Acoustical Imaging

Volume 28

Acoustical Imaging

Recent Volumes in This Series:

Volume 10	Proceedings of the Tenth International Symposium October 12–16, 1980, edited by Pierre Alais and Alexander F. Metherell
Volume 11	Proceedings of the Eleventh International Symposium May 4–7, 1981, edited by John P. Powers
Volume 12	Proceedings of the Twelfth International Symposium July 19–22, 1982, edited by Eric A. Ash and C. R. Hill
Volume 13	Proceedings of the Thirteenth International Symposium October 26–28, 1983, edited by M. Kavch, R. K. Mueller, and J. F. Greenleaf
Volume 14	Proceedings of the Fourteenth International Symposium April 22–25, 1985, edited by A. J. Berkhout, J. Ridder, and L. F. van der Wal
Volume 15	Proceedings of the Fifteenth International Symposium July 14–16, 1986, edited by Hugh W. Jones
Volume 16	Proceedings of the Sixteenth International Symposium June 10–12, 1987, edited by Lawrence W. Kessler
Volume 17	Proceedings of the Seventeenth International Symposium May 31–June 2, 1988, edited by Hiroshi Shimizu, Noriyoshi Chubachi, and Jun-ichi Kusibiki
Volume 18	Proceedings of the Eighteenth International Symposium September 18–20, 1989, edited by Hua Lee and Glen Wade
Volume 19	Proceedings of the Nineteenth International Symposium April 3–5, 1991, edited by Helmut Ermert and Hans-Peter Harjes
Volume 20	Proceedings of the Twentieth International Symposium September 12–14, 1992, edited by Yu Wei and Benli Gu
Volume 21	Proceedings of the Twenty-First International Symposium March 28–30, 1994, edited by Joie Pierce Jones
Volume 22	Proceedings of the Twenty-Second International Symposium September 3–7, 1995, edited by Piero Tortoli and Leonardo Masotti
Volume 23	Proceedings of the Twenty-Third International Symposium April 13–16, 1997, edited by Sidney Lees and Leonard A. Ferrari
Volume 24	Proceedings of the Twenty-Fourth International Symposium September 23–25, 1998, edited by Hua Lee
Volume 25	Proceedings of the Twenty-Fifth International Symposium March 19–22, 2000, edited by Michael Halliwel and Peter N. T. Wells
Volume 26	Proceedings of the Twenty-Sixth International Symposium September 9–12, 2001, edited by Roman Gr. Maev
Volume 27	Proceedings of the Twenty-Seventh International Symposium March 24–27, 2003, edited by W. Arnold and S. Hirsekorn
Volume 28	Proceedings of the Twenty-Eighth International Symposium March 20–23, 2005, edited by Michael P. André

Volume 28

Edited by

Michael P. André

University of California and San Diego Veterans Affairs Healthcare System, San Diego, California, USA

Springer

A C.I.P. Catalogue record for this book is available from the Library of Congress.

ISBN-10 1-4020-5720-2 (HB)
ISBN-13 978-1-4020-5720-5 (HB)
ISBN-10 1-4020-5721-0 (e-book)
ISBN-13 978-1-4020-5721-2 (e-book)

Published by Springer,
P.O. Box 17, 3300 AA Dordrecht, The Netherlands.

www.springer.com

Printed on acid-free paper

28th International Acoustical Imaging Symposium

Chairman: Michael P. André

International Advisory Board

Iwaki Akiyama, Japan
Michael Andre, USA
Walter Arnold, Germany
Jeff Bamber, United Kingdom
Valentin Burov, Russia
Noriyoshi Chubachi, Japan
Kenneth Erikson, USA
Helmut Ermert, Germany
Mathias Fink, France
Woon S. Gan, Singapore
Bernd Granz, Germany
James Greenleaf, USA
Jiankai Hu, China
Joie P. Jones, USA
Pierre Khuri-Yakub, USA
Pascal Laugier, France
Hua Lee, USA
Sidney Lees, USA
Vadim M. Levin, Russia
Roman Maev, Canada
Leonardo Masotti, Italy
Andrzej Nowicki, Poland
William O'Brien, Jr., USA
Manika Prasad, USA
Patrick Rafter, USA
Daniel Rouseff, USA
Johan Thijssen, Belgium
Bernard Tittmann, USA
Piero Tortoli, Italy
Anton Van der Steen, The Netherlands
Robert Waag, USA
Peter Wells, United Kingdom

Contents

Acknowledgements

By its nature any list of acknowledgements will be incomplete. Nonetheless, I wish to express my sincere gratitude to the following wonderful people who for many years have offered wise counsel, good friendship and fine spirits. Without their support Acoustical Imaging 28 would not have been possible: Roman Maev, Ph.D., James Greenleaf, Ph.D., William O'Brien, Jr., Ph.D., Walter Arnold, Ph.D., Kenneth Erikson, Ph.D., Manika Prasad, Ph.D., Joie Jones, Ph.D., Piero Tortoli, Ph.D., Hua Lee, Ph.D., and most especially, Janice André, M.A.

Preface

The International Acoustical Imaging Symposium has been held continuously since 1968 as a unique forum for advanced research in all areas of acoustical imaging. The interdisciplinary nature of the Symposium and the wide international participation are two of its main strengths. Scientists from around the world present papers in all fields of acoustical imaging in an informal environment conducive to lively discussion and cross-fertilization.

Acoustical Imaging remains the unique Symposium in the world that promotes the sharing of technology, developments, methods and theory among all areas of acoustics. The fact that a loyal community of scientists has supported this Series since 1968 is evidence of its impact on the field. The Symposium Series continues to thrive in a busy calendar of scientific meetings without the infrastructure of a professional society. It does so because those who attend and those who rely on the Proceedings as a well-known reference work acknowledge its value.

The 28th International Acoustical Imaging Symposium was held in San Diego, California USA during March 20–23, 2005. Volume 28 of the Proceedings contains an excellent collection of papers presented in six major categories:

- Acoustic Microscopy
- Components and Systems
- Computed Tomography
- Biological and Medical Applications
- Non-Destructive Evaluation
- Physics and Mathematics

As it has for nearly 40 years, this volume of *Acoustical Imaging* offers both a broad perspective on the state of the art in the field as well as an in-depth look at its leading edge research. It is my privilege to be able to offer this collection and I express my sincere thanks to the contributing authors for continuing to make this series a success.

The 29th International Acoustical Imaging Symposium will be held April 16–18, 2007 in Kamakura, Japan.

Michael P. André

ACOUSTIC MICROSCOPY

AIR-COUPLED IMAGING METHOD APPLIED TO THE STUDY AND CONSERVATION OF PAINTINGS

A.M. Siddiolo, A. Maeva, R.Gr. Maev
Dipartimento di Meccanica, University of Palermo, Viale delle Scienze, 90128 Palermo, Italy; Centre for Imaging Research and Advanced Materials Characterization, University of Windsor, 401 Sunset Str., Ontario, N9B 3P4, Canada

Abstract: An air-coupled acoustical imaging method for the study of wooden panel paintings is presented. After a brief overview of the state of the art, an introduction is given regarding the production technique of the art object under investigation. The technology employed is described in detail, as well as the proposed method. After a feasibility campaign of experiments, real ancient paintings have been investigated by means of a through-transmission and a single-sided lay-out. Defects were imaged in all the objects examined and in both the configurations adopted

Key words: Air-coupled; acoustical imaging; wooden painting

1. INTRODUCTION

In the last decade, an increasing interest in the cultural heritage has been registered[1]. Art works are now considered as a personal cultural patrimony; nevertheless they are endangered more than ever and it is necessary to continuously check the artwork's state of conservation. Ultrasound techniques, borrowed from other fields or developed ad hoc, can make a strong contribution to the safeguarding and exploitation of cultural heritage[2].

In this work, attention is focused on wooden panel paintings. In most cases today, the standard procedures to find defects are visual and manual. These methods rely completely on the skill and experience of the operator and do not provide quantitative results. Recently developed techniques applied to the art work study are: infrared thermography, radiography, holography[3], electro-optic

M.P. André (ed.), Acoustical Imaging, 3–12.

holography[4] and the Scanning Laser Doppler Vibrometer[5]. Defects are not always detectable; radiography, for instance, cannot reveal delaminations parallel to the painting surface. The used apparatus often involves high cost and some techniques have stability requirements that are different to realize in *in situ* applications.

Before going further, it is necessary to proper understand the object of the present investigation. A wooden panel painting can be thought as a layered structure with a support; the last one provides a base for the paint. After a first thin layer of animal glue, the wood support is coated with a number of superimposed priming layers (called "ground") made by mixtures of gesso and glue. After these operations, the design layers usually include: a preparatory design, the paint layer, the varnish, and any retouching[6]. The layers of this structure are characterized by different rigidity and thickness. In time, the ground becomes more and more fragile, loosing its former elasticity. Hence, it cannot follow the deformations of the wood support any more: detachments between layers and cracks appear and propagate through and under the painting surface.

2. AIR-COUPLED TECHNIQUE

In this study an air-coupled ultrasonic technique is employed. Many researchers have performed NDEs on works of art by means of contact ultrasound. Only a single work is reported in literature in which wooden paintings are investigated in a non-contact fashion by the use of ultrasound[7]. The results of those investigations were really promising, even if the available technology was characterized by lower performances than what nowadays researchers dispose.

By using air as coupling medium - in order to avoid contaminations and damages of the object to be tested - several problems must be overcome in setting-up a feasible measurement technique; first of all the enormous acoustical mismatch between air and the materials involved. Other problems arise if we consider the high attenuative nature of wood. In the past decades, many ways to overcome these problems have been tried; now the technology is ready and a lot of air-coupled applications are found in literature[8–10].

The ultrasonic pulser-receiver instrument "NCA1000-2E" (Ultran Laboratories) is implemented into the measurement system. This device can work in non-contact, contact and immersion modality. It is characterized by a total dynamic range up to 150 dB and by a time resolution of about 1 ns; it can operate between 50 kHz and 5 MHz. The pulse compression technique[11] is implemented into the system, in order to extend the detection range for a given peak-power, and still have a good time resolution.

Three couples of last generation piezoelectric transducers have been utilized (Ultran Laboratories), whose manufacturing codes and characteristics are here summarized (f_c = Center Frequency; B = Bandwidth; D = Active Diameter):

- T#1: Code NCT-102. Characteristics: f_c=221 kHz, B=78 kHz, D=25 mm;
- T#2: Code NCT-55. Characteristics: f_c=485 kHz, B=148 kHz, D=12.5 mm;
- T#3: Code NCT-510. Characteristics: f_c=910 kHz, B=290 kHz, D=12.5 mm.

Beam field and lateral resolution were measured for each couple of transducers, confirming the good element properties. The lateral resolution has been determined, providing the following values: 15.2 mm for T#1; 4.6 mm for T#2; 3.6 mm for T#3.

Two different types of ultrasonic configurations were employed: a through-transmission configuration (TTC) and a single-sided configuration (SSC). The commercial scanning system used to control the position of the non-contact transducers is the "Techno Stepper DaVinci"; this device is characterized by a 10 μm resolution and repeatability of positioning.

In TTC, the transducer on the back of the painting generates ultrasound and the other one receives it. A precise period in time of the received signal is stored and analyzed by the system; it corresponds to the first perturbation arriving to the receiving transducer located on the painted side of the wooden panel. The gated wave packet is processed and some parameters are measured. Besides ToF, the system measures a quantity usually named Integrated Response (InR). It corresponds to the area underneath a definite time interval of the compressed pulse; therefore, it is a quantity related to the energy of the received ultrasound. Whenever sound encounters discontinuities during its path, such as air pockets, the perturbation cannot penetrate, or the measured InR becomes smaller than what it is possible to measure in a sound region. InR value can then be interpreted to deduce properties and conditions of the painting.

In SSC, both transducers are placed on one side of the model. This configuration was adopted not only to test the feasibility of a more comfortable lay-out, but also to properly face situation in which the back painting is not thoroughly accessible or the wooden painting thickness is highly variable. Dealing with a really complicated structure, no theoretical data (i.e. dispersion curves) were available to set-up the proper geometrical layout. After some experiments, it was possible to find out suitable angles for each layered structure. The generated waves were mixed vibration modes: angles vary with thickness, material and frequency. Due to the highly orthotropic nature of wood, the geometrical set-up was good as long as the fiber direction remained almost unaltered. The generated guided waves allowed us to properly detect the presence of a delamination in almost all the models tested, as well as in the real paintings examined.

3. EXPERIMENTAL RESULTS AND DISCUSSION

In order to check the capabilities of the air-coupled ultrasound technique, samples were made to mimic panel paintings and the typical occurrence of defects. These models were prepared using the same techniques and materials that were common in paintings since the twelfth and thirteenth centuries[6]. They were realized using different supports [red oak (ROK); maple (MPL) and hemlock (HML)] and thickness of the ground. Several kinds of defects have been simulated: cracks in the wood support; cracks in the ground; detachments of different shape and location between the animal glue layer and the preparation made by gesso and animal glue; high curvature of the panel (See Table 1).

Ultrasound data are displayed by using two-dimensional representations known as C-scans. These images were contrast enhanced by means of an algorithm originally developed by the authors to analyze fringe pattern images[12]. In fact, due to the really weak signal we are dealing with, the signal to noise ratio is critical; C-scans present noise and corrupted regions that can be profitably enhanced by the use of this algorithm. Simple median filtering operations do not lead to the same good result, since the corrupted regions are often characterized by great extension.

Table 1. Samples characteristics.

ID code	Detachment	Wood crack	Ground crack	Curvature [mm]	
ROK01		Sound sample		1140	Medium Curvature
ROK02	Rectangle		Present	∞	Flat
ROK03	Strip		Present	∞	Flat
ROK04		Present		∞	Flat
ROK05		Sound sample		450	High Curvature
ROK06	Strip		Present	1660	Almost flat
ROK07	Rectangle			1820	Almost flat
ROK08	Rectangle		Present	1270	Medium Curvature
MPL01	Rectangle			850	High Curvature
MPL02		Present		1350	Medium Curvature
MPL03	Strip			1130	Medium Curvature
MPL04	Rectangle			2100	Almost flat
HML01	Rectangle		Present	1890	Almost flat
HML02	X strip		Present	2100	Almost flat
HML03		Sound sample		1950	Almost flat

The prepared models were analyzed in TTC and SSC, by means of the piezoelectric transducers above mentioned, both in painted and not painted configuration. The scan-step was set equal to 1.27 mm. The monitored parameter was the InR of the first peak in TTC, and the InR of the fastest

guided wave in SSC. The performed scans are shown as gray images, from the smaller InR value (black) to the bigger one (white). The checked region for each sample was an inset of the real model dimensions, in order to avoid border distortions of the measured pressure field; as a consequence, the border gray region of each scan defines the real dimensions of the wooden panel. The black segment in the upper left corner indicates the diameter of the used transducer in TTC, and the wave path length and direction in the sample in SSC. By using white lines, cracks in the ground and the wood support are shown; while, by using black ones, borders of simulated delaminations inside the model are pointed out.

In what follows, results regarding three models that present almost all the simulated defects are discussed: a ROK support with a rectangular delamination and cracks in the ground (#02); a MAP support having medium curvature with a strip delamination (#03); a HML support, almost flat but thick, with a crossed strip delamination and cracks in the ground (#02).

For each model, four scans are shown: two regarding TTC (T#1 and T#3) and two regarding SSC (T#1 and T#2). Delaminations were imaged both in TTC and in SSC in all the fifteen samples examined. It was not possible to generate useful guided waves by using T#3; guided waves generated by means of this high frequency involved just the ground layer, since they were not influenced by the presence or absence of a delamination between the ground and the wood support. Nevertheless, they were fruitfully used in detecting crack in the ground; wood and ground cracks were, in fact, more easily detected in SSC than in TTC, since they were sometimes oriented perpendicularly to the guided wave path and their extension was also perpendicular to the sample surface. By using T#1 in TTC, delaminations were easily detected. If there is no flaw, ultrasound energy can penetrate the layered structure without any problem. On the other hand, ultrasound is stopped, if an air gap is encountered during the path (Fig. 1.a-column). By using this frequency, model orientations even considerably different from the ideal condition normal to the beam axis do not lead to ambiguous C-scans. The scans of Fig. 1 (HML02-a/b) were performed by using just one fifth of the maximum power and, even if the model thickness was relevant (20.3 mm), the detached zones were perfectly located. The only drawback is the limited lateral resolution (about 15 mm); this is an inherent transducer feature due to the dimensions of the radiating surface (25 mm). This drawback is overcome by using T#3. The better lateral resolution (about 3.6 mm) allows a precise definition of the delaminated region (Fig. 1.b-column). This pro is however alleviated by the critical behavior when the model surface is not perfectly perpendicular to the beam field propagation axis and when the wooden panel painting thickness becomes greater in value (Fig. 1.b-HML). T#2 has an intermediate behavior. It was not possible, in through-transmission,

to detect the presence of ground or wood cracks; nevertheless, the detection of these defects is feasible by using focused transducers.

By using SSC, the uncomfortable necessity of reaching both sides of the wooden painting is overcome; on the other hand, the ultrasonic layout becomes more and more critical. The guided wave generation requires a fine positioning of both transducers, which must be rotated of the same angle with respect to the model surface normal (See Table 2); angle variations within one degree could cause no formation of the vibration mode. Hence, care has to be given to the interpretation of high-curvature panel C-scan. Besides, angles are not a priori known and computer simulations do not seem to help much to this purpose. Then, there is the need of proper calibration operations, in order to create a sort of database to allow real applications of the presented technique.

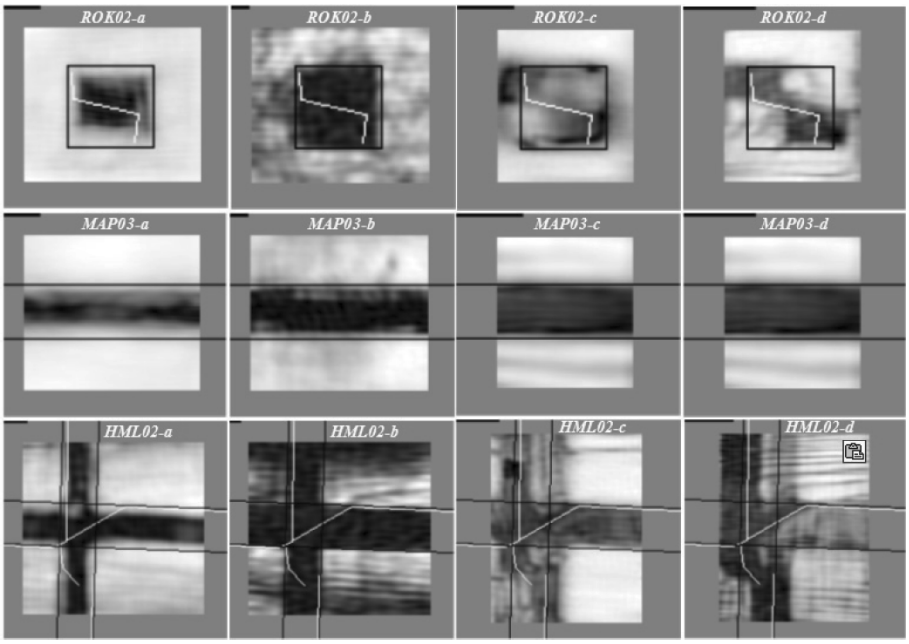

Figure 1. Feasibility analysis. a–b: TTC (200 and 1000 kHz); c–d: SSC (200 and 500 kHz).

An inherent drawback of the SSC is the limited resolution. Each measured point of the scan is a linear integration from the generating to the receiver transducer. The distance between transducers was reduced until it was possible to unambiguously gate in time the selected wave packet. Actually, it is possible to block the propagation of disturbing waves by interposing a suitable barrier between transducers and increasing, as a consequence, image resolution. A relevant pro of this set-up is its capability

to verify the presence of cracks perpendicularly disposed with respect to the direction of wave propagation (Fig. 1.c–d, related to ROK and HML).

Table 2. Angles of rotation to generate guided waves.

	200 kHz		500 kHz	
	Angle [degrees]	Path [mm]	Angle [degrees]	Path [mm]
Oak (thick=7.9 mm)	18º	39.3	16º	49.5
Maple (thick=7.5 mm)	19º	44.9	17º	48.7
Hemlock (thick=20.0 mm)	19º	44.9	17º	52

Finally, investigations on four real ancient paintings were performed. The four wooden paintings came from a private collection and two of them were almost four hundred years old. Results about the two older paintings are here presented and discussed (Fig. 2.a and b).

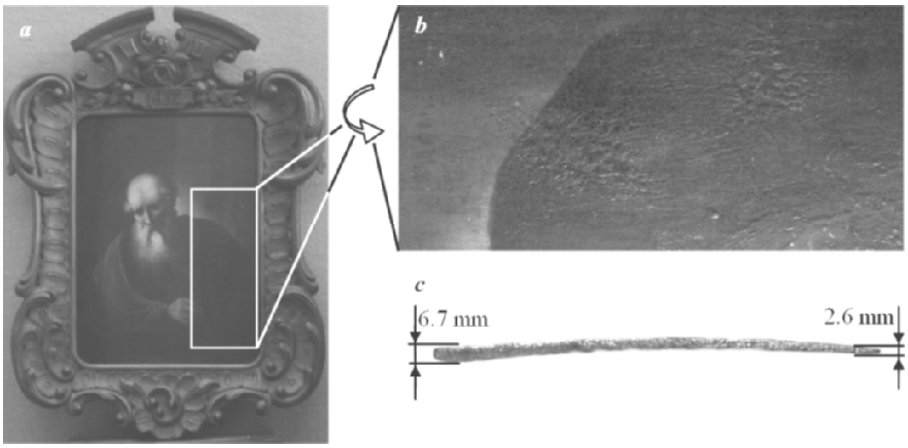

Figure 2. a) Wooden painting; b) Particular of the defective region; c) Variable thickness.

The first painting (187x263 mm^2) presented a highly variable thickness (Fig. 2.c) and the lower right region of it showed a system of bubbles that let us foresee the presence of some detachments in the inner region (Fig. 2.b). Investigations of the painting in TTC by using T#1 seemed to confute this idea; just the variable thickness was recorded during this scan and no clear defect was imaged (Fig. 3.a).

The following scans performed by using T#2 and T#3 revealed, at different resolution, the presence of low transmission regions, due to the existence of some discontinuity in the ultrasound path (Fig. 3.b and c). Observing these scans, it is easy to visually locate probable defective regions (darker ones), even if in T#2 data, the resolution is not good enough.

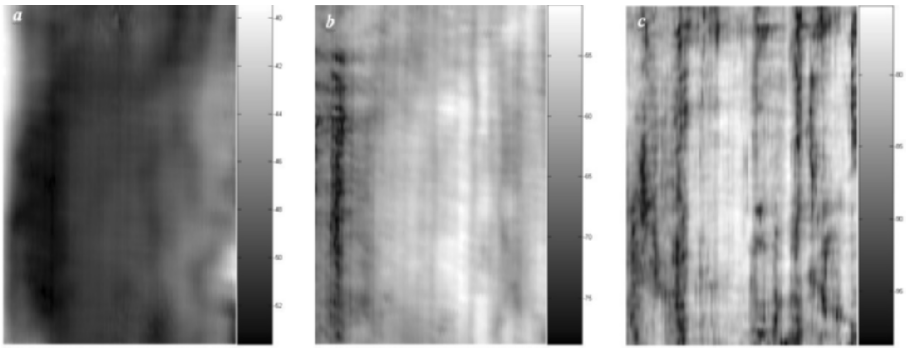

Figure 3. TTC results. a) f=200 kHz; b) f=500 kHz; c) f=1000 kHz.

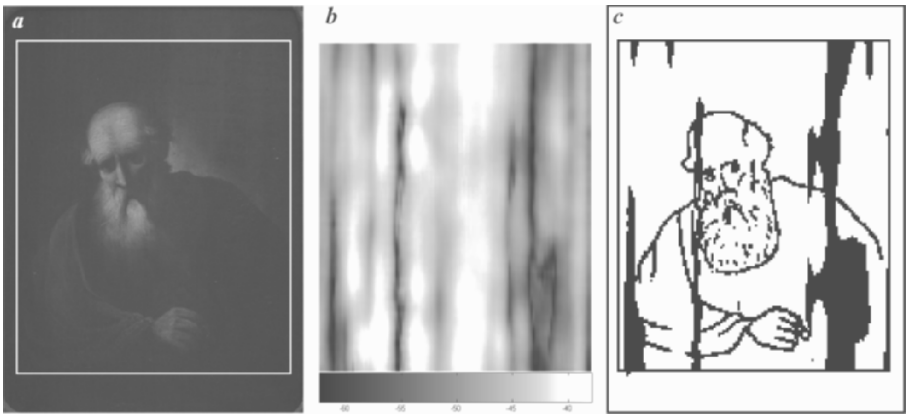

Figure 4. SSC results. a) Wooden painting; b) Scan; c) Summarizing binary image.

Further analyses in SSC by using T#1 definitely established the defective nature of the regions above highlighted, confirming the results provided by the TTC scans. In a pretty clear fashion, the defective regions are imaged in Fig. 4.b. The wooden painting (Fig. 4.a) is shown on the left; the scan in the middle (Fig. 4.b) and a binary image on the right (Fig. 4.c). This last image was created by thresholding the scan performed in SSC (the black regions are the localized detached ones) and superimposing on it a symbolic representation of the subject of the painting.

The second painting (183x263 mm^2) did not show any visible defect. As the first painting, it presented a highly variable thickness (Fig. 5.a and b). Investigations of the painting in TTC by using T#1, T#2 and T#3 allowed us to detect – with different resolution – the presence of detachments in the inner structure of the panel painting. Further analyses in SSC by using T#1

confirmed the results obtained in TTC. The experimental results of this investigation are shown in Fig. 6: the wooden painting is displayed on the left (Fig. 6.a); the scan in the middle (Fig. 6.b) and the usual binary image on the right (Fig. 6.c).

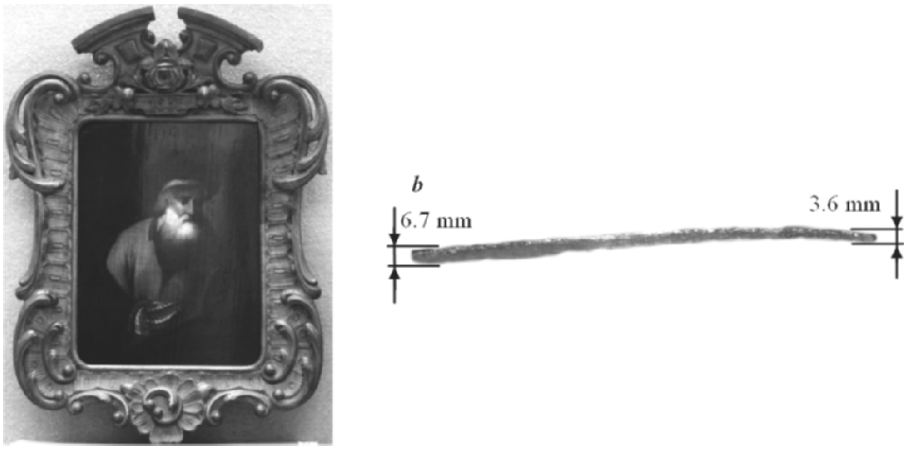

Figure 5. a) Wooden painting; b) Variable thickness.

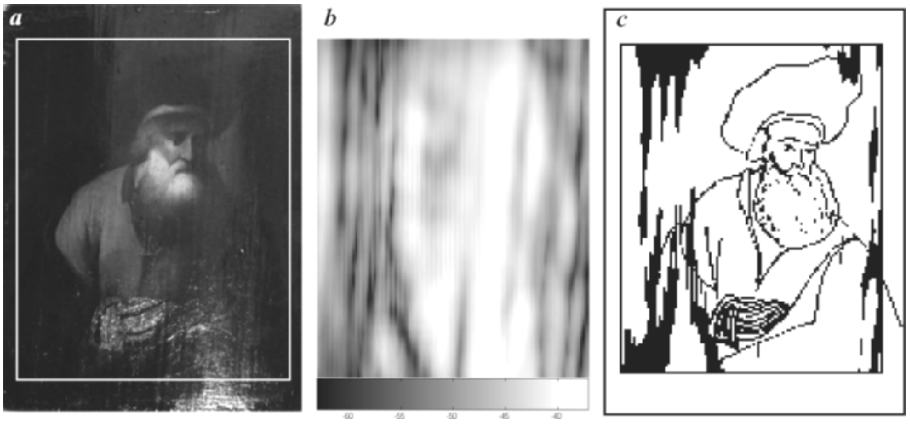

Figure 6. SSC results. a) Wooden painting; b) Scan; c) Summarizing binary image.

4. CONCLUSIONS

An air-coupled technique applied to the study and conservation of wooden panel paintings has been presented. The method is described in detail, as well as the technology employed and the techniques adopted to overcome

the absence of a coupling medium between transducers and object of investigation. In order to check the capabilities of the technique, several models were made to mimic wooden panel paintings and the typical occurrence of defects, such as delaminations between the ground and the wood support and cracks in the ground itself. Almost all the simulated defects were clearly located in through-transmission and single-sided configuration. Four ancient paintings were afterwards checked to establish their state of conservation. Results regarding two of them (four hundred years old paintings coming from a private collection) have been here presented and commented.

REFERENCES

1. UNESCO Our Creative Diversity: Report of the World Commission on Culture and Development (Paris: UNESCO Publishing), (1995)
2. Maev R.Gr., Green R.E. Jr., Siddiolo A.M., "Advanced acoustical imaging techniques for non-destructive evaluation of art-objects – Review" and Siddiolo A.M., Grube O., Maeva A., D'Acquisto L., Maev R.Gr., "Air-coupled acoustical imaging NDE for art object study", "ART'05", Lecce (Italy), (2005)
3. Amadesi S., Gori F., Guattari G., Grella R., Holographic methods for painting diagnostics, Appl. Opt. 13, 2009–2013, (1974)
4. Schirripa Spagnolo G., Ambrosini D., Guattari G., Electro-optic holography system and digital image processing for in situ analysis of microclimate variation on artworks, J. Opt. 28, 99–106, (1997)
5. Castellini P., Paone N., Tomasini E.P., The laser Doppler Vibrometer as an instrument for non intrusive diagnostic of works of art: application to fresco paintings, Optics Lasers Eng. 25, 227–246, (1996)
6. Cennino d'Andra Cennini, Il libro dell'arte (The Craftsman's Handbook), (1437)
7. Murray A., Boltz E.S., Renken M.C., Fortunko C.M., Mecklenburg M.F., Green R.E. Jr., Air-coupled ultrasonic system for detecting delaminations and cracks in paintings on wooden panels, Nondestructive characterization of materials 6, ed. Green R.E. Jr., New York: Plenum Press. 103–10, (1994)
8. McIntyre C.S., Hutchins D.A., Billson D.R., Stor-Pellinen J., The Use of Air-Coupled Ultrasound to Test Paper, IEEE Trans. Ultras. Ferr. Freq. Contr. 48, 717–727, (2001)
9. Cinquin M., Castaings M., Hosten B., Brassier P., Pérès P., Monitoring of the moisture content in carbon-epoxy plates using Lamb waves, NDT & E International 38, 37–44, (2005)
10. Robertson T.J., Hutchins D.A., Billson D.R., Rakels J.H., Schindel D.W., Surface metrology using reflected ultrasonic signals in air, Ultrasonics 39, 479–486, (2002)
11. Furgason E.S., Newhouse V.L., Bilgutay N.M., Cooper G.R., Application of random signal correlation techniques to ultrasonic flaw detection, Ultrasonics 13, 11–7, (1975)
12. D'Acquisto L., Siddiolo A.M, "A novel bi-dimensional Fourier transform method to surface measurement by shadow moiré", 12th International Conference on Experimental Mechanics, Bari (Italy), (2004)

STUDY OF BIOMEDICAL SPECIMENS USING SCANNING ACOUSTIC MICROSCOPY

D. Doroski, B.R. Tittmann, C. Miyasaka
The Pennsylvania State University, University Park, PA, 16802

Abstract: Microscopy is a paramount part of science and the medical field. The optical microscope (OM), scanning electron microscope (SEM), and atomic force microscope (AFM) are commonly used for the imaging of biomedical cells and tissues. Unfortunately, these conventional micro–scopes have major disadvantages. The atomic force microscope is still underdeveloped in imaging of living biomedical specimens. The OM and SEM require dead specimens for imaging, and cannot image the subsurface of thick specimens. Development of the scanning acoustic microscope (SAM) is a solution to these problems. The SAM has the ability to image living specimens for extended periods of time without harming them, can image the subsurface of the sample, can image thick specimens, and can obtain information about mechanical properties of the specimen. In this study images of esophagus tissue were obtained using an OM, SEM, and SAM. While OM and SEM have been established as valuable tools for imaging of biological tissue samples not much basic imaging of histological structures of biological specimens has been done using the SAM. The goal was to create an imaging baseline for the SAM that showed that it could function at the level of the OM and the SEM. When imaging the tissues, all three of the microscopes yielded similar images

Key words: acoustic microscopy, scanning electron microscopy, laser scanning confocal optical microscopy, esophagus

M.P. André (ed.), Acoustical Imaging, 13–20.

1. INTRODUCTION

Microscopy holds an integral place in modern science. Microscopy is medically useful in diagnosing patients and conducting research for new cures. For these uses the imaging of human cells and tissues is paramount. Ideally the imaging would be done quickly and non-invasively without need to take a tissue sample from the patient. Many medical diagnoses are conducted by taking a tissue sample from the patient. Unfortunately if the patient's problem is not localized in the area of an organ where the tissue sample was taken, a negative diagnosis could result while a problem actually exists. With conventional microscopes this problem can not be remedied without taking tissue samples in multiple areas of the organ. Such a solution is not always feasible. Since the SAM can penetrate below the surface of a specimen and does not kill the specimens that it images, SAM may be adapted for imaging of multiple areas of an organ. It may be possible to create a SAM whose sensors would be on the tip of an endoscope and would allow detailed and useful microscopic imaging of internal organs and tissues. This SAM function would allow a more accurate diagnosis of many ailments.

2. MICROSCOPES COMMONLY USED FOR IMAGING OF BIOMEDICAL SPECIMENS

2.1 Optical Microscope (OM)

The OM is a microscope that is often used in biological studies. The most commonly used OM in this study was the laser scanning confocal optical microscope (LSCOM). The LSCOM has the ability to focus on the surface of the specimen or on some point below the surface that is inside as long as the specimen is sufficiently thin. This allows it to focus on multiple vertical planes. By focusing on different vertical planes the LSCOM can image a thin slice of the specimen. The LSCOM can take multiple distinct thin slices in the vertical direction and combine these images into one cohesive image that gives an overall shape of the specimen[1]. The slices can be less than a micron (10^{-6} m) apart which provides the possibility of relatively detailed images. In addition to being able to give an overall picture of the specimen the LSCOM's ability to focus in distinct vertical planes allows it image the inside of the specimen. To prepare a specimen for imaging with an OM it must first be cut into very thin sections (5–10 μm)[1].

This process involves many steps and therefore can take multiple days. The OM requires thin specimens because thin specimens are more transparent than thick ones. The OM requires transparency for imaging because it shines light through the specimen and the light can only be transmitted if the specimen is transparent. This need for meticulous preparation limits the usefulness of OM since the preparation is costly in terms of time and also requires the slicing of tissue that can be invasive.

2.2 Scanning Electron Microscope (SEM)

Figure 1. Schematic Diagram of the SEM (Model: JOEL, JSM 5400) used in this study.

The SEM can image the surface of a specimen with great resolution and at a high magnification[2] (Figure 1). Unlike the SAM, the SEM does not have the ability to obtain images below the specimen's surface. When a tissue or cell is prepared for the conventional vacuum chamber SEM, it goes through a process that includes cutting of the tissue or cell. This cutting often cleaves the cell leaving the inside exposed. The SEM also requires a conductive sample for imaging purposes. Non-conductive biological samples must be coated with a 10 nm thick gold-palladium coating to facilitate imaging. Once the specimen is prepared it is inserted into a chamber attached to the SEM. This chamber is evacuated to create a vacuum inside. The cutting of the specimen, the gold-palladium coating, and the vacuum created in the SEM chamber results in the death of the tissues or cells. As a result the SEM's effectiveness in visualizing living specimens is non-existent.

2.3 Summary

These conventional microscopes that are used to image cells and tissues often must kill the specimens to successfully image them. In the cases when the microscopes can image living specimens the limitations of the imaging can be problematic. Therefore, it is desirable to have a microscope that allows imaging of living specimens without the limitations of the conventional microscopes. The SAM has been shown to have the ability to image living tissue and cells without killing them[3]. Additionally, SAM can image living specimens without the drawbacks that accompany imaging using conventional microscopes. However, the SAM is still a relatively new microscopy technique and therefore experiments to image living biological samples using SAM should be continued.

3. ESOPHAGUS IMAGING STUDY

Unlike the OM, SEM, or, AFM, the SAM has the ability to image relatively thick biological specimens while also penetrating to image the interior of the specimens. The pictures below offer a comparison of images that have been obtained with an optical microscope, a SEM, and the SAM under similar conditions (Figures 2 and 3). The images are of tissues of esophagus using the OM, SEM, and SAM. The SAM is the only microscope that images the subsurface of the specimens[3].

3.1 Image obtained by Optical Microscope

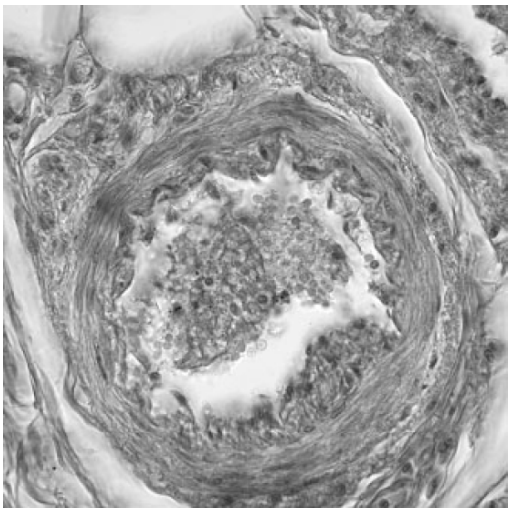

Figure 2. Esophagus, Thickness: 10 µm, Magnification: 400x.

3.2 Image obtained by Scanning Electron Microscope

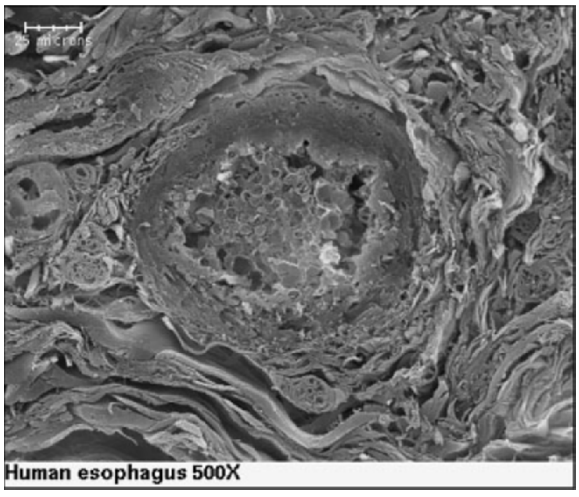

Figure 3. Esophagus, Thickness: 3 µm, Magnification 500x.

3.3 Images obtained using SAM

In the SAM image seen below the focal position of the lens is at the surface of the specimen (z = 0 µm) (Figure 4). The frequency used for this image is 200 MHz.

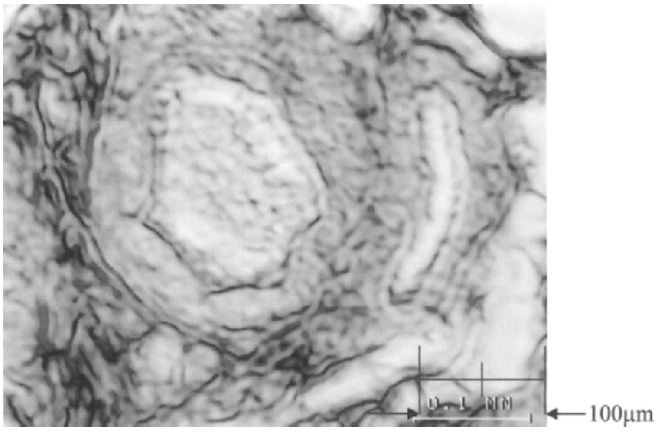

Figure 4. Esophagus, Thickness: 10 µm.

In the SAM image below the focal position of the lens is at the subsurface of the specimen (z < 0) (Figure 5). The frequency used for this image is 200 MHz.

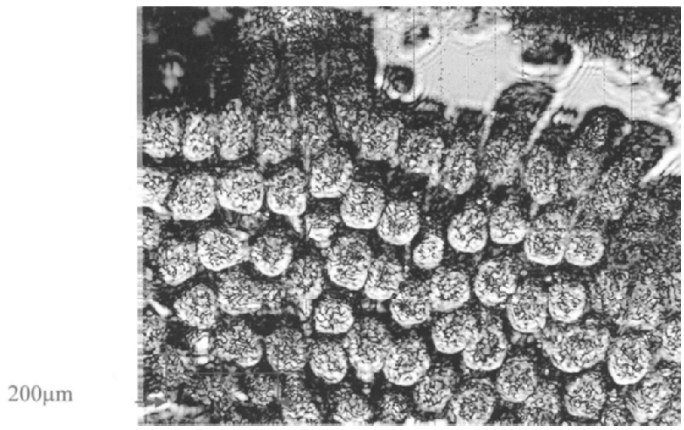

Figure 5. Esophagus, Thickness: 150 µm, Focal Position: (z = -20 µm).

These esophagus images show the great ability of the SAM. Similar specimens were imaged using the OM, the SEM, and the SAM. The first

two SAM images are very comparable to the OM and SEM images. In this instance the SAM is shown to have a very similar ability to image specimens as more conventional microscopes. Similar amounts of surface detail are shown in the images at similar tissue thicknesses.

In the second set of SAM pictures the tissues are much thicker, and the SAM is imaging the subsurface of the specimen with a similar amount of detail as was shown in imaging the specimen surface. The SEM does have the ability to image such thick specimens and in this way is comparable to the SAM. However the SEM does not have any ability to image the subsurface of the specimen as the SAM has been shown to be able to. The OM in this case can neither image specimens of the thickness that the SAM has the ability to image, nor can it penetrate into the subsurface as the SAM can.

4. RESULTS

The pictures that were obtained using the SAM did not have as high resolution as those obtained using the LSCOM and the SEM. However the SAM was still able to obtain meaningful images of the tissues being imaged. All three microscopes were able to obtain images of esophagus tissue to similar degree of resolution and contrast.

The relative preparation time in this experiment was similar with all of the microscopes. Extra time was required by the SEM to create a conductive gold-palladium coating on the specimens in order to make imaging possible. The staining of the specimens was an extra step that was required only by the LSCOM. The SAM required neither the conductive coating nor the staining process. In addition the LSM required thin specimens (~5 μm) for in order to form an image. The SAM and the SEM were able to image thicker tissues and thus made it easier to prepare specimens.

Preparation of the specimens was increased using the LSCOM and the SEM, but the actual imaging of the specimens was most time consuming when using the SAM. With the LSCOM and the SEM movement of the lens was quick and real-time imaging was possible. This enabled quick scanning of a large area. Thus, areas with interesting features could be found rather quickly. The scanning of the SAM was much slower and scanning a large area was thus more tedious. When actually obtaining and saving images, a similar amount of time was required by all of the microscopes.

5. CONCLUSIONS

SAM is a viable alternative to the OM and the SEM in the imaging of biological specimens in order to distinguish relevant cellular structures. While the resolution of the SAM was not as good as those of the OM and the SEM, the SAM was still able to image the relevant structures imaged by the OM and the SEM.

The preparation time required for the SAM was minimal compared to the OM and the SEM. The preparation time required for the OM and the SEM was similar. The conductive layer required by the SEM and the staining required by the OM are fatal to living specimens so SAM is the only viable method of the three for imaging of living specimens. In fact when using the SAM cutting may not be needed at all. The SAM has been shown to have the ability to penetrate specimens (~ 30 μm below the surface) so subsurface imaging need not require an incision. When using the SAM for imaging preparation of the specimen is minimal.

The OM and the SEM were faster in scanning of the specimens than the SAM. The SAM would be greatly improved with an upgrade in the speed of scanning specimens. Overall the SAM was comparable in ability and ease of obtaining relevant images of the esophagus tissue.

REFERENCES

1. Bradbury and Savile. *The optical microscope in biology*, London: Edward Arnold, 1976.
2. Hearle, J.W., Sparrow, J.T., and Cross, P.M., *The Use of the Scanning Electron Microscope*, New York: Pergamon Press, 1972.
3. Tittmann, B.R., and Miyasaka C., (2003), Imaging and Quantitative Data Acquisition of Biological Cells and Soft Tissues with Scanning Acoustic Microscopy. In *Science, Technology and Education of Microscopy: An Overview,* Edited by A. Méndez-Vilas, pp. 325–344. Formatex: Badajoz, Spain.

IMAGE PROCESSING OF ACOUSTIC MICROSCOPY DATA TO ESTIMATE TEXTURAL SCALES AND ANISTROPY IN SHALES

T. Mukerji, M. Prasad
Stanford University; Colorado School of Mines

Abstract: We estimate different statistical measures for quantifying heterogeneity and textures from scanning acoustic microscope images of shale microstructures. The analyzed shales covered a range of depths, kerogen content, and maturity. We observed quantifiable and consistent patterns linking texture, shale maturity, and elastic P-wave impedance. The textural heterogeneity and P-wave impedance and velocity, and density increase with increasing maturity (decreasing kerogen content), while there is a general decrease in textural anisotropy with maturity. We also found a reasonably good match between elastic impedance estimated from SAM images and impedance computed from ultrasonic measurements. The textural anisotropy ranges from 10% to about 70% and tends to decrease with increasing depth and maturity

Key words: Kerogen shales, acoustic microscopy, Image processing, Fourier transform

1. INTRODUCTION

Microgeometry plays an important role in the overall effective elastic properties of shales. Therefore characterizing and understanding the microgeometry, their textures, scales, and textural anisotropy is important for better understanding the effect of microgeometry on effective elastic properties. Microstructural characteristics of organic rich shales can give important insights on the maturation processes and on oil generation from such formations (Vernik and Nur, 1994). Optical and scanning electron

M.P. André (ed.), Acoustical Imaging, 21–29.

microscopy methods to analyze kerogen shale microstructure have been utilized in the past. However, due to the opaque nature of the kerogen and the associated pyrite, such methods are rather difficult to implement. For example, studies have shown that microgeometry, textural heterogeneity, and textural anisotropy have significant effects on the effective elastic properties of rocks. On the other hand, Prasad et al. (2002) have shown we can map textural changes with shale maturity with acoustic microscopy.

2. METHODS

The acoustic images were made with an acoustic microscope and image analyses techniques are used to detect changes in texture and heterogeneity in these images.

2.1 Acoustic Microscopy

We used a non-destructive technique to map the impedance microstructure of kerogen-rich shales with a Scanning Acoustic Microscope. The C-scan surface images were made at 1 GHz. With this technique we were able to map changes in elastic properties as the shales undergo maturation. The method and sample description and impedance measurement on a micrometer-scale is given in detail in Prasad et al. (2002).

2.2 Image Processing

The heterogeneity was quantified by the coefficient of variation (CV, standard deviation/mean) of the image pixel values. Textures were quantified using spatial autocorrelation functions. We used Fourier transform based autocorrelation estimation. Radial profiles of the autocorrelation function along azimuths ranging from 0^o to 180^o were computed, and the correlation length estimated at each azimuth. The texture anisotropy was quantified by the anisotropy ratio (AR) defined as the ratio between the maximum and minimum correlation lengths obtained over all azimuths.

We used statistical descriptors to quantify the heterogeneity and textures observed in the images. The heterogeneity was quantified by the coefficient of variation (CV) given by the ratio of the standard deviation to the mean of the image pixel values. Spatial textures can be quantified using spatial autocorrelation functions R(m,n). As an example, Fig. 1 shows how a smoothly varying image has a broad, slowly decaying autocorrelation

function. In contrast a rough "salt-and-pepper" image has a very narrow spiky autocorrelation function.

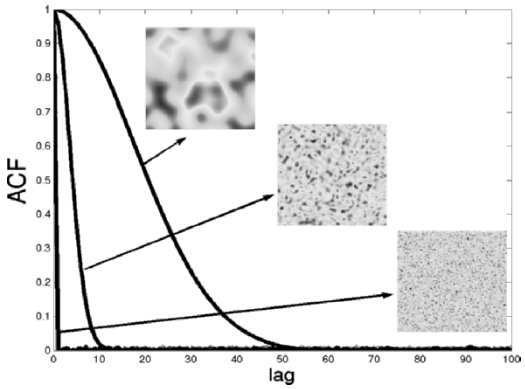

Figure 1. Relation between the autocorrelation function and synthetic images.

We used Fourier transform based autocorrelation estimation where

$$R(m,n) = F^{-1}\left[S(kx,ky)\right]$$

$$S(kx,ky) = \hat{I}(kx,ky)\hat{I}^{*}(kx,ky)$$

$$\hat{I}(kx,ky) = F[I(x,y)]$$

In the above equations I(x,y) denotes the image intensity, while F and F^{-1} denote the forward and inverse Fourier transforms. The 2-d Fourier transform of the image I(x,y) is denoted by $\hat{I}(kx, ky)$ where kx, ky are the spatial wavenumbers in the Fourier domain. The power spectrum S(kx,ky) is obtained by multiplying $\hat{I}(kx, ky)$ with its complex conjugate. Finally the 2-d ACF R(m,n) is obtained by taking the inverse Fourier transform of S.

In Fig. 2, the synthetic textures image is shown on the left and its corresponding 2-d autocorrelation function (ACF) is on the right. Peak intensity is the autocorrelation at zero lag distance (maximum) and decays away on all sides with increasing lag. The rate of decay is a quantitative measure of texture. Radial profiles of the autocorrelation function along azimuths ranging from 0 to 180 degrees were computed by interpolation along the different directions, and the correlation length estimated at each azimuth. This analysis, shown in Fig. 3, allowed us to quantify the azimuthal changes in ACF due to textural anisotropy. As Fig. 3 shows, the correlation length at each azimuth is taken to be the lag value where the correlation function falls to 1/e of its maximum value at zero lag. The texture anisotropy was quantified by the anisotropy ratio (AR) defined as the ratio between the

maximum and minimum correlation lengths obtained over all azimuths. All 180 ACF profiles are plotted in Fig. 3. Figs. 4 and 5 show examples of actual shale SAM images and corresponding radial profiles of the ACF.

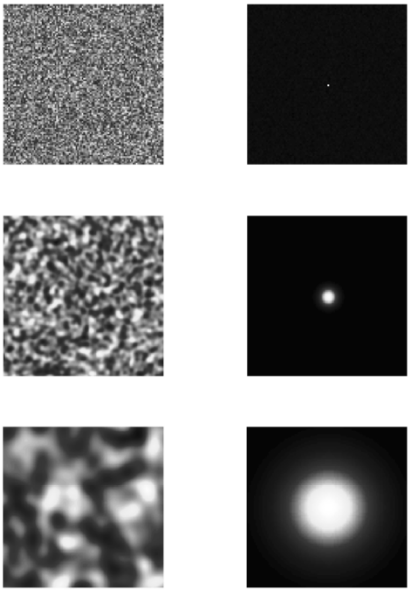

Figure 2. Synthetic textures and their two-dimensional ACF.

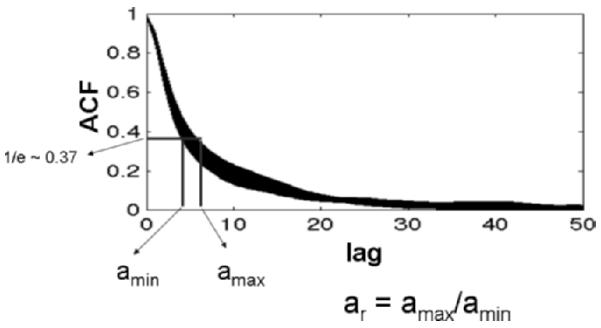

Figure 3. Radial profiles of the 2D autocorrelation along all azimuths from 0^o to 180^o.

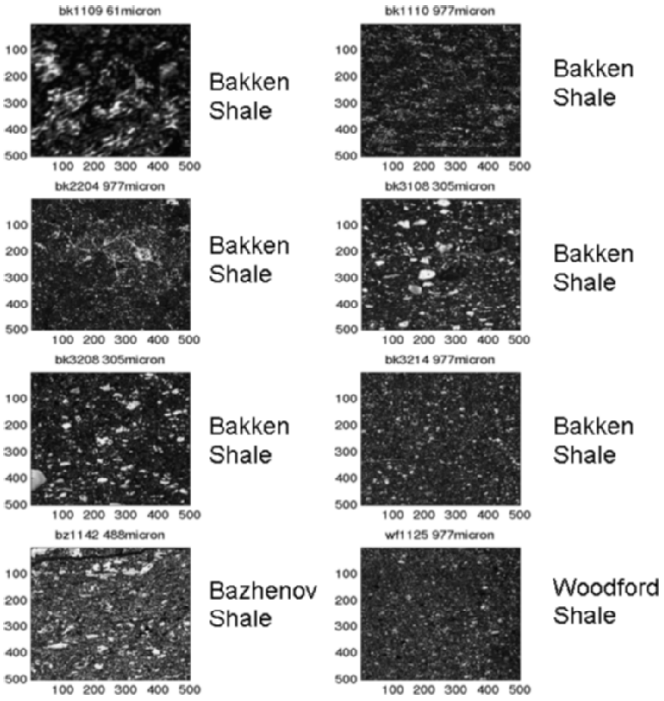

Figure 4. C-scan images made at 1 GHz with the Scanning Acoustic Microscope (SAM).

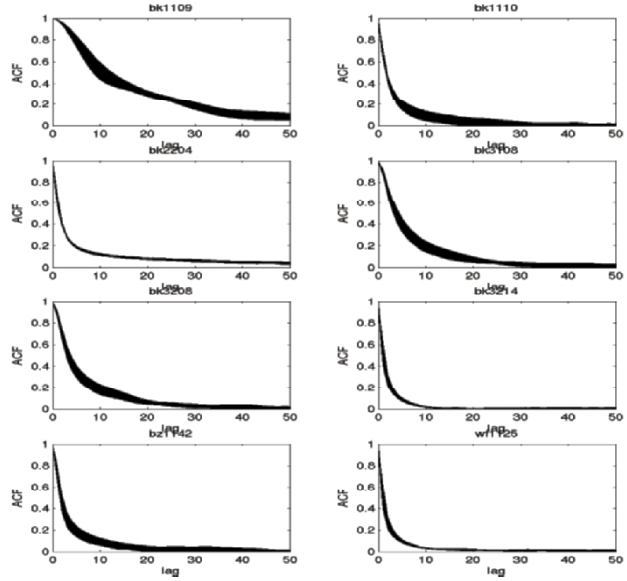

Figure 5. Radial profiles of the ACF from 0 to 180 for the SAM images in Fig. 8.

Thus, we define three parameters for textural analysis:

- The Coefficient of Variation (CV) that describes textural heterogeneity. A larger contrast of heterogeneity leads to high values of CV
- The Anisotropy Ratio (AR) that describes the textural anisotropy. Textural anisotropy leads to a directional dependence of the ACF.
- The Mean Correlation Length that describes textural scale in the images. Larger sized heterogeneities lead to longer correlation lengths

In the following, we present analysis of all the shales.

3. RESULTS

This paper shows how can we quantify textural changes and relate them to maturation and ultrasonic properties of Vp, density, and impedance. Of the dataset used in Prasad et al. (2002), we have analyzed 3 shales: Bakken, Bazhenov, and Woodford. These are organic rich shales with varying amounts of kerogen content, at different maturation stages, and from different depths. We analyzed over 280 SAM images takes at different scales ranging between ~0.1 – 1 mm image size and ~0.2 – ~2μm pixel resolution.

3.1 Image Processing Results

The results of texture analyses are discussed below and shown in the following figures. The data points plotted in the figures are averages over multiple samples, with one standard deviation bars around the estimated average. The coefficient of variation (CV) of the impedance heterogeneities ranged from about 7% to 12%. The mean correlation length ranged from 2 to 10 microns while the textural anisotropy ratio ranged from 1.1 to 1.7 (10% to 70%). We will examine the patterns between textural anisotropy and mean correlation length (Fig. 6), and between textural heterogeneity and correlation length (Fig. 7). We will also see how these patterns change with depth and maturity.

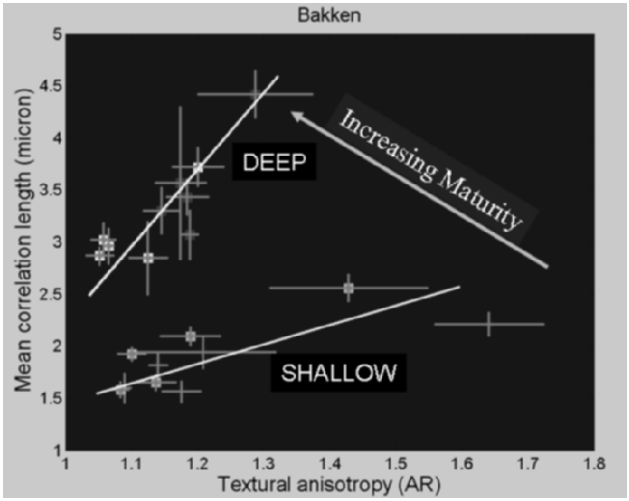

Figure 6. Mean correlation length as a function of textural anisotropy (AR). Woodford shale are shown as circles; Bazhenov shale as triangles; and Bakken shale as squares.

In general, textural anisotropy (AR) increases with increasing mean correlation length (Fig. 6). With depth (= maturity), textural anisotropy increase is lower while the mean correlation length increase is larger. Deeper samples have lower anisotropy but larger heterogeneities. This trend can be sub-divided further within each set. For example, in Bakken shales, the AR vs. mean correlation length trend steepens with depth; that is, textural anisotropy decreases while mean correlation length increases as we go from shallow (less mature) to deeper (more mature) shales.

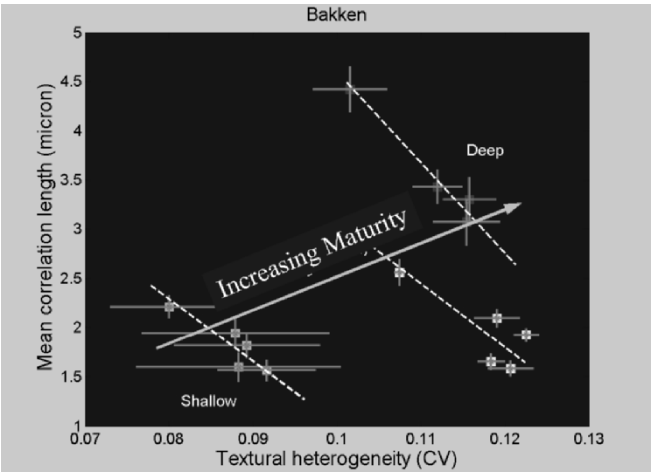

Figure 7. Mean correlation length as a function of textural heterogeneity (AR).

The textural heterogeneity and mean correlation length show a en-echelon correlation pattern when we plot the Bakken samples seperated by depths (Fig. 7). For each depth we see a negative trend between heterogeneity and correlation length, but overall there is a trend of increasing heterogeneity and correlation length with increasing depth and maturity. This is consistent with the observed trend of increasing heterogeneity (CV) with decreasing kerogen content and total organic content (TOC) (Fig. 8).

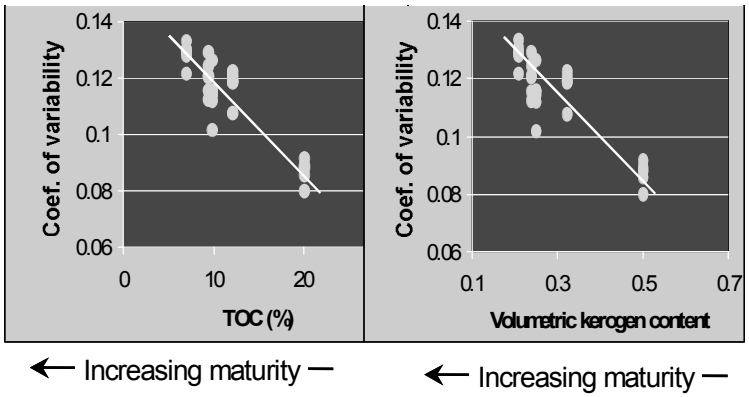

Figure 8. Coefficient of variability (textural heterogeneity) increases with decreasing kerogen content and total organic content.

3.2 Correlations with Other Measurements

A satisfying match was obtained between P-wave impedance derived from the SAM images and the corresponding impedance from ultrasonic data on core samples (Fig. 9). Fig. 9 shows the ultrasonic impedance derived from measured V_P along both the fast and the slow directions (small dots), along with the SAM impedance (large red and orange dots) for Bakken shales. Elastic impedance, density and textural heterogeneity all increase with increasing maturity (Fig. 9).

4. DISCUSSION / CONCLUSIONS

Our analysis of textural parameters of SAM images from Bakken, Bazhenov, and Woodford shales showed quantifiable and consistent patterns linking texture, shale maturity process, and elastic P-wave impedance. Image derived impedances matched reasonably well with impedances estimated from ultrasonic data. The coefficient of variation, CV, (textural

heterogeneity) ranges from 7% to about 12% for these samples. Textural heterogeneity, elastic impedance, P-wave velocity, and density all tend to increase with increasing shale maturity. The mean spatial correlation length generally tends to increase with increasing heterogeneity. The textural anisotropy (AR) ranges from 10% to about 70% and tends to decrease with increasing depth and maturity.

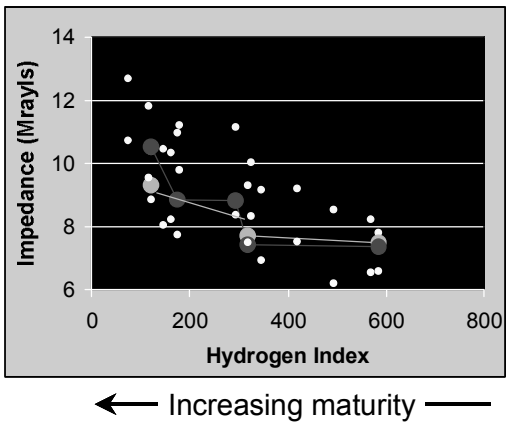

Figure 9. Consistency between P-wave impedance from SAM images (large red and orange spots) and impedance estimated from ultrasonic data (small dots). Ultrasonic data is from Vernik and Nur, 1994). Impedance shows a general increase with increasing shale maturity (from Prasad et al., 2002).

5. ACKNOWLEDGEMENTS

We acknowledge the support of the sponsors of the Stanford Rock Physics Project. This work was performed under the auspices of the National Science Foundation (Grant No. EAR 0074330) and the U. S. Department of Energy (Award No. DE-FC26-01BC15354). M.P. also acknowledges support from the sponsors of the Colorado School of Mines - University of Houston Fluids / DHI Consortium.

REFERENCES

1. Prasad, M., Reinstaedler, M., Nur, A., Arnold, W., 2002, Quantitative acoustic microscopy: Applications to petrophysical studies of reservoir rocks: Acoustical Imaging 25, Kluver Publications.
2. Vernik L. and Nur, 1994; Ultrasonic velocity and anisotropy of hydrocarbon source rocks: Geophysics, 57, no. 5, 727–7351.

NEAR-FIELD ACOUSTICAL IMAGING USING LATERAL BENDING MODE OF ATOMIC FORCE MICROSCOPE CANTILEVERS

Applications to fracture mechanics of NC-Zirconia

A. Caron, U. Rabe, J. Rödel, W. Arnold

Fraunhofer-Institute for Non-Destructive Testing (IZFP), Bldg. 37, University, D-66123 Saarbrücken, Germany; Institute of Materials Science, University of Technology, Darmstadt, D-64287 Darmstadt, Germany

Abstract: Scanning probe microscopy techniques enable one to investigate surface properties such as contact stiffness and friction between the probe tip and a sample with nm resolution. So far the bending and the torsional eigenmodes of an atomic force microscope cantilever have been used to image variations of elasticity and shear elasticity, respectively. Such images are near-field images with the resolution given by the contact radius typically between 10 nm and 50 nm. We show that the flexural modes of a cantilever oscillating in the width direction and parallel to the sample surface can also be used for imaging. Additional to the dominant in-plane component of the oscillation, the lateral modes exhibit a vertical component as well, provided there is an asymmetry in the cross-section of the cantilever or in its suspension. The out-of-plane deflection renders the lateral modes detectable by the optical position sensors used in atomic force microscopes. We studied cracks which were generated by Vickers indents, in submicro- and nanocrystalline ZrO_2. Images of the lateral contact stiffness were obtained by vibrating the cantilever close to a contact-resonance frequency. A change in contact stiffness causes a shift of the resonant frequency and hence a change of the cantilever vibration amplitude. The lateral contact-stiffness images close to the crack faces display a contrast that we attribute to altered elastic properties indicating a process zone. This could be caused by a stress-induced phase transformation during crack propagation. Using the contact mode of an atomic force microscope, we measured the crack-opening displacement as a function of distance from the crack tip, and we determined the crack-tip toughness K_{tip}. Furthermore, K_{1c} was inferred from the length of radial cracks of Vickers indents that were measured using classical scanning acoustic microscopy

Key words: Atomic Force Microscopy; Atomic Force Acoustic Microscopy; Scanning Acoustic Microscopy; Crack-tip toughness; Process zone

M.P. André (ed.), Acoustical Imaging, 31–41.

1. INTRODUCTION

The Atomic Force Microscope (AFM) [1] has found wide applications in biology, physics and material science. Most AFM operation modes measure the deflection of the cantilever caused by the forces acting between the tip and the sample while it is scanned. This allows mapping of surface properties such as topography, elasticity, magnetic or piezoelectric domains and other quantities with nm resolution. Forces lateral and normal to the sample surface contribute to the total tip-sample interaction [2]. In friction force microscopy lateral tip-sample forces are measured [3]. In early experiments the lateral deflection of a bent tungsten wire [4] or the buckling of the cantilever in its length direction [5] were exploited to image atomic-scale friction. In commercial instruments friction and lateral forces are detected by measuring the torsion of AFM cantilevers. In a recent publication we showed that the lateral bending modes of an AFM cantilever can be used for imaging variations of shear elasticity [6] in the so-called atomic force acoustic microscopy mode (AFAM) [7]. Here we present results on the measurement of the crack-tip toughness of submicro- and nanocrystalline stabilized zirconia. For this purpose the crack opening displacement (COD) was measured, using a commercial AFM (Dimension 3000 from Veeco/DI S. Barbara). The purpose of this work was to determine whether stress-induced phase transformation of stabilized zirconia still occurs at small grain sizes. Therefore AFAM images have been recorded along the crack and at its tip in order to quantify the extension of the process zone.

1.1 Fracture Mechanics

The theory of Griffiths' fracture mechanics postulates that crack propagation in materials occurs when the elastic work provided equals the energy to create two new surfaces [8]. This is expressed by the following equation:

$$G_c = \frac{dU}{dc} = 4\gamma_0 \tag{1}$$

where G_c is the energy release per crack increment, dU is the energy supplied to the system, dc is the crack extension per unit width, and γ_0 is the surface energy. In some technical ceramics like SiC, Al_2O_3, and ZrO_2 energy-dissipative processes take place that occur simultaneously when a crack propagates. Such processes consume energy and are thus responsible for an increase of G_c. In such cases one speaks of resistance curve (R-curve)

behavior [9]. For example coarse-grained Al_2O_3 exhibits a typical resistance curve for G_c versus crack propagation [10]. Two effects contribute to this behavior of Al_2O_3. Firstly the friction caused by serrated crack-walls and secondly micro-cracks generated in a process zone [10, 11]. In order to take the contribution of energy dissipative processes into account, Eq. 1 has to be extended by a further term:

$$G_c = R_0 + R_\mu = 2\gamma_0 \tag{2}$$

Here, R_0 and R_μ are the intrinsic contribution and the contribution of energy-dissipative processes to the total fracture energy R, which balances the mechanical energy release per crack increment G_c.

Zirconia undergoes a reversible martensitic transformation from the tetragonal high-temperature to the monoclinic phase. The phase transformation starts in pure zirconia at 1220 °C and ends at 600 °C. This transformation is associated with a volume strain of 4% and a deformation of 16%. Alloying with stabilizing elements like MgO, YO_2, CaO or CeO_2 enables one to adjust the transformation-starting temperature in such a way that the high-temperature phase is still metastable at room temperature. This stabilized phase can then experience a stress-induced martensitic transformation at room temperature. Thermodynamics delivers a critical grain size D_c under which the phase transformation can no longer occur [12]:

$$D \geq D_c = 6\left(\gamma_m - g_s\gamma_t\right) \Big/ \left[\left|\Delta G^c\right| - \Delta U_{se}\right] \tag{3}$$

Here $\gamma_{m,t}$ are the surface energies for the monoclinic phase and the tetragonal one respectively, g_s is the ratio of the surfaces of the tetragonal to the monoclinic particles, ΔG^c is the chemical free energy, and ΔU_{se} is the deformation energy associated with the phase transformation.

With the emergence of new polycrystalline materials with grain sizes in the sub-micrometer and nanometer range and the importance of the energy-dissipative phase transformation for fracture-toughness enhancement, the grain size effect becomes crucial. As it is difficult to determine the necessary thermodynamical quantities, measurements of the critical grain size remains the only way to obtain an optimal microstructure.

For the investigation of the fracture processes the crack-opening displacement was measured. This method follows from Irwin's work on stress concentration at a crack tip [13]. The crack-opening displacement (Fig. 1) profile has a parabolic shape if no closure stresses are present close to the crack tip [14]:

$$u(x) = u_y(x) = \frac{K_{tip}}{E'}\left(\frac{8x}{\pi}\right)^{1/2}, \quad (x > 0) \tag{4}$$

Here, x is the distance from the crack tip, $E' = E/(1-\upsilon^2)$ is the reduced Young's modulus, and K_{tip} is the crack-tip toughness at the crack tip. In the case where a stress-induced transformation takes place parallel to crack propagation, closure-stresses emerge in the vicinity of the crack tip as a consequence of the strain associated with the transformation. Then the plot of the crack opening deviates from the parabolic shape. From such a deviation it is possible to quantify the closure stresses [15].

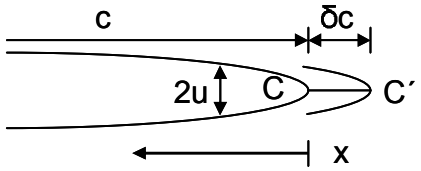

Figure 1. Definition of the crack-opening displacement (COD) u(x). The path CC' symbolizes an incremental crack extension δc of unit width, see [14].

Furthermore the fracture toughness can be determined by measuring the length c_{rad} of the so-called radial cracks in a Vickers indent [16]:

$$K_{Ic} = 0.067\left(c_{rad}/a\right)^{-3/2} Ha^{-1/2}\left(H/E\right)^{2/5} \tag{5}$$

Here, 2a is the diagonal of the Vickers indent, $H = F/2a^2$ is the hardness and E is Young's modulus. Eq. 5 is valid under the assumption that a half-penny shaped crack forms under the indentation zone, which is an idealization for materials exhibiting transformation toughening.

2. EXPERIMENTAL METHODS

In this work several microscopy techniques have been used for investigating the toughness and the crack-tip toughness. Crack opening profiles have been measured by means of AFM in contact mode and by measuring the length of the radial cracks of the Vickers indent using scanning acoustic microscopy [17]. Employing AFAM, imaging of the process zone in the vicinity of cracks has been carried out.

The AFM measurements were carried out with a Dimension 3000 from Digital Instruments/Veeco [18]. In the contact mode of AFM operation, the sharp sensor tip at the end of a micro-fabricated elastic beam is scanned over the sample surface. The tip radius is a few tens of nm, the contact radius, however, typically remains below 10 nm. The interaction forces between sensor tip and sample surface cause a deflection of the cantilever which is measured with a position-sensitive photo-diode. If the deflection of the cantilever and thus the interaction forces are kept constant by a feedback

loop, the topography of the sample surface can be measured with a nanoscale resolution. This allows one to follow the contour of cracks and to measure the COD and compare it to the theoretically expected curve (Eq. 4).

In AFAM the resonances of the cantilever are excited by using an ultrasonic transducer coupled to the sample [7], or by using a piezoelectric element mounted in the cantilever holder [19]. In contact with the sample surface the resonance frequency of the cantilever is determined by the contact stiffness between sensor tip and sample, which represents one of the two boundary conditions of the cantilever eigenmode. The contact stiffness is in turn determined by the elastic properties of the investigated sample. AFAM can be operated in two different working modes. In the spectroscopic mode resonance spectra are collected at one point of the surface from which the indentation modulus of the sample and information on friction can be gained [2, 7]. In this work the imaging mode of AFAM has mainly been used. In this mode a fixed frequency is chosen next to the resonance frequency. Due to local variations of the contact stiffness the resonance frequency shifts, so that the oscillation amplitude of the cantilever changes. The amplitude is then digitized and plotted as an image. Unlike in the spectroscopic mode, the information gained with this method is only qualitative regarding the elastic properties of the sample.

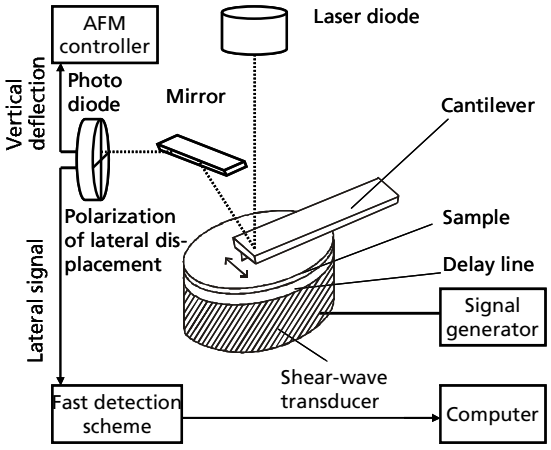

Figure 2. Principle of an atomic force acoustic microscope using lateral bending modes.

In earlier work of AFAM, bending modes have been excited by injecting longitudinal ultrasonic waves through the sample causing out-of-plane displacements of the surface [2, 7, 20]. Furthermore, torsion modes of the cantilever can be excited and used for friction investigation [2, 21]. Torsion modes can be excited by using a shear-wave transducer with its polarization perpendicular to the length axis of the cantilever. Recently we measured the vibration spectra of cantilevers made of single silicon crystal by using an optical scanning interferometer. We found that eigenmodes of the cantilever

can be excited by in-plane displacements, which are neither *torsional nor flexural* modes [6] (Fig. 2). Furthermore, this mode has been characterized regarding its sensitivity to variations of elastic stiffness [6].

3. SAMPLES AND PREPARATION

Sub-microcrystalline zirconia stabilized with 3 mol% Y_2O_3 was investigated in order to measure the crack-tip toughness. Two samples with different mean grain sizes (500 nm and 98 nm) were prepared in order to observe the influence of the grain size on the martensitic transformation and on the crack-tip toughness. The samples were ground with SiC abrasive paper and polished with a diamond suspension with a particle size down to 0.25 μm. A final polish with alumina particles again of 0.25 μm size was used to reveal the grain structure.

For the crack initiation a Vickers indent with a load of ~ 200 N was made. For the separate hardness measurements a micro-indenter from Leica, type VMHT Mot was used. In order to avoid parallel crack initiation, the loading forces were kept small (4.9 N and 9.8 N).

4. MEASUREMENTS AND DISCUSSION

Fig. 3 and 4 show the COD measured with the AFM as a function of the distance to the crack tip for both samples. As concerns the sample having a mean grain size of 98 nm, several cracks were measured, whereas in the case of the sample with 500 nm mean grain size one crack was measured at different times after indentation. For evaluating the COD according to Eq. 4 the Young's modulus of zirconia was assumed to be 210 GPa and its Poisson ratio 0.29. The crack-tip toughness slightly decreases with grain size from 4.1 to 3.2 $\mathrm{MPa}\sqrt{\mathrm{m}}$, with decreasing grain size from 500 nm to 98 nm. This result can be compared with measurements of the crack-opening displacement, using a high-resolution electron microscope where values of 2.8 to 2.3 $\mathrm{MPa}\sqrt{\mathrm{m}}$ were obtained for the large and the smaller grain size, respectively [22]. The crack-tip toughness is altered by phase transformation due to shear stresses, whereas the phase transformation due to dilatational stresses affects the shielding term R_μ. The difference between both types of samples occurs as the phase transformation is restrained at a smaller grain size. Moreover, the deviation of the crack opening profiles from the parabolic shape supports this explanation. This effect is still more remarkable with the sample of 500 nm mean grain size (Fig. 4). Fig. 4 also includes the time dependence of the crack-tip toughness. Sub-critical crack

growth leads to a small contribution to crack propagation, which unloads the crack tip and provides a smaller crack-tip stress-intensity factor, albeit with a small effect only.

For comparison, the fracture toughness was also determined by measuring the length of the radial cracks c_{rad} of the Vickers indent in scanning acoustic microscope images (ELSAM, Leica, Wetzlar, Germany) at a frequency of 1 GHz (Fig. 5). From the images the radial crack length c_{rad}, the size 2a of the Vickes indent, and the hardness H were determined in order to calculate K_{1c} from Eq. 5. For the sample with a grain size of 98 nm the following values were obtained from the images: 2a = 162 (± 8) µm, 2_{crad} = 422 (± 8) µm. This leads to a hardness of H = 14.9 (± 1.5) GPa and a value of 1400 (± 140) for the Vicker hardness using the standard definition for HV. With these data, a value of $K_{1c}= 3.7 \pm 0.26$ MPa$\sqrt{m}$ is obtained. As discussed elsewhere [22], a very small grain size in 3-YTZP over stabilizes the tetragonal crystal structure, such that very little transformation toughening occurs and fracture toughness and crack tip toughness almost coincide.

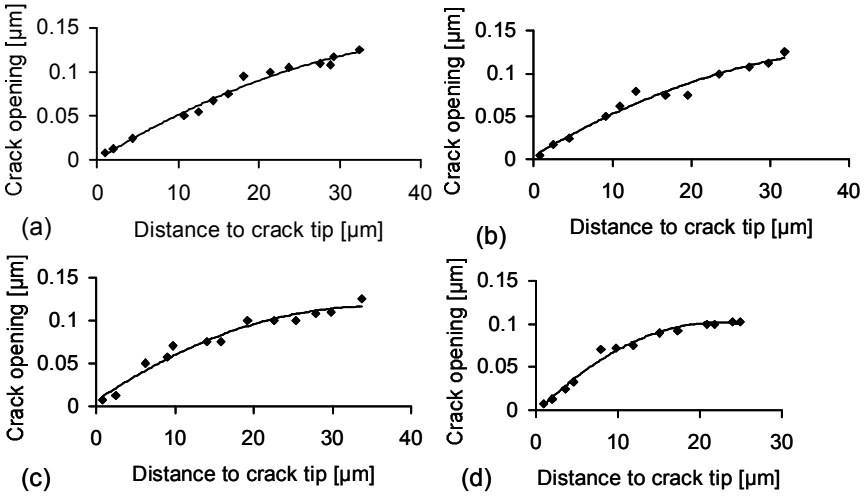

Figure 3. COD u(x) for different cracks on the 3Y-ZrO_2 sample with 98 nm mean grain size. Eq. 4 delivers a crack-tip toughness K_{tip} = 3.15 MPam$^{1/2}$ averaged over all profiles.

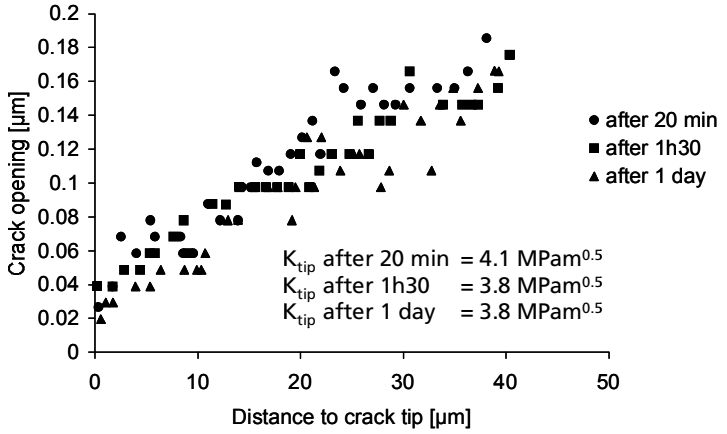

Figure 4. Crack opening displacement as a function of the distance to the crack tip and of the time for the 3Y-ZrO_2 sample with 500 nm mean grain size.

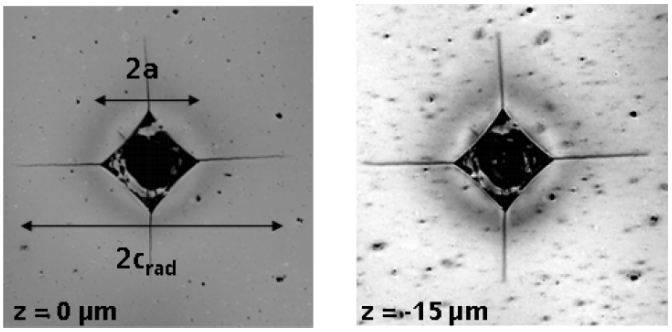

Figure 5. Scanning acoustic microscopy images of a Vickers indent in the zirconia sample with 98 nm grain size at two different defocusing distances z. The indent was made with a loading force of 196.2 N. K_{1c} is obtained from the radial crack length c_{rad} whose apparent length became slightly larger with decreasing z. Images size is 500×500 µm^2.

Table 1. Results of the crack-tip toughness of 3Y-ZrO_2 with tow different grains sizes.

Grain size	Measuring technique	Hardness [GPa]	$K_{tip,}$ $K_{Ic,}$ [MPa$\sqrt{m}$]
98 nm	COD		3.15 ± 0.15
500 nm	COD		4.1 ± 0.20
98 nm	SAM	14.9 ± 1.5	3.67 ± 0.26
98 nm	SEM		2.3
500 nm	SEM		2.8

A further aim of this work was to quantify the width of the process zone in the vicinity of the crack tip and thus to measure the extension of the closure stress-field caused by the stress-induced phase transformation (Table 1). On

the sample with 500 nm mean grain size we observed a depression of the topography close to the crack walls (Fig. 6(a)) and of the crack tip. This depression is connected to the deformation associated with the martensitic transformation. By measuring this topography contrast, the process zone was estimated to be 600 nm wide and about 15 nm deep. Parallel to the topography image, AFAM images using the first contact bending mode (f = 349 kHz) and the first contact lateral bending mode (f = 676 kHz) of a cantilever with stiffness 1.7 N/m were recorded at the same location. The image obtained, using the first contact bending mode, does not show a direct correlation with the topography contrast which could be associated with a process zone. The lateral bending mode seems to be more sensitive in this case. Indeed a band of higher amplitude along the crack fronts can be observed which coincides with the depression observed in topography image (see Figs. 6(b), 6(c)). This implicates a change of the shear elastic properties in the vicinity of the crack. Figs. 6(b) and 6(c) reveal different contrasts in the grain structures. In Fig. 6(c) the grain structure is far better resolved. We believe that the difference between both images is caused by the fact that by using a bending mode local variations of the indentation modulus $M = E/(1-\upsilon^2)$ [7, 20] are emphasized, whereas by using a lateral bending mode local variations of the shear modulus G become more pronounced in the contrast. At the moment we assume that in zirconia the anisotropy of the shear modulus is larger than the anisotropy of the indentation modulus.

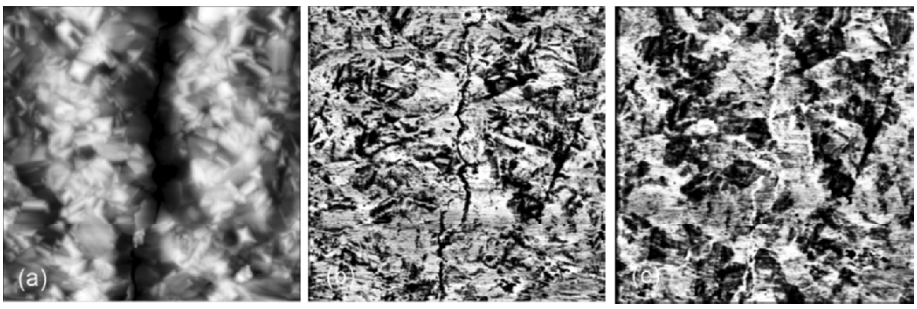

Figure 6. (a) AFM topography image of a crack in a 3Y-ZrO_2 sample with 500 nm mean grain size (z-scale: 70 nm); (b) AFAM image at the same place using the first contact bending mode (f = 349 kHz). Parallel to the crack walls there is a bright contrast indicating the change in shear elasticity; (c) AFAM image at the same location using the first contact lateral bending mode (f = 676 kHz). The static load was 147 nN in all three images; Size: 5×5 μm².

5. CONCLUSION

The influence of the grain size on the crack-tip toughness of zirconia and thus on the stress-induced martensitic transformation was verified on two samples with different mean grain sizes (98 nm and 500 nm) since the crack-tip toughness is slightly smaller for the zirconia sample having the smaller grain size. This can be explained by the restriction of the process zone at the smaller grain size. Furthermore, a process zone could be identified with contact atomic force microscopy and also by atomic force acoustic microscopy using the first *lateral* bending mode in contact. The contrast in this new imaging mode depends on the surface shear elasticity. Finally quantitative measurements of the crack-tip toughness K_{tip} were made by measuring the crack-opening displacement with an AFM revealing a grain-size dependence. The fracture toughness was determined by measuring the radial crack-length of Vickers indents with a scanning acoustic microscope. Future measurements are planned in order to determine the critical grain size above which the phase transformation sets in.

REFERENCES

1. G. Binnig, C.F. Quate, and Ch. Gerber, “Atomic Force Microscope”, Phys. Rev. Lett., **56**, 930 (1986).
2. V. Scherer, M. Reinstädtler, and W. Arnold, “Atomic Force Microscopy with Lateral Modulation” in *Applied Scanning Probe Methods*, Eds. H. Fuchs, B. Bhushan, and S. Hosaka (Springer, Berlin, 2003), pp. 76–115, and references therein.
3. B. Bhushan, in *Handbook of Nanotechnology*, edited by B. Bhushan (Springer, Berlin, 2004), pp. 497ff, and references therein.
4. C.M. Mate, G.M. McClelland, R. Erlandsson, and S. Chiang, “Atomic-scale friction of a tungsten tip on a graphite surface”, Phys. Rev. Lett., **59**, 1942 (1987).
5. T. Göddenhenrich, S. Müller, and C. Heiden, “A lateral technique for simultaneous friction and topography measurements with the atomic force microscope”, Rev. Sci. Instrum., **65**, 2870 (1994).
6. A. Caron, U. Rabe, M. Reinstädtler, J.A. Turner, and W. Arnold, “Imaging using lateral bending modes of atomic force microscope cantilevers”, Appl. Phys. Lett. **85**, 6398 (2004).
7. U. Rabe, S. Amelio, E. Kester, V. Scherer, S. Hirsekorn, and W. Arnold, “Quantitative Determination of Contact Stiffness Using Atomic Force Acoustic Microscopy”, Ultrasonics, **38**, 430 (2000), and reference contained therein.
8. A.A. Griffiths, “The Phenomena of Rupture and Flaw in Solids”, Phil. Trans. R. Soc. London, **A221**, 163 (1920).
9. T.L. Anderson, Fracture Mechanics - Fundamentals and Applications, Chapter 6: Fracture Mechanics in Nonmetals, Boston: CRC Press (1991).
10. E. Babilon, G. Kleist, R.W. Steinbrech, and H. Nickel, “Untersuchung von Mikrorissfeldern in der Umgebung eines Makrorisses in Al_2O_3-Keramik mittels der Röntgenkleinwinkelstreuung”, *Konferenzberichte des FZ Jülich*, 7, Eds. H. Nickel and R.W. Steinbrech, 175 (1991).

11. W. Arnold, G. Weides, and S. Faßbender "Measurement of Elastic Properties Related to the R-Curve-Behavior of Ceramics", *Proc. Asian Pacific Conf. Fract. & Strength 2001 and Int. Conf. Adv. Technol. in Exp.. Mech.*, Jap. Soc. of Mech. Eng., Tokyo, 2001, 517.
12. F.F. Lange, "Transformation Toughening. Part 1: Size Effects Associated with the Thermodynamics of Constrained Transformations", J. Mat. Sci., **17**, 225 (1982).
13. G.R. Irwin, "Fracture", *Handbuch der Physik*, Springer Verlag, Berlin, **6**, 551, (1958).
14. B.R. Lawn, "Fracture of Brittle Solids – Second Edition", *Sol. State Sci. Ser*. Cambridge University Press, (1993).
15. J. Rödel, G. Kelly, and B.R. Lawn, "In-Situ Measurements of Bridged Cracked Interfaces in the SEM", J. Am. Ceram. Soc., **73**, 3313 (1990).
16. D. Munz, and T. Fett, Mechanisches Verhalten keramischer Werkstoffe, in *Werkstoffforschung und –Technik*, B. Ilschner (Ed.), Springer, Heidelberg, 1989.
17. G.A.D. Briggs, "*Scanning Acoustic Microscopy*", Oxford University Press, 1992.
18. AFM – Digital Instrument, www.veeco.com.
19. K. Yamanaka, H. Ogiso, and O. Kosolov, "Analysis of Subsurface Imaging Effect of Contact Elasticity in the Ultrasonic Force Microscopy", Jpn. J. Appl. Phys., **33**, 3197 (1994).
20. M. Kopycinska-Müller, M. Reinstädtler, U. Rabe, A. Caron, S. Hirsekorn, and W. Arnold, "Ultrasonic modes in atomic force microscopy", *Proc. 27th Int. Symp. Acoustical Imaging*, Kluwer Plenum Press, Eds. W. Arnold and S. Hirsekorn, 699–704 (2004).
21. M. Reinstädtler, U. Rabe, V. Scherer, U. Hartmann, A. Goldade, B. Bhushan, and W. Arnold, "On the nanoscale measurement of friction using atomic force microscope cantilever torsional resonances", Appl. Phys. Lett., **82**, 2604 (2003).
22. J. Eichler, "Mechanical Properties of Nanocrystalline Zirconia", Ph.D. Thesis, Fachbereich Material- und Geowissenschaften, University of Technology, Darmstadt, Germany (2004).

MEASUREMENTS OF PARAMETERS OF LEAKY WAVES USING ULTRASONIC MATERIAL CHARACTERIZATION SYSTEM WITH ELECTRONIC SCANNING

R.Gr. Maev, S.A. Titov
University of Windsor, Windsor, N9B 3P4, Canadna; Institute of Biochemical Physics of RAS, 4 Kosygin St., Moscow, 119991, Russia

Abstract: In this paper, we present an ultrasonic material characterization system with electronic scanning. In this system, leaky acoustic waves are generated by a single transducer whose focus is located at the water-specimen interface, and the spatial field distribution of the reflected wave is recorded by a linear array of receiving transducers. The relative position of the transmitting transducer and the receiving linear array is constant in this experimental setup, and the measurement time is only limited by the time of the wave propagation and speed of the electronic data acquisition system. The parameters of the leaky waves can be obtained by processing the set of the output waveforms

Key words: material characterization; leaky acoustic wave; linear array; mechanical and electronic scanning

1. INTRODUCTION

Recently, many methods have been proposed for quantitative material characterization[1]. In typical measurement scheme, the output voltage of the transducer is recorded as a function of time and relative position of the transducer and the specimen. The velocity and attenuation of the leaky surface acoustic waves can be obtained from the output spatio–temporal data. The experimental arrangements with longitudinal movement of the transducer (the V(z) scheme[2–5]) and lateral translation of the receiving

M.P. André (ed.), Acoustical Imaging, 43–48.

transducer (the V(x) scheme[6–8]) are well known systems. However, the mechanical scanning of the transducer is associated with slow data acquisition, and precision mechanics is required.

In this paper, we consider an ultrasonic material characterization system with electronic scanning. In the system, an unmovable array is used for receiving of leaky waves, which propagate along the specimen–immersion liquid interface under investigation.

2. RAY MODEL OF THE SYSTEM

The ray model of the ultrasonic system is shown in Fig. 1. Suppose the leaky wave propagates along B_1B_2 leaking into upper liquid half–space at the critical angle θ_R. This wave is received by the ultrasonic array having pitch p. The array is tilted at the angle θ_0, and only two of the neighboring elements of the array with centers O_1 and O_2 are shown in Fig. 1.

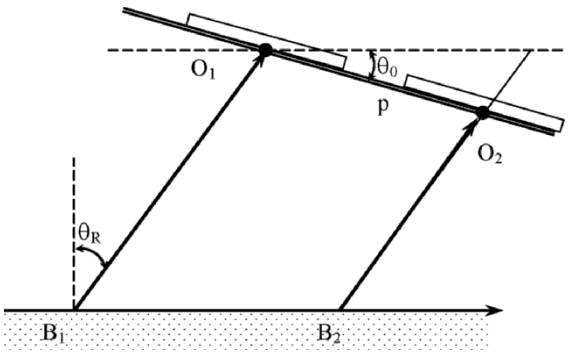

Figure 1. Ray model of the system.

The relative time delay Δt between responses of the leaky wave, received by these two neighbor elements of the array, is related to the critical angle θ_R by the following equation:

$$\Delta t = \frac{p}{C}\sin(\theta_R - \vartheta_0) \tag{1}$$

where C is the sound velocity in the liquid. Using the measured value of Δt, the phase velocity of the non dispersive leaky wave C_R can be calculated according to Snell's law:

$$C_R = \frac{C}{\sin\theta_R} \tag{2}$$

For a particular frequency f_0, the amplitude ratio of the responses of the neighbor elements η can be written as:

$$\eta = \frac{A_2}{A_1} = \frac{\exp(-\alpha \cdot B_1B_2 - \alpha_w \cdot B_2O_2)}{\exp(-\alpha_w \cdot B_1O_1)} \tag{3}$$

where α_w, and α are the attenuation factors of the longitudinal wave in the immersion liquid and the leaky wave, respectively.

$$\eta = \exp\{(-\alpha \cdot \cos(\theta_0 - \theta_R) + \alpha_w \cdot \sin\theta_0) \cdot \frac{p}{\cos\theta_R}\} \tag{4}$$

Using the handbook value of α_w, the critical angle θ_R determined according to Eq. (2), and the measured amplitude ratio η, the attenuation factor of the leaky wave α can be obtained by solving this equation.

3. EXPERIMENT

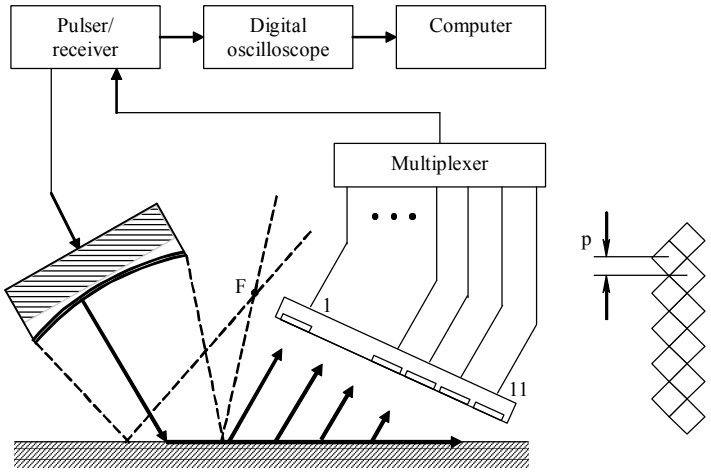

Figure 2. Experimental setup.

The experimental setup is shown in Fig. 2. A leaky wave is generated along the water–specimen interface by a single spherically focused transducer (IS-HR-1/4-20, Xactec Inc., USA). The central frequency of the transducer is 20 MHz, the diameter and focal distances are 6 and 19 mm, respectively. The receiving array consists of 11 identical 1.25 mm square elements located in a zigzag manner as shown in the picture. The pitch of the array is 0.884 mm and the array is tilted at an angle of θ_0=27°.

Relative positions of the array, transmitting transducer and specimen are adjusted in such a way that the wave directly reflected from the interface propagates aside of the array and responses of the array elements are entirely produced by the leaky wave. A standard ultrasonic pulse/receiver with an analog multiplexer are used for acquisition of the output waveforms $V_n(t)$, where n=1…11 is channel number.

Several materials with known properties were tested using this experimental setup. The $V_n(t)$ data recorded for fused quartz, and aluminum alloy are shown in Fig. 3 as grayscale images and waterfall plots. In the graphs, the vertical axes represent the time t, whereas the horizontal axes correspond to the channel number n.

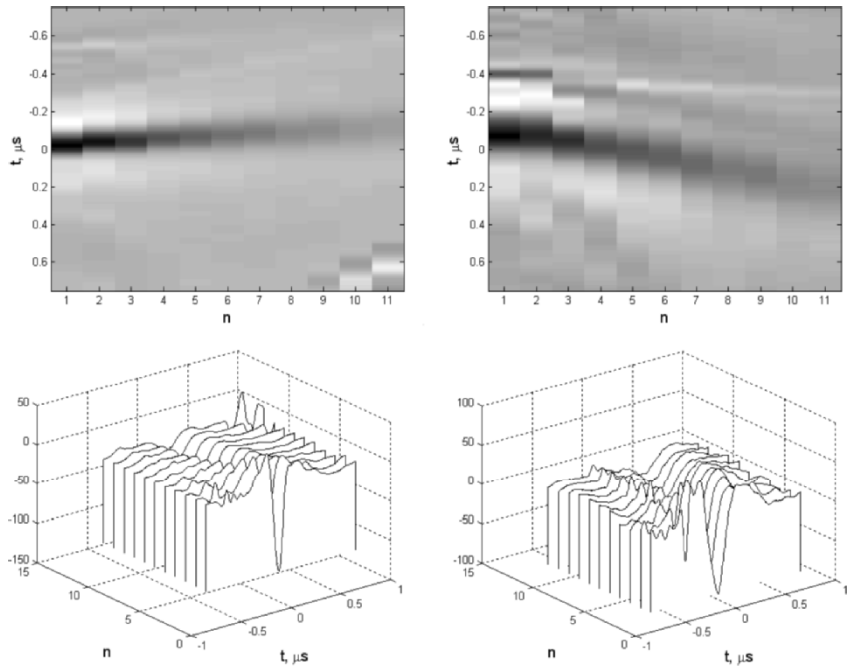

Figure 3. Output waveforms Vn(t) recorded for fused quartz (left) and aluminum alloy (right) presented as grayscale images (upper pictures) and waterfall plots (bottom graphs).

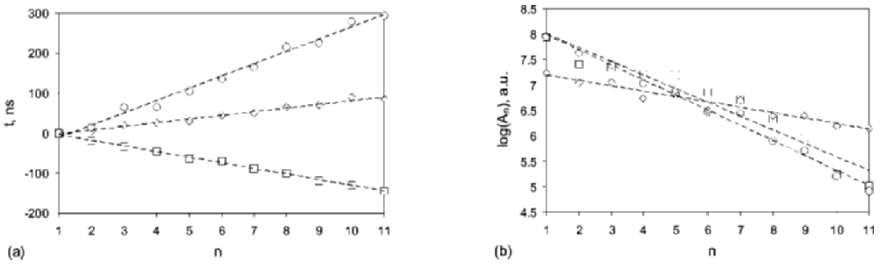

Figure 4. The time of flight (a) and spectral magnitude (b) vs. the channel number n; (o – fused quartz, ◊ – steel, □ – aluminum alloy).

The number of the elements of the array is small (n=11), therefore the discrete structure of the images is quite evident. The slopes and decaying rates of the responses vary between the tested specimens. These responses are produced by the leaky Rayleigh waves and their behavior depends on the elastic properties of the materials.

To measure the velocity of the leaky wave, the time delay t of the negative peak of wave R was determined as a function of n (Fig. 4(a)). The average value of Δt was then calculated, and the velocity C_R was found according to Eqs. (1)–(2) for each material. To estimate the attenuation of the leaky wave, the spectra of the recorded waveforms $S_n(f)$ were calculated first. Then, for a particular frequency f_0=4 MHz, the average value of η was estimated based on the decay of the spectral magnitudes $A_n=|S_n(f_0)|$ with increasing channel number n (Fig. 4(b)). Finally, the attenuation factor of the leaky wave α was found by solving Eq. (4).

4. RESULTS AND DISCUSSION

The values of the velocity C_R and attenuation factor α measured for the test specimens by the proposed ultrasonic material characterization system are summarized in Table 1.

Table 1. Measured and calculated leaky Rayleigh wave parameters.

Material	C_R, m/s	α, 1/mm (f_0=4 MHz)	C_{Rcal}, m/s	α_{cal}, 1/mm (f_0=4 MHz)
Fused quartz	3430	0.30	3426	0.282
Steel	3173	0.10	3163	0.077
Aluminum alloy	2973	0.27	2960	0.235

The leaky Rayleigh wave velocity and attenuation were also calculated from the location of the pole of the reflectance function. To calculate the reflectance function, the velocity of the longitudinal and shear waves were measured for the particular material used in the experiment. The measurement of the bulk wave velocities was conducted according to the ordinary pulse–echo method.

Comparison of measured and calculated values of leaky wave parameters shows a satisfactory agreement, however the attenuation factors obtained by the proposed method are slightly larger than the calculated values because of additional attenuation of ultrasound in a material and diffraction.

REFERENCES

1. A. Briggs, *Acoustic Microscopy* (Clarendon Press, Oxford, 1992).
2. K.K. Liang, G.S. Kino and B.T. Khuri–Yakub, Material characterization by the inversion of V(z), *IEEE Trans. Sonics and Ultrasonics*, **SU–32**, 213–224 (1985).
3. J. Kushibiki and N. Chubachi, Material characterization by line–focus–beam acoustic microscope, *IEEE Trans. Sonics and Ultrasonics,* **SU–32**, 189–212 (1985).
4. M.-H. Nadal, P. Lebrun and C. Gondard, Prediction of the impulse response of materials using a SAM technique in the MHz frequency range with a lensless cylindrical-focused transducer, *Ultrasonics*, **36**, 505–512 (1998).
5. N. Nakaso, K. Ohira, M. Yanaka and Y. Tsukahara, Measurement of acoustic reflection coefficients by an ultrasonic microspectrometer, *IEEE Trans. Ultrason. Ferroelec. Freq. Contr*., **41**(4), 494–502 (1994).
6. O.I. Lobkis and D.E. Chimenti, Three–dimensional transducer voltage in anisotropic materials characterization, *J. Acoust. Soc. Amer*., **106**(1), 36–45 (1999).
7. S. Titov, R. Maev and A. Bogatchenkov. Wide–Aperture, Line–focused Ultrasonic Material Characterization System Based on Lateral Scanning. *IEEE Trans. Ultrason., Ferroelec. Freq. Cont.*, **50**(8), 1046–1056 (2003).
8. M. Pluta, M. Schubert, J. Jahny and W. Grill, Angular spectrum approach for the computation of group and phase velocity surface of acoustic waves in anisotropic materials, *Ultrasonics*, **38,** 232–236 (2000).

APPLICATION OF AN ACOUSTIC MICROSCOPE FOR THE INVESTIGATION OF EMBRYONIC DEVELOPMENT IN QUAILS COTURNIX COTURNIX

L.A. Denisova, R.Gr. Maev, E.A. Khramtsova, T.S. Gurieva,
O.A. Dadasheva, A.F. Denisov, E.V. Snetkova
Emanuel's Institute for Biochemical Physics, RAS, Moscow; Institute of Biomedical Problems, Moscow

Abstract: The aim of the present study was to investigate potentials of acoustic microscopy in the evaluation of embryonic development of the quail. The study has been conducted with the quail embryos in the period from the 7th to 11th day of incubation

Key words: Acoustic microscopy, quail embryos, development, internal structures

1. INTRODUCTION

Quail is a traditional object of space biology. This species is one of the prospective parts of life-support system for future long-term space missions. Also, they are often used as an object for fundamental studies on the influence of weightlessness and other space flight factors upon living organisms, their mineral metabolism, and to clarify the role of gravitation in the formation of terrestrial vertebrates skeleton.

Experimental investigations aboard space vehicles are expensive and usually have been conducted with a limited volume of biological materials. So an opportunity to non-destructively obtain morphological data on an embryo's internal organs and skeleton condition and then further utilize the same embryo in other kinds of analysis, substantially increases the efficiency and decreases the costs of the study.

M.P. André (ed.), Acoustical Imaging, 49–56.

New opportunities for non-destructive micro-anatomical analyses of the whole embryo could be realized using acoustic microscopy. An acoustic microscope, similarly to medical ultrasound, is capable of producing visual images of the internal structure of dense optically opaque objects. However, due to the use of a focused beam and higher frequencies it provides higher resolution and can be employed for the investigation of small objects with dimensions of about several millimeters (Foster et al. 1993; Maev et al. 2004, 1988; Denisova et al. 2004).

The aim of the present study was to investigate the potential of acoustic microscopy to evaluate of embryonic development of quail.

2. MATERIALS AND METHODS

The study has been conducted with quail embryos in their 7th to 11th day of incubation. Immediately after taking the eggs from the incubator, the egg shell has been dissected, the embryo has been extracted from the shell and placed into a dish filled with physiological solution at room temperature. Then it has been examined with a scanning acoustic microscope "Tessonix" designed by Maev R.G. The investigation has been conducted with short focused ultrasound signal, using a frequency 50 MHz that provides lateral resolution of about 30 microns and depth of ultrasound penetration up to 10 millimeters. After scanning in the acoustic microscope, the embryos have been dissected and examined with a light microscope, with x20 magnification.

3. RESULTS AND DISCUSSION

In the left part of Fig. 1 there is an acoustical image, called B-scan that corresponds to the image of the surface of the slice performed through the head of the 7-day quail embryo in one plane with the acoustic lens axis.

At the B-scan one is able to determine the form of eyeballs, sclera and retina thickness. The width of the image corresponds to the transversal dimension of the embryo's head in millimeters, and the height of the image corresponds to the depth of the "acoustical cut" in microseconds. Velocity of ultrasound in soft watered embryonic tissues is similar to that in water (about 1450 m/c), therefore using the presented B-scan we can determine some linear dimensions: skin thickness on the head, and the eye-balls dimensions at different levels. If we assume the most obtrusive parts of the head surface to be zero, then we can determine the depth of the disposition of various structures as well as evaluate the levels of the C-scan planes

(C-scans – "acoustical slices" obtained at the planes, perpendicular to the lens axis). The B-scan, presented in Fig. 1, reproduces tissues in the volume with the depth approximately 10 millimeters.

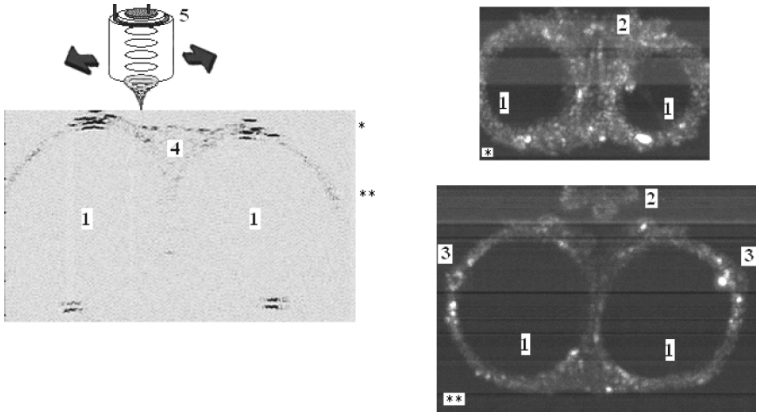

Figure 1. Acoustical images of quail embryo head from the crown of the head. 1 – eyeballs, 2 – base of beak, 3 – eye lens, 4 – front part of cranium, 5 – acoustic lens position during scanning, * - level of upper C-scan, ** - level of lower C-scan. Frequency 50 MHz.

The upper C-scan is the acoustical image of the layer 0.5 microseconds in thickness that corresponds 360 micron. It includes head skin and eyes tissues in their upper part. In the lower C-scan there is a layer of the same thickness (360 micron), which is bedded deeper. This "acoustical slice" includes both eyeballs, and one can also see the eye lenses. Between the eyeballs, there is olfactory organ partition.

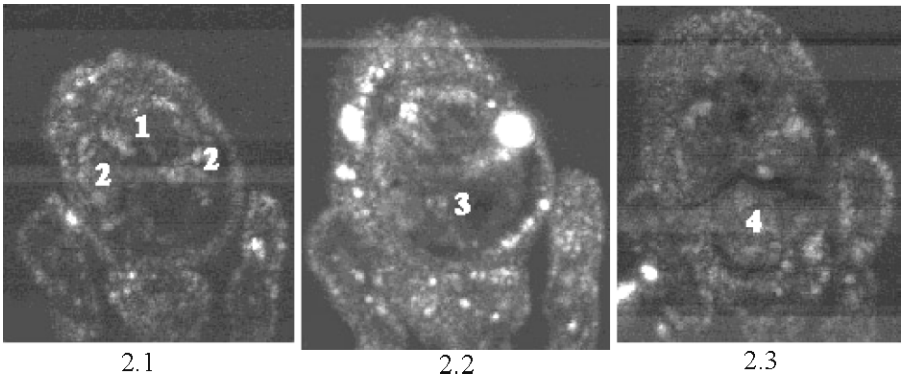

Figure 2. Acoustical images (C-scans) of the 7-day quail embryo body: 1 – heart, 2 – left and right lungs, 3 – stomach, 4 – liver. Frequency 50 MHz.

In the next figure there are C-scans of a 7-day quail embryo body (Fig. 2). The embryo has been placed on its back, abdomen upwards. Gate width for each image is about 0.1 microseconds, therefore the thickness of each "acoustical cut" is approximately 75 micron. First image has been obtained at the depth of 1 mm from the most prominent (obtrusive) part of the abdomen surface, on which the ultrasound signal had been focused. The distance between the levels of the 1st and 2nd acoustical images is 300 micron, and between 2nd and 3rd – 225 micron.

In the thorax, there is the heart, which is between the left and right lungs. At the C-scan №1 (Fig. 2.1) in the left part of the abdomen one can see the stomach (Fig. 2.2), and in C-scan №3 (Fig. 2.3) in the right part we see the liver, which at this stage has a shape of a ball. The results of the ultrasonic study in acoustic microscope have been confirmed by subsequent dissection of the embryo body in the levels corresponding to the planes of C-scans and examination of cuts in light microscope at x20 resolution.

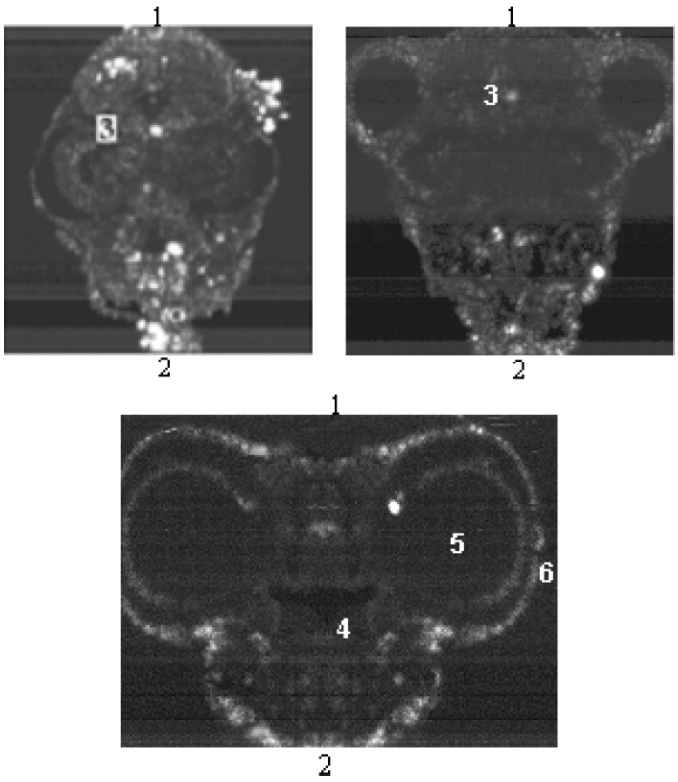

Figure 3. Acoustical images (C-scans) of 8-day quail embryo head. 1 – head crown, 2 – neck, 3 – brain, 4 – oral cavity, 5 – eyeball, 6 – eye lens. Frequency 50 MHz.

In the next group of acoustical images (Fig. 3), there are C-scans, obtained from the back side of the head in the process of scanning towards the beak. Ultrasound signal has been focused at the skin on the back of the head. Gradually moving the C-scan plane from the back of the head to the beak, one can see the disposition of the cerebellum in the cranium, shape of the medulla cavity and diencephalon. In the upper part of the images, there is the distal part of the cerebral hemispheres. In the middle C-scan the image includes eye sockets, in the right-side image there are eyeballs with retina, lenses and vitreous humor.

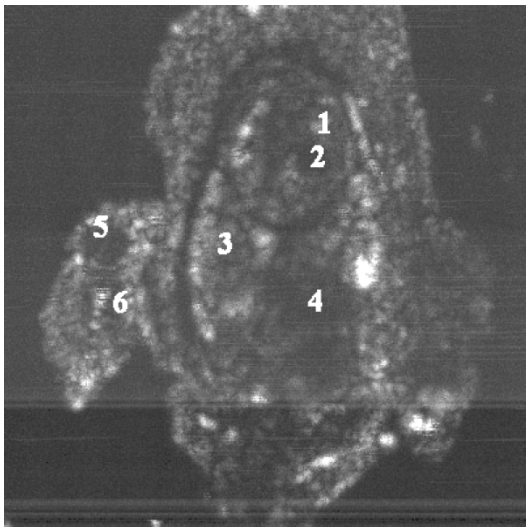

Figure 4. Acoustical image (C-scan) of the 8-day quail embryo body: 1 – myocardium, 2 – heart ventricle, 3 – lung, 4 – stomach, 5 – knee-joint, 6 - shin-bone. Frequency 50 MHz.

In the next figure there is an acoustical image, which corresponds to the plane of the frontal longitudinal cut (Fig. 4). One can distinctly see the contours of the internal organs: heart ventricles, lungs, stomach. In the right shank (in the figure it is from the left side) there is an area of knee-joint, which still has no mineralized tissue and looks transparent. Below this, one can see some piece of ossified shinbone (tibia). The same set of organs can also be seen on acoustical images of the 11-day quail embryo, made from its right side (Fig. 5).

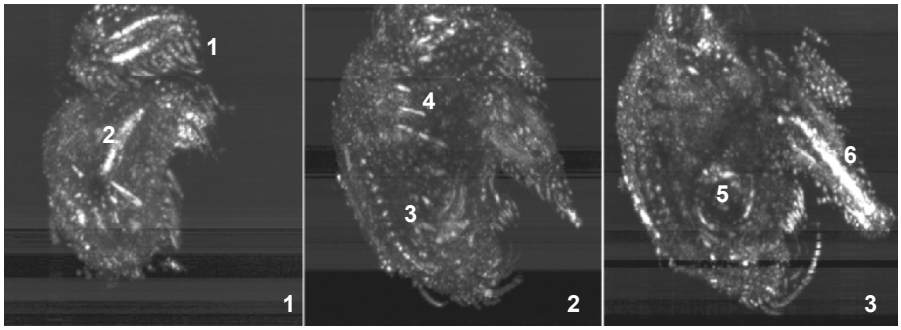

Figure 5. Acoustic images (C-scans) of the 11-day quail embryo body from its right side: 1-ulna and radial bone in the wing, 2-femoral bone in the leg, 3-ossification centers in dorsal vertebrae, 4-ribs, 5-femoral joint, 6-tibia and fibula bones in the leg; C-scans height 18 mm.

In the next acoustical image, there is a knee-joint of a 12-day quail embryo. The contours of the joint are distinctly determined under the skin (Fig. 6.1). The next picture represents the image of the femoral bone and knee joint surfaces under skin and muscles (Fig. 6.2) in 13-day old embryo.

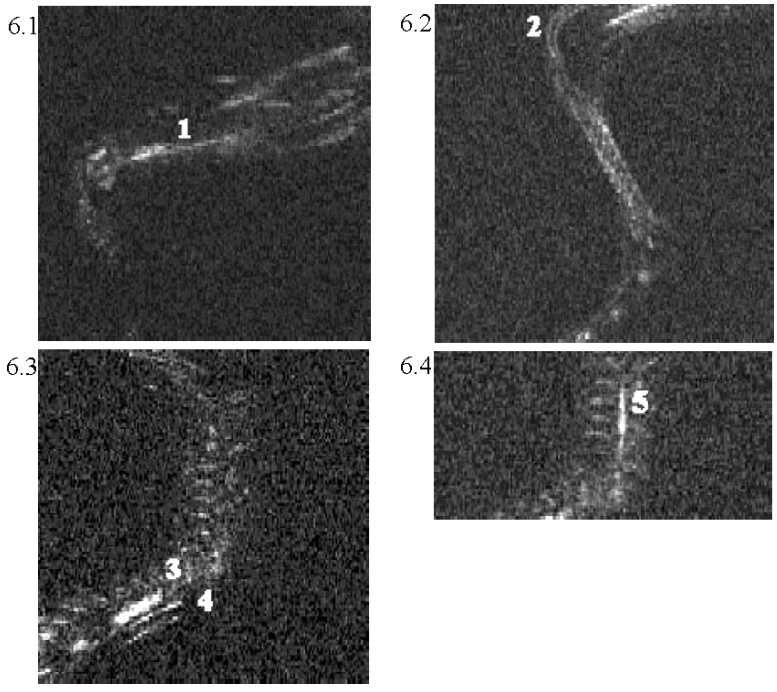

Figure 6. Acoustical images (C-scans) of quail embryo limbs. 1 - thigh-bone, 2 - knee-joint, 3 – radius, 4 – ulna, 5 – humerus. Frequency 50 MHz.

Analogous acoustical images have been obtained for the upper limbs bones: humeral bone (Fig. 6.3) and radial bone (Fig. 6.4) of the wing.

Thus, comparative analysis of the results obtained non-invasively in acoustic microscope and the data of micro-anatomical study conducted with the use of light microscope on dissected biomaterial proved identification of some internal organ and their disposition in the whole embryo. It has been established, that in the process of formation of an acoustical image no substantial distortions arise when reflecting typical form and dimensions in separate profiles or sections.

In the scientific literature there are just scant data on the internal organs development after the period of organogenesis, when their typical shape has been formed and the further embryogenesis is characterized by progressive gain of organ weight and dimensions. It is caused, in some degree, by the small size of the objects. They are too small for traditional morphological or anatomical examination or medical ultrasound, but are too large for classic histology and can be investigated not as a whole, but fragmentarily.

Recently the results by Turnbull et al., (1999) have been published on the application of scanning acoustic microscope for the investigation of internal structure of a mouse embryo. Until now, investigations with the other species' embryos have not been conducted. Alternative methods of investigating the internal structure in dense optically opaque objects 0.5–5.0 cm in size could be micro-roentgen or computer micro-tomography (DeClerk et al., 2003). However, with reference to the developmental biology objects those methods could have only limited application. From one side the difficulties in interpretation of the obtained images are caused by weak contrast of embryonic tissues. From the other side those methods work in transmission mode and the images of superficial and deeper layers are superimposed on each other.

4. CONCLUSIONS

Significant advantages of acoustic microscopy are the following:

- Ultrasound, with the parameters used, is harmless for both the living organisms and the researcher;
- Ultrasound can be used for the examination of dense optically opaque objects;
- In an acoustic microscope, biological tissues can be examined without fixation, dehydration, staining, contrasting and so on. It should be mentioned, that some of these phenomena, such as shape and spatial distribution of chondrocytes lacunae, could be explored with a light

microscope after fixation, dehydration, demineralization, staining, slicing etc. With an acoustic microscope we can obtain even more information without any processing: the cut surface has not been polished or stained. Such a reduction of preparation procedures allows us to observe cartilage immediately after cutting into two cuts and therefore closely investigate cartilage in its natural condition.

REFERENCES

1. De Clerck, N.M., Van Dyck, D., Postnov, A.A., 2003, Non-invasive high-resolution μCT of the inner structure of living animals, *Microscopy and analysis*, **81**, pp. 13–15.
2. Denisova, L.A., Denisov, A.F., Maev, R.G., Matveichuk, Yu.I., Maslennikova, T.V., 2004, Acoustic microscopy methods in morphological study of the articular cartilage and subchondral bone. *Proceed. 27th Intern. symp. on acoustical imaging*, Saarbrucken, Germany, "Acoustical Imaging", Vol. 27, Eds. Arnold W. and Hirsekorn, S., Kluwer Academic/Plenum Publishers, Dordrecht & New York, pp. 535–541.
3. Foster, F.S., Pavlin, C.J., Lockwood, G.R., Ryan, L.K., Harasiewicz, K.A., Berube L., Rauth A.M., 1993, Principles and application of ultrasound backscatter microscopy, *Proceed. IEEE Transaction UFFC*, **40**, pp. 608–616.
4. Maev, R.G., 1988, Scanning acoustic microscopy of polymeric and biological substances, *Tutorial Archives of acoustics*, **13**(1–2), pp. 13–43.
5. Maev, R.G., 2004, Recent advances in quantitative acoustic microscopy. *Proceed. 27th Intern. symp. on acoustical imaging*, Saarbrucken, Germany, 2003, "Acoustical Imaging", Vol. 27, Eds. Arnold W. and Hirsekorn, S., Kluwer Academic/Plenum Publishers, Dordrecht & New York, pp. 407–414.

ULTRASONIC CHARACTERIZATION OF THE BIOLOGICAL OBJECTS OF SPHERICAL OR CYLINDRICAL SHAPE USING AN ACOUSTIC MICROSCOPE

A.R. Maeva, E.Yu. Bakulin, A. Sinisac, N. Bajic, L.A. Denisova,
F.M. Severin, R.Gr. Maev, E.A. Khramtsova
Windsor University, Dept. of Physics, 401, Sunset ave., Windsor, ON, N9B 3P4, Canada;
e-mail: maev@uwindsor.ca

Abstract: The ability of an acoustic microscope in the investigation of biological objects with irregular surface, layered structure, different physical and acoustical properties has been estimated. Acoustic images and the results of tissue layers thickness measurements have been analyzed with 3 objects: extracted human tooth, cats' knee joint in vitro and human nail in vivo. It has been demonstrated, that unlike metal or polymeric samples the biological objects of a ball or cylindrical shape due to the fine surface irregularities can produce acoustic images of their internal structures, which are in a good correspondence with the real microanatomical parameters. Morphological resemblance of the biological objects shape in acoustical and optical images provides precise measuring of separate tissue layers in a noninvasive mode that can not be performed with any other method

Key words: acoustic microscopy, high-frequency ultrasound, tooth, joint cartilage, finger nail, biological tissue mechanical properties, ultrasound morphometry

1. INTRODUCTION

In agreement with the general law of physical acoustics, the angle of the incident ultrasonic beam is equal to the angle of the reflected beam. Therefore, when investigating smooth objects in an acoustic microscope the ultrasonic signals can widely deviate from the irregular surface. This phenomenon makes it impossible to precisely receive and register the

M.P. André (ed.), Acoustical Imaging, 57–64.

reflected ultrasound energy with an acoustic lens due to its complete or partial loss. In the acoustical images (Fig. 1) we can see that only the small central part of the objects provides proper reflection of the ultrasound signal. Other areas reflect focused ultrasound beam at angles greater than aperture angle of the acoustic lens, which causes the loss of information.

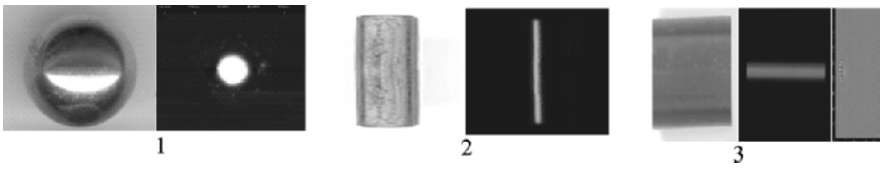

Figure 1. Appearance of a metal ball (1), metal and PVC cylinders (2 and 3) and their acoustical images: C-scans (1 and 2) and B-scan (3), - obtained by the focusing ultrasound beam on the upper surface of the objects; frequency 50 MHz; (ball – 8 mm in diameter; metal cylinder – 4.23 mm in diameter; PVC-cylinder 15 mm in diameter).

As a result, acoustic microscopy has been applied mainly for the investigation of flat-parallel samples. Biological objects usually have complicated irregular shape, which is often similar to the shape of a ball or cylinder (Fig. 1). It is practically impossible to mathematically describe the propagation of ultrasound in such objects. The aim of this study is to investigate possible ways to apply acoustic microscopy for biological objects morphology and physical properties characterization without any special preparation or the necessity to create flat-parallel slices.

2. MATERIALS AND METHODS

The objects of the study were human teeth and finger-nails that have cylindrical shape, and cat's knee joint heads, which have spherical shape. Whole human teeth, extracted for orthodontic reasons, have been obtained from dental clinics, and cats' joints have been obtained from veterinary clinics. Human fingernails have been investigated in vivo in male and female volunteers (18 years old). For the TOF measuring and obtaining visual images, two scanning acoustical microscopes (Sonix, Sonoscan, USA, and Tessonix-1103 (Maev R.G 2004)) have been used (frequency 20 and 50 MHz, water immersion). Using TOF method, the thickness of enamel, dentin, cartilage and nail plate has been nondestructively determined. After the ultrasonic investigation, the teeth and cats' joints have been dissected along the line of the acoustical microscope B-scanning, and the results, obtained with ultrasound methods have been verified using a light microscope at x20 resolution. Precise thickness of the tissue layers has been

measured in slices using an ocular-micrometer. Nails' thickness has been measured in vivo in their distal projected part using a micrometer and the assumption was made that it does not significantly change along the nail plate from its proximal to distal part. The nails density has been determined with Archimedes "wet" method using the samples of clipped tissue. The values of the acoustic impedance (Z) and longitudinal (dynamic) elasticity module (E) have been calculated using the formulae: $Z=\rho C$, $E= \rho C^2$, where ρ is density and C- longitudinal ultrasound velocity.

3. RESULTS AND DISCUSSION

The tooth, whose acoustic images are presented in Fig. 2, looks like a cylinder with the diameter about 4 mm (Fig. 1.2). However, due to the fine enamel roughness, the small areas of the surface contribute to the reflection of the ultrasound signal. Therefore, in the B-scan (Fig. 2.1) we can distinctly determine the shape of the tooth and measure enamel thickness in this region. In the tooth's equator, enamel thickness varies from 300 to 1000 μm. In the case presented in Fig. 2.1 and 2.2 the TOF in the enamel layer is 0.27 μs, therefore the enamel thickness is 810 μm. The determination of the enamel thickness in the optic image (Fig. 2.3) is more difficult due to the partial superposition of upper and lower structures, but in the C-scan (Fig. 2.4) of the slice surface we can precisely measure it: 0.81±0.09 mm.

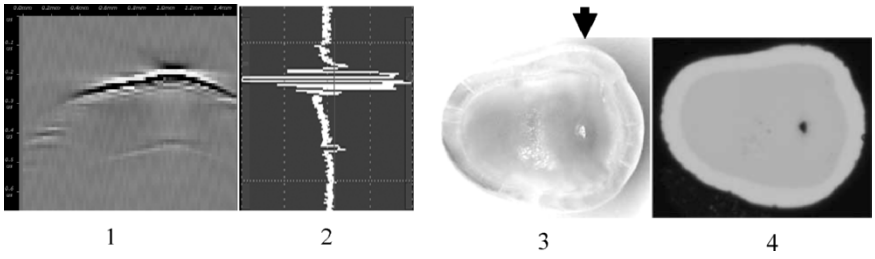

Figure 2. B-scan (1) and A-scan (2) of a whole human tooth. Optical image of the surface of the transversal slice, made in the area where the B- and A-scans have been obtained (3). Acoustic image of the surface of the same slice, scan size 7.5 x 9 mm (4). Frequency 50 MHz.

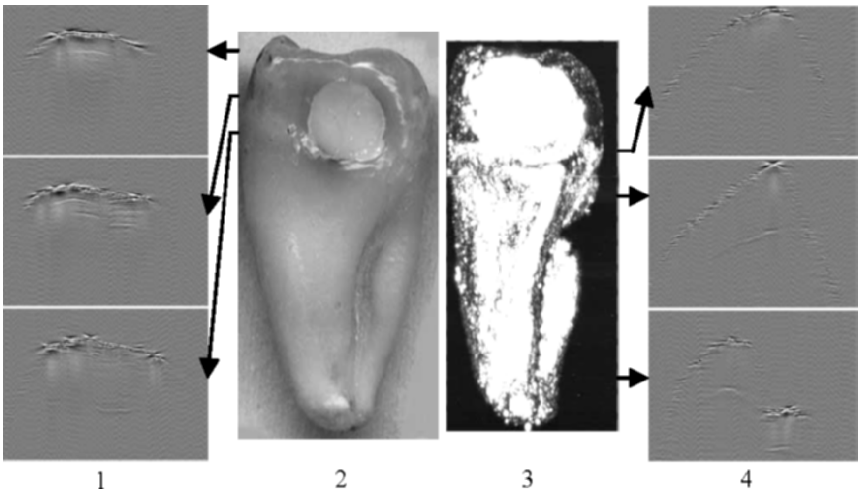

Figure 3. Digital photo of the human molar (2), its acoustic image (3, C-scan obtained with the acoustic gate 3 μsec), transversal B-scans (1,4) obtained at the levels indicated with black arrows. Frequency 50 MHz.

In Fig. 3 there is an extracted human molar, whose shape partly resembles a ball (Fig. 3.2), cylinder or cone. From the B-scans obtained at different levels along the tooth's length, one can discern normal enamel layer (Fig. 3.1, upper B-scan), filling disbond (Fig. 3.1, middle and lower B-scans), pulp chamber (Fig. 3.4, upper and middle B-scans), and root channels (Fig 3.4, lower B-scan). Providing that the ultrasound velocity is about 6000 m/s in enamel, 4500 m/s in dentin and 3500 m/s in the filling material, we can readily calculate the thickness of the tooth tissues, presented in the B-scans. At the levels of the obtained B-scans the enamel thickness is 0.35 μs = 1.05 mm, depth of the maximum filling thickness is 1.31 μs = 2.29 mm, the distance from the tooth surface to the pulp in the tooth's neck area is about 1.40 μs = 3.15 mm; the thickness of the root dentin is 0.78–0.95 μs = 1.76–2.14 mm. These parameters, determined in a non-destructive manner with the acoustic microscope, are in good agreement with the data obtained from the measurements made after the awing the tooth transversely in the same locations.

The second object of our study has been a human finger-nail. Its curvature and dimension (Fig. 4.1) can be compared with that of the PVC-cylinder, presented in Fig. 1.3. However, the B-scan obtained focusing on the most convex area of the nail surface (Fig. 4.2) distinctly shows the character of the shape and even allows us to determine the thickness of the nail plate. In Fig. 4.3 the nails longitudinal B-scans can be compared with the scheme of the microanatomical structure by Cormack (1984) (Fig. 4.4).

In the non-invasively obtained acoustic images, one can readily reveal the main details of the nail anatomical structures.

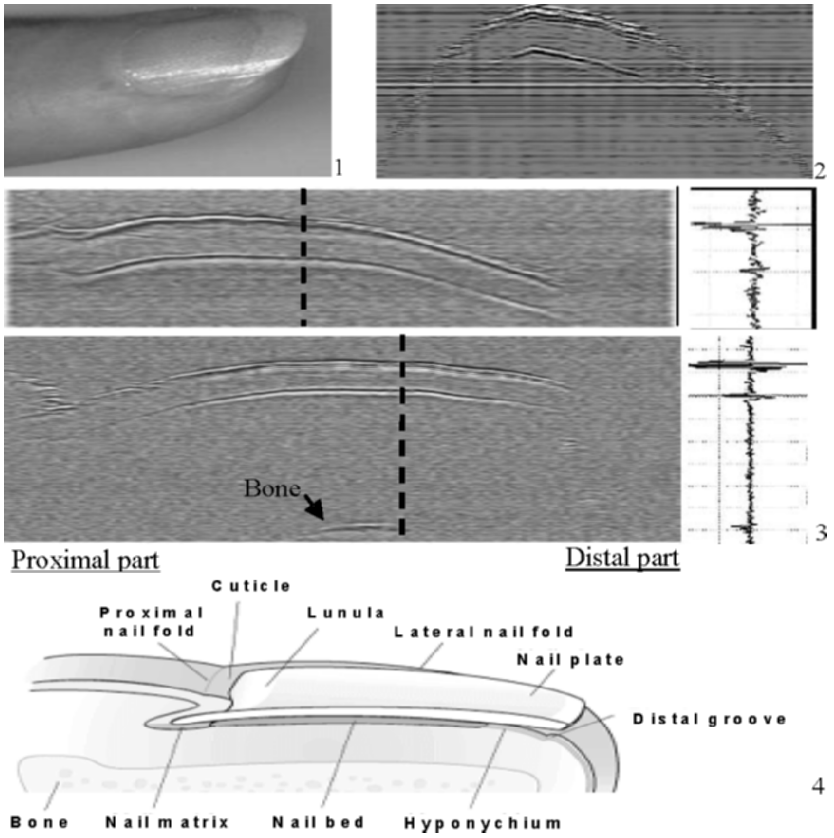

Figure 4. Human finger-nail (1) and its transversal B-scan (2), 50 MHz. Longitudinal B-scans and the corresponding A-scans of male (upper) and female (lower) volunteers, 50 MHz (3) in comparison with the scheme of anatomical structure (4).

It has been shown that nail thickness in male volunteers is higher than in female volunteers, this is in agreement with the data published by Finlay et al. (1990). In some nails the interface between the dorsal and intermediate layer described by Jemec and Serup (1989) can be easily distinguished (Fig. 4.3, the lower B-scan).

Application of the acoustical pulse-echo technique, allows us to determine the ultrasound velocity values. In the Fig. 5 there is a distribution of the nail plate sound velocity in the different fingers of 3 different persons. The data presented in Fig. 5 confirms that there are expressed differences in

the sound velocity of the nails either between persons or between different fingers of the same hand.

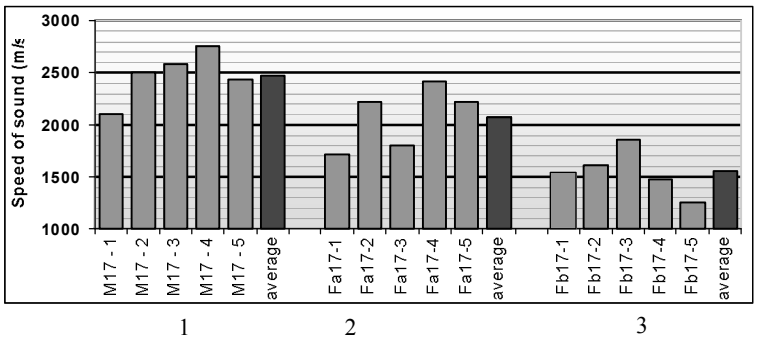

Figure 5. Distribution of the ultrasound speed values in the nails of different fingers of male (1) and female (2,3) volunteers, the figures under the columns are the numbers of fingers from thumb to the little one.

Using ultrasound velocity values we can nondestructively characterize elastic properties of the nail tissue. The data presented in Table 1 demonstrate that significant deviations of acoustic and mechanical tissue properties can be revealed while the density remains almost the same.

Table 1. Acoustic parameters, density and elasticity of the finger-nails in males (group 1) and females (group 2), Means and standard deviation.

Group	Ultrasound velocity, m/s	Density, g/cm^3	Acoustic impedance, 10^6 kg/m^2 s	Elasticity, GPa
1	2480 ± 100	1.30 ± 0.07	3.22 ± 0.20	8.0 ± 1.0
2	2070 ± 130	1.37 ± 0.05	2.84 ± 0.20	6.0 ± 0.9

To display the structure of the knee-joint heads the acoustical lens has been focused above the upper point of its spherical surface, therefore the B-scans obtained correspond to the sagittal histological cross-sections. In the A-scans (Fig. 6) the upper signals correspond to the surface of the cartilage, the middle signal to the cartilage-bone interface, the lower signals are caused by the reflections on the trabeculas of the cancellous bone. In our previous study the average ultrasound velocity in the normal cartilage was determined using flat-parallel joint heads' slices: 1680 m/s (Denisova et al., 2004). Using this value and obtained TOF we have calculated the thickness of the cartilage layers in cats' knee joints. In the group of 9 younger animals (age 1–7 years) the cartilage layers thickness has been 0.34±0.01 mm; in the

group of older animals (8–15 years) without visible osteoarthritic changes the cartilage layers thickness has been 0.53±0.02 mm. After the non-destructive investigation in the acoustic microscope the joint heads have been sectioned (Fig. 6) by the line of B-scanning. The cartilage thickness values have been measured using an ocular-micrometer. The difference between the acoustical data and direct measurements on average has not exceeded 3%.

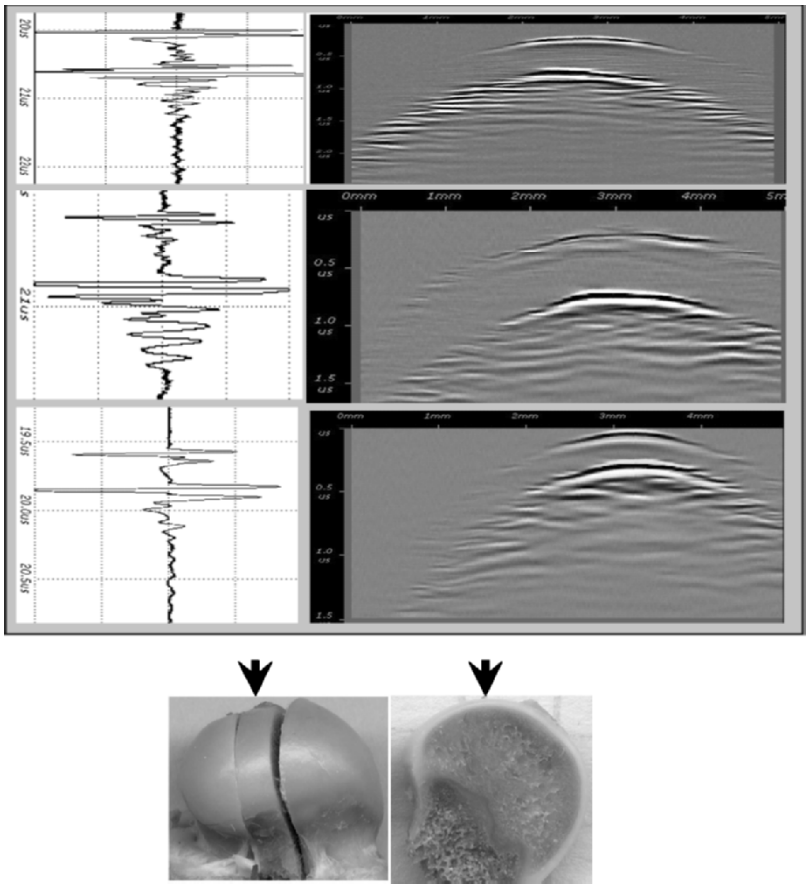

Figure 6. In the upper part of the figure, there are B-scans (on the right) and corresponding A-scans (on the left) of the 3 cats' joint heads. The photos in the bottom part show the direction of the acoustic lens scanning and the following section of the joint head for the cartilage thickness measurement.

4. CONCLUSION

The results obtained by comparing acoustical and optical images demonstrate that unlike in metal or polymeric samples, in biological objects due to the fine surface irregularities, one can obtain visual images of their internal structures by application of an acoustic microscope, which are in good agreement with the real microanatomical parameters. Morphological resemblance of the biological objects shape in acoustical and optical images provides grounds for precise measuring of tissue layers in a noninvasive mode that cannot be performed with any other method. It has been found that when focusing the ultrasound beam perpendicularly to the convex surface of the object, we achieve the least distortion of the quantitative characteristics of the tissue layer's thickness. The results of the study confirm that acoustic microscopy can be effectively used for the in vivo characterization of the spherical or cylindrical shaped biological objects ranging in size from several hundred microns up to several centimeters.

REFERENCES

1. Cormack D.H., 1984, *Introduction to Histology*, J.B. Lippincott company, Philadelphia.
2. Denisova L.A., Denisov A.F., Maev R.G., Matveichuk Yu.I., Maslennikova, T.V., 2004, Acoustic microscopy methods in morphological study of the articular cartilage and subchondral bone. In: *"Acoustical Imaging", Proceed. 27-th Intern. Symp.*, vol. 27, Eds. W. Arnold, S. Hirsekorn, Kluwer Academic/Plenum Publishers, Dordrecht & New York, 535–541.
3. Finlay A.Y., Western B., Edwards C., 1990, Ultrasound velocity in human fingernail and effects of hydration: validation of in vivo nail thickness measurement techniques, *British Journal of Dermatology*, **123**, 365–373.
4. Jemec G.B.E., Serup J., 1989, Ultrasound structure of the human nail plate, *Archives of Dermatology*, **125**, 643–646.
5. Maev R.G., 2004, Recent advances in quantitative acoustic microscopy. In: *"Acoustical Imaging", Proceed. 27-th Intern. Symp.*, vol. 27, Eds. W. Arnold, S. Hirsekorn, Kluwer Academic/Plenum Publishers, Dordrecht & New York, 407–414.

OSTEOBLAST ADHESION OF BREAST CANCER CELLS WITH SCANNING ACOUSTIC MICROSCOPY

C. Miyasaka, R.R. Mercer, A.M. Mastro
Department of Physics, Idaho National Laboratory, Idaho Falls, ID 83415, USA;
Department of Biochemistry and Molecular Biology, 431S Frear, The Pennsylvania State University, University Park, PA16802, USA

Abstract: Conditioned medium was collected from a bone-metastatic breast cancer cell line, MDA-MB-231, and cultured with an immature osteoblast cell line, MC3T3-E1. Under these conditions the osteoblasts acquired a changed morphology and appeared to adhere in a different way to the substrate and to each other. To characterize cellular adhesion, MC3T3-E1 osteoblasts were cultured with or without MDA-MB-231 conditioned medium for two days. With mechanical scanning acoustic reflection microscopy, we were able to detect a change in the adhesive condition of the interface between the cell and the substrate, but not with optical microscopy

Key words: acoustic microscope, laser scanning confocal microscope, cellular adhesion, bone cancer, osteoblasts

1. INTRODUCTION

Once breast cancer has progressed to an advanced stage, it is likely to metastasize to bone, and is usually fatal. However, the process by which breast cancer affects bone tissue is poorly understood[1]. When breast cancer metastasizes to bone, the osteoclasts are constitutively activated, resulting in osteolytic lesions[2]. Kureja *et al* examined nude mice with bone metastasis, and found a significant decrease in bone formation[3]. Similar results have

M.P. André (ed.), Acoustical Imaging, 65–72.

also been reported elsewhere[3–5]. Therefore, these observations suggest that breast cancer cells affect osteoblasts in addition to osteoclasts.

When MC3T3-E1 osteoblasts were cultured in cancer cell condition medium, they took on a fibroblast-like morphology and exhibited adhesion characteristics different from those observed in normal medium. The osteoblasts were fixed and stained for actin visualization and for observation of the focal adhesion plaques with optical microscopy. However, since fixation kills the cells, some characteristics of the adhesion could be missed. On the other hand, an acoustic image formed by reflected ultrasonic waves is based on the elastic properties of the living cells. Therefore, fixing and staining are not required for mechanical scanning acoustic reflection microscopy[6] (hereinafter called simply "SAM"). Hence, living cells can be easily observed. Further, SAM allows observation not only of the surface but also of the internal structure of the specimen with sub-micrometer resolution[7–12]. This report presents the visualization of adhesive conditions of living osteoblasts grown on the substrate using SAM. The results are compared with those obtained with laser scanning confocal microscopy.

2. SPECIMENS

For the SAM experiments, MC3T3-E1 osteoblasts were plated at 10^4 cells/cm^2 in differentiation medium (MEM + 10% FBS, 50 ug/ml ascorbic acid, and 10 m, glycerophosphate) and incubated overnight. The following day, media were replaced with 50% 2x differentiation medium (MEM + 20% FBS, 100 ug/ml ascorbic acid, and 20 mM, glycerophosphate) plus 50% MDA-MB-231 conditioned medium or vehicle control medium (serum free medium). Cells were cultured in a humidified 37^o incubator containing 5% CO_2 and 95% air, receiving media changes every other day. For the laser scanning confocal microscopy experiments, cells were fixed in 4% paraformaldehyde and stained with either AlexaFluor 568 phalloidin (twenty minutes), or monoclonal anti-tubulin cy-3 conjugate (one hour).

3. SCANNING ACOUSTIC MICROSCOPY

Fig. 1 shows the local adhesion plaques visualized with interference reflection microscopy[13–15]. The focal adhesions as black spots are not clearly visualized. Further, the shapes of the cells are totally different from those of the living cells visualized with SAM. Our assumption is that the fixing procedure for the cells, when we try to observe the adhesive conditions with optical microscopy, may have an effect on the interface.

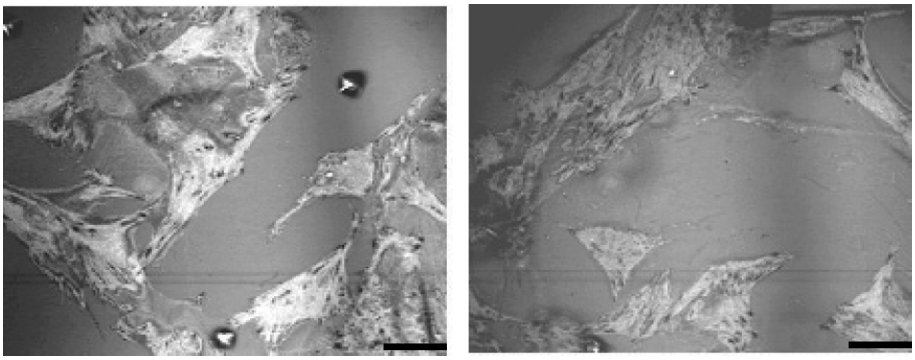

Figure 1. Focal adhesion plaques visualized with optical interference reflection microscopy. [Left] Vehicle Control MDA-MB-231; [Right] Conditioned Medium. Bar is 50 μm.

Osteoblasts are relatively thick (thickness range: 7~13 μm), so that the attenuation is too high to visualize the interface between the cells and the sapphire substrate with higher ultrasonic frequency such as 1.0 GHz in the culture liquid at the temperature of 37 °C. The frequency to visualize them is limited to approximately 600 MHz in this study (see Fig. 2).

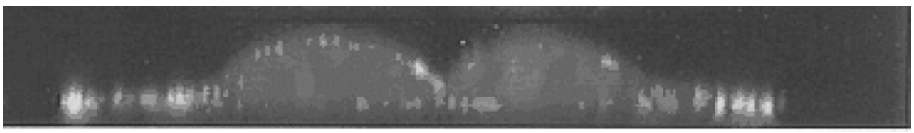

Figure 2. A vertical cross-sectional optical image for measuring the thickness of the cell. The average thickness of osteoblasts is typically 10 μm. Based on these images, we can select an appropriate frequency to observe the condition of the interface between the cell and the substrate with SAM.

The SAM instrument comprises a transmitting/receiving section, an X-Y scanning section, a Z scanning section, a computer section for controlling the SAM, and a display section for observing a specimen. The transmitting/receiving section includes a transmitter, a receiver having an amplifier, and a circulator. The X-Y scanning section comprises an X-Y stage including a temperature-controlled chamber for containing living cells grown on a substrate in a coupling medium (*i.e.*, a culture liquid). The Z scanning section includes a Z-stage and an acoustic lens. An electrical signal (*i.e.*, tone-burst wave) generated by a transmitter inputs to a

piezoelectric transducer (*i.e.*, zinc oxide), located on the top of a buffer rod through a circulator. The input voltage from the transmitter to the transducer is approximately 5V. The electrical signal is converted into an acoustic signal (*i.e*., ultrasonic plane wave) by the transducer. The ultrasonic plane wave travels through the buffer rod made of sapphire to a spherical recess (hereinafter called simply the "lens") located at the bottom of the buffer rod, wherein the lens is coated by the acoustic impedance matching layer which is a so-called "acoustic anti-reflection coating" made of silicon oxide (hereinafter called simply "AARC"). The lens converts the ultrasonic plane wave to an ultrasonic spherical wave (*i.e.*, ultrasonic beam).

The ultrasonic beam is focused within the cells grown on the substrate located at the bottom of the chamber, and reflected from the cells via the culture liquid. The temperature of the culture liquid is constantly maintained at 37 °C. The reflected ultrasonic beam, which carries acoustic information of the cells, is again converted into an ultrasonic plane wave by the lens. The ultrasonic plane wave returns to the transducer through the buffer rod. The ultrasonic plane wave is again converted into an electrical signal by the transducer. The voltage of the electrical signal ranges from 300 mV to 1 V. When the operating frequencies range from 100 MHz to 2.3 GHz, the corresponding values for the insertion loss range from approximately 30 dB to 80 dB. Therefore, the electrical signal must be amplified by 30 dB to 80 dB at a receiver. Furthermore, the electrical signal comprises transmission leaks, internal reflections from the interface between the lens and the AARC, and reflections from the specimen. Therefore, the reflections must be selected by a rectangular wave from a double balanced mixer (hereinafter called simply "DMB") that is so-called the "first gate." Then, the peak of the amplitude of the electrical signal is detected by a circuit, which includes a diode and a capacitor (*i.e.*, the peak detection technique). The gate noise is removed by using the second gate existing within the first gate (*i.e.*, the blanking technique). The peak-detected signal is stored into a memory through an analog-to-digital signal (hereinafter called simply "A/D") converter. The stored signal is again converted into an analog signal by a digital-to-analog signal (hereinafter called simply "D/A") converter. This flow of processes allows the information that is collected at a single spot on a cell to be displayed as intensity at a certain point on the CRT monitor.

In order to form a two-dimensional acoustic image, an acoustic lens and an X-Y stage are mechanically scanned across a certain area of the cells. The scanned area determines the magnification of the image. The acoustic lens is able to translate axially along the z direction to vary the distance between the cells and the lens for sub-surface visualization. That is, when visualizing the bottom of the cells, the acoustic lens is focused on the

substrate (we denote $z = 0$ μm), and when visualizing a subsurface of the cells, the acoustic lens is mechanically defocused toward the lens (we denote z = +x μm, where x is the defocused distance).

An acoustic beam (*i.e.*, spherical longitudinal wave) emitted from the lens via the culture liquid is focused onto the substrate in Fig. 3(a). The acoustic impedance of gas, such as air, is significantly lower than that of the cell. Therefore, theoretically, if the interface between the cell and the substrate has an adhesive problem (*e.g.*, a delamination), the acoustic wave will reflect strongly from the interface. The contact area having the adhesive problem is observed as a high intensity (white) region in the acoustic image. In Fig. 3(a), we can unclearly observe such areas. We can think of at least two reasons for this phenomenon; first, the acoustic impedance of the cell is close to that of the culture liquid; second, the gap may be too thin compared to the wavelength of the longitudinal ultrasonic beam.

Since the aperture angle of the lens is large (*i.e.*, 120°), we propose that we defocus the acoustic lens toward the substrate to generate a surface acoustic wave (SAW) when observing the adhesive problem at the interface. The wavelength of the SAW is substantially less than half of that of the longitudinal wave. Furthermore, the SAW is very sensitive to discontinuities. Therefore, we have an opportunity to see the adhesive problem at the interface.

Figs. 3(b), 3(c) and 3(d) show the adhesive problem (*i.e.*, "white" areas) at the interface that the conventional optical microscopy cannot visualize. In addition, we can see some internal details of the cells.

4. CONCLUSIONS

There are at least two important results in this study. One is that the SAM has the advantage of allowing surface and subsurface imaging of biological living cells. Comparison with the images obtained with optical microscopy shows astonishing differences because the staining and fixing process appears to dramatically deform the cells. Another is that the defocusing of the acoustic lens toward to the substrate brings out many important features in the cell imaging. This is seen in part as a result of constructive interference between longitudinal and leaky surface waves which agrees with the well known V(z) curve theory[16–18].

We have been successful in evaluating an adhesive portion between a cell and a substrate with a mechanically scanned acoustic image. However, the

image could not provide much physical and quantitative information. Work at the Idaho National Laboratory (INL) is ongoing utilizing laser based ultrasonic microscopy to form images of the ultrasonic motion resulting from the SAM. This method forms images of the ultrasonic waves traversing within the cell, and can allow a direct measurement of the ultrasonic wave propagation caused by the cellular structures.

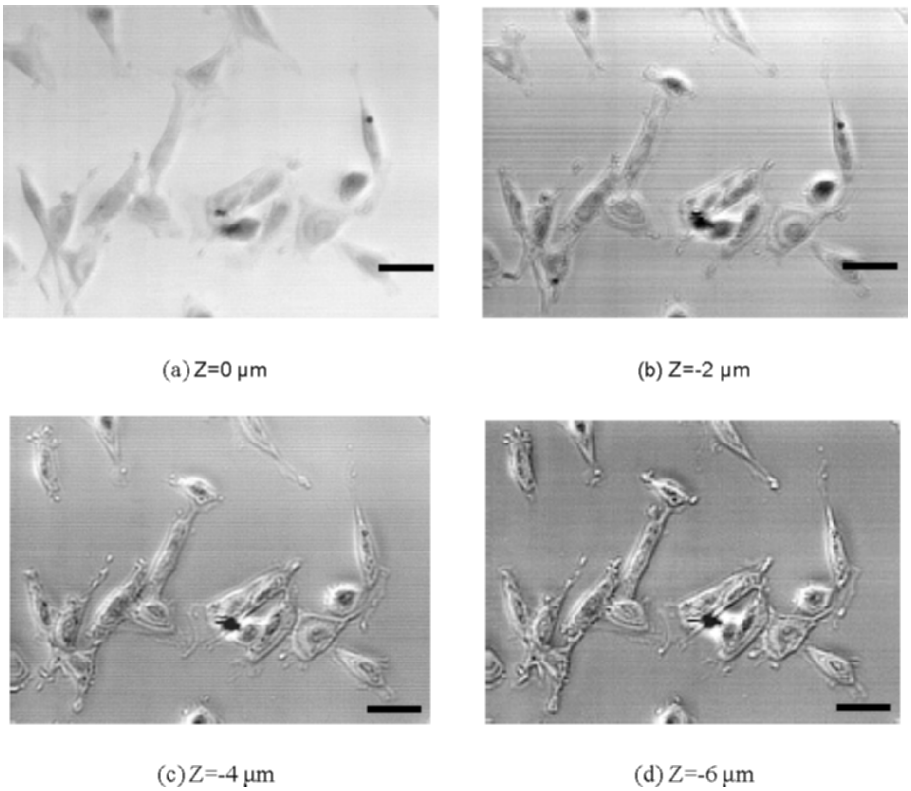

Figure 3. SAM images of MC3T3-E1 osteoblasts cultured with 50% MDA-MB-231 conditioned medium for 2 days. Bar is 50 µm.

5. ACKNOWLEDGEMENT

Robin. R. Mercer was supported by a pre-doctoral grant from the US Army Medical Research Materiel Command under DAMD 17-02-1-0358. Research was supported in part by a Biotechnology Grant, Life Sciences Consortium, the Pennsylvania State University, PA Tobacco Settlement

Fund, the National Foundation for Cancer Research, Center for Metastasis Research, the USMC Research university that resides at the Pennsylvania State University under Contract M67004-99-0-0037, U.S. Department of Energy, Office Basic Energy Sciences, Materials and Engineering Physics under DOE Idaho Operations Office Contract DE-AC07-99ID13727.

REFERENCES

1. S.H. Landis, T. Murray, S. Bolden, P.A. Wingo. Cancer statistics, CA Cancer J Clin 49(1), 31, pp. 8–31, 1999.
2. C.S. Galasko, Mechanisms of lytic and blastic metastatic disease of bone, *Clin Orthop* (169), pp. 20–27, 1982.
3. P.D. Delmas, B. Demiaux, L. Malaval, M.C. Chapuy, C. Edouard, P.J. Meunier, "Serum bone gamma carboxyglutamic acid-containing protein in primary hyperparathyroidism and in malignant hypercalcemia. Comparison with bone histomorphometry," *J Clin Invest* 77(3), pp. 985–991, 1986.
4. A.F Stewart, A. Vignery, A. Silverglate, N.D. Ravin, V. LiVolsi, A.E. Broadus, R. Baron, "Quantitative bone histomorphometry in humoral hypercalcemia of malignancy: uncoupling of bone cell activity." *J Clin Endocrinol Metab* 55(2), pp. 219–227, 1982.
5. T. Taube, I. Elomaa, C. Blomqvist, M.N. Beneton, J.A. Kanis, "Histomorphometric evidence for osteoclast-mediated bone resorption in metastatic breast cancer," *Bone* 15(2):161–166, 1994.
6. A. Atalar, C.F. Quate, H.K. Wickramasinge, "Phase imaging in reflection with acoustic microscope," *Appl. Phys. Lett.*, **31**, p. 791, 1977.
7. J.A. Hildebrand, D. Rugar, R.N. Johnston, C.F. Quate, "Acoustic microscopy of living cells," *Proc. National Academy of Science*, **78(3)**, p. 1656, 1981.
8. J.A. Hildebrand, "Observation of Cell-Substrate Attachment with the Acoustic Microscope," IEEE Transction on Sonic and Ultrasonics, Vol. SU-32, No. 2, pp. 332–340, 1985.
9. J. Bereiter-Hahn, "Scanning acoustic microscopy visualizes cytomechanical responses to cytochalasin D," *J. Microsc*. **146**, p. 29, 1986.
10. J. Bereiter-Hahn, H. Lüers, "Shape changes and force distribution in locomoting cells. Investigation with reflected light and acoustic microscopy," *Eur. J. Cell Biol.* **53**: Suppl. 31, p. 85, 1990.
11. B.R. Tittmann, C. Miyasaka, "Imaging and Quantitative Data Acquisition of Biological Cells and Soft Tissues with Scanning Acoustic Microscopy". In *Science, Technology and Education of Microscopy: An Overview.* Fomatex: Badajoz, Spain, p. 325, 2003.
12. B.R. Tittmann, C. Miyasaka, "Thermal and Acoustical Insult to Cells as Studied by In-Vivo Acoustic Microscopy," Presented at the 2002 ASME Pressure Vessels and Piping Conference, Aug. 4–8, Vancouver, British Columbia. *NDE Engineering: Applications* edited by G. Ramirez, C. Miyasaka, and O. Hedden, PVP-Vol. 450, NDE-Vol. 22, The American Society of Mechanical Engineers, New York, NY, p. 43, 2002.
13. D. Gingel, I. Todd, "Interference Reflection Microscopy: A Quantitative Theory for Image Interpretation and its Application to Cell-Substrate Separation Measurement, " *Byophys.* J., Vol. 26, pp. 507–526, 1979.
14. J. Bereiter-Hahn, C.H. Fox, B. Thorell, "Quantitative Reflection Contrast Microscopy of Living Cells," *J. Cell Biol.* Vol. 82, pp. 767–779, 1979.

15. R. Mercer, C. Miyasaka, A.M. Mastro, "Metastatic Brest Cancer Cells Suppress Osteoblast Adhesion and Differentiation," Clinical and Experimental Metastasis. (in Press).
16. R.D. Weglein: "A model for predicting acoustic materials signatures", *Appl. Phys. Lett.*, Vol. 34, pp. 179 – 181, (1979).
17. W. Parmon, and H.L. Bertoni: "Ray interpretation of the material signature in the acoustic microscope", *Electron. Lett.*, Vol. 15, pp. 684–686, (1979).
18. A. Atalar: "An angular spectrum approach to contrast in reflection acoustic microscopy", *J. Appl. Phys.*, Vol. 49, pp. 5130 – 5139, (1978).

MEASURING CELL VOLUME REGULATION WITH TIME RESOLVED ACOUSTIC MICROSCOPY

E.C. Weiss, F. Wehner, R.M. Lemor
Fraunhofer-Insitute for Biomedical Technology, Biomedical Ultrasound Research, Ensheimer Strasse 48, St.Ingbert, Germany;
Max-Planck-Insitute for Molecular Physiology, Otto Hahn Strasse 11, Dortmund, Germany

Abstract: Cell volume regulation in biological systems is of key significance for a variety of physiological processes including apoptosis and proliferation. Many different methods like scanning confocal laser microscopy, light scattering and the coulter method are used to measure the cell volume. Major limitations of these techniques are a rather high error, a low time resolution, the limitation to certain experimental conditions and, possibly, photo damage of cells. This contribution describes the potency of time resolved acoustic microscopy for measuring the cell volume. The major advantages of acoustic microscopy for cell volume measurement are the high accuracy, the absence of any radiation damage and photobleaching and the opportunity to use non-transparent samples and substrates

Key words: Cell volume measurement; cell volume regulation; time resolved acoustic microscopy

1. INTRODUCTION

Regulation of cell volume is a fundamental mechanism of cell homeostasis. Moreover, it plays key roles in a variety of cell physiological processes like the coordination of transepithelial transport, cell locomotion, gene expression, the triggering of metabolic processes in the liver as well

M.P. André (ed.), Acoustical Imaging, 73–80.

as the interplay between cell proliferation and apoptosis[1]. To carefully investigate the physiology and pathology associated with cell volume regulation, a technique that allows the quantitative and high-resolution characterization of cell volume while retaining cell functionality is a prerequisite[2].

Many different methods are currently used to measure the cell volume. A first group of techniques is based on the continuous monitoring of the intracellular concentration of loaded reagents (fluorescent dyes) or ions. The concentration of these intracellular markers depends on the amount of cell water, and thus changes whenever cell water volume is altered. By monitoring these concentrations the relative changes in cell water volume can be determined.

Some investigators determine the volume of spherical cells by classical light microscopy; others use impedance analysis on cell suspensions. In all instances, however, these techniques are limited to special experimental conditions, i.e. they are only applicable to cells of nearly spherical shape in suspension.

Light microscopy methods, such as video-enhanced contrast optical microscopy, light microscopy with spatial filtering, and laser light-scattering systems have been used to estimate cell shape and cell volume. The most accurate optical method consists of fluorescence labelling of the cytoplasma or the cell membrane and using confocal laser scanning microscopy (CLSM). Image sets of thin optical sections across the cell are obtained. A three dimensional model of an individual cell is then reconstructed from these images.

Yet, photodynamic damage to the biological sample remains a serious problem of any method using light especially with high intensity laser confocal microscopy. In many instances, the need for sample or substrate transparency limits the use of optical methods further e.g. when cell growth requires special substrate conditions.

Acoustic reflection microscopy was proposed[3] as a method to access the cell volume with high accuracy and high temporal resolution without inflicting photodynamic damage to the cell[4]. The method is base on the fact that, in addition to the acoustic echo from the substrate on which the cells are grown, an echo at the front surface of the cell occurs. In narrowband acoustic microscopy the local cell height can be deduced from interference fringes, which are generated by interference of the front echo of the cell and the substrate echo.

However, since the actual interference depends on the distance in terms of wavelength between front and substrate it also depends on the local sound speed in the cell, which reduces the accuracy of this method considerably.

In this report we propose the use of time resolved acoustic reflection microscopy to measure the cell volume. In this mode, the echo from the cell surface can clearly be separated from the substrate echo. The cell height can be deduced from the local distance of the cell surface to the acoustic lens.

2. METHODS

2.1 Time Resolved Acoustic Microscopy

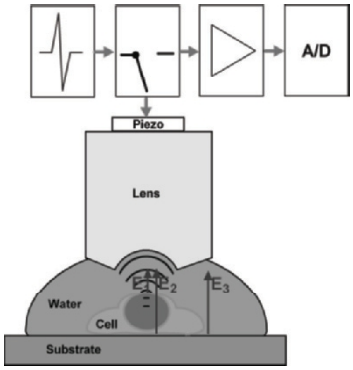

Figure 1. Setup for time resolved acoustic microscopy of single cells.

To measure the cell volume we use a time resolved acoustic microscope with broadband excitation as shown in Figure 1. A short electric pulse with 1 ns duration is generated and a piezoelectric thin film converts the electrical current to an acoustic wave travelling through the sapphire rod of the acoustic lens. The acoustic waves are focussed onto the cell grown on a substrate by a small round cavity in the sapphire. A reflection occurs at the top surface of the cell and at the substrate. The acoustic waves travelling back to the lens are focussed onto the piezoelectric transducer and converted into electrical current. The amplified radio frequency signal is digitized using a fast analogue to digital converter and transferred to a personal computer.

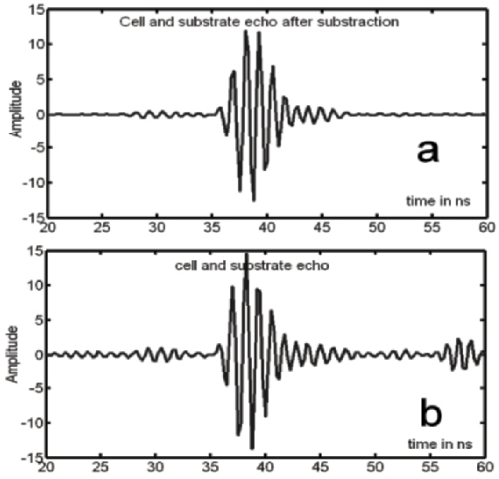

Figure 2. a) rf-Signal from a L-929 fibroblast at 1 GHz after subtraction of static echoes b) the original unprocessed signal.

Up to 5000 signals are recorded at every position and averaged to reach the needed signal to noise ratio to clearly resolve the front echo.

Additional echoes that are comparable in magnitude to the front echo arise from reflection of the excitation pulse inside the rf-chain of the microscope due to impedance mismatches and from internal reflections inside the sapphire rod. Therefore these echoes are static and can be eliminated by subtracting a pre-recorded transient from the actual transient as shown in Figure 2. The front echo of the cell becomes clearly visible before the large substrate echo.

2.2 Measurement Time

The measurement time is mostly depending on the number of points to be recorded and the number of averages needed to achieve the signal to noise ratio. A maximum pulse repetition rate of 1 MHz is feasible with currently available lenses and electronics. Therefore, a single measurement at a single position takes 1 ms to 5 ms for 1000 to 5000 fold averaging.

The time to transfer the data from a single point to the computer is 2 ms to 10 ms. Additional time is required to move the lens to the next measuring position. This amounts to some ms but can actually be achieved in parallel to the data transfer. This gives minimal recording time from 3 to 15 ms per point resulting in a maximum of 300 points that can be measured per second. Around 5000 points are needed to cover the area of a single cell which may amount to up to 60 µm times 60 µm when scanning the full rectangle area

evenly spaced with a step size of 0.8 µm which is approx. equivalent to the spot size of a 1 GHz lens.

As shown in Figure 3, most of the pixels are not within the cell surface area and therefore are not necessary to measure the cell volume. Using a programmable scanner and synchronous optical microscopy[5] to cover only the points necessary, the scan time can be reduced to approx. 5 s for the total determination of cell volume.

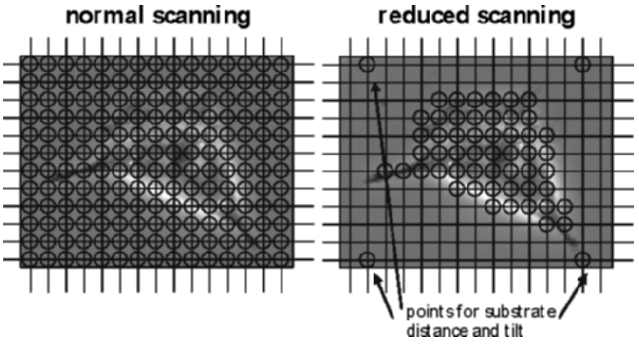

Figure 3. Using a programmable scanner to decrease scanning time.

2.3 Volume Reconstruction using B-Scans

From all transients recorded along a mechanical scan line brightness mode (b-mode) images similar to images used in medical ultrasound can be generated by using hilbert reconstruction of the amplitude signals of the received radio frequency signals and converting the amplitude values to greyscale values. These b-mode scans are used to reconstruct the surface of the cell using commercial software.

3. MATERIALS

To prove the feasibility of the proposed method L-929 fibroblast were grown on glass cover slips. The cells were either fixed using a 3.7% formalin solution or left untreated. Unfixed cells were kept in a Hepes buffered physiological solution with additional glucose.

Records were taken from single cells on the substrate with a 1 GHz 100° acoustic lens at room temperature (22 °C). 70 by 70 pixel with a pixel distance of 0.8 µm were recorded. The radio frequency signal was digitized with a sample rate of 4GS/s and a resolution of 8bit with a maximum upper

frequency of 1.1 GHz. A 3000 fold averaging was used and a pre-recorded echo transient was subtracted to reduce the unwanted spurious echoes. The surface was reconstructed using brightness scans and the amira (Indeed, Germany) software package.

4. RESULTS

Figure 4 shows brightness-mode scans from different positions of a fixed L-929 fibroblast. The surface echoes of the cell are clearly visible but the thin areas of the cell, especially the lamellopodium, can not be resolved due to the large substrate echo. The brightness of the surface echo varies greatly over the cell area and sometimes the echo is barely detectable. This renders advanced surface reconstruction mandatory.

Figure 5 shows the reconstructed surface of the same cell. Now even the thin areas are detectable which could not be resolved in the simple brightness-mode scans. Figure 6 shows the same results for a living L-929 fibroblast.

For three different cells the absolute volume could be measured from the reconstructed surfaces yielding values of 2460 μm^3, 3282 μm^3 and 2133 μm^3.

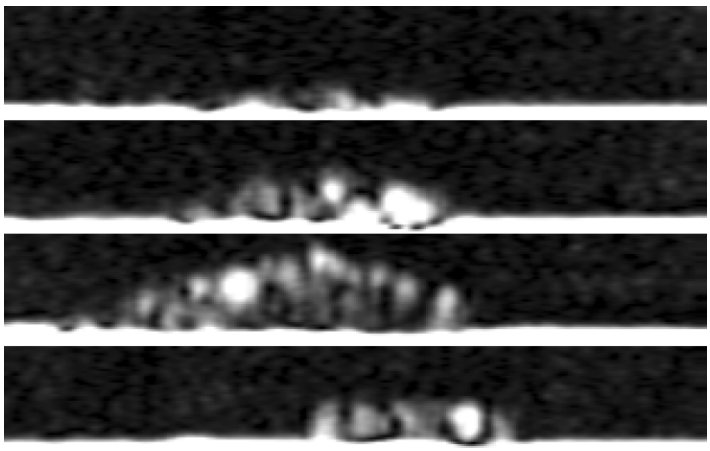

Figure 4. Brightness-Scans of a fixed L-929 fibroblast at different positions showing the surface reflection. Image dimensions are 6 µm by 56 µm.

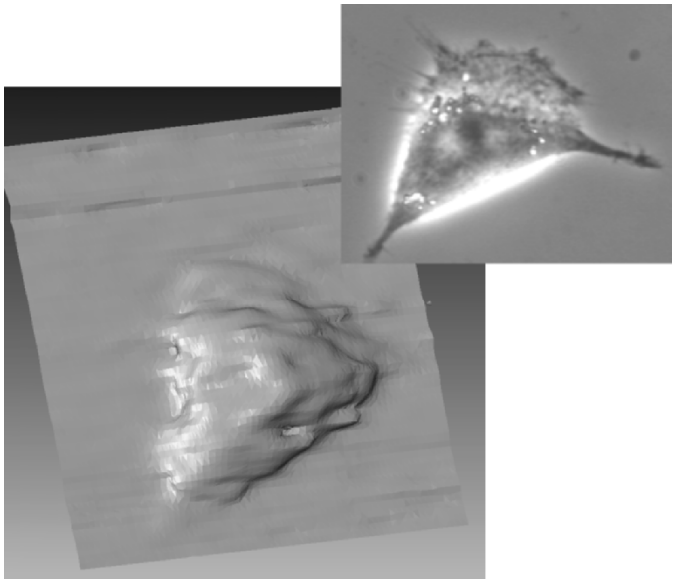

Figure 5. Surface Reconstruction of fixed L-929 fibroblast using brightness-scans. The small inset shows the optical phase contrast image of the same cell.

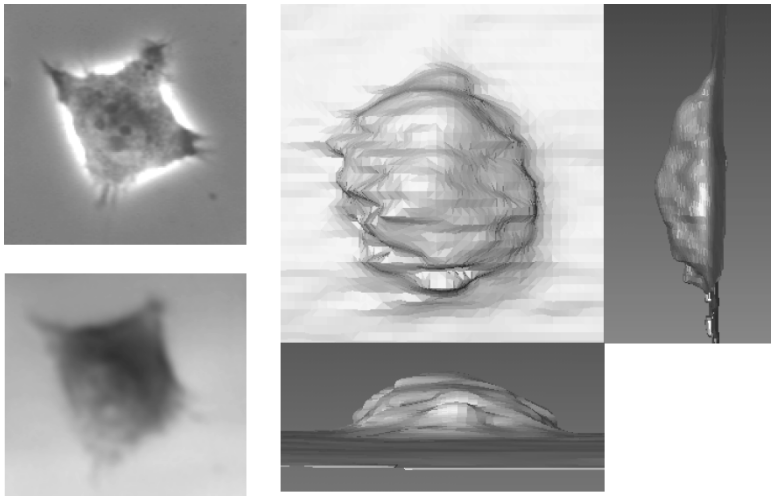

Figure 6. Surface Reconstruction of a living L-929 fibroblast. The upper left image shows the optical phase contrast image. The bottom left image is the acoustic image while on the right side the top and side views of the reconstructed surface using brightness-mode scans are shown. The acoustic image dimension are 56 µm by 56 µm.

5. DISCUSSION

In this report we show that time resolved acoustic microscopy together with surface reconstruction techniques is a powerful tool for long-term measurements of cell volumes. No fluorescent dyes are needed and no irradiation damage of cells is detectable, which is the major advantage of this technique. The measuring time for a single determination of cell volume is approximately 5 s which is comparable to high speed confocal laser scanning microscopes.

The lateral resolution of acoustic microscopy at 1 GHz is somewhat smaller than that of optical microscopy. The axial resolution, however, is much higher and may considerably be further increased by using the radio frequency data and interpolation techniques. With an additional surface reconstruction algorithm, which is currently developed in our laboratory, time resolved acoustic microscopy will achieve an accuracy comparable to high-resolution confocal laser scanning microscopy.

REFERENCES

1. Wehner F, Sauer H, Kinne RKH, Hypertonic stress increases the Na^{2+} conductance of rat hepatocytes in primary culture. J. Gen. Physiol. 105, 507–535 (1995)
2. Wehner F, Olsen H, Tinel H, Kinne-Saffran E, Kinne RK, Cell volume regulation: osmolytes, osmolyte transport, and signal transduction, Rev Physiol Biochem Pharmacol. 2003; 148:1–80
3. Litniewski J, Bereither-Hahn J, Measurement of cells in culture by scanning acoustic microscopy, Journal of Microscopy, Vol. 158, April 1990, pp. 95–107
4. Briggs GAD, Wang J, Gundle R, Quantitative acoustic microscopy of individual living human cells, Journal of Microscopy Vol. 172:3–12, (1993)
5. Lemor R, Pilarczyk G, Westphal I, Weiss EC, Combination of acoustic and optical microscopy for investigation of biological cell properties, in Acoustical Imaging, Vol. 27, Edited by W. Arnold and S. Hirsekorn, Kluwer Academic/Plenum Publishers, Dordrecht & New York, pp. 563–572 (2004)

FUNDAMENTAL POTENTIAL FOR ACOUSTIC MICROSCOPY EVALUATION OF DENTAL TISSUES

L.A. Denisova, R.Gr. Maev, F.S. Rusanov, A.R. Maeva, A.F. Denisov, D.Yu. Gavrilov, E.Yu. Bakulin, F.M. Severin
Windsor University, Dept. of Physics, 401, Sunset ave., Windsor, Ontario, N9B 3P4, Canada; Emanuel's Institute for biochemical problems, RAS, Moscow, Russia

Abstract: Comprehensive analysis of the present-day acoustic microscopy experimental approaches from the standpoint of their potential application in dental research and diagnostics has been performed. Whole extracted human teeth and specially prepared dental tissue samples have been investigated. The results of the study demonstrate that there are several experimental techniques that can be used for precise quantitative evaluation of the tissues local mechanical properties in flat-parallel teeth slices, for the pathomorphological investigation of the tissues strength spatial distribution in flat cuts. In the whole tooth, the acoustic microscopy techniques allow us to precisely measure the enamel and dentine layers thickness, the distance between the external surface and pulp, to reveal hidden caries and restoration disbonding. These opportunities form a real ground for the further design of the special acousto-microscopical methods and new equipment for the clinical diagnostics

Key words: acoustic microscopy, focused ultrasound, human tooth, dentin, enamel, caries, tissue micromechanics

1. INTRODUCTION

The significance of developing acoustic microscopy approaches for the application in the dental tissues investigation is based on several positions: 1) ultrasound, with the parameters used (low intensity, high frequency), has no substantial harmful effects upon living organisms – we mean patient and personnel; 2) ultrasonic techniques allow us to conduct investigation in a reflection mode, therefore 1-side access is sufficient; 3) the visual images of

M.P. André (ed.), Acoustical Imaging, 81–88.

the internal structures can be obtained at any depth without reciprocal superimposition; 4) ultrasonic wave yields information concerning local elastic-mechanical properties, which is of paramount importance with regard to the hard dental tissue, whose main function is a mechanical one. A number of studies on this subject has been conducted from 1963 till present. S. Lees, S.D.Peck, G.A.D.Briggs, J.Kushibiki, et al., among others, have made the significant contributions. A detailed review of the results obtained at that period was presented in our previous papers (Maev, et al., 2000, 2002). The aim of the present study is to reconsider the acoustic microscopy potential value for dental diagnostics with regards to the last achievements in this field.

2. MATERIALS AND METHODS

The experimental studies have been conducted with human teeth extracted for orthodontic reasons. One experiment has been conducted with dog's teeth, obtained from a veterinary clinic. Whole teeth, flat-parallel slices and specially prepared model samples have been used. Ultrasound investigations have been performed using ELSAM (Leitz, Germany) and 2 short-pulse scanning acoustic microscopes: "SONIX" (Sonoscan Ltd, USA) and "Tessonix" (designed by Maev, R.G).

3. RESULTS AND DISCUSSION

Since our experiments have been conducted from 5 hours to 3–4 days after extraction, it is important to clarify how the storage conditions influence acoustic properties of tooth tissue. For this reason, flat-parallel longitudinal human teeth sections (thickness 1.2–1.5 mm) have been prepared in 2–5 hours after extraction; the ultrasound time-of-flight and the sample thickness in the corresponding locations have immediately been measured in 10–12 areas on each sample. After that, the samples have been placed into 50 ml of water, physiological solution, formalin or ethyl alcohol, and stored in a refrigerator at 4 °C. The measurements of the ultrasound time-of-flight and local sample thickness have been repeated 24 hours and 5 days after the first procedure. The results presented in Table 1 demonstrate that no significant changes occur in acoustical properties of teeth during short (up to 5 days) storage in any of the investigated liquid media.

Table 1. Longitudinal ultrasound velocity in the hard dental tissues during the storage in different liquid media, mean and standard deviation.

Storage media		Number of samples	Ultrasound Velocity, m/s		
			Storage duration		
			Control	1 day	5 days
Distilled water	Enamel	12	5870 ± 190	5860 ± 210	5850 ± 240
	Dentin	12	4030 ± 240	4020 ± 260	4000 ± 220
0.9% NaCl with thymol	Enamel	12	5900 ± 170	5920 ± 170	5910 ± 180
	Dentin	12	3980 ± 130	4000 ± 120	4000 ± 160
Neutral 10% formalin (pH=7.2)	Enamel	12	5960 ± 190	6150 ± 280	6160 ± 240
	Dentin	12	4350 ± 180	4550 ± 290	4590 ± 320
Ethyl alcohol, 40%	Enamel	12	5900 ± 130	6060 ± 160	6050 ± 170
	Dentin	12	4280 ± 180	4550 ± 190	4580 ± 180

The second part of the study has to clarify anisotropy manifestation in enamel and dentin as well as to evaluate the possible role of the anatomical status. For this purpose, the flat-parallel sections of dogs' teeth, prepared in longitudinal and transversal planes, have been investigated separately for 4 different teeth groups. The results of this part of the study (Table 2) show that there are no expressed differences between acoustical properties of enamel and dentin in the teeth, belonging to different anatomical groups.

Table 2. Longitudinal ultrasound velocity (m/s) in dog's hard dental tissues.

Tissue		Type of teeth			
		Incisors, n=8	Canine, n=4	Premolars, n=8	Molars, n=8
Trans-versal sections	Enamel	4750 ± 220	4920 ± 190	4630 ± 240	4900 ± 200
	Dentin in bulk	3200 ± 240	3440 ± 200	3300 ± 170	3600 ± 190
	Peripulp. dentin	2740 ± 170	2890 ± 230	2680 ± 180	2900 ± 220
Longi-tudinal sections	Enamel	4720 ± 170	4900 ± 280	4580 ± 280	4820 ± 210
	Dentin in bulk	3120 ± 260	3460 ± 220	3280 ± 250	3500 ± 190
	Peripulp. dentin	2580 ± 220	2780 ± 260	2800 ± 260	2890 ± 250

Also, no significant distinction has been found between ultrasound velocity values in longitudinal and transversal sections, therefore at the frequency 50 MHz the direction of enamel rods or dentin canals does not substantially contribute to the acoustic signal traveling inside the tooth. So far, one can presume that heterogeneous hydroxyapatite crystals distribution in enamel

rods and around dentin canals in its morphology resembles isotropic fine-grained composite.

The aim of the next part of the study has been to investigate the spatial distribution of acoustic impedance variations in the flat surface of the transversal or longitudinal cuts of human teeth. Fig. 1A and 1B show the acoustical images of the surface of the human teeth longitudinal slices in the area of caries.

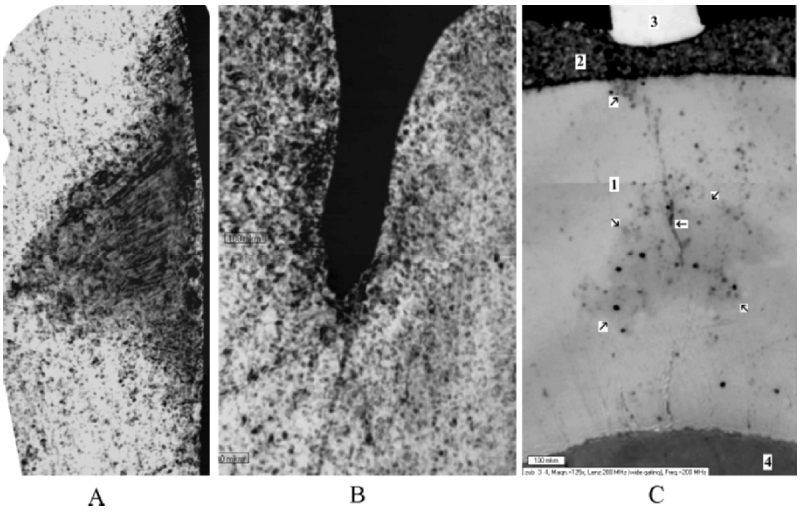

Figure 1. Acoustic images (200 MHz) of the surfaces of the sections of the teeth in the area of white spot caries lesion (A), fissure caries (B) and enamel changes under the bracket leg (C). 1-enamel, 2 – siller, 3 – bracket, 4 – dentin.

One can see that in the area of the carious lesion the acoustic impedance is lower than in the sound enamel. It is typical that the external surface of the tooth above the carious lesion is denser than in the central part of the carious tissue. In accordance with that, we can see that there is a thin layer with high acoustic impedance at the surface of the tooth over the carious enamel. Comparative morphometric analysis of the same slices in the light and acoustic microscopes reveals that in the acoustical image the carious lesions always have larger dimensions than in the optical image. The difference can achieve 20–30%. That is in good agreement with the earlier findings of Peck and Briggs (1987). This fact demonstrates that the changes of the mechanical properties of enamel or dentin in pathological conditions can be expressed more obviously than the changes of physical density. Due to that, particularly in the acoustic images, we can find early manifestations of pathological changes in enamel or dentin, which cannot be revealed by any other methods. One of the examples is presented in Fig. 1C. We can see fine

changes developed in the enamel under the attached bracket. A crack (indicated with the horizontal arrow) spreads across the enamel layer and acoustic impedance of the enamel around this crack is lower (oblique arrows). In our previous study it was shown that acoustic impedance correlates with mineral content and mechanical strength of hard biological tissues. Therefore, decreasing impedance is evidence of early mechanical properties changes of the enamel under the area of the bracket attachment.

A series of experimental studies have been conducted using special samples with one side polished to a flat condition. This allows us to evaluate the possible artifacts that curved internal tooth cavities could produce in the process of the acoustical imaging. The images obtained with the acoustic microscope (Fig. 2.1–2.4) have been compared with the structures revealed after transversal or longitudinal dissection of the teeth. The comparison confirms that there is no significant distortion and we can nondestructively determine the distribution of filling materials inside the dental channel. Experiments on the acoustical imaging of flat samples demonstrate that in spite of the curved shape of internal structures, the distortion is not dramatic and an acoustic microscope enables one to reveal some internal structures with good correspondence to the real microanatomy.

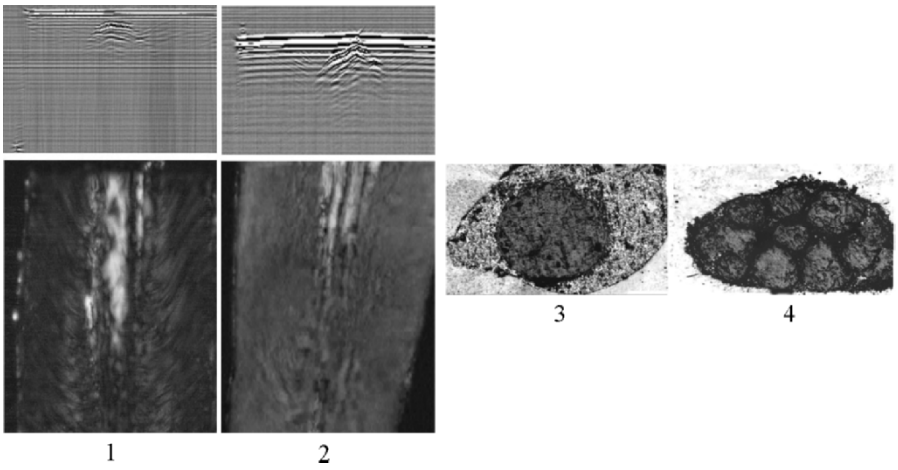

Figure 2. B- and C-scans of the teeth in the area of the root filled with one large (1) or several small (2) gutta-percha posts; C-scans obtained at the depth 1 mm under the surface correspond to longitudinal sections of the teeth roots through the channels, 50 MHz. (3) and (4) - the gutta-percha posts position inside root channels in the transversal sections.

The next experiments have been performed with whole teeth without preparing any grinded flat surfaces. In Fig. 3 there are two B-scans obtained from the intact enamel of the tooth. In the lower B-scan the normal enamel

layer and a good enamel-dentin interface are presented, in the upper B-scan the thinner enamel and additional reflections at the dentin-enamel interface can be detected. After the examination in the acoustic microscope, the tooth has been cut longitudinally and a hidden carious cavity has been found (Fig. 3, below), which confirms the acoustic microscope sensitivity to such kind of dental pathology.

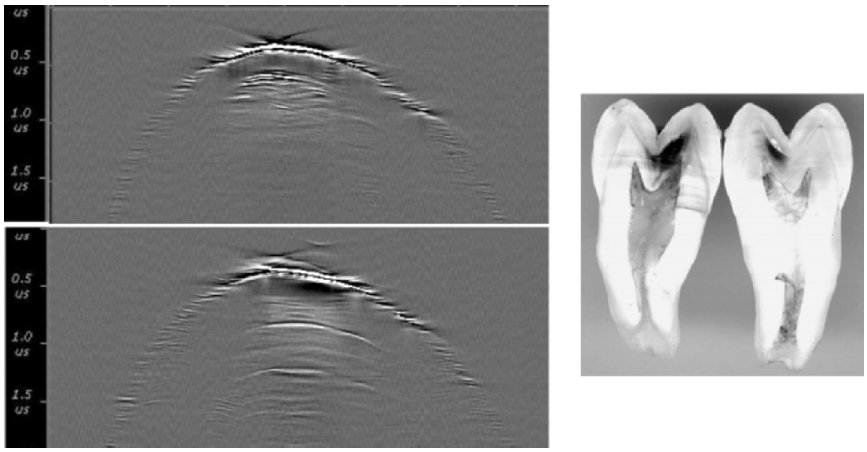

Figure 3. B-scans (50 MHz) of the tooth with a hidden caries, obtained from the side of the intact enamel (above) in comparison with optic images of the same tooth after its sectioning.

In the process of the preparation of a tooth for the crown mounting or the preparation of a cavity for the restoration, it is particularly important to evaluate a precise distance from the processing surface to the pulp chamber to prevent pulp injury. Using X-ray image (Fig. 4.1–4.3) of the tooth prepared for the crown mounting one can determine the approximate pulp chamber shape, but cannot measure the distance to the pulp. Scanning that tooth in the acoustic microscope enables one to reveal the shape of the pulp chamber as it is, at any depth under the surface either in C- or in B-scan mode.

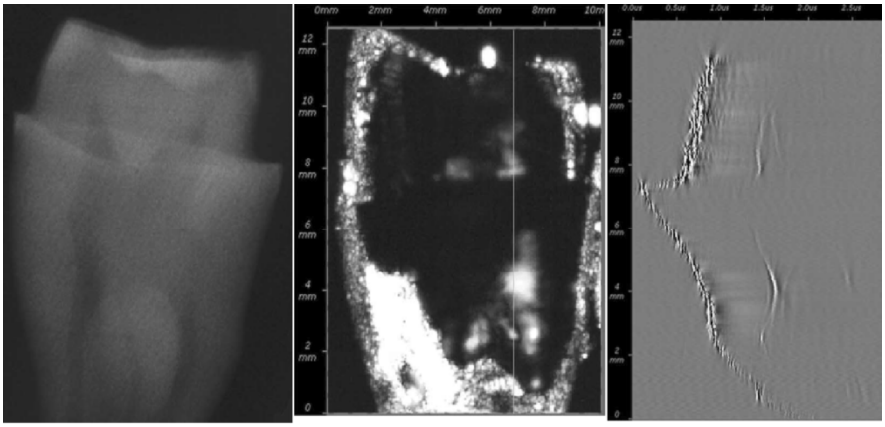

Figure 4. X-ray image of the tooth with the partly removed tissues prepared for the crown mounting (1), C-scan of the same tooth at the depth 2 mm, in which pulp chamber and root channels can be seen (2). The light vertical line (2) indicates the B-scan (3) position; 50 MHz.

Scanning a tooth with 2 different restorations (Hybrid and Microfil), we have managed to demonstrate, that acoustic microscope enables one to obtain a visual image of the dental restorative material's disbond (Fig. 5.1 and 5.3).

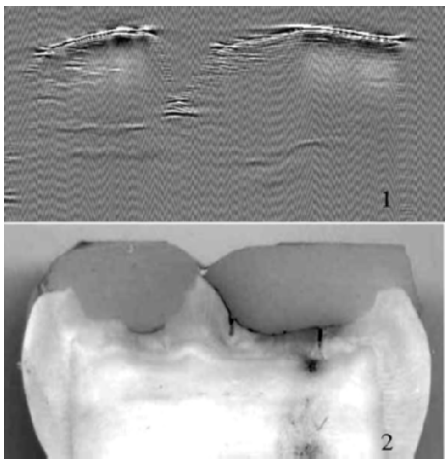

Figure 5. B-scan, 50 MHz (1), obtained from the masticatory surface of the whole molar in comparison with the real structure in the section (2).

4. CONCLUSION

The results obtained show that in the whole extracted tooth, the focused ultrasound can easily determine the thickness of enamel and dentine, the distance from the tooth's surface to the pulp cavity, and reveal deep-seated carious cavities under the enamel. In some cases, acoustic microscopy enables one to obtain a visual image of the dental restorative material's disbond. The results of the study demonstrate that acoustic microscopy provides new promising approaches for the evaluation of dental tissues either with slices and specially prepared samples or on the whole tooth. These new approaches could be useful for pathomorphological analysis of an extracted tooth in flat-parallel slices or in the surface of transversal or longitudinal cuts. Acoustic microscopy methods turn out to be valuable methods for dental materials research, especially for the investigation of the dental restorative materials interaction with the tooth's tissues. It also is a promising base for the development of new devices and methods for clinical dental diagnostics.

REFERENCES

1. Maev R.G., Denisova L.A., Maeva E.Yu., Denisov A.F. (2000) Mineralized tooth tissue study using scanning of acoustic microscopy. Proceedings of the 25th International Acoustical Imaging Symposium, Bristol, UK, Kluwer Academic/Plenum Publishers, v.25, 501–506.
2. Maev R.G., Denisova L.A., Maeva E.Yu., Denissov A.A. (2002) New data on histology and physico-mechanical properties of human tooth obtained with acoustic microscopy. *Ultrason.Med.Bio.*, **28**, 1:131–136.
3. Peck S.D., Briggs G.A.D. The caries lesion under the scanning acoustic microscope (1987) Adv. Dent. Res., v.1, No. 1, 50–63.

COMPONENTS AND SYSTEMS

PERFORMANCE IMPROVEMENT OF ALGORITHMS BASED ON THE SYNTHETIC APERTURE FOCUSING TECHNIQUE

P. Acevedo, A. Sotomayor, E. Moreno
DISCA-IIMAS.Universidad Nacional Autónoma de México. Apdo. Postal 20-726 Admon. No. 20, 01000, México, D.F. México; CENUS, Instituto de Cibernética Matemáticas y Física, Cuba. Calle 15 No. 551, Vedado, La Habana, 10 400, Cuba

Abstract: An analysis to improve the performance of the ultrasonic synthetic aperture focusing technique (SAFT) on a PC platform is presented in this paper. Some useful processing techniques like apodization, dynamic focusing, envelope detection and image composition are used to improve the quality of the image. Finally, results of the algorithm implemented using MATLAB and C/C++ and the respective images are presented

Key words: Synthetic aperture focusing, ultrasonic imaging, data processing

1. INTRODUCTION

Synthetic Aperture Focusing Technique (SAFT) has become popular in the field of ultrasonic imaging. Basically, this technique, which constitutes a reception focusing technique, can be based mainly on software; therefore, hardware needs are minimal. A more detailed physical description of this technique and comparison with some other conventional focusing techniques may be consulted in references [1,2].

The general operating principal is shown in figure 1[1,2]. It is observed that there is only one electronic processing chain for transmission and reception that is shared by all the elements of the array using a multiplexer.

M.P. André (ed.), Acoustical Imaging, 91–99.

SAFT allows the sequential capture of signals from the transducer substituting the necessary parallelism for the acquisition and processing of a signal from an array.

Using this technique we are able to acquire signals with a broad range of information and when we apply focusing algorithms we are able to discriminate specific information from different space regions.

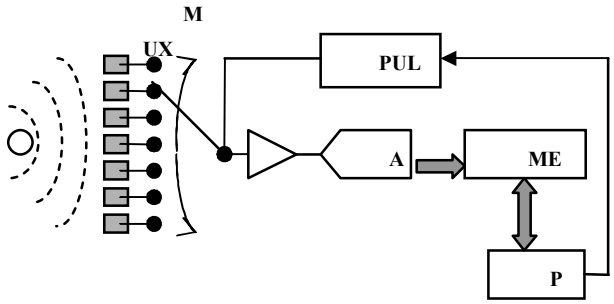

Figure 1. Diagram of the electronic implementation of SAFT [1].

This information allows obtaining images with a good lateral resolution but with the disadvantage of being more sensitive to the influence of sidelobes, which produce unwanted distortion [1, 3].

2. FOCUSING USING THE VIRTUAL ELEMENT MODEL

The virtual element is modeled as a spherical wave supply with a certain aperture angle as it is shown in figure 2. The divergence angle can be approximately expressed as [4]:

$$\frac{\beta}{2} = \tan^{-1}\frac{A}{2F} \tag{1}$$

where:
β is the divergence angle,
A is the transducer aperture, and
F is the distance to the focal point *Pf.*

This angle will determine the size of the sub-aperture at an established depth.

The algorithm is based in the implementation of the coherent sum of different lines obtained using a transducer that moves in the *x*-axis direction with a resolution or step *d*. The coherent sum can be expressed as [4]:

$$A(t) = \sum_{j=1}^{l} w_j * s_j(t - \Delta t_j) \tag{2}$$

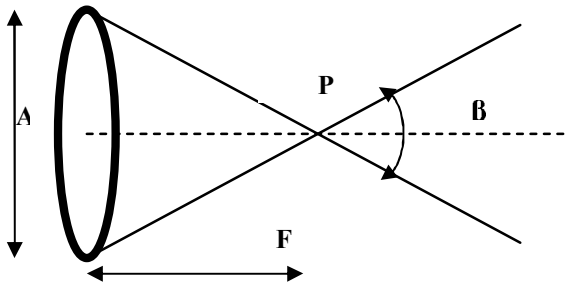

Figure 2. Formation of a virtual element from a focal point of the scanned line.

where:

w_j, are the coefficients of the apodization applied to the sub-aperture under focusing.

S_j, are the A-Scan lines of the window.

Δt, is the delay applied to the signal that is located around the current sub-aperture.

A(t), is the focused RF line in a sub-aperture.

l, is the number of A-scan lines that give information in the coherent sum.

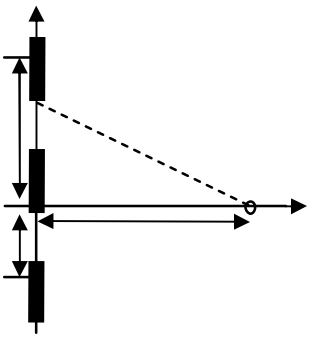

Figure 3. Calculation of Δt_j to focus the Z_i point.

Based on figure 3, the calculation of the Δt delay is made using the Pythagoras theorem:

$$\Delta t = \frac{2}{c} * (Z_i - L_x) \tag{3}$$

$$L_x = \sqrt{Z_i^2 + x_j^2} \tag{4}$$

Substituting (4) in (3) gives:

$$\Delta t = \frac{2}{c}(Z_i - \sqrt{Z_i^2 + x_j^2}) \tag{5}$$

Equation 5 is applied to each sub-aperture, i.e., to the line under analysis (central position of the transducer in the sub-aperture under analysis).

The calculation of the number of lines to be considered in a sub-aperture for a focus Z_i is obtained using the Pythagoras theorem and the aperture angle of the transducer calculated using equation 1 (see figures 2 and 3).

$$j = 2 * \left(\frac{Z_i * \tan(\frac{\beta}{2})}{d} \right) \tag{6}$$

where:

j is the number of lines in the sub-aperture,
Z_i is the focus deepness,
β is the divergence angle, and
d is the separation between the elements of the array.

Using equation 6 the size of the sub-aperture is adjusted in a dynamic form according to the focus deepness and the apodization window.

3. DESCRIPTION OF THE PROCESSING TECHNIQUES

Apodization reduces the influence of secondary sidelobes. It consists in applying a spatial windowing over the sub-aperture, varying the gain of the receiving element the side effects are reduced. Different types of windows are normally used: Hanning, Hamming, Triangular, Square, Cosine, etc. The Cosine window is the one with a better performance when there is a trade off

between improving the lateral resolution and reducing the lateral sidelobes [4].

Dynamic Focusing takes into account the sample frequency to give the delays in a number of samples of the signal using equation 5. A lookup table was implemented aiming to reduce the calculation time of the dynamic focusing in reception.

Envelope Detection helps to have a better quality in B-scan images. Two techniques were used, one based on the Hilbert transform (using the FFTPack [5, 6]) and another based on the implementation of a non-linear filter (EDFilter) proposed by Fritsch et al. [7].

Image Composition: B-scan lines are grouped in order to form the final image.

4. DESCRIPTION OF THE EXPERIMENT

Data acquisition was performed using a commercial measurement system and a 3.5 MHz Krautkramer transducer; the resolution in the X axe direction was 250 μm storing 400 RF lines. Signals were sampled at 50 MHz using a digital Oscilloscope connected to a PC using a GPIB port.

A phantom with 10 cylindrical acrylic bars with a 5 mm diameter was used as shown in figure 4. The initial storage deepness was 12.3 mm and the final storage deepness was 107.8 mm.

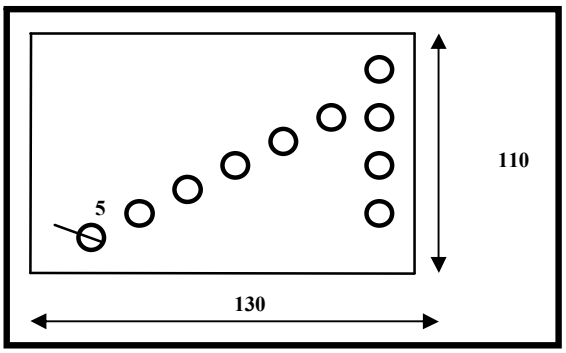

Figure 4. Diagram of a phantom with 10 cylindrical acrylic bars with a 5 mm diameter.

Firstly the SAFT algorithm was developed using MATLAB 6.5 and then its performance was measured incorporating different processing techniques.

This same procedure was repeated but now the SAFT algorithm was developed using C/C++ programming language. In both cases the elapsed time was measured.

5. RESULTS

Programs developed in MATLAB and C/C++ use the following parameters:

Apodization Window (lookup table): Cosine Type.
Sub-aperture Size: 80 and 40 lines.
Number of calculated foci (lookup table): 1024.
Size of the total aperture: 400 y 200 lines.

To measure the performance of the algorithm the total elapsed time was calculated which is the sum of the elapsed time of the following modules:

SAFT algorithm,
Envelope detection. In this case two algorithms were used: Hilbert and EDFilter.
Logarithmic compression

Tables 1 and 2 shows the performance of the algorithm implemented using MATLAB 6.5.

Table 1. Envelope detection method: **Hilbert**.

Test	Aperture	Sub-aperture	Time (s)
1	400	80	359.6
2	400	40	204.7
3	200	80	136.0
4	200	40	90.9

Table 2. Envelope detection method: **EDFilter**.

Test	Aperture	Sub-aperture	Time (s)
1	400	80	365.2
2	400	40	210.7
3	200	80	137.0
4	200	40	92.3

Tables 3 and 4 show the performance of the algorithm implemented using C/C++.

Table 3. Envelope detection method: **Hilbert (FFTPack)**.

Test	Aperture	Sub-aperture	Time (s)
1	400	80	0.484
2	400	40	0.297
3	200	80	0.187
4	200	40	0.141

Table 4. Envelope detection method: **EDFilter**.

Test	Aperture	Sub-aperture	Time (s)
1	400	80	0.453
2	400	40	0.281
3	200	80	0.172
4	200	40	0.125

Figure 5 shows the figure of the phantom without SAFT. Figures 6 and 7 show the figure of the phantom with SAFT and apodization, envelope detection and logarithmic compression algorithms.

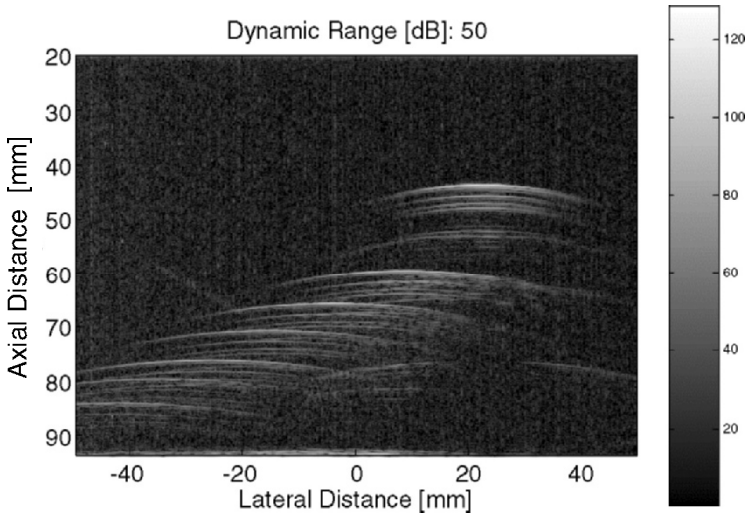

Figure 5. Image of the phantom without SAFT.

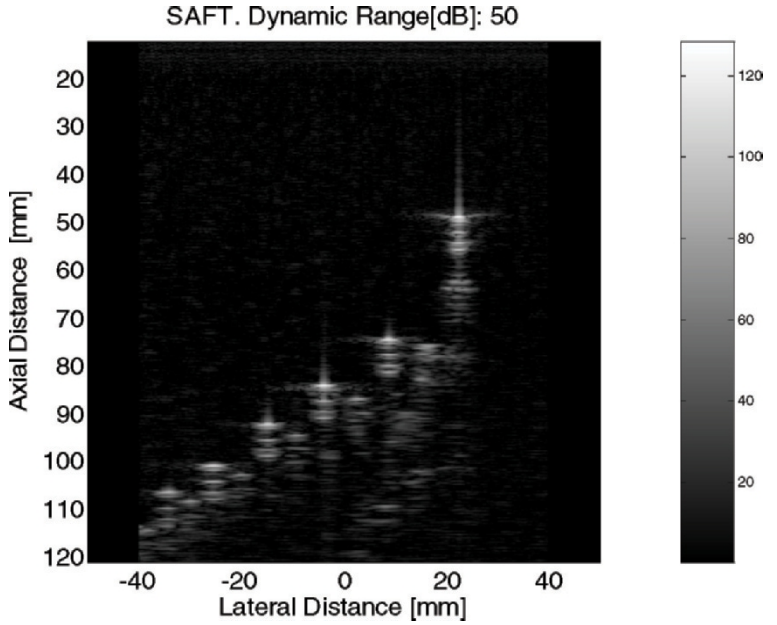

Figure 6. Image of the phantom with SAFT, Cosine type apodization, 80 lines sub-aperture and envelope detection using Hilbert transform.

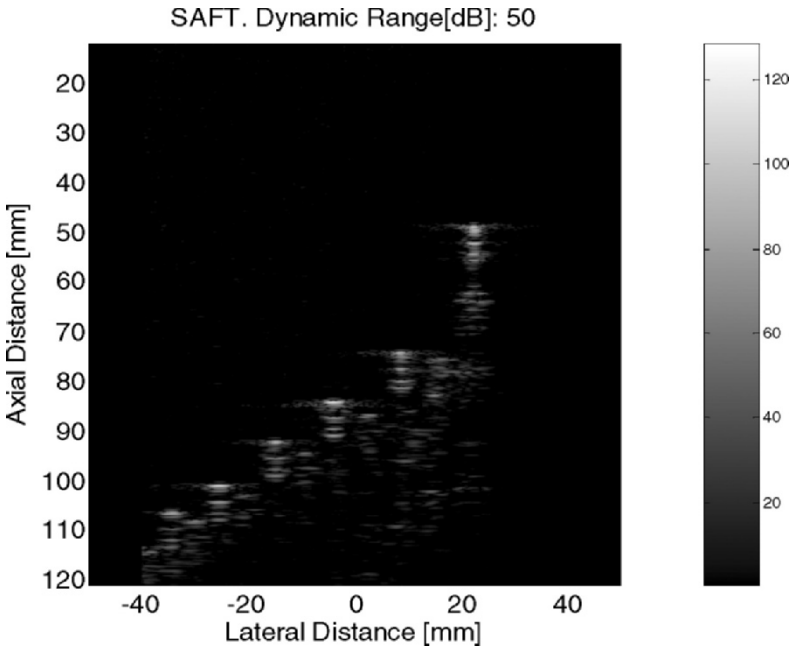

Figure 7. Image of the phantom with SAFT, Cosine type apodizacton, 80 lines sub-aperture and envelope detection using a non-linear filter (EDFilter).

6. CONCLUSIONS

Based on the results showed in figures 5 to 7 and in tables 1 to 4, it is clearly seen that the algorithm firstly implemented in MATLAB works, this implementation was made in order to check the correct performance of the algorithm in conjunction with the different applied processing techniques. Then the same algorithm was implemented in C/C++ and it is also clearly seen that the corresponding elapsed time was reduced allowing displaying approximately 8 images per second.

7. ACKNOWLEDGEMENTS

The authors acknowledge the support of UNAM (PAPIIT IN-111303) and M. Fuentes for his participation in this work.

REFERENCES

1. Martínez, C.O., Parrilla, M., Izquierdo, M.A.G. and Ullate, L.G. "*Application of Digital Signal Processing Techniques to Synthetic Aperture Focusing Technique Images*", Elsevier, Sensors and Actuactors, No. 76, 1999.
2. Ludwig, R. and Roberti, D. "*A Non destructive ultrasonic imaging system for detection of flaws in metal blocks*". IEEE Trans. on instrumentation and measurement, Vol. 45, No. 1, 1989.
3. Frazier, H. and O'Brien, W.D. "*Synthetic aperture techniques with a virtual source element*", IEEE Trans. Ultrason., Ferroelec., Freq. Contr., Vol. 45, No. 1, January 1998.
4. Fritsch, C. "*Técnicas Electrónicas de Focalización de Haces Ultrasónicos*", Jornadas Iberoamericanas de Ultrasonido Huelva, España, 2001.
5. http://www.netlib.org/fftpack/
6. http://www.scd.ucar.edu/softlib/mathlib.html
7. Fritsch, C., Ibáñez, A. and Parrilla, M. "*A Digital Envelope Detection Filter for Real-Time Operation*", IEEE Transaction on Instrumentation and Measurement, Vol. 48, No. 6, December 1999.

ULTRA-BROADBAND ULTRASONIC IMAGING USING BI-LAYER STRUCTURE PROBE

I. Akiyama, A. Ohya, S. Saito
Shonan Institute of Technology, Fujisawa 251-8511 Japan; Graduate School of Systems and Information Engineering, University of Tsukuba, Tsukuba, 305-8573 Japan; School of Marine Science and Technology, Tokai University, Shizuoka, 424-8610, Japan

Abstract: An ultrasonic imaging system to employ ultrasounds whose bandwidth is over two times compared to the conventional ultrasonic diagnosis equipment is invented. Assuming a receiving transducer and a transmitting transducer separately, the present system is improved to get high signal to noise ratios even at high frequencies by using a broadband transducer made from polymer piezoelectric materials particularly for the reception. Two transducers are unified in a bi-layer structure so as to be used for the conventional equipment. A bi-layered probe consisting of a ceramic transmitter and PVDF receiver is prototyped. A capability of detecting the second to tenth harmonic sounds contained in the echo signal, which are generated during the propagation, is experimentally demonstrated. The images for a phantom are then generated using each harmonic component. Finally, it is shown that the superposition of higher harmonic images reduces the speckle noise

Key words: PVDF, higher harmonics, speckle noise reduction, nonlinear propagation

1. INTRODUCTION

It is well known that the use of a broadband ultrasonic pulse for generating a B-mode image enhances the resolution and quality of the image. Since the bandwidth of ultrasonic pulses conventionally employed for the ultrasonic diagnosis equipment are limited by that of the transducer, the practical fractional bandwidth is as small as 60%. On the other hand, since the ultrasound generates higher harmonics due to nonlinear

M.P. André (ed.), Acoustical Imaging, 101–109.

propagation within biological media, the echo signal contains higher harmonics even if the bandwidth of an initially radiated sound is limited narrow. As an imaging system using such higher harmonics, a harmonic imaging to utilize the second harmonic component has recently been equipped in ultrasonic diagnosis equipments. In spite of its low S/N ratio, the harmonic image has been widely used for clinical diagnosis because of better image qualities compared to the conventional image that is primarily generated by the fundamental component of the sound.

Meanwhile, granular patterns called speckle that appears in ultrasonic images are known as the main cause to reduce the quality of images[1]. Therefore, provided the speckle noise is reduced, the ultrasonic image would be drastically improved[2]. The present author previously showed that the speckle noise could be reduced when the images generated by higher harmonics over third order in addition to the second harmonic were superposed with each other[3].

To receive the higher harmonics over third order contained in echo signals, a broadband transducer unlike a transmitting transducer is necessary only for reception. In this study, attaching a PVDF film on the front surface of a transmitting ceramic transducer, a unified probe of a bi-layer structure is prototyped. The system is also built for generating the harmonic image of each harmonic component in the echo signal received with this probe. Further the speckle reduction by superposing these images is demonstrated.

In the present paper, after formulating the higher harmonic echoes, the capability of reducing the speckle by averaging the higher harmonic images is theoretically shown. Using a prototype probe with a bi-layer structure, the imaging for a phantom is experimentally conducted. The formation of higher harmonic image and its speckle reduction effect are then discussed.

2. SPECKLE REDUCTION BY SUPERPOSING HIGHER HARMONIC IMAGES

Scatterers are randomly distributed on a two dimensional plane. The ultrasound is emanated from a transducer located at the origin. The transmitting waveform consists of a carrier $\cos\omega_0 t$ and an envelope $f(t)$. The profile of the ultrasound beam is approximated as the Gaussian function, where the beam width is defined by the standard deviation b of its Gaussian distribution. The echo from n scatterers randomly distributed on the x-y plane is approximated as

$$r(t) \cong \sum_{i=0}^{n-1} \gamma_i \exp(-\frac{y_i^2}{2b^2}) f(t-\frac{2l_i}{c}) \cos\omega_o (t-\frac{2l_i}{c}), \quad (1)$$

where γ_i is the scattering coefficient of i-th scatterer, and c is the sound speed. In addition, l_i represents the distance of i-th scatterer from the transmitter, that is approximated as the distance from the origin. This approximation is equivalent to the employment of a point receiver like a needle-type hydrophone. Supposing the location of i-th scatterer to be (x_i, y_i), l_i is expressed as

$$l_i = \sqrt{x_i^2 + y_i^2}. \quad (2)$$

The quadrature detection for $r(t)$ with respect to the carrier frequency component gives

$$\left|\tilde{r}(t)\right|^2 = \sum_{i=0}^{n-1}\sum_{j=0}^{n-1} \gamma_i \gamma_j e^{-\frac{b_i^2}{2b^2}} e^{-\frac{b_j^2}{2b^2}} f(t-T_i) f(t-T_j) \cos(\theta_i - \theta_j), \quad (3)$$

where $T_i=2l_i/c$ and $\theta_i=2\omega_0 l_i/c$.

Since $f(t)$ expresses the envelope of the emanated sound, $f(t-T_i)f(t-T_j)$ vanishes when the back scattered wave from an i-th scatterer does not temporally overlap with that from a j-th scatterer similar to an example shown in Fig. 2. Hence the pair of scatterers whose mutual distance is greater than the width of the envelope can be excluded for the summation in Eq.(3). An echo from the vicinity of focus, whose distance is l_f, is considered first. Assuming that the echoes from n_f scatterers located near the focus overlap with each other, an approximation holds as follows.

$$\left|\tilde{r}(\frac{2l_f}{c})\right|^2 \cong \gamma^2 f^2(t-\frac{2l_f}{c}) \sum_{i=0}^{n_f-1}\sum_{j=0}^{n_f-1} \exp(-\frac{y_i^2 + y_j^2}{2b^2}) \cos(\theta_i - \theta_j). \quad (4)$$

The scattering coefficient γ is assumed constant here. θ_i-θ_j is expressed as

$$\theta_i - \theta_j = 2k_0(l_i - l_j), \quad (5)$$

where k_0 is the wavenumber, and l_i-l_j is the difference in distance from the origin. In addition to the replacement of this distance with d_i, taking into

consideration the echoes only from n_{bf} scatterers located in the region within the width of envelope in x-direction and the beam width b in y-direction, the summation in Eq.(4) is rewritten as follows.

$$\sum_{i=0}^{n_f-1}\sum_{j=0}^{n_f-1}\exp(-\frac{{y_i}^2+{y_j}^2}{2b^2})\cos(\theta_i-\theta_j)=n_{bf}+\sum_{i=0}^{n_{bf}(n_{bf}-1)-1}\cos 2k_0 d_i\ . \tag{6}$$

Using Eq.(6), Eq.(4) becomes

$$\begin{aligned}\left|\tilde{r}(\frac{2l_f}{c})\right|^2 &\approx n_{bf}\gamma^2 f^2(t-\frac{2l_f}{c})+\gamma^2 f^2(t-\frac{2l_f}{c})\sum_{i=0}^{n_{bf}(n_{bf}-1)-1}\cos 2k_0 d_i \\ &= n_{bf}\gamma^2 f^2(t-\frac{2l_f}{c})\left\{1+\frac{1}{n_{bf}}\sum_{i=0}^{n_{bf}(n_{bf}-1)-1}\cos 2k_0 d_i\right\}.\end{aligned} \tag{7}$$

When the summation of the right side of Eq.(6) is expressed by $N(k_0)$, Eq.(7) is rewritten as

$$\left|\tilde{r}(\frac{2l_f}{c})\right|^2 \approx n_{bf}\gamma^2 f^2(t-\frac{2l_f}{c})\{1+N(k_0)\}. \tag{8}$$

Consequently the speckle noise is considered to be a noise that gets mixed in the product process. Logarithmic expression of Eq.(8) leads to

$$\log\left|\tilde{r}(\frac{2l_f}{c})\right|=\frac{1}{2}\log n_{bf}+\log\gamma+\log f(t-\frac{2l_f}{c})+\frac{1}{2}\log\left|1+N(k_0)\right|. \tag{9}$$

$N(k_0)$ which has been given as

$$N(k_0)=\frac{1}{n_{bf}}\sum_{i=0}^{n_{bf}(n_{bf}-1)-1}\cos 2k_0 d_i\ , \tag{10}$$

is the value averaging the cosine of distance between each scatterer and transducer, that accompanies a statistical fluctuation. This is the speckle. Since this fluctuation is given by $N(k_0)$, the change in k_0 causes the change of fluctuation.

The number of scatterers n_{bf} is related to the density of scatterers along the x-axis, $\rho(x)$, as follows,

$$n_{bf} = \rho(x) b \frac{cw}{2}, \tag{11}$$

where w is the temporal width of the pulse envelope. Substituting Eq.(11) into Eq.(9) and then putting the fourth term to be 0 by the speckle reduction, the equation to give the intensity of echoes at $x=2l_f/c$ is derived as follows.

$$\log\left|\tilde{r}(\frac{2l_f}{c})\right| = \frac{1}{2}\left[\log\rho(\frac{2l_f}{c}) + \log w + \log b + \log c\right]$$

$$+ \log\gamma + \log f(t - \frac{2l_f}{c}). \tag{12}$$

Since only $\rho(x)$ is a variable, the density distribution of the scatterers can be obtained along the x axis when the speckle is reduced. In commercially supplied ultrasonic diagnosis equipments, the images around the focus are synthesized by means of techniques such as dynamic focusing. If the beam width b changes with x for various focal distances, the distribution including the variance of beam width are obtained through Eq.(12).

The echo that contains higher harmonics generated by the nonlinearity in an ultrasonic propagation is expressed as

$$r(t) = \sum_{m-1}^{M} r_m(t)$$

$$\cong \sum_{m-1}^{M}\sum_{i-0}^{n-1} \gamma_{mi} g_m^2(x) \exp\{-\frac{y_i^2}{2b_m^2}) f_m(t - \frac{2l_i}{c}) \cos m\omega_o(t - \frac{2l_i}{c}). \tag{13}$$

where $g_m(x)$ describes the m-th order harmonic component at the position $(x,0)$. The beam has been approximated by the Gaussian one whose standard deviation is b_m.

Then it is supposed that the envelope is extracted with the quadrature detection for each harmonic component of the echo signal after passing through band-pass filters. Using the approximation similar to those

employed in the preceding section, the envelope of the echo returned from the vicinity of the focus is derived as

$$\left|\tilde{r}_m(\frac{2l_f}{c})\right|^2 \cong n_{bf}{\gamma_m}^2 g_m^2(\frac{2l_f}{c}){f_m}^2(t-\frac{2l_f}{c})\{1+N(mk_0)\}, \tag{14}$$

where m is the order of the higher harmonic. The logarithmic expression for Eq.(14) is

$$\begin{aligned}\log\left|\tilde{r}_m(\frac{2l_f}{c})\right| &= \frac{1}{2}\log n_{bf} + \log\gamma_m + \log g_m(\frac{2l_f}{c}) \\ &+ \log f_m(t-\frac{2l_f}{c}) + \frac{1}{2}\log\left|1+N(mk_0)\right|.\end{aligned} \tag{15}$$

Since the value $N(mk_0)$ significantly changes with m, the fifth term can be converged to 0 provided the higher harmonic components are superposed.

3. HIGHER HARMONIC IMAGING

In order to receive the higher harmonic components contained in the echo signals, a unified probe to have a bi-layer structure where a PVDF film was bonded on the front surface of a transducer of piezoelectric ceramic materials was produced. The transmitting transducer has a 2-MHz center frequency, an approximately 60% fractional bandwidth, a 20-mm diameter and a concavity with a 70-mm focal length. The receiving PVDF transducer has an 8-MHz center frequency, a 120% fractional bandwidth, a 20-mm diameter and a concavity with a 70-mm focal length. The prototype probe is overviewed in Fig. 1. Fig. 2 shows the pressure waveform observed at the focus, and compares the observed and computed spectra[4]. They agree well with each other. It is seen that the observed higher harmonics are generated due to the nonlinear propagation in water. The imaging for a phantom immersed in water was carried out. After amplified with a 50-dB power amplifier (ENI, model 2100L), the 5-cycle cosine wave with the envelope of Hanning window generated by an arbitrary waveform generator drives the transmitting transducer. The echo signal received with the receiving transducer is amplified and transformed to 8-bit digital signals of 100-MHz sampling frequency. Since the 8-bit digitization lacks a dynamic range, digital signals equivalent to 14 bits are obtained by a 64-time averaging.

Scanning the probe set at an *x*-stage with an interval of 0.2 mm, an image was generated for the internal region of 24 mm ×24 mm in the phantom. Dividing the received signal to each higher harmonic component after passing through band-pass filters, the envelope was detected for each component. The higher harmonic image was obtained with a brightness modulation for the envelope signal. Fig. 3 shows the harmonic images of fundamental to sixth harmonic. After a logarithmic compression, these images are superposed for reducing the speckle. Fig. 4 is the superposed image. Comparing with the fundamental and the second harmonic images of Fig. 3, the smoothened speckle improves the image quality.

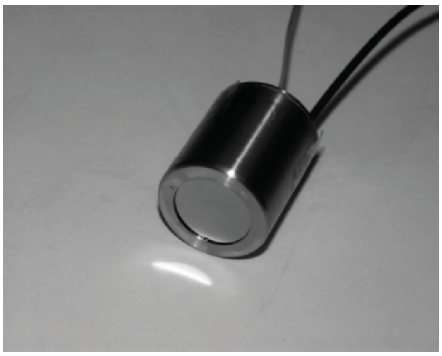

Figure 1. Prototype unified probe with bi-layer structure.

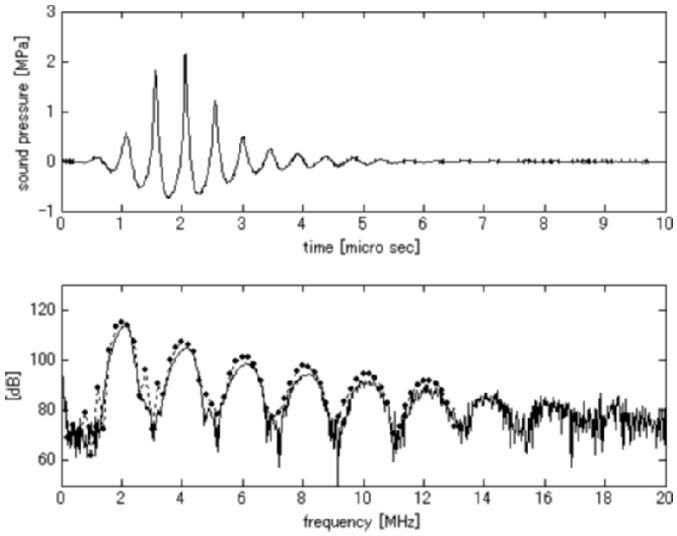

Figure 2. Measured waveform (upper) and its spectrum. Circles are computed plots.

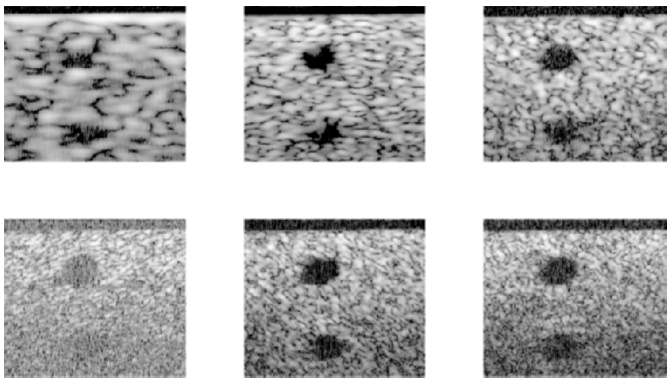

Figure 3. A fundamental image (upper left), a second harmonic image (upper middle), a third harmonic image (upper right), a forth harmonic image (lower left), a fifth harmonic image (lower middle) and a sixth harmonic image (lower right).

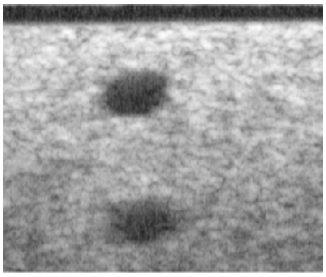

Figure 4. Speckle reduced image by superposing fundamental through sixth harmonic images.

REFERENCES

1. R.F. Wagner, S.W. Smith, J.M. Sandrik, et.al: Statistics of speckle in ultrasound B-scans. IEEE Trans on Ultrason 30(3), 156–163,1983
2. P.A. Magnin, O.T. Ramm and F.L. Thurstone: Frequency compounding for speckle contrast reduction in phased array images. Ultrasonic imaging 4, 267–281, 1982
3. I. Akiyama, H. Yamamoto, G. Ohashi and A. Ohya: Speckle reduction by summation of higher order harmonic images, Acoustical Imaging Vol. 27, (Kluwer Academic Publishers, Dordrecht, The Netherlands, 2004), pp. 651–657
4. I. Akiyama, A. Ohya and S. Saito: Speckle noise reduction by superposing many higher harmonic images, JJAP, (accepted)

DEVELOPMENT OF A 40-MHZ ANNULAR ARRAY

J.A. Ketterling, S. Ramachandran, F.L. Lizzi
Riverside Research Institute, 156 William St., New York, NY 10038

Abstract: The design and testing of a 5-ring, focused annular array is presented. The array has a total aperture of 6 mm, a geometric focus of 12 mm, and a nominal center frequency of 40 MHz. The active element of the transducer is a 9-μm polyvinylidene fluoride (PVDF) membrane and the array pattern is formed on a copper clad polyimide film. A system has been developed to permit testing of the array. The system consists of a XYZ axis scanning component, a pulser/receiver, a crosspoint switch module, a digital storage oscilloscope, and a PCI digital acquisition card. The system permits a single ring of the array to be pulsed, and then the radio-frequency echo of all five array elements to be simultaneously digitized. Data from all 25 transmit/receive ring pairs were collected and then post-processed with a synthetic focusing technique to establish an improved depth of field. To accomplish this testing, a wire phantom with nine 25-μm diameter wires spaced in 1 mm by 1 mm increments was utilized. An improved depth of field was observed for data processed with the synthetic focus technique versus data with no focusing

Key words: Annular array; high-frequency ultrasound; synthetic focus; ophthalmic imaging

1. INTRODUCTION

High frequency ultrasound (HFU) imaging is typically undertaken utilizing single element, focused transducers [1–3]. These transducers have been effectively used for a wide variety of applications requiring resolution on the order of 100 μm or less [4–7]. The drawbacks of single-element transducers are their relatively limited depth of field and the need to mechanically scan the transducer to form a B-mode image.

M.P. André (ed.), Acoustical Imaging, 111–118.

Arrays provide a method to address these two problems. The ideal solution would be a multi-element array similar to conventional low MHz probes that permits real time imaging. However, the small array element sizes required for HFU imaging create many technical challenges that need to be overcome before HFU array probes can be made widely available [8,9]. An intermediate solution is to employ annular arrays [10–13]. These arrays permit an increased depth of field but still require a mechanical scan to form a B-Mode image.

In this article, we present the design, instrumentation, and testing of a polyvinylidene fluoride (PVDF) based annular array. The array has a PVDF membrane as the acoustic layer and the array pattern is formed on a copper clad polyimide film. The assembled array is tested with an experimental system that permits a single array element to be pulsed and the radio-frequency (RF) echo data to be simultaneously digitized for all array elements. The digitized data are processed with a synthetic focusing algorithm to establish an improved depth of field. To test the array and experimental system, RF echo data are acquired from a wire phantom with a 25 μm diameter wire.

2. METHODS

2.1 Theory

2.1.1 Spatial Impulse Response Model

To assist in testing the synthetic focusing algorithm and to better evaluate the experimental performance of the array, the sound fields of the annular array elements were modeled using the spatial impulse response (SIR) method [14]. The SIR model was used to generate both spatial beam profiles and simulated B-mode images of a point scatterer target.

For a transducer of surface area **S**, the SIR at a point **r** in the sound field is [14]

$$\mathbf{h}(\mathbf{r}, t) = \frac{1}{2\pi} \int_S \frac{\delta(t - r'/c)}{r'} d\mathbf{S} \tag{1}$$

where r' is the distance between **r** and d**S**, δ(t) is the Dirac delta function, and c is the speed of sound. If we assume there is a point source at **r**, the transmit/receive voltage $E(\mathbf{r}, t)$ at the transducer is then found from the convolution of the transmit SIR, $\mathbf{h}_T(\mathbf{r}, t)$, and the receive SIR, $\mathbf{h}_R(\mathbf{r}, t)$, [15]

$$E(\mathbf{r}, t) \propto -\upsilon_0(t) * \frac{\partial \mathbf{h_T}(\mathbf{r}, t)}{\partial t} * \frac{\partial \mathbf{h_R}(\mathbf{r}, t)}{\partial t} \tag{2}$$

To characterize the beam, we assume there is a point scatterer at axial depth **r** and then calculate $E(\mathbf{r},t)$ as the transducer is laterally incremented. The process is repeated for all 25 transmit/receive pairs and then the collected data are summed with no time delays or processed with the synthetic focusing algorithm. The summed data with no time delays simulate the case of a single element transducer with a 12 mm geometric focus and a 6 mm aperture. The data processed with synthetic focusing permit the focus of the array to be axially shifted.

2.1.2 Synthetic Focusing

A synthetic focusing algorithm was developed to permit the focus of the annular array to be axially shifted by post-processing the acquired RF data. To focus the array to a depth f on transmit, the time delay t_n required for ring n of the array is [16]

$$t_n = \frac{a_n^2(1/\mathrm{R} - 1/f)}{2c} \tag{3}$$

where R is the geometric focus and a_n is the average radius of ring n. The round trip delay is then the sum of the transmit and receive delays giving $t_n^{tot} = t_n^T + t_n^R$.

To focus at a depth f, t_n^{tot} is calculated for all 25 transmit/receive pairs. The delays are then applied to the RF A-lines and the resulting signals are summed. In order to increase the depth of focus over a fixed axial span, f is shifted in intervals of Δf. An overall image is then formed by windowing the data at each focal depth and assembling the windowed data into a final composite image.

2.1.3 Experimental System

The annular array is constructed from a 9-μm PVDF membrane with a single conductive side and a copper clad polyimide film that has the array pattern etched onto it (Fig. 1). The films are bonded with epoxy, press fit into a tube with a ball bearing, and then back filled with epoxy. The array was designed to have a total aperture of 6 mm, a geometric focus of 12 mm, and 5 equal area rings. The center frequency of the array elements is ≈40 MHz. Fig. 2 shows the annular array mounted in a hollowed out UHF

connector. The electrical connections to the annuli are established via the flex circuit visible in the left part of the image. The UHF connector acts as a path to ground. A more detailed description of the fabrication method and array element properties may be found in Ref. [17].

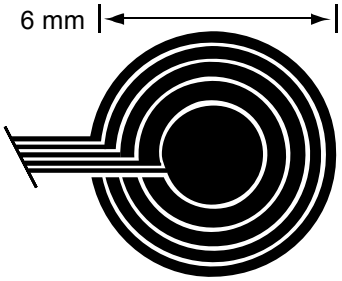

Figure 1. Array pattern etched onto the copper clad polyimide film. Electrical trace lines allow electrical access to the annuli. The trace lines are 100 μm in width. The center element is Ring 1 and the outermost annulus is Ring 5.

Figure 2. The annular array transducer mounted in an UHF connector. The UHF connector and PVDF membrane are electrically joined with silver epoxy.

We assembled a data acquisition system to permit collection of digitized RF data by scanning the transducer across a reflective target. The system permitted a single element to be pulsed and receive RF data to be captured on all 5 array elements simultaneously. A collection of digitized RF data for

all 25 transmit/receive pairs could then be achieved with five lateral scans of the array. The experimental system was composed of a bi-directional crosspoint switch (CXL/8X8 Cytec, Penfield, NY), a pulser/receiver (Panametrics 5900, Waltham, MA), a digital oscilloscope (6050A LeCroy, Chestnut Ridge, NY), a PCI digitizer card (DP110 Acqiris, Monroe, NY), and a XYZ axis scanning system. The crosspoint switch was used in a 5x5 input/output configuration with five input lines connected to the array, one output line to the pulser/receiver, and the other four output lines to the digital oscilloscope. This configuration permitted any array element to be pulsed and then the received signals to be digitized from all five array elements. By making five translational passes across the sample and pulsing on a separate array element each pass, RF echo data for all 25 transmit/receive ring pairs could be digitized. LabVIEW program (National Instruments, Austin, TX) controlled all aspects of the data acquisition system.

3. RESULTS

A wire phantom having nine 25 μm diameter wires spaced in 1 mm by 1 mm increments was used to test the ability of the array to focus at different depths. Fig. 3 shows a comparison of experimental and theoretical two-way lateral beam profiles at three wire depths without applying any delays to the RF data. This represents the case of a single element transducer with a 6 mm aperture and 12 mm focus. For this case, the peak amplitude is at the geometric focus of 12 mm [Fig. 3(b)] and then the reflected signal drops drastically when moving away from the geometric focus [Fig. 3(a) and 3(c)].

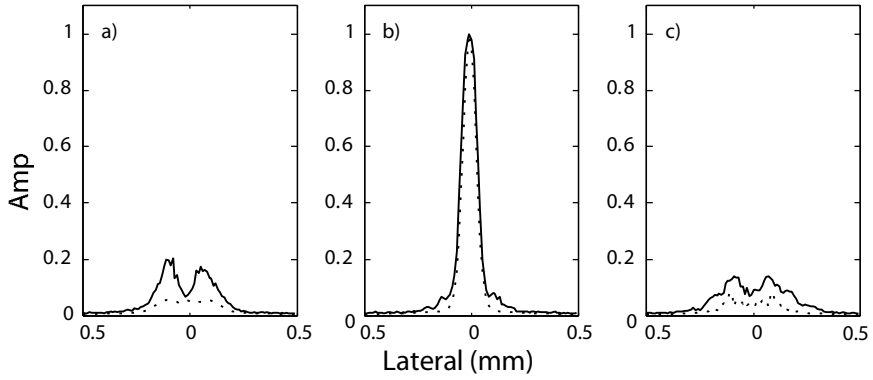

Figure 3. Experimental (solid) and theoretical (dotted) two-way lateral beam profiles for non-time-shifted data at depths of (a) 11 mm, (b) 12 mm, and (c) 13 mm.

Fig. 4 shows a comparison of experimental and theoretical two-way lateral beam profiles at three wire depths where the RF data has been processed with the synthetic focusing algorithm. For the processed data, the lateral beam profile does not change at 12 mm [Fig. 4(b)] because no delays are applied at this depth. However, away from the geometric focus, we see a strong improvement in the reflected signal [Fig. 4(a) and 4(c)].

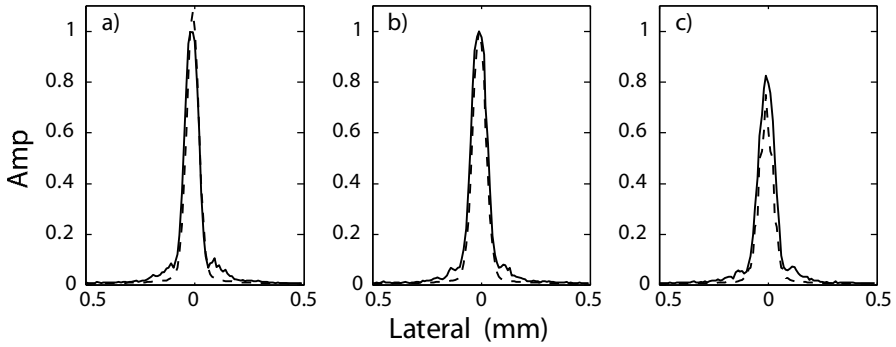

Figure 4. Experimental (solid) and theoretical (dotted) lateral beam profiles for time-shifted data at depths of (a) 11 mm, (b) 12 mm, and (c) 13 mm.

Fig. 5 shows an example of experimental data with and without synthetic focusing. The figure shows a B-mode scan with wires at three depths: 17, 18, and 19 mm. With no time shifts applied [Fig. 5(a)], the wires at each depth are smeared out due to the beam being wide away from the geometric focus. When the data were processed with the synthetic focusing algorithm, the wires at each depth are brought into focus. Note that the intensity scale of Fig. 5(b) is 10 times that of Fig. 5(a).

4. CONCLUSION

We have fabricated and tested a 5-ring annular. The array was constructed from a PVDF active layer and a copper clad polyimide film with the array pattern etched onto it. A numerical model was developed to generate RF transmit/receive echo waveforms from a point scatterer. By moving the scatterer laterally, B-mode images and two-way lateral beam profiles could be generated. Axial beam profiles were generated by moving the scatterer axially. Experimental data were also acquired for the transmit/receive waveforms from a wire scatterer at a fixed axial depth.

Experimental and theoretical data were acquired for all 25 transmit/receive pairs and then processed with a synthetic focusing algorithm to establish the

ability of the array to focus at some depth *f*. The data were also summed with no time delays to simulate a single element transducer with the same focus and aperture as the array. For wires away from the geometric focus, the transmit/receive echoes were significantly enhanced for the data processed with synthetic focusing. With the wire phantom, the usable depth of field was roughly from 8 to 19 mm, in agreement with theoretical predictions. For *in vivo* imaging, this range will be reduced to roughly 9 to 15 mm because of acoustic attenuation and a finite signal to noise ratio (SNR).

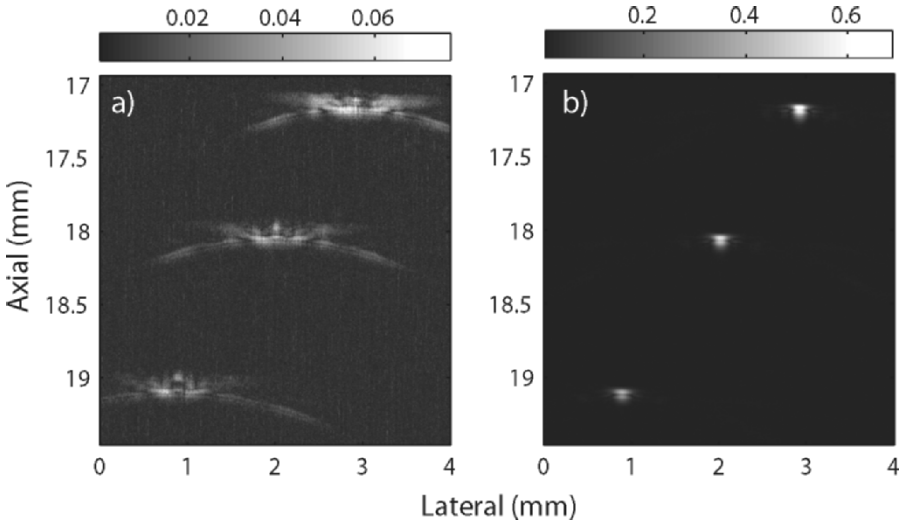

Figure 5. Experimental RF B-mode data (a) with and (b) without synthetic focusing processing. The wires are at the axial depths of 17, 18, and 19 mm.

REFERENCES

1. M.D. Sherar, and F.S. Foster, "The design and fabrication of high-frequency poly(vinylidene fluoride) transducers," *Ultrason. Imaging* **11**, 75–94 (1989).
2. J.M. Cannata, T.A. Ritter, W.H. Chen, R.H. Silverman, and K.K. Shung, "Design of efficient, broadband single-element (20–80 MHz) ultrasonic transducers for medical imaging applications," *IEEE Trans. Ultrason. Ferroelect. Freq. Contr.* **50**, 1548–1557 (2003).
3. G.R. Lockwood, D.H. Turnbull, and F.S. Foster, "Fabrication of high frequency spherically shaped ceramic transducers," *IEEE Trans. Ultrason. Ferroelect. Freq. Contr.* **41**, 231–235 (1994).
4. G.R. Lockwood, D.H. Turnbull, D.A. Christopher, and F.S. Foster, "Beyond 30 MHz - applications of high-frequency ultrasound imaging," *IEEE Eng. Med. Biol. Mag*. **15**, 60–71 (1996).

5. R.H. Silverman, M.J. Rondeau, F.L. Lizzi, and D.J. Coleman, "Three-dimensional high-frequency ultrasonic parameter imaging of anterior segment pathology," *Ophthalmology* **102**, 837–843 (1995).
6. D.H. Turnbull, B.G. Starkoski, K.A. Harasiewicz, J.L. Semple, L. From, A.K. Gupta, D.N. Sauder, and F.S. Foster, "40–100 MHz B-scan ultrasound backscatter microscope for skin imaging," *Ultrasound Med. Biol*. **21**, 79–88 (1995).
7. F.S. Foster, C.J. Pavlin, K.A. Harasiewicz, D.A. Christopher, and D.H. Turnbull, "Advances in ultrasound biomicroscopy," *Ultrasound Med. Biol.* **26**, 1–27 (2000).
8. T.A. Ritter, T.R. Shrout, R. Tutwiler, and K.K. Shung, "A 30-MHz piezo-composite ultrasound array for medical imaging applications," *IEEE Trans. Ultrason. Ferroelect. Freq. Contr*. **49**, 217–230 (2002).
9. J.A. Cannata, T.R. Shrout, and K.K. Shung, "A 35 MHz linear ultrasonic array for medical imaging," in *Proc. IEEE 13th Int. Symp. Appl. Ferroelect.*, (Nara, Japan), 343–346 (2002).
10. C.H.F. Alves, K.A. Snook, T.A. Ritter, and K.K. Shung, "High frequency single element and annular array transducers incorporating PVDF," in *Proc. SPIE Med. Imag.*, **3982**, 116–121 (2000).
11. K.A. Snook, J.Z. Zhao, C.H.F. Alves, J.M. Cannata, W.H. Chen, J.J. Meyer, T.A. Ritter, and K.K. Shung, "Design, fabrication, and evaluation of high frequency, single-element transducers incorporating different materials," *IEEE Trans. Ultrason. Ferroelect. Freq. Contr*. **49**, 169–176 (2002).
12. C.E. Morton, and G.R. Lockwood, "Design of a 40 MHz annular array," in *Proc. IEEE Ultrason. Symp.*, (Atlanta, GA), 1135–1138 (2001).
13. J.A. Brown, C.E.M.Démoré, and G.R. Lockwood, "Design and fabrication of annular arrays for high-frequency ultrasound," *IEEE Trans. Ultrason. Ferroelect. Freq. Contr*. **51**, 1010–1017 (2004).
14. M. Arditi, F.S. Foster, and J.W. Hunt, "Transient fields of concave annular arrays," *Ultrason. Imaging* **3**, 37–61 (1981).
15. J.P. Weight, and A.J. Hayman, "Observations of the propagation of very short ultrasonic pulses and their reflection by small targets," *J. Acoust. Soc. Amer*. **63**, 396–404 (1978).
16. M. Arditi, W.B. Taylor, F.S. Foster, and J.W. Hunt, "An annular array system for high-resolution breast echography," *Ultrasonic Imaging* **4,** 1–31 (1982).
17. J.A. Ketterling, O. Aristizábal, D.H. Turnbull, and F.L. Lizzi, "Design and fabrication of a 40-MHz annular array transducer," *IEEE Trans. Ultrason. Ferroelect. Freq. Contr*., (to appear 2005).

MEASURING PHASE OF VIBRATION OF SPHERES IN A VISCOELASTIC MEDIUM USING VIBROMETRY

M.W. Urban, R.R. Kinnick, J.F. Greenleaf
Department of Physiology and Biomedical Engineering, Mayo Clinic and Foundation, 200 First St SW, Rochester, MN 55905, Email: urban.matthew@mayo.edu

Abstract: Vibro-acoustography is a method that uses ultrasound radiation force at low frequency as an excitation mechanism to create images of the acoustic response of an object. At certain frequencies the magnitude image of an object consisting of materials of different densities may not provide sufficient contrast to distinguish each of the materials from one another so the phase of vibration is assessed as another modality for contrast. An experiment is described to address the efficacy of using the phase of vibration relative to the magnitude of vibration to assess mass density. Experimental data are compared with theoretical simulations. The authors discuss the usefulness of the phase images compared with the magnitude images. Possibilities for obtaining better contrast of materials of different density in a viscoelastic medium are explored

Key words: Vibro-acoustography, phase, contrast, density, viscoelastic

1. INTRODUCTION

Microcalcifications in the breast can be associated with the presence of cancerous tissue[1]. These microcalcifications are composed of apatite, calcite, calcium oxalate, and other materials[2]. Since these minerals are denser and harder than soft tissue, an imaging modality that is sensitive to material properties including hardness and density may be useful in detection of these microcalcifications *in vivo*[3]. For this reason we will explore detection of spheres of different density embedded in a viscoelastic medium. We choose spheres because they can be used as models for

M.P. André (ed.), Acoustical Imaging, 119–126.

microcalcifications and the theory for vibration of spheres in a viscoelastic medium is well developed.

Vibro-acoustography is an imaging modality that uses the radiation force of ultrasound to produce images of the acoustic response that are related to the material properties of an object. This method has been used previously to identify microcalcifications in breast tissue[4]. However, the images used for that study were only formed using the magnitude of the acoustic response of the tissue being inspected. Images can also be formed using the phase of the acoustic response. These phase images may provide a modality to improve image contrast and provide better detection of microcalcifications.

2. MATERIALS AND METHODS

2.1 Vibro-Acoustography

Vibro-acoustography is a recently developed method that uses the low-frequency acoustic radiation force created from the interference of two ultrasound beams at slightly different frequencies[5,6]. The force occurs at the beat frequency of the two ultrasound waves, Δf, which is usually in the kHz range. The oscillatory force is localized only to the focal region of the transducer where the two beams interfere, so an object within the focal region will undergo vibration at Δf. This vibration causes an acoustic response from an object in the focal region and that acoustic response is measured by a sensitive hydrophone. In this paper we are using the same excitation scheme as in vibro-acoustography but measuring the velocity directly as opposed to the acoustic response.

2.2 Theory for Spheres in Viscoelastic Medium

The radiation force resulting from a plane wave incident on a sphere immersed in a fluid is given by $\langle F \rangle = \pi a^2 Y \langle E \rangle$ where πa^2 is the projected area of the sphere, Y is the radiation force function and $\langle E \rangle$ is the energy density of the ultrasound[7]. The dynamic radiation force from two interfering plane waves is given by $\langle F_d \rangle = \pi a^2 \overline{Y} \langle E_0 \rangle \cos((\omega_1 - \omega_2)t)$ where $\langle E_0 \rangle = 2P_0^2/\rho c^2$. The velocity of the sphere can be calculated with Eq. (1).

$$V = \frac{\langle F_d \rangle}{Z_r + Z_m} \tag{1}$$

The terms Z_r and Z_m are the radiation and mechanical impedances, respectively given in Eqs. (2) and (4), where $k = \sqrt{\rho\Delta\omega^2 / (2\mu + \lambda)}$, $h = \sqrt{\rho\Delta\omega^2 / \mu}$, $\mu = \mu_1 + i\Delta\omega\mu_2$, and $\lambda = \lambda_1 + i\Delta\omega\lambda_2$, a is the radius of the sphere, ρ is the density of the medium, c is the speed of sound of the medium, μ_1 and μ_2 are shear elasticity and viscosity of the medium, respectively, and λ_1 and λ_2 are the bulk elasticity and viscosity of the medium, respectively[8]. For soft tissues, $\lambda_1 \sim 10^9$ Pa, $\lambda_2 \sim 0$ Pa·s, $\mu_1 \sim 10^4$ Pa and $\mu_2 \sim 10^{-2}$ Pa·s[8,9].

$$Z_r = -i\frac{4\pi a^3}{3}\rho\Delta\omega\frac{\left(1-\frac{3i}{ah}-\frac{3}{a^2h^2}\right)-2\left(\frac{i}{ah}+\frac{1}{a^2h^2}\right)\left(3-\frac{a^2k^2}{aki+1}\right)}{\left(\frac{i}{ah}+\frac{1}{a^2h^2}\right)\frac{a^2k^2}{aki+1}+\left(2-\frac{a^2k^2}{aki+1}\right)} \tag{2}$$

For a sphere with mass m vibrating with velocity $Ve^{i\Delta\omega t}$ the force required to overcome the inertia of the sphere is given by Eq. (3). The mechanical impedance is the ratio of the force to the velocity given in Eq. (4), where ρ_s is the density of the sphere material. Using these relationships, we can calculate the response of spheres of varying density over a range of frequencies.

$$F = m\frac{dVe^{i\Delta\omega t}}{dt} = im\Delta\omega Ve^{i\Delta\omega t} \tag{3}$$

$$Z_m = \frac{-F}{Ve^{i\Delta\omega t}} = -im\Delta\omega = -i\rho_s\frac{4\pi a^3}{3}\Delta\omega \tag{4}$$

The theory presented above has been implemented in MATLAB 7.0 (Mathworks, Inc., Natich, MA) to explore how the velocity of a sphere embedded in a viscoelastic medium changes with density of the sphere. Fig. 1 shows the dispersion curves for velocity magnitude and phase for spheres of five different materials, acrylic, soda lime glass, silicon nitride, 440-C stainless steel, and brass having densities 1190, 2468, 3210, 7840, and 8467 kg/m^3, respectively. The medium parameters for this simulation are μ_1 = 6.7 × 10^3 Pa, μ_2 = 0.5 Pa·s, λ_1 = 10^9 Pa, λ_2 = 0 Pa·s, c = 1500 m/s, ρ = 1000 kg/m^3 and the spheres have a diameter of 3.175 mm. The magnitude curves

show resonances at different frequencies for each sphere. The shear elasticity and viscosity of the surrounding medium affects the shape of these curves. From the simulation results, it is important to note that the phase of the velocity is proportional to increasing density.

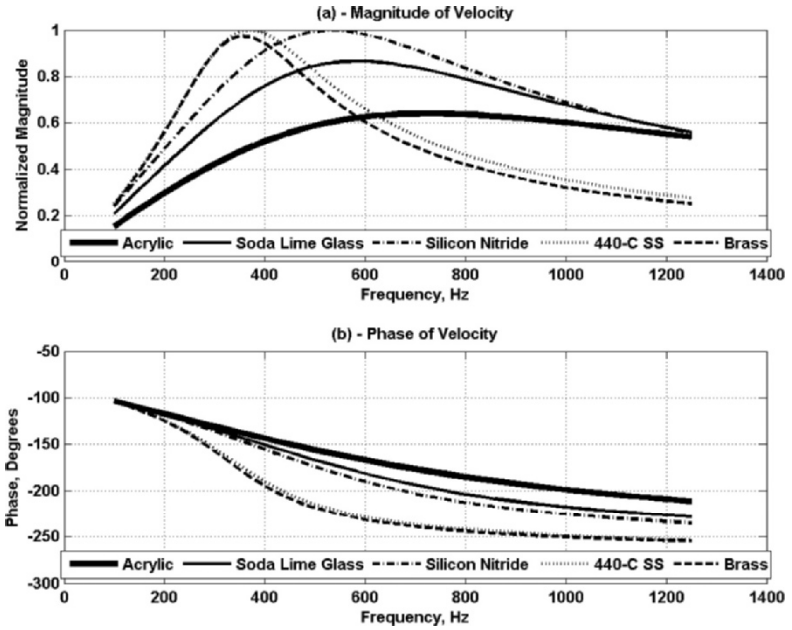

Figure 1. Simulation results for magnitude and phase of velocity, (a) Magnitude of velocity (normalized to maximum of all velocities) for spheres of different density, (b) Phase of velocity for spheres of different density in degrees.

2.3 Experimental Setup

Spheres of equal diameters (3.175 mm) and different materials including acrylic, soda lime glass, silicon nitride, 440-C stainless steel, and brass with respective densities 1190, 2468, 3210, 7840, 8467 kg/m^3 were suspended in an optically clear gelatin phantom. The spheres were spray painted white to provide a reflective surface for the laser vibrometer. The gelatin phantom was made using 300 Bloom gelatin powder (Sigma-Aldrich, St. Louis, MO) with a concentration of 10% by volume. A confocal, two-element transducer with a nominal frequency of 3.0 MHz and a focal distance of 70 mm was used to excite each sphere. A pulse echo technique was used to position the transducer so that the sphere was in the focal region. A laser

vibrometer (Polytec, Waldbronn, Germany) was used to measure the velocity of the sphere being excited by the radiation force. The signal was processed by a lock-in amplifier (Signal Recovery, Oak Ridge, TN) to obtain the magnitude and phase of the velocity (Fig. 2). The phase was computed using a sinusoidal reference signal at the vibration frequency, which was created by mixing the two ultrasound drive signals and applying a low-pass filter.

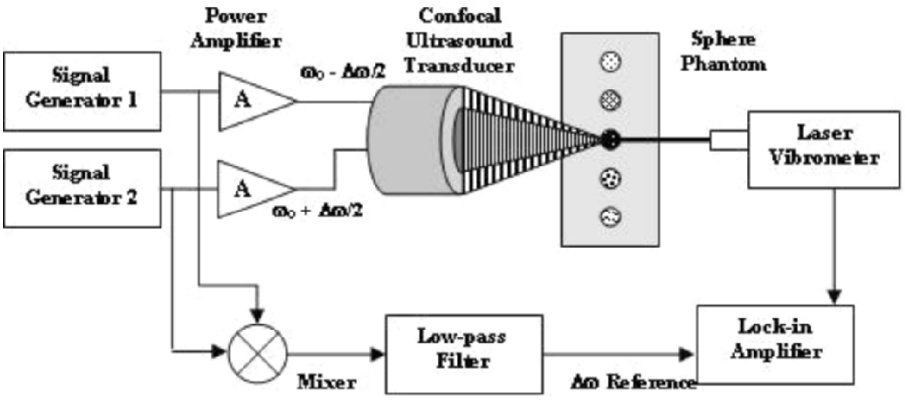

Figure 2. Setup for measurement of magnitude and phase of velocity with vibrometry.

The difference frequency was varied from 100–1250 Hz in increments of 50 Hz. The magnitude and phase of vibration at each frequency was measured while the transducer was fixed spatially on each sphere. A magnitude and phase image was also created for each sphere at $\Delta f = 700$ Hz. We chose this difference frequency to be beyond the resonance peaks of the spheres to provide more predictable contrast between the spheres both in the magnitude and phase images. During scanning, the laser was focused on one sphere while the transducer was raster-scanned across the phantom. The same field of view was scanned for each sphere to insure registration of the resulting images.

3. RESULTS

The measured magnitude and phase results for this phantom are shown in Fig. 3(a) and 3(b). While the laser vibrometer was focused on each sphere, the transducer was scanned across the same field of view. The magnitude and phase images from each of the five scans performed at $\Delta f = 700$ Hz were combined to create composite images for the phantom. The phase composite images were created using threshold masks made from the magnitude

images. As a result, the phase composite image had a blocky appearance so it was low-pass filtered to make the objects look more like spheres. The composite images for this phantom are shown in Fig. 4. From left to right, the spheres are acrylic, soda lime glass, silicon nitride, stainless steel, and brass. The brass and stainless spheres appear dark in the phase image because brass was used as the reference and stainless steel has a phase value very close to the brass.

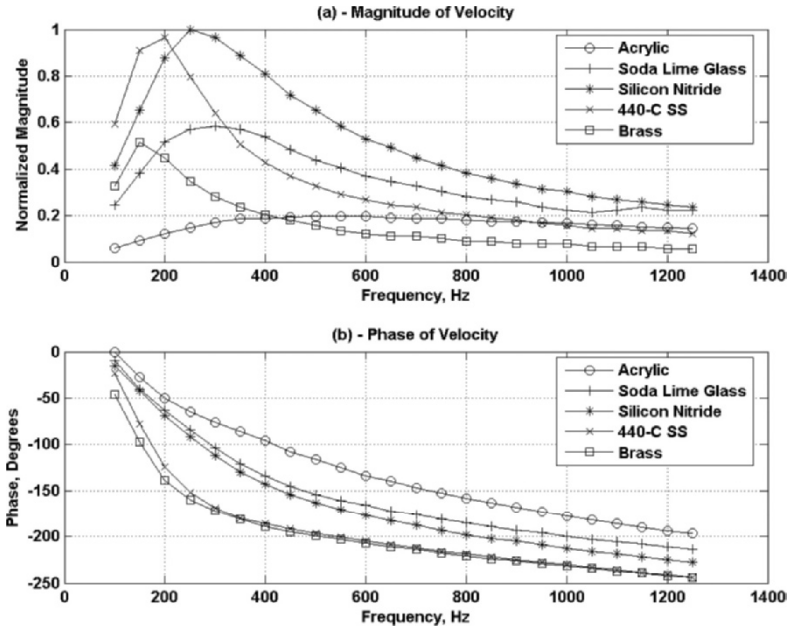

Figure 3. Experimental results for magnitude and phase of velocity, (a) Magnitude of velocity (normalized to maximum of all velocities) for spheres of different density, (b) Phase of velocity for spheres of different density in degrees.

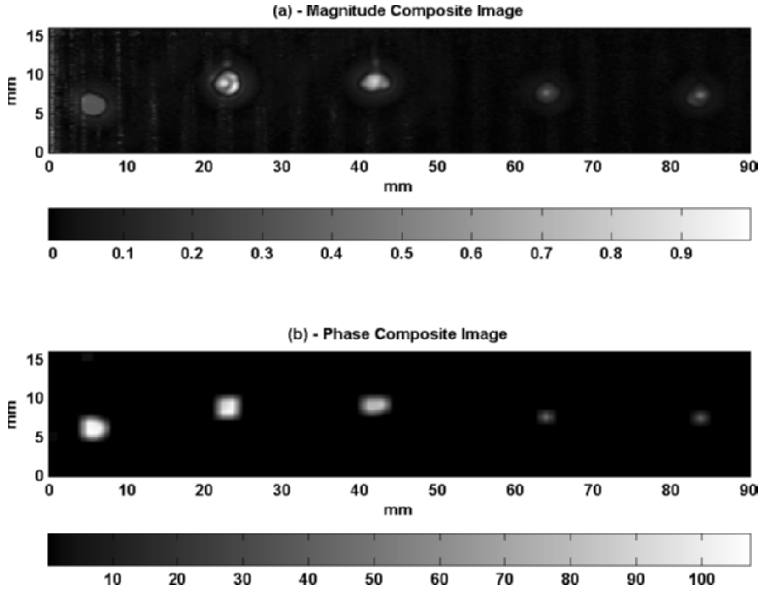

Figure 4. Composite images of sphere phantom, (a) Magnitude of velocity (normalized to maximum of all velocities) for spheres of different density, (b) Phase of velocity for spheres of different density in degrees. (The spheres from left to right are acrylic, soda lime glass, silicon nitride, 440-C stainless steel, and brass.)

4. DISCUSSION

Comparing the phase responses in Figs. 1 and 3, we find that the spheres follow the same pattern, that is, the phase shift for the less dense spheres is less than the phase shift of the more dense spheres.

If we consider the magnitude image in Fig. 4(a), we may not visually be able to tell the difference between the acrylic, stainless steel, or brass spheres. Also, the soda lime glass and silicon nitride appear similar. In the phase image (Fig. 4(b)), the distinction between the acrylic and stainless steel spheres is very evident. There is also a noticeable difference between the soda lime glass and silicon nitride spheres in the phase image. The phase image depicts the same phase shift progression as in the measurements, that is, compared to the most dense sphere made of brass, spheres of less dense material have larger phase shifts.

The ability to identify different materials in an image is of great import in medical diagnosis. We have shown that we can provide predictable

contrast between different density objects so that when we look at an image we can compare the density of different objects in the image. Finding the magnitude and phase responses of small spheres may give us more insight into how to choose the difference frequency when imaging microcalcifications in the breast. We may be able to provide better contrast in the phase images so that we can identify microcalcifications among other structures in the image, which would aid in diagnosis and treatment.

5. ACKNOWLEDGEMENTS

This study was supported by grants EB002640 and EB002167 from the National Institute for Biomedical Imaging and Bioengineering.

REFERENCES

1. V. Kumar, A.K. Abbas, and N. Fausto, *Robbins and Cotran Pathologic Basis of Disease, Seventh Edition*. (Elsevier Saunders, Philadelphia, 2005).
2. A. Fandos-Morera, M. Prats-Esteve, J.M. Tura-Soteras, and A. Traveria-Cros, Breast tumors: composition of microcalcifications. *Radiology*. **169**, 325–327 (1988).
3. D.R. Lide, (ed.) *CRC Handbook of Chemistry and Physics*, *72nd Edition*. (CRC Press, Boca Raton, 1991).
4. A. Alizad, M. Fatemi, L.E. Wold, and J.F. Greenleaf, Performance of vibro-acoustography in detecting microcalcifications in excised human breast tissue: a study of 74 tissue samples. *IEEE Transactions on Medical Imaging*. **23**(3), 307–312 (2004).
5. M. Fatemi, and J.F. Greenleaf, Ultrasound-stimulated vibro-acoustic spectrography. *Science*. **280**, 82–85 (1998).
6. M. Fatemi, and J.F. Greenleaf, Vibro-acoustography: an imaging modality based on ultrasound-stimulated acoustic emission. *Proceedings of the National Academy of Sciences USA*. **96**, 6603–6608 (1999).
7. S. Chen, M. Fatemi, and J.F. Greenleaf, Remote measurement of material properties from radiation force vibration of an embedded sphere. *Journal of the Acoustical Society of America*. **112**(3), Pt. 1, 884–889 (2002).
8. H.L. Ostreicher, Field and impedance of an oscillating sphere in a viscoelastic medium with an application to biophysics. *Journal of the Acoustical Society of America*. **23**(6), 707–714 (1951).
9. L.A. Frizzell, E.L. Carstensen, and J.F. Dyro, Shear properties of mammalian tissue at low megahertz frequencies. *Journal of the Acoustical Society of America*. **60**(6), 1409–1411 (1976).

ACOUSTIC RHINOMETRY (AR): AN ALTERNATIVE METHOD TO IMAGE NASAL AIRWAY GEOMETRY

S.P. Straszek
University of Aarhus, Institute of Public Health, Department of Environmental and Occupational Medicine, Vennelyst blvd. 6, 8000, Aarhus. SPVS@mil.au.dk

Abstract: In acoustic rhinometry (AR) a sound pulse enters the nasal cavity, where it is reflected due to changes in the local impedances. From the incident and reflected sound signal we use the Ware-Aki algorithm to calculate an area-distance relationship. The method has been validated in nasal cavity models with known dimensions, and in humans and animals, where the dimensions were measured by other methods as well, (CT-scanning, MR scanning and fluid displacement). In small animals AR seems to underestimate the cross-sectional areas, probably due to violation of several assumptions for the method. Future studies should aim at development of better-scaled equipment, better sound generation, better microphones, better algorithms, and better validation

Key words: Acoustic Rhinometry; Nasal airway volume; nasal obstruction; airway pharmacology

1. INTRODUCTION

Acoustic rhinometry (AR) is increasingly used to evaluate pharmaceutical compounds with effect on the nasal mucosa. A number of studies used guinea pigs[1–7], cats[8–11] or dogs[12–13] as models for testing mucosa

M.P. André (ed.), Acoustical Imaging, 127–135.

active substances in the nasal cavity. There have so far been few attempts to validate AR by comparison to other methods, including nasal casting, fluid-displacement and magnetic resonance imaging (MRI). Kaise et al.[2] 1994 estimated that AR only measured 70% of nasal cavity volume in guinea pigs, and data by Straszek et al.[14] suggest 88% in dogs and 71% in cats. We have validated acoustic rhinometry *post mortem* in guinea pigs and rats by comparison to a previously described fluid-displacement-method (FDM).[14] We quantified AR measurement errors in guinea pig and rat, small laboratory animals used in comparative pharmacological evaluations.

We have also carried out a feasibility study with *in vivo* histamine provocation. We found that it was possible to measure relative changes in nasal cavity volume, but that optimization of equipment and computing were likely to improve measurements. So far there is only one published study applying AR in rats and attempts to include mice as potential study objects has not succeeded.

Our aim is to improve AR through innovative input and make pharmacological testing in small laboratory animals more sensitive and reliable.

2. MATERIALS AND METHOD

2.1 Acoustic Rhinometry

The underlying principle is quite simple although in practice the technique is based on certain assumptions and complex computational algorithms. When a sound pulse travels along a tube and encounters an area change, part of the pulse is reflected and part is transmitted. The reflected pulse travels back along the tube. If the sound speed is known, it is easy to calculate the distance to where the sound is reflected. An intuitive approach to describe how an area distance function can be derived from an incident and reflected sound pulse is presented in Figure 1.

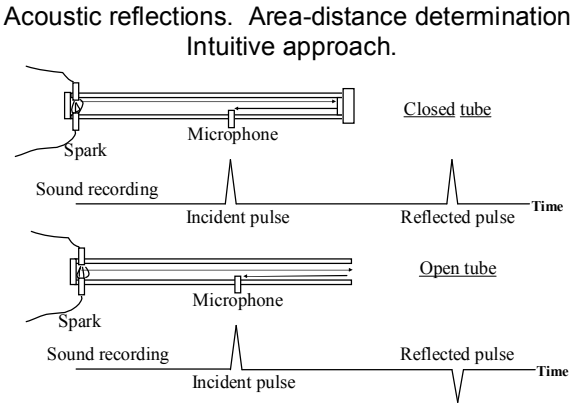

Figure 1. Incident and reflected waves in closed and open tube.

O.F.Pedersen. Airway geometry determined by acoustic reflections.
In: Mechanics of Breathing. Pathophysiology, Diagnosis and Treatment.
(Aliverti A, Brusasco V, Macklem PT, Pedotti A, eds)
Springer-Verlag Milano, Italia 2002.

In the upper panel of Figure 1 a spark near the bottom of a closed tube creates an acoustic pulse. The pulse travels along the tube and is recorded as a positive spike, when it passes a microphone in the wall. The pulse travels further, hits the closed end of the tube and is reflected. When the reflected signal returns to the microphone, another positive spike is recorded. The time between the two spikes is the time taken for the pulse to travel the double distance from the microphone to the closed end of the tube.

In the lower panel the tube is open-ended. The reflected signal now becomes negative. But the time between the two is the same as above. It is now intuitively understood that a change in airway dimension (here either to zero cross-sectional area or to an infinite area) will give either a positive reflection signal (a narrowing) or a negative signal (a widening), and that the time from the incident to the reflected pulse is a measure of the distance to the change in the area.

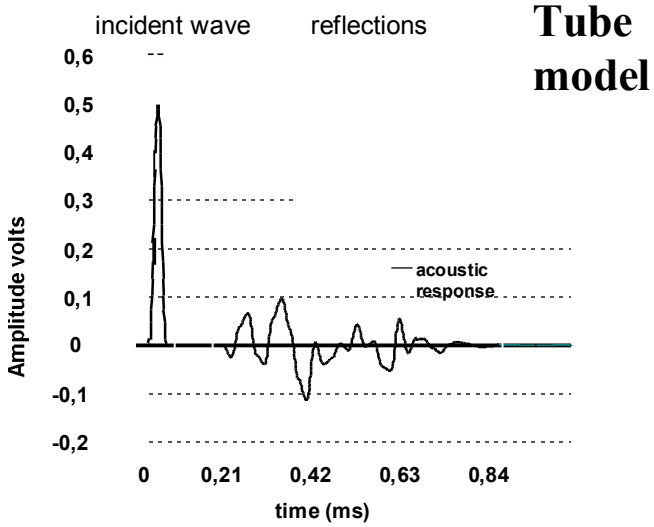

Figure 2. Area-distance curve created by Ware and Aki algorithm.

O.F.Pedersen. Airway geometry determined by acoustic reflections.
In: Mechanics of Breathing. Pathophysiology, Diagnosis and Treatment.
(Aliverti A, Brusasco V, Macklem PT, Pedotti A, eds)
Springer-Verlag Milano, Italia 2002.

Ware and Aki[15] developed an algorithm to calculate cross-sectional area as a function of distance. The area-distance curve calculated by use of this algorithm is shown in Figure 2.

The sound spike created by the spark contains a broad spectrum of frequencies and this gives possibilities for a high resolution. However, continuous sound patterns can also be applied, but this requires an adaptation of the calculation algorithm.

In theory an accurate area distance function can only be obtained, if the walls of the airway are rigid, there are no energy losses due to viscous dissipation, and if the airway is branching, then the bifurcations are regular. Finally the wave must be one-dimensional. It is not allowed to bounce between the walls

of the tube (cross-modes). The ability of the method to separate two points on the distance scale depends on microphone characteristics, high pass filtering, sound wave length and speed (gas property and temperature). However, to avoid cross-modes the sampling frequency must be kept under a certain limit, c/2d, where c is the speed of sound, and d is the diameter of the conduit[16–17].

2.2 Fluid-Displacement-Method

The nasal cavity is placed with the axis of the nasal cavity in a vertical position. It is filled from below with perfluorocarbon, a fluid with low surface tension, through the nostril by a constant flow from a Harvard pump. Changes in the slope of the pressure-time curve at the inlet are proportional to changes in the cross-sectional areas of the nasal cavity with distance. The cross-sectional area of the cavity (A) is then

$$A \propto \frac{dV}{dt} \Big/ \frac{dP}{dt}.$$

Pressure is measured consecutively at every 0.5 second. For a detailed description of the fluid-displacement-method, physical properties of perfluorocarbon, and potential errors, we refer to a previous study by Straszek et al.[14] A moving average algorithm was applied to reduce noise in the measurements.

3. EXPERIMENTAL PROTOCOL

3.1 Validation in Guinea Pig and Rat *Post Mortem*

We (Straszek et al. 2004)[18] used 5 guinea pigs and 5 rats injected intraperitoneally with a lethal dose of 1 ml pentobarbital (50 mg/ml) and decapitated prior to the experiments. The head was placed with the nasal cavity in the horizontal plane with the back of the nose upwards. Five acoustic measurements were obtained with alternating measurements on each

nostril. The sound waves travel through the cavity, reach the end of the nasal septum and continue backwards through the contralateral cavity as well as forwards into a common conduit leading to the nasopharynx. AR beyond the septum thus measures the sum of the cross-sectional areas of the common conduit as well as the contralateral cavity.

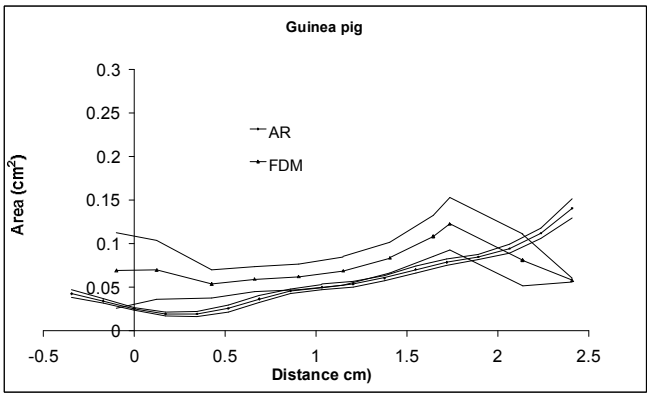

Figure 3. Mean cross-sectional area from five guinea pigs (10 cavities) by acoustic rhinometry (AR)and fluid-displacement-method (FDM)[18].

The fluid-displacement study was carried out on all guinea pigs and rats immediately after the acoustic measurements. Nosepieces were connected one at a time to a Harvard pump delivering a constant flow of 0.0063 mL/s, in a way so that resistance would be kept to a minimum. Five consecutive FDM measurements were performed with the opposite nostril blocked, and hereby filling the entire cavity completely, before fluid rose through the nasopharynx and ran out of the mouth. FDM was always done with the contralateral cavity filled with fluid, thus measuring only the cross-sectional area of the common conduit after the fluid surface had passed the end of the nasal septum. See Figure 3 for a comparison of mean AR and FDM measurements in guinea pig[14].

3.2 Histamine Provocation in Guinea Pig and Rat

This is two *in vivo* feasibility studies where guinea pigs and rats were anaesthetized with urethane. Joynson et al.[19] tested the histamine H1 receptor antagonist cetirizine (CE, 5 mg/kg), the alpha agonist oxymetazoline (OM, 3 mg/kg) or saline vehicle on guinea pigs. Compounds were administered intravenously 15 minutes after intranasal histamine treatment. The congestion response to a sub maximal dose of histamine was

inhibited by pre-treatment with cetirizine (65%, $p<0.01$) and oxymetazoline (57%, $p<0.01$), (n=3–6 per group).

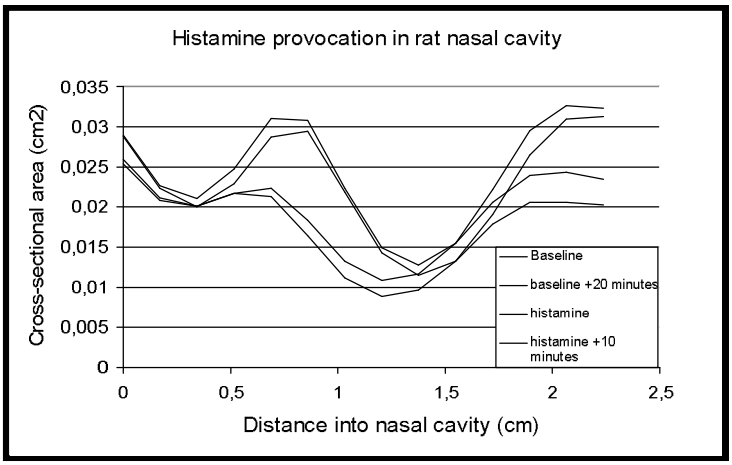

Figure 4. Histamine provocation in rat in vivo. Measurements at baseline and after appliance of histamine. (Joynson and Straszek 2004).

We also did a non-published feasibility study with rats (Joynson and Straszek 2004). As described above intranasal histamine was applied to the nostrils and measurements of nasal volume were taken in 10-minute intervals. Only histamine treatment was applied. We did succeed to measure a histamine response as described above, but the experiments did not include decongestion. A histamine response in a rat nasal cavity is seen in Figure 4.

4. RESULTS AND DISCUSSION

The study compared measurements obtained *post mortem*. There is reason to believe that some physiologic changes take place shortly after death. However, the aims of this study were to validate how AR measures the complex geometry of nasal cavities in small laboratory animals, and to investigate the methodological aspects for future *in vivo* comparative pharmacological studies. It has been shown that AR can measure *relative* changes in nasal congestion in guinea pigs, and we also believe that AR can measure relative changes in rats, as preliminary data suggests.

A number of assumptions concerning planar waves, symmetrical structure and minimal losses inside the cavity may be violated, and the errors increase with distance into the cavity. A constriction with a cross-sectional

area below a certain threshold may result in severe underestimation by AR of the cross-sectional areas beyond the constriction. The exact value of the threshold area is not known, but most likely below 0.01 cm². Finally, a combination of errors including capillary effects in the nostril and slight differences in position of the head in relation to the direction of gravity may contribute to the differences between FDM and AR but are considered of lesser importance.

The considerations expressed above regarding comparability of AR and FDM also apply to the rat study. However, rats have a narrower but longer nasal cavity than guinea pigs, and internal structures possibly reflect sound waves with greater loss.

To examine even smaller animals we (Straszek SP and Pedersen OF) tried to measure mice in our experiments. However, we discarded the measurements because of methodological difficulties, including a too narrow nostril for satisfactory readings, both with AR and FDM. We estimated the volume of a nasal cavity to be 25 μL, hardly enough for intranasal application of pharmacological compounds, although it cannot be excluded with future technical development.

5. CONCLUSION

The main findings are an underestimation of cross-sectional areas by AR compared to FDM, both in guinea pig and rat. In previous studies it has been possible to measure *relative* changes in guinea pig nasal congestion, making them interesting to pharmacological evaluation studies. Based on these studies we believe this is also possible in the rat. Both species have a nasal cavity volume large enough for intranasal application of mucosa active substances. Future improvements of equipment and software are likely necessary to make better and more reliable measurements.

REFERENCES

1. Kaise T, Ohmori K, Sakakura Y, and Ukai K. The effect of KW-4679, an antiallergic drug, on experimental allergic rhinitis in guinea pigs: effects on nasal blockade. *Jpn J Pharmacol* 69: 435–438, 1995.
2. Kaise T, Ukai K, Pedersen OF, and Sakakura Y. Accuracy of measurement of acoustic rhinometry applied to small experimental animals. *Am J Rhinol* 13: 125–129, 1999.

3. Nakamato S, Sakakura Y, Pedersen OF, and Ukai K. Evaluation of nasal passage patency after antigen and histamine challenge in guinea pigs by acoustic rhinometry. *Am J Rhinol* 11: 85–89, 1997.
4. Ohkawa C, Ukai K, Miyahara Y, and Sakakura Y. Acoustic rhinometry evaluation of nasal response to histamine and antigen in guinea pigs. *Am J Rhinol* 13: 67–71, 1999.
5. Ohkawa C, Ukai K, Miyahara Y, Takeuchi K, and Sakakura Y. Histamine H1 receptor and reactivity of the nasal mucosa in sensitized guinea pigs. *Auris Nasus Larynx* 26: 293–298, 1999.
6. Pedersen OF, Yamagiwa M, Miyahara Y, and Sakakura Y. Nasal cavity dimensions in guinea pigs measured by acoustic reflections. *Am J Rhinol* 8: 299–304, 1994.
7. Sakaguchi M, Mase A, Ikeda Y, Iizuka A, Imamura S, Komatsu Y, Ukai K, and Sakakura Y. Effects of Sho-seiryu-to on experimental allergic rhinitis in guinea pigs. *Exp Clin Pharmacol* 21: 303–308, 1999.
8. Erickson CH, McLeod RL, Mingo GG, Egan RW, and Pedersen OF. Comparative oral and topical decongestant effects of phenylpropanolamine and d-pseudoephedrine. *Am J Rhinol* 15: 83–90, 2001.
9. Mcleod RL, Erickson CH, Mingo GG, Hey JA. Intranasal application of the alpha2-adrenocepter agonist BHT-920 produces decongestion in the cat. *Am J Rhinol* 15: 407–415, 2001.
10. McLeod RL, Mingo GG, Herczku C, Corboz MR, Ramos SI, DeGennaro-Culver F, Pedersen OF, and Hey JA. Changes in nasal resistance and nasal geometry using pressure and acoustic rhinometry in a feline model of nasal congestion. *Am J Rhinol* 13: 375–383, 1999.
11. Mcleod RL, Mingo GG, Herczku C, DeGennaro-Culver F, Kreutner W, Egan RW, and Hey JA. combined histamine H1 and H3 receptor blockade produces nasal decongestion in an experimental model of nasal congestion. *Am J Rhinol* 13: 391–399, 1999.
12. Koss MC, Yu Y, Hey JA, and McLeod RL. Acoustic rhinometry in the dog: a novel large animal model for studies of nasal congestion. *Am J Rhinol* 16: 49–55, 2002.
13. Koss MC, Yu Y, Hey JA, and Mcleod RL. Measurement of nasal patancy in anaesthetized and conscious dogs. *J Appl Physiol* 92: 617–621, 2002.
14. Straszek SP, Taagehoej F, Graff S, and Pedersen OF. Acoustic Rhinometry in dog and cat compared to a Fluid-Displacement-Method and Magnetic Resonance Imaging. *J Appl Physiol* 95: 635–642, 2003.
15. Ware JA, and Aki K. Continuous and discrete inverse scattering problems in a stratified elastic medium.I. Plane waves at normal incidence. *J Acoust Soc Am* 1969; 45: 911–921.
16. Fredberg JJ, Wohl ME, Glass GM, and Dorkin HL. Airway area by acoustic reflections measured at the mouth. *J Appl Physiol* 1980; 48: 749–758.
17. Hoffstein V, and Fredberg JJ. The acoustic reflection technique for noninvasive assessment of upper airway area. *Eur Respir J* 1991; 4: 602–611.
18. Straszek SP, Pedersen OF. Nasal cavity dimensions in guinea pig and rat measured by acoustic rhinometry and fluid-displacement method. *J Appl Physiol*. 2004 Jun; 96(6): 2109–14. E pub 2004 Feb 13.
19. Joynson VM, Liu WLS, Pedersen OF, Straszek SP, and Yeadon M. P-16–18, Characterization of a guinea pig acoustic model of nasal congestion. *Journal of the World Allergy Organization: Abstracts*. Sup. No. 1, 2003.

A NEW HIGH FREQUENCY ULTRASOUND SKIN IMAGING SYSTEM: IMAGING PROPERTIES AND CLINICAL IN VIVO RESULTS

M. Vogt, R. Scharenberg, G. Moussa, M. Sand, K. Hoffmann, P. Altmeyer, H. Ermert

Institute of High Frequency Engineering, Ruhr-University Bochum, IC 6/133, 44780 Bochum, Germany, Michael.Vogt@rub.de; taberna pro medicum GmbH, Lüneburg, Germany; Dermatological University Hospital, Ruhr-University Bochum, Germany; Ruhr-Center of Excellence for Medical Engineering (KMR), Bochum, Germany

Abstract: In this paper, a new high frequency ultrasound (HFUS) system for high-resolution skin imaging is presented. For imaging, mechanical scans are performed with spherically focused single element transducers. Two separate applicators with different transducers are utilized to fulfill the different requirements for imaging the skin with 20 MHz ultrasound and for lower range high resolution imaging of the uppermost skin layers with HFUS in the 100 MHz range. Clinical images were acquired in the imaging lab of the Dermatological University Hospital. Imaging results of wound healing process and skin lesion nevus investigations are presented

Key words: High frequency ultrasound; ultrasound imaging; skin imaging; dermatology; ultrasound biomicroscopy

1. INTRODUCTION

The design of the new imaging system is aimed at utilizing HFUS in the 20 to 100 MHz range for in vivo skin imaging applications. Pulse echo measurements are performed driving the transducers with broadband pulsed signals and amplifying echo signals with broadband receivers. Special care

M.P. André (ed.), Acoustical Imaging, 137–144.

was taken to preserve the bandwidth in connecting the pulser / receivers to the transducers. The electrical coupling was analyzed and optimized using time domain reflectometry (TDR) and network analysis (NWA) measurements[1]. Furthermore, the frequency dependent attenuation of the water path between the transducer and the skin was analyzed and identified as a limiting factor concerning the spectral characteristics and spatial resolution[2]. The implemented system was initially tested on phantoms. Spatial resolution and spectral characteristics were analyzed by measurements on a glass plate surface, wire targets and speckle phantoms.

2. METHODS

HFUS is applied for non invasive and high resolution imaging of tissues and organs like skin and eye on a microscopic level in terms of ultrasound biomicroscopy (UBM)[3–13]. In this section, some fundamental design criteria, the system design and the system performance (spectral characteristics and resulting resolutions) of the implemented HFUS imaging system are discussed.

2.1 High Frequency Ultrasound (HFUS) Skin Imaging

In dermatology, skin imaging with HFUS in the 20 MHz range is already well established as a diagnostic tool. With the help of this technique, skin morphology can be assessed non invasively over depth. While the advantage of standard 20 MHz sonography is the capability to image the whole skin, spatial resolution is relatively poor. Utilizing higher frequencies and increasing the bandwidth, resolution can significantly be improved while the penetration depth decreases at the same time because of the frequency dependent attenuation[13–16]. High resolution imaging of the uppermost skin layers is especially of interest with respect to skin lesion investigations. It was found that HFUS in the range up to 100 MHz delivers a good compromise between the contradictory demands for good spatial resolution and a large penetration depth[13,16]. A new HFUS skin imaging system, which was developed to enhance the capabilities of the already available and established sonography in dermatology, is presented below.

2.2 Design of HFUS Imaging System

In Fig. 1, a block diagram of the implemented HFUS imaging system is shown. Because of the lack of HFUS transducer arrays, which cover high

frequency ranges above 30 MHz, single element transducers are utilized. Consequently, mechanical scans have to be performed for imaging. The transducer is moved by a direct current (DC) motor and consecutive A-lines are acquired at equidistant positions along the lateral coordinate x. Spherically focused, rotationally symmetric transducers are utilized to obtain high measurement sensitivity as well as a good resolution with respect to the lateral and the elevational direction in the transducer focus.

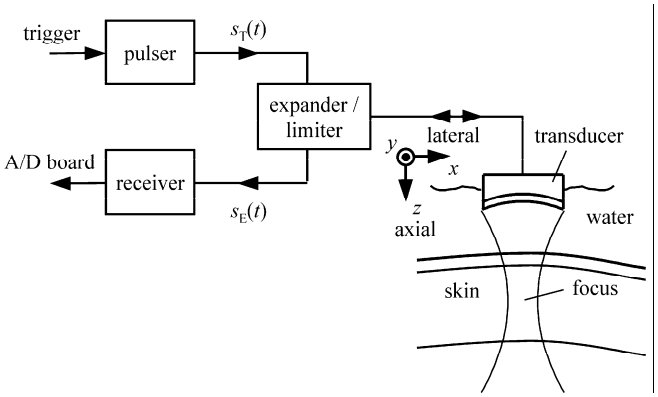

Figure 1. Block diagram of implemented HFUS imaging system: Transmit signal $x_S(t)$, echo signal $x_E(t)$.

Two different applicators are available, from which one can easily be selected by means of a switch. The 20 MHz applicator can be utilized for imaging the whole skin, while the 100 MHz range applicator is capable of high resolution imaging of the uppermost skin layers. Transducers are driven with broadband pulser / receivers for transmit signal generation and echo signal reception. In order to prevent the receiver against the large transmit signal voltages and to hold noise signals off, an expander / limiter network was inserted between the pulser, transducer and receiver[1]. Radio frequency (rf) echo signals are amplified and digitized with an analog to digital conversion (A/D) board with 8 bit amplitude resolution and 100 MHz and 500 MHz sampling frequency for the 20 MHz and 100 MHz applicator, respectively. Each A-line consists of 1024 samples, leading to maximum axial imaging ranges of 8.2 mm and 1.6 mm, respectively, based on a speed of sound $c = 1600$ m/s in the skin.

2.3 Spectral Characteristics

The driving pulsers have to have a sufficient bandwidth to cover the transducer's spectral characteristics. As *pulsed* transmit signals are applied

and the signal's amplitude is limited, the signal's energy decreases with increased bandwidth and cut-off frequency. Taking into account a Gaussian model for the low pass filtered transmit signal $s_T(t)$ with a -6db pulse width Δt, the following conditions result for the transmit signal spectrum $S_T(f)$ and the -6db cut-off frequency f_c:

$$s_T(t) = \hat{s} \cdot e^{-4 \cdot \log 2 \cdot (t/\Delta t)^2}, \left|S_T(f)\right| = \hat{s}' \cdot e^{-\ln 2 \cdot (f/f_c)^2}, f_c = 2 \cdot \ln 2 / (\pi \cdot \Delta t)$$

The cut-off frequencies of utilized receivers have to be sufficiently large as well as to cover the transducer's spectral characteristics. In Fig. 2, the transmit signal $s_T(t)$ (Fig. 2(a)) and the magnitude of the corresponding spectrum $s_T(f)$ (Fig. 2(b))of the 100MHz range pulser are shown[2]:

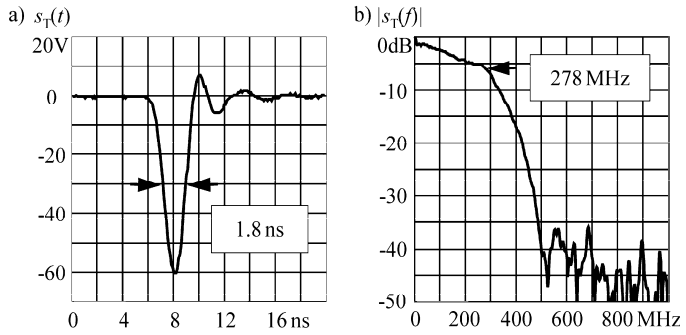

Figure 2. Pulser characteristics (100 MHz range applicator): a) Measured transmit signal $s_T(t)$; b) Corresponding spectrum $|s_T(f)|$ (magnitude)

The signal was measured with a digital storage oscilloscope (DSO, LeCroy 9450) at a 50Ω load, and the spectrum was obtained by Fast Fourier Transform (FFT) calculations[2]. In the implemented system, transmit signals with 132V and 60V peak voltages, 16ns and 1.8ns pulse widths (-6dB), covering frequency bands up to 25MHz and 278MHz cut-off frequencies (-6dB) are utilized. The broadband receivers have 61MHz and 174MHz cut-off frequencies (-6dB) and the receiver's gains are 36dB and 43dB, respectively.

The utilized transducers emit ultrasound in broad frequency bands around 20MHz and 100MHz center frequencies. However, with increasing frequencies the attenuation of the water, which is used as coupling medium between the transducer and the skin, increases as well. Consequently, center frequencies and bandwidths are reduced during propagation due to the low path characteristics of the water path[2].

3. RESULTS

Two separate applicators with different transducers are employed for imaging. The spectral characteristics and spatial resolutions, which have been analyzed by measurements with a glass plate surface and a wire target as well defined imaging objects, are summarized in Table 1:

Table 1. Specifications of implemented HFUS imaging system.

	Applicator #1:	Applicator #2:
Frequency range:	5 to 25 MHz	24 to 97 MHz
Axial resolution (–6 dB):	39 µm	9.9 µm
Lateral resolution (–6 dB):	210 µm	84 µm

With conventional 20 MHz range sonography the whole skin as well as the subcutaneous fat beneath can be imaged with a 39µm / 210µm minimum axial / lateral resolution. Also, HFUS in the 100 MHz range is utilized for high resolution imaging of the uppermost skin layers (epidermis / upper dermis) with a 9.9µm / 84µm minimum axial / lateral resolution.

HFUS images were acquired in vivo with the standard 20 MHz range technique as well as with the new high resolution 100 MHz range sonography. In Fig. 3, B-mode images, which were acquired at an index finger, are shown. For a comparison of the imaging properties, the 20 MHz range B-mode images are shown over the same axial imaging range of 1.6 mm as the 100 MHz range images. In both cases, a number of 384 A-lines was acquired along a distance of 12.8 mm in lateral direction.

The image series show a wound healing process over time. Acquisitions were performed on a fresh wound, Fig. 3a) and b), and after 44 hours, Fig. 3c) and d). The water between the transducer and the skin is a homogeneous sound propagation medium, which causes no echoes. Because of the significantly different acoustic impedances of water and tissue, strong echo signals appear at the skin surface. The hypoechoic band beneath is the epidermis, which was incised at the location of the wound. The dermis underneath shows a high echoic texture. Analyzing the acquired B-mode images, the reformation of skin structures during the wound healing process can be studied.

In the images, the advantage of applying larger frequency ranges can clearly be seen. Utilizing HFUS in the 100 MHz range, the structures in the uppermost skin layers can be imaged with much better resolution and, consequently, much more details can be identified[17]. Furthermore, a much finer echo texture is visible in the dermis, which indicates the better spatial resolution as well.

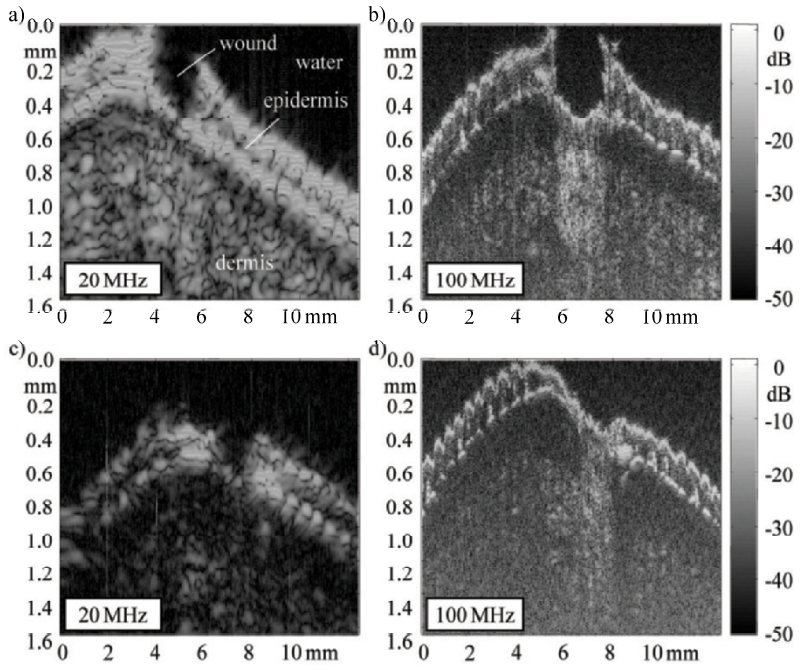

Figure 3. HFUS imaging of wound healing process (index finger): Fresh wound (top row) and after 44 hours (bottom row); 20 MHz sonography (left) and 100 MHz sonography (right).

In dermatological diagnostics, skin lesions are of great relevance[13,16,18]. Established 20 MHz range sonography (Fig. 4a) is so far mainly applied to non invasively measuring the depth of lesion penetration into healthy skin tissue for surgery planning. With the improved spatial resolution of the implemented 100 MHz range imaging system (Fig. 4b), the capabilities for analyzing skin lesions should be improved as well.

In Fig. 4, B-mode images of a nevus, which have been acquired using booth the 20 MHz range and the 100 MHz range sonography are shown. The lesion shows a low echogeneity in the B-mode images, which easily allows to measure the invasion depth.

Again, the advantage of utilizing large ultrasound frequencies becomes obvious. The echo texture, which is visible in the 100 MHz range image, is much finer than the texture in the 20 MHz range image. Consequently, much more details of the lesion are visible.

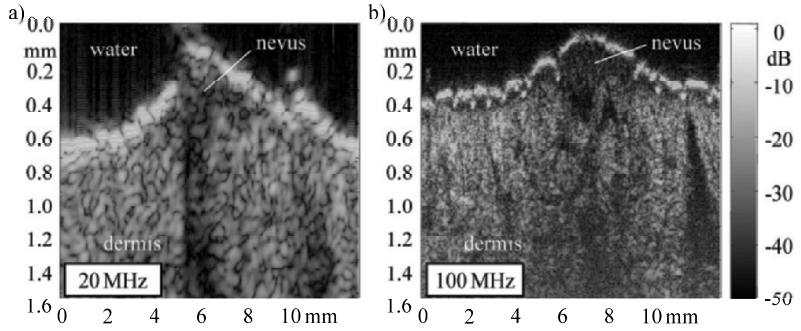

Figure 4. HFUS imaging of nevus: a) 20 MHz sonography; b) 100 MHz sonography.

4. SUMMARY AND CONCLUSIONS

In this paper, a new HFUS based imaging system, which utilizes ultrasound in the 20 MHz and the 100 MHz range, was presented. The system design was discussed and the imaging properties were analyzed with the help of measurements on technical objects. Furthermore, in vivo B-mode images were presented and discussed in order to analyze the potential of the new system in clinical applications. In conclusion, the high resolution imaging properties of the new implemented 100 MHz range system are much better than those of standard 20 MHz range sonography. Consequently, skin structures can be imaged in much more detail. It was shown that the new system allows a detailed imaging of the epidermis and the upper dermis. Furthermore, skin lesions can be differentiated from the surrounding tissue with much better accuracy. The implemented system has proven to significantly improve the diagnostic value of HFUS imaging in dermatology.

5. ACKNOWLEDGEMENT

A project of the Ruhr Center of Excellence for Medical Engineering (KMR), Bochum, Germany, supported by the German Federal Ministry of Education and Research (BMBF), No. 13N8079.

REFERENCES

1. Vogt M, Paul B, Scharenberg S, Scharenberg R, Ermert H (2003) Development of a high frequency ultrasound skin imaging system: Optimization utilizing time domain reflectometry and network analysis, *IEEE Ultrasonics Symposium Proceedings*, 744–747.
2. Vogt M, Paul B, Scharenberg S, Scharenberg R, Ermert H (2004) Analysis and measurement of spectral characteristics and spatial resolution of high frequency ultrasound imaging systems, *IEEE Ultrasonics Symposium Proceedings*, 2137–2140.
3. Foster FS, Pavlin CJ, Lockwood GR, Ryan LK, Harasiewicz KA, Berube L, Raut AM (1993) Principles and applications of ultrasound backscatter microscopy, *IEEE Transactions on Ultrasonics, Ferroelectrics, and Frequency Control* 40 (5), 608–617.
4. Foster FS, Pavlin CJ, Harasiewicz KA, Christopher DA, Turnbull DH (2000): Advances in ultrasound biomicroscopy, *Ultrasound Med Biol* 26 (1), 1–27.
5. Knapik DA, Starkoski B, Pavlin CJ, Foster FS (1997) A realtime 200 MHz ultrasound B-scan imager, *Proceedings IEEE Ultrasonics Symposium Proceedings*, 1457–1460.
6. Knapik DA, Starkoski B, Pavlin CJ, Foster FS (2000) A 100–200 MHz ultrasound biomicroscope. *IEEE Transactions on Ultrasonics, Ferroelectrics, and Frequency Control* 47 (6), 1540–1549.
7. Lockwood GR, Turnbull DH, Christopher DA, Foster FS (1996) Beyond 30 MHz, *IEEE Engineering in Medicine and Biology* 15 (6), 60–71.
8. Turnbull DH, Starkoski BG, Harasiewicz KA, Semple JL, From L, Gupta AK, Sauder DN, Foster FS (1995) A 40–100 MHz ultrasound backscatter microscope for skin imaging. *Ultrasound Med Biol* 21 (1), 79–88.
9. Berson M, Vaillant L, Patat F, Pourcelot L (1992) High-resolution, real-time ultrasonic scanner, *Ultrasound in Medicine and Biology* 18 (5), 471–478.
10. Yano T, Fukukita H, Ueno S, Fukumoto A (1987) 40 MHz ultrasound diagnostic system for dermatologic examination, *IEEE Ultrasonics Symposium Proceedings*, 875–878.
11. Chen WH, Gottlieb EJ, Cannata JM, Chen YF, Shung KK (2000) Development of sector scanning ultrasonic backscatter microscope. *IEEE Ultrasonics Symposium Proceedings*, 1681–1684.
12. Erickson S, Kruse D, Ferrara K (2001) A hand-held, high frequency ultrasound scanner. *IEEE Ultrasonics Symposium Proceedings*, 1465–1468.
13. Passmann C, Ermert H (1996) A 100-MHz ultrasound imaging system for dermatologic and ophthalmologic diagnostics. *IEEE Transactions on Ultrasonics, Ferroelectrics, and Frequency Control* 43 (4), 545–552.
14. Ermert H, Vogt M, Passmann C, el Gammal S, Kaspar K, Hoffmann K, Altmeyer P (1997) High frequency ultrasound (50–150 MHz) in dermatology, in: Altmeyer P, Hoffmann K, Stücker M (eds.) *Skin cancer and UV Radiation*, Springer, Berlin, Heidelberg, New York, 1023–1051.
15. Ermert H, Vogt M (1999) High frequency ultrasonic imaging and its applications in skin, *Proceedings of the International Society for Optical Engineering (SPIE)*, 44–55.
16. Vogt M, Kaspar K, Altmeyer P, Hoffmann K, El Gammal S (2001) High frequency ultrasound for high resolution skin imaging, *Frequenz* 55 (1–2), 12–20.
17. El Gammal S, El Gammal C, Kaspar K, Pieck C, Altmeyer P, Vogt M, Ermert H (1999) Sonography of the skin at 100 MHz enables in vivo visualization of stratum corneum and viable epidermis in palmar skin and psoriatic plaques. *J Invest Dermatol* 5, 821–829.
18. Bamber JC, Harland CC, Gusterson BA, Mortimer PS (1992): Correlation between histology and high resolution echographic images of small skin tumors, *Acoustical Imaging* 19, 369–374.

COMPUTED TOMOGRAPHY

NON-INVASIVE BREAST TISSUE CHARACTERIZATION USING ULTRASOUND SPEED AND ATTENUATION

In Vivo Validation

S.A. Johnson, T. Abbott, R. Bell, M. Berggren, D. Borup, D. Robinson, J. Wiskin, S. Olsen, B. Hanover

Techniscan Medical Systems Inc, Salt Lake City, Utah USA

Abstract: TechniScan Medical Systems, Inc. is using novel inverse scattering methods to provide a unique method for calculating ultrasound characteristics of speed and attenuation of sound traveling through human tissue. In this paper we describe basic system parameters and results of the first in vivo patient studies. It is concluded that this novel inverse scattering method provides a unique method for noninvasive breast tissue characterization that could assist physicians in assigning probability of cancer to breast abnormalities identified but not resolved with currently available imaging techniques. This application could have a major impact on patient management decisions and has the potential to reduce the number of currently unavoidable breast biopsies that result in a benign outcome

Key words: inverse scattering methods; ultrasound; computerized tomography; breast tissue characterization

1. INTRODUCTION

It has long been recognized that the full potential of ultrasound imaging for discriminating healthy from pathological or abnormal tissue cannot be realized with conventional pulse echo (reflection mode or B-scan) methods. Transmission methods using data representing time of flight and energy attenuation were advanced about thirty years ago based on the analogy of acoustic rays with the geometry of x-ray CT. The first and natural

M.P. André (ed.), Acoustical Imaging, 147–154.

application was breast cancer imaging, and early results were promising in that quantitative images of acoustic speed and absorption discriminated between cancerous and benign tumors. However, the spatial resolution remained about 8 mm to 10 mm and at this lesion size breast cancer is detectable by palpation and mammography. When the fine-resolution barrier was traced to the failure of the ray-based models to treat the *diffraction* of ultrasound, it became clear that wave propagation models rather than ray-based models were needed.

First order perturbation wave equation models (e.g. Born and Rytov approximations) were tried, but these so-called "Diffraction Tomography" methods proved to be inadequate for imaging an object as large the human breast in terms of quantitative accuracy, high spatial resolving power and freedom from severe artifacts[3,4].

TechniScan Medical Systems, Inc. has overcome the limitations in both accuracy and spatial resolution of ray-based and diffraction tomography by utilizing full wave data combined with non-perturbation-based, wave equation approaches[1,2]. Utilization of full wave data means that all or most of the secondary scattering information that arrives at the receivers at different times is used in the reconstruction algorithm that produces an image. The use of such multiple scattered data sets requires a non-perturbation theory based approach that is non-linear in nature. This is made clear by observing that the scattered field emitted by a small region within a body is dependent on the acoustic properties of the small region and the total field at the small region. However, the total field at the small region is dependent on the acoustic properties of all regions (not just regions coupled by a common ray) of the body. In the method used by TechniScan Medical Systems, Inc., both the internal fields and the acoustic properties of the body are treated as independent variables and calculated, however only the acoustic body properties are saved. The boundary conditions are, for each transmitting transducer position, the incident fields within the body and on the receivers, and the measured total fields on the receivers. Thus, the boundary conditions plus the wave equation model are the inputs to the imaging method and the acoustic properties of the body are the quantitative image outputs. This method is called inverse scattering.

2. THEORY AND IMAGING ALGORITHMS

The theory and algorithms for breast imaging by inverse scattering are related to the incident fields, the scatter within a body, and the fields recorded on the receivers. We define the temporal Fourier transform of the incident field between the transmitting transducer and the receiving

transducer by $f^{(inc)}(\theta, \omega_o, \mathbf{x}, \gamma o)$, with the constraint that there is only water (at constant temperature, spatially and temporally) present between the transmitting and receiving transducers. The acoustic properties of water are given by γ_o, while the acoustic properties of breast tissue are given by $\gamma(\mathbf{y})$. Here, θ is the vector of transmitting transducer location components, ωo is the angular frequency of the transmitted wave, and $\mathbf{x}$ is the vector location of a point within the closed space between the transmitting transducer and the receiving transducer. The scattered field, $f^{(sc)}(\theta, \omega_o, \mathbf{x}, \gamma(\mathbf{y}))$, is defined mathematically as the total field, $f(\theta, \omega_o, \mathbf{x}, \gamma(\mathbf{y}))$, minus the incident field $f^{(inc)}(\theta, \omega_o, \mathbf{x}, \gamma_o)$, i.e. $f^{(sc)}(\theta, \omega_o, \mathbf{x}, \gamma(\mathbf{y})) = f(\theta, \omega_o, \mathbf{x}, \gamma(\mathbf{y})) - f^{(inc)}(\theta, \omega_o, \mathbf{x}, \gamma_o)$. Let z be the receiver elements locations relative to the receiving transducer. We next define the actual measured scattered field on the receivers z as $f^{(m\text{-}sc\text{-}rec)}(\theta, \omega_o, \mathbf{z}, \gamma(\mathbf{y}))$ and the residual or difference between the calculated/predicted $f^{(c\text{-}sc\text{-}rec)}$ and measured f(m-sc-rec) scattered fields on the detector by

$$r(\theta, \omega_o, \mathbf{z}, \gamma(\mathbf{y}),), f^{(inc)}) = f^{(m\text{-}sc\text{-}rec)}(\theta, \omega_o, \mathbf{z}, \gamma(\mathbf{y})), f^{(inc)}) - f^{(c\text{-}sc\text{-}rec)}(\theta, \omega_o, \mathbf{z}, \gamma(\mathbf{y}), f^{(inc)}) \quad (1)$$

We next form a long residual vector $\mathbf{r}(\omega_o, \mathbf{y}, \gamma(\mathbf{y}), f^{(inc)})$, whose sub-vectors comprise components of $(\theta, \mathbf{z})$. Let $\gamma(\mathbf{y}) = \boldsymbol{\gamma}$. Define an error functional (scalar range) $\varepsilon(\omega_o, \gamma(\mathbf{y})), f^{(inc)}) = \|r(\theta, \omega_o, \mathbf{z}, \gamma(\mathbf{y}),), f^{(inc)})\|_2$ and note that ω_o and $\gamma(\mathbf{y})$ are known and fixed by the data collection process, but $\gamma(\mathbf{y})$ is unknown and minimizes $\varepsilon(\gamma)$ (where we now drop the implicit other variables ω_o, $\mathbf{y}$, $f^{(inc)}$) when the calculated $\boldsymbol{\gamma}$ best matches the true $\boldsymbol{\gamma}$ in the breast. The degree of match (smallness of ε) depends on accurate modeling of scanner geometry, scanner electronics, its transducers, and the inversion algorithm. Also important are adequate sampling of the scattered signals in space, quantized amplitude sample distribution, and number/location of incident fields. A Taylor's series expansion of $\varepsilon(\boldsymbol{\gamma})$ to quadratic accuracy gives: $\varepsilon(\boldsymbol{\gamma} + \boldsymbol{\delta}) = \varepsilon(\boldsymbol{\gamma}) + \mathbf{g}\boldsymbol{\delta} + \tfrac{1}{2}\boldsymbol{\delta}\mathbf{G}\boldsymbol{\delta}$, where gradient vector $\mathbf{g} = \nabla_{\boldsymbol{\delta}}[\varepsilon(\boldsymbol{\gamma})]$ and the Hessian matrix $\mathbf{G} = \nabla_{\boldsymbol{\delta}}[\mathbf{g}^T]$. The minimum of the LHS is found when the gradient of the RHS equal to 0. This gives $\mathbf{G}\boldsymbol{\delta} = -\mathbf{g}$.

A general iterative algorithm for finding $\boldsymbol{\gamma} = \gamma(\mathbf{y})$ is now given: (1) solve the forward problem for $f^{(c\text{-}sc\text{-}rec)}$; (2) form $\varepsilon(\boldsymbol{\gamma}^{(n)})$ and compute $\mathbf{g}^{(n)}$ and $\mathbf{G}^{(n)}$; (3) solve the linear equation $\mathbf{G}^{(n)}\boldsymbol{\delta}^{(n)} = -\mathbf{g}^{(n)}$ for $\boldsymbol{\delta}^{(n)}$; (4) minimize $\varepsilon(\boldsymbol{\gamma}^{(n)} + \alpha^{(n)}\boldsymbol{\delta}^{(n)})$ by a line search over $\alpha^{(n)}$; (5) replace $\boldsymbol{\delta}^{(n)}$ with $\alpha^{(n)}\boldsymbol{\delta}^{(n)}$; (6) update $\boldsymbol{\gamma}$ by $\boldsymbol{\gamma}^{(n+1)} = \boldsymbol{\gamma}^{(n)} + \boldsymbol{\delta}^{(n)}$; (7) if $\varepsilon(\boldsymbol{\gamma})$ is sufficiently small then stop, else repeat iteration steps.

The approximation $\mathbf{G} = 2\mathbf{J}\mathbf{J}^T$ provides fast computation of $\mathbf{G}$ for small $\mathbf{r}$, where the rectangular Jacobian matrix $\mathbf{J}$ is given by $\mathbf{J} = (\nabla_{\delta} r_1, \nabla_{\delta} r_2, \nabla_{\delta} r_3, \ldots \nabla_{\delta} r_{max})$. Fast methods for solving the forward problem for fields on the receiver in step (1) above, and for the search direction $\alpha^{(n)}\delta^{(n)}$ in steps (3–4) above, are important and require a balance between speed and accuracy. Computing steps (1, 3) by conjugate search directions, by Fletcher Reeves methods and/or by incorporating recursive or marching methods are useful.

3. CONSTRUCTION OF THE LABORATORY PROTOTYPE SCANNER

The electronic and mechanical systems necessary to image the breast by inverse scattering have been researched for over three decades. Previous generations of laboratory scanners were constructed to support modeling, provide interim images of excised tissue and small animal organs, and support the development of ultrasound array and mechanics to finally allow in vivo imaging.

Trial subsystems included mechanical scanners with a single transmitter and receiver transducers, electronic scanning using transmit and receive multiplexed 1-D arrays that circumscribed the image area, hybrid scanners with 1-D or 2-D arrays combined with mechanical motion, multiplexers using reed relay and/or digitally controlled analog switches, and arrays with a wide variety of frequencies, sizes and element arrangements.

The first in vivo images were obtained using an early laboratory prototype of the UltraSound CT ™ system. This prototype employed a fixed table with an opening into a water bath that enabled the breast to hang pendant. The buoyancy of the breast was constrained against motion at the nipple by an EKG electrode attached to a small magnet docked to a magnet-topped rod within the water bath. The Ultrasound CT™ laboratory prototype used two ultrasound transducers in a water bath to obtain the sound transmission information used to generate images. As an additional feature, acoustic reflection data was also gathered to assess the ability of the system to support traditional reflection imaging at low frequency.

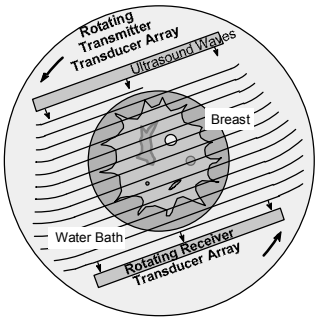

Figure 1. Top View of the Inverse Scattering Tomography Scanning Process. This drawing illustrates a planar cross-section, parallel to the chest wall, of a pendant breast in a cylindrical water tank.

The transducers were oriented with their active faces parallel and fixed relative to each other and were mounted to opposing sides of the water bath. Both the transmitter and receiver transducers were a single row of 512 transmitter/receiver elements spaced at 0.375 mm. The transmit side was wired together to allow all of the elements to operate in unison as a single element. The receiver side was operated as 512 individual elements that received the transmitted ultrasonic energy. The operating bandwidth of the transmitter and receiver transducers was 500 kHz to 3 MHz, and a chirp containing energy from 0.5 to over 2 MHz was used. Images were processed using up to 1.8 MHz.

A single computer-controlled rotation stage was used to drive the arrays mounted on the water bath in a circular motion. During the rotation sequence, the transmitting array emitted an ultrasound signal into and through the breast at 180 different locations (every 2 degrees) around the entire breast. The resulting waveforms were received by the opposing receiver array. A reflection pulse was emitted at 20 different locations (every 18 degrees) around the entire breast. The reflection signals were received at the same array that generated the ultrasonic energy. Once a slice was completed the operator physically elevated the table up or down to allow scanning of different slices of the breast.

Each slice took approximately 20 minutes and each patient had 3 or 4 slices imaged. The area to be imaged was selected prior to scanning by a radiology technician using the patient's mammograms and/or ultrasound examination as a reference. The center of the area of interest was physically marked on the breast. The transducers were aligned with the mark using a laser which passed through the clear walls of the water tank.

Water was used to couple the ultrasound signal into the breast being scanned. The temperature was maintained in the scanning tank at skin temperature with a tubing coil mounted on the base of the water bath through which warm water was circulated. Overflow protection was provided through the use of two overflow weirs at opposite ends of the scanning tank.

The data management system electronics in the prototype scanner were designed around industry-standard GAGE A/D cards and custom-built amplifier and MUX circuits, all controlled with a standard PC computer. The data acquisition system also included software that controlled and monitored the position of the arrays and the patient's breast in the water bath, and accounted for water temperature fluctuations and other factors that could affect image quality. The system was operated manually from a 350 MHz Pentium PC.

4. IN VIVO CONCEPT VALIDATION USING THE USCT LABORATORY PROTOTYPE SCANNER

TechniScan formed a Clinical Advisory Board in 1999. Members include national and local physicians and physicists who meet regularly to review TechniScan's direction and progress in development of the UltraSound CT™ scanner. Local physicians from this board were asked to refer patients who had been scheduled for breast biopsy, based on results of screening mammography and/or diagnostic mammography or ultrasound. This preliminary investigation was approved by the University of Utah Institutional Review Board and all patients underwent informed consent procedures. Patients were asked "to volunteer for an experimental imaging study which would not alter the course of their diagnostic treatment in any way" prior to undergoing biopsy. In this way, twenty-six women (age 38 to 81 years) were scanned over a period of 6 months.

Mammogram films and patient files were obtained for each of the volunteers. A certified radiology technologist used these sources to triangulate the area of interest (biopsy target area) for each patient and placed a permanent-ink mark on the breast at the level to be scanned. The targeted level plus a level above and below were scanned. Each level represented a 2.6 mm thick slice of breast tissue. Pre-biopsy findings represented within the patient group included complex cysts (n=1), circumscribed lesions (n=9), spiculated lesions (n=7), microcalcification clusters (n=4), and other breast abnormalities (n=5). Overall, 14 of the biopsies in this group proved benign and 12 were malignant. It should be noted that this was a highly selected convenience sample (and therefore not

representative of population parameters), as the goal of the investigation was to demonstrate feasibility of scanning human volunteers and investigate relationships between acoustic speed and attenuation values in benign and malignant tissues.

Analog values provided by the engineering prototype were digitized and subjected to inverse scattering analysis based on the algorithms described in this paper. Resulting images were manually segmented to isolate areas of interest identified on mammogram film and evident in the sound speed images. Sound speed and attenuation values were determined for each pixel (representing 0.375 x 0.375 mm^2 of tissue) within the segmented area and an overall average of the speed and attenuation values within the area was calculated. A scatter plot of the speed and attenuation values was then constructed, using biopsy outcome to differentiate individual patient points. Preliminary visual analysis indicated little overlap between benign and malignant outcomes, with attenuation measures having the greatest predictive value for this select sample. Mean comparisons indicated higher average attenuation values for the malignant lesions (3.05 dB/cm/MHz, standard deviation of 0.290 dB/cm/MHz) than for the benign abnormalities (1.50 dB/cm/MHz, standard deviation of 0.474 dB/cm/MHz). Speed of sound was not a reliable predictor of malignancy, with less than .01mm/microsecond separating averages for malignant and benign lesions.

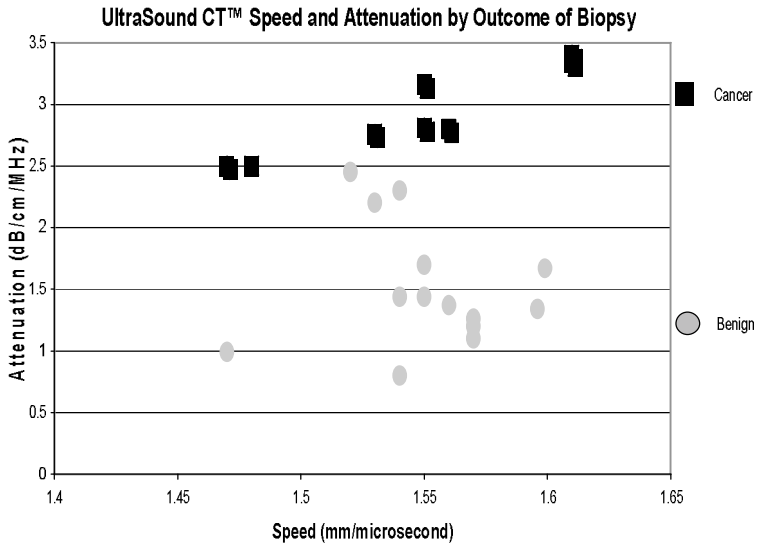

Figure 2. Results.

5. CONCLUSION

This first study of tissue characterization using UltraSound CT and TechniScan's inverse scattering methods was extremely encouraging. The association between higher attenuation values and cancerous tissue as confirmed by biopsy suggested that this technology could provide physicians and patients with information that could impact patient management decisions in cases where results of other breast imaging procedures proved equivocal. It was clear that further development of the technology was warranted including methods for increasing the speed of data collection and further refinements in the inverse scattering algorithms and calibration procedures. These efforts and results are described in the companion paper.

REFERENCES

1. Borup, D.T., Johnson, S.A., and Berggren, M.J., 1992, Nonperturbative diffraction tomography via Gauss-Newton Iteration applied to the scattering integral equation, *Ultrasonic Imaging*, **14**: 69–85.
2. Johnson, S.A. et al. "Apparatus and Method for Acoustic Imaging Using Inverse Scattering Techniques," US Patent #4: 622–222.
3. Sponheim, N., Johansen, I., and Devaney, A.J., 1991, Initial testing of a clinical ultrasound mammograph, in *Acoustical Imaging* (Vol. 18) , G.W.H. Lee, ed. Plenum Press.
4. Slaney, M., Kak, A.C., and Larsen, L.E., 1984, Limitations of imaging with first-order diffraction tomography, IEEE Trans. MTT, MTT-32: 860–874.

DATA SYMMETRIES AND THEIR USE IN ACOUSTIC DIFFRACTION TOMOGRAPHY

M.A. Anastasio, X. Pan, D. Shi
Department of Biomedical Engineering, Illinois Institute of Technology, Chicago IL 60616; Department of Radiology, The Univerity of Chicago, Chicago, IL 60637

Abstract: In this article, we review certain Fourier space symmetries that exist in formulations of ultrasonic diffraction tomography that assume either constant or variable density objects. It is demonstrated that the symmetries can be exploited for the development of novel reconstruction algorithms. Computer-simulation studies are presented to demonstrate the resulting reconstruction algorithms

Key words: Ultrasonic diffraction tomography, image reconstruction

1. INTRODUCTION

The development of ultrasonic diffraction tomography[1] (DT) systems for biomedical imaging applications remains an active area of research[2–6]. Such tomographic-based imaging systems promise several advantages over conventional B-scan imaging methods. The reconstructed image in ultrasonic DT represents a three-dimensional (3D) map of the object's acoustic properties that can convey quantitative information regarding tissue properties that is not produced easily in B-scan imaging techniques. Moreover, because it is a truly tomographic technique, it can reveal the 3D object geometry without being contaminated by overlapping structures. Another advantage of ultrasonic DT over B-scan methods is that it employs a fixed scanning geometry. Therefore, the quality and reproducibility of the reconstructed images is not related to the skill of the operator who conducts the imaging scan.

M.P. André (ed.), Acoustical Imaging, 155–171.

Although a variety of reconstruction algorithms have been developed for ultrasonic DT, there remains a great need for the development of improved algorithms that address the specific requirements of clinical applications. Such requirements include robustness to measurement noise, applicability to scanning geometries of clinical relevance, and the potential to compensate for the effects of density variations and higher-order scattering effects introduced by strong tissue inhomogeneities.

Recently, we have investigated the identification and exploitation of explicit data symmetries for the development of novel ultrasonic DT reconstruction algorithms[7–14]. Due to the tomographic nature of DT, the measurement data collected at different view angles must satisfy certain mathematical constraints in order to ensure data consistency. By forcing a collection of measurement data to satisfy these conditions, known as *consistency conditions*, a component of data that represents certain noise or other inconsistencies can effectively be suppressed. Assuming that the consistency conditions are known explicitly, they can be enforced in different ways to remove different inconsistent components of the measurement data. This can permit, for example, control of the statistical properties of the reconstructed image. Utilization of consistency conditions can also lead to novel reconstruction algorithms that may have numerical and computational properties superior to that of the convention algorithms.

In this article, we review different data symmetries in ultrasonic DT, and demonstrate how they can facilitate the development of new DT reconstruction algorithms. We will consider both the constant and variable density formulations of ultrasonic DT. In the constant density DT case, we demonstrate that data symmetries can be employed to convert the DT problem into a conventional X-ray computed tomography (CT) problem. In the variable density case, we describe how the use of data symmetries can facilitate the separate reconstructions of the density and compressibility variations of an object. In each case, numerical examples are provided to demonstrate the resulting reconstruction algorithms.

2. CONSTANT DENSITY FORMULATION OF DT

In this section, we consider the classic ultrasonic DT reconstruction problem in which the object is characterized by its spatially variant complex-valued

refractive index distribution. The variable density formulation of DT is presented in Section 3.

2.1 Tomographic Scanning Geometry and Imaging Model

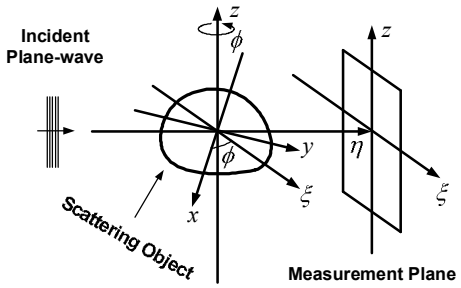

Figure 1. The classic scanning geometry of 3D DT.

The classic scanning geometry of 3D DT is shown in Fig. 1. A plane-wave $\exp[ik\eta]$ with wavenumber k that propagates along the η-axis is incident upon the object that is contained within a volume V. The complex amplitude of the forward scattered wavefield is measured on the detector plane located at $\eta = l$ that is spanned by the coordinates ξ and z. Tomographic scanning is achieved by simultaneously rotating the plane-wave source and detector plane about the z-axis through the tomographic view angle ϕ. From knowledge of a collection of tomographic measurements, DT seeks to reconstruct the scattering potential $f(\vec{r})$ that is related to the objects complex-valued refractive index distribution $n(\vec{r})$ as

$$f(\vec{r}) = \frac{k^2}{4\pi}\left(n^2(\vec{r}) - 1\right). \tag{1}$$

The wavefield on the detector plane at view angle ϕ can be expressed as

$$U(\xi, z, \phi) = \exp[ik\eta + \psi(\xi, z, \phi)], \tag{2}$$

where $\psi(\xi, z)$ denotes the complex-phase perturbation. In this work, we assume that the object is weakly scattering in the sense that the first-order Rytov approximation is valid[1]. However, the results that follow can provide the basis for nonlinear reconstruction algorithms that can account for

higher-order scattering effects[15,16]. Let $\hat{\psi}(u_r, v, \varphi)$ denote the two-dimensional (2D) Fourier transform of $\psi(\xi, z, \phi)$ with respect to the detector plane coordinates. It is has been demonstrated[1] that the Fourier transform of $\psi(\xi, z, \phi)$ is related to the scattering potential $f(\vec{r})$ as

$$M(u_r, v, \phi) = \int_V d\,\vec{r}\, f(\vec{r})\ \exp\left[-i(u_r\xi + vz + \omega(u_r, v)\eta\right], \tag{3}$$

where

$$M(u_r, v, \phi) \equiv \frac{\omega(u_r, v)}{i4\pi^2} \exp\left[-i\omega(u_r, v)l\right] \hat{\psi}(u_r, v, \phi), \tag{4}$$

and

$$\omega(u_r, v) \equiv \sqrt{k^2 - u_r^2 - v^2} - k. \tag{5}$$

Equation (3), which is known as the Fourier diffraction projection (FDP) theorem, indicates that the Fourier transform of the complex phase $\psi(\xi, z, \phi)$ is linearly related to the 3D Fourier transform of $f(\vec{r})$ evaluated on a hemi-sphere of radius k that is centered at position $(0, 0, -k)$ in a rotated Fourier coordinate system that is conjugate to the (ξ, η, z) spatial system. We will assume that $k^2 \geq u_r^2 + v^2$, reflecting that evanescent wave modes are not typically measurable.

2.2 Fourier Space Data Symmetries

The FDP theorem provides the basis for data-symmetry identification in DT. Because $M(u_r, v, \phi)$ is a periodic function of the view angle ϕ, it can be represented by a Fourier series with expansion coefficients given by

$$M_m(u_r,v)=\frac{1}{2\pi}\int_0^{2\pi} d\phi\, M(u_r,v,\phi)\ \exp\left[-im\phi\right], \tag{6}$$

where $m\in\mathbb{Z}$. On substitution from Eq. (3) into Eq. (6), it can be verified that

$$M_m(u_r,v)=(-1)^m\left[\gamma(u_r,v)\right]^{-2m} M_m(-u_r,v), \tag{7}$$

where $\gamma(u_r,v)\equiv\dfrac{\sqrt{u_r^2+\omega^2(u_r,v)}}{u_r-i\omega(u_r,v)}$. Equation (7) describes a data symmetry. This symmetry results from the fact that a double coverage of the scattering potential's Fourier space is produced as the tomographic view angle varies from 0 to 2π. Equation (7) can be interpreted as a consistency condition in the sense that it must be satisfied by consistent measurement data. We demonstrate below that this consistency condition can be enforced explicitly during the reconstruction procedure.

2.3 Reconstruction Algorithms that Exploit Explicit Data Symmetries

Let $f^{cyl}(r,\theta,z)$ denote $f(\vec{r})$ expressed in the cylindrical coordinate system. For a given *z*, consider the 2D Radon transform of $f(r,\theta,z)$ that is defined as

$$p(\xi,z,\phi)=\int_{\infty} d\eta\, f^{cyl}(r,\theta,z). \tag{8}$$

Equation (8) describes a stack of 2D Radon transforms of $f^{cyl}(r,\theta,z)$ along the *z*-axis. From knowledge of $p(\xi,z,\phi)$, $f^{cyl}(r,\theta,z)$ can be reconstructed on a slice-by-slice basis by use of the computationally efficient and numerically stable filtered backprojection (FBP) algorithm of parallel beam X-ray CT.

Let $P(u_a,v,\phi)$ denote the 2D Fourier transform of $p(\xi,z,\phi)$ with respect to the detector coordinates ξ and z. The Fourier series expansion coefficients of the periodic function $P(u_a,v,\phi)$ as defined as

$$P_m(u_a,v) = \frac{1}{2\pi}\int_0^{2\pi} d\phi\, P(u_a,v,\phi)\ \exp\left[-im\phi\right]. \tag{9}$$

On substitution from Eq. (8) into Eq. (9) and performing the integration over ϕ, it can be verified that[7,8]

$$P_m(u_a,v) = \left[\gamma(u_r,v)\right]^m M_m(u_r,v), \tag{10}$$

and

$$P_m(u_a,v) = (-1)^m \left[\gamma(u_r,v)\right]^{-m} M_m(-u_r,v), \tag{11}$$

where $u_a = \left[u_r^2 + \omega^2(u_r,v)\right]^{1/2}$. (12)

Equations (10) and (11) are identical mathematically, and will produce identical estimates of $P_k(u_a,v)$ in the absence of data inconsistencies such as noise or finite sampling effects. However, in the presence of data inconsistencies, these equations will produce estimates of $P_k(u_a,v)$ that are distinct in general. In order to produce an estimate with a potentially reduced noise level, Eqs. (10) and (11) can be combined as[7,8]

$$\begin{aligned} P_m^c(u_a,v) = {} & c(u_r,v)\left[\gamma(u_r,v)\right]^m M_k(u_r,v) \\ & + \left[1 - c(u_r,v)\right](-1)^m \left[\gamma(u_r,v)\right]^{-m} M_m(-u_r,v), \end{aligned} \tag{13}$$

where $c(u_r,v)$ is a generally complex-valued combination coefficient. The superscript on $P_k^c(u_a,v)$ denotes that the estimate was produced by use of a combination coefficient $c(u_r,v)$. Equation (13) describes an infinite family of methods for estimation of $P_k^c(u_a,v)$ that are indexed by the choice of the

combination coefficient $c(u_r, v)$. Different choices of $c(u_r, v)$ specify different reconstruction algorithms that will produce images generally possessing distinct noise properties. If knowledge of the measurement-noise statistics is available, $c(u_r, v)$ can be chosen in such a way that Eq. (13) produces an estimate $P_k^c(u_a, v)$ that has an optimally reduced variance, which will result in minimization of the global variance of the reconstructed image. The use of Eq. (12) enforces automatically the consistency conditions described in Eq. (7). From knowledge of $P_k^c(u_a, v)$, $p(\xi, z, \phi)$ can be determined, from which $f^{cyl}(r, \theta, z)$ can be reconstructed readily by use of the FBP algorithm. For 3D problems, this reconstruction procedure has a tremendously reduced computational burden as compared to the filtered backpropagation algorithm[17] of DT. It is interesting to note that the filtered backpropagation algorithm can be obtained by use of Eq. (13) by consideration of the special case $c(u_r, v) = \frac{1}{2}$.

3. VARIABLE DENSITY FORMULATION OF DT

Conventional formulations of ultrasonic DT assume that the object's density is constant and equal to that of the background medium. When applied for reconstruction of a variable density object, conventional ultrasonic DT reconstruction algorithms will produce a composite image that reflects both the compressibility and density variations of the object[18,19]. Although such images may reveal certain geometric features of the object, they do not provide direct quantitative information regarding the object's physical properties. The goal of variable density ultrasonic DT is to produce separate images of the compressibility and density variations of the object, which can contain useful diagnostic information.

A reconstruction theory for variable density ultrasonic DT has been established by Devaney[18]. In that work, reconstruction algorithms of filtered backpropagation form were developed and demonstrated. Below we identify explicit data symmetries for variable density DT, and utilize these symmetries for the development of novel reconstruction algorithms.

3.1 Tomographic Scanning Geometry and Imaging Model

For simplicity, we will consider the 2D scanning geometry in Fig. 2. The tomographic measurement protocol is identical to that described in Section 2. The results that follow can readily be extended to the 3D case. We will adopt the imaging model and physical assumptions described in the seminal work of Devany[18]. Let $\kappa(\xi,\eta)$ and $\rho(\xi,\eta)$ denote the compressibility and density distributions, respectively, of the object, expressed in the rotated coordinate system shown in Fig. 2. The goal of variable density DT is to reconstruct, separately, the quantities

$$\chi_\kappa(\xi,\eta) \equiv \frac{\kappa(\xi,\eta)-\kappa_0}{\kappa_0} \qquad and \qquad \chi_\rho(\xi,\eta) \equiv \frac{\rho(\xi,\eta)-\rho_0}{\rho_0}, \quad (14)$$

which describe the object's normalized compressibility and density variations.
Let

$$\tilde{\chi}_\kappa[u_r,\phi] = \int_V d\xi\, d\eta\, \chi_\kappa(\xi,\eta)\ \exp\left[-i(u_r\xi+\omega(u_r)\eta\right] \quad (15)$$

and

$$\tilde{\chi}_\rho[u_r,\phi] = \int_V d\xi\, d\eta\, \chi_\rho(\xi,\eta)\ \exp\left[-i(u_r\xi+\omega(u_r)\eta\right], \quad (16)$$

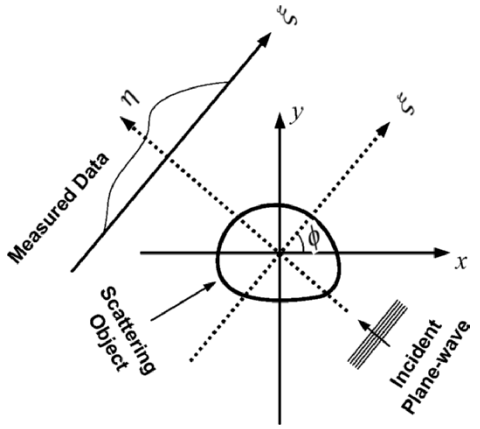

Figure 2. Scanning geometry for 2D variable density DT.

denote the 2D Fourier transforms of $\chi_\kappa(\xi,\eta)$ and $\chi_\rho(\xi,\eta)$, respectively, evaluated on semi-circular arcs that intersect the origin and have an orientation ϕ. The function $M(u_r,\phi)$ is specified by the measured complex phase in analogy to Eq. (4), and $\omega(u_r)$ is defined by Eq. (5) with $v=0$. Assuming the validity of the first-order Rytov approximation, it has been shown[18] that the Fourier transform of the measured complex phase is related to the object properties as

$$M(u_r,\phi)=\left(-\tilde{\chi}_\kappa[u_r,\phi]+\left[\frac{u_r^2+\omega^2(u_r)}{2k^2}-1\right]\tilde{\chi}_\rho[u_r,\phi]\right). \tag{17}$$

Equation (17) can be regarded as the FDP theorem for variable density media. This result demonstrates that an image reconstructed from $M(u_r,\phi)$ directly by use of a conventional DT reconstruction algorithm will contain a mixture of information regarding the compressibility and density variations of the object.

3.2 Fourier Space Symmetries

We will assume that the object is dispersionless, and therefore $\chi_\kappa(\xi,\eta)$ has no dependence on the temporal frequency of the insonifying wavefield. Consider that two tomographic scans of the object are performed that correspond to insonifying plane-waves with wavenumbers k_1 and k_2. The quantities $M^{(1)}(u_r,\phi)$ and $M^{(2)}(u_r,\phi)$ will denote the modified data functions that correspond to k_1 and k_2, respectively. The Fourier series expansion coefficients of these quantities will be denoted as $M_m^{(1)}(u_r)$ and $M_m^{(2)}(u_r)$, respectively. $\tilde{\chi}_\kappa^{(n)}[u_r,\phi]$ and $\tilde{\chi}_\rho^{(n)}[u_r,\phi]$ will be used to denote the object property Fourier data residing on semi-circular arcs of radius k_n, $n=1,2$. Similarly, ω_n will denote ω evaluated with $k=k_n$.

Due to the rotational invariance of the imaging model, it can be verified that the following Fourier space symmetries hold true[14]:

$$\tilde{\chi}_\kappa^{(1)}[u_r,\phi]=\tilde{\chi}_\kappa^{(2)}[u_r',\phi+\phi'] \tag{18}$$

$$\tilde{\chi}_{\rho}^{(1)}[u_r,\phi] = \tilde{\chi}_{\rho}^{(2)}[u_r',\phi+\phi'], \tag{19}$$

where

$$u_r' = R\sqrt{1-\frac{R^2}{4k_2^2}}, \tag{20}$$

$$R \equiv \sqrt{u_r^2+\omega_1^2}, \tag{21}$$

and

$$\phi' = \arctan\left(\frac{u_r}{\omega_1}\right) - \arctan\left(\frac{u_r'}{\omega_2}\right). \tag{22}$$

3.3 Reconstruction Algorithms that Explicitly Exploit Fourier Space Symmetries

According to Eq. (17), the data functions $M^{(1)}(u_r,\phi)$ and $M^{(2)}(u_r,\phi)$ are related to the Fourier transform of the compressibility and density distributions as

$$M^{(1)}(u_r,\phi) = \left(-\tilde{\chi}_{\kappa}^{(1)}[u_r,\phi] + \left[\frac{u_r^2+\omega_1^2(u_r)}{2k_1^2}-1\right]\tilde{\chi}_{\rho}^{(1)}[u_r,\phi]\right) \tag{23}$$

and

$$M^{(2)}(u_r,\phi) = \left(-\tilde{\chi}_{\kappa}^{(2)}[u_r,\phi] + \left[\frac{u_r^2+\omega_2^2(u_r)}{2k_2^2}-1\right]\tilde{\chi}_{\rho}^{(2)}[u_r,\phi]\right). \tag{24}$$

Equations (23) and (24) constitute a system of two equations containing the four unknowns $\tilde{\chi}_{\kappa}^{(n)}[u_r,\phi]$ and $\tilde{\chi}_{\rho}^{(n)}[u_r,\phi]$, $n=1,2$. In order to circumvent this difficulty, we can utilize the Fourier space symmetries described in Section 3.2. Evaluating Eq. (24) at $u_r = u_r'$ and utilizing Eqs. (18) and (19), we find that

$$M^{(2)}(u_r',\phi) = \left(-\tilde{\chi}_{\kappa}^{(1)}[u_r,\phi-\phi'] + \left[\frac{u_r^2+\omega_2^2(u_r')}{2k_2^2} - 1 \right] \tilde{\chi}_{\rho}^{(1)}[u_r,\phi-\phi'] \right). \quad (25)$$

The unknown Fourier data that appear in Eq. (25) are now found to reside on semi-circular arcs of radius k_1 that are rotated by an angle ϕ' with respect to the corresponding quantities in Eq. (23). This angular shift will pose no difficulties if we exploit the rotational invariance of the imaging model.

Let $A_m(u_r)$ and $B_m(u_r)$ denote the Fourier series expansion coefficients of $\tilde{\chi}_{\kappa}^{(1)}[u_r,\phi]$ and $\tilde{\chi}_{\rho}^{(1)}[u_r,\phi]$, respectively. By calculating the Fourier series expansion coefficients of both sides of Eqs. (23) and (25) and making use of the Fourier shift theorem, one obtains readily a system of two equations containing two unknowns that can be solved as[14]

$$A_m(u_r) = \frac{1}{W} \begin{vmatrix} M_m^{(1)}(u_r) & \dfrac{u_r^2+\omega_1^2(u_r)}{2k_1^2} - 1 \\ M_m^{(2)}(u_r') & \left[\dfrac{(u_r')^2+\omega_2^2(u_r')}{2k_2^2} - 1 \right] \exp[im\phi'] \end{vmatrix} \quad (26)$$

and

$$B_m(u_r) = \frac{1}{W} \begin{vmatrix} -1 & M_m^{(1)}(u_r) \\ -\exp[im\phi'] & M_m^{(2)}(u_r') \end{vmatrix}, \quad (27)$$

where

$$W = \begin{vmatrix} -1 & \dfrac{u_r^2 + \omega_1^2(u_r)}{2k_1^2} - 1 \\ -\exp[im\phi'] & \left[\dfrac{(u_r')^2 + \omega_2^2(u_r')}{2k_2^2} - 1\right]\exp[im\phi'] \end{vmatrix}. \quad (28)$$

From knowledge of $A_m(u_r)$ and $B_m(u_r)$, estimates of the Fourier data $\tilde{\chi}_\kappa^{(1)}[u_r, \phi]$ and $\tilde{\chi}_\rho^{(1)}[u_r, \phi]$ can be determined. In turn, estimates of the object properties $\chi_\kappa(\xi, \eta)$ and $\chi_\rho(\xi, \eta)$ can subsequently be reconstructed separately by use of a DT reconstruction algorithm for constant density objects, such as the one presented in Section 2.

4. NUMERICAL EXAMPLES

We conducted computer-simulation studies to demonstrate the reconstruction algorithms presented in Sections 2 and 3. Although our reconstruction theories can accommodate 3D objects, in the presented numerical studies 2D objects were considered.

4.1 Constant Density DT

For the constant density DT case, the numerical phantom shown in Fig. 3, top row, was taken to represent the complex refractive index distribution of the object. The 2D scanning geometry in Fig. 2 was employed, in which the linear detector array contained 1024 elements and measurements were acquired at 360 view angles that were evenly spaced over a 2π angular range. Assuming a wavelength $\lambda = 0.001m$, the FDP theorem (Eq. 3) was employed for computation of the simulated complex amplitude of the transmitted wavefields. Noisy versions of the wavefield data were created by addition of 1% Gaussian noise. Images were reconstructed from the noiseless and noisy data sets by use of the algorithm described in Section 2. Specifically, Eq. (13) was employed for estimation of $P_m^c(u_a, v)$ followed by application of the FBP algorithm for reconstructing estimates of $f(\vec{r})$. Two different values of the combination coefficient $c(u_r, v)$ were considered, namely $c(u_r, v) = 0.5$ and $c(u_r, v) = 0.9$. The matrix size of the reconstructed images was 256^2 pixels.

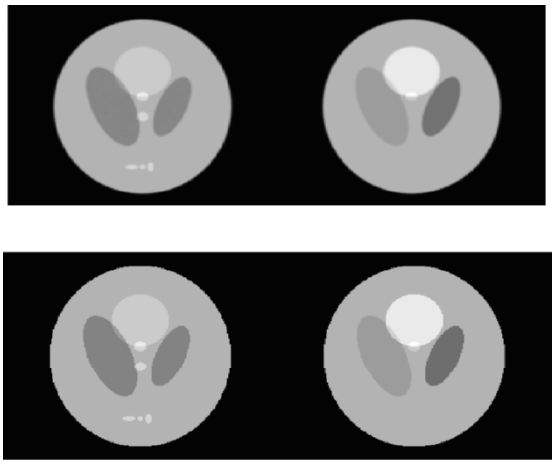

Figure 3. Top row: The real (left panel) and imaginary (right panel) components of the simulated refractive index distribution. Bottom row: Corresponding images reconstructed from the noiseless simulation data.

Images reconstructed from the noiseless simulation data by use of the algorithm specified by $c(u_r, v) = 0.5$ are shown in Fig. 3, bottom row. Although not shown, the corresponding images reconstructed by use of the algorithm specified by $c(u_r, v) = 0.9$ are virtually identical to those shown in Fig. 3. This is consistent with our assertion that the algorithms specified by different choices of $c(u_r, v)$ are equivalent mathematically. The images reconstructed from the noisy simulation data by use of the algorithms specified by $c(u_r, v) = 0.5$ and $c(u_r, v) = 0.9$ are contained in the top and bottom rows of Fig. 4, respectively. As expected, different reconstruction algorithms produced noisy images that are distinct. This reflects that our reconstruction methods provide the opportunity to suppress noise propagation through a suitable choice of combination coefficient $c(u_r, v)$.

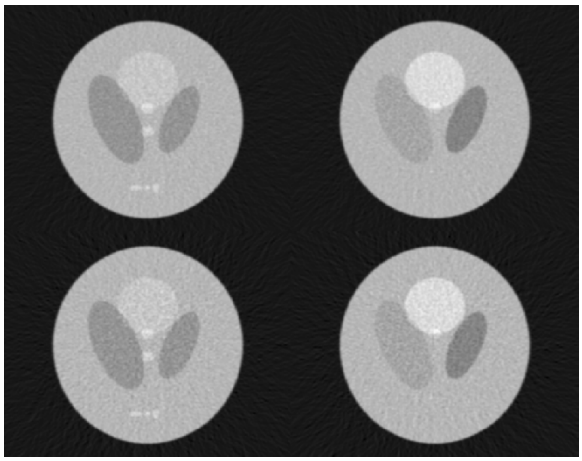

Figure 4. Images reconstructed by use of the noisy simulation data. See the text for a description.

4.2 Variable Density DT

For the variable density DT case, the numerical phantom shown in Fig. 5 was taken to represent the compressibility (left panel) and density (right panel) distributions of the object. The 2D scanning geometry in Fig. 2 was employed, in which the linear detector array contained 512 elements and measurements were acquired at 360 view angles that were evenly spaced over a 2π angular range. The distance between the center of rotation and detector line was $0.65m$. At each of the wavelengths $\lambda_2 = 0.002m$ and $\lambda_1 = 0.006m$, the FDP theorem for variable density DT (Eq. 17) was employed for computation of the complex amplitude of the transmitted wavefields. Noisy versions of the wavefield data were created by addition of 0.05% Gaussian noise. Equations (26) and (27) were employed for determination of $\tilde{\chi}_{\kappa}^{(1)}[u_r, \phi]$ and $\tilde{\chi}_{\rho}^{(1)}[u_r, \phi]$. From this data, estimates of the object properties $\chi_{\kappa}(\xi, \eta)$ and $\chi_{\rho}(\xi, \eta)$ were reconstructed individually by use of the DT reconstruction algorithm described in Section 2 with $c(u_r, v) = 0.5$.

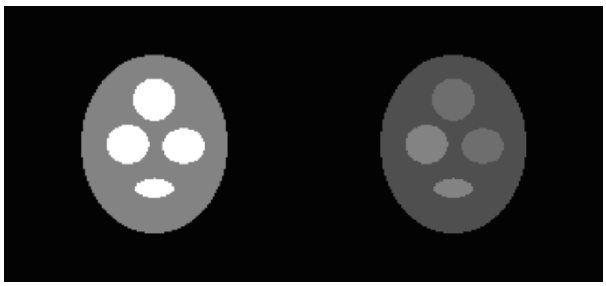

Figure 5. The numerical phantom representing the compressibility (left panel) and density (right panel) variations in the object.

The images reconstructed from the noiseless and noisy simulation data are shown in the top and bottom rows, respectively, of Fig. 6. The reconstructed distributions of compressibility and density variations are contained in the left and right columns, respectively. These results confirm that our algorithm can indeed produce accurate reconstructions of the compressibility and density variations.

5. SUMMARY

In this work, we have discussed Fourier space symmetries that exist in ultrasonic DT, and demonstrated that they can facilitate the development of novel reconstruction theories. Specifically, for the constant DT problem, symmetries were utilized to exploit redundancies in the measurement data, which permitted control of the statistical properties of the reconstructed images. For the variable density DT problem, the identification and exploitation of Fourier space symmetries resulted in the development of a novel algorithm for independently reconstructing images of an object's compressibility and density variations.

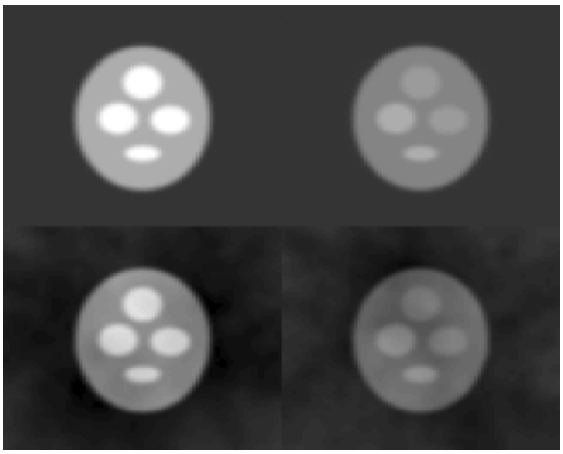

Figure 6. Reconstructed images of the compressibility (left column) and density (right column) variations. The images in the top and bottom rows were reconstructed from noiseless and noisy simulation data, respectively.

6. ACKNOWLEDGEMENT

We thank Mr. Thomas Deffieux for useful interactions regarding the variable density DT problem.

REFERENCES

1. R. Muller, M. Kaveh, and G. Wade, Reconstructive tomography and applications to ultrasonics, *Proceedings of the IEEE*, **67**, 567–587, 1979.
2. M.P. Andre et al., A New Consideration of Diffraction Computed Tomography for Breast Imaging: Studies in Phantoms and Patients*, Acoustical Imaging* J.P. Jones, Ed., 379–390, 1995.
3. J.F. Greenleaf, J. Ylitalo, and J.J. Gisvold, Ultrasonic Computed Tomography for Breast Examination*, IEEE Engineering in Medicine and Biology Magazine*, 27–32, 1987.
4. M.P. Andre, et al., High-Speed Data Acquisition in a Diffraction Tomography System Employing Large-Scale Toroidal Arrays, *International Journal of Imaging Systems Technology*, **8**(1): p. 137–147, 1997.
5. N. Sponheim, L.J. Gelius, I. Johansen, and J.J. Stamnes, Quantitative Results in Ultrasonic Tomography of Large Object Using Line Sources and Curved Detector

Arrays, *IEEE Transactions on Ultrasonic, Ferroelectrics, and Frequency Control*, **38**(4): p. 370–379, 1991.
6. T. Mast, Wideband quantitative ultrasonic imaging by time-domain diffraction tomography, *Journal of the Acoustical Society of America*, **106**, 3061–3071, 1999.
7. X. Pan, Unified reconstruction theory for diffraction tomography with consideration of noise control, *Journal of the Optical Society of America A*, **15**, 2312–2326, 1998.
8. M.A. Anastasio, and X. Pan, Computationally efficient and statistically robust image reconstruction in three-dimensional diffraction tomography**,** *Journal of the Optical Society of America A*, **17**(3), 391–400, 2000.
9. X. Pan, and M.A. Anastasio, Short-scan filtered backpropagation algorithms for diffraction tomography, *Journal of the Optical Society of America A,* **16**, 2896–2903, 1999.
10. M.A. Anastasio, and X. Pan, A new reconstruction algorithm for reflection mode diffraction tomography, *IEEE Transactions on Image Processing*, **9**, 1262–1271, 2000.
11. M.A. Anastasio, and X. Pan, Investigation of the noise properties of an infinite class of reconstruction methods in diffraction tomography, *International Journal of Imaging Systems Technology,* **10**, 437–446, 2000.
12. X. Pan, and M.A. Anastasio, On a limited-view reconstruction problem in diffraction tomography, *IEEE Transactions on Medical Imaging*, **21**, 413–416, 2002.
13. M.A. Anastasio, and X. Pan, An improved reconstruction algorithm for 3D diffraction tomography with spherical-wave sources, *IEEE Transactions on Biomedical Engineering*, **50**, 517–521, 2003.
14. M.A. Anastasio, D. Shi, and T. Deffieux, Image reconstruction in variable density acoustic tomography, *Proceedings of the SPIE*, 5750, 326–331, 2005.
15. Z.Q. Lu, et al., Acoustical Tomography Based on the Second-Order Born Transform Perturbation Approximation. *IEEE Transactions on Ultrasonics, Ferroelectrics, and Frequency Control*, **43**(2), 296–302, 1996.
16. C. Lu, et al., Image Reconstruction with Acoustic Measurement Using Distorted Born Iteration Method, *Ultrasonic Imaging*, 1996, **18**, 140–156, 1996.
17. A.J. Devaney, A filtered backpropagation algorithm for diffraction tomography, *Ultrasonic Imaging*, **4**, 336–350, 1982.
18. A.J. Devaney, Variable density acoustic tomography, *Journal of the Acoustical Society of America*, **78**, 120–130, 1985.
19. A. Witten, J. Tuggle, and R.C. Waag, A Practical Approach to Ultrasonic Imaging Using Diffraction Tomography, *Journal of the Acoustical Society of America*, **83**(4), 1645–1652, 1988.

COMPUTERIZED ULTRASOUND RISK EVALUATION (CURE): FIRST CLINICAL RESULTS

N. Duric, P. Littrup, O. Rama, E. Holsapple
Karmanos Cancer Institute, 4100 John R, Detroit MI 48201, USA.

Abstract: The Karmanos Cancer Institute has developed an ultrasound (US) tomography system, known as Computerized Ultrasound Risk Evaluation (CURE), for detecting and evaluating breast cancer, with the eventual goal of providing improved differentiation of benign masses from cancer. We report on our first clinical findings with CURE.

A preliminary study imaged 19 patients with CURE between October 1 and December 1, 2004. Patients were recruited on the basis of having a suspicious mass after mammography and follow-up ultrasound. The CURE exam was interposed between the standard US exam and subsequent biopsy. Biopsy results were therefore available for all 19 patients. Typically, 45 tomograms were taken of each patient with the CURE device. For each tomogram, images of reflectivity and sound speed were made with automated algorithms. In five cases, attenuation images had to be produced by a manual technique due to gain instability of the current transducer ring.

Based on the preliminary CURE data we have currently utilized six CURE diagnostic criteria for cancer. In this small sample, when each criterion is given equal weight, it appears that women with higher scores are more likely to have cancerous masses. More definitive results await the conclusion of a larger, ongoing study

Keywords: Ultrasound tomography, breast cancer, diagnostic criteria, tissue characterization

M.P. André (ed.), Acoustical Imaging, 173–181.

1. INTRODUCTION

Ultrasound tomography may provide a more operator independent alternative to current breast ultrasound, while presenting hope for a highly specific , non-ionizing screening adjunct to mammography. Mammography screening has been shown to reduce the mortality rate up to 30% in multiple screening trials. However, mammography also generates many abnormal findings not related to cancer which leads to additional, costly imaging procedures and up to 80% benign biopsies. If marked improvements in tissue-specific imaging could be achieved, up to one million benign biopsies could be eliminated each year in the United States[1], saving several billion dollars[2]. Recent studies have demonstrated the effectiveness of ultrasound (US) imaging in detecting breast cancer[1], particularly for women with dense breasts. At the same time, other studies have raised questions about the efficacy of mammography[2]. However, despite these developments, US is used only as an adjunct to X-ray mammography. A major reason for ultrasound's adjunctive role is its limited imaging capabilities. Specifically, the operator dependence, limited resolution and contrast, the presence of speckle noise and artifacts are key factors which have prevented US imaging from playing a greater role in standard diagnostic evaluation.

Efforts to improve the diagnostic accuracy of current US may be best represented by the success of the 'Stavros/Colorado' criterion for mass margin evaluation[3]. Further advances have led to compound imaging[5] (SonoCT, ATL/Phillips) resulting in better mass margin identification by reduction, of speckle, clutter and ultrasound artifacts [6]. As a result of these advancements, US is increasingly being studied for its potential as a screening tool. The ongoing ACRIN 6666 study, funded by the Avon foundation and the National Cancer Institute, represents a definitive trial evaluating the potential of US as a screening tool[7,8,9]. However, its anticipated positive results could also highlight the difficulties of mass acceptance and replication at the community level due to the persistent operator dependent nature of conventional US.

Several investigators demonstrated the early promise of ultrasound tomography but lacked the appropriate hardware/software technology advances that are currently available to make a fast, practical system (10–12). Current work is being carried out on a number of fronts and includes Johnson et al[13] (TechniScan Inc), Marmarelis' group at USC[14], and the work at the Karmanos Cancer Institute (KCI) in Detroit[15–21]. However, due to continued practical constraints of hardware and/or software combinations, we are the only group that has obtained full breast data acquisition in approximately 1 minute or less for both reflection and transmission imaging.

1.1 Ultrasound Tomography and CURE

We are developing the Computerized Ultrasound Risk Evaluation System (CURE)[14–20] to be a fast, operator independent data acquisition tool with a high degree of flexibility for continued incremental improvement on both hardware and software aspects as dictated by initial outcomes. Its current operating characteristics are summarized in Table 1.

Table 1. Summary of CURE performance characteristics.

Operating frequency	Number of data acquisition channels	Data acquisition time (one slice)	Data acquisition time for entire slice set (50 slices)	Spatial Resolution (reflection–in plane)	Minimal detectable sound speed variations	Minimal detectable variations in attenuation	Patient in and out time
1.5 MHz	256	0.1s	30s	0.4–0.7 mm	5 m/s	10%	5 min

Our approach differs from those cited earlier[13–14] for two major reasons. First, because CURE embodies a ring transducer that surrounds the breast, we collect the entire 2-D scattered field, which allows us to perform both transmission tomography and reflection tomography. As detailed below, this approach allows for measurement of a larger number of cancer detection criteria than is possible with transmission or reflection only. Second, the high data acquisition speed of the CURE scanner completely eliminates inter and intra-slice image motion artifacts. We believe that these two unique aspects of our approach will allow us to fully probe the clinical potential of US tomography.

The first clinical prototype has been integrated into the normal patient flow of the Walt Comprehensive Breast Center located at KCI. The purpose of this paper is to report on the initial clinical tests.

2. DATA COLLECTION AND ANALYSIS

2.1 Phantom Studies

The prototype device was installed in August, 2005 and first evaluated with phantoms. The breast phantom was built by Dr. Ernie Madsen of the University of Wisconsin and represents tissue-equivalent scanning characteristics of highly scattering, predominantly parenchymal breast tissue. It also mimics the presence of benign and cancerous masses embedded in glandular tissue, including a subcutaneous fat layer. The

phantom was scanned with CURE and representative images are shown in Fig. 1a–d.

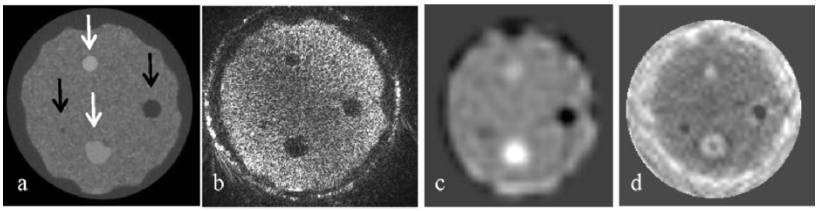

Figure 1. CURE Imaging of the breast phantom. From left to right: (a) an X-ray CT slice containing two fat spheres (black arrows) and two "cancerous tumors" (white arrows). The corresponding CURE images show (b) reflection, (c) sound speed and (d) attenuation. All four masses are detected in the three CURE images. Note the significantly different sound speed and attenuation of the benign and cancerous masses (c and d). Sound speed and attenuation values increase from black to white.

The phantom mass assessment was largely successful. The resolution, contrast and location accuracy met our milestone targets of 0.5 mm, SNR > 3 and +/- 5 mm, respectively. The sound speed characterization of the various phantom components also met the milestone targets, reaching an accuracy of 5 m/s. The targeted goal of measuring accurate mass attenuation, however, was not met. The primary reason for this was an unforeseen design flaw in the first transducer that led to random gain variations among the elements that make up the transducer. Since these gain variations were a function of time, it was not possible to calibrate them. Therefore, relative attenuation values were determined from manual calculations along each ray projection. Despite the labor-intensive nature of these manual calculations, proof of principle was demonstrated by generating attenuation images for 5 of the patients and the breast phantom (Figure 1d). Fortunately, these images serve as good estimates of future attenuation imaging capabilities with our new transducer ring, which is better matched to the attenuation algorithm. If necessary for the next series of patients, the flexible system architecture will allow continuous incremental design implementations upon the transducer and/or algorithm software in order to make any further design modifications a minor adjustment, rather than an impediment to further clinical progress.

Overall, CURE performance reached or exceeded most of our milestone targets, allowing us to proceed with the in-vivo testing. The clinical implications of these in-vivo tests are now described.

2.2 In-Vivo Testing

Patients were selected if they exhibited a suspicious mass after mammography and/or follow-up ultrasound at the Karmanos Cancer Institute (Walt Comprehensive Breast Center). The CURE exam was interposed between these conventional examinations and subsequent biopsy. Biopsy confirmation was therefore available for all recruited patients. Typically, 45 tomograms were taken of each patient with the CURE device. (Fig. 2a–f).

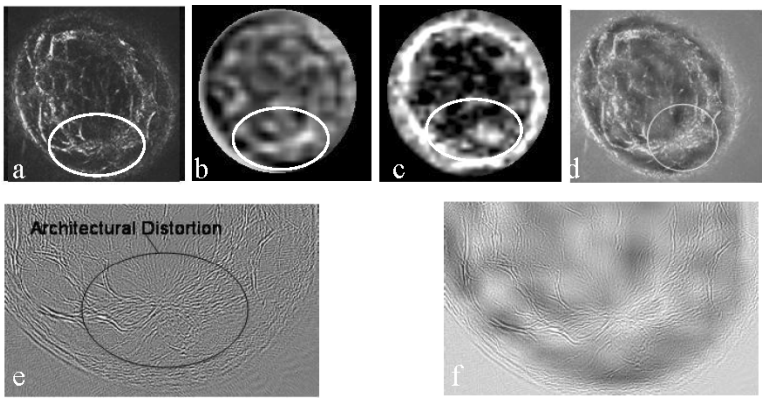

Figure 2. Images showing a 1 cm Invasive Ductal Carcinoma. (a) The reflection intensity image showing the region of architectural distortion, (b) the sound speed image showing elevated sound speed, (c) the attenuation image showing elevated attenuation, (d) reflection – sound speed overlay, (e) close up of edge reflection image showing the details of the architectural distortion and (f) detailed reflection – sound speed overlay showing the correlation of architectural distortion with elevated sound speed. The grey scale on the sound speed and attenuation images reflects quantitative changes in values. White indicates high sound speed/attenuation while black indicates low values. The CURE images reveal architectural distortion, elevated sound speed and elevated attenuation in the region of the tumor, all risk factors for cancer.

Analysis of the CURE images of the 19 patients in our initial sample, suggested that we could image a number of attributes relating to the mass shape, acoustic mass properties and architecture of the surrounding tissue. These attributes are listed below.

1. **Aspect** ratio (width to height) < 1.4: The mass appears more round than elliptical.
2. Irregular **Shape**: The tumor has an irregular contour, including a branching pattern or ductal extension.
3. Irregular **Margins**: includes spiculation, angular margins and/or microlobulation.

4. Architectural **Distortion**: Surrounding tissue shows altered anatomy (e.g. mass effect and/or retraction).
5. Elevated **Sound Speed**: Higher sound speed than surrounding tissue is noted within the mass. Typically the sound speed is elevated by 50 to 150 m/s relative to fat.
6. Elevated **Attenuation**: Higher attenuation than surrounding tissue is noted within the mass. The amount of enhancement varies but is typically about 0.5 dB/cm relative to fat at 1.5 MHz.

The first three attributes are linked to the acoustic shape of the mass as defined by the appearance of the mass in the CURE reflection images. They represent straightforward applications of the "Stavros" criteria[3]. The fourth attribute is linked to the architecture of the tissue surrounding the tissue. Architectural distortion is an attribute commonly measured in mammography. In the CURE data it is defined by the appearance of the tissue in our reflection images. The fifth and sixth attributes are unique to transmission ultrasound and were first defined by Greenleaf[10]. They represent the internal acoustic properties of the mass and are defined by the quantitative values measured in the CURE transmission images.

The above attributes are defined such that the probability of cancer increases with the number of attributes that are present. Despite the relatively small sample of patients in our data and the limits on attenuation measurements a trend is beginning to emerge in the application of these attributes. For the masses known to exist in each patient we determined, from the CURE images, whether a given attribute was present or not. The presence of each attribute was denoted qualitatively with a binary decision; 1 = "yes" or 0 = "no". The numbers assigned to the six attributes were then summed to provide a total score; the higher the score the greater the chance that a mass is cancerous. The results are shown in Fig. 3.

Figure 3 shows that an apparent separation exists in the cancer and benign patient distributions. The 9 patients with cancer have an average CURE score of 4.9 ± 0.8, while those with benign masses have an average score of 0.8 ± 0.6, ($p<0.0001$). These numbers suggest that a reasonable cutoff value for separating the two populations is 3. Despite the low number of patients analyzed thus far, a highly significant difference between the average probability score for benign and malignant masses was identified. Obviously, this is a highly selective series for patients with relatively large masses. A larger series appears likely to define a distinct cut-point in the probability score for differentiating benign from malignant masses.

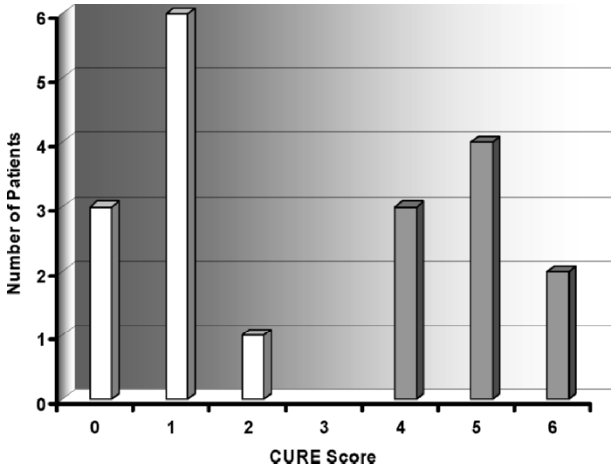

Figure 3. CURE scoring results.

Although the small sample size precludes a rigorous statistical analysis, these results demonstrate the feasibility of diagnostic imaging of breast lesions using the first-generation CURE device and justify its continued development as guided by the clinical results from our continuing studies. Future studies will focus on fine tuning of the CURE machine for reflection, sound speed and attenuation measurements as well as the statistically rigorous development of prognostic tables relating imaging findings to tissue characterization and differentiation of benign from malignant findings.

REFERENCES

1. Kolb TM., Lichy J and Newhouse JH. Comparison of the Performance of Screening Mammography, Physical Examination and Breast US and Evaluation of Factors that Influence Them: An Analysis of 27, 825 Patient Evaluation.Radiology, 2002; 225:165–175.
2. Gotzsche PC, and Olsen O. Is screening for breast cancer with mammography justifiable? Lancet 2000; 355:129–134.
3. Stavros AT, Thickman D, Rapp CL, Dennis MA, Parker SH, and Sisney GA. Solid breast nodules: use of sonography to distinguish between benign and malignant lesions. Radiology. 1995;196:123–34.
4. Federal Register 60712–60713. 1996. (www.rsna.org/REG/research/regulatory/wfprfcexamples.html).

5. Entrekin RR, Porter BA, Sillesen HH, Wong AD, Cooperberg PL, and Fix CH. Real-time spatial compound imaging application to breast, vascular, and musculoskeletal ultrasound. Semin Ultrasound CT MR 2001 Feb; 22(1):50–64
6. Shapiro RS, Simpson WL, Rausch DL, and Yeh HC. Compound spatial sonography of the thyroid gland: evaluation of freedom from artifacts and of nodule conspicuity. AJR Am J Roentgenol 2001 Nov; 177(5):1195–8
7. Dakins DR. Breast ultrasound trial finds keys to better performance. In Review. A Special Supplement to Diagnositc Imaging, Jan; 2005: 17–17.
8. ACRIN website: www.acrin.org .
9. Lucas-Fehm L. Sonographic mammographic correlation. Applied Radiology, Feb; 2005:20–25.
10. Greenleaf JF, Johnson A, Bahn RC, and Rajagopalan B:*Quantitative cross-sectional imaging of ultrasound parameters*. 1977 Ultrasonics Symposium Proc., IEEE Cat. # 77CH1264-1SU, pp. 989–995, 1977.
11. Carson PL, Meyer CR, Scherzinger AL and Oughton TV. Breast imaging in coronal planes with simultaneous pulse echo and transmission ultrasound. Science 1981 Dec; 4;214(4525): 1141–3.
12. Andre MP, Janee HS, Martin PJ, Otto GP, Spivey BA, and Palmer DA, "High-speed data acquisition in a diffraction tomography system employing large-scale toroidal arrays," International Journal of Imaging Systems and Technology 8, pp.137–147, 1997.
13. Johnson SA., Borup DT, Wiskin JW, Natterer F, Wuebbling F, Zhang Y, and Olsen C. *Apparatus and Method for Imaging with Wavefields using Inverse Scattering Techniques*. United States Patent 6, 005, 916 (1999).
14. Marmarelis VZ, Kim T, and Shehada RE. Proceedings of the SPIE: Medical Imaging 2003; San Diego, California; Feb; 23–28, 2002. Ultrasonic Imaging and Signal Processing – Paper 5035-6.
15. Littrup PJ, Duric N, Azevedo S, Chambers DH, Candy JV, Johnson S, Auner G, Rather J and Holsapple ET. Computerized ultrasound risk evaluation (CURE) system: Development of combined transmission and reflection ultrasound with new reconstruction algorithms for breast imaging. Proceedings of the 26th International Acoustical Imaging Symposium; Windsor, Canada; Sept; 9–12, 2001.
16. Littrup PJ, Duric N, Leach Jr. RR, Azevedo SG, Candy JV, Moore T, Chambers DH, Mast JE and Holsapple ET. *Characterizing tissue with acoustic parameters derived from ultrasound data.* Proceedings of the SPIE: Medical Imaging 2002; San Diego, CA; Feb. 23–28, 2002. Ultrasonic Imaging and Signal Processing – Paper 4687-43.
17. Leach Jr. RR, Azevedo SG, Berryman JG, Bertete-Aguirre HR, Chambers DH, Mast JE, Littrup PJ, Duric N, and Wuebbeling F. *A comparison of ultrasound tomography methods in circular geometry.* Proceedings of the SPIE: Medical Imaging 2002; San Diego, CA; Feb. 23–28, 2002. Ultrasonic Imaging and Signal Processing – Paper 4687-44.
18. Duric N, Littrup PJ, Leach Jr. RR, Azevedo SG, Candy JV, Moore T, Chambers DH, J. Mast JE and Holsapple ET. *Using Data Fusion to Characterize Breast Tissue.* Proceedings of the SPIE: Medical Imaging 2002; San Diego, California; Feb; 23–28, 2002. Ultrasonic Imaging and Signal Processing – Paper 4687-39.
19. Azevedo SG, Moore T, Huber RD, Ferguson W, Leach Jr. RR, Benson S, Duric N, Littrup PJ and Holsapple ET. *Apparatus for circular tomographic ultrasound measurements.* Proceedings of the SPIE: Medical Imaging 2002; San Diego, California; Feb. 23–28, 2002. Ultrasonic Imaging and Signal Processing – Paper 4687-12.

20. Duric N, Littrup P, Holsapple E, Babkin A, Duncan R, Kalinin A, Pevzner R and Tokarev M. *Ultrasound Imaging of Breast Tissue*. Proceedings of the SPIE: Medical Imaging 2003; San Diego, California; Feb. 21–26, 2003. Ultrasonic Imaging and Signal Processing – Paper 5035-4.
21. Huang LJ, Duric N, and Littrup, P. Ultrasonic Breast Imaging Using a Wave-Equation Migration Method. Proceedings of the SPIE: Medical Imaging 2003; San Diego, California; Feb. 21–26, 2003. Ultrasonic Imaging and Signal Processing – Paper 5035-4.

FULL-WAVE, NON-LINEAR, INVERSE SCATTERING

High Resolution Quantitative Breast Tissue Tomography

J. Wiskin, D.T. Borup, S.A. Johnson, M. Berggren, T. Abbott, R. Hanover
TechniScan, Inc., 1011 Murray Holladay Rd., Salt Lake City, Utah USA 84117; Dept. Bioengineering, Univ. of Utah, Salt Lake City, Utah 84112; St. Mark's Hospital, Salt Lake City, Utah 84106

Abstract: A full wave nonlinear inverse scattering algorithm is presented and resulting images shown

Key words: Full Wave Inverse Scattering, Quantitative Ultrasound Computed Tomography

1. INTRODUCTION

Ultrasound has been proposed as an adjunct diagnostic modality for 25+ years [3,5]. The present mode of hand-held ultrasound incorporates the use of tissue characteristics indirectly inferred from 'speckle behavior' and other image hints [2]. Although there are companies and research groups attempting to minimize the effect of the operator (e.g. U-systems in San Jose, California), TSI is unique in its goal to yield quantitative estimates of the tissue properties. For example the attenuation characteristics of the tissue within a suspected lesion can be indirectly inferred from the shadowing/lack of shadow behind the lesion. These methods have had some success in the hands of well-trained experts, [2], however, it is clear that if accurate physics could be brought to bear on the problem, it should be possible to accurately model the propagation of ultrasound through a human breast, thereby resulting in quantitative and high resolution imaging. Early work in this direction used time of flight algorithms to estimate the speed and a similarly crude algorithm to estimate the attenuation.

M.P. André (ed.), Acoustical Imaging, 183–193.

In the intervening years there has been a virtual explosion of papers in the 'so-called' inverse-scattering literature. Some of these papers have focused on the mathematical aspects, while others have dealt with algorithms that can be applied to laboratory data. We discuss the mathematical side of the algorithm below. A large number of the laboratory-applicable algorithms have arisen from the Microwave imaging literature. Here we follow [1] in notation and presentation of theory.

We present some preliminary results using Ultrasound Computed Tomography (USCT), and discuss possible reasons for the discriminatory value of attenuation. In particular, it appears that malignant tissue has a high attenuation value. We make no claims as to the validity of the medical hypothesis at this point. We present a scientific hypothesis (that cancer has an abnormally high attenuation coefficient) and refer to [Johnson, et al.], papers presented in this conference for some preliminary evidence that may be supportive.

2. FORWARD PROBLEM

The forward problem is well-known: given an incident field and some distribution of speed of sound and attenuation, $c(\boldsymbol{x})$, $\alpha(\boldsymbol{x})$, determine the pressure field $f(\mathbf{x})$. By contrast, the inverse problem is: Given the pressure field $f_{\omega\phi}(\mathbf{x})$ as measured for some transmitter positions, $\phi = 1,...,\Phi$, (known incident fields) and frequencies, $\omega = 1,...\Omega$, determine the distribution of speed of sound and attenuation, $c(\boldsymbol{x})$, $\alpha(\mathbf{x})$ in some region (e.g. the breast).
Once the data has been collected it must be properly processed in order to yield an image. This is a computationally very intensive task. We have developed several algorithms over the past 5 years that dramatically reduce the computation time. We outline the basis of our algorithm in operator theory and integral equation notation due to its flexibility, and continuity with [1], but leave the details to several patent publications [e.g. USPTO# 6,005,916].

The frequency domain scattering problem is modeled by the Helmholtz equation.

$$\nabla^2 f(\mathbf{x}) + k^2(\mathbf{x}) f(\mathbf{x}) = 0$$

In this equation $f(\mathbf{x})$ is pressure, and k is the wavenumber, which is given by: $k(\mathbf{x}) = \frac{\omega}{c(\mathbf{x})} + i\alpha(\mathbf{x})$, with $\omega = 2\pi f_o$, where f_o is the frequency of insonification. Using the object function $\gamma \equiv \frac{k^2(\mathbf{x})}{k_o^2} - 1$, the Helmholtz equation is written: $\nabla^2 f(\mathbf{x}) + k_o^2 f(\mathbf{x}) = -k_o^2 \gamma(\mathbf{x}) f(\mathbf{x})$. The total field

also satisfies the Sommerfeld radiation condition (substantially weakened by Wilcox) which states that asymptotically the scattered field behaves like an outgoing spherical wave: $f^{sc}_{\omega\theta}(\mathbf{x}) = \frac{e^{-ik_o\|\mathbf{x}\|}}{\|\mathbf{x}\|}\left(f^{\infty}(\hat{\mathbf{x}}) + O\left(\frac{1}{\|\mathbf{x}\|}\right)\right)$, where $\hat{\mathbf{x}} \equiv \frac{\mathbf{x}}{\|\mathbf{x}\|} \in S^2$ is a unit vector. The forward operator for dimensions *N=2,3, is defined by* $\gamma \in C_o^2(B_\rho) \xrightarrow{\phi_\omega} \left[\phi_\omega(\gamma)\right] \in Hom\left(C(B_\rho), C^2\left(\mathbb{R}^{N-1}\right)\right)$. The operator $\left[\phi_\omega(\gamma)\right]$ maps incident fields defined on the disk $B_\rho \equiv \left\{\mathbf{x} \in \mathbb{R}^3 \,\middle|\, |\mathbf{x}| \le \rho\right\}$ to total fields there. Here $C(B_\rho)$=continuous functions on B_ρ, $C^2(B_\rho)$, $C_o^2(B_\rho)$=continuous functions on B_ρ with continuous second derivatives, and compact support, respectively. These are simple Banach spaces. A more complete mathematical description including the appropriate Sobolev spaces is carried out in [4], where it is shown that the Far-Field Operator is well defined $\mathbf{F}: H_0^2(B_\rho) \to L^2\left(S^2 \times S^2\right)$, in the following way: The Sommerfeld radiation condition defines the scattering function: $f^{\infty}(\hat{\mathbf{x}})$. The map $\gamma \in H_0^2(B_\rho) \to f^{\infty}(\hat{\mathbf{x}}) \in L^2\left(S^2 \times S^2\right)$ is the required (nonlinear) map **F.** Note that the Sobolev imbedding theorem (B_ρ is a compact manifold with boundary) guarantees that $H_0^2(B_\rho) \subset H_0^{3/2}(B_\rho) \subset C(B_\rho)$, so that γ is indeed continuous in $B_\rho \equiv \left\{\mathbf{x} \in \mathbb{R}^3 \,\middle|\, |\mathbf{x}| \le \rho\right\}$.

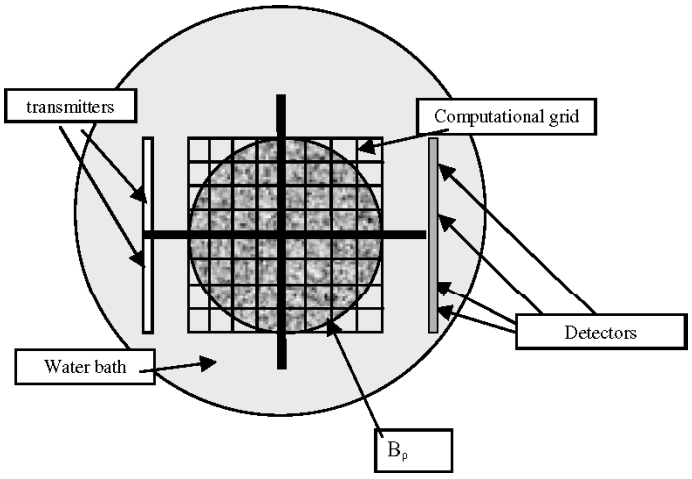

Hohage [4] shows that the Frechet derivative of **F,** $\mathbf{A} \equiv \mathbf{F}'(\gamma_0)$, at a solution γ_o, is a compact operator, indicating that the inversion problem will be severely ill-posed. In fact, he shows that the singular values of this operator actually decrease *exponentially.* This is in accord with the fact that the far-field pattern is guaranteed to be an analytic function on $S^2 \times S^2$.

The numerical process by which f^{sc} is determined in the forward problem is a two-step process. As shown by several authors, the solution of the Helmholtz scattering problem with Sommerfeld-Wilcox radiation condition is equivalent to the 'Lippmann-Schwinger equation' (which is Fredholm of the second kind):

(1) Solve the Fredholm integral equation of the second kind for the total field $f_{\omega\theta}(\mathbf{x})$.

$$f^{inc}_{\omega\theta}(\mathbf{r}) = f_{\omega\theta}(\mathbf{r}) - k_0^2 \iiint_\Gamma \gamma(\mathbf{r}') f_{\omega\theta}(\mathbf{r}') G_\omega(|\mathbf{r}-\mathbf{r}'|)dx'dy'dz'$$

where $\Gamma \equiv \operatorname{supp}\gamma$, is the support of the "object function" γ and $\mathbf{r},\mathbf{r}' \in \Gamma$. This gives the total field, $f_{\omega\theta}$, which is then converted to the measured scattered field by

(2) computing the integral:

$$f^{sc}_{\omega\theta}(\mathbf{r}_i) = k_0^2 \iiint_\Gamma \gamma(\mathbf{r}') f_{\omega\theta}(\mathbf{r}') G_\omega(|\mathbf{r}_i-\mathbf{r}'|)dx'dy'dz'$$

3. THE INVERSE SCATTERING PROBLEM

The inverse problem is the following: given an imperfect estimate of $\phi_\omega(\gamma)$, determine the scattering parameters γ. The inverse problem of determining the γ from the scattered data: $f^\infty(\hat{\mathbf{x}}) \to \gamma$, is, according to the discussion above, exponentially ill-posed, *and,* when solved as a minimization problem, suffers the additional defect of having *multiple local minima, due to the 'phase problem'*.

The inverse problem cannot be carried out analytically or explicitly in the vast majority of cases; in fact, one rarely determines the scattering operator $\phi_\omega(\gamma)$ explicitly. However, by carefully analyzing the recorded scattered waveform for several different frequencies and source/receiver positions the scatter parameters can be estimated by a least squares minimization. We introduce the operator theoretic notation:

$$\left(k_0^2 G_\omega[\gamma]\right) f_{\omega\theta} \equiv k_0^2 \iiint_\Gamma \gamma(\mathbf{r}') f_{\omega\theta}(\mathbf{r}') G_\omega\left(|\mathbf{r}_i-\mathbf{r}'|\right) dx'dy'dz' .$$

This can be interpreted as an infinite dimensional operator, or as a finite dimensional operator acting on the discretized version of the total field:

$$f^{sc}_{\omega\theta}(\mathbf{r}_{rec}) = k_0^2 G_{\omega r}[\gamma] f_{\omega\theta} = k_0^2 G_{\omega r}[\gamma]\left(I - k_0^2 G_\omega[\gamma]\right)^{-1} f^{inc}_{\omega\theta} .$$

$f^{sc}_{\omega\theta}(\mathbf{r}_{rec})$ is the scattered field at the receiver positions. We can make the (reasonable) assumption that the data at receiver *j*, for frequency ω and incident field θ, is $d_{\omega\theta j} \equiv A\iint_{\Omega_j} f_{\omega\theta}(\mathbf{r}')d\mathbf{r}'$, where Ω_j is the support of the *jth* receiver, and *A* is some constant of proportionality, characteristic of the system. . Alternatively, the characteristics of the transducer element can be incorporated directly via $T_k(f(\mathbf{r}')) \equiv \langle f_{x'} | f_{x',R_k} \rangle_{L_2(\mathbb{R}^2)}$, where $\langle f_{x'} | f_{x',R_k} \rangle_{L_2(\mathbb{R}^2)} \equiv \iint_{S_o} f(\mathbf{r}') f_{R_k}(\mathbf{r}') dS_{\mathbf{r}'}$, where S_o is the plane at the edge of the image grid that is closest to the receiver array. (see diagram), and where $f_{x',R_k}(y,z) \equiv f_{R_k}(x = x', y, z)$, is the field generated by the *kth* receiver element, evaluated at the edge of the computational grid. There is a similar definition for $f_{x'}$, and $\langle f_{x'} | f_{x',R_k} \rangle_{L_2(\mathbb{R}^2)}$ is the standard inner product in the Hilbert space, $L_2(\mathbb{R}^2)$. In this case the forward operator is given via:

$$T(f(\mathbf{r}')) \equiv \sum_{k=1}^{N_R} \langle f_{\omega\theta x'_N} | f_{x',R_k} \rangle_{L_2(\mathbb{R}^2)},$$

where $f_{\omega\theta} \equiv f^{inc}_{\omega\theta} + f^{sc}_{\omega\theta} = \left(I - k_0^2 G_\omega[\gamma]\right)^{-1} f^{inc}_{\omega\theta}$ is the total field and $dS_{\mathbf{r}'}$ is the standard Lebesgue measure along the plane defined by $x = x'_N$, the last grid plane in an NxN grid

4. NONPERTURBATIVE IMAGING – MULTIPLE VIEW, MULTIPLE FREQUENCY CASE

It may be the case that we have limited views available to us due to experimental limitations. If so we must rely upon multiple frequencies to ameliorate the ill-posedness (in the sense of Hadamard) of the problem. Furthermore, multiple frequencies can help to overcome the multiple minimum problem. To solve the multiple view and multiple frequency problem we solve the holomorphic (in γ) system $\left[\phi_\omega(\gamma) f^{inc}_{\omega\theta}\right]_k \equiv T_k\left(I - k_0^2 G_\omega[\gamma]\right)^{-1} f^{inc}_{\omega\theta}$, $k = 1,\ldots,N_R$ (number of receivers). Note that in the discretized version, $\phi_\omega(\gamma) f^{inc}_{\omega\theta} \in \mathbf{C}^{N_R}$, and form the 'residual vectors': $\mathbf{r}_{\omega\theta}(\gamma) \equiv \left(\phi_\omega(\gamma)\left(f^{inc}_{\omega\theta}\right) - \mathbf{d}_{\omega\theta}\right) \in \mathbf{C}^{N_R}$. From

these we form the functional: $F(\gamma,\overline{\gamma}) \equiv \frac{1}{2}\sum_{\omega\theta} \overline{\mathbf{r}}_{\omega\theta}^{T}\mathbf{r}_{\omega\theta}$, $F:\mathbf{C}^{NxN} \to \mathbf{R}$.

Note that *F,* cannot be holomorphic, however, each $F:\mathbf{C}^{NxN} \to \mathbf{R}$ is manifestly holomorphic. Note that: $\frac{\partial}{\partial\overline{\gamma}}F(\gamma,\overline{\gamma}) = \frac{1}{2}\left(\frac{\partial F}{\partial\gamma_R} + i\frac{\partial F}{\partial\gamma_I}\right)$, which conveniently splits the real and imaginary parts up into derivatives with respect to the real and imaginary parts of γ (speed and attenuation models). Also, in accordance with the Polak-Ribiere formula, the gradient must be calculated:

$$\frac{\partial}{\partial\overline{\gamma}}F(\gamma,\overline{\gamma}) \equiv \frac{1}{2}\sum_{\omega\theta}\left(\frac{\partial\overline{\mathbf{r}}_{\omega\theta}}{\partial\overline{\gamma}}(\overline{\gamma})\right)^{T}\mathbf{r}_{\omega\theta}(\gamma)$$

Note that the holomorphic character of the Jacobian gives: $\frac{\partial\overline{\mathbf{r}}_{\omega\theta}}{\partial\overline{\gamma}}(\overline{\gamma}) = \overline{\left(\frac{\partial\mathbf{r}_{\omega\theta}(\gamma)}{\partial\gamma}\right)}$. It can be shown that the action of the Jacobian on a perturbation in γ, i.e. $\frac{\partial\mathbf{r}_{\omega\theta}(\gamma)}{\partial\gamma}\delta\gamma = T\left[\left(I - k_0^2 G_\omega[\gamma]\right)^{-1} k_0^2 G_\omega\right]\left[f_{\omega\theta}\right]\delta\gamma$, can be interpreted as follows: A 'pseudo-scattered field' is calculated: $f_{\omega\theta}^{\delta\gamma} \equiv k_0^2 G_\omega\left[f_{\omega\theta}\right]\delta\gamma$, i.e. the total field from $\gamma$is used in place of the total field from $\delta\gamma$. Note that this pseudo-scattered field is different from the true scattered field. It is a kind of 'distorted Born' scattered field. Then, this 'distorted scattered field' is used as the 'incident field' from which a 'total field' is calculated. This 'total field' is action of the Jacobian on the γ perturbation.

4.1 Gradient Calculation

Now the gradient itself is:

$$\frac{\partial}{\partial\overline{\gamma}}F(\gamma,\overline{\gamma}) = \frac{1}{2}\sum_{\omega\theta}\overline{\left(T_k\left[\left(I - k_0^2 G_\omega[\gamma]\right)^{-1} k_0^2 G_\omega f_{\omega\theta}\right]\right)}^{T}\mathbf{r}_{\omega\theta}(\gamma),$$

from which it immediately follows that:

$$\left(\frac{\partial F}{\partial\gamma_R} + i\frac{\partial F}{\partial\gamma_I}\right) = \sum_{\omega\theta}\overline{\left(T_k\left[\left(I - k_0^2 G_\omega[\gamma]\right)^{-1} k_0^2 G_\omega f_{\omega\theta}\right]\right)}^{T}\mathbf{r}_{\omega\theta}(\gamma)$$

This is the gradient of the functional *F* to be minimized. This requires the action of the Hermitian conjugate (the adjoint) of the Jacobian

$J \equiv \left(\frac{\partial \mathbf{r}_{\omega\theta}(\gamma)}{\partial \gamma} \right)$ on the residual vectors, $\mathbf{r}_{\omega\theta}(\gamma)$. It is advantageous to calculate the complex conjugate of the gradient: which can be calculated as

$$\overline{\frac{\partial}{\partial \bar{\gamma}} F(\gamma, \bar{\gamma})} = \frac{1}{2} \sum\nolimits_{\omega\theta} \left[f_{\omega\theta} \right] \left(I - k_0^2 G_\omega [\gamma] \right)^{-1} k_0^2 G_\omega T^T \mathbf{r}_{\omega\theta}(\gamma),$$

which has the following physical interpretation: First, form the total field generated by the data:

$f_{\mathbf{r}_{\omega\theta}} \equiv T^T \mathbf{r}_{\omega\theta}(\gamma) = \sum_{k=1}^{N_{rec}} T_k^T \mathbf{r}_{\omega\theta k}$, from which $f^{inc}_{\mathbf{r}_{\omega\theta}} \equiv k_0^2 G_\omega f_{\mathbf{r}_{\omega\theta}}$ is calculated. This is then interpreted as 'an incident field'. The total field resulting from this 'incident field' is calculated. The resulting '**adjoint total field**', $f^{adj}_{\mathbf{r}_{\omega\theta}} \equiv \left(I - k_0^2 G_\omega [\gamma] \right)^{-1} k_0^2 G_\omega f_{\mathbf{r}_{\omega\theta}}$ is pointwise multiplied by the true total field: $\overline{\frac{\partial}{\partial \bar{\gamma}} F(\gamma, \bar{\gamma})} = \frac{1}{2} \sum\nolimits_{\omega\theta} \left[f_{\omega\theta} \right] f^{adj}_{\mathbf{r}_{\omega\theta}}$

4.2 Polak Ribiere Nonlinear Conjugate Gradient Algorithm

For multiple view and multiple frequency inversion then, the inversion scheme reads:

1. Choose an initial guess for the scattering potential, $\boldsymbol{\gamma}^{(0)}$.
   Set n = 0

solve the forward problems $(\boldsymbol{I} - \boldsymbol{G}[\boldsymbol{\gamma}])\boldsymbol{f}_{\theta\omega} = \boldsymbol{f}^{\mathrm{inc}}_{\theta\omega}, \quad \forall \begin{matrix} \theta = 1,\ldots,\Theta \\ \omega = 1,\ldots,\Omega \end{matrix}$, and use the result to compute the ϕ-forward maps $\boldsymbol{\phi}_{\theta\omega}(\boldsymbol{\gamma}^{(\mathrm{n})})$ and residuals $\boldsymbol{r}^{(\mathrm{n})}_{\theta\omega} \equiv \boldsymbol{\phi}_{\theta\omega}(\boldsymbol{\gamma}^{(\mathrm{n})}) - \boldsymbol{d}_{\theta\omega} = \boldsymbol{0} \quad \forall \begin{matrix} \theta = 1,\ldots,\Theta \\ \omega = 1,\ldots,\Omega \end{matrix}$.

Determine the $\mathbf{L_2}$ norm of the total residual vector:

Determine the gradient, $\mathbf{g}_o \equiv \frac{\partial}{\partial \bar{\gamma}} F(\gamma, \bar{\gamma}) \equiv \frac{1}{2} \sum\nolimits_{\omega\theta} \left(\frac{\partial \bar{\mathbf{r}}_{\omega\theta}}{\partial \bar{\gamma}}(\bar{\gamma}) \right)^T \mathbf{r}_{\omega\theta}(\gamma)$, set

$\mathbf{d}_o \equiv -\mathbf{g}_o$

2. **Begin:** set $\alpha_n \approx -\frac{\mathbf{g}_n^T \mathbf{d}_n}{\mathbf{d}_n^T J^T J \mathbf{d}_n}$, or use a line search, and set

$\delta\gamma^{(n)} \equiv \alpha_n \mathbf{d}_n$

Update $\boldsymbol{\gamma}^{(n+1)} = \boldsymbol{\gamma}^{(n)} + \delta\boldsymbol{\gamma}^{(n)}$

solve the forward problems $(\boldsymbol{I} - \boldsymbol{G}[\boldsymbol{\gamma}])\boldsymbol{f}_{\theta\omega} = \boldsymbol{f}^{\text{inc}}_{\theta\omega}, \quad \forall \begin{matrix} \theta = 1,\ldots,\Theta \\ \omega = 1,\ldots,\Omega \end{matrix}$, and use the result to compute the ϕ-forward maps $\boldsymbol{\phi}_{\theta\omega}\left(\boldsymbol{\gamma}^{(n)}\right)$ and residuals $\boldsymbol{r}^{(n)}_{\theta\omega} \equiv \boldsymbol{\phi}_{\theta\omega}\left(\boldsymbol{\gamma}^{(n)}\right) - \boldsymbol{d}_{\theta\omega} = \boldsymbol{0} \quad \forall \begin{matrix} \theta = 1,\ldots,\Theta \\ \omega = 1,\ldots,\Omega \end{matrix}$.

3. Determine the $\mathbf{L_2}$ norm of the total residual vector:

If $\left|\boldsymbol{tr}^{(n)}\right|^2 \equiv \sum_{\omega=1}^{\Omega}\sum_{\theta=1}^{\Theta}\left\|\boldsymbol{r}^{(n)}_{\theta\omega}\right\|^2 < \varepsilon$ then stop.

4. Form the gradient:

$$\mathbf{g}_{n+1} \equiv \frac{\partial}{\partial\overline{\gamma}} F\left(\gamma^{(n+1)}, \overline{\gamma}^{(n+1)}\right) \equiv \frac{1}{2}\sum\nolimits_{\omega\theta}\overline{\left(\frac{\partial \mathbf{r}_{\omega\theta}\left(\gamma^{(n+1)}\right)}{\partial\gamma}\right)}^{T} \mathbf{r}_{\omega\theta}\left(\gamma^{(n+1)}\right)$$

And using the Polak-Ribiere formula, set: $\beta_n \equiv \frac{\left(\mathbf{g}_{n+1} - \mathbf{g}_n\right)^T \mathbf{g}_{n+1}}{\left\|\mathbf{g}_n\right\|^2}$, and create the new search direction: $\mathbf{d}_{n+1} \equiv -\mathbf{g}_{n+1} + \beta_n \mathbf{d}_n$.

Set n = n+1, go to **begin (2)**

5. RESULTS

As a verification of our mathematical algorithm, data was collected on an engineering prototype described in [other TSI papers in these proceedings]. These papers also detail the correlation procedure we used to ascertain that we were imaging the suspected lesion that was being sent to biopsy (in the patients where this was relevant). The initial results are very promising. Regions of high attenuation appear to be correlated to malignancy. The chart shown below (figure 3) displays the results of biopsies that were carried out. The patients were imaged with the TechniScan engineering prototype before the biopsy was performed. The results indicate that not only is high resolution obtainable with the above nonlinear optimization algorithm, but as well, the quantitative values of the relevant tissue parameters are imaged. We have carried out phantom studies (see the accompanying TSI papers in these proceedings) to verify the accuracy of our speed of sound and attenuation quantitative values.

The figures 1 through 3 below show the high degree of resolution that can be obtained via our methods. The high resolution is in part due to the

fact that we have included the full nonlinear nature of the inversion process, we have modeled the wave propagation very accurately, and we have incorporated the characteristics of the transducing elements via an accurate calibration.

The inversion process is extremely computationally intensive. A rough estimate of the number of operations is $M_{RP}\Theta\Omega M 6\left(2N\right)^2 \log N$ for the relatively simple algorithm described herein. Where M_{RP} is the number of Ribiere-Polak iterations, Θ is the number of transmitter positions used, Ω is the number of frequencies used in the inversion, M represents the number of iterations required to solve the forward problem, and N is the edge dimension (pixels) of the 2D image space. The 3D problem introduces another factor of 2N. We achieve 2D images in approximately 10 seconds, the 3D algorithm requires approximately 2 hours for a 30 slice breast, on a 2 node cluster of Pentium IV workstations running LINUX.

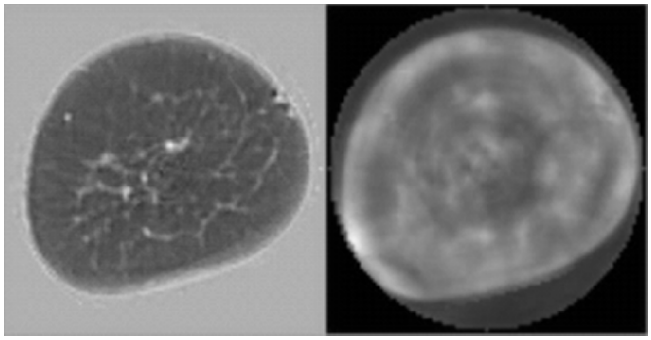

Figure 1a. Speed image, of right breast of 81-year-old patient with non-invasive tumor. Ductal tissue is seen as light gray. The skin line is clearly visible, and subcutaneous veins are visible. *1b*: Attenuation image of same breast. Both images are 394 by 394 pixels, pixels are 0.325 mm square, image is 12.8 cm across. Higher attenuation is shown as lighter gray. Attenuation ranges from 0. to 3.0 dB/cm/MHz.

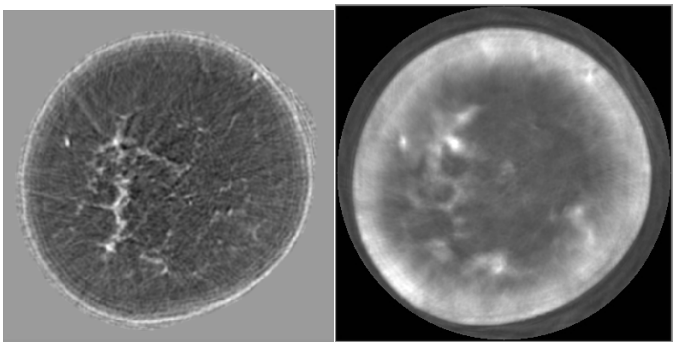

Figure 2. The speed image is on the left, the attenuation image is on the right. The speed image is scaled from 1.35 mm/μsec to 1.6 mm/μsec. The attenuation image (right) is scaled from 0. to 3.0 dB/cm/MHz. Our model assumes a

linear relationship of the attenuation coefficient with frequency. The volunteer had no history of disease. The images are 394 pixels by 394 pixels, each pixel is 0.375 mm by 0.375 mm.

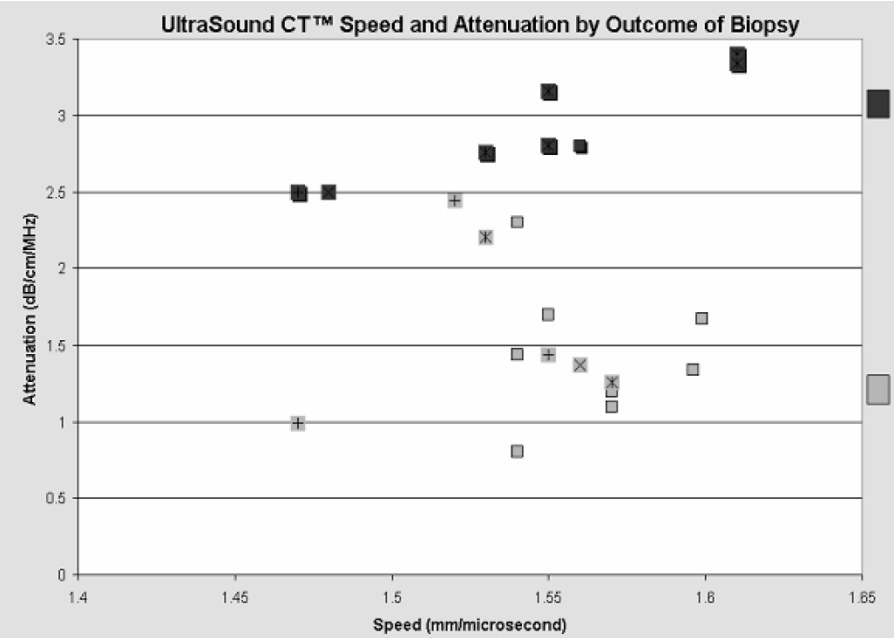

Figure 3. A chart showing some preliminary results of our study. The horizontal axis shows speed, and the vertical axis shows attenuation. The red squares represent malignant lesions, and the green diamonds are benign.

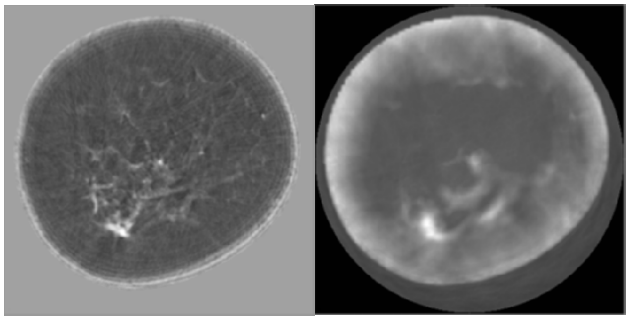

Figure 4. P35: speed and attenuation images. Pixel size is 0.375mm by 0.375mm This patient was diagnosed with Lobular Carcinoma via biopsy. P35: attenuation image, 394 by 394 pixels, Note the region of high attenuation corresponding to the Lobular carcinoma diagnosed via biopsy.

REFERENCES

1. Wiskin J., Borup, Johnson S, Inverse Scattering from arbitrary two-dimensional objects in stratified environments via a Green's Operator," J. Acoust. Soc. America, **102**(2), Pt. 1, August, 1997.
2. Stavros, Thomas A., Rapp, Cynthia L., in Steve H. Parker, Thomas A. Stavros, "*Breast Ultrasound*", Lippincott Williams & Wilkins, 28 December, 2003.
3. Johnson SA, et al, "Apparatus and Method for Acoustic Imaging Using Inverse Scattering Techniques," US Patent #4, 622– 222.
4. Hohage T. On the numerical solution of a three-dimensional inverse medium scattering problem. Inverse Problems, 2001; 17:1743–1763.
5. Greenleaf JF, Bahn RC, "Clinical Imaging with Transmissive Ultrasonic Computerized Tomography", IEEE Trans. Biomed. Eng., BME-28, No.2, February, 1981.

HIGH-RESOLUTION 3-D IMAGING AND TISSUE DIFFERENTIATION WITH TRANSMISSION TOMOGRAPHY

V.Z. Marmarelis, J. Jeong, D.C. Shin, S. Do
Alfred E. Mann Institute for Biomedical Engineering, University of Southern California, 1042 West 36th Place, Los Angeles, CA 90089

Abstract: A three-dimensional High-resolution Ultrasonic Transmission Tomography (HUTT) system has been developed recently under the sponsorship of the Alfred Mann Institute at the University of Southern California that holds the promise of early detection of breast cancer (mm-size lesions) with greater sensitivity (true positives) and specificity (true negatives) than current x-ray mammograghy. In addition to sub-mm resolution in 3-D, the HUTT system has the unique capability of reliable tissue classification by means of the frequency-dependent attenuation characteristics of individual voxels that are extracted from the tomographic data through novel signal processing methods. These methods yield "multi-band signatures" of the various tissue types that are utilized to achieve reliable tissue differentiation via novel segmentation and classification algorithms. The unparalleled high-resolution and tissue differentiation capabilities of the HUTT system have been demonstrated so far with man-made and animal-tissue phantoms. Illustrative results are presented that corroborate these claims, although several challenges remain to make HUTT a clinically acceptable technology. The next critical step is to collect and analyze data from human subjects (female breasts) in order to demonstrate the key capability of the HUTT system to detect breast lesions early (at the mm-size stage) and to differentiate between malignant and benign lesions in a manner that is far superior (in terms of sensitivity and specificity) to the current x-ray mammography. The key initial application of the HUTT imaging technology is envisioned to be the early (at the mm-size) detection of breast cancer, which represents a major threat to the well-being of women around the world. The potential impact is estimated in hundreds of thousands lives saved, millions of unnecessary biopsies avoided, and billions of dollars saved in national health-care costs every year – to say nothing of the tens of thousands of relieved Radiologists worldwide, who will finally have at their disposal a reliable and effective diagnostic tool for early detection of breast cancer.

M.P. André (ed.), Acoustical Imaging, 195–206.

Numerous other potential applications of this medical imaging technology are possible, following proper adjustments to the specific scanning requirements of each particular application

Key words: mammogram; ultrasound imaging; tissue differentiation; transmission tomography

1. INTRODUCTION

The gravity of breast cancer as a major threat to public health is widely recognized, since it represents the leading cancer among women and exhibits alarming trends of incidence rates worldwide. It is estimated that one-in-seven women will face the threat of breast cancer in her lifetime, and the incidence rate is rising among all demographic, racial, ethnic and age groups. In the U.S. alone, more than 200,000 new cases are diagnosed every year and mortality rates rise to about 75,000 annually in spite of progress in surgical and pharmacological treatments. Furthermore, more than 1,000,000 unnecessary biopsies (resulting from false-positive outcomes of the current screening procedure of x-ray mammography) are performed annually in the U.S. alone, resulting in considerable hardship and health-care cost for numerous families. It is estimated that the annual total cost associated with breast cancer diagnosis amounts to ~$8 billion in the US alone.

Conventional, hand-held (reflection mode) ultrasound imaging is currently used as an adjunct to x-ray mammography, primarily for the purpose of differentiating between cysts and tumors, after such sizable lesions are detected in the x-ray mammogram. However, this conventional imaging modality is limited in resolution and scope, and it remains operator-dependent (because it is hand-held), thus failing to achieve the requisite performance capability that would give it the credibility of a reliable screening procedure. These shortcomings are removed by the new HUTT technology that achieves high-resolution in a 3-D fixed-coordinate system (i.e., it is operator-independent), and can provide reliable tissue-differentiation capability.

The objective of this new sonomammography system is to reduce signi-icantly both the number of false-negative and false-positive outcomes - thus reducing the mortality rates (since early detection of malignant lesions at the mm-size range improves immensely the chances of survival) and the unnecessary biopsies. In addition to the primary benefit in human lives and suffering, this development will have the additional benefit of reducing significantly the health-care cost associated with breast cancer, because of

the reduction in unnecessary biopsies and the avoidance of expensive treatments of latter stage breast-cancer patients.

Although the idea of ultrasonic computerized tomography (UCT) was first introduced 30 years ago,[1–4] it did not deliver on its initial promise because of poor implementation that was due in part to the technological limitations of those early years (viz. the large ultrasonic transducers and cumbersome electronics) as well as the lack of advanced methods of signal processing. As a natural consequence of the inaccuracies and limitations of the imaging results of the early UCT applications, the impression was formed in the peer community that this approach is not a viable or preferred alternative to the established x-ray mammography.

The new HUTT technology seeks to redress this misconception by improving the resolution in all three dimensions (with a combination of better scanning technology and advanced signal processing) and by securing accuracy of measurement (using proper data collection and preprocessing procedures), as well as reducing scanning time to clinically acceptable levels. Last, but not least, the HUTT system offers a unique capability for reliable tissue classification/differentiation.[5–10]

An experimental prototype of the HUTT system has been developed over the last four years under the sponsorship of the AMI-USC, which has demonstrated the basic capabilities of the HUTT technology and serves as proof-of-principle for the underlying physical/acoustic processes, as well as for the innovative concepts of the employed technology and signal processing methods. Illustrative results from man-made and animal-tissue phantoms are presented below.

The tissue differentiation capability of the HUTT system relies on "multi-band signatures" of distinct tissue types to classify individual voxels of the 3-D image with great reliability. These multi-band signatures are comprised of "attenuation indices" at various frequency bands and represent measures of acoustic attenuation through each specific tissue type at the various frequency bands. This multi-band tissue differentiation capability has been initially demonstrated in animal-tissue phantoms and the results have been published recently in [8].

The safety of ultrasound (non-ionizing radiation), the comfort of the HUTT scanning system (fixed-coordinate water-bath), its modest cost, and, most importantly, its 3-D high-resolution capability (sub-mm voxels) combined with its unique capability for reliable tissue classification (ability to differentiate between malignant and benign lesions) offer an exceptionally attractive modality for medical imaging with key initial application to the early detection of breast cancer.

2. METHODS

The aforementioned experimental prototype has been used to demonstrate the key capabilities of the HUTT imaging approach and the validity of the underlying physical principles. This experimental HUTT prototype employs transmit-receive pairs of sub-mm piezoelectric transducers (0.4 mm × 0.4 mm in active area) by which the data collection is performed in transmission mode at 8 MHz center-frequency and with 100 MHz sampling rate over successive elevation planes separated by 0.4 mm. The tomographic images are created for each elevation plane by use of the inverse Radon transform, and the stack of 2-D images forms the 3-D image volume that is visualized with commercial software.

In order to reduce scanning time, we fire several elements of the transmitting array simultaneously (and receive at the respective elements of the receiving array). To alleviate problems arising from cross-talk between different transmit-receive elements, we utilize the concept of orthogonal coding (code-division multiplexing) whereby each transmit-receive pair of elements in the two arrays uses its own distinctive binary code which corresponds to positive (+1) and negative (-1) pulses – since the ultrasonic pulses are bipolar, "negative" pulse means reverse polarity.

Because these binary codes are nearly orthogonal (by construction) and of sufficient length relative to the number of co-active elements, the integrity of each transmit-receive pair "channel" can be secured by cross-correlational decoding at each receiving element (using the respective orthogonal code). The (near) orthogonality of the codes eliminates the contributions of the other "undesired" transmissions and, furthermore, enhances the output signal-to-noise ratio (SNR) of the received "home signal" proportionally to the length of the binary code. The dual benefit of cross-talk elimination and output SNR enhancement makes the orthogonal coding/decoding an important innovation in this particular application context.

Figure 1(a) shows a schematic of the parallel-beam scanning configuration, and Figure 1(b) shows a rendering of the envisioned clinical prototype under development. At each scanning position in 3-D space (azimuth, angle, elevation), the first-arrival pulse is extracted and compared with a reference from a water-only path by computing the logarithm of the ratio of the two Discrete Fourier Transform (DFT) magnitudes. The resulting frequency-dependent profile gives the relative (to water-path) attenuation along the travel-path of the propagating pulse at the specific scanning position for all the frequency bands in the measurement. For each frequency band of interest, the corresponding relative attenuation values for all azimuths (single-band projection) constitute one column in the sinogram of the imaged object for this band. The collection of all single-band projections

for all view-angles forms the sinogram of the imaged object for this frequency band.

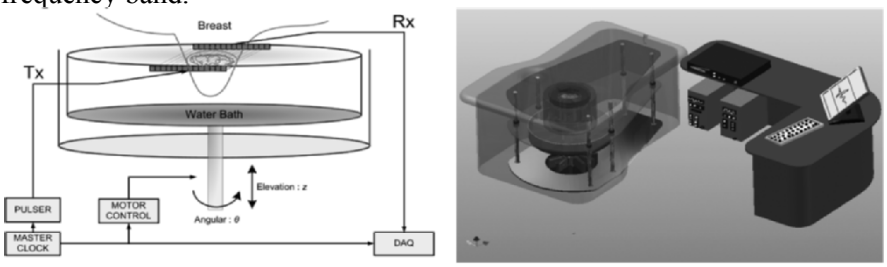

Figure 1. (a) A schematic of the parallel-beam scanning configuration emulated by the existing single-pair experimental prototype and (b) artist's rendering of the HUTT imaging system.

The inverse Radon transform of this sinogram (implemented via the well-established Filtered Back-Projection algorithm) yields the tomographic image at the respective elevation plane *for this specific frequency band*. Thus, at each elevation plane, we obtain a set of 2-D tomographic images (termed *multi-band images*) corresponding to the various frequency bands of interest, as illustrated in Figure 2. This set of images provides the powerful potential capability of "multi-band" analysis of the constituent parts of the image for the purpose of tissue differentiation.

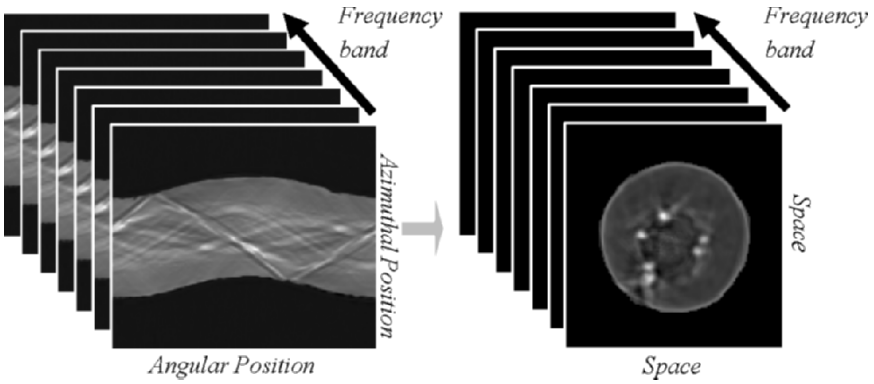

Figure 2. The set of 2-D multi-band tomographic sinograms (left) and reconstructed images (right) corresponding to the various frequency bands of interest. The phantom is a portion of bovine kidney.

The underlying key hypothesis is that distinct tissue types will have distinct "multi-band attenuation profiles or signatures" that are measurable with sufficient accuracy by the HUTT system for reliable tissue

classification. Some preliminary results are shown below that appear to corroborate this hypothesis.

3. ILLUSTRATIVE RESULTS

An initial illustrative example of high-resolution 3-D imaging of a man-made phantom, composed of a breast tissue mimicking agar-gel phantom with five small metallic spheres inserted, is shown in Figure 3 (for the frequency band corresponding to the 7–8 MHz center-frequency of forcing) and demonstrates the ability of the HUTT system to image sub-mm objects with satisfactory clarity (the smallest sphere has a diameter of 0.3 mm). The diffraction pattern (halo or ring) is evident around each spherical object and it is especially pronounced because of the large mismatch of acoustic impedance between the agar-gel medium and the metallic spheres. Such diffraction patterns are expected to be much weaker for real tissue acoustic images, as demonstrated in subsequent real-tissue images.

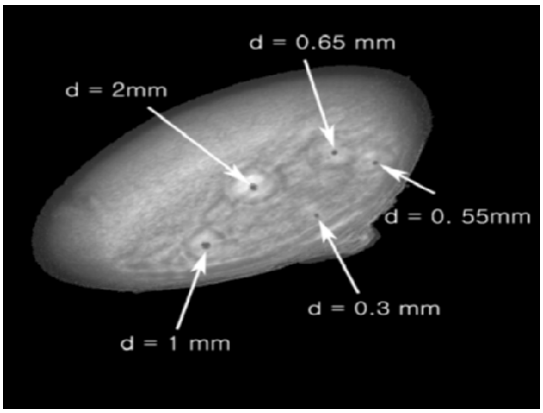

Figure 3. An initial example of HUTT imaging of the 3-D image of a man-made phantom composed of a breast tissue mimicking agar-gel phantom with five small metallic spheres inserted. Four of the spheres have sub-mm diameter (the smallest diameter is 0.3 mm).

Comparison of a 2-D HUTT image of a sheep kidney with a co-registered MRI image and an optical image (high-resolution photograph of the corresponding slice) is given in Figure 4. It is evident that the HUTT image captures the key features seen in the other two images and contains additional "information/features" that remain to be validated and interpreted.

This intriguing fact is also illustrated in the zoomed images of the projections of calyces into the renal medulla shown in Figure 4 (bottom panels). Note that the potential advantages of HUTT imaging become more eminent when multi-band analysis is used for tissue classification or differentiation (see below).

An illustrative example of a 3-D HUTT image of a sheep kidney after multi-band tissue classification is shown in Figure 5, where three classes of anatomical structures have been identified and color-coded to assist visual inspection. Note that this 3-D image has a resolution of 0.4 mm in each of the three dimensions and contains the information extracted by the HUTT system for all frequency bands of interest (in this case from 6 to 24 MHz). The procedure of the multi-band analysis for tissue differentiation is detailed in our recent publication in the *IEEE Transactions on Medical Imaging* [8].

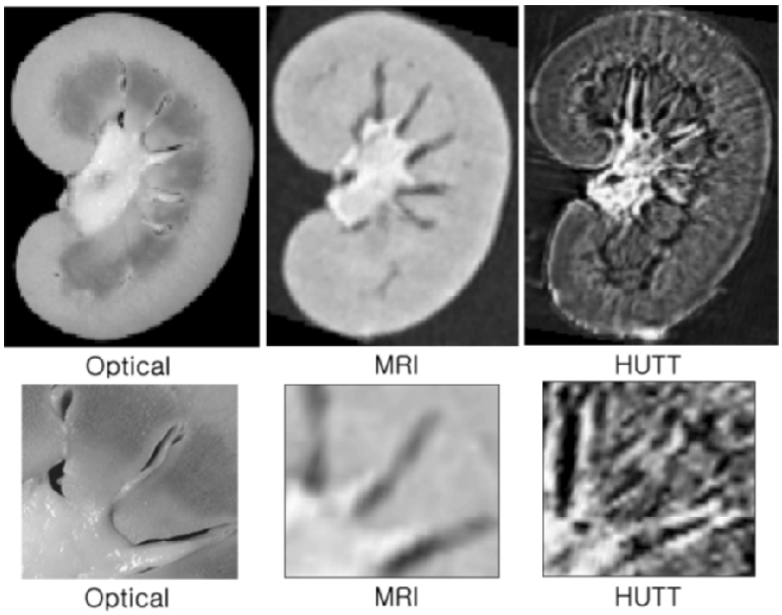

Figure 4. Comparison of the 2-D HUTT image (right) of a sheep kidney with a co-registered MRI (middle) and an optical image (left) that is a high-resolution photograph of the corresponding slice. Zoomed details of the calyces projecting into the renal medulla are shown in the bottom panels for the three imaging modalities.

In order to assist the reader with the understanding of the multi-band analysis procedure, we present an illustrative example in Figure 6, where the multi-band signatures and the classification results are shown for an animal-tissue phantom, composed of a cylindrical piece of bovine kidney with two

insertions: a piece of chicken tissue (roughly spherical with approximately 5 mm diameter) and three Styrofoam balls (with 1 mm diameter each).

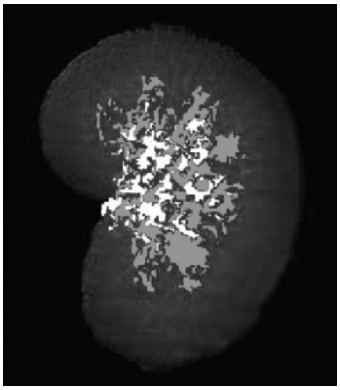

Figure 5. A 3-D HUTT image of a sheep kidney after multi-band analysis, where three classes of anatomical structures have been identified and color-coded.

The results appear promising, since the two known (inserted) object-classes are clearly identified and correctly classified. Two types of vessel structures are also identified with distinct multi-band signatures and appear to correspond to the two known classes of blood vessels and collecting (papillary) ducts in the kidney. Another illustrative result is the 3-D HUTT image of a sheep kidney shown in Figure 7, where the main anatomical renal structures are evident (pelvis, calyces, medulla, papillary ducts, blood vessels, cortex). Of course, these results are preliminary and simply illustrative at this point. Their confirmation will require far more extensive and thorough examination. Nonetheless, these preliminary results appear promising in pursuing a goal that has been long viewed as the "holy grail" of medical imaging.

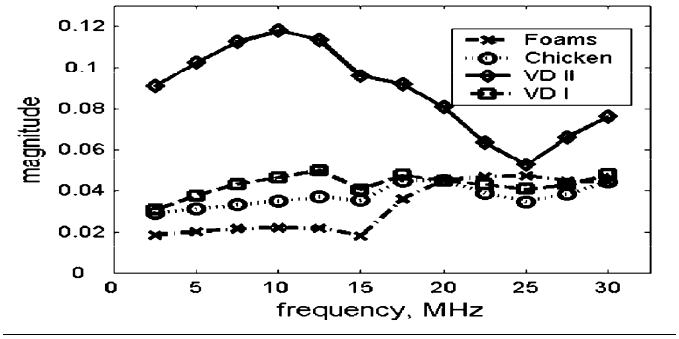

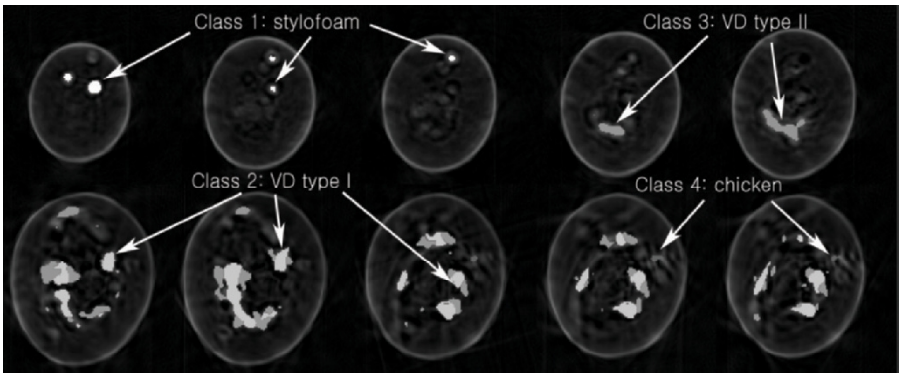

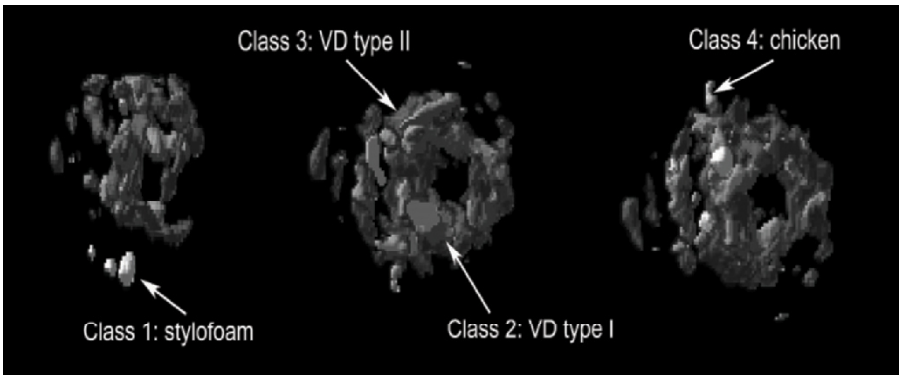

Figure 6. The multi-band signatures (top) from an animal-tissue phantom composed of bovine kidney with two insertions: a piece of chicken tissue (about 5 mm in diameter) and three styrofoam balls (about 1mm diameter each), the classification results in ten selected slices (middle) and the 3-D visualization (bottom).

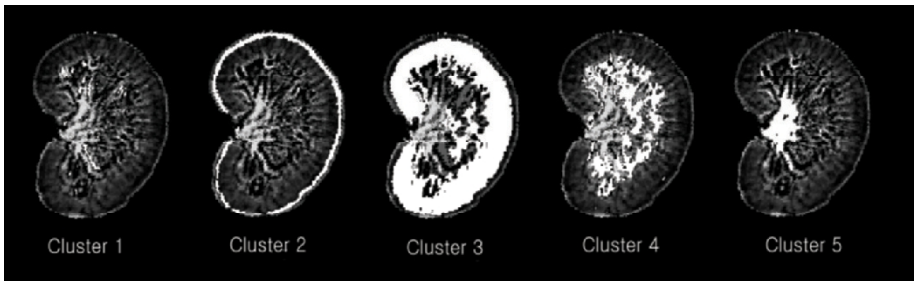

Figure 7. Results of the proposed segmentation algorithm: the optimal five clusters having the minimum total within-cluster distance after k-means agglomerative clustering.

The critical competitive advantage of the HUTT technology is the combination of 3-D high resolution (sub-mm) with the tissue classification/differentiation capability of the multi-band analysis. The latter advantage was illustrated above. Let us illustrate now the advantage of 3-D representation versus the 2-D projections of conventional x-ray mammography that inevitably obscure the breast anatomy (because of occlusion by overlaying anatomical structures on the 2-D projection). This issue may attain cardinal importance in the comparative evaluation by the Radiologists.

To illustrate this point, we consider the previously presented 3-D HUTT image of the bovine kidney phantom (see Figure 6). We compute two orthogonal 2-D projections of the fused 3-D HUTT image, that are shown in Figure 8 along with the appropriate 2-D slices of the fused 3-D HUTT image and of the co-registered MRI (two views: coronal and sagittal). The presence of the two Styrofoam balls and of the piece of chicken tissue is visually evident, although not identifiable as such – the latter is possible only via the multi-band analysis of the HUTT data, as also shown in Figure 8 with color-coding after applying our tissue classification algorithm.

It is evident that the 2-D projection has obscured our ability to discern the presence of the Styrofoam balls and the piece of chicken tissue (although this is not an x-ray image, similar occlusion problems will exist in the 2-D x-ray mammograms). Note also that the piece of chicken tissue is not visually discernible in the co-registered MRI, and the Styrofoam balls, although visible, may not be readily identifiable as such in the MRI. Nonetheless, both types of inserted objects (real tissue and man-made) are clearly discernible and identifiable in the HUTT images, owing to the tissue classification capability using HUTT multi-band data. The latter capability is akin to color vision in differentiating tissues.

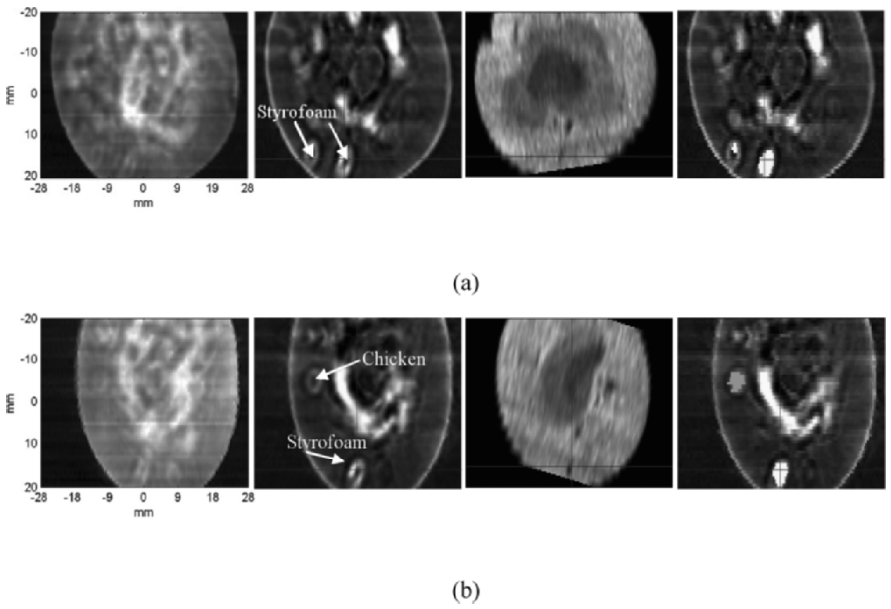

Figure 8. Comparison of the 2-D projections of the fused 3-D HUTT image (1st column), with the 3D-HUTT slices showing the inserted Styrofoam balls and the piece of chicken tissue (2nd column), and the corresponding co-registered MRIs (3rd column), given in the coronal (a) and sagittal (b) views. The images of the 4th column show the color-coded results on the HUTT slices of the 2nd column, after application of our segmentation-classification algorithm: chicken tissue in orange and Styrofoam balls in yellow (see text).

These results demonstrate the potential capability of the HUTT imaging technology to provide 3-D high-resolution images of real tissue with the unique ability to classify (i.e., differentiate) different tissue types. The implications for assisting clinical diagnosis are compelling.

4. CONCLUSIONS

The significance of the novel HUTT technology in the fight against breast cancer can hardly be overstated. Since early detection is the key to successful treatment and survival, it is expected that the HUTT technology will offer the means for reducing significantly the number of deaths associated with the leading cancer among women, as well the number of unnecessary biopsies. It is also expected to improve the efficacy and cost of treatments for those patients who are correctly diagnosed, since the

diagnosis will occur at a much earlier stage (about 1 mm size tumors) and with better localization (due to the 3-D fixed-coordinate system of the HUTT images).

Furthermore, the safety of ultrasound (non-ionizing radiation) will allow frequent repetitions of the imaging procedure (if needed) and the effective screening of dense/younger breasts as well as cosmetically augmented breasts (e.g., with silicon implants) that cannot be screened with current x-ray mammography. Lastly, the comfort of the HUTT imaging procedure will encourage women to maintain a more consistent and frequent schedule of mammographic examination. All these factors are expected to cause a considerable increase of mammographic examinations that is sorely needed in order to provide the proper preventive care against breast cancer to all women.

Successful demonstration of the 3-D high-resolution and the tissue-differentiation capabilities of the HUTT system for early detection of breast cancer will lead to full clinical trials and a host of potential applications for cancer detection in other internal organs. If successful, the potential clinical benefits are immense.

REFERENCES

1. J.F. Greenleaf, and R.C. Bahn, "Clinical imaging with transmissive ultrasonic tomography", *IEEE Trans. Biomed. Eng.*, vol. 28, pp. 177–185, Feb. 1981.
2. P.L. Carson, C.R. Meyer, A.L. Scherzinger, and T.V. Oughton, "Breast imaging in coronal planes with simultaneous pulse echo and transmission ultrasound", *Science*, vol. 214, pp. 1141–1143, 1981.
3. J.S. Schreiman, J.J. Gisvold, J.F. Greenleaf, and R.C. Bahn, "Ultrasound transmission computed tomography of the breast", *Radiology*, vol. 150, pp. 523–530, Feb. 1984.
4. J.F. Greenleaf, J. Ylitalo, and J.J. Gisvold, "Ultrasonic computed tomography breast examination", *IEEE Eng. Med. Biol. Mag.*, vol. 6, pp. 27–32, Dec. 1987.
5. V.Z. Marmarelis, T.-S. Kim, and R.E.N. Shehada, "High Resolution Ultrasonic Transmission Tomography," *Proc. SPIE Medical Imaging*, San Diego, Feb. 2003.
6. T.-S. Kim, R.E.N. Shehada, and V.Z. Marmarelis, "Nonlinear modeling of ultrasonic transmit-receive system using Laguerre-Volterra networks," *SPIE International Symposium, Medical Imaging*, San Diego, Feb. 2003.
7. T.-S. Kim, S. Do, and V.Z. Marmarelis, "Multi-band tissue differentiation in ultrasonic transmission tomography," *Proc. SPIE Medical Imaging*, San Diego, 2003.
8. J.W. Jeong, T.S. Kim, D.C. Shin, S. Do, M. Singh, and V.Z. Marmarelis, "Soft Tissue Differentiation Using Milti-band Signatures of High Resolution Ultrasonic Transmission Tomography," *IEEE Transactions on Medical Imaging*, vol. 24, no. 3, pp. 399–408, March 2005.
9. J.W. Jeong, T.S. Kim, D.C. Shin, S. Do, and V.Z. Marmarelis, "Multiband Tissue Classification for Ultrasonic Transmission Tomography Using Spectral Profile Detection", *Proc. SPIE Med. Imag.*, vol. 5373, pp. 87–97, 2004.
10. J.W. Jeong, D.C. Shin, S. Do, and V.Z. Marmarelis, "Automatic Tissue Segmentation Algorithm for Ultrasonic Transmission Tomography Using Active Contours Segmentation and Unsupervised Clustering", *Proc. SPIE Med. Imag.*, vol. 5750, pp. 356–365, Feb. 2005.

USING DIFFRACTION TOMOGRAPHY TO ESTIMATE MARINE ANIMAL SIZE

J.S. Jaffe, P. Roberts
Marine Physical Lab, Scripps Insitution of Oceanography, La Jolla, CA 92093-0238

Abstract: In this article we consider the development of acoustic methods which have the potential to size marine animals. The proposed technique uses scattered sound in order to invert for both animal size and shape. The technique uses the Distorted Wave Born Approximation (DWBA) in order to model sound scattered from these organisms. The use of the DWBA also provides a valuable context for formulating data analysis techniques in order to invert for parameters of the animal. Although 3-dimensional observations can be obtained from a complete set of views, due to the difficulty of collecting full 3-dimensional scatter, it is useful to simplify the inversion by approximating the animal by a few parameters. Here, the animals are modeled as 3-dimensional ellipsoids. This reduces the complexity of the problem to a determination of the 3 semi axes for the x, y and z dimensions from just a few radial spokes through the 3-dimensional Fourier Transform. In order to test the idea, simulated scatter data is taken from a 3-dimensional model of a marine animal and the resultant data are inverted in order to estimate animal shape

Key words: Diffraction tomography, limited angle tomography

1. INTRODUCTION

One of the basic goals of biological oceanography is to understand the abundance and distribution of organisms in the sea. Over centuries of measurement various schemes have been devised, many of which use remote sensing techniques. Since light is severely attenuated a common technique uses acoustics. Although echo sounders are now commonplace for

M.P. André (ed.), Acoustical Imaging, 207–212.

recreational use, scientific description requires a higher degree of specificity than can ordinarily by obtained with such devices. Underwater researchers have therefore tried various techniques whose goal is to obtain a higher level of specificity in characterizing marine populations. To date, almost all work in acoustics has concentrated on exploiting various features of the 180-degree backscatter from marine organisms (McClennan and Simmonds, 1992). This provides a convenient geometry however suffers from a lack of specificity. Unfortunately, due to the variability in animal morphology and its consequences for differences in acoustic impedance, the correspondence between the magnitude of animal backscatter and size, and especially biomass, is degenerate.

An additional degree of freedom, rarely exploited, is to measure animal scatter at a multiplicity of angles. Although this is more challenging from a technical point of view, the benefits of these additional measurements can make it worthwhile. A mathematical framework for inverting for animal morphology from a multiplicity of scattered waves exists within the theory of diffraction tomography. Although various assumptions can be made about whether the scattering potential is weak or strong, the theory provides important insights into how to interpret multiple-angle scatter data. In one case, the Distorted Wave Born Approximation, researchers have used this forward modeling scheme in order to predict animal backscatter from crustacean zooplankton (Lavery et al. 2002). The theory provides a convenient way to understand the relationship of scattered radiation to the scattering potential which can ultimately lead to a complete inversion for animal morphology. Here we propose the use of inverse techniques from wide band scatter at a few observation angles.

2. THEORETICAL BACKGROUND

2.1 A Forward Model

The starting point for this work is the prediction of the four dimensional scattering function which describes the scatter of sound as a function of source receiver separation and animal orientation. An interesting, and well-studied case, occurs when the sound is weakly scattered, such as by either copepods or euphausids. Lavery et al. (2002) modeled the scatter using the Distorted Wave Born Approximation (DWBA). The expression (and its application to the modeling of fluid-like zooplankton) for the complex backscatter amplitude is

$$f_{bs} = \frac{k_1^2}{4\pi} \iiint_V (\gamma_k - \gamma_p) e^{2ik_{2i} \cdot r_v} dV. \tag{1}$$

Here, $\mathbf{k}_1$ is the wave number of the incident sound, $\mathbf{k}_{2i}$ is the wave vector of the incident sound evaluated in the interior of the volume and $\mathbf{r}_v$ is the position vector of any volume element within the animal volume: V. Also note $\gamma_k = \kappa_2 - \kappa_1 / \kappa_1 = (1 - gh^2) / gh^2, \gamma_p = (\rho_2 - \rho_1) / \rho_2 = (1 - g) / g,$ where $g(=\rho_2 / \rho_1)$ and $h(=c_2 / c_1)$. Therefore, $\kappa_1(=(\rho_1 c_1^2)^{-1})$ and $\kappa_2(=(\rho_2 c_2^2)^{-1})$, are the compressibility in the surrounding medium and body interior. Interestingly enough, the expression reveals that the value of the complex backscatter amplitude can be obtained via evaluation of the Fourier transform of the three dimensional function $(\gamma_\kappa - \gamma_p)$ (henceforth called the "gamma contrast") evaluated at the spatial frequency $-2k_{2i}$, normalized by the factor $k_1^2/4\pi$. Hence, using Fourier theory, the three-dimensional gamma contrast can be obtained by "filling" in Fourier space and then taking a three dimensional inverse transform of the resultant information.

The interpretation of the Born Approximation, subsequent DWBA improvement, and its relationship to the Fourier Transform was first considered by E. Wolf (1969). Further work by others (Devaney 1982, Devany and Oristalglio 1983, Wombell and Fiddy 1988) resulted in several proposed methods for inverting for the three dimensional structure, referred to as the scattering potential, from the multiplicity of views made possible by observation of the scattered wave field at a multitude of angles from a multitude of incident waves. Equation (1) can thus be modified for a non collocated source and receiver as:

$$f_{bs} = \frac{k_1^2}{4\pi} \iiint_V (\gamma_k + \gamma_p \cos(\varphi_{obs,0}) e^{i(k_{obs} - k_0)_{2i} \cdot r_v} dV, \tag{2}$$

where k_0 is now an incident wave number vector, k_{obs} is the wave number observation vector (both taken as the wave vectors inside the scattering region as considered in the DWBA) and $\varphi_{obs,0}$ is the angle between k_{obs} and k_0 (Morse and Ingard, 1968) Given, now, a forward model, the development of inverse techniques can be considered.

2.2 Inverse Procedures

In the case that the object is a 3-dimensional sphere with radius r (or any spherically symmetric object), the theory of reconstruction from projections can be used to invert for the spherically symmetric profile from a

single projection (Kak and Slaney, 2001). A 3-dimensional solid ellipsoid with semi-axes *a*, *b*, and *c* is somewhat more complicated, however can be simply defined by these three parameters. Interestingly enough, the Fourier Transform of the ellipsoid can be related to that of a sphere in a straightforward way.

Stated without proof, the following mathematical theorem provides a way to approach the inversion:

There exists an equivalent sphere that can be estimated from a single radial spoke of the observed 3D Fourier transform of the 3D-ellipsoid. Moreover, the diameter of this sphere is defined by the distance between the planes tangent to the 3D-ellipsoid at the given observation angle.

In a practical sense, this says that any single radial spoke of the 3D transform of the ellipse will uniquely define an equivalent sphere in real space. Call this the "equivalent spherical radius" or ESR for the data observed at scattering angle $(\theta_{obs}, \varphi_{obs})$ from the incident set of angles (θ_0, φ_0). Also note that this function is almost periodic in that it consists of a series of nulls that are a function of the radius of the object. An additional theorem states that the position of these nulls totally characterizes the ESR. The proposed algorithm then uses these estimates of the ESR as a function of incident and look angle in order to estimate the three parameters for the semi-axes of the ellipse (*a, b, c*) and its orientation via a refinement of the observed data against a set of predicted values. We conjecture, however have not proved, that this provides a unique answer for perfect data.

3. NUMERICAL EXPERIMENTS

In order to provide initial tests of the above ideas a set of numerical simulations were performed. Since the procedure was expected to work well with perfect 3D ellipsoidal data, a 3-dimensional model of a zooplankton was used in order to judge the algorithm's performance on quasi-realistic data. The simulations were facilitated via obtaining a set of data from a web site dedicated to scattering models of zooplankton (McGehee et al., 2005). A model of a Calanus Finmarchicus (an extremely abundant crustacean zooplankton) adult female was used in order to generate a cylindrically symmetric three-dimensional matrix model of a zooplankton. Figure 1a shows a projected view of the animal obtained by integrating the three-dimensional function along the animal's short axis. The magnitude of the 3D Fourier transform is shown in Figure 1b. Since the numerical object is cylindrically symmetric, a single plane through the axis of symmetry

completely characterizes it. The 3D Fourier transform is therefore also cylindrically symmetric and it can be completely characterized by a single plane (as shown in Figure 1b). Simulated data consisted of the observation of both 180-degree backscatter and bistatic scatter at several angles. Based on the above schemes (that of using the null spacing to estimate animal dimensions) the ESR for the species was computed and found to be within 30% of the true values.

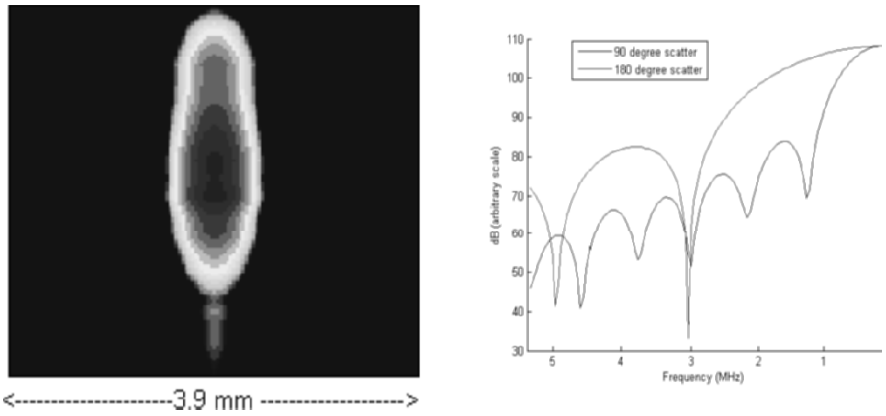

Figure 1. Left: A projected view of a 3-dimensional Calanus (adult female). Right: Radial spokes through its Fourier Transform corresponding to the 180-degree "broadside" backscatter case (red) and the scatter that would be measured by having a receiver at an angle of 90 degrees (blue).

4. DISCUSSION AND CONCLUSIONS

The idea of using multiple angular observations of scattered sound from marine organisms has been proposed. Under the assumptions of the DWBA model for organism scatter and a 3D ellipsoidal model for organism shape, a small number of observation angles can be used in order to estimate both size and orientation. Theorems indicate that if the organism under observation is similar in shape to a 3-dimensional ellipse that tangent planes at the observation angles can be estimated. It has been conjectured that these set of tangent planes will permit an inversion for 3-dimensional shape.

Note that the question of how many views, what view separation, what bandwidth, and what signal to noise is necessary for practical inversion have not been answered. These questions will be addressed in further research.

Of course, the ultimate goal of this work is to fabricate a new class of ocean observing instruments that might take advantage of this methodology

in order to provide a more detailed and accurate view of marine animals in their natural habitat.

REFERENCES

1. Devaney, A.J., "Inversion formula for inverse scattering within the Born approximation", Optics Letters, 7 (3) pp 111- 112, 1982.
2. Devaney, A.J., and Oristaglio, M.L., "Inversion Procedure for Inverse Scattering within the Distorted Wave Born Approximation", Physical Review Letters, 51 (4), pp 237–240, 1983.
3. Kak, A.C., and Slaney, M., "Principles of Computerized Tomographic Imaging" Society of Industrial and Applied Mathematics, 2001.
4. Lavery, A.C., Stanton, T. K., McGehee, D.E., and Chu, D., "Three-dimensional modeling of acoustic backscattering from fluid-like zooplankton", J. Acoust. Soc. Am, 111 (3) pp 1197–1210, 2002.
5. McGehee, D.E., Benfield, M., Holliday, D.V., and Greenlaw, C., "Advanced multifrequency inversion methods for classifying acoustic scatterers", 2005.
6. http://zooplankton.lsu.edu/scattering_models/MultifreqInverseMethods.html.
7. MacLennan, D.N., and Simmonds, E.J., "Fisheries Acoustics", Chapman & Hall, Fish and Fisheries Series 5, 1992.
8. Morse, P.M. and Ingard, K.U., "Theoretical Acoustics", Princeton University Press, 1968.
9. Wombell, R.J., and Fiddy, M.A., "Inverse scattering within the distorted-wave Born approximation, Inverse Problems 4, L23-L27, 1988.
10. Wolf, E. "Three-dimensional structure determination of semi-transparent objects from holographic data", Optics Communications, 1 (4), pp 153–156, 1969.

BREAST DUCTAL COMPUTER PHANTOM

E. Franceschini, S. Mensah, D. Amy, J.-P. Lefebvre
CNRS-LMA (Laboratoire de Mécanique et d'Acoustique), 31 Chemin Joseph Aiguier, 13402 Marseille Cedex 20, France; University of Medecine Montpellier-Nîmes,UFR Kennedy, 30908 Nîmes Cedex 2, France

Abstract: A breast ductal computer phantom is designed in order to evaluate ultrasound imaging procedures: Ductal Echography and Diffraction Tomography are compared

Key words: Diffraction tomography, Ductal Echography, breast model, MFEM, near-field

1. NEED FOR AN ANATOMICALLY-LED METHOD OF INVESTIGATION

Breast cancer and all the specific diseases of the breast present the common property of originating from the epithelium and developing first in the ductolobular structures. Therefore, the observation of these structures provides direct means for detecting alterations induced by breast diseases as soon as they become perceptible. Echography is well adapted to soft tissue examinations but, in conventional echography, transductal scans are performed perpendicularly to the ductal course. This mode of scanning cannot match the radial arrangement of breast anatomy. Cancers are detected only when they show an abnormality with a contrast and have a sufficient three dimensional volume, perceptible whatever the sweeping orientation (5 mm size lesions). The lack of anatomic guidance in breast ultrasound has been responsible for its failure [1][2].

An anatomically led method of investigation based on the identification of internal mammary structures, **Ductal Echography** (DE), was introduced in 1987. This technique is based on a radial scanning. Ductal-axial scans are

M.P. André (ed.), Acoustical Imaging, 213–221.

performed along the ductal course. With this new technique, the observer investigates the epithelial structures actively by systematically following the ductal system in each mammary lobe.

Our research aims at developing ultrasound tomography techniques that will reduce the operator-dependency observed in echography and provide an intelligible visualization of the epithelium. Indeed, tomographic methods in medical ultrasound are the subject of increasing interest. Current research work aims mainly at improving the differentiation of breast tissues (and cancers) by quantifying the sound speed, the elasticity and the attenuation of tissues [3] [4] [5] [6]. We propose to differentiate the breast tissues by using not only these parameters but also the breast anatomy identification as performed in DE.

In order to compare DE and our tomographic approach [7], ultrasonic pulse propagation through breast tissues has been simulated using a 2D realistic breast phantom that respects the anatomy of the breast as much as possible. The tissues of the breast are modeled as a random inhomogeneous continuum [8] [9]. For the echography, that serves as a common reference, we simulate a linear probe, a semi-circular antenna is used for the tomography. Tomographic and echographic reconstructions can then be compared.

2. NUMERICAL PHANTOM

2.1 Tissue Random Media

C. Tsogka has developed the numerical method we use to compute the solution of the wave equation. This method models the time domain acoustic wave propagation in fluid media and is based on the discretization of the mixed velocity-pressure formulation for acoustics. The space discretization of the problem is based on a mixed finite element method [10] and for the discretization in time, a 2^{nd} order-centered finite difference scheme is employed. The simulation grid is surrounded with an absorbing layer (PML) for simulating unbounded domains [11].

The numerical tissue-like materials are characterized in terms of density and celerity. We assume each parameter to consist of a heterogeneous mean value and the realization of a stationary random medium. The differences between the material parameters and their mean values are defined by correlation functions assumed to be isotropic. This assumption is not realistic, but locally, it is acceptable. Nevertheless, large-scale fluctuations

within each kind of tissue (connective tissue, lobe, fat) should also be considered, but they are not introduced in our models. Thus, we realize the stationary random medium in terms of a white noise filtered by a spectral filter, whose power spectrum is the radial Fourier Transform of the correlation function [8] [9].

A Gaussian filter is used since it produces tissue-like echographic patterns. It allows us to adjust the correlation length, and is quite simple to use. It leads to a correlation function of the type (a is the Gaussian correlation length): $c\left(\underline{y}\right) = \left[\alpha / \left(\pi a^2\right)\right] \cdot \exp\left(-y^2 / a^2\right)$.

2.2 "Realistic" Numerical Phantom

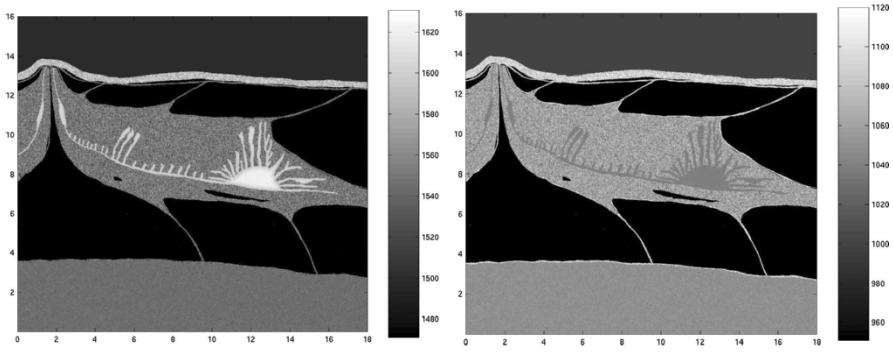

Figure 1. Numerical breast phantom for echography. Sound speed and density maps.

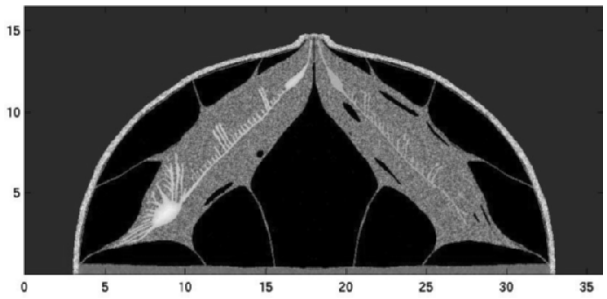

Figure 2. Numerical breast phantom for tomography. Sound speed map (mm).

The density and sound speed grids used for the computation were obtained by mapping a schematic view of a diametric section of the breast passing through the nipple. The drawings [figures 1 and 2] display the successive elements observed in the breast with ultrasound: the skin, the fat (including the superficial fatty layer and the deep fatty layer), the lobe, the connective tissue that supports the lobe and the intra-lobular structures. Cooper's ligaments link the lobes to the superficial layer of the superficial

fascia lining the skin, and to the deep layer of the superficial fascia that lines the thoracic wall [1]. Each pixel of the map is then assigned a sound speed and density value determined from the results found in the relevant literature and assumed to be representative of the local tissue type [3], [4], [5], [6] and [12]. Random media, defining the standard deviation and the correlation length for each tissue, are realized thanks to a DE analysis. The correlation lengths (and respectively the standard deviations) of the connective tissue (fasciae and Cooper's ligament), the hyper echogenic skin and the lobe are chosen smaller (respectively bigger) than the fat and the pectoralis muscle. We display a duct infiltration (ectasia) that has a fine texture; its correlation length is the smallest. The parameter values employed in the present study are summarized in Table 1.

The finite element code was employed to compute the propagation of cylindrical waves (2D simulations) through the phantom. The spatial step size of the finite element grid was chosen to be one fortieth of the wavelength. Each simulation was performed on IDRIS (Institute for Development and Resources in Intensive Scientific computing) using a Compaq Linux Cluster incorporating 24 Alpha EV68 processors cadenced at 836 MHz (1.5 Gigaflop peak performance per processor).

Table 1. Reference values for sound speed and density.

Medium	Average		Random medium	
	Sound speed (m/s)	Density (kg/m³)	Standard deviation (%)	Correlation length (mm)
Water	1500	1000	-	-
Skin	1590 [4] [6]	1090 [12]	2	0.21
Connective tissue	1545 [4] [6]	1090 [12]	2	0.21
Fat	1470 [3] [4]	950 [12]	-	-
Lobe	1550 [3] [4]	1060 [12]	2	0.21
Ectasia	1570–1620 [3] [5]	1040 [12]	0.8	0.02
Pectoralis muscle	1545 [3] [4]	1050 [12]	0.8	0.42

Numerical breast phantom for echography. During a clinical examination, the patient lies on her back, her breast is flattened; a water bag is placed on the probe, thus the skin appears quite rectilinear [figure 1]. For the Finite Element Code, a grid of 2400×2600 pixels (Δx=0.0075mm, 1.8cm×1.95cm) was employed. Signals were recorded by 168 receivers simulating a linear probe placed about 4.5 mm from the skin surface. The computation time for the whole simulation was of the order of 1340 hours.

Numerical breast phantom for tomography. During an ultrasound examination, the patient lies prone on an examination bed, her breast immersed in a water bath, with a semi-circular antenna around it [figure 2].

For the Finite Element Code, a grid of 2400×1200 pixels (Δx=0.015mm, 3.6cm×1.8cm) was employed. Short pulses were transmitted along the acquisition circle at every 0.25° (720 shots). For each shot, numerical signals were registered by means of receivers over a finite aperture of 20° centred on the transmitter, with a step of 0.25°. The computation time for the whole simulation was of the order of 1440 hours.

3. IMAGING TECHNIQUES

Diffraction tomographic reconstruction. Starting from measurements of the scattered field to recover the various parameter maps, one has to solve the forward problem (prediction). For that purpose, soft biological tissues are classically described by their density and their compressibility distributions. Provided the receiving aperture is large enough, this formulation has the advantage of leading to a single parameter reconstruction that corresponds to the Laplacian of the compressibility map [13]. This allows us (linearity of the problem) to neglect right now the density echo contributions, under the condition we limit our reconstruction procedure to the large aperture reflection tomography. Let $\gamma_\chi = \left(\chi - \chi_0\right)/\chi_0$ be the relative compressibility fluctuations, we can then introduce the forward problem.

Forward problem. Let us consider a pressure source in the infinite homogeneous host medium, the scattered field p_d meets the classical wave equation based on the assumption that the total field inside the region of interest is very close to the incident field (first order Born approximation),

$$-\frac{1}{c_0^2}\frac{\partial^2 p_d}{\partial t^2} + \nabla^2 p_d = \frac{\gamma_\chi}{c_0^2}\frac{\partial^2 p_i}{\partial t^2}. \tag{1}$$

This equation (1) can be resolved by the 3D Green function. We assume that the medium is excited by a spherical wave of infinite bandwidth, transmitted from a point source $\underline{x}_E$, and measured at the receiver location $\underline{x}_R$. In order to simplify the formulation, we can introduce a new parameter: $\gamma(\underline{x}) = \gamma_\chi(\underline{x})/\left[16\pi^2 c_0^2 |\underline{x}_R - \underline{x}\| \underline{x} - \underline{x}_E|\right]$. Therefore, the scattered field is:

$$p_d(\underline{x}_E, \underline{x}_R, t) = \int_{\mathbb{R}^3} \left[\delta\left(|\underline{x}' - \underline{x}_E| + |\underline{x}_R - \underline{x}'| - c_0 t\right) * f''(t)\right] \gamma(\underline{x}')\, d\underline{x}' \tag{2}$$

where $f''(t)$ is the second derivative of the wave form function $f(t)$. For a fixed time delay t and a given acquisition geometry ($\underline{x}_E, \underline{x}_R$), the locus of the point for which the argument of the delta function is zero is the ellipsoidal surface described by the equation $c_0 t = |\underline{x} - \underline{x}_E| + |\underline{x}_R - \underline{x}|$.

Considering this acquisition geometry, the amplitude of the scattered field results from the integral of the compressibility distribution over the surface of the ellipsoid of revolution. This is why we use a qualitative algorithm, presented in [7], based on elliptical back-projection, which deals with these data in order to recover the 2D distribution of $\gamma(\underline{x})$.

Echographic reconstruction. We simulate a 168 element transducers with a central frequency of 5 MHz, using an aperture with 12 active elements. The piezoelectric transducers are represented by punctual sources (used both in emission and reception), and are spaced at $\lambda/3$. Each punctual source transmits a cylindrical wave (2D simulation). We use transmission and reception focusing at 6.3 mm, 8.85 mm, 11.4 mm, 13.95 mm and 19.05 mm, offering a dynamic range scanning from 5 mm up to 20.3 mm.

4. RESULTS

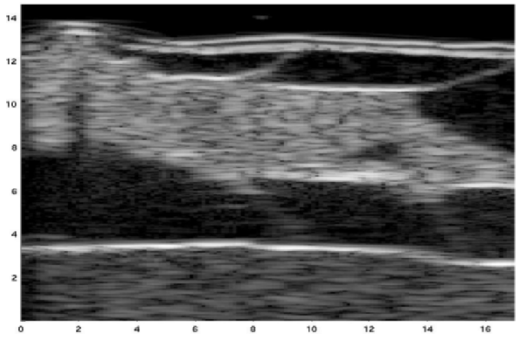

Figure 3. Echographic simulation [2.5–7.5 MHz], linear scanning (mm).

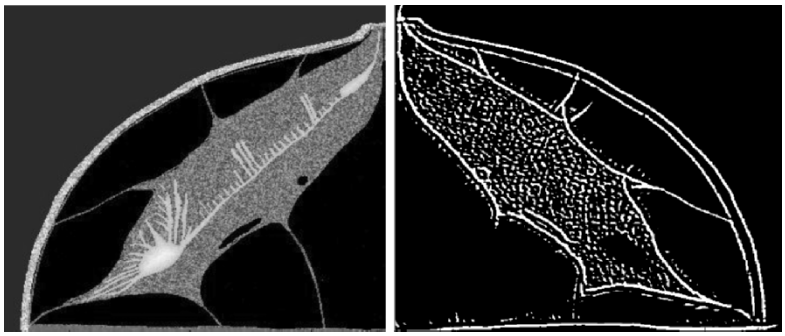

Figure 4. Numerical phantom and tomographic reconstruction [1.5–4.5 MHz].

The simulated echographic view [figure 3] has to be compared with the phantom of figure 1. One may observe that the main features (lobe, ligaments, fat and retro-areola zone) are restituted. The lesion is visible, but

not the fatty inclusions in the lobe. The speckle noise is important as it is expected from low frequency echography. In the Tomographic Image (TI) [figure 4], all the interfaces (connective tissues) are clearly revealed; some intra-lobular fatty zones visible in TI are not restituted by DE. The TI is free of speckle even if a reconstruction noise is still noticeable. Compared with DE, the contrast in TI is greatly improved. In addition the border of the lesion is nicely delineated although the central frequency of the tomographic signals is half that of the echographic pulses. In both cases, the ducts are not visible, since the impedance contrast is weak and their size smaller than the wavelength. The use of lower frequency responds to the computing limitation trade off between resolution and acceptable computing time. Indeed, in comparison with the flattened breast, the uncompressed breast occupies an apparently larger volume. In spite of this low frequency activation, the image resolution is improved, which augurs new possibilities for current working frequencies comprised between [5–10 MHz].

5. CONCLUSION

This work focuses on the design of a 2D numerical acoustic model of the breast, making it possible to simulate ultrasonic wave propagation and measurement. The main features of this phantom are, on the one hand, its taking into account of anatomic details of sub-millimeter size and on the other hand, the respect of the ultrasonic characteristics of the various types of tissues (lobe, connective tissues, fat, muscle) constituting the breast which are expressed in terms of density and celerity maps.

Nevertheless, this phantom still presents two major limitations. Firstly, the acoustic model neglects the attenuation phenomenon that is of prime importance, especially as far as breast ultrasound semiology is concerned. Secondly, it is a 2D phantom that cannot permit full 3D measurements of the scattered field. Concerning the first item, our team is currently working on a visco-acoustic extension of the Finite-Element code by introducing a complex, frequency dependent visco-acoustic modulus (constant quality factor Q). Besides, signal pre-processing is required upstream the tomographic reconstruction in order to extract from the ultrasonic data, the integral attenuation along the propagation paths. The second point is more difficult to solve. Indeed, nowadays, 3D simulations seem to be beyond the capacity of middle of the range computers (computation time).

Nevertheless, this 2D breast phantom enables us to simulate 2D Ductal Echographic images by using [2.5–7.5] MHz linear array probes. These images have been compared with the large aperture tomographies. In the latter case, [1.5–4.5] MHz cylindrical waves were transmitted and measured

by point transducers uniformly distributed on a semi-circular antenna. The comparison of these images leads to a comfortable superiority of the tomographic reconstruction both in terms of contrast and in resolution. In addition, tomography will open the way to quantitative imaging that means, to computer-assisted diagnoses. This is the next challenge of ductal ultrasound computed tomography and a push for realistic breast phantom designing and numerical experimentation based on clinical data.

6. ACKNOWLEDGEMENT

This study has been supported by Ville de Marseille, Region Provence-Alpes-Côte d'Azur, CNRS-LMA, and an "Action Concertée Incitative" of the French Ministry of Research and Technology (2001–2004). We are grateful to Veronique Bourrillon (ENSPM) for her participation in the echographic reconstruction developments.

REFERENCES

1. Teboul M., *Practical ductal echography, guide to intelligent and intelligible ultrasonic imaging of the breast* (editorial Medgen, 2004).
2. Amy D., *Critères échographiques de bénignité*, in *Echographie mammaire, De l'image à la thérapeutique* (Collection d'imagerie radiologique, Ed. Masson, 1998), pp.23–31.
3. Kossoff G., Fry E.K., Jellins J., Average velocity of ultrasound in the human female breast , *J. Acoust. Soc. Am.* **53**(6), pp.1730–1736 (1973).
4. Goss S.A., Johnston R.L., Dunn F., Comprehensive compilation of empirical ultrasonic properties of mammalian tissues, *J. Acoust. Soc. Am.* **64**(2), pp.423–457 (1978).
5. Glover G.H., *Characterization of in vivo breast tissue by ultrasound time of flight computed tomography, Ultrasonic tissue characterization II*, M. Linzer, Ed. National Bureau of Standards Spec. Pub. 525, pp.221–225 (1979).
6. Foster F.S., Strban M., Austin G., The ultrasound macroscope: initial studies of breast tissue, *Ultrasonic imaging* **6**, pp.243–261 (1984).
7. Mensah S., Ferriere R., Near field diffraction tomography, *Ultrasonic Imaging* **24**, pp.135–146 (2002).
8. Insana M.F., Wagner R.F., Brown D.G., Hall T.J., Describing small-scale structure in random media using pulse-echo ultrasound, *J. Acoust. Soc. Am.* **87**(1), pp.179–192 (1990).
9. Klimes L., *Correlation functions of random media*, Pure and Applied Geophysics, 159 (2002).
10. Bécache E., Joly P., Tsogka C., An analysis of new mixed finite elements for the approximation of wave propagation problems, *SIAM J. Numer. Anal.* **37**(4), pp.1053–1084 (2000).
11. Collino F., Tsogka C., Application of the pml absorbing layer model to the linear elastodynamic problem in anisotropic heteregeous media, *Geogysics* **66**, pp.294–305 (2001).

12. Woodard H.Q., White D.R., The composition of body tissues, *The British Journal of Radiology* **59**, pp.1209–1219 (1986).
13. Mensah S., Lefebvre J.-P., Enhanced Compressibility Tomography, *IEEE Trans. Ultras. Ferro. Freq. Contr.* **44**(66), pp.1245–1252 (1997).

COMPOUND QUANTITATIVE ULTRASONIC TOMOGRAPHY OF LONG BONES USING WAVELETS ANALYSIS

P. Lasaygues
Laboratoire de Mécanique et d'Acoustique, UPR CNRS 7051, 31 chemin Joseph AIGUIER 13402 Marseille cedex 20

Abstract: Compound Quantitative Ultrasonic Tomography (*CQUT)* is used to long bones imaging. We showed that an iterative tool might be used to provide, from reflection tomography, qualitative images of the shape of the object, and to provide, from transmission tomography, quantitative images of the velocity map. Both tomographies are based on ultrasonic propagation in bones, particularly perturbed by this high-contrasted heterogeneous medium. Reflected and transmitted signal are composed of several packages of waves. We propose a novel algorithm based on the wavelet analysis tool adapted to ultrasonic signals that allow the transmitted signals to be cleaned and filtered and the useful information to be separated from the unwanted noise

Key words: Ultrasonic tomography, bone imaging, wavelets analysis

1. INTRODUCTION

Quantitative ultrasonic tomography is used to long bones imaging. In previous works, we showed that an iterative tool might be used to provide, from reflection tomography, qualitative images of the shape of the object, and to provide, from transmission tomography, quantitative images of the velocity map. Both tomographies are based on ultrasonic propagation in bones, particularly perturbed by this high-contrasted heterogeneous medium. Reflected and transmitted signal are composed of several packages of waves, which had followed various pathways within the cortical shell of long bones. Signal and image processing have a large important part in the complete process.

M.P. André (ed.), Acoustical Imaging, 223–229.

Transmission tomography is based on the knowledge of the Time-Of-Flight (TOF) measured on the extracted ultrasonic signal and related to the useful velocities of the ultrasonic waves throughout the shell. To optimise our TOF detection processing, we propose a novel signal processing based on the wavelet analysis adapted to ultrasonic signals that allow the transmitted signals to be cleaned and filtered and the useful information to be separated from the unwanted noise.

2. COMPOUND ULTRASONIC TOMOGRAPHY

Ultrasonic Tomography (UT) is based on a linearization of the inverse acoustic scattering problem. It allows perturbations (theoretically small) of a reference medium to be visualized.

For long bones, the acoustic impedance of the cortical is highly contrasted compared to the surrounding soft tissues (or water), and so, perturbs ultrasonic propagation (refraction, attenuation and diffraction). Therefore, bone imaging is a non-linear inverse problem with no single solutions. However, for some hypotheses (weak heterogeneous medium, straight lines waves propagation) and *a priori* knowledge of the analyzed bones, we showed that one solution is possible [1].

Our algorithm combines two tomographies, Ultrasonic Reflection Tomography (URT) and Ultrasonic Transmission Tomography (UTT). URT [2] provides the realistic shape of the bodies and UTT is especially adapted to mapping local velocities inside the area defined. On the final image, the mean geometrical and acoustical parameters may be measured and used to improve the dimensioning and the quantification, ensuring, the complete iterative Compound UT in which the behaviour and the convergence are excellent.

Long human bones are effectively irregular hollow tubes (Figure 1) and should support the propagation of more complex waves similar to elastic volume waves.

Close to the external water/bone interface, the wave is deviated from its initial position because of the refraction throughout the shell. The corrections of this refraction are based on the knowledge of the dimensions and on a velocity ground level (Snell-Descartes laws).

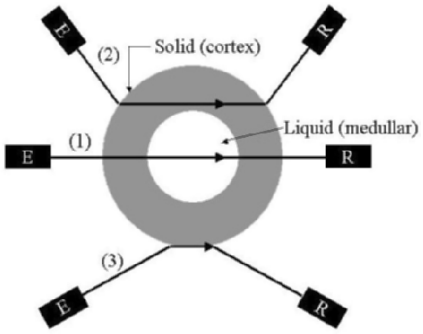

Figure 1. Supposed pathways of the wave propagation throughout cortical long bone for CQUT.

3. WAVELET ANALYSIS OF TRANSMITTED SIGNALS

For transmission tomography, projections must be constructed from determination of the TOF between both transducers. The experimental ultrasonic acquisition protocol enabled us, according to the compensation procedure, to digitize correctly the transmitted signals [3], composed of several packages of waves which had followed various pathways within the object (cortex and/or medullary and/or cortex) [4].

Various algorithms of existing *T.O.F.* measurements are based on various definitions of transit times of pulse, such as zero-crossing or thresholding. Our algorithm was based on detecting the arrival time of the signal corresponding to the wave propagating at, or close to, the longitudinal velocity within the shell ("fluid" modeling).

The level of the detection accepted for each signal was fixed by a subjective threshold. Then, the number of bad *T.O.Fs* detected increased because these thresholds are very sensitive to the signal-to-noise ratio (SNR), and are not correctly adapted to all the values (usually 15^6 or 20^6) that we had to automatically treat. Indeed, the choice of the lower limit of the threshold was fixed for each view angle in relation to the noise. If we extracted the useful signal from this noise and if we standardized all the packages with a criterion that did not perturb their temporal position, the errors decrease.

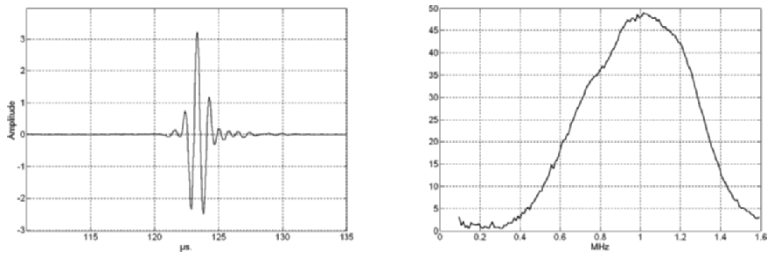

Figure 2. Transmitted signal in water.

Our idea was to exploit wavelet analysis, which allowed simultaneous joint studies in the time and frequency domains.

Two aspects were considered in particular: the significant spectral bandwidth of the emitted signal; that is, the transmitted signal without the object (Figure 2) and the axial resolution of the transducer, brought back to the support of this emitted signal. Then we defined a Region-Of-Interest (*R.O.I.*) consisting of this time and frequency bandwidth for the wavelet analysis, filtering and synthesis (sum of the wavelet coefficients).

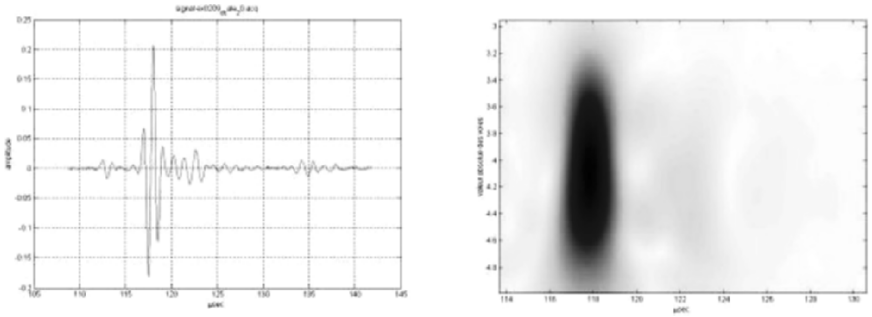

Figure 3. Wavelets analysis of a transmitted signal through the medullary hollow zone (Zone 1).

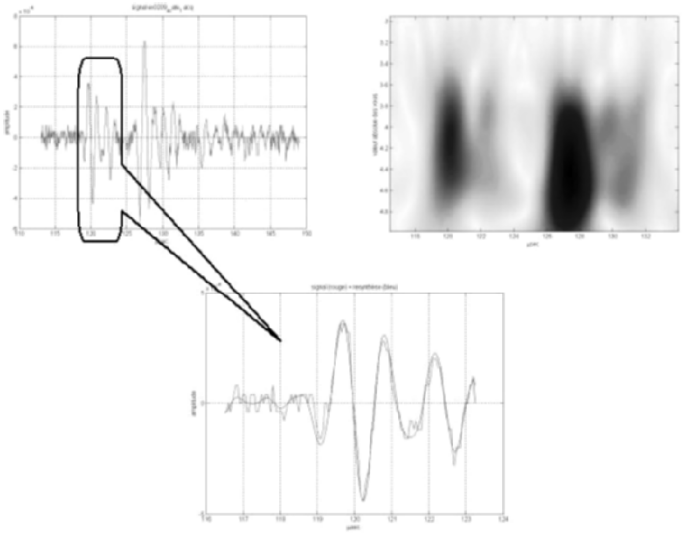

Figure 4. Filtering the transmitted signal corresponding to the wave propagating close to the boundary bone/water (zone 3).

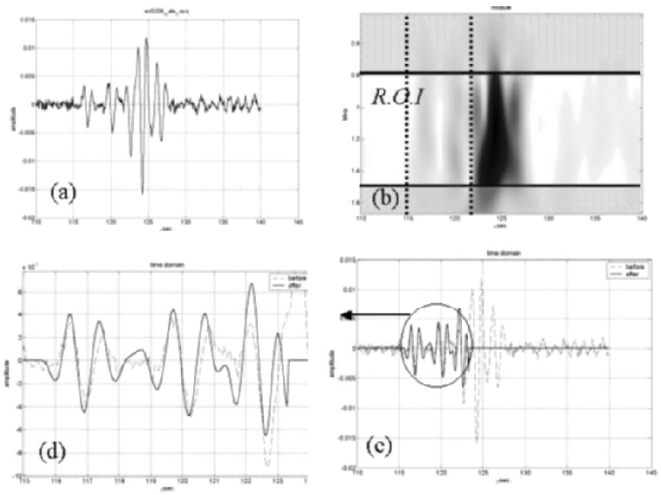

Figure 5. Filtering transmitted signals in solid cortex area (zone 2) (a) - temporal representation; (b) - wavelet decomposition – modulus – and visualization of the R.O.I. on the bandwidth [0.8 - 1.5] MHz (at –25 dB) X [115 – 123.35] μs; (c) - comparison between the initial signal and its synthesis on the R.O.I.; (d) – zoom, the SNR and the resolution of the first-arriving signal increase.).

In the medullary hollow zone, the processing of the signals is generally easy and the *T.O.F.* are calculated with a margin for error lower than 2% (Figure 3). In the solid cortex (Figure 4 & 5), signals are much more disturbed.

For example, on the Figure 5, three lots of waves were distinguished with different amplitudes and the first-arriving signal was the lowest and the arbitrary first-time could be 115 μs. The upper signal arrived in water after the *T.O.F.* (123.35 μ*s*) and so, did not correspond to a direct propagation inside the shell.

This signal was analyzed and the *R.O.I.* was defined. Figure 4d display the curves after filtering. The SNR was higher than before processing, and the signal was filtered for low and high frequencies. The resolution and the quantification of the first two packages had improved.

Hence, the *T.O.F.* detections increased and the false values decreased. The same threshold can be used for all filtering signals for all view angles. The advantage of our algorithm was that the noise reduction, the thresholding and the *T.O.F.* detection could be made simultaneously on the image of the wavelet coefficients.

4. CQUT OF FEMUR

The human sample was a femoral specimen of approximately 32 ± 5 mm for the external diameter and 16 ± 2 mm for the internal diameter. The *a priori* mean-velocities were 3400 m/s in bone and 1478 m/s in water. In previous studies, the femur was compared to a circular tube, but this approximation (Figure 6-left) was not suitable enough. Figure 6-right displays the final image obtained by CQUT.

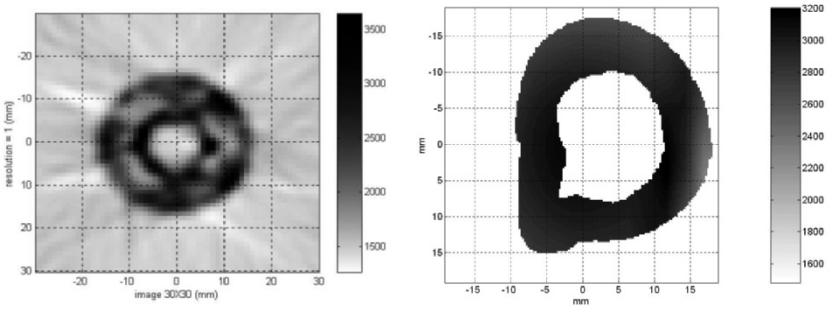

Figure 6. Human femur CQUT, without (left) and with(right) signal processing.

The fluid in the internal shape was reconstructed with a correct velocity value (≈ 1500 m/s) and the dimension of this cavity was 15 – 17 mm. The greatest external shape (30 – 34 mm) was exact and the mean-velocity estimated in the cortical shell was 3150 m/s.

REFERENCES

1. Ouedraogo E., Lasaygues P., Lefebvre J.P., Gindre M., Talmant M., Laugier P., Contrast and velocity ultrasonic tomography of long bones, Ultrasonic Imaging 24, (2002) 135 – 146.
2. Lasaygues P., Lefebvre J.P., Cancellous and cortical bone imaging by reflected tomography, Ultrasonic Imaging 23, (2001) 55–68.
3. Ouedraogo E., Lasaygues P., Lefebvre J.P., Talmant M, Gindre M., Laugier P., Multi-step compensation technique for ultrasound tomography of bone, Acoustical Imaging 26, (2001), 153–160.
4. Ouedraogo E., 2002 Caractérisation géométrique et Acoustique des os long par tomographie ultrasonore, *Ph.D Thesis* University of Cergy-Pontoise.

DATA REDUNDANCIES IN REFLECTIVITY TOMOGRAPHY USING OFFSET SOURCES AND RECEIVERS

A 'Layer-Stripping' Perspective

X. Pan, J. Zhang, M.A. Anastasio

Department of Radiology, The University of Chicago, Chicago, IL 60637; Department of Biomedical Engineering, Illinois Institute of Technology, Chicago, IL 60616

Abstract: In this work, we investigate the existence and utilization of data redundancies in reflectivity tomography employing offset source and receiver transducers, which we refer to as bistatic reflectivity tomography. A layer-stripping procedure is described heuristically and mathematically, which reveals that a two-fold redundancy exists in a complete data set. This indicates that knowledge of the measured data function over any half of its domain is, in principle, sufficient for image reconstruction. Computer-simulation studies are presented for demonstrating the numerical feasibility of half-data image reconstruction

Key words: Reflectivity tomography, ultrasound tomography, inverse scattering

1. INTRODUCTION

Ultrasound reflectivity tomography is a noninvasive imaging technique that holds great promise for biomedical imaging applications [1–3]. In reflectivity tomography, a weakly scattering object is probed by use of ultrasonic pulses that are generated by point-like sources that reside on a measurement aperture. The resulting backscattered, or reflected, wavefields are measured as functions of time at specified receiver locations on the measurement aperture. The goal of reflectivity tomography is to reconstruct, from knowledge of this measurement data, a function that represents the

M.P. André (ed.), Acoustical Imaging, 231–245.

difference between the normalized compressibility and density variations of the object[2]. We will refer to this function as the object function.

The explicit form of the imaging model in reflectivity tomography depends on the relative locations at which the reflected wavefields are measured with respect to the source positions. As investigated in the seminal work of Norton and Linzer[2], when the source and measurement locations coincide, the imaging model takes the form of a spherical Radon transform. In the case where the source and measurement locations differ, the imaging model is described by a generalized Radon transform that integrates the object function over elliptical surfaces. Using terminology borrowed from the radar literature, these two cases correspond to "monostatic" and "bistatic" measurement configurations, respectively[8].

Norton and Linzer[2] and Finch *et al.*[4] have derived explicit and exact reconstruction formulae for 3D reflectivity tomography using a monostatic measurement configuration. These algorithms assume that the source-receiver positions cover a spherical measurement aperture that encloses the object. In medical imaging studies such as breast imaging, it is clearly not possible to use a measurement aperture that completely encloses the object. We have recently identified and formulated mathematically data redundancies in monostatic 2D and 3D reflectivity tomography[5,6]. By use of these redundancies, we demonstrated that knowledge of measurements over (any) half of the measurement aperture is sufficient for exact image reconstruction, and proposed half-scan reconstruction methods for achieving such reconstructions[5,6].

In this article, we extend our study of data redundancies in reflectivity tomography to the bistatic measurement configuration. A layer stripping procedure, which we have referred to previously as a "potato peeler procedure,"[7] is described heuristically and mathematically. This formulation reveals that knowledge of bistatic measurements over any half of the data space is sufficient for exact image reconstruction. Numerical simulations are conducted to corroborate our theoretical assertions.

2. IMAGING MODEL

2.1 Measurement Geometry

We will assume the two-dimensional (2D) measurement geometry shown in left panel of Fig. 1. However, the results that follow can readily be generalized to the three-dimensional (3D) case. A 2D object that is characterized by its object function $f(r,\theta)$ is embedded in an acoustically homogeneous background medium. The object is assumed to reside completely within a disk of radius R_f. A collection of wide-band point-like transducers are evenly positioned along a circle of radius R_m that encloses the object. The position of each transducer will be denoted by the polar coordinates $(r = R_m, \theta)$. At time $t = 0$, a single transducer at location (R_m, θ_s) emits an infinitesimally short pulse of sound, and the wavefield that is backscattered, i.e., reflected, from the object is measured at transducer location (R_m, θ_r), where $\theta_s \neq \theta_r$. Furthermore, we assume that the receiver location (R_m, θ_r) satisfies the condition that the chord connecting it with the source location (R_m, θ_s) does not intersect the support disk of the object.

In order to describe conveniently the resulting measurement data, we will utilize an aperture-point coordinate system (x', y') that is specified by the source and measurement locations. As described in Fig. 1 (left panel), the y'-axis coincides with the line containing the points (R_m, θ_s) and (R_m, θ_r). The x'-axis intersects the y'-axis at a location midway between these points, and has an orientation denoted by the angle

$$\theta_{1/2} \equiv \frac{1}{2}[\theta_s + \theta_r], \tag{1}$$

measured with respect to the x-axis of the fixed system. In terms of the aperture-point coordinates the source and receiver locations can be denoted as $(R_m, \theta_s) = (x' = 0, y' = c)$ and $(R_m, \theta_r) = (x' = 0, y' = -c)$, respectively. Here, $\pm c$ denotes the distance from the origin of the aperture-point system to the source and receiver locations, respectively.

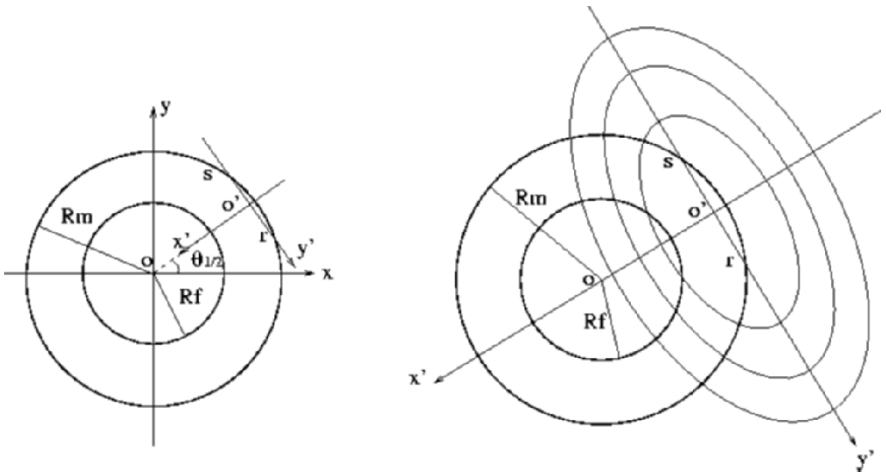

Figure 1. The measurement geometry of bistatic reflectivity tomography.

2.2 Imaging Model

Assuming weak scattering conditions, the measurement data represent a collection of line integrals of the object function computed over a family of ellipses with different eccentricities[2]. The foci of each ellipse are the same and, as shown in Fig. 1 (right panel), coincide with the locations of the source and receiver. This family of ellipses is described in the aperture-point coordinates as

$$\frac{(x')^2}{b^2}+\frac{(y')^2}{b^2+c^2}=1, \tag{2}$$

where c (the foci locations) remains fixed, while the length of the semiminor axis b is permitted to vary. This indicates an imaging model of the form

$$g(\xi,\theta_r;\theta_s)=\int\limits_{L(\xi,\theta_r;\theta_s)} f(r,\theta)\ ds, \tag{3}$$

where $g(\xi,\theta_r;\theta_s)$ denotes data acquired at receiver location (R_m,θ_r) when the source is located at (R_m,θ_s). The coordinate ξ describes the

signed distance from the center of the measurement aperture, $L(\xi,\theta_r;\theta_s)$ denotes the integration path over an ellipse given by Eq. (1) with $b=\xi+R_0$, where R_0 is the distance from the center of the measurement aperture to the origin of the aperture-point-coordinate system, and *ds* denotes the appropriate integration measure. Note that $R_0 < R_m$. In this work, we will consider that the location of the receiver relative to source remains fixed. Accordingly, the measured data will be denoted simply as $g(\xi,\theta_r)$, with the dependence of the parameter θ_s suppressed. If the measurement process is repeated by simultaneously varying θ_r and θ_s, the data function $g(\xi,\theta_r)$ can be interpreted as a 2D function of ξ and θ_r. The reconstruction problem is to determine $f(r,\theta)$ from knowledge of $g(\xi,\theta_r)$ by inversion of Eq. (2).

3. HEURISTIC IDENTIFICATION OF DATA REDUNDANCIES

In our previous studies[5,6] of monostatic reflectivity tomography, we employed a "potato peeling" procedure[7] to heuristically and mathematically identify redundancies in the measured data function. In this procedure, which is conceptually a layer stripping method, each thin layer of the object function $f(r,\theta)$ is determined and subsequently peeled away to reveal the next innermost layer. By repeating this procedure, $f(r,\theta)$ could be determined completely. Based on this procedure, we demonstrated that $f(r,\theta)$ could be reconstructed from knowledge of the data function over any half of its domain. Below we extend our heuristic layer stripping approach for identifying data redundancies to the bistatic reflectivity tomography problem. A mathematical formulation of this procedure is provided in Section 4.

As stated earlier, without loss of generality we assume that $f(r,\theta)$ is compactly supported on a disk of radius R_f centered at the origin of the measurement aperture. This indicates that $f(r,\theta)\neq 0$ for $r \le R_f$ and $f(r,\theta)=0$ for $r > R_f$. According to Eq. (2), we therefore can identify a value $\xi_{\max} > 0$ such that $g(\xi_{\max},\theta_r)\neq 0$ and $g(\xi,\theta_r)=0$ for $\xi > \xi_{\max}$. Because $f(r,\theta)$ has compact support on the disk or radius R_f, it must be true that

$$\xi_{\max} = R_f . \tag{4}$$

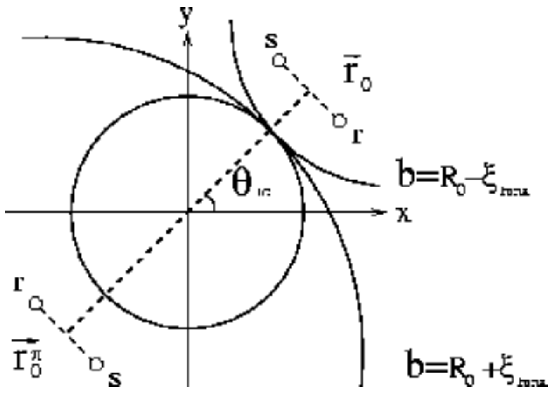

Figure 2. A schematic of the integration at the end of the object's support.

As shown in Fig. 2, the ellipse $L(\xi_{\max}, \theta_r; \theta_s)$ intersects $f(r,\theta)$ at only the single point $\left(R_f, \theta_{1/2}\right)$. If we neglect, for the moment, the fact that a point represents a set of measure zero, these observations imply that

$$g(\xi_{\max}, \theta_r) = f(R_f, \theta_{1/2}). \tag{5}$$

From Fig. 2, in a similar way we find that

$$g(-\xi_{\max}, \theta_r + \pi) = f(R_f, \theta_{1/2}). \tag{6}$$

Equations (5) and (6) indicate that the value of $f(r,\theta)$ at its outermost edge can be specified by either of the two measurements $g(\xi_{\max}, \theta_r)$ or $g(-\xi_{\max}, \theta_r + \pi)$. This observation forms the basis for a heuristic layer stripping procedure for the determination of $f(r,\theta)$. The procedure is comprised of the following steps:

1. Utilize Eq. (5) or (6) to determine the value of $f(r,\theta)$ at its outermost edge of its support.

2. Create a modified data function $g_M(\xi,\theta_r)$ by removing from $g(\xi,\theta_r)$ the contribution due to the components of $f(r,\theta)$ that were determined in Step 1. Specifically, $g_M(\xi,\theta_r)$ is given by

$$g_M(\xi,\theta_r) = \int_{L(\xi,\theta_r;\theta_s)} f_M(r,\theta)\, ds, \tag{7}$$

where $f_M(r,\theta)$ is obtained from $f(r,\theta)$ by removing its outermost edge.

3. Determine $f_M(r,\theta)$ at all points on the outermost edge of its support from knowledge of $g_M(\xi'_{\max},\theta_r)$ or $g_M(-\xi'_{\max},\theta_r+\pi)$. The new value $\xi'_{\max}$ satisfies the condition $g_M(\xi'_{\max},\theta_r)\neq 0$ and $g_M(\xi'_{\max},\theta_r)=0$ for $\xi>\xi'_{\max}$.

4. Repeat Steps 1–3 to determine the next innermost layer of $f_M(r,\theta)$.

By use of this procedure, each layer of $f(r,\theta)$ is determined and subsequently "stripped away" for the determination of the next innermost layer. A key observation is that each stage of the layer-stripping procedure, the values of $f(r,\theta)$ can be determined by either of two points in the data space. This indicates a presence of a two-fold redundancy in the data function $g(\xi,\theta_r)$. A framework for formalizing this observation mathematically is presented next.

4. MATHEMATICAL FORMULATION OF LAYER-STRIPPING PROCEDURE

4.1 Some Useful Definitions

Consider the schematic shown in Fig. 3, which shows a portion of an elliptical integration path that intersects the support of the object function. The foci $y'=\pm c$ of the ellipse coincide with the locations of the source and receiving transducers, and the definition of the aperture point coordinates

(x', y') was provided in Section 2.1. The angle γ_0 describes the angle between the x'-axis and the line that connects the origin of the aperture point system to the point of intersection of the ellipse and the support of the object function. This angle is defined as

$$\gamma_0(R_f) = \tan^{-1}\left(\frac{R_f \sin\vartheta}{R_0 - R_f \cos\vartheta}\right), \tag{8}$$

where the angle ϑ, shown in Fig. 3, is defined as

$$\cos\vartheta = \left[(b^2 + c^2)R_0 - b\sqrt{c^2(b^2 + c^2 - R_f^2) + (b^2 + c^2){R_0}^2}\right]/(c^2 R_f). \tag{9}$$

In terms of these quantities, the path-length of the elliptical segment within the object is given by

$$l = \int_{-\gamma_0(R_f)}^{\gamma_0(R_f)} d\gamma \sqrt{\rho^2 + (d\rho/d\gamma)^2}\ , \tag{10}$$

where γ is a polar angle in the aperture-point system and $\rho = \rho(\gamma)$ is a radial coordinate that describes the distance from the origin of the aperture-point system to a point on the ellipse. When the elliptical arc approaches the edge of the support of $f(r,\theta)$, i.e. when $b \to R_0 \pm R_f$, γ_0 tends to zero. In this case, it can be shown mathematically $d\rho/d\gamma \to 0$ and consequently

$$l = 2b\gamma_0(R_f). \tag{11}$$

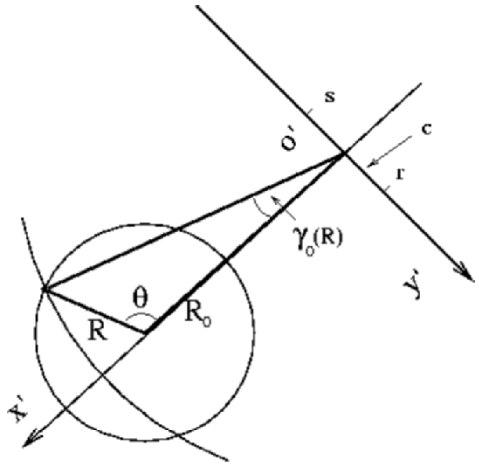

Figure 3. Geometry employed in the mathematical layer-stripping development.

Moreover, if we consider that $b = R_0 + R_f - \Delta$, where Δ is a small parameter, when $\Delta \to 0$ it can be shown that

$$l = 2\sqrt{\frac{2R_f(c^2 + R_f^2 + {R_0}^2 + 2R_f R_0)}{c^2 + {R_0}^2 + R_0 R_f}}\sqrt{\Delta} + \mathrm{O}(\Delta). \tag{12}$$

In the special case where the source and the detector coincide, $c = 0$, and the elliptical integration arc becomes circular. In this case, Eq. (12) reduces to

$$l = 2\sqrt{2R_f(R_f + R_0)/R_0}\sqrt{\Delta} + \mathrm{O}(\Delta). \tag{13}$$

4.2 Variable Data Function

To formulate mathematically the layer-stripping procedure, we will introduce a *variable data function*[5] that is defined as

$$n(R,\xi,\theta_r) = \int_{-\gamma_0(R)}^{\gamma_0(R)} d\gamma \sqrt{\rho^2 + (d\rho/d\gamma)^2}\, f_{ap}(\rho,\gamma), \tag{14}$$

where $0 \le R \le R_f$. The function $f_{ap}(\rho,\gamma)$ denotes $f(r,\theta)$ expressed in the polar coordinates of the aperture point system. Recall that the orientation angle $\theta_{1/2}$ of the aperture-point-coordinate system is specified by θ_r alone, because the source location θ_s is fixed relative to θ_r. It can be verified that

$$n(R = R_f,\xi,\theta_r) = g(\xi,\theta_r). \tag{15}$$

However, when $R < R_f$, $n(R,\xi,\theta_r)$ represents a new data function that corresponds to a version of the object function that has been masked, or multiplied, by a uniform disk of unit height and radius R. In the layer-stripping procedure, the variable data function $n(R,\xi,\theta_r)$ represents the data produced by the object at various stages of stripping. Below we derive equations that relate $n(R,\xi,\theta_r)$ to $f(r,\theta)$, thereby formulating mathematically the layer-stripping procedure.

4.3 Mathematical Formulation

Consider the variable data function when ξ is near R. For $\xi = R - \Delta$ with $\Delta \approx 0$, it is true that $\gamma_0(R) \approx 0$. In the case, by use of Eq. (12), Eq. (14) can be written as

$$n(R, R-\Delta,\theta_r) = 2\sqrt{\frac{2R(c^2 + R^2 + {R_0}^2 + 2RR_0)}{c^2 + {R_0}^2 + R_0 R}}\, f(R,\theta_{1/2}+\pi)\sqrt{\Delta} + \mathrm{O}(\Delta), \tag{16}$$

where $f(R,\theta_{1/2}+\pi) = f_{ap}(R+R_0,0)$ by the definition of the aperture point coordinate system Because $n^2(R,R,\phi) = 0$, we have the following equation for $n^2(R,\xi,\phi)$:

$$n^2(R,R,\theta_r) - n^2(R,R-\Delta,\theta_r)$$

$$= -\frac{8R(c^2 + R^2 + {R_0}^2 + 2RR_0)}{c^2 + {R_0}^2 + R_0 R} f^2(R,\theta_{1/2} + \pi)\Delta + \mathrm{O}(\Delta^{3/2}). \tag{17}$$

In the limit $\Delta \to 0$ we obtain

$$\frac{\partial n^2(R,\xi,\theta_r)}{\partial \xi}\Big|_{\xi=R} = -\frac{8R(c^2 + R^2 + {R_0}^2 + 2RR_0)}{c^2 + {R_0}^2 + R_0 R} f^2(R,\theta_{1/2} + \pi). \tag{18}$$

In a similar manner, one can show that

$$\frac{\partial n^2(R,\xi,\theta_r + \pi)}{\partial \xi}\Big|_{\xi=-R} = -\frac{8R(c^2 + R^2 + {R_0}^2 - 2RR_0)}{c^2 + {R_0}^2 - R_0 R} f^2(R,\theta_{1/2} + \pi). \tag{19}$$

Equations (18) and (19) indicate that, at each stage of the layer-stripping procedure, the variable data function at conjugate views contain redundant information. Specifically, they indicate that

$$\frac{(c^2 + R^2 + {R_0}^2 - 2RR_0)}{c^2 + {R_0}^2 - R_0 R}\left[\frac{\partial n^2(R,\xi,\theta_r)}{\partial \xi}\right]_{\xi=R}$$

$$= \frac{(c^2 + R^2 + {R_0}^2 + 2RR_0)}{c^2 + {R_0}^2 + R_0 R}\left[\frac{\partial n^2(R,\xi,\theta_r)}{\partial \xi}\right]_{\xi=-R} \tag{20}$$

Equation (20) reveals mathematically the two-fold data redundancy that was predicted by the heuristic layer-stripping procedure. This redundancy

indicates that the object function can be determined uniquely from knowledge of the data function over any half of its domain.

Equations (18) and/or (19) formulate mathematically step 1 of the heuristic layer-stripping procedure described in Section 3. In order to formalize steps 2 and 3, an equation is needed that relates $n(R,\xi,\theta_r)$ and $n(R-\Delta,\xi,\theta_r)$, where Δ is a small positive number. Although not presented, this equation can be derived in analogy to the analysis in reference 6.

5. NUMERICAL RESULTS

5.1 Simulation Studies

Computer-simulation studies were conducted to corroborate our theoretical assertions. The numerical phantom shown in Fig. 4 was taken to represent the object function $f(r,\theta)$. The radius of support of $f(r,\theta)$ was $R_f = 1$ (arbitrary units). The object was assumed to reside at the center of a circular measurement aperture of radius $R_m = 1.2$. Along the measurement aperture, source-receiver point transducers were evenly spaced in 1 degree angular intervals. When the object was insonified by use of a source at orientation θ_s, we assume that the resulting reflected signal was measured at receiver location $\theta_r = \theta_s + 10$ degrees. The data function $g(\xi,\theta_r)$ was computed by approximating Eq. (1) by use of numerical integration for each of 257 values of $\xi = b - R_0$ such that b spanned the support of the object. A collection of these measurements was performed by simulating rotating the source and receiver locations in 1 degree intervals over the circumference of the aperture. Accordingly, the discrete data function $g(\xi,\theta_r)$ was represented by a matrix of size 257×360.

Our layer-stripping analysis indicated a presence of a two-fold redundancy in the data function. To confirm this numerically, two reduced data sets were created by keeping only half of the complete data set $g(\xi,\theta_r)$. A "half-scan" data function $g_{hs}(\xi,\theta_r)$ was defined as $g_{hs}(\xi,\theta_r) = g(\xi,\theta_r)$ for $0 \le \theta_r < \pi$ and $g_{hs}(\xi,\theta_r) = 0$ otherwise. This data function corresponds to the use of a semi-circular measurement aperture. We also created a "half-time" data function $g_{ht}(\xi,\theta_r)$ that was defined as $g_{ht}(\xi,\theta_r) = g(\xi,\theta_r)$ for $\xi \le 0$ and $g_{ht}(\xi,\theta_r) = 0$ otherwise. The half-time data function assumes a complete circular aperture, but only utilizes half of data acquired at each receiver location. Noisy versions of

these data sets were produced by use of an uncorrelated Guassian noise model. The standard deviation of the noise was approximately 1% of the maximal value of the data $g(\xi,\theta_r)$. From the noiseless and noisy data sets, images were reconstructed by use of the expectation maximization (EM) algorithm. In all cases, the EM algorithm was terminated after 120 iterations. Details regarding the application of the EM algorithm to reflectivity tomography can be found in reference 5.

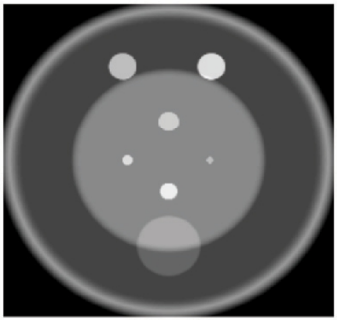

Figure 4. Numerical phantom representing the object function.

5.2 Reconstructed Images

Images reconstructed from the noiseless simulation data are displayed in Fig. 5. The images in the left, center, and right panels were reconstructed from the complete, half-time, and half-scan data functions, respectively. The images reconstructed from the complete (left panel) and half-time (center panel) appear virtually identical. This result is consistent with our claim that knowledge of the data function over only half of its domain is necessary for accurate image reconstruction. The image reconstructed from the half-scan data function (right panel) also appears very similar to the other two images. It does, however, contain some subtle artifacts in its lower half, indicating that features residing outside the convex hull of the measurement aperture may not always be reconstructed stably. This aspect of half-scan reconstruction methods in monostatic reflectivity tomography has been investigated previously[5].

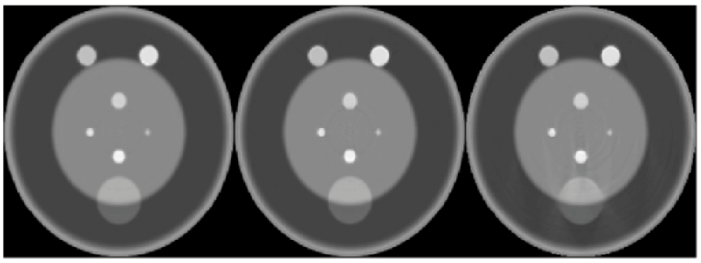

Figure 5. Images reconstructed from the complete (left), half-time (center), and half-scan (right) noiseless simulated data sets.

Images reconstructed from noisy simulation data are displayed in Fig. 6. The images in the left, center, and right panels were reconstructed from the complete, half-time, and half-scan data functions, respectively. It is found that the noise texture is distinct in the images, reflecting that different components of the noisy data are utilized when reconstructing each image. Also, as expected, the image reconstructed from the complete data function has a reduced noise level as compared to the images reconstructed from the half-scan and half-time data functions. This can be attributed to the fact that statistically complementary information is contained in the complete data function.

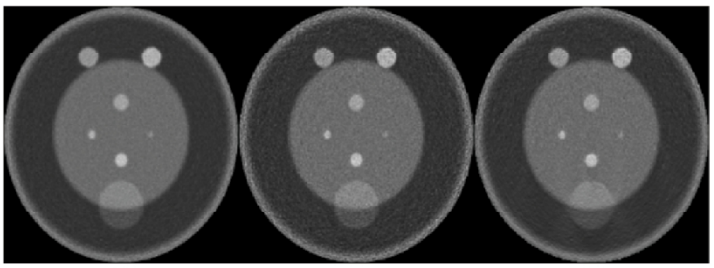

Figure 6. Images reconstructed from the complete (left), half-time (center), and half-scan (right) noisy simulated data sets.

6. SUMMARY

In this work, we have investigated the existence and utilization of data redundancies in reflectivity tomography employing offset source and receiver transducers, which we refer to as bistatic reflectivity tomography. A layer stripping procedure was described heuristically and mathematically, which revealed that a two-fold redundancy exists in a complete data set. This indicates that knowledge of the measured data function over any half of its domain is, in principle, sufficient for image reconstruction. Computer simulation studies were presented that demonstrated the numerical feasibility of half-data image reconstruction.

REFERENCES

1. S. Norton, Reconstruction of a two-dimensional reflecting medium over a circular domain: Exact solution, Journal of the Acoustical Society of America, 67, 1266–1273, 1980.
2. S. Norton and M. Linzer, Ultrasonic reflectivity imaging in three dimensions: Exact inverse scattering solutions for plane, cylindrical, and spherical apertures, IEEE Transactions on Biomedical Engineering, 28, 202–220, 1981.
3. N. Duric, et al., Ultrasound tomography of breast tissue, Proc. SPIE (Medical Imaging Conf.) 5035, 24–32, 2003.
4. D. Finch, S. Patch and Rakesh, Determining a function from its mean values over a family of spheres, SIAM J. Math. Anal., 35, 1213–1240, 2004.
5. X. Pan, Y. Zou and M.A. Anastasio, Data redundancy and reduced-scan reconstruction in reflectivity tomography, IEEE Transactions on Image Processing, 12, 784–795, 2003.
6. M.A. Anastasio, J. Zhang, E.Y. Sidky, Y. Zou, D. Xia and X. Pan, Feasibility of half-data image reconstruction in 3-D reflectivity tomography with a spherical aperture, IEEE Transactions on Medical Imaging, 24, 1100–1112, 2005.
7. E. Y. Sidky and X. Pan, Variable sinograms and redundant information in SPECT with nonuniform attenuation, Inverse Problems, 18, 1483–1497, 2002.
8. Y. Vardi and D. Lee, From image deblurring to optimal investiments: Maximum likelihood solutions for positive linear inverse problems, J. Roy. Statist. Soc. B., 55, 569–612, 1993.

BIOLOGICAL AND MEDICAL APPLICATIONS

EXPERIMENTAL VALIDATION OF THE SPECTRAL FIT ALGORITHM USING TISSUE MIMICKING PHANTOMS

T.A. Bigelow, W.D. O'Brien, Jr.
Bioacoustics Research Laboratory, Department of Electrical and Computer Engineering, University of Illinois, 405 North Mathews, Urbana, Illinois 61801 USA

Abstract: Characterizing tissue by measuring its physical properties has potential for improving the diagnostic capabilities of medical ultrasound. One parameter that is estimated using the power spectrum of backscattered ultrasound echoes is the characteristic size or correlation length of the tissue microstructure responsible for the scattering. Unfortunately, the characteristic size measurement has traditionally been corrupted by uncertainties in the frequency-dependent attenuation along the propagation path. Recently, this problem was addressed by estimating the characteristic size and attenuation along the propagation path simultaneously using an algorithm termed the Spectral Fit (SF) algorithm. Using computer simulations to study the SF algorithm, the accuracy and precision of the attenuation estimate improved as the frequency range (largest frequency minus smallest frequency used by the algorithm when obtaining estimates) was increased. Similarly, the accuracy and precision of the scatterer size estimates were improved as the Δka_{eff} (largest wavenumber times scatterer radius minus smallest wavenumber times scatterer radius used by the algorithm) was increased. In this study, the simulation results were validated using a tissue mimicking phantom. The phantom had an attenuation of 0.83 dB/cm-MHz with glass beads with a radius range between 22.5 and 26.5 μm at a concentration of 47.7/mm^3. The SF algorithm accurately estimated the size of the glass beads and the precision of the size and attenuation estimates improved with increasing Δka_{eff} and frequency range respectively in the same manner as was observed in the simulation studies

Key words: Effective scatterer radius, Attenuation estimation, Frequency range

M.P. André (ed.), Acoustical Imaging, 249–256.

1. INTRODUCTION

In the past, many different investigators have worked at extending the diagnostic capabilities of medical ultrasound by providing quantitative measures of tissue properties based on an analysis of the backscattered RF waveforms. One tissue property that has shown diagnostic potential is the effective radius, a_{eff}, of the tissue microstructure (Lizzi et al. 1983; Lizzi et al. 1986; Insana et al. 1990). Oelze et al. (2004) showed that the tissue microstructure could distinguish between fibroadenomas and carcinomas. Likewise, Tateishi et al. (1998) demonstrated that the tissue microstructure could be used to diagnose axillary lymph node metastases in breast cancer, and Feleppa et al. (1996; 1997) used tissue microstructure to identify cancer in the prostate. As well as these examples involving tumors, Insana et al. (1995) used the properties of the tissue microstructure obtained from backscattered ultrasound signals to measure the structural properties of the kidney.

Despite these successes, determining a_{eff} on a clinical basis has had only limited success due to the patient specific frequency-dependent attenuation along the propagation path, $\sim\alpha f$ where f is frequency and α is the attenuation coefficient, masking the frequency dependence of a_{eff} in the backscattered RF waveforms. The earlier successes were obtained when α could be measured or reasonably estimated *a priori*. Recently, we proposed a new algorithm, termed the Spectral Fit (SF) algorithm, that would overcome this shortcoming by estimating a_{eff} and α simultaneously (Bigelow and O'Brien, submitted). Using computer simulations, we demonstrated that the accuracy and precision of the a_{eff} estimate improved as the $\Delta k a_{eff}$ (largest wavenumber, k, minus the smallest wavenumber multiplied by a_{eff}) used to obtain the estimate was increased. Similarly, the accuracy and precision of the α estimate improved as the frequency range (largest frequency minus the smallest frequency) used to obtain the estimate was increased.

In this work, we wanted to verify our simulation results by using the SF algorithm to analyze the backscattered RF waveforms from a glass bead tissue-mimicking phantom. In addition, we wanted to explore the impact the initial frequency/initial ka_{eff} value used to obtain the estimates had on the accuracy and precision of the SF algorithm also using the waveforms from the glass bead phantom.

2. REVIEW OF SF ALGORTIHM

Before proceeding with the discussion, the SF algorithm will be reviewed. Assuming weakly focused sources and small window lengths, the

expected backscattered voltage spectrum returned from a tissue region containing weak scatterers satisfying the Born approximation is given by (Bigelow and O'Brien, submitted)

$$E\left[\left|V_{scat}(f)\right|^2\right] \propto k^4 \left|V_{plane}(f)\right|^2 e^{-4\alpha f z_T} F_\gamma\left(ka_{eff}\right) \tag{1}$$

where $V_{plane}(f)$ is the voltage spectrum returned from a reference plane placed at the focal plane, z_T is the distance from the region of interest (ROI) to the aperture plane of the transducer, and $F_\gamma\left(ka_{eff}\right)$ is the form factor that depends on the scatterer geometry. The geometry of the scatterer must be known before an accurate estimate of a_{eff} can be obtained.

The SF algorithm solves for a_{eff} and α, by finding the values that minimize

$$ASD = \underset{f}{\text{mean}}\left[\left(X\left(f, a_{eff}, \alpha\right) - \bar{X}\left(a_{eff}, \alpha\right)\right)^2\right] \tag{2}$$

where

$$X\left(f, a_{eff}, \alpha\right) = \ln\left(E\left[\left|V_{scat}(f)\right|^2\right]\right) - \ln\left(k^4 \left|V_{plane}(f)\right|^2 e^{-4\alpha f z_T} F_\gamma\left(ka_{eff}\right)\right)$$
$$\bar{X}\left(a_{eff}, \alpha\right) = \underset{f}{\text{mean}}\left[X\left(f, a_{eff}, \alpha\right)\right]. \tag{3}$$

In the algorithm, an $E\left[\left|V_{scat}(f)\right|^2\right]$ is obtained by

$$E\left[\left|V_{scat}(f)\right|^2\right] \cong \frac{1}{N}\sum_{i=1}^{N}\left(\left|V_i(f)\right|^2\right) \tag{4}$$

where N was 25 in our initial evaluation of the algorithm. Subtracting by the modified $\left|V_{plane}(f)\right|^2$ term in X removes the system dependence of the backscattered power spectra. Also, subtracting by $\bar{X}$ removes the effects of any multiplicative constants allowing estimation of a_{eff} and α independent of the acoustic concentration (Insana et al., 1990).

3. SIMULATION AND EXPERIMENTAL SETUP

The simulations (Bigelow and O'Brien, submitted) used a spherically focused source with an f-number of 4 and a focal length of 5 cm. The voltage spectrum returned from a plane placed at the focal plane for the simulated source was given by

$$\left|V_{plane}(f)\right| \propto |f|^2 \exp\left(-2\left(\frac{f-f_o}{\sigma_o}\right)^2\right) \tag{5}$$

where f_o was 8 MHz and σ_o was varied as 2, 4, and 6 MHz to change the bandwidth of the source. The source exposed an infinite homogeneous half-space where the attenuation of the half-space was varied from 0 to 1 dB/cm-MHz to test the impact of attenuation. The half-space contained Gaussian scatterers, $F_\gamma\left(ka_{eff}\right) = \exp\left(-0.827\left(ka_{eff}\right)^2\right)$, of the same size at a density of 35/mm^3 where a_{eff} varied from 5 to 150 μm to test the impact of scatterer size. For each attenuation, scatterer size, and source bandwidth, the simulations generated and analyzed 1000 waveforms whose power spectrum were averaged in sets of 25 when determining $E\left[\left|V_{scat}(f)\right|^2\right]$ for a total of 40 estimates of a_{eff} and α per case. Also, prior to the analysis, the waveforms were time gated with a Hamming window corresponding to 3 mm about the focus.

The phantom experiment also used a spherically focused source with an f-number of 4 and a focal length of 5.35 cm. The focus of the transducer was positioned 2 cm into the phantom. The transducer used in the experiment had a center frequency of 9.4 MHz and a -3 dB bandwidth of 3.8 MHz as measured from the reflection off of a wire placed at the focus, and a f_o value of 6.9 MHz and a σ_o value of 9.0 MHz as described by Eqn. (5) when measured from the reflection off of a plane placed at the focal plane. The phantom had an attenuation of 0.83 dB/cm-MHz and contained glass beads, $F_\gamma\left(ka_{eff}\right) \cong \left[\sin\left(2ka_{eff}\right)/\left(2ka_{eff}\right)\right]^2$, with radii between 22.5–26.5 μm at a density of 47.7/mm^3. 350 waveforms were acquired from the phantom and time gated with a Hamming window corresponding to 3 mm about the focus. In the phantom experiment, the initial and final ka_{eff} values used by the SF algorithm were manually selected. Once again, the waveforms were averaged in sets of 25 to obtain 14 estimates of for each set of ka_{eff} values used by the SF algorithm.

4. RESULTS

4.1 Results for Initial ka_{eff} and Initial Frequency

The first analysis performed on the phantom data was to vary the initial ka_{eff} value used by the SF algorithm while maintaining a constant Δka_{eff} of 0.5. The results for this analysis are shown in Figure 1(a)–1(d). The error in the *aeff* estimate for the phantom experiment is based on a size of 24.5 μm, the median size for the glass beads.

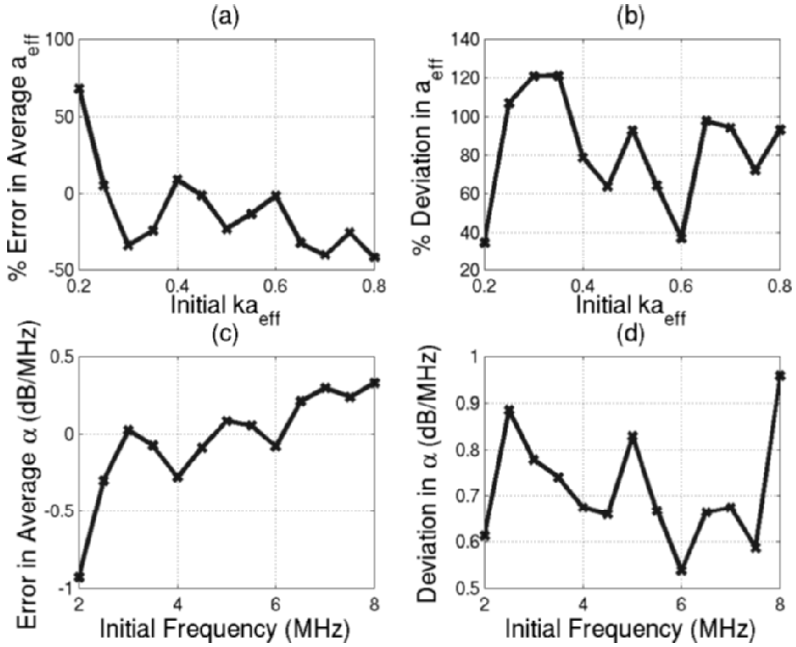

Figure 1. Phantom estimation results for different initial ka_{eff} for a Δka_{eff}=0.5. (a) Accuracy of a_{eff} estimate, (b) precision of a_{eff} estimate, (c) accuracy of α estimate, and (d) precision of α estimate.

The accuracy of the a_{eff} and α estimates improves significantly as the initial ka_{eff} is increased from 0.2 to 0.3. After an initial ka_{eff} of 0.3, the accuracy of the estimates exhibits only a weak dependence on initial ka_{eff}. The improvement at low initial ka_{eff} is probably due to the weak frequency dependence of $F_\gamma(ka_{eff})$ at low values of ka_{eff}.

4.2 Results for Δka_{eff} and Frequency Range

After exploring the importance of the initial ka_{eff} value used by the SF algorithm, the significant impact of Δka_{eff} and frequency range as observed in the earlier simulation study was verified using the phantom waveforms. This time the initial ka_{eff} was maintained at 0.3 while Δka_{eff} was varied from 0.2 to 1. The results from the phantom experiment are shown with a summary of the results from the earlier simulation study in Figure 2(a)–2(d).

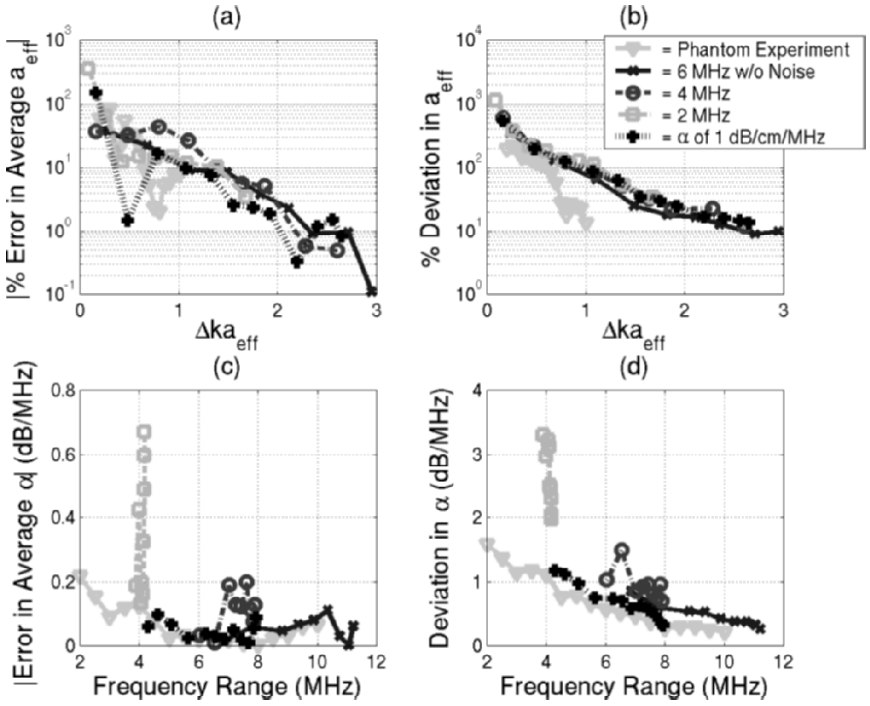

Figure 2. Results for different Δka_{eff} and frequency ranges from Phantom experiment ( ) and simulations, σ_o of 6 MHz and α of 0 dB/cm-MHz ( ), σ_o of 4 MHz and α of 0 dB/cm-MHz ( ), σ_o of 2 MHz and α of 0 dB/cm-MHz ( ), σ_o of 6 MHz and α of 1 dB/cm-MHz ( ). (a) Accuracy of a_{eff} estimate, (b) precision of a_{eff} estimate, (c) accuracy of α estimate, and (d) precision of α estimate.

In both the simulation study and the phantom experiment there is improvement in the accuracy (Figure 2(a)) and precision (Figure 2(b)) of the a_{eff} estimate with increasing Δka_{eff}, and improvement in the precision of the α estimate (Figure 2(d)) with increasing frequency range. However, the phantom

results tend to be slightly more precise than the simulation results for the same Δka_{eff} and frequency range.

5. CONCLUSIONS

The SF algorithm can estimate both a_{eff} and α simultaneously as was demonstrated by phantom experiments and computer simulations. Also, the accuracy of the SF algorithm exhibits only weak dependence on the initial ka_{eff} value for initial $ka_{eff} > 0.3$ as was illustrated by the phantom experiment. However, the accuracy and precision of the of the a_{eff} estimate drastically improves with increasing Δka_{eff} while the precision of the attenuation estimate drastically improves with increasing frequency range. The estimates obtained with the glass bead phantom exhibit the same trends observed in the Gaussian scatterer simulations but with improved precision. The improved precision is probably due to the stronger ka_{eff} dependence of the form factor for the glass beads as compared to the form factor for Gaussian scatterers as is illustrated by the ka_{eff} dependence for both form factors shown in Figure 3.

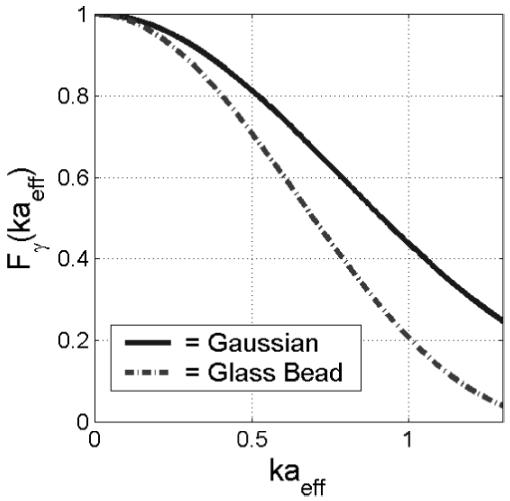

Figure 3. ka_{eff} dependence of the form factor for the glass bead and Gaussian scatterer.

REFERENCES

1. Bigelow, T.A., and O'Brien, W.D. Jr., submitted, Evaluation of the Spectral Fit algorithm as functions of frequency range and Δka_{eff}, *IEEE Trans. Ultrason. Ferroelect. Freq. Contr.*
2. Feleppa, E.J., Kalisz, A., Sokil-Melgar, J.B., Lizzi, F.L., Liu, T., Rosado, A., Shao, M.C., Fair, W.R., Wang, Y., Cookson, M.S., Reuter, V.E., and Heston, W.D.W., 1996, Typing of prostate tissue by ultrasonic spectrum analysis, *IEEE Trans. Ultrason. Ferroelect. Freq. Contr.* **43:** 609–619.
3. Feleppa, E.J., Liu, T., Kalisz, A., Shao, M.C., Fleshner, N., Reuter, V., and Fair, W.R., 1997, Ultrasounic spectral-parameter imaging of the prostate, *Int. J. Imaging Syst. Technol.*, **8:** 11–25.
4. Insana, M.F., Wagner, R.F., Brown, D.G., and Hall, T.J., 1990, Describing small-scale structure in random media using pulse-echo ultrasound, *J. Acoust. Soc. Am.* **87:** 179–192.
5. Insana, M.F., Wood, J.G., Hall, T.J., Cox, G.G., and Harrison, L.A., 1995, Effects of endothelin-1 on renal microvasculature measured using quantitative ultrasound, *Ultrasound in Med. & Biol.* **21:** 1143–1151.
6. Lizzi, F.L., Greenebaum, M., Feleppa, E.J., and Elbaum, M., 1983, Theoretical framework for spectrum analysis in ultrasonic tissue characterization, *J. Acoust. Soc. Am*. **73:** 1366–1373.
7. Lizzi, F.L., Ostromogilsky, M., Feleppa, E.J., Rorke, M.C., and Yaremko, M.M., 1986, Relationship of ultrasonic spectral parameters to features of tissue microstructure, *IEEE Trans. Ultrason. Ferroelectr. Freq. Control.* **33:** 319–329.
8. Oelze, M.L., O'Brien, W.D. Jr., Blue, J.P., and Zachary, J.F., 2004, Differentiation and characterization of rat mammary fibroadenomas and 4T1 mouse carcinomas using quantitative ultrasound imaging, *IEEE Trans. Med. Imaging.* **23:** 764–771.
9. Tateishi, T., Machi, J., Feleppa, E.J., Oishi, R., Jucha, J., Yanagihara, E., McCarthy, L.J., Noritomi, T., and Shirouzu, K., 1998, In vitro diagnosis of axillary lymph node metastases in breast cancer by spectrum analysis of radio frequency echo signals, *Ultrasound in Med. & Biol.* **24:** 1151–1159.

ACOUSTICAL IMAGING OF INDIVIDUAL MICROBUBBLES

F. Guidi, H.J. Vos, F. Nicchi, E. Boni, P. Tortoli
Electronics & Telecommunications Department, University of Florence, via Santa Marta 3 50139 Firenze, Italy

Abstract: This paper describes an acoustical approach for imaging the behavior of individual microbubbles in ultrasound fields. The experimental set-up includes a tank where small concentrations of encapsulated microbubbles are suspended in distilled water. When insonified by a programmable transmitter (TX), each microbubble is pushed away by the US radiation force to an extent which depends on its size and composition as well as on the TX parameters. For each transmitted ultrasound burst, the RF echo-signals backscattered by microbubbles over the ROI are processed in a high-speed digital board. The acquired data is used to produce two real-time displays. Tests performed in different experimental conditions clearly show bubbles accelerating in the focal region and moving slower elsewhere. It is seen in particular that all velocities measured for a full population of microbubbles are lower than- or equal to- the maximum velocities predicted for resonating bubbles. Finally, the destruction of a bubble is identified by a sudden interruption of the corresponding trace in the M-mode display. By controlling the TX parameters and monitoring the bubble movements, information about their dimension and elastic features can be obtained

Key words: Real-time processing; Doppler imaging; Contrast agents; Microbubbles; Radiation force

1. INTRODUCTION

Different phenomena may be involved when ultrasound (US) contrast agents (microbubbles encapsulated by a shell) are hit by acoustic waves [1]. Depending on the insonifying pressure, they can linearly or non linearly

M.P. André (ed.), Acoustical Imaging, 257–265.

oscillate, move along the US propagation direction, coalesce, fragment or be destroyed.

The behavior of contrast agents during insonation is typically observed through optical methods making use of high-speed cameras [2, 3]. Such an approach requires that the observation area be limited to a very small region (1 or 2 order of magnitudes larger than the microbubble diameter). Hence, the microbubbles must be fixed in a gel, immobilized on Petri dishes [4] or, when suspended in a fluid, they can move only along short paths in small transparent tubes.

In this paper, an acoustical approach is described, and shown capable of displaying in real time the response to insonation of individual bubbles which can freely move in a fluid. The experimental set-up includes a programmable US transmitter-receiver (TX-RX), coupled to a single element transducer immersed in a water tank, where small concentrations of microbubbles are suspended. For each transmitted US burst, the RF echo signals backscattered by microbubbles over a deep region of interest (ROI) are sampled by a special digital processing board. The acquired data is used to produce in real time two simultaneous displays showing the instantaneous backscattered intensity, position and velocity for each bubble of a given population.

When insonified, each microbubble is seen to be pushed away by the US radiation force to an extent which depends on its size and composition as well as on the TX parameters. A sophisticated simulation model is demonstrated capable of accurately predicting such behavior. It is shown, in particular, that all velocities measured for a population of microbubbles are lower than- or equal to the peak velocities predicted for resonating bubbles.

The possibility of indirectly estimating the bubble diameter through the comparison of measured and simulated bubble displacements is also discussed. Finally, the acoustical method described in this paper is shown suitable to detect the phenomenon of bubble destruction due to high insonation pressures.

2. METHODS

2.1 Experimental Set-Up

In order to study the effects of US on contrast agent micro-spheres, the experimental set-up shown in Figure 1 has been developed. Here, small concentrations (typically 10 μg/liter) of microbubbles are suspended in distilled water and insonified by a single element US transducer. The latter is controlled by an electronic board containing the following building blocks:

- A wideband pulsed-wave front-end, capable of performing standard TX/RX functions. The TX section excites the transducer with bursts whose amplitude, shape, frequency, phase, length and PRF can be arbitrarily fixed. In the RX section, the RF echo-signal backscattered by microbubbles are pre-amplified and digitally converted at 14-bit resolution and 64 MHz rate.

- A real-time acquisition and processing section. For each transmitted burst, 2048 signal samples are taken from the ROI. The board can process the acquired data in real-time through a high speed Digital Signal Processor (TMS320C6713 Texas Instruments, Dallas, Texas) and a high density FPGA device (Stratix I, Altera, San Jose, CA). Both the raw data (temporarily stored in 64 Mbyte of on-board SDRAM) and the processed data can be transferred to the host personal computer via a USB 2.0 interface.

A software program controls the electronic board and the pc user-interface producing two real-time displays. The first is a classic M-mode display in which distinct traces show the backscattered amplitude and position of individual bubbles as a function of time. The second is a multigate Doppler display, which shows the instantaneous backscattered intensity, depth and velocity of each bubble within the ROI.

The system is completed with a single element US probe. Different transducers in the 2–10 MHz range have been used. In all cases the level of transmitted acoustical signals was measured using a calibrated capsule "golden lipstick" hydrophone (Onda Corp., Sunnyvale, CA). Pressure measurements have an uncertainty of about 13 %.

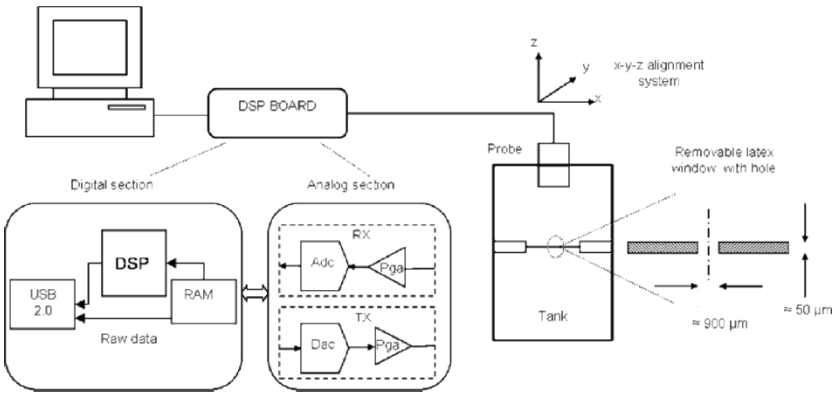

Figure 1. Experimental setup.

The achievable signal-to-noise ratio has been evaluated by comparing the echoes obtained with and without bubbles suspended in the water tank. For a 1 MHz system bandwidth, an RMS noise level of about 3.5 µV and bubble echo-signal on the order of 1 mV have been obtained.

It is possible to transversely insert an US-transparent sheet with a small hole in correspondence of the transducer beam axis (see Figure 1). In this way, only the echoes produced by bubbles passing through the hole and experiencing the US beam peak pressure are selected.

2.2 Simulation Model

The microbubbles used in the experiments (Microsphere F-04E, Matsumoto Yusi-Seiyaku Co. Ltd., Osaka, Japan) consist of a PVC-AN copolymer shell, with a mixture of hydrocarbon gasses (C_3H_8 and C_4H_{10}) inside [5]. They can be modelled as encapsulated spherical gas bubbles in a viscous fluid. The shell is assumed to behave visco-elasticity, and the shell mass is conserved during vibration. The radial movement of this type of encapsulated bubbles is described by the Rayleigh - Plesset equation [6, 7]:

$$\rho\left(R\ddot{R}+\frac{3}{2}\dot{R}^2\right)=p_0\left(\frac{R_0}{R}\right)^{3\gamma}-\frac{4\mu\dot{R}}{R}-12G_s d_{Se}\left(\frac{R_0}{R}\right)^3\left(\frac{1}{R_0}-\frac{1}{R}\right)-12\mu_{sh}d_{Se}\left(\frac{R_0}{R}\right)^2\frac{\dot{R}}{R^2} \qquad (1)$$
$$-\left(\delta_{th}+\frac{\omega R_0}{c}\right)\omega\rho R\dot{R}-\left(p_0+p_{driv}(t)\right)$$

The terms in this expression are discussed separately.

The left hand side describes the inertial effects of the bubble surrounding liquid. R is the outer diameter of the sphere and ρ the density in the surrounding medium (998 kg/m^3). The first term on the right hand side, containing the resting radius R_0 of the bubble (1 μm to 20 μm, mean value 4.5 μm [5]), calculates the internal pressure of the gas, with γ the polytrophic exponent and V the gas volume. The value of the polytrophic exponent is calculated as shown by Hoff [7] and Medwin [6]. The second term in the equation is the viscous damping of the fluid, with μ the medium viscosity (1.0 10^{-3} Pas)[7].

The third term is the shell elasticity [7, 8], accounting for conservation of mass in the shell. The parameter G_s denotes the shear modulus of the shell material; $G_s = E/2(1+\nu)$[9], with E Young's modulus (200 MPa) and ν Poisson's ratio (0.4). The initial shell thickness d_{Se} is estimated 2.7 % of the radius. The fourth term describes the shell friction due to viscosity, incorporating the shell viscosity parameter μ_{sh} (0.25 Pas) [7, 8]. The shell parameter values are estimated from comparison between the model and population measurements, and should be considered preliminary.

The fifth term takes the thermal and reradiation damping of the bubble into account [6, 7]. The radiation damping is calculated using $\delta_{rad} = \omega R_0 / c$ [7], with ω the driving radial frequency, and c the speed of sound in the medium (1480 m/s). The final term on the right hand side contains the ambient and driving pressure, p_0 (101 kPa) and $p_{\mathrm{driv}}(t)$.

In the case of encapsulation, the surface tension σ is the sum of the inner and outer surface tensions of the shell and liquid. However, for the plastic-shelled microballoon, the influence of elasticity of the shell is much larger [9]. Hence the surface tension is absent in the equation.

2.3 Bubble Displacement

The US radiation force, due to a pressure wave acting on a volume, for objects having dimensions smaller than the wavelength, reads [10]:

$$\vec{F}_{US} = -V_b(t) \cdot \vec{\nabla} p(z,t) \tag{2}$$

with $V_b(t)$ the instantaneous volume of the bubble and the spatial derivative of the pressure. The microballoons are assumed to move and vibrate freely, thus neglecting secondary Bjerknes forces. By assuming plane progressive undamped acoustic waves, the spatial derivative of pressure can be calculated as:

$$\vec{\nabla}_z p = -\frac{1}{c}\frac{\partial p}{\partial t} \tag{3}$$

This force is counteracted by four forces [10], which we discuss next.

The bubble velocity due to buoyancy was estimated 50 μm/s for a bubble with a diameter of 10 μm and density of 200 kg/m^3 [5]. This velocity is two orders lower than the US-induced velocities, so buoyancy forces are neglected. The second is the inertia of the bubble itself, given by the product of its density, volume and acceleration. The third is the viscous drag [11]:

$$F_D = -\frac{1}{4}\pi C_D \,\mathrm{Re}\, R\mu u_b \tag{4}$$

with C_d the drag coefficient [11], μ the dynamic viscosity of the fluid (1.0 10^{-3} Pas), u_b the bubble velocity, and Re the Reynolds number, $\mathrm{Re} = 2R\rho|u_b|/\mu$.

The fourth force is the less-known added mass force. This accounts for the fact that a moving bubble pushes its surrounding liquid around, and is a function of the instantaneous bubble velocity [12, 13]:

$$\vec{F}_{am} = -\frac{1}{2}\rho\left(V_b \frac{\partial u_b}{\partial t} + u_b \frac{dV}{dt}\right) \tag{5}$$

Equating all forces, and expanding the volume change into the first order time derivative of the bubble radius, we get the final differential equation describing the bubble velocity and acceleration:

$$\rho_b V_b \frac{du_b}{dt} = V_b \frac{1}{c}\frac{dP}{dt} - \frac{1}{4} C_D \,\mathrm{Re}\, \pi\mu R u_b - \frac{3}{2}\rho V_b u_b \frac{\dot{R}}{R} - \frac{1}{2}\rho V_b \frac{du_b}{dt} \tag{6}$$

Eqs. (1) and (6) are recursively solved for the radial vibration and bubble translation with a 5th order Runga-Kutta method in Matlab (The Mathworks, Natick, MA). The driving pressure amplitude is obtained by hydrophone measurements of the US beam. As the bubbles are diplaced only during the insonation, the average velocity is calculated by the product of the displacement corresponding to each burst and the PRF.

3. RESULTS

As a qualitative approach, Figure 2 shows the basic displacement phenomenon. Each trace is produced by the echoes corresponding to an individual bubble. For example, the brightest and steepest trace indicates a bubble close to resonance, clearly moving faster away from the transducer. Furthermore, some traces interrupt abruptly, indicating the bubble rupture.

A closer observation of the latter phenomenon revealed a bubble echo disappearance within hundreds of milliseconds.

Figure 3 shows the distribution of bubble velocities estimated at each depth after averaging the recordings that covered a long time interval. Resonating bubbles that experience the maximum pressure along the beam axis have the peak velocities. Both non-resonating bubbles and resonating bubbles in lower pressure regions will achieve lower velocities. These are distributed between zero and the peak for each depth. The simulated peak velocity profile is superimposed on the display showing that around the focal region the experimental values do not exceed the peak velocity estimated for resonating bubble on the beam axis.

Figure 4 shows some bubbles in M-mode display, acquired when the latex sheet was inserted at a depth of 16.5 mm. At lower depths, multiple traces are appreciated, while few traces can be observed below the sheet. The traces that cross the sheet correspond to bubbles passing through the hole. The lines superimposed on the experimental traces demonstrate the model capability of predicting the displacements of bubbles with different diameters. In particular, two bubble diameters have been found to produce equivalent displacements, both well fitting the experimental one.

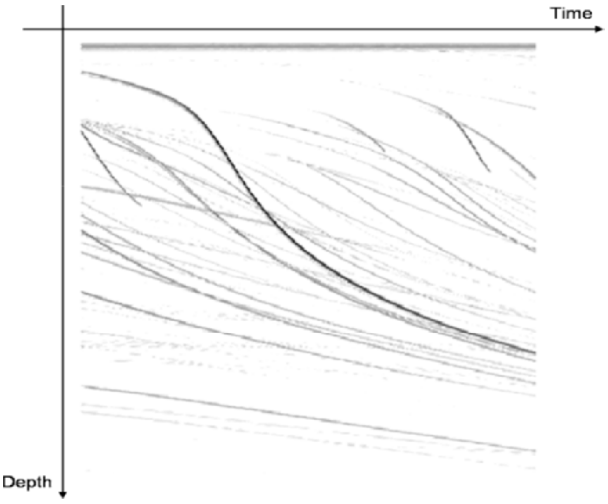

Figure 2. M-mode display of a low concentration bubble population insonified by a focussed wide-band transducer excited at 10 MHz.

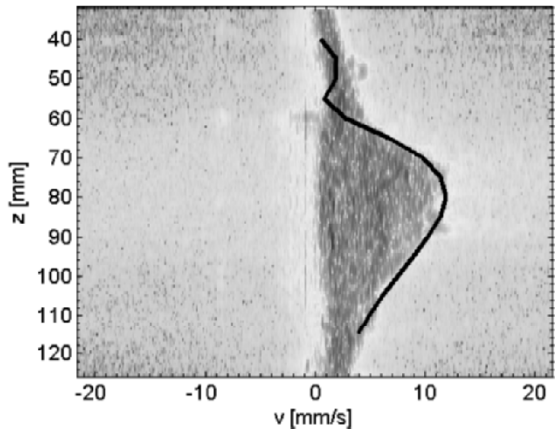

Figure 3. Experimental velocity profile and simulated peak velocities of a bubble population insonified with a 2.5 MHz transducer focussed at 80 mm.

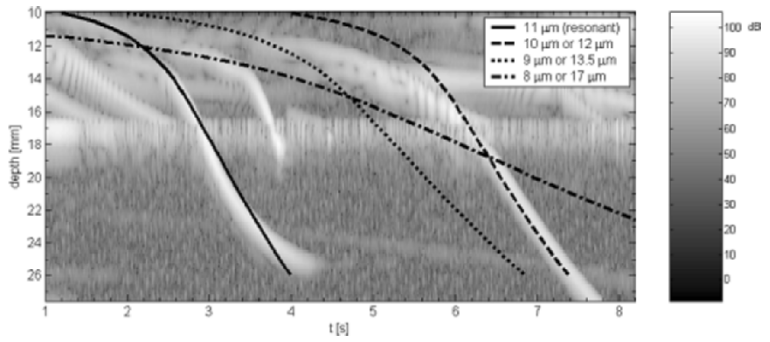

Figure 4. Measured and simulated traces in the M-mode display. The simulated traces show that the peak velocities achieved at the focus (18 mm) are between 2.5 and 9 mm/s. The transducer was excited at 4MHz producing a peak pressure of 850 kPa.

4. DISCUSSION

This paper has shown an experimental set-up capable of acoustically imaging the behavior of individual microbubbles. A simulation model has also been presented which is capable of accurately predicting the movements of microbubbles in known experimental conditions. The model has been validated through the comparison between simulated data and both

experimental displacements of individual bubbles and peak velocities of a full population.

In principle, this approach can be exploited to derive information on microbubble dimensions and elastic parameters. For example, the diameter can be estimated from the trajectory traced in the M-mode display. However, the balance of different forces acting on the bubbles produces the same displacement for a couple of them, having diameters smaller and larger than the resonant diameter, respectively. Future work will be addressed to solve this ambiguity through more sophisticated transmission strategies.

5. ACKNOWLEDGEMENT

This work was supported by the EU grant QLG1-CT-2002-01518(UMEDS Project).

REFERENCES

1. Postema, M.A.B., et al., *Ultrasound-Induced Encapsulated Microbubble Phenomena.* Ultras. Med. Biol., 2004. **30**(6): p. 827–840.
2. Chin, C.T., et al., *Brandaris 128: A 25 million frames per second digital camera with 128 highly sensitive frames.* Rev. Sci. Instr., 2003. **74**(12): p. 5026–5034.
3. Dayton, P.A., J.S. Allen, and K.W. Ferrara, *The Magnitude of radiation force on ultrasound contrast agents.* J. Acoust. Soc. Am., 2002. **112**(5): pp. 2183–2192.
4. Klibanov, A.L., et al., *Destruction of contrast agent microbubbles in the ultrasound field: the fate of the microbubble shell and the importance of the bubble gas content.* Acad. Radiol., 2002. **9**(1 (Supp.)): p. S41-S45.
5. Takeuchi, Y. *Industrial Use Thermoplastic Microballoon to mimic the contrast agents and its in-vitro behavior including released gas dynamics*. In *IEEE Ultras. symp*. 1997. pp. 1579–1582.
6. Medwin, H., *Counting Bubbles acoustically: a review.* Ultrasonics, 1977: p. 7–13.
7. Hoff, L., P.C. Sontum, and J.M. Hovem, *Oscillations of polymeric microbubbles: Effect of the encapsulating shell.* J. Acoust. Soc. Am., 2000. **107**(4): p. 2272–2280.
8. Church, C.C., *The effects of an elastic solid surface layer on the radial pulsations of gas bubbles.* J. Acoust. Soc. Am., 1995. **97**(3): p. 1510–1521.
9. De Jong, N., *Acoustic properties of ultrasound contrast agents*, in *Erasmus Medical Center*. 1993, Erasmus University Rotterdam: Rotterdam. p. 150.
10. Rensen, J., et al., *Spiraling bubbles: How acoustic and Hydrodynamic Forces Compete.* Phys. Rev. Lett., 2001. **86**(21): p. 4819–4822.
11. Tortoli, P., M. Pratesi, and V. Michelassi, *Doppler Spectra from Contrast Agents Crossing an Ultrasound Field.* IEEE Transact. Ultras., Ferroelec. Freq. Contr., 2000. **47**(3): p. 716–726.
12. Matula, T.J., *Bubble levitation and translation under single-bubble sonoluminescence conditions.* J. Acoust. Soc. Am., 2003. **114**(2): p. 775–781.
13. Magnaudet, J. and D. Legendre, *The viscous drag force on a spherical bubble with a time-dependent radius.* Phys. fluids, 1998. **10**(3): p. 550–554.

OPTIMIZATION OF A BREAST MASS CLASSIFIER FOR COMPUTER-AIDED ULTRASOUND ANALYSIS

M.P. André, M. Galperin, G. Contro, N. Omid, L. Olson
University of California, San Diego, San Diego VA Healthcare System, San Diego, California USA

Abstract: The goal of this research was to optimize performance of a Computer-Aided Diagnostic system to identify, analyze and compare breast masses based on parameters measured in the ultrasound image. We compared case-based reasoning using Relative Similarity to an Artificial Neural Network in order to implement an objective form of the ACR BIRADS scheme to describe and score breast masses. The image feature set was reduced to nine including margins, shape, echogenicity, echo texture, orientation and posterior acoustic attenuation. Both classifiers performed well with a high ROC A_Z although RS performed significantly better than the ANN in Specificity, PPV and achieved the goal of very high Specificity without a reduction in Sensitivity. Compared to a preliminary version of the RS classifier this optimized version of RS has significantly higher A_Z (0.96 vs. 0.93)

Key words: Breast cancer; computer-aided diagnosis; image processing; relative similarity; artificial neural network; ROC analysis

1. INTRODUCTION

The American College of Radiology (ACR) developed a structured Breast Imaging Reporting And Data System (BIRADS) approach to interpretation and reporting of breast ultrasound exams and is detailing a program to accredit the clinical practice of breast ultrasound[1,2]. A detailed lexicon is defined for use by radiologists to standardize descriptions of findings on breast sonography and to provide a numerical score (1–5) for the

M.P. André (ed.), Acoustical Imaging, 267–278.

level of suspicion cancer. The major goal of the efforts of these medical organizations is to improve quality of care by increasing accuracy and reducing variability of interpretation, but it has proven difficult to teach and implement the BIRADS method. Many authors have felt uncomfortable with the number of benign and malignant masses that overlap in appearance. The present status of breast ultrasound is generally acknowledged to be that if a lesion is solid or indeterminate, biopsy is to be recommended even though current definitive estimates of the False Negative (FN) rate and Positive Predictive Value (PPV) for diagnostic ultrasound are not available.

The purpose of this study was to refine and optimize aspects of our novel approach that combine Computer Aided Detection with breast ultrasound in order to reduce high variability among breast US interpreters with the goal to implement an objective form of the BIRADS scheme. If successful, in the future we hope to use this Computer-Aided Imaging System (CAIS) to: 1) significantly reduce the false-positive rate of biopsies without impacting FN, and 2) provide an improved methodology to screen younger women and women with high risk and/or dense breasts.

In previous work we showed the feasibility of our method and conducted preliminary studies with a sample of breast sonography examinations[3,4]. This work enabled us to design the optimization studies presented in this paper with sufficient statistical power to measure meaningful improvements.

2. MATERIALS AND METHODS

The specific BIRADS guidelines for differentiation of breast lesions are shown in Table 1 and the preliminary mapping of quantitative image parameters developed in our earlier study for lesion classification is shown in Table 2[5,6].

2.1 Computer-Aided Imaging System

The core technology of the software for this project was originally developed for satellite image processing and analysis. It employs a wide range of algorithms for image enhancement, segmentation and classification and provides the user with the means to easily insert a new analysis or combine processes with a macro language capability, but without the need for scripting. The components of the software may be summarized as: *Image Processing*: image in $\rightarrow$ image out; *Image Segmentation*: image in $\rightarrow$ object out; *Image Analysis*: object in $\rightarrow$ measurements out; *Image Understanding*: measurements in $\rightarrow$ high-level description or classification out. The overall steps of the process are illustrated in Figure 1. One of the goals of this study

was to compare performance of two classifiers: Relative Similarity (RS) vs. Artificial Neural Network (ANN).

Table 1.

Criteria Associated with Benign Lesions	Criteria Associated with Malignant Lesions
Spherical/ovoid/lobulated	Irregular shape
Linear margin	Poorly defined margin
Homogeneous texture	Central shadowing
Isoechoic/anechoic	Distorted architecture
Edge shadow	Calcifications
Parallel to the skin	Skin thickening
Distal enhancement	
Dilated duct/mobile	

Table 2.

Image Criteria	Sample of Associated Parameters
Spherical/ovoid vs. irregular shape	Form factor Equivalent circular diameter/Form factor Perimeter/Area Perimeter/Equivalent circular diameter Aspect ratio
Linear margin vs. poorly defined margin	Edge gradient
Homogeneous texture vs. internal echoes Isoechoic/anechoic vs. echoic Calcifications	Homogeneity (multiple texture parameters) Relief Contrast Optical density Integrated density Scatterer density, scatterer size 2^{nd}, 3^{rd}, 4^{th} moments of inertia
Edge shadowing vs. Central shadowing Distal enhancement	Density measures of a Distal ROI defined by X- and Y-Ferret coordinates
Parallel to skin vs. irregular	X-Ferret/Y-Ferret Aspect ratio Relative angle

2.1.1 Image Processing and Segmentation of the Mass

Image Segmentation is accomplished by a sequence of methods including multi-level pixel thresholding, region growing and radial gradient edge detection described elsewhere with task-specific criterion to yield the most accurate results[3–6]. Pre-processing reduces speckle, increases contrast, enhances edge gradient and reduces shading effects to facilitate segmentation of the borders of the mass as shown in Figure 2. The automatically segmented lesion border may be modified by the radiologist if needed with manual segmentation by cursor outline. The process is successful in all cases but the radiologist may choose to guide or edit more difficult masses. Additional improvement is expected in segmentation accuracy but it is our intention that the radiologist always be "in the loop" for this process.

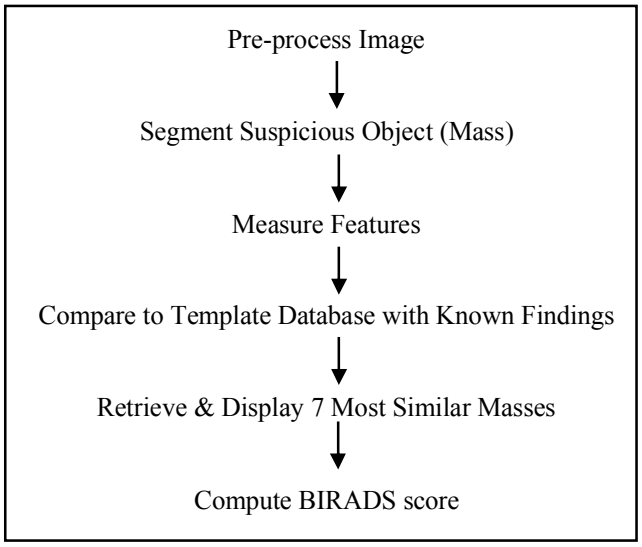

Figure 1. Overview of computer-aided image analysis.

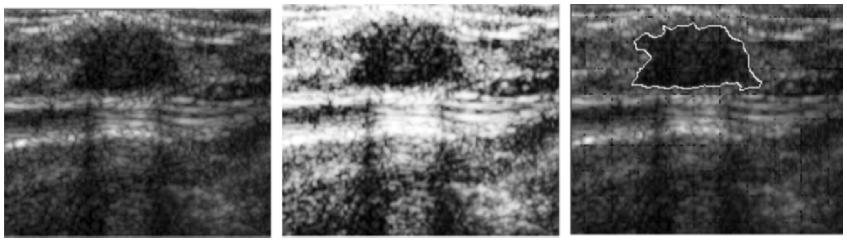

Figure 2. US original image (left) of a complex debris-filled cyst preprocessed and automatically segmented (white boundary, right). The lesion was scored BIRADS Category 2 by CAIS despite the suspicious "look."

The current software system contains a very large number of filtering, shading and image sharpening tools. Each function may be cascaded into a series of operations by the user for any specific application. These steps may be recorded and used again by applying the macro feature to provide automated image processing and segmentation methods, which was extensively tailored for breast ultrasound in this research. The system also supports import/export of convolution and other processing masks.

2.1.2 Relative Similarity CAD Classifier

The combinations of object features and others to be derived from this work, may be represented by an N-dimensional vector **P** used to calculate the "Relative Similarity," **R**, of one lesion to another,

$$\overline{R} = \left(\sum_{k=1}^{L} \left(p_k^t - P_k^t \right)^s \cdot \omega_k \right)^{1/s} \tag{1}$$

Appropriate weighting factors, ω, may be applied to these results to further enhance the classification; they are established by multi-factorial regression analysis of cases with known findings. A new case with an "unknown" finding is compared directly to the database of stored images and a measure of **R** is computed for different benign and malignant lesions. Similarity is calculated for a particular lesion $\mathbf{P}_{it}$ (the index of this "template" object) compared to the other lesions, $\mathbf{P}_k$ (k=1,…L), where L is the number of objects, s is the number of features, although other distance measures may be applied. The term Relative Similarity means that the detected lesion is compared not to a hypothetical "golden template" of the disease but to the database of previously analyzed patients and the cases most "similar" to this suspicious mass are automatically retrieved and displayed. Only the lesion portion of the stored image that is most similar to the unknown is initially retrieved, so performance is nearly instantaneous.

Figure 3 (below) illustrates this method for a complex cyst compared to a collection of different breast masses. The "un-known" mass in the upper left portion of the screen is a dark, relatively echo-free mass consistent with fluid-filled cyst but with irregular indistinct margins more consistent with a solid mass that might have a higher suspicion for cancer. The CAIS software automatically locates the mass contour. The border is confirmed by radiologist after which measurements are made of the mass. Its Relative Similarity is compared to a digital template database with known findings. Cases most "similar" to this suspicious mass are automatically retrieved and displayed in the thumbnail images on the right listed in rank order of this

value (light contours in the right half of the screenshot). In this case, all of the "similar" masses were proven to be benign.

2.1.3 Artificial Neural Network

The ANN system we implemented combines a statistical tool that first performs clustering of input variables by Euclidean distances in multi-dimensional space. The clusters are trained on output variables by the ANN performing non-linear discrimination on cluster averages. The data set used to train the neural network with and without pre-processing has previously been analyzed by other methods and published elsewhere;[7] the first was by a discriminant function with stepwise addition and removal of variables and the second was by a method using Kullback-Leiber entropy to find the optimum decision values for the predictor variables. In a related study applying this new agent system to the diagnosis of acute myocardial infarction with EKG, we demonstrated that for optimum clustering distance the number of classes is minimized with efficient training on the neural network. The software agent also performs a random partitioning of the patients' data into training and testing sets, one-time neural network training, and an accuracy estimate on the testing data set.

The ANN technique, for readers accustomed to classical statistics, can be viewed as an extension of multivariate regression analysis with such new features as non-linearity and ability to process categorical data. Categorical (not continuous) variables represent two or more levels, groups, or classes of correspondent features and this concept is used to signify patient condition, for example existence or not of acute myocardial infarction.

The ANN is an acyclic directed graph with input and output nodes corresponding respectively to input and output variables. There are also "intermediate" nodes, comprising so-called "hidden" layers. Each node n_j is assigned the value x_j that has been evaluated by the node's "processing" element, as a non-linear function of the weighted sum of values x_i of nodes n_i, connected with n_j by directed edges (n_i, n_j).

$$x_j = f(w_{i(1),j}x_{i(1)} + w_{i(2),j}x_{i(2)} + ... + w_{i(l),j}x_{i(l)}), \quad (2)$$

where x_k is the value in node n_k and $w_{k,j}$ is the "weight" of the edge (n_k, n_j). In our research we used the standard function f(x), a "sigmoid", defined as $f(x)=1/(1+\exp(-x))$. This function is suitable for categorical output, allows use of an efficient back-propagation algorithm for calculating the optimal values of weights, providing the best fit for the learning set of data and eventually the most accurate classification[8].

2.2 Database of Ultrasound Images

Under Institutional Review Board approval a pool of breast ultrasound cases were retrieved chronologically from the medical center image archive for patients examined in January 2002 to January 2003 with ultrasound masses with findings known through either biopsy or two-year follow up. The age range was 40–71 and the database consisted of: 30% simple cysts, 18% intra-cystic masses, 30% solid benign, 22% carcinoma. This distribution of findings follows very closely that of the average mixture in the U.S. reported as 36% cysts, 7% complex cysts, 34% fibroadenomas and 22% malignant[8]. Each case was reviewed by participating radiologists and 332 cases were found to be of acceptable quality for BIRADS scoring (lesion border was visible to radiologists eyes, minor contrast adjustments were acceptable during this preliminary review, minimal artifacts, etc.). We have developed this protocol with the intent that the physician is always "in the loop." The CAIS does not select an ultrasound view or determine the adequacy of image quality, the radiologist does. CAIS may be seen as a confidence-building tool and works for the radiologist on the same image data that the radiologist is willing to review. If the image is of poor quality, has extensive artifacts or if distortion of the lesion geometry is present in the image, the radiologist will reject it even before using CAIS.

3. RESULTS

The database of 332 cases was divided into two equivalent sets: a Development Set and a Test Set each with 166 cases. The Development Set was used to examine if the number of measured parameters could be reduced and it was used to compare performance of five different schemes for converting Relative Similarity to a BIRADS score. The same Development Set of 166 was used to train the ANN. The second Test Set of 166 masses was used to compare the two classifiers: CAIS with Relative Similarity vs. a feed-forward back-propagation Artificial Neural Network. The 166 cases in each Set were randomly selected from two groups, malignant and benign. This preserved our occurrence rate of 22% malignant and 78% benign in each Set. Receiver Operator Characteristic (ROC) analysis was the performance metric for validation in this study. The ROC Area (A_Z) under the curve with standard deviation was analyzed (Analyze-It®).

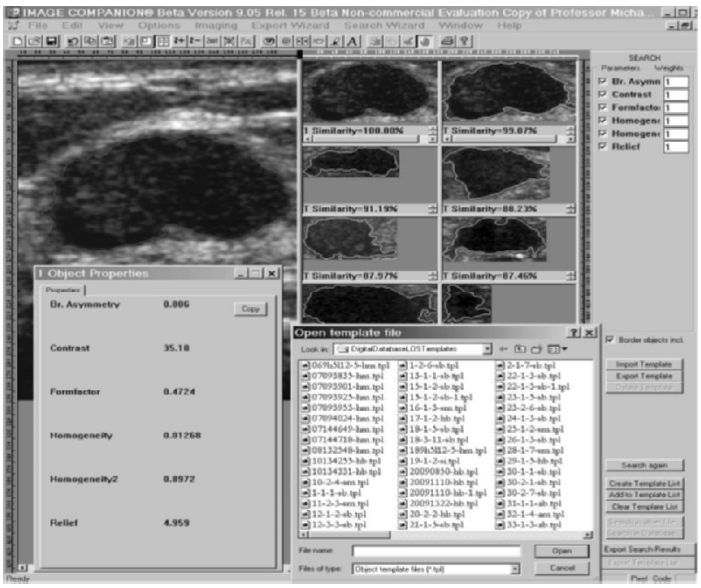

Figure 3. Intra-cystic mass (benign) is compared to other images in the template database.

3.1 Reducing Dimensionality of Measured Parameters

In a previous study an initial collection of 50 parameters were selected *ad hoc* to correspond to the BIRADS description of mass features in Table 1. We utilized more than one texture feature including: 1) those measured from the pixel histogram of a defined region of interest, considered first order statistics, 2) second order parameters that involve spatial distribution and features of co-occurrence matrices, 3) probability distributions including measures of the angular second and third moments, sum and difference entropy, sum and difference variance, correlation, contrast, etc. The most relevant from a statistical point of view were selected through objective analysis, removing parameters that were statistically co-linear and therefore redundant. This process reduced the original ad hoc set to 15 parameters. Multifactor, round-robin, leave-one-out analysis was used to reduce this set of 15 parameters to 9 numeric parameters in the categories of geometry, texture and density. Numeric parameters for each mass are computed on a relative scale and normalized; therefore there is no bias toward images with larger masses. This method of reducing dimensionality was successfully used in a variety of life science and biomedical applications[9].

The "optimized" set of features includes:

Form factor

Integrated density

Optical density

Aspect ratio

Relief

Homogeneity

Average energy/area

Second order homogeneity

Brightness asymmetry

3.2 BIRADS Scoring Methods

Five different methods to convert the Relative Similarity value to a BIRADS score were evaluated with the Development Set of 166 cases. The CAIS calculates RS for a particular image against the entire database of 332 cases with known findings and returns the seven most similar. Ground truth is known for the database so the number of benign vs. malignant images returned may be used to assign a score 1–5. The scoring methods included a "winner take all" approach and other schemes to compute a threshold average value. Although the differences in A_Z between the scoring methods were not major, best performance was found with a non-rounded average that includes a "cost for position" correction when the value (direct impact) of the score is increased or decreased on a certain percentage depending on the position of the template in the retrieved cluster of the most similar templates.

3.3 Comparison of Classifiers: RS vs. ANN

The second Test Set of 166 masses was used to compare the two classifiers: CAIS with Relative Similarity vs. a feed-forward back-propagation Artificial

Neural Network. Performance of the two classifiers was very good, although CAIS performed significantly better than the ANN in Specificity, PPV and achieved the desired goal of very high Specificity (>92%) without a reduction in Sensitivity. Statistical power was 93%. The CAIS also performs with higher accuracy than other recently published results for other CAD systems (Table 3).

Table 3. Relative Similarity vs. ANN.

	A_Z	Sensitivity	Specificity	PPV	NPV	CAD Efficiency
CAIS	0.96±0.02	87.8%	97.3%	90.3%	96.5%	95.2%
ANN	0.94±0.03	85.3%	89.2%	67.4%	95.9%	88.4%

4. CONCLUSIONS

Compared to the version of the preliminary classifier tested in our early feasibility study[1,2], this optimized version of the CAIS has statistically significantly higher A_Z (0.96 vs. 0.93), higher positive predictive value (PPV 90% vs. 83%), higher sensitivity (88% vs. 71%), with comparable specificity (97% vs. 98%), NPV (97% vs. 96%) and CAD Efficiency (95% vs. 95%). Thus our goals were achieved. Comparison the CAIS performance to that of four experienced radiologists is presented in the companion paper in this volume.

It is our premise that for clinical settings, the open "white-box" approach of RS may be preferred to the close "black box" of an ANN. With RS the reasons for every classification are apparent to the radiologist—the value of each measured parameter may be displayed--as opposed to the closed ANN that may also suffer from over- and under-training effects.

It is important to emphasize that the set of 9 features used in our Relative Similarity classifier are all relative and dimensionless. In a companion study it appears that this fact, in part, helps to make RS calculation less sensitive to machine-dependent effects. Nonetheless, a more extensive study is planned in the future, both in phantoms and in volunteer women with known masses.

Our collaborative radiologists have identified several possible advantages of the CAIS we are currently developing in the context of diagnostic decision-making. These include: 1) CAIS takes advantage of large fund of clinical knowledge with a rule-base method for interpretation; 2) CAIS uses a "white box" classifier to clearly show reason for classification; 3) CAIS may be better acceptance by radiologists than an ANN; 4) nearly instantaneous classification; 5) nearly instantaneous retrieval of similar cases; 6) the knowledge base (Template Database) may be updated with new

cases; 7) there is no need to retrain system as the database grows; 8) it is not prone to under- or over-training; 9) additional Expert Templates (reference works or atlases) may be incorporated in the clinical tool; 10) the CAIS has a built-in teaching database; finally and possibly most importantly CAIS is directly upgradeable to include additional risk factors such as BIRADS mammogram findings, mammogram CAD output, patient history, MRI results, etc.

In addition to the study of ultrasound machine-dependence of CAIS, the following factors are being examined: 1) determine the impact of the use of CAIS on decision-making by radiologists; 2) incorporate the output from x-ray mammogram CAD; 3) refine user interface; 4) incorporate CAIS in a standard PACS workstation; 5) utilize CAIS to train less experienced radiologists and sonographers on the BIRADS protocol; 6) utilize "objective observer" aspect of CAIS to measure ultrasound scanner quality control.

5. ACKNOWLEGEMENTS

This research was supported in part by the Gustavus and Louise Pfeiffer Research Foundation and the NIH/NCI STTR Program.

REFERENCES

1. Stavros AT, Thickman D, Rapp CL, Dennis MA, et al., "Solid Breast Nodules: Use of Sonography to Distinguish between Benign and Malignant Lesions," Radiology 196, pp. 123–134, 1995.
2. American College of Radiology: ACR Standards 2000–2001. Reston, VA: American College of Radiology, 2000.
3. André MP, Galperin M, Olson LK, et al, "Preliminary investigation of a method to assess breast ultrasound level of suspicion," SPIE Medical Imaging 4322:507–512, 2001.
4. André MP, Galperin M, Olson LK, et al.: "Improving the accuracy of diagnostic breast ultrasound," Acoustical Imaging 26:453–460, 2002.
5. Andre MP, Galperin M, Phan P, Chiu P, "ROC analysis of lesion descriptors in breast ultrasound images," SPIE Medical Imaging 5034, 2003.
6. André MP, Galperin M, Green CT, Olson L: "A Case-Based Reasoning System to Aid Interpretation of Breast Ultrasound Images", SPIE Medical Imaging 5749, 2003.
7. Mackay, DJC. (1992): A practical Bayesian framework for back-propagation networks. *Neural Computation*, 4(3), 448–472.
8. Mhitaryan V, Mayzlin I, Troshin L: "Determining the optimal decisions points for the parameters of the classified objects," Methods of Computational Mathematics and its Application, Institute of Economics and Statistics, Moscow, 1985.
9. Kupinski MA, Giger ML, "Feature selection with limited dataset," Med. Phys. 26(10), pp. 2176–2182, 1999.

EX VIVO BREAST TISSUE IMAGING AND CHARACTERIZATION USING ACOUSTIC MICROSCOPY

I. Bruno, R.E. Kumon, B. Heartwell, E. Maeva, R.Gr. Maev
Centre for Imaging Research and Advanced Materials Characterization, Department of Physics, University of Windsor, 401 Sunset Ave., Windsor, Ontario N9B 3P4, Canada; _Hôtel-Dieu Grace Hospital, 1030 Ouellette Ave., Windsor, Ontario N9A 1E1, Canada

Abstract: As part of a pilot project, roughly-cut slices of ductal carcinoma from human mastectomies were imaged using acoustic microscopy in the range 15 to 50 MHz. C-scan images of the 2 to 5 mm thick specimens were shown to correlate well with corresponding optical images and showed higher contrast. By selective gating, internal structures could be highlighted in C-scan images that were not visible from the surfaces of the slice. Velocity and attenuation image maps of the sample were also made and then used to try to identify the tumor regions based quantitative criteria. Our results suggest that acoustic microscopy shows promise as an adjunctive method for pathologists to rapidly measure tumor size and resection margin status during intraoperative consultation and provide more complete specimen assessment during gross examination

Key words: acoustic microscopy; breast cancer; ductal carcinoma; tissue characterization

1. INTRODUCTION

At the time of surgery, surgeons sometimes have difficulty determining if they have achieved an adequate margin of normal tissue around an excised tumor. Currently, it often takes a day or more for pathologists to determine margin status via the creation of permanent sections and examination of these sections by optical microscopy. Frozen sections may be rapidly attained, but can exhibit undesirable image artifacts and are contraindicated for small lesions and some pathologies. Hence a method to accurately and rapidly determine margin status on arbitrary unfixed tissue at the time of

M.P. André (ed.), Acoustical Imaging, 279–287.

surgery would reduce re-operative rates, patient anxiety, and local recurrence rates and free up limited resources.

Acoustic microscopy has the potential to provide pathologists an adjunctive method to allow determination of tumor dimensions and the width of resection margins on gross specimens at the time of initial surgery and during subsequent gross examination. It can be performed without any special sample preparation on both unfixed and fixed tissue and yet still achieve high contrast imaging. Without the need for dehydration and paraffin-embedding, acoustic microscopy is able to provide images of tissue closer to its native state, while still achieving sub-millimeter to micron-scale resolution. Finally, it can detect sub-surface features throughout the volume of optically opaque tissue even when the specimen has macroscopically large dimensions (mm or cm) and thus provide more thorough specimen sampling than thin sampling of permanent sections will allow.

Among breast cancers, ductal carcinoma is the most common type. Its characteristics relevant to ultrasound include a solid core, indurations, comedo necrosis, above-normal density and collagen content, and sometimes clustered micro-calcifications[1]. These parameters influence ultrasound reflection and propagation, resulting in visualization of tumor boundaries with diagnostic ultrasound[2]. Early studies using 600 MHz transmission acoustic microscopy demonstrated normal and diseased tissue could be distinguished[3]. Studies have also been performed to measure the velocity[4–8], attenuation[5–10], and backscatter coefficient[5,6,8,11–13] of normal, benign, and malignant breast tissue both *in vivo* and *ex vivo*, although all of these measurements were done in the diagnostic ultrasound frequency range (1 to 13 MHz). Foster et al.[5,6] used a scanning acoustic microscope at 3 to 7 MHz and 13 MHz to produce images and make quantitative measurements of thick breast tissue specimens. While they found that malignant tissue could be distinguished from other tissue based on ultrasound measurements, their results also suggest that the distinction could be enhanced at higher frequencies, particularly with respect to attenuation and backscatter. In light of the literature discussed above, we anticipated noticeable differences between cancerous and healthy tissue in images obtained with an acoustic microscope at frequencies of 15 MHz and above. This work extends our group's recent research on acoustical characterization of skeletal and dental tissue[14,15] into the soft tissue domain[16,17].

2. EXPERIMENT AND THEORY

Specimens of human breast tissue were investigated using acoustic microscopy in the frequency range 15 to 50 MHz. Imaging was performed in

reflection mode using Sonix HS-1000 and Tessonics AM1103 scanning acoustic microscopes. The hardware and software for the latter device were custom-designed at our center. Roughly-cut samples from a mastectomy were examined, each of which was approximately 2 x 2 cm in size and 2 to 5 mm thick. The specimens were fixed in formalin and never frozen. All samples were immersed in degassed water at room temperature during imaging. A plastic plate was secured on top of the sample to minimize scattering due to surface topography, and a glass plate was used in some cases as a substrate to increase the amount of reflected signal. The transducer was raster-scanned over the specimen and the resulting A-scan data was recorded at every point. B-scan and C-scan images could then be constructed by assigning grayscale values to the appropriately-gated sections of the A-scan data.

To generate quantitative image maps of velocity and attenuation, an insertion method was employed, whereby the properties of the tissue are computed in reference to a position without tissue (i.e., only water). For the purposes of the calculations, the acoustic beam is assumed to be planar throughout the specimen. Point-to-point variations in the sample thickness were accounted for by computing the distance between the top and bottom plates, assuming the bottom plate is flat. In the case where the bottom plate is level, the velocity at position (x, y) is then given by

$$c(x,y) = \frac{2L(x,y)}{t_s(x,y) - t_c(x,y)} = \frac{t_s^0 - t_c(x,y)}{t_s(x,y) - t_c(x,y)} c_0 \,, \tag{1}$$

where L is the distance between the bottom of the cover plate and top of the substrate, t_s and t_c are the signal travel times to the tissue-substrate and cover-tissue interfaces, respectively, t_s^0 is the travel time to the cover-water interface at the reference point, and c_0 is the velocity of the water. The attenuation in decibels per unit length is given at each position by

$$\alpha_{\tau}(x,y) = \frac{-20}{2L(x,y)} \log_{10}\left[\frac{A(x,y)}{A_0}\right], \tag{2}$$

where A and A_0 are the peak amplitudes of the signal after passing through the specimen and water reference locations, respectively. Note that this equation does not account for frequency-dependent effects, and therefore is essentially an estimate of the attenuation at the center frequency of the transducer.

3. RESULTS AND DISCUSSION

To begin, a qualitative study of the specimens was performed. Figure 1 shows a comparison of optical (Fig. 1a) and acoustical images (Fig. 1b) of Specimen I. The acoustical C-scan image is produced using a 25 MHz focused transducer focused at the bottom of the sample. While the carcinoma can be seen in the optical image (lighter shade of gray; in color it is typically white while the surrounding tissue is flesh-colored), the acoustical image exhibits higher contrast and shows more of the sub-surface tissue structure. The black and white arrows in the images point to common regions where the carcinoma is branching into the surrounding margin. In addition, the acoustical image clearly shows a clear dark band starting near the vertical gray arrow and proceeding around the tumor and corresponds to a yellow band surrounding the tumor in the optical image. Figure 2 shows images of Specimen II and provides an example of placing the transducer focus at the top and bottom of the sample. In the former case (Fig. 2a), the reflected signal is primarily a function of the reflection coefficient at the cover-tissue interface and thus represents an image of the local acoustic impedance. The higher acoustic impedance of the tumor is indicative of higher density, higher velocity, or both. In the latter case (Fig. 2b), the image is primarily a function of the round-trip attenuation of the signal as it passes through the specimen. In contrast to Fig. 1b, a distinct border of higher attenuation is observed around the perimeter of the tumor, not just at some distance around it. This result may be in part due to the fact that a plastic substrate was used in Fig. 2(b).

Because changes in tissue velocity cause the received signals to arrive at slightly different times, different regions of the specimen can be selectively displayed by narrowly gating the A-scan data. Figure 3 shows C-scan images produced from a single scan of Specimen II using the Tessonics microscope at 50 MHz with the focus of the transducer placed at the tissue-glass interface. These images highlight (Fig. 3a) the tumor margin as well as thin extensions of the tumor extending into the surrounding tissue, (Fig. 3b) the main body of the carcinoma, and (Fig. 3c) a sinuous structure, possibly a microvessel. The latter feature was not visible from the surface and appears when the specimen is imaged from either side, suggesting that it is internal to the volume of the slice.

Next, quantitative measurements of the velocity and attenuation were calculated at each scan point using the method described in Sec. 3 for Specimen II but using the Tessonics microscope. Figure 4 shows an image map of the velocity as a function of position and a corresponding histogram of the measured values. The measurements show two major peaks in ranges 1480–1485 m/s, corresponding to the water, and 1550–1570 m/s, corresponding to the tumor. The latter range is in line with previous velocity

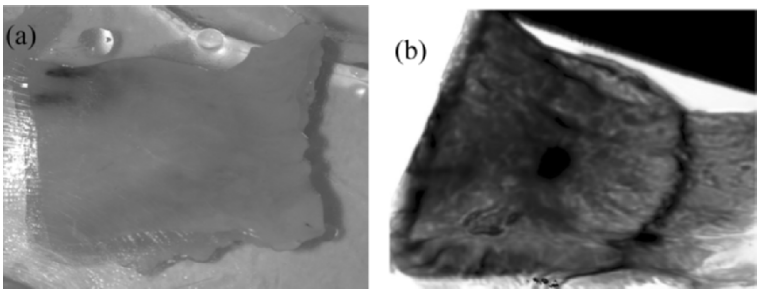

Figure 1. Comparison of (a) optical and (b) acoustical images of a ductal carcinoma**.** The optical image is not stained. The acoustical image was produced at 25 MHz using the Sonix microscope with the transducer focused on the back side of the 4 mm thick, roughly-cut slice and a glass substrate (the acoustical image is slightly stretched horizontally). The arrows point to common features, as described in the text.

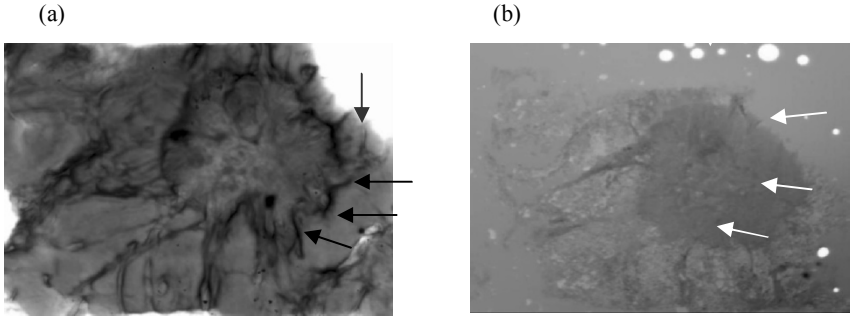

Figure 2. Acoustical images of a ductal carcinoma with transducer focused on the (a) top and (b) bottom of the specimen. These images were produced on an approximately 2 mm thick specimen using the Sonix microscope with a 50 MHz transducer and plastic substrate.

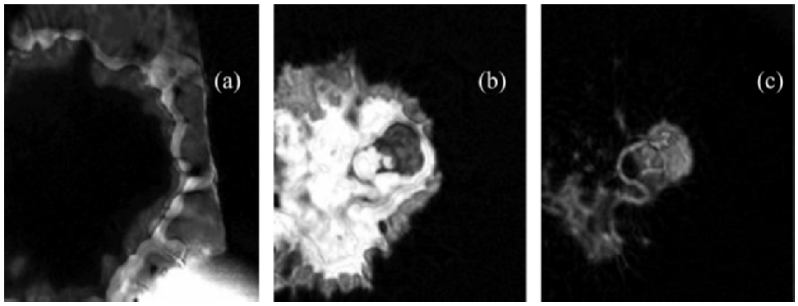

Figure 3. Examples of acoustical images created by gating A-scan data to highlight (a) margin, (b) tumor, and (c) an internal feature. All three images were created from the data obtained from a single scan of the Tessonics microscope for the same specimen as in Fig. 2.

measurements of breast carcinoma[5,7]. Figure 5 shows an image map of the attenuation. (The white spots inside the tissue image correspond to regions where small bubbles were trapped on top of the specimen thereby preventing meaningful attenuation measurements in those regions.) The attenuation of the carcinoma at 50 MHz is seen to be significantly lower than the surrounding tissue. This result is qualitatively consistent with previous measurements in the diagnostic ultrasound frequency range (5–13 MHz)[5–10], although the measured values are less than what might be expected by simple extrapolation from these previous measurements.

To determine if the velocity and attenuation data from Figures 4 and 5 could be combined to identify regions of abnormal tissue development, a two-dimensional histogram was constructed, as shown in Fig. 6a, where the grayscale is proportional to the area corresponding to each (c, α) pair. The rectangular regions drawn on the histogram are two subsets of the velocity and attenuation data: (1) 1550–1590 m/s and 0 to 1 dB/mm, enclosed by the gray rectangle, and (2) 1500–1590 m/s and 0 to 2 dB/mm, enclosed by the black rectangle. The image regions corresponding to these parameter subsets were then marked with corresponding colors on the C-scan of Fig. 6b, with the result shown in Fig. 6(c). (Fig. 6b is a C-scan image generated from the same data set as in Figure 3). The gray region, corresponding approximately to the range of velocity values found in the literature for breast carcinoma[4–8], appears to underestimate the extent of the tumor, whereas the larger black region seems to identify the tumor region better. This type of approach could be useful for computerized sizing of tumors and/or margins, a desired capability for pathological assessment. For example, the areas of the gray and black marked regions in Fig. 6c were computed to be 27 mm^2 and 49 mm^2, with equivalent circular diameters of 6 mm and 8 mm, respectively.

4. CONCLUSION

Our pilot study has examined the use of acoustic microscopy in the range of 15 to 50 MHz to image ductal carcinoma specimens up to 5 mm in thickness. Although these results are promising, additional work needs to be done to make acoustic microscopy a robust and reliable tool for gross tissue examination in the pathology laboratory. Future efforts will include a detailed analysis of the specimen pathology via permanent sections, examination of additional fixed and unfixed specimens with different kinds of benign and malignant lesions, and measurement of acoustical backscatter.

This project was supported by the Canadian Institutes of Health Research (CIHR) and the Natural Science and Engineering Research Council (NSERC) of Canada.

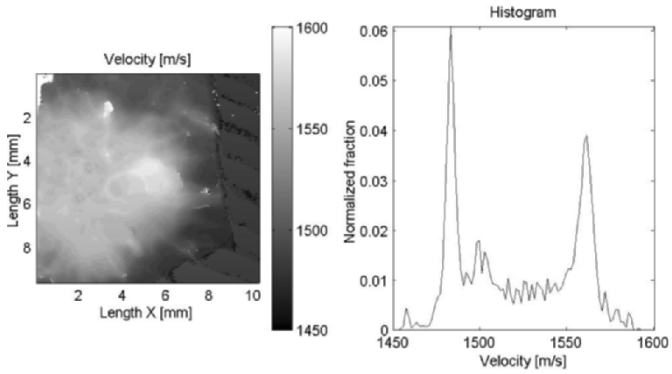

Figure 4. Image map of velocity data for ductal carcinoma and corresponding distribution of measured values**.** The tumor has noticeably higher velocity than the surrounding tissue. In Fig. 6, this data is combined with attenuation measurements of Fig. 5.

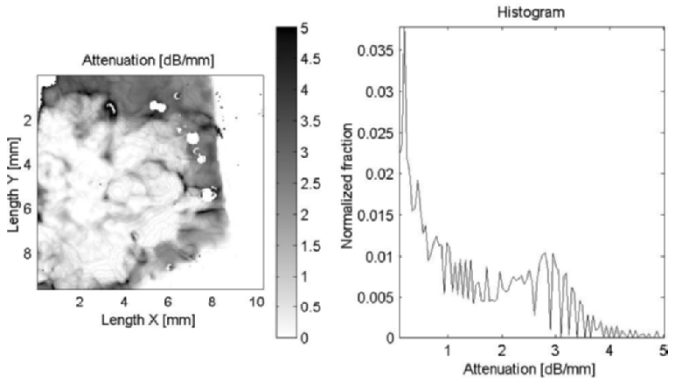

Figure 5. Image map of attenuation data for ductal carcinoma and corresponding distribution of measure values. The tumor has noticeably lower attenuation than the surrounding tissue. In Fig. 6, this data is combined with the velocity measurements of Fig. 4.

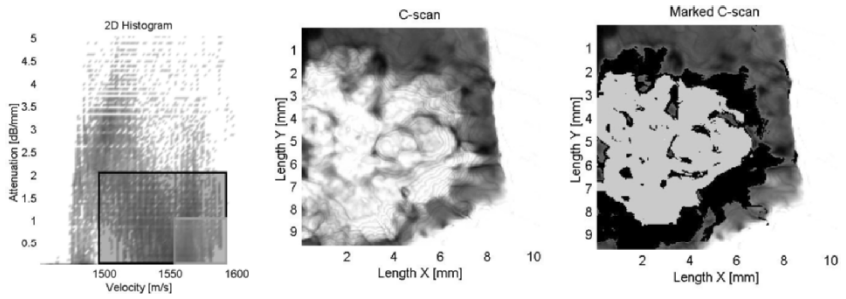

Figure 6. C-scan marking using quantitative data analysis**.** The figure shows (a) a two-dimensional histogram of velocity and attenuation data, (b) an unmarked C-scan image, and (c) a marked C-scan image. The parameter subsets enclosed by the gray and black rectangles in the histogram (a) correspond with the gray and black regions marked in image (c).

REFERENCES

1. M.E. Anderson, M.S. Soo, R.C. Bentley, and G.E. Trahey, The detection of breast micro-calcifications with medical ultrasound, *J. Acoust. Soc. Amer.* **101**, 29–39 (1997).
2. M.P. André, M. Galperin, L.K. Olson, K. Richman, S. Payrovi, and P. Phan, Improving the accuracy of diagnostic breast ultrasound in: *Acoustical Imaging, v. 26,* edited by R.Gr. Maev (Kluwer Academic/Plenum Press, New York, 2002), pp. 453–460,.
3. R.A. Lemons and C.F. Quate, Acoustic microscopy: Biomedical application, *Science* **188**, 905–914 (1975).
4. G. Kossoff, E.K. Fry, and J. Jellins, Average velocity of ultrasound in the human female breast, *J. Acoust. Soc. Am.* **53**, 1730–1736 (1973).
5. F.S. Foster, M. Strban, and G. Austin, The ultrasound macroscope: Initial studies of breast tissue, *Ultrasonic Imaging* **6**, 243–261 (1984).
6. F.T. D'Astous, and F.S. Foster, Frequency dependence of ultrasound attenuation and backscatter in breast tissue, *Ultrasound Med. Biol.* **12**, 795–808 (1986).
7. P.D. Edmonds, C.L. Mortensen, J.R. Hill, S.K. Holland, J.F. Jensen, P. Schattner, A.D. Valdes, R.H. Lee, and F.A. Marzoni, Ultrasound tissue characterization of breast biopsy specimens, *Ultrasonic Imaging* **13**, 162–185 (1991).
8. C.L. Mortensen, P.D. Edmonds, Y. Gorfu, J.R. Hill, J.F. Jensen, P. Schattner, L.A. Shifrin, A.D. Valdes, S.S. Jeffrey, and L.J. Esserman, Ultrasound tissue characterization of breast biopsy specimens: Expanded study, *Ultrasonic Imaging* **18**, 215–230 (1996).
9. C. Calderon, D. Vilkomerson, R. Mezrich, K.F. Etzold, and M. Haskin, Differences in the attenuation of ultrasound by normal benign and malignant breast tissue, *J. Clin. Ultrasound* **4**, 249–254 (1976).
10. E. Kelly Fry, N.T. Sanghvi, and F.J. Fry, Frequency dependent attenuation of malignant breast tumors studied by the fast Fourier transform technique, in: *Ultrasonic Tissue Characterization II, NBS Spec. Publ. 525,* edited by M. Linzer (U.S. Government Printing Office, Washington, DC, 1979), pp. 85–91.
11. R.M. Golub, R.E. Parsons, B. Sigel, E.J. Feleppa, J. Justin, H.A. Zaren, M. Rorke, J. Sokil-Melgar, and H. Kimitsuki, Differentiation of breast tumors by ultrasonic tissue characterization, *J. Ultrasound Med.* **12**, 601–608 (1993).

12. T.M. Burke, T.A. Blankenberg, A.K.Q. Siu, F.G. Blankenberg, and H.M. Jensen, Preliminary investigation of ultrasound scattering analysis to identify women at risk for later invasive cancer, *Ultrasound Med. Biol.* **21**, 295–303 and 305–311 (1995).
13. M.E. Anderson, M.S.C. Soo, and G.E. Trahey, In vivo breast tissue backscatter measurements with 7.5- and 10-MHz transducers, *Ultrasound Med. Biol.* **27**, 75–81 (2001).
14. L.A. Denisova, R.Gr. Maev, I.V. Matveichuk, Yu.I. Denisov-Nikolsky, A.A. Denisov, and E.Yu. Maeva, Investigating bone microstructure and mechanical properties using acoustic microscopy in: *Acoustic Imaging, v. 26,* edited by R. Gr. Maev (Kluwer Academic/Plenum Press, New York, 2002), pp. 61–68.
15. R. Maev, L. Denisova, E. Maeva, and A. Denissov, New data on histology and physico mechanical properties of human tooth tissue obtained with acoustic microscopy, *Ultrasound Med. Biol.* **28**, 131–136 (2002).
16. E. Maeva, I. Bruno, M. Docker, B. Zielinsky, F. Severin, and R.Gr. Maev, Method of acoustic microscopy for sex determination of sea lamprey, petromyzon marinus larvae, *J. Fish Biol.* **65**, 148–156 (2004).
17. R.E. Kumon, I. Bruno, B. Heartwell, and E. Maeva, Breast tissue characterization with high-frequency scanning acoustic microscopy, *J. Acoust. Soc. Am.* **115**, 2376(A) (2004).

AN ULTRASOUND BASED SYSTEM FOR NAVIGATION AND THERAPY CONTROL OF THERMAL TUMOR THERAPIES

R.M. Lemor, S.H. Tretbar, H.J. Hewener, C. Guenther, K. Schwarzenbarth, J.-P. Ritz, K. Lehmann

Fraunhofer-Institute for Biomedical Technology, Biomedical Ultrasound Research, Ensheimer Str. 48, 66386 St. Ingbert, Germany; Charité, Campus Benjamin Franklin, Department of Surgery II, Berlin, Germany

Abstract: Interstitial thermal therapies such as laser induced interstitial thermal therapy (LITT) and radio frequency induced interstitial thermal therapy (RFITT) are widely used in treatment of focal lesions of tumors and metastasis. For improving the results and the safety of these therapies it is necessary to optimize the precise heat applicator placement and to control the energy deposition into the tissue. In this paper we present a dedicated system for navigation and therapy control of thermal ablation therapies for liver applications based on ultrasound technology. The navigation scenario offers the possibility to use single or multiple applicators and allows on line three-dimensional puncturing guidance inside and outside the imaging plane of the transducer. Using attenuation changes as an ultrasound parameter for defining the thermal ablation zone the therapy process can be controlled and monitored. Differential attenuation data are derived by using a coded excitation scheme for acquiring multi band attenuation images, which are reconstructed into 3d volume data. The volume data sets are then coregistered with and compared to pretreatment data. A strong increase in attenuation change correlates with tissue coagulation

Key words: ultrasound therapy control, thermal ablation, attenuation

M.P. André (ed.), Acoustical Imaging, 289–294.

1. INTRODUCTION

Interstitial Thermal therapies are widely used for treatment of focal soft tissue lesions of tumors or metastasis [1]. For improving the efficacy of the treatment the correct placement of the heat applicators in the tissue as well as the control of the heat deposition into the tissue are crucial factors. These tasks, i.e. puncture guidance and therapy control, can be performed with medical imaging modalities like x-ray and magnetic resonance imaging. Also ultrasound has been proposed by several groups for both tasks [2] but until now no dedicated ultrasound system was available on the market.

In this paper we describe an ultrasound-based system for supporting the clinician in performing thermal liver therapies. The real time capabilities of ultrasound imaging allow the guidance and control of applicator placement and parametric ultrasound imaging allows the visualization of the heat-induced lesion [3][4][5].

Figure 1. System prototype, including rf generator, ultrasound beamformer, personal computer and optical tracking device.

2. MATERIAL AND METHODS

The system consists of a personal computer system that connects a digital ultrasound beamformer (Fraunhofer-IBMT, Diphas) and a position tracking device (Northern Digital Instruments, Polaris Accedo) to constitute a freehand 3D ultrasound system (Figure 1). The ultrasound system is adapted to a radio frequency ablation system (Celon, ProSurge) and the software provides scenarios for guiding the applicator placement and the three-dimensional imaging of thermal ablation.

The software is structured in modules leading the clinician in single steps through the therapy. The graphical user front end comprises modules for diagnosis, planning of applicator placement and heat deposition, puncturing guidance and therapy control.

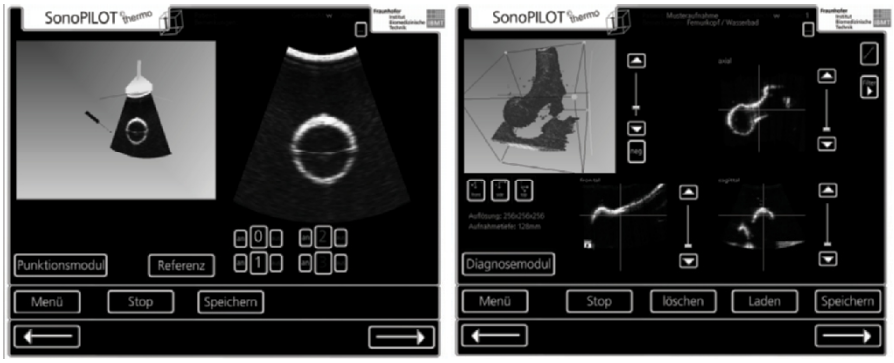

Figure 2. Graphical user frontend of puncture guidance and therapy control.

The module for puncture guidance (Figure 2, left) visualizes in real time next to the common ultrasound b-mode image and a three dimensional scenario of the applicator, the projected puncturing channel and the ultrasound transducer with the online ultrasound image in correct geometric relation, allowing the clinician to place the applicator in a controlled way.

The control module visualizes the reconstructed 3d-volume and 3 freely selectable slice planes of the rf data. Different filters and interpolation techniques can be selected by the user and the visualized data can be chosen to be either b-mode data or attenuation change data. Movable markers allow for measurement of geometric dimensions and the volume data can be exported into raw type files for further evaluation.

3. EXPERIMENTAL EVALUATION

The system was evaluated under in vitro and in vivo conditions. An animal study was performed on pigs in vivo using two bipolar rf-applicators and multipolar radio frequency heating. The thermal heating was performed in the liver for 20 min duration with 30 W. Before, during and after the therapy, freehand 3D-ultrasound data was acquired. For motion artifact reduction during acquisition the controlled respiration of the narcotized pigs was halted during the data acquisition period of 15–20 sec. Acoustic radio frequency reflection data were acquired using a four pulse excitation with bursts of 2,25 MHz, 3,5 MHz, 5 MHz and a 6 MHz - pulse for each scan

line. Each volume data set contains approximately 200 images of 4*96 scan lines each. After the therapy the livers were excised and gelatin fixed deep frozen for later thin sectioning for optical measurement.

3.1 Acoustic Measurement

After narrow band pass filtering and amplitude detection of each rf line in one scan the amplitude decay of the signal over runtime in each of the four excited frequency band was analyzed. Using a windowing technique the local attenuation in multiple segments was calculated. The local frequency dependence of attenuation was calculated using a linear interpolation between local attenuation in the different frequency bands. For measuring differential attenuation changes, the calculated values for each volume segment during and after treatment were compared to pretreatment values. For this comparison each volume data set was geometrically coregistered with the pretreatment data set with a best fit algorithm using the heat applicator positions as artificial landmarks.

3.2 Optical Reference

For comparing the acoustically derived change in attenuation slope to the actual lesion geometry the procedure described in [6] was used. The thin sectioned liver slices were photographed and from the optical images 3-dimensional data volumes were generated consisting of native image data and binarized lesion data segmentation of the thermal lesion according to a procedure described in [6].

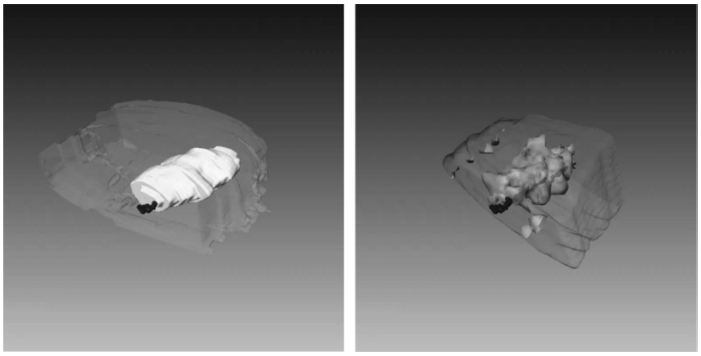

Figure 3. Optically reconstructed and acoustically measured lesion volume.

4. RESULTS AND DISCUSSION

The puncturing scenario with the visualization of the applicator and transducer using the optically tracked positions allows good placement of multiple applicators. The three-dimensional dataset with integrated applicator visualization is very helpful for controlling the correct applicator placement. Freehand data acquisition of volume data with 15 to 20 seconds of acquisition time is well feasible. The extraction of frequency dependence of attenuation and the comparison to the coregistered pretreatment data allows the visualization of attenuation change. Thresholding and isosurface calculation of attenuation change data allow a clear definition of a lesion volume as seen in Figure 3 (right). The coregistered optical and acoustical data volumes allow the visualization and comparison of the optically measured binarized lesion and the acoustically derived lesion. The lesion location and size in the optical and acoustical dataset correspond well. Preliminary data shows that using a threshold value of 0.7 [dB/cm/MHz] for attenuation change the acoustically measured lesion volumes differ from the optically measured lesion volume by 10 percent (Figure 4).

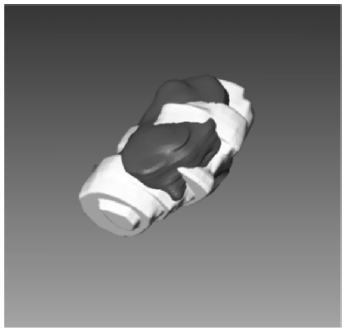

Figure 4. Volume and shape difference in optical (white) and acoustical (blue) measurement. Acoustic attenuation change isosurface of 0.7 [dB/cm/MHz].

5. CONCLUSION

In this paper we presented a dedicated ultrasound based system for supporting the clinician in performing thermal ablation therapies for cancer treatment. The system seems to be a valuable tool for treatment planning and applicator placement as well as therapy control. The precision in lesion size characterization by means of ultrasound attenuation change measurement has to be further evaluated.

6. ACKNOWLEDGEMENT

This work was funded in parts by the German Ministry for Education and Research (BMBF) and was carried out in the Center of Competence for Miniaturised Monitoring and interventional Systems MOTIV, partner of the German Medical Technology Alliance GMTA.

REFERENCES

1. Scoggins CR, Gleason JF, Martin RCG, Kehdy FJ, Hutchinson JR, McMasters KM, Thermal ablation of liver tumors, Review Article, Cancer Therapy, Vol 2, 455–462 (2004).
2. Solbiati L, Ierace T, Goldberg SN, Sironi S, Livraghi T, Fiocca R, Servadio G, Rizzato G, Mueller PR, Del Maschio A, Gazelle GS, Percutaneous US-guided radio frequency tissue ablation of liver metastasis: treatment and follow up in 16 patients, Radiology 202, 195–203 (1997).
3. Lemor RM, Kleffner BV, Tretbar S, Schmitt RM, Ultrasound temperature and Attenuation Monitoring for Controlling the Laser Induced Thermo Therapy, Acoustical Imaging, Vol 25, Kluwer Academic/Plenum Publishers, Dordrecht & New York, pp 395–400 (2000).
4. Varghese T, Zagzebski JA, Lee FT (Jr), Elastographic imaging of thermal lesions in the liver in vivo following radiofrequency ablation: preliminary results, Ultrasound in Medicine & Biology, 28 (11/12):1467–1473, 2002 .
5. Clarke RL, Bush NL, Ter Haar GR, The changes in acoustic attenuation due to in vitro heating, Ultrasound in Medicine & Biology, 29 (1):127–135, 2003.
6. Lutter A, Cappius HJ, Schütz R, Lemor R, Müller GJ, Preparation and optical measurement of coagulated tissue samples, 15th World Congress of the International Society for Laser Surgery and Medicine (ISLSM) , Proc. of the 14th Congress of the International YAG-Laser Society and 14th Annual Meeting of Deutsche Gesellschaft fuer Lasermedizin (DGLM e. V.) München, 25.-27. June, 2003.

CLASSIFICATION OF THERMALLY ABLATED TISSUE USING DIAGNOSTIC ULTRASOUND

S. Siebers, U. Scheipers, J. Hänsler, M. Frieser, D. Strobel, C. Welp, J. Werner, E. Hahn, H. Ermert

Institute of High Frequency Engineering, Ruhr-University, 44780 Bochum, Germany; Department of Internal Medicine, University Erlangen-Nürnberg, Ulmenweg 18, 91054 Erlangen, Germany; Institute of Biomedical Engineering, Ruhr-University, 44780 Bochum, Germany

Abstract: In this work the application of an ultrasound based classification system for the detection of thermally ablated tissue is presented. In-vitro and in-vivo experiments have been carried out using an RF ablation device. A conventional diagnostic ultrasound device was used for measurements. Several features from spectral and spatial domain were extracted from ultrasound RF data and processed by the classifier. Classification results are presented in binary coagulation maps

Key words: tissue characterization; classification; monitoring; RF ablation; thermal therapy; coagulation

1. INTRODUCTION

Tissue characterization has been widely used throughout the ultrasound research community for various applications[1,2], amongst others for differentiating pathological from healthy tissue. In this work, a classification system for automated tissue characterization is investigated towards its ability for monitoring thermal therapies as RF ablation. In this context, a differentiation of thermally coagulated and noncoagulated or viable tissue is desired. In several research projects, tissue characterizing ultrasound parameters have been used for this purpose, however, in general a single

M.P. André (ed.), Acoustical Imaging, 295–300.

parameter has been used on its own[3,4,5]. In this work, more than 40 parameters from spectral and spatial domain have been evaluated in a first step, regarding their potential in detecting coagulated tissue. The best combination has been processed by a linear classifier. The classification result is presented in binary coagulation maps indicating the thermally ablated zone.

2. EXPERIMENTS AND DATA ACQUISITION

2.1 RF Ablation

For RF Ablation a conventional device (Elektrotom HiTT 106, Integra ME GmbH, Tuttlingen, Germany) was used. The system consists of a 60 W, 375 kHz RF generator to which needle and neutral electrode are connected, and of a piston pump which delivers saline solution to the needle electrode for open perfusion. Tissue impedance is measured by the device throughout the application. Saline flow can be controlled automatically. If necessary, a bolus of saline is given to compensate for variation in tissue impedance. The hollow needle electrodes consist of isolated steel except for the 15mm active tip. The active tip has 6 micro holes for infusion of saline solution into the tissue. During ablation, temperature of up to 100°C are reached in the surrounding of the needle tip, inducing thermal coagulations of up to 5 cm in diameter.

2.2 Data Acquisition

Data were acquired using two conventional diagnostic ultrasound systems, the Siemens Antares for in vitro measurements, and the Siemens Elegra for in vivo measurements.

The Siemens Antares was equipped with the Siemens Axius Direct Ultrasound Research Interface (URI), which provides RF data at 40 MHz sampling frequency and 16 bit resolution. Using the Siemens Elegra, baseband data were obtained accessing its internal operating system via telnet and downloading the data via FTP. All features needed for controlling the Elegra were provided by custom made software. With both systems, a 3.5 MHz curved array transducer was used.

2.3 In Vitro Experiments

Samples of bovine liver have been used for in vitro experiments. The samples were placed in a custom made holder. The needle electrode was placed perpendicular to the imaging plane to avoid artifacts in the images. The imaging depth was set to 60 mm. The power of the RF generator was set to 20 W for 5 to 8 minutes, leading to relatively smooth coagulations without larger gas bubbles that also might cause artifacts in the images. Ultrasound RF data were acquired after the coagulation process and stored on a PC. Afterwards the liver specimens were sliced in the imaging plane. Photographs were taken to serve as a reference for later analysis.

2.4 In Vivo Experiments

All animal experiments were performed according to the German animal protection law and official permission to perform the animal experiments was obtained. 10 domestic pigs were included in this study. The anesthetized animals were placed in supine position on the operating table. RF ablation was performed intraoperatively. The livers were excised, sliced and also photographed.

3. DATA PROCESSING

3.1 Extraction of Tissue Characterizing Parameters

To obtain spatially resolved tissue characterizing parameter images, each set of RF data was subdivided in up to 1700 overlapping ROIs. The size of the ROIs was set to 128 samples (2.5 mm) axially and 16 lines (4 degrees) laterally. Overlap was set to 50%, both axially and laterally. For each ROI a set of 40 spectral and textural features was calculated. Spectral features take into account changes in spectral behavior of coagulated tissue, like increase in attenuation.

To consider changes in spectral properties due to the coagulation process, 21 parameters from the frequency domain were calculated. Spectral estimates were obtained using Fourier transform (FT) as well as autoregressive modeling (AR) using the Burg method. The optimal order of the AR-model was determined using the Akaike information criterion to be 14.

As backscatter measures midband, slope and intercept values of a straight-line fit to the spectrum were used. Frequency dependent attenuation coefficients were also used. The center frequency for attenuation estimation was determined using spectral moments as well as a least square fit to the spectrum. Estimates of attenuation coefficients were obtained using multi-narrowband[7] and spectral shift method[8]. Furthermore, estimated coefficients of the autoregressive model of order 14 were used as tissue characterizing parameters. All texture parameters were calculated after demodulating the RF signals using Hilbert transform. Moreover, for the calculation of second order texture parameters, image data were quantized to 64 intensity levels. First order texture parameters account for variations in intensity without spatial reference, second order texture parameters account for changes in the spatial arrangement of intensities. First order parameters used in this study were maximum, minimum, mean value, signal-to-noise ratio, squared signal-to-noise ratio, standard deviation, contrast, entropy, kurtosis, skewness, and full-width-at-half-maximum of intensities. Second order texture parameters were extracted from normalized cooccurrence matrices[6] and include contrast, inverse difference moment, entropy, second angular moment, and correlation.

3.2 Classification

In a first step, features have been evaluated regarding their potential in discriminating coagulated from noncoagulated tissue. For that purpose, the coagulated and a noncoagulated region were manually delineated in the B-Mode images according to the photographs and transferred to the parameter images. Two groups of ROIs were created thereby, each representing coagulated and noncoagulated tissue, respectively. The distribution of each feature for both groups was obtained calculating histograms. Defining a threshold k_c, sensitivity and specificity and hence the receiver operating characteristic (ROC) curve were determined for each feature. The area under the ROC curve served as a quality criterion for selectivity of each feature.

The Maximum-Likelihood measure was used to classify each ROI separately. Classification was done by leave-one-out validation over cases, i.e. to classify one ROI the ROIs of the same case were not included in the training data set. The classification results were presented in binary coagulation maps. To evaluate the classification result, sensitivity and specificity for each map were determined.

To find the best combination of features to be processed by a classifier, all possible combinations of features must be tried, as a matter of principle. Since this exhaustive scheme would call for an enormous computational cost, an approximation for the best combination was alternatively found by

sequential forward selection. Initially, the feature with the largest area under the ROC curve was processed separately by the classifier. Subsequently, the feature with the second largest area under the ROC curve was added. If the sum of sensitivity and specificity improved with the new feature, it was included for classification, otherwise it was excluded. This procedure was repeated for all remaining features.

4. RESULTS AND DISCUSSION

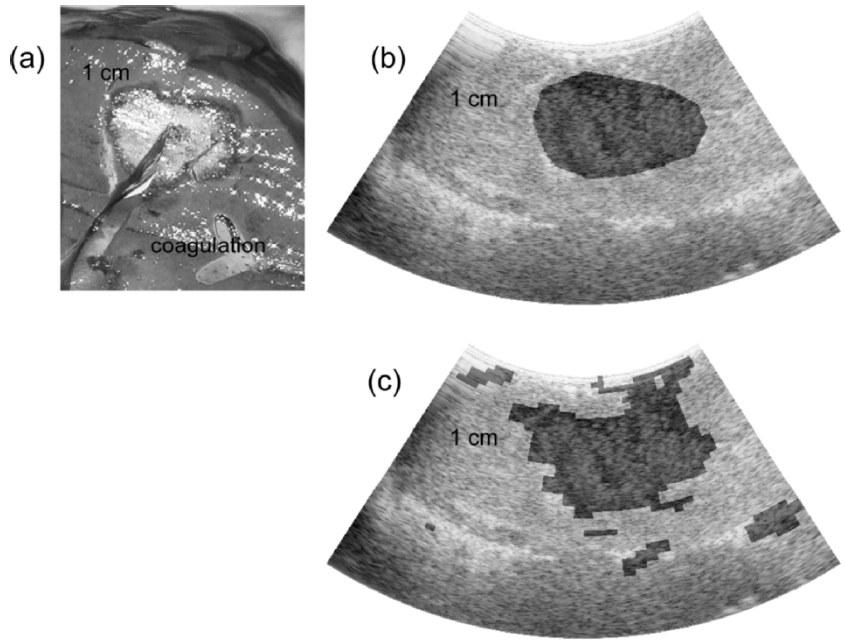

Figure 1. In vivo results. Photograph of coagulation (a), manually delineated coagulated region (b), coagulation map obtained by classification system (c).

15 in vitro experiments were included in this study. The training data set consisted of 1802 ROIs representing group 1 (coagulated), and 2092 ROIs representing group 2 (noncoagulated). Sensitivity and specificity reached 0.9±0.12 and 0.84±0.09, respectively. The lower specificity is mainly due to an overestimation of the coagulated zone, possibly caused by the size of the ROIs. Future work will therefore incorporate the influence of the ROI size to the classification result.

The training data set for in vivo experiments included 2122 ROIs representing group 1 and 1388 ROIs representing group 2. Overall 10 datasets were acquired and classified. Sensitivity and specificity achieved thereby were 0.86±0.11 and 0.76±0.09.

Classification results were displayed in scan converted binary images, serving as coagulation maps. The maps can be superimposed to the B-Mode image for better visualization of the coagulated region.

5. ACKNOWLEDGEMENTS

This work is a project of the Ruhr Center of Excellence for Medical Engineering (Kompetenzzentrum Medizintechnik Ruhr, KMR) Bochum. It is supported by the German Federal Ministry of Education and Research (Bundesministerium für Bildung und Forschung), grant No. 13N8079, and Siemens Medical Solutions, Siemens AG.

REFERENCES

1. Scheipers U, Ermert H, Sommerfeld HJ, Garcia-Schürmann M, Senge T, Philippou S: Ultrasonic multifeature tissue characterization for prostate diagnostics. Ultrasound Med Biol 29(8): 1137–1149, 2003.
2. Siebers S, Geier B, Scheipers U, Vogt M, Mumme A, Ermert H: Classification of Venous Thrombosis combining Ultrasound Elastography and Tissue Characterization. Proc 2004 IEEE Ultrason Symp, in press, 2004.
3. Bevan PD, Sherar MD: B-scan ultrasound imaging of thermal coagulation in bovine liver: Frequency Shift attenuation mapping. Ultrasound Med Biol 27(6): 809–817, 2001.
4. Lemor R, Kleffner B, Tretbar S, Schmitt R: Ultrasound temperature and attenuation monitoring for controlling the laser induced thermo therapy. Acoust Imag, 25: 395–400, 2000.
5. Righetti R, Kallel F, Stafford R, Price R, Krouskop T, Hazle J, Ophir J: Elastographic Chracterization Of HIFU-Induced Lesions In Canine Livers. Ultrasound Med Biol 25(7): 1099–1113, 1999.
6. Haralick RM, Shanmugam K, Dinstein I: Textural Features For Image Classification. IEEE Trans Syst Man Cybern, SMC-3(6), 1973.
7. Cloostermans MJTM, Thijssen JM: A beam corrected estimation of the frequency dependent attenuation of biological tissues from backscattered ultrasound. Ultrason Imaging 5: 136–147, 1983.
8. Fink M, Hottier F, Cardoso JF: Ultrasonic signal processing for in vivo attenuation measurement – short time fourier analysis. Ultrason Imaging 5: 117–135, 1983.

HIGH FREQUENCY QUANTITATIVE ULTRASOUND IMAGING OF SOLID TUMORS IN MICE

M.L. Oelze, W.D. O'Brien, Jr., J.F. Zachary
Department of Elecrtical and Computer Engineering, University of Illinois at Urbana-Champaig; Department of Bioengineering, University of Illinois at Urbana-Champaign; Department of Veterinary Pahtobiology, University of Illinois at Urbana-Champaign

Abstract: A mammary carcinoma and a sarcoma were grown in mice and imaged with ultrasound transducers operating with a center frequency of 20 MHz. Quantitative ultrasound (QUS) analysis was used to characterize the tumors using the bandwidth of 10 to 25 MHz. Initial QUS estimates of the scatterer properties (average scatterer diameter and acoustic concentration) did not reveal differences between the two kinds of tumors. Examination of the tumors using light microscopy indicated definite structural differences between the two kinds of tumors. In order to draw out the structural differences with ultrasound, a higher frequency probe (center frequency measured at 70 MHz) was used to interrogate the two kinds of tumors and new models were applied to the QUS analysis. QUS scatterer diameter images of the tumors were constructed using the high frequency probe. Several models for scattering were implemented to obtain estimates of scatterer properties in order to relate estimated scatterer properties to real tissue microstructure. The Anderson model for scattering from a fluid-filled sphere differentiated the two kinds of tumors but did not yield scatterer property estimates that resembled underlying structure. Using the Anderson model, the average estimated scatterer diameters were 25.5 ± 0.14 μm for the carcinoma and 57.5 ± 2.90 for the sarcoma. A new cell model was developed, which was based on scattering from a cell by incorporating the effects of the cytoskeleton and nucleus. The new cell model yielded estimates that appeared to reflect underlying structure more accurately but did not separate the two kinds of tumors. Using the new cell model, the average estimated scatterer diameters were 15.6 ± 2.2 μm for the carcinoma and 16.8 ± 3.82 μm for the sarcoma. The new cell model yielded estimates close to the actual nuclear diameter of the cell (13 μm)

Key words: tissue characterization, ultrasound backscatter

M.P. André (ed.), Acoustical Imaging, 301–306.

1. INTRODUCTION

Cancer has become the leading cause of death in the United States of America [1]. An important factor in improving the prognosis of cancer is the early detection of cancer. Conventional ultrasound imaging can identify some types of cancerous lesions but in most cases cannot specify whether the lesion is malignant or benign.

Recent advances in a novel ultrasound imaging technique, called quantitative ultrasound imaging (QUS), have exhibited the capability to differentiate malignant tumors from benign tumors in rat and mouse models [2]. QUS imaging utilizes the frequency-dependent information that is not used in conventional ultrasound imaging [3]. The goal of QUS imaging is twofold. The first goal of QUS imaging is to distinguish between tissues that are not distinguishable through conventional ultrasound. The second goal of QUS imaging is to relate quantitative estimates (e.g. scatterer size and acoustic concentration of scatterers) to underlying microstructure.

In a recent study, three types of solid tumors in rats and mice were examined with ultrasound [4]. The tumors were a spontaneously occurring fibroadenoma, a carcinoma and a sarcoma. QUS imaging techniques were used to differentiate the three kinds of tumors at frequencies below 25 MHz. The QUS techniques were able to differentiate the benign fibroadenomas from the other two kinds of tumors. However, QUS was not able to differentiate between the carcinoma and sarcoma. Examination of optical photomicrographs of the three tumors showed distinct features of the microstructure.

In order to distinguish between the carcinoma and sarcoma, a new high frequency scanning system was used to create images. In addition, new models were developed to relate the backscatter to structures observed from optical photomicrographs of the tissues.

2. MEASUREMENT SYSTEM

Measurements of the carcinoma and sarcoma tumors were conducted using a high frequency transducer. The transducer was a lithium niobate transducer (Penn State). The transducer had a center frequency of 70 MHz measured from a planar glass reflector at the focus. The diameter of the transducer was 2 mm with a 7-mm focus. The analysis bandwidth used with the transducer was 30 – 90 MHz. The transducer was found to be highly sensitive to tissue scattering measurements.

The tumors were obtained from commercially available tumor cell lines, the 4T1 MMT carcinoma for mice and the EHS sarcoma for mice. The cells

were cultured in medium and then injected subcutaneously into the fatpad of mice (balb/c mice for the carcinoma and C57BL/6 mice for the sarcoma). Tumors were grown to a little over a centimeter in size and then examined using QUS techniques.

3. MODELS

Three models were used or developed to describe the scattering from tissues. Each model assumed the Born approximation. The Born approximation is valid when there is weak scattering and no multiple scattering. The first model was the spherical Gaussian model [5], the second model was derived from the Anderson model for fluid-filled sphere [6], and the third model was constructed by considering the cytoskeleton of cells.

The spherical Gaussian model was used to describe the high frequency scattering initially because the spherical Gaussian model has been used previously to estimate scatterer properties in may tissues [3]. The spherical Gaussian model assumes that the spatial impedance distribution within the scatterers is continuously increasing over the background. The spatial variation of impedance follows a Gaussian distribution, with the largest impedance value at the center of the scatterer.

The Anderson model for fluid-filled spheres was used to describe scattering from the tissues because examination of optical photomicrographs of the carcinomas indicated that cells were the dominant source of scattering. Specifically, the nuclei of the cells were hypothesized to be a strong scatterer relative to the rest of the cell [2,7]. Therefore, the nuclei of the cells were modeled as fluid-filled spheres and the cell cytoplasm and extracellular matrix were modeled as a uniform background.

The third model incorporated not only the nucleus but also the cytoskeletal structure of the cell cytoplasm from the networks of actin filaments and microtubules. The new cell model yielded a combination of the fluid sphere model and the Gaussian model. Application of the new cell model yielded estimates of nuclear diameter.

4. RESULTS

QUS images of the tumors were constructed for the tumors. Figure 1 shows a QUS scatterer diameter image of a carcinoma tumor using the spherical Gaussian model. Scatterer property estimates were obtained from the carcinoma and sarcoma tumors and from pellets of the carcinoma cells. Scatterer property estimates were obtained using the three models. Relative

chi-square values indicating the goodness-of-fit between the three models and measured data were also obtained. The average scatterer diameter and chi-square values are displayed in figure 2.

Examination of the scatterer diameter estimates indicated that the spherical Gaussian model did not yield scatterer diameter estimates that differed significantly from one tumor to the next. In addition, the chi-square value was the largest for the spherical Gaussian model indicating that the model did not fit the measured data as well as the other models.

Estimates of scatterer diameter from the Anderson model were significantly different between the carcinoma and sarcoma (average scatterer diameter of 26 μm for the carcinoma versus 58 μm for the sarcoma). Furthermore, the chi-square value was smaller for the Anderson model than for the spherical Gaussian model but approximately equal to the value for the new cell model. While the Anderson model distinguished between the two tumors, the diameter estimates were much larger than the actual nuclear diameters (~ 13 μm) as measured using the optical photomicrographs.

Estimates of the scatterer diameter from the new cell model yielded good fits but did not distinguish between the sarcoma and carcinoma. However, diameters estimates were very close the nuclear diameters estimated from optical photomicrographs of the tissues.

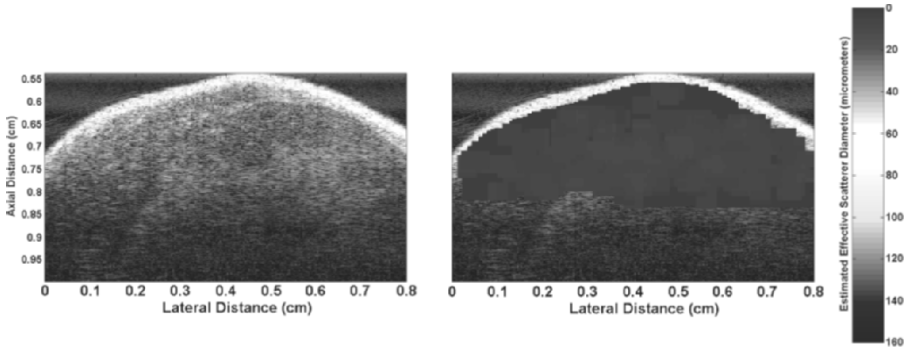

Figure 1. Ultrasound B-mode image of mouse carcinoma (left) and QUS scatterer diameter image of tumor (right) using the 70 MHz transducer.

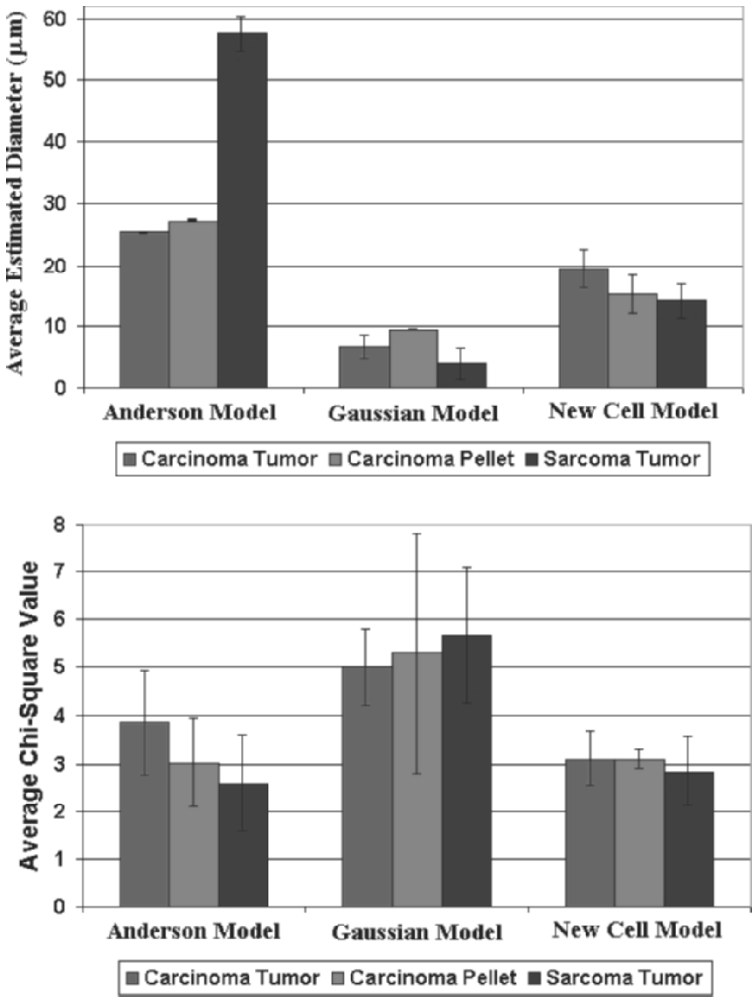

Figure 2. Average scatterer diameter estimates for the carcinoma, sarcoma and carcinoma cell pellet using the three models (left). Chi-square estimates of model fits (right). The error bars represent one standard deviation about the mean.

5. CONCLUSIONS

High frequency QUS imaging (30 to 90 MHz) was applied to two tumor models that were indistinguishable with lower frequency QUS analysis (< 25 MHz). Three new models were tested to determine if estimates of scatterer

properties could be related to tissue microstructure and could distinguish between the two tumor models.

Use of the Anderson model for the fluid-filled sphere allowed the differentiation of the two tumor models. However, the Anderson model did not allow the correlation of scatterer property estimates to microstructure observed from optical photomicrographs of the tumor.

Use of the new cell model did not allow the differentiation of the two tumor models. However, estimates of scatterer properties derived from the model appeared to fit the underlying microstructure it was intended to model.

Differences exist between the two tumor models. These differences were exploited using the backscattered power spectrum and models to extract meaningful quantitative parameters about the microstructure. The goal of future models will be to highlight these differences and correlate with underlying structure.

6. ACKNOWLEDGEMENTS

The authors would like to thank James P. Blue and Rita J. Miller. This work is supported by NIH Grant F32 CA96419 to MLO.

REFERENCES

1. Jemal, A., T. Murray, E. Ward, A. Samuels, R.C. Tiwan, A. Ghafoor, E.J. Feuer, and M.J. Thun, "Cancer statistics, 2005," CA Cancer J. Clin., 55, 10–30, (2005).
2. Oelze, M.L., J.F. Zachary, and W.D. O'Brien, Jr., "Differentiation and characterization of mammary fibroadenomas and 4T1 Carcinomas using ultrasound parametric imaging," IEEE Trans. Med. Imag., 23, 764–771, (2004).
3. Oelze, M.L., J.F. Zachary, and W.D. O'Brien, Jr. "Characterization of tissue microstructure using ultrasonic backscatter: theory and technique optimization using a Gaussian form factor," J. Acoust. Soc. Am., 112, 1202–1211, (2002).
4. Oelze, M.L., W.D. O'Brien, Jr., and J.F. Zachary, "Characterization of solid tumors in mice using ultrasound backscatter over a broad range of frequencies (10 to 90 MHz)," 4th Int. Conf. Ultra. Backscat. Micro., Arden House, New York, 2004.
5. Insana, M.F., R.F. Wagner, D.G. Brown, and T.J. Hall, "Describing small-scale structure in random media using pulse-echo ultrasound," J. Acoust. Soc. Am., 87, 179–192, (1990).
6. Anderson, V.C., "Sound scattering from a fluid sphere," J. Acoust. Soc. Am., 22, 426–431, (1950).
7. Kolios, M.C., L. Taggert, R.E. Baddour, et al., "An investigation of backscatter power spectra from cells, cell pellets and microspheres," Proc. 2003 Ultrason. Symp., 752–757, (2003).

STUDY AND CHARACTERIZATION OF SUBHARMONIC EMISSIONS BY USING SHAPED ULTRASONIC DRIVING PULSE

L. Masotti, E. Biagi, L. Breschi, E. Vannacci
Ultrasonic and Non-Destructive Testing Lab, Dept. of Electronics and Telecommunications, Via S. Marta 3, 50 139 Firenze, Italy

Abstract: Subharmonic emissions from Ultrasound Contrast Agents (UCA_s) were studied by a Pulse Inversion method in order to assess the feasibility of implementation of this technique to subharmonic imaging. Interesting results concerning the dependence of the subharmonic emission with respect to initial pulse shape are presented. The experimentation was performed also by varying the acoustic pressure and concentration of the contrast agent (SonoVue®)

Key words: Contrast agents; subharmonic emission; pulse inversion; signal processing

1. INTRODUCTION

Many research groups are deeply involved in contrast agents characterization in order to investigate the mechanisms of interaction with ultrasounds[1]. Many authors investigated the subharmonic emissions from contrast agents in order to find out new and peculiar responses from the contrast bubbles that allow a specific detection during perfusion[2–5]. In the previous AI conference our group presented a work concerning the ½ subharmonic stable emission as a tool for increasing the contrast to tissue ratio[6].

In this paper subharmonic emission features were studied by a Pulse Inversion (PI)[7] technique in order to evaluate the possibility to employ this technique for ½ subharmonic imaging. A comparison between PI ½

M.P. André (ed.), Acoustical Imaging, 307–315.

subharmonic imaging and a PI second harmonic imaging was performed in different measurement conditions. In particular, a complete characterization of a commercial contrast agent (SonoVue®) response was performed in terms of spectral contents, by varying the measurement condition such as acoustic pressure and the contrast agent concentration. FEMMINA (Fast Echographic Multi parameters Multi Image Novel Apparatus)[8], a real time echographic platform realized in our lab, was employed to perform multiparameter extraction and multi image data representation starting from the acquired Radio Frequency (RF) echo signal.

By considering that subharmonic emission is strongly affected by the driving pulse phase, a further investigation was performed to investigate the shape influence of the driving pulse.

2. MATERIALS AND METHODS

All the presented results were produced by means of FEMMINA, a hardware-software platform developed by our group. The platform completely integrates the architecture of a Personal Computer (PC). The PC also constitutes the user interface, as a flexible and intuitive visualization support, and performs some software signal processing, by custom algorithms and commercial libraries.

The platform, used in conjunction with an analog front-end hardware for driving the ultrasonic transducers of any commercial echograph, with its capability to access the RF echo signal, makes it possible to dispose of a powerful echographic system for experimenting any processing technique, also in clinical environment, where real time operation mode is an essential prerequisite.

For this experimentation, FEMMINA was also connected to a modified echograph (Esaote, Technos) through an optical link and is able to acquire RF frames sequences in a real time modality at the echograph frame rate (43 Frame/s).

Technos was modified in order to transmit two ultrasonic pulses with phase opposition for each line of sight and then to produce two echographic frames.

In Fig. 1 a block diagram of the entire acquiring system is reported. FEMMINA is also able to acquire RF data which came from a single element transducer or from a hydrophone placed in front of the echographic probe for acoustic pressure evaluation.

In Fig. 1 the adopted test-object is reported. The test-object consists of a latex tube filled with the contrast agent solution and then immersed in a water tank. A plexiglass slab is placed behind the tube acting as reflector.

In a different acquiring system set-up the echograph was replaced by an arbitrary waveform generator (Agilent, 33120A) connected to a linear power amplifier (ENI 350L, Gain 50dB, Bandwidth 250 kHz-105MHz). In this second set-up the slab was removed and replaced by an ultrasonic transducer in order to receive the transmitted ultrasonic signal. This set-up allows the insonation of the contrast agent by ultrasonic pulses of different waveform shapes.

3. RESULTS

The performed experimentation allows us to affirm that it is possible to employ a PI scheme to develop a contrast imaging technique based on subharmonic emission from contrast agents.

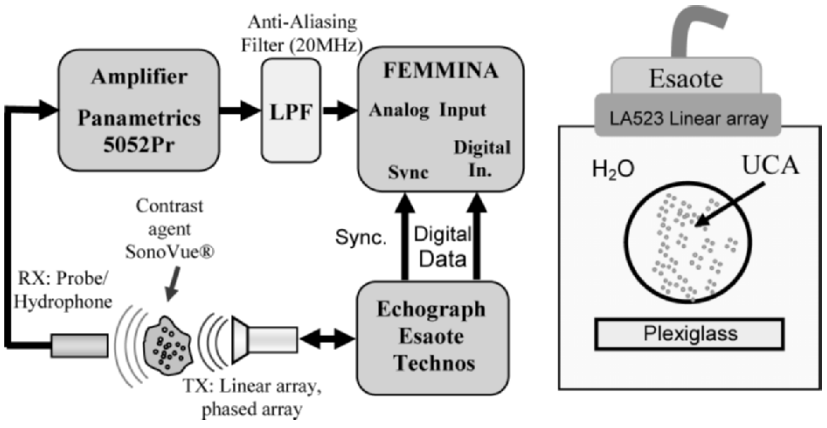

Figure 1. Block diagram of the acquiring system is reported on the left. Two measurements set-up were adopted. In the figure the first set-up appears. The second one is obtained by replacing the echograph with an arbitrary waveform generator (Agilent, 33120A) connected to a linear power amplifier (ENI 350L, Gain 50dB, Bandwidth 250 kHz-105MHz). On the right a schematic representation of the employed test-object is reported. The test-object consists of a latex tube filled with the contrast agent solution and a plexiglass slab positioned behind the tube.

In Fig. 2 a PI scheme is implemented on the echographic RF frames coming from the test-object of Fig. 1. The slab interface behaves like a reflector and thus its echo-signals received by the echographic probe contains spectral contents which are cumulated during its propagation. On the left of Fig. 2 PI was applied to the left portion of the first slab interface

directly invested by the ultrasonic beam, without passing through the latex tube.

On the right the results obtained from a slab portion placed behind the latex tube are reported. In this case this portion interface reflects a signal derived from the ultrasound contrast agent interaction.

By comparing these two different results it can be observed that PI is able to remove the fundamental band while the non-linear contents are maintained.

In particular, the second harmonics occur in both the selected portions, while subharmonic appears only in the portion under the test-object. This can lead to the consideration that only the subharmonic is a typical feature of the contrast agents while second harmonic is generated also by non-linear propagation in water.

By comparing the spectral distribution of the two employed signals, an appreciable difference can be observed on their subharmonic emissions while no differences are detected on second harmonic components. The contrast agent seems to exhibit different non-linear emissions versus the signal phase.

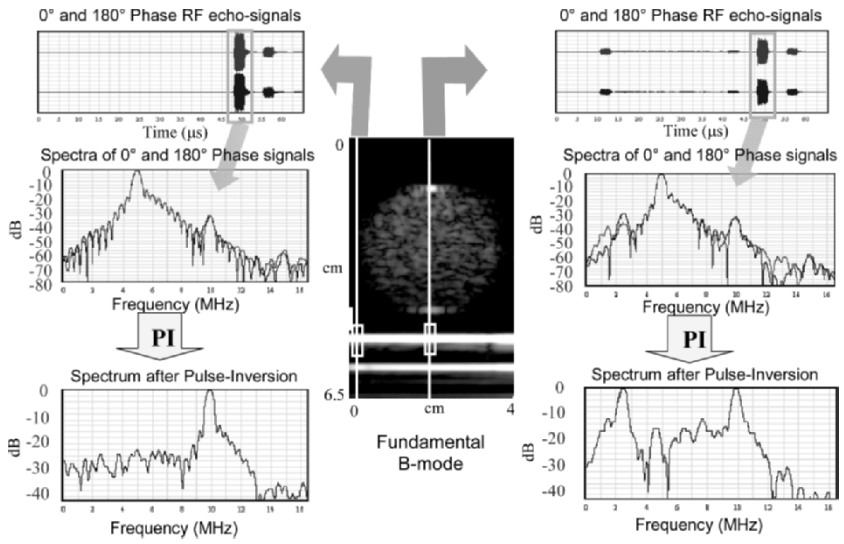

Figure 2. In middle a fundamental B-Mode image of the Fig. 1 test-object is reported. On the left, the RF echo-signals (0°–180° phase), their spectral distributions and PI results appear respectively. These graphs are referred to a signal portion (first slab interface) of the sight line selected by the left white cursor on the B-Mode. On the right, the same sequence of data for the signal portion behind the latex tube, is reported.

In Fig. 3 the PI subharmonic and PI second harmonic images were added to the fundamental B-Mode image. As discussed above, in the subharmonic images only the two portions of the interfaces located behind the latex tube appear. The filtered RF echo-signals for subharmonic and second harmonic are also reported.

Both the RF tracks show that the two signals become phase locked after an initial phase. The differences of the subharmonic emission are confirmed by observing how the two subharmonic filtered echo-signals appear more mismatched if compare with second harmonic ones.

We focus our experimental tests to investigate this phenomenon by using the second measurement set-up.

The following results concern the evaluation of harmonic and subharmonic emissions versus acoustic pressure and contrast agent concentration.

In Fig. 4 a sequence of spectral distributions obtained at a fixed acoustic pressure (P_{pk-}= 50 kPa) for different values of contrast agent concentration C is reported on left column. On the right the results produced with variable pressure and concentration are shown ($C = 3{,}75 * 10^{-3}$).

The difference between the subharmonic for 0° phase signal and for 180° signal are pressure and concentration dependent with a non-linear law.

By observing Fig. 4 different subharmonic contributions (1/3 order and 2/3 order) appear for concentration values higher then $C=1.3*10^{-3}$ and for acoustic pressure higher than P_{pk-}= 30 kPa.

To investigate how the shape of the transmitted pulse influences the harmonic and subharmonic emission we performed several tests with sinusoidal bursts characterized by different Transition Cycles (TC); where TC is the number of starting cycles necessary to reach the maximum pulse amplitude following a linear ramp. These tests are carried on without using PI technique. In Fig. 5 these results are reported for fixed concentration and acoustic pressure in order to demonstrate how the subharmonic is strongly affected by the shape of the transmitting pulse and in particular how it is influenced by the initial portion of the transmitting pulse.

The maximum subharmonic emission occurs when TC approaches zero.

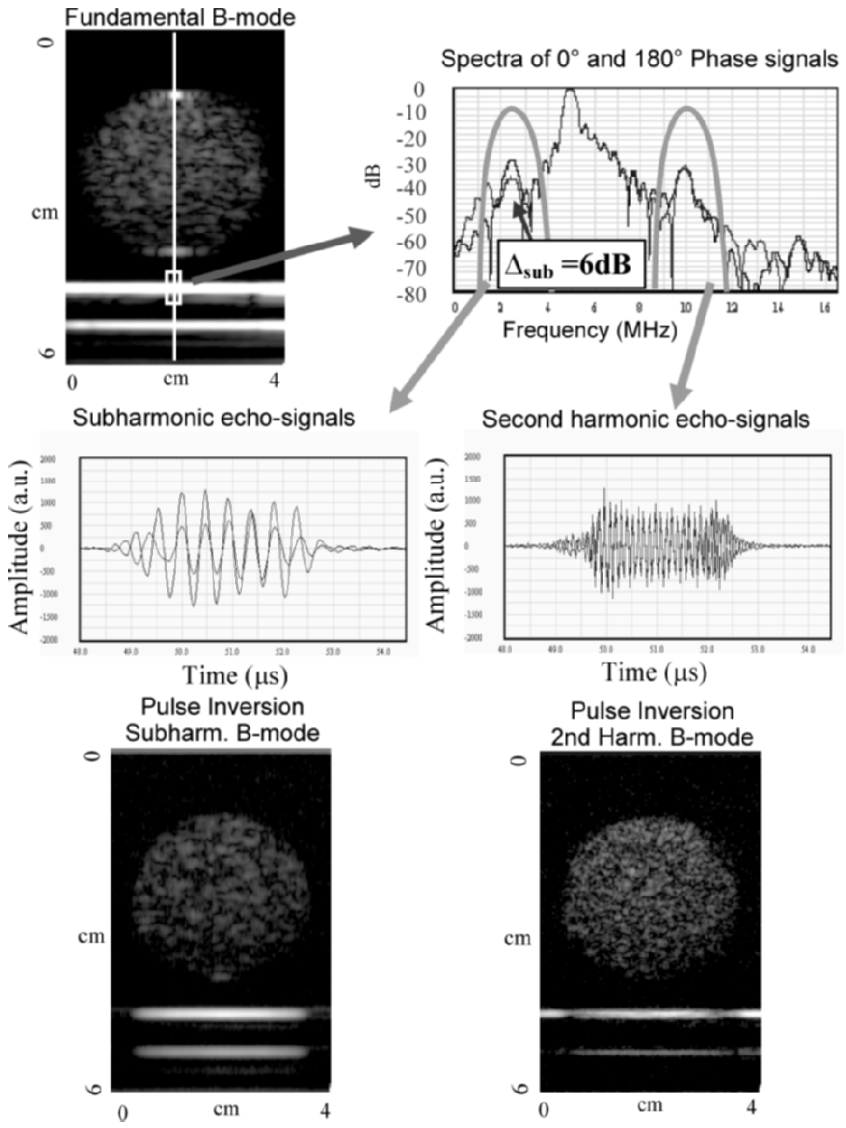

Figure 3. The results obtained on the right of Fig. 2 are enriched by adding PI subharmonic and PI second harmonic images (on the bottom). In the middle the two RF filtered signals are reported for subharmonic and second harmonic content.

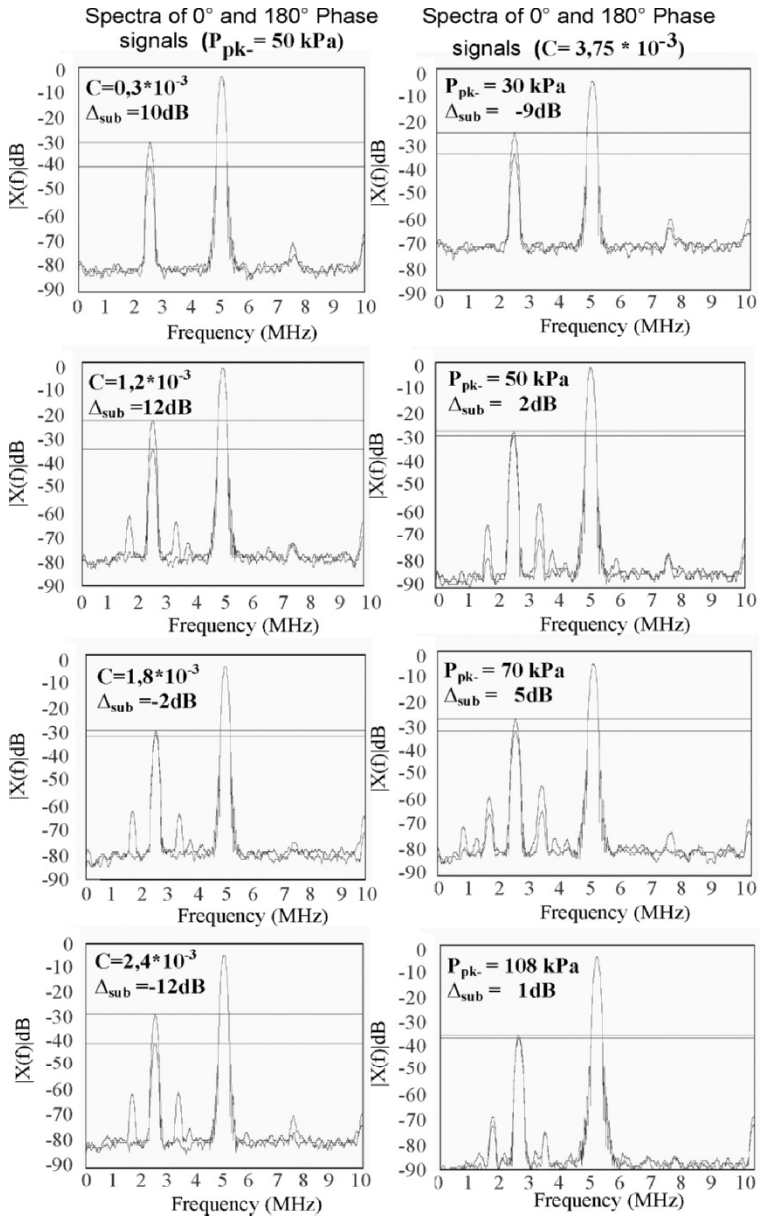

Figure 4. These results concern the second measurement set-up (transmitting technique). On the left a sequence of spectra obtained at different contrast agent concentration and for a fixed value of acoustic pressure (50 kPa) are reported. On the right the sequence is referred to a fixed concentration (C =3.75*10^{-3}) by varying the acoustic pressure.

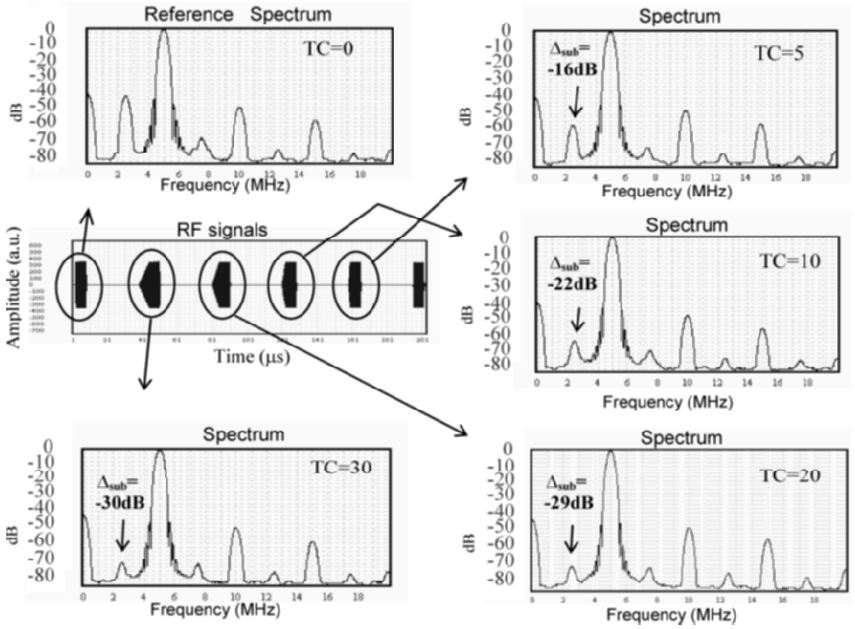

Figure 5. Harmonic and subharmonic emission spectra for different shaped transmitting bursts. The bursts are constituted by 30 cycles preceded by Transition Cycles (TC). TC is the number of starting cycles necessary to reach the maximum pulse amplitude following a linear ramp. (Ppk-= 70 kPa) ($C=1.2*10^{-3}$).

4. CONCLUSION

In this work we study the subharmonic emission by employing a pulse inversion technique. A different behavior between subharmonic and 2nd harmonic emission was detected. In particular, subharmonic emission is a phase dependent phenomenon.

Several experimental procedures were presented by employing transmitting-receiving ultrasonic techniques in order to investigate the subharmonic response as a function of the transmitting pulse shape.

It was experimentally demonstrated that subharmonic response is strongly affected by concentration of contrast agents and acoustic pressure.

Subharmonic imaging[2,5,6] has an high Contrast to Tissue Ratio (CTR) due to lack of subharmonic emission from biological tissue in the frequency and pressure range commonly employed for diagnostics.

Transmitting pulse shape, contrast agent concentration and acoustic pressure constitute the key-factors to take carefully into account for proposing novel imaging techniques based on subharmonics.

REFERENCES

1. P. Dayton, K.E. Morgan, A.L. Klibanov, G.H. Brandenburger and K.W. Ferrara, "Optical and acoustical observations of the effects of ultrasound on contrast agents", *IEEE Trans. Ultrason., Ferroelect., Freq. Contr.,* **46**, 220–232, (1999).
2. F. Forsberg, J.S. Raichlen, L. Needleman and B.B. Goldberg, "Pressure dependence of subharmonic signal from contrast microbubbles", *Ultrasound in Med. & Biol.*, **25**, 275–283, (1999).
3. E. Biagi, L. Masotti, L. Breschi, M. Scabia and S. Granchi "Echographic examination method using contrast media" US Patent App. No.: 10/809,758 Filing date: March 25, (2004).
4. E. Biagi, L. Breschi and L. Masotti, "Transient subharmonic and ultraharmonic acoustic emission during dissolution of free gas bubbles," *IEEE Trans. Ultrason., Ferroelect., Freq. Contr.*, to be published.
5. F. Forsberg, W.T. Shi, R.Y. Chiao, A.L. Hall, S.D. Lucas and B.B. Goldberg, "Implementation of subharmonic imaging", *IEEE Ultrason. Symp.*, **2,** 1673–1676, **(**1999).
6. E. Biagi, L. Masotti, L. Breschi, M. Gentile, S. Mazzanti, A. Ricci and M. Scabia, "Harmonic and subharmonic acoustic response of microbubbles," presented at the *27th International Symposium Acoustical Imaging,* Saarbrücken, Germany, March 24–27, (2003).
7. D. Hope Simpson, C.T. Chin and P.N. Burns, "Pulse Inversion Doppler: A new method for detecting nonlinear echoes from microbubble contrast agents," *IEEE Trans. Ultrason., Ferroelect., Freq. Contr.,* **46**, 372–382, (1999).
8. M. Scabia, E. Biagi and L. Masotti, "Hardware and software platform for real-time processing and visualization of echographic RF signals", *IEEE Trans. Ultrason., Ferroelect., Freq. Contr.*, **49**(10), 1444–1452, (2002).

VOLUMETRIC IMAGING USING ACOUSTICAL HOLOGRAPHY

T.F. Garlick, G.F. Garlick
Advanced Imaging Technologies Inc., 2400 Stevens Drive, Suite B, Richland WA 99354

Abstract: Transmission acoustical holography holds tremendous promise for medical imaging applications. As with optical holography, an image is obtained using the interference of two coherent acoustic sources, the transmitted object wave with a reference wave. Although resultant images are true holograms, depth can be difficult to quantify and an entire volume in one image can often result in "too much" information. Since Physicians/Radiologists are often interested in viewing a single plane at a time, techniques have been developed to generate acoustic holograms of "slices" within a volume. These primarily include focused transmission holography with spatial and frequency filtering techniques. These techniques along with an overview and current status of acoustical holography in medical imaging applications will be presented

Key words: Acoustical holography, axial resolution, lateral resolution, diffraction, slice thickness

1. OVERVIEW

In recent years acoustical holography has shown considerable promise in the detection, characterization and instrument guidance of lesions in the breast. There are a number of compelling advantages of this technology such as:

- Large field of view
- Real time imaging
- Multi-planar imaging modality
- High penetration at low insonification levels

M.P. André (ed.), Acoustical Imaging, 317–329.

- No Ionizing radiation
- Diffraction sensitive imaging

While there are a number of feature sets used to identify and characterize lesions, in most cases identification is principally dependant upon spatial resolution and contrast resolution. In acoustical holography, lateral resolution (resolution in the cross plane) exceeds axial resolution (resolution along the axis of propagation). As the emphasis and need for volumetric imaging has increased in recent years, focus has been placed on efforts to increase axial resolution. Previous research has indicated that source motion yields certain advantages in image quality[1]. Current research, and the subject of this paper deals with an analysis of techniques used to reduce the depth of field including optimization of source motion.

2. BACKGROUND OF THE TECHNOLOGY

Acoustical holography relies on the same principles as optical holography with the one exception that the hologram is constructed in sound[2–4]. Figure 1 illustrates a typical acoustical holography imaging chain. The object is insonified with a plane wave of ultrasound causing scattering and absorption within the volume. The resultant wave front combines with an unperturbed reference wave at the detecting surface creating a hologram. In acoustical holography it is advantageous to focus a region of the object into the detecting surface, thus the use of an ultrasonic lens system.

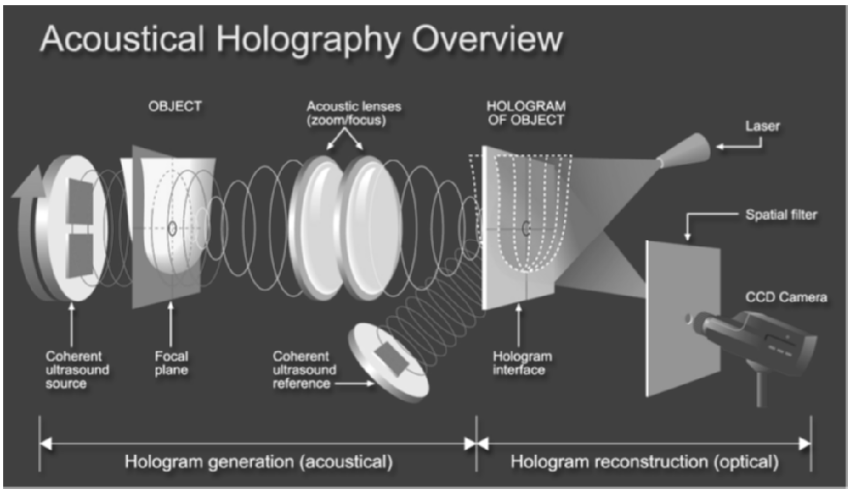

Figure 1. Acoustical holography imaging chain.

Although the object information is recorded in the hologram formed by coherent ultrasound, it is reconstructed by coherent light. Due to the difference in wavelength from the acoustical to optical domain a lens is required for direct viewing. Furthermore, it should be noted that this is off axis holography, thus the image information will be found in the +/- 1 diffracted order requiring a spatial block to isolate the desired image.

3. VOLUMETRIC IMAGING

Given an object to interrogate it is often convenient to divide the volume up into sub volumes comprised of slices of a given thickness as illustrated in Figure 2.

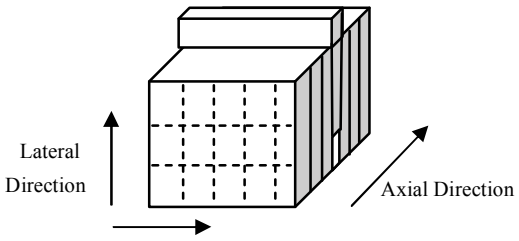

Figure 2. Volume interrogation.

Ideally we would like to image precisely what is in the slice without any interference or influence from structures on either side of the slice. In addition, the slice thickness should be the same dimension as the lateral resolution yielding a cubic resolution element for every point in the volume. It is apparent that given this information it is easy to characterize structures of interest at any location within the volume. Unfortunately this is difficult to accomplish with most imaging systems.

3.1 Acoustical Holography Considerations

If a plane wave of ultrasound is used to interrogate the object (as in Figure 2), then in principle objects or structures within in any given slice will alter the wave by attenuation (be it by reflection and or absorption), refraction, and diffraction. Through transmission acoustical holography makes use of attenuation and all the forward scattering interactions or the diffraction components present in the wave.

3.1.1 Imaging Attenuation

Attenuation does not affect the spatial frequency content of the hologram but rather the amplitude of the carrier (or put another way the amount of light reflected in the 1st order is proportional to the amplitude of the ultrasonic object wave), thus attenuation of objects can be accurately characterized. Figure 3 illustrates this concept from a simple plot of the frequency domain. The "carrier" frequency (f_1) is created from the interference of the unperturbed plane wave with the reference wave and is fixed by the relative angle between them. This simple relationship between amplitude of the transmitted acoustic wave and the amplitude of the optical counterpart affords the opportunity to make characterizations using contrast resolution alone. Furthermore with a typical dynamic range greater than 30 dB these measurements can be very sensitive well within the ranges described by Goss[5] and Fry[6] for distinguishing lesions in the breast.

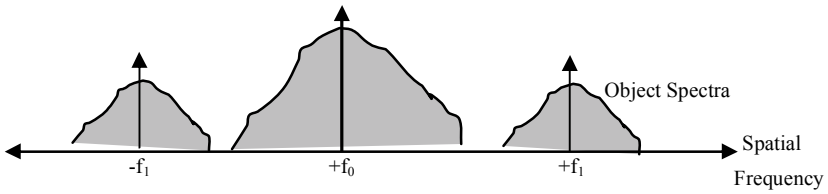

Figure 3. Acoustical holography spatial frequency domain[3].

3.1.2 Imaging Diffraction

The great strength of holography comes from its ability to accurately reconstruct edges from the diffracted portion of the sound. Again referring to the frequency domain, the process of holography will shift the object spectra to center on f_1 as shown in Figure 3. This object spectrum represents a complete wave front reconstruction and the shift allows the ability to isolate it from the central wave front. Thus the resultant image captures the attenuation and diffraction components of the object.

Figure 4 illustrates a volumetric data set of a diseased breast, collected using acoustical holography. Note both edge (diffraction) and attenuation components present.

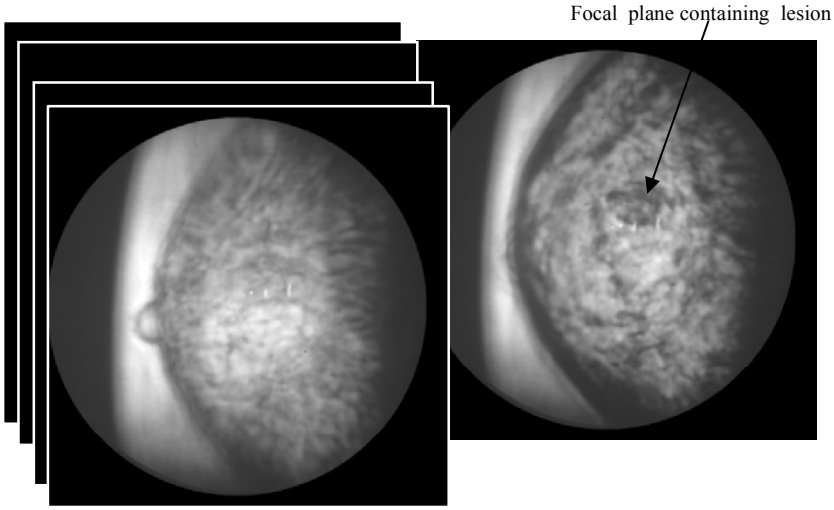

Figure 4. Illustration of acoustical holography volumetric data set.

3.2 The Slice Thickness

In a study conducted by Lehman[7], et. al., acoustical holography demonstrated promise for breast imaging applications. Nevertheless there remains a driving factor to reduce the thickness of the slice since it is greater than the lateral resolution. This does not cause a great concern in fairly homogenous objects with few scatterers. However, in complex structures (such as the breast) the resultant image often contains too much information and it becomes more difficult task to accurately characterize tissue characteristics. In addition, it is obviously more difficult to locate a structure in the axial direction. While a stereo-tactic approach could be used (rotate the object by 90^{o}) to increase location accuracy it still does not isolate the plane of interest for detailed analysis. Finally real time instrument guidance demands not only high lateral resolution but axial resolution as well.

It must be noted that the techniques presented in this paper are primarily concerned with improving axial resolution in the presence of complex structures.

4. FOCUSING

In focused ultrasonic holography we use the concepts of transmission holography with the modification that a single slice within the volume becomes the object. This is accomplished with the use of ultrasonic lens to

focus this slice into the hologram interference pattern. In this scenario, the slice thickness is determined by the F number of the acoustical lens system.

4.1 Ultrasonic Lens

Although a multiple lens system is typically employed it can be modeled and tested as a single lens. As shown by Kino[8], the focus of the lens system is defined by the 3 dB points on either side of the maximum as given by Eqn. 1 and illustrated by Figure 5.

$$I(z) \propto \left| \left(\frac{f}{z} \operatorname{sinc}\left[\frac{a^2}{2f\lambda} \left(\frac{f}{z} - 1 \right) \right] \right)^2 \right| \tag{1}$$

Where f = focal length of the lens a is the radius of the aperture, and λ is the wavelength of the source.

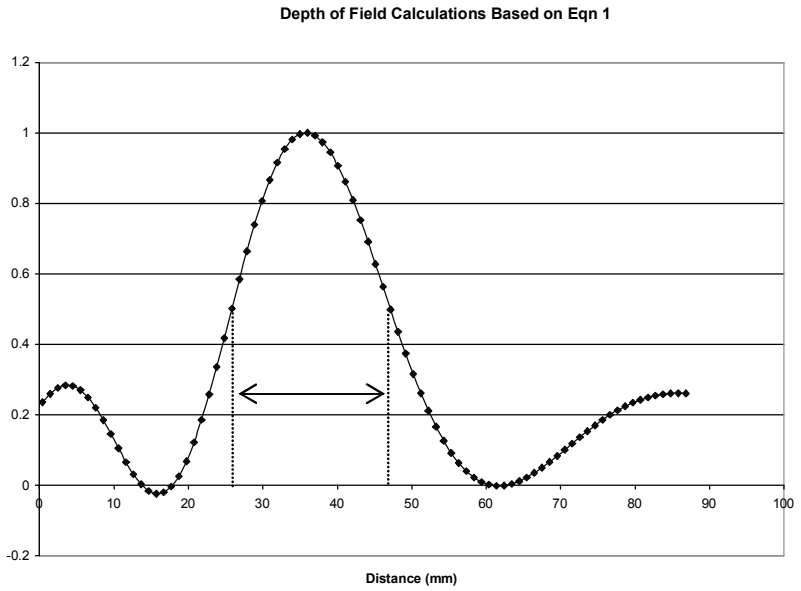

Figure 5. Depth of field.

This model correlates well to the empirical data taken on an acoustical holography system and was used as a metric to compare changes to the depth of field for each technique evaluated. This model also works well in predictive analysis of various lens configurations and designs.

Further effort in improving the ultrasonic lens is the principal mechanism to reduce the depth of field. Other techniques are primarily focused on achieving this depth of field in the presence of complex structures.

5. SOURCE MOTION

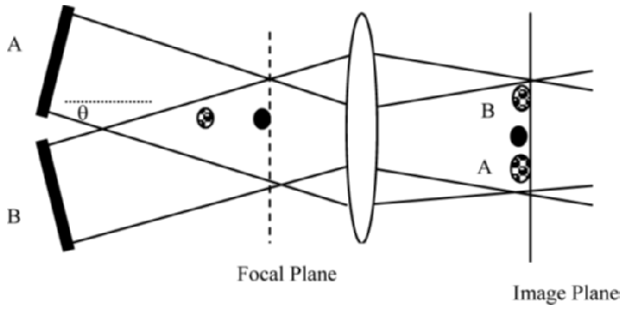

Figure 6. Optimal source positions for preferential insonification.

A further enhancement to axial resolution is to average the images resulting from a number of preferential views created by changing the source location. There are a number of advantages to this technique. First as illustrated in Figure 5, multiple source angles will increase the contribution of scatters within the focal slice when shadowing structures are present outside of the focal plane. This is obvious from the standpoint that different source position and angles can provide more insonification of the object by "shining around shadowing structures".

The greater the angle the greater the effect. However, since the object is placed at or near the focal length of the lens, the maximum angle is clearly limited. Assuming specular scattering and using geometrical

approximations, an angle given by Eq. 2 would ensure that half of the scattered wave from structures at the extreme edge of the object would be collected by the lens.

$$\theta = \tan\text{-}1(b/f) \tag{2}$$

Where b = the radius of the object and *f* is the focal length of the lens.

The second principle advantage is the spatial filtering concept where structures outside of the focal plane appear at different locations in the image depending on position of the source (see Figure 6 positions A & B). When averaged together, the resultant contribution of these structures to the final image is further diminished.

A similar analysis for averaging images at different frequencies yields the advantages of an incoherent imaging system. However, once again we are limited by the number of frequencies due to limited bandwidth in the transducer and nonlinear attenuation with increase in frequency. In practice, a combination of both techniques is utilized to optimize resolution in the slice thickness.

To illustrate the power of this technique consider the following experiment. A series of wire mesh screens are placed in a random orientation on the source side of the focal plane a distance of 25 mm from the target as illustrated in Figure 7. These screens are intended to replicate a worst-case scenario of the complex structures within the breast.

Without source motion it was difficult to distinguish separation at the minimum level of the standard resolution block (.86 mm). However, as illustrated in Figure 8d with source motion the smallest line pairs were distinguishable. Finally Figure 9 looks at the focal slice containing the target and the focal slice containing the screens.

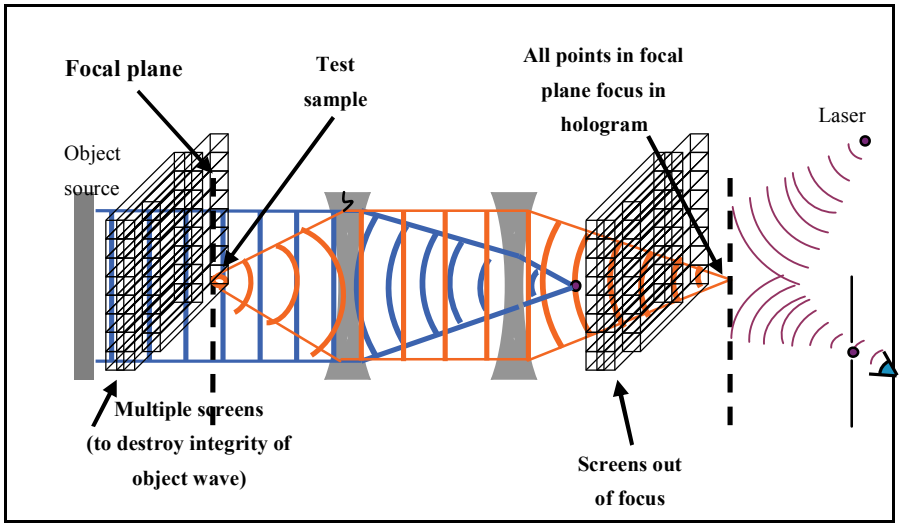

Figure 7. Example of minimizing out of focal slice interference.

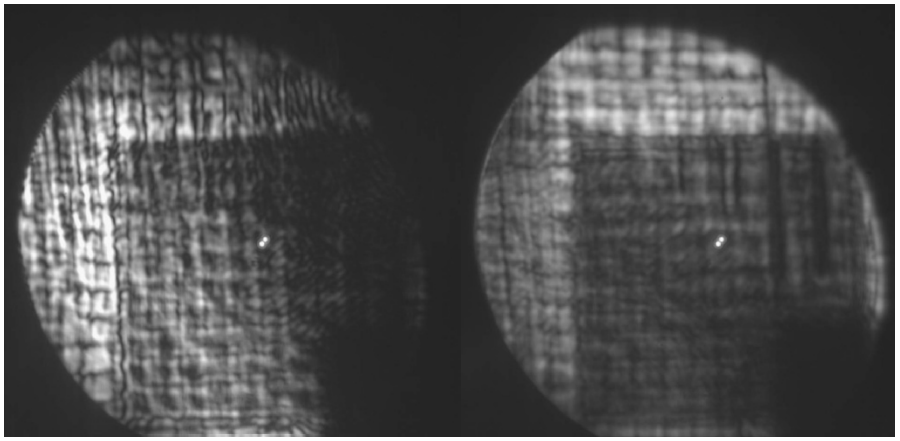

(a). Single frequency with no source motion

(b). Multiple frequency with no source motion

(Continued)

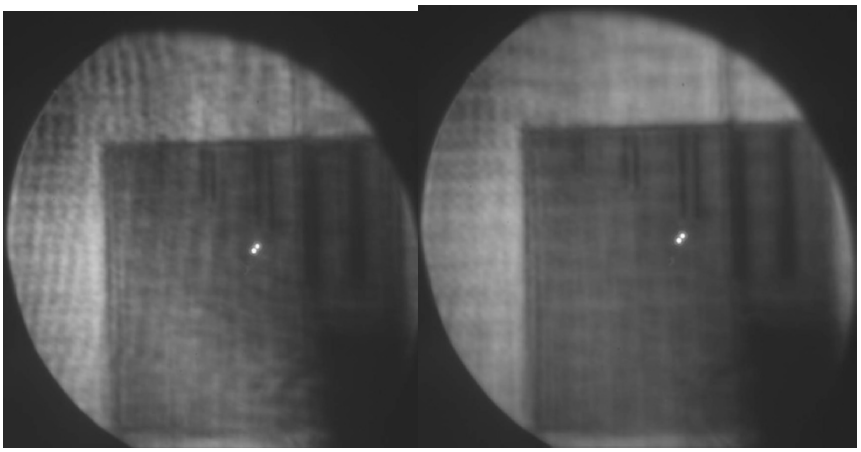

(c). Single frequency with source motion

(d). Multiple frequencies with source motion

Figure 8. Images obtained from the screen experiment.

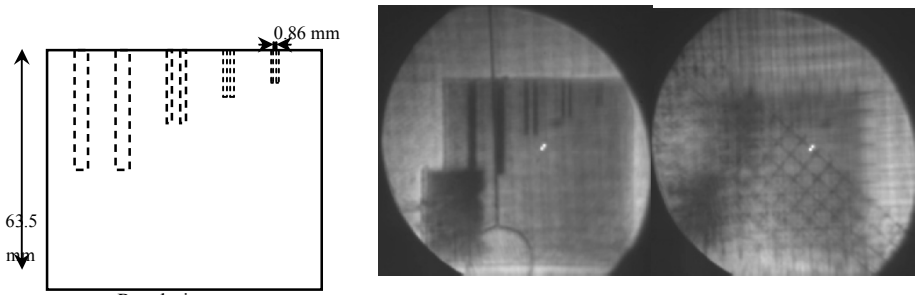

Resolution target dimensions

Focal plane located on resolution target

Focal plane located on 1st screen

Figure 9. Different focal slices in the screen experiment.

6. DIFFRACTION ONLY IMAGING

Another technique to be explored is to remove the contribution of the plane wave component. This can be accomplished by placing a spatial block at the focus of the plane wave component (see Figure 7). The resultant image is comprised of the diffractive component only (Figure 8). This powerful technique has the advantage of increasing the effective dynamic range and increasing the SNR by essential removing the bias. However, this technique

when combined with frequency compounding provides a further reduction of the depth of field (Figure 9).

7. POST PROCESSING TECHNIQUES

Image processing techniques have progressed considerably in recent years and, due to the low capital expenditures required, are attractive approaches to the depth of field problem. Despite the obvious benefits, processing techniques still remain an underutilized approach to improved focal plane location in acoustical holography. A recent study by R. Yin[9], et. al. explored several techniques to better define the center of focus. These included

- Gradient Magnitude
- Modulus Difference
- Laplacian
- Gray Level Variance

Of these, the gray level variance technique performed best providing approximately a 15% improvement over the other selected techniques. While these studies show promise they have yet to be validated in a clinical setting.

8. USER DEFINED FOCUS

In many ways textbook definitions of resolution, depth of field, etc. are somewhat arbitrary and often do not adequately reflect the true usefulness of the system. This is evident from the very nature of analog processes since in the case of focus there is no quantized jump from in focus to out of focus but rather a slow blur into the background. While rigorous definitions are important for system characterization and often the only means to accurately quantify incremental improvements, they do not capture such intangibles as operator experience. In this case, focal plane thickness is best modeled using probability theory.

Using data from a recent study conducted by Jensen et al[10], where operators of various backgrounds were required to locate the center of the focal plane, an operator dependent specification of focal plane thickness can be derived. In the experiment, a phantom containing simulated lesions of a mean diameter of 8.2 mm was placed in an acoustical holography breast imaging system. The subjects were then asked to focus in on a lesion and

then direct a biopsy needle into the phantom penetrating the center of the lesion (see Figure 10). The trial was repeated numerous times.

As expected, all participants correctly positioned the needle in the x-y plane 100% of the time regardless of their medical or acoustical holography experience. However correct z position varied from 93% (those with system experience) to 22%. This result clearly indicates that the effective slice thickness for a trained operator is much less than the definition based on 3 dB points. In fact, if a uniform focus between the 3dB points is used then the probability of a correct hit would be 8.2/25 = 32% Further using Bayesian estimation techniques an effective focal plane thickness can be developed based on operator classification.

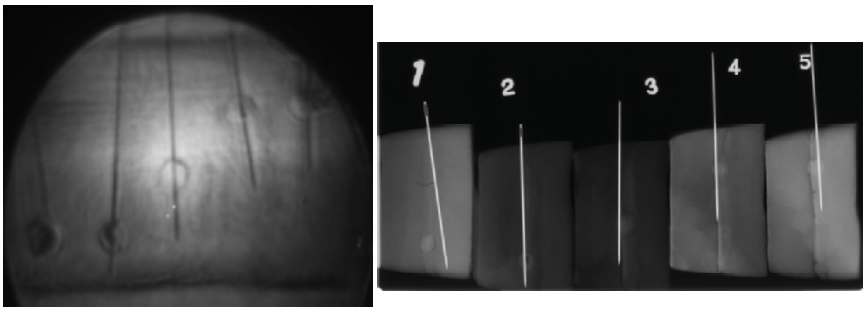

Acoustical holography image used for needle guidance

X-Ray validation of placement in axial direction

Figure 10. Test subjects from focal plane study.

9. CONCLUSIONS

Acoustical holography allows imaging of structures from information imparted on a through-transmitted ultrasonic wave. Such a process has separate contributions from the structures attenuation and diffraction of the incident wave. Furthermore the image resolution is greater in the lateral direction than the axial direction. A number of techniques have been investigated that have demonstrated improvement in axial resolution in the presence of complex structures. It must be kept in mind that most of these techniques can be used in various combinations to optimize performance for any given application.

Techniques discussed include:

1. Focusing using ultrasonic lenses.
2. Source motion averaging

3. Frequency compounding
4. Diffraction imaging
5. Post processing technique

Further work is directed primarily at improving ultrasonic lenses, further optimization to source motion profiles, and exploitation of the diffraction only techniques.

In summary the use of Acoustical Holography as practiced by Advanced Imaging Technologies shows great promise for medical imaging applications. Early work on depth of field optimization has demonstrated great progress and holds even greater potential for future efforts.

REFERENCES

1. B.A. Fecht, M.P. André, G.F. Garlick, R.L. Shelby, J.O. Shelby, C.D. Lehman, "Investigation of an Acoustical Holography System for Real-time Imaging," *Physics of Medical Imaging SPIE 3336*: 106–112 (1998).
2. B.B. Brenden, "UItrasonic holography: a practical system," *Ultrasonic Imaging and Holography,* G.W. Stroke, W.E. Kock, Y. Kikuchi and J. Tsujiuchi, Eds, Plenurn Press, New York, NY, 1973.
3. J.W. Goodman, *Introduction to Fourier Optics*, McGraw-Hill, San-Fransico, California pp. 213–214.
4. B.B. Brenden, *An Introduction to Acoustical Holography Ultrasonic Imaging and Holography,* Plenurn Press, New York, NY, 1974.
5. S. Goss, R. Johnston, F. Dunn, "Compilation of empirical ultrasonic properties of mammalian tissue. I," J. *Acoust. Soc. Am*. 64, pp. 423–457, 1978.
6. E.K. Fry, N.T. Sanghi, F.J. Fry, "Frequency Dependent Attenuation of Moalignant Breast Tumors Studied by the Fast Fourier Transform Technique." Ultrasonic Tissue Characterization II (edited by M. Linzer) National Bureau of Standards, Special Publication 525, pp. 85–90, 1979.
7. C.D. Lehman, M.P. André, B.A. Fecht, J.M. Johansen, R.L. Shelby, J.O. Shelby, "Through-transmission US Applied to Breast Imaging," *Academic Radiology*, **7**(2): 100–107 (2000).
8. G.S. Kino, *Acoustic Waves,* Prentice hall, Englewood Cliffs, New Jersey, pp. 190–191.
9. R. Yin, S.L. Broschat, P.J. Flynn, "Focus Directed Processing of Acoustic Holography Images," *ASA* 1064, p. 2135.
10. B.A. Fecht, P.S. Jensen, "Toward Guided Breast Biopsy using Diffractive Energy Imaging," *Physics of Medical Imaging SPIE 4681*: 226–232 (2002).

RECENT ADVANCES IN ULTRASONIC TISSUE-TYPE IMAGING OF THE PROSTATE

Improving Detection and Evaluation

E.J. Feleppa, C.R. Porter, J.A. Ketterling, S. Dasgupta, S. Ramachandran, D. Sparks

Riverside Research Institute, New York, NY; VIrgnia Mason Medical Center, Seattle, WA

Abstract: The purpose of our prostate tissue-typing studies is to develop more sensitive and specific imaging methods for identifying and characterizing cancerous prostate tissue and thereby improving the effectiveness of biopsy guidance, therapy targeting, and treatment monitoring. We acquired ultrasonic radio-frequency echo-signal data, and clinical variables, e.g., prostate-specific antigen, during biopsy examinations; computed spectra of the radio-frequency signals in each biopsied region; and trained neural network classifiers using biopsy results as the gold standard. Lookup tables returned scores for cancer likelihood on a pixel-by-pixel basis from spectral parameter and PSA values to generate tissue-type images (TTIs). ROC curves based on a leave-one-patient-out approach were used to minimize the chance of biased classification. The ROC-curve area for neural-network-based classification derived from the values of ultrasound spectral parameters plus PSA level was 0.84 +/– 0.02; in comparison, the ROC-curve area for B-mode-based classification was only 0.64 +/- 0.03. Furthermore, the sensitivity of neural-network-based classification was more than 50% better than the sensitivity of B-mode-based classification at ROC specificity values corresponding to a B-mode, biopsy-guidance sensitivity of 50% to 60%

Key words: ultrasound, spectrum analysis, tissue typing, neural networks, cancer imaging, cancer staging, treatment planning, prostate cancer, TTI

M.P. André (ed.), Acoustical Imaging, 331–339.

1. INTRODUCTION

Our studies of prostate cancer imaging were initiated with the purpose of improving means of biopsy guidance, staging, treatment planning, and treatment monitoring. Currently, the standard imaging means of guiding biopsies is conventional, B-mode, transrectal ultrasound (TRUS), and conventional TRUS is not capable of reliably imaging cancer in the prostate. Examination of data regarding the incidence of positive biopsies in repeat TRUS-guided biopsies of men with initially negative biopsies reveals that the fraction of positive cores only increases slightly when second biopsies are performed. Analysis of these data suggests that the sensitivity of the current ultrasound-guided procedure is no better than 60%.[1]

Clinical staging, which is essential for effective treatment selection and planning, relies upon clinical indicators along with TRUS imaging and in some cases, CT or MR imaging. However, typically 30% of surgically removed glands show histological evidence of extracapsular spread, which indicates under staging and an inappropriate treatment selection.[2] (Surgery is considered to be appropriate only if the cancer is gland confined.)

Because gland-confined cancer cannot be reliably depicted in any current imaging modality, all current prostate-cancer treatments are directed toward the entire gland; for example surgical treatment performs a complete excision of the gland, and radiation-therapy irradiates the full gland volume. However, if cancerous and non-cancerous regions could be distinguished reliably, then nerve-sparing surgeries (to preserve sexual function) could be performed with greater confidence, and the side effects of irradiating the bladder, rectum, and urethra might be reduced while concomitantly escalating the dose delivered to cancerous regions.

TRUS remains the primary means of imaging to evaluate the prostate and in effect is the only means of guiding biopsies. TRUS is useful in the great majority of cases for identifying the anatomy of the gland, e.g., its borders (capsule), seminal vesicles, urethra, etc., for the purpose of directing biopsies into the peripheral zone, and in some cases, into the transition zone or seminal vesicles. In a small minority of cases, biopsies are directed toward uniform slightly hypoechoic regions that occasionally indicate a cancerous lesion. However, this image feature does not have sufficient sensitivity or specificity to be used reliably either for assessing gland status or for guiding biopsies. Other methods have not proven to be advantageous in terms of imaging sensitivity or specificity, and their generally higher costs leave them at a disadvantage compared to TRUS.

Based on our experiences characterizing intraocular tissues, liver lesions, thrombi and plaque using spectrum-analysis methods, we undertook a study to characterize prostate tissue using similar ultrasonic methods.[3] The

NIH-funded portion of this study began with the collaboration of the late William R. Fair, MD, Chief of Urologic Surgery at the Memorial Sloan-Kettering Cancer Center (MSKCC) in 1992. Initial MSKCC results proved promising. Currently, we are obtaining equivalent results using data obtained from biopsy patients at MSKCC and separately from patients at the Washington, DC, Veterans Affairs Medical Center (DCVAMC) – despite the large differences in the racial composition and ages of the two patient populations. This article describes our latest DCVAMC studies and their results.

2. METHODS AND MATERIALS

2.1 Data Acquisition

2.1.1 Biopsy-Examination Data

Ultrasonic, radio-frequency (RF), echo-signal data were acquired during transrectal ultrasound-guided biopsy examinations by digitizing the radio-frequency (RF) echo signals accessed within a Hitachi (Twinsburg, OH) EUB 525 scanner using a EUP V53W end-fire curved-array probe with a nominal center frequency of 7.5 MHz. (The measured effective bandwidth was 4.5 MHz, extending from 3.5 to 8.0 MHz, i.e., the effective center frequency was 5.75 MHz.) Digitization was performed by a GaGe (Lashine, QC, Canada) Compuscope 1250-1M data-acquisition board sampling at 50 MS/sec. Each scan plane consisted of 155 digitized scan vectors and each vector spanned 3,600, 12-bit samples. Acquisition was controlled by custom software implemented using LabVIEW (National Instruments, Austin, TX).

Each patient's blood level of prostate-specific antigen (PSA) was entered into the RF data-file header. A key header entry was the level of suspicion (LOS) for cancer assigned by the examining urologist to the biopsied region of each scan. This LOS assignment was based on the appearance of the conventional B-mode image at the biopsy site combined with any other clinical information available to the urologist, e.g., PSA level. The LOS served as our baseline for assessing the relative performance of our classification methods.

2.1.2 Patient Population

Patients for the study described here were recruited from the pool of patients undergoing biopsy at the Washington DC Veterans Affairs Medical Center. Our latest, data set consisted of ultrasonic, clinical and histology data from 617 biopsy core-needle specimens obtained from 64 patients; the racial composition of this patient population was predominantly Black of African descent. (Our previously reported results were based on the predominantly white patient population at MSKCC.) Cancer was detected by biopsy in 23 (35.9%) of the 64 patients and in 103 (16.7%) of the 617 biopsy cores. The fractions of positive biopsies and of patients with detected cancer were notably higher in this data set than in other patient populations; e.g., in our prior MSKCC data about 10% of the biopsies were positive and about 30% of the patients were determined to have cancer.

2.2 Data Analysis

We analyzed RF echo-signal data using the methods described in previous articles.[4] Data analysis utilized custom LabVIEW-based software. This software computed spectral-parameter values from the log power spectrum using 64-sample sliding Hamming windows applied to the RF data of each scan vector in 8-sample steps along all 155 vectors in each digitized scan. The slope and intercept values were computed over a frequency range of 3.5 to 8.0 MHz using linear regression. At each window location, the slope value was corrected for the assumed attenuation of 0.5 dB/MHz-cm. A region of interest (ROI) was carefully placed to match with the biopsy location. This required moving the proximal (to the rectal wall) end of the region to coincide with the proximal border of the gland and by assuring that the distal end of the ROI did not extend past the distal border of the gland. The long axis of the ROI was coincident with the known axis of the needle trajectory (which is in a fixed location relative to the scan plane). Average values of slope, intercept, and midband parameters were computed over the area defined by the ROI. Average spectral parameters values and clinical variables (e.g., PSA value) were entered into a FoxPro (Microsoft, Redmond, WA) data base.

2.3 Classification

We used the MATLAB (MathWorks, Natick, MA) neural-network toolbox to classify spectral-parameter values and PSA for biopsy-proven prostate tissues.[5] Our classification efforts only sought to differentiate cancerous from non-cancerous peripheral-zone tissue from the prostate.

We used a custom script to limit the test set either to a single patient (placing all the biopsies for that patient in the test set) or using only one biopsy at a time in the test set; we termed these a "leave-one-patient-out" or "leave-one-biopsy-out" approach. All remaining data were randomly assigned to the training set (90%) and validation set (10%). Each run of the network produced a score for the likelihood of cancer based on the input values of midband, intercept, and PSA level.

2.4 ROC Analyses

For evaluation purposes, the scores of all runs of each neural network configuration were merged into a single set and analyzed as a whole, i.e., a score was computed for every biopsy in each of the 64 runs, and all the scores for a given configuration were combined into a single set of 617 scores for ROC evaluation.[6]

To asses the relative tissue-typing efficacy of our best artificial neural network classifier, we compared its classification performance to classification based on the LOS from conventional B-mode and clinical data.

2.5 Imaging

To expedite tissue-type image (TTI) generation we used a lookup table (LUT) to translate input spectral-parameter and PSA values to a pixel value for cancer likelihood. We used the MLP configuration that gave the best ROC areas for this purpose. The entire collection of 617 biopsy-proven cases served as the training set, and 64,000 combinations of 40 values of midband, intercept and PSA level that spanned the range of values in the database were used as the test set. Each combination was classified by the MLP and assigned a score for cancer likelihood.

Spectral-parameter values were computed at each pixel and were referred with the PSA level to the LUT, which returned a cancer-likelihood score for that pixel location. Software then translated the score into a pixel value, e.g., for gray-scale TTIs, the lowest score translated to a value of 0 and the highest translated to a value of 255. In the resulting image, bright pixels identified a region having a high likelihood of cancer. The software also was able to generate false-color TTIs by presenting different score ranges in different colors to indicate different ranges in cancer likelihood, e.g., red above a certain threshold to indicate the greatest likelihood of cancer, orange between two thresholds to indicate a somewhat lesser likelihood, on down to green to indicate a minimal likelihood.

3. RESULTS

3.1 Classifiers

The best classifier performance was obtained using an MLP having four hidden layers containing 5, 4, 4, and 2 nodes respectively. The ROC curve for the leave-one-patient-out approach is shown as the upper curve in Fig. 1. Its area is 0.844 with a standard error of 0.018 for the area estimate; it compares very favorably with the baseline ROC-curve area (derived from B-mode-based LOS assignments) of 0.638 with a standard error of 0.031, which is the lower curve in Fig. 1. The area difference of 0.206 is four times 0.049, the sum of the errors, which indicates that the two curves are significantly different. At the operating point where the base-line curve shows a sensitivity of 0.5 to 0.6, the MLP curve shows a sensitivity of 0.85 to 0.90, which represents a sensitivity improvement of 50% to 70%.

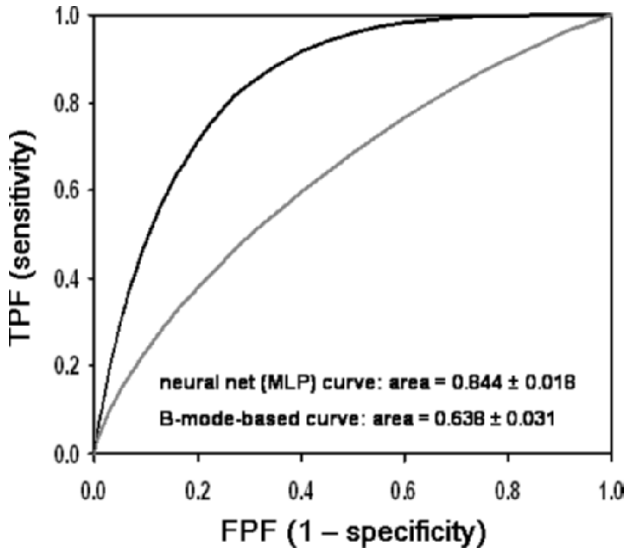

Figure 1. ROC curves for MLP and LOS.

ROC-curve areas for the leave-one-biopsy-out approach generally were the same as or very slightly greater than those for the leave-one-patient-out approach. Although the differences were too small to be significant, they hint at the possibility that having the same tissue type of a given patient in

the training and test sets may favorably bias the classifier if samples of the same tissue for that patient are correlated.

3.2 LUTs and TTIs

The LUT generated using the optimal MLP showed expected behavior: scares increased with increasing PSA level, and the counter of the surface depicting scores vs. midband and intercept values changed dramatically as a function of PSA level. This is shown in Fig. 2 (reproduced with permission from *Ultrasonic Imaging*) where A, B, C, and D respectively show score contours as a function of midband (lower-left axis, values increasing to the left) and intercept (lower-right axis, values increasing to the right) for PSA = 1, 8, 15, and 22. For PSA levels of 15 and lower, the contour peaks are consistent with the anecdotal observations that uniform hypoechoic (low midband values) regions occasionally are indicative of tumor sites.

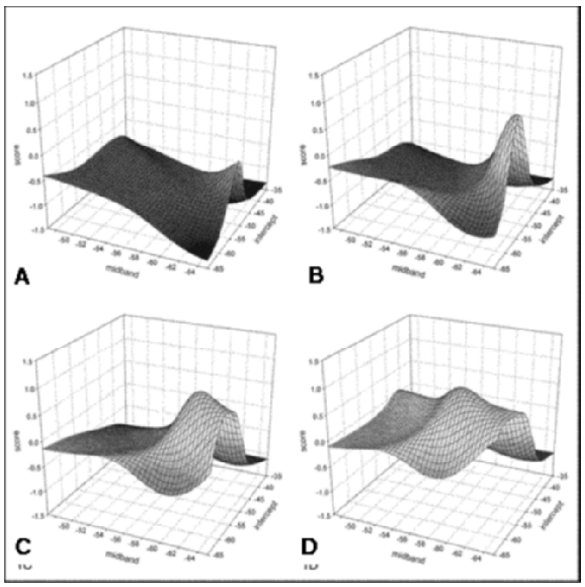

Figure 2. LUTs for PSA = 1, 8, 15, 22.

When applied to different scans of the same patient, this LUT produced image results best illustrated in color.[7] They showed high likelihood of cancer as indicated by a red overlay in the region corresponding to a positive biopsy in one scan and low likelihood as indicated by green in a region corresponding to a negative biopsy in another; both scans were obtained

from different locations within one gland.[7] Furthermore, ROC curves made directly from biopsy-site-matched pixel values in the full set of 617 TTIs generated from this LUT had areas consistent with those of the basic classifier.

4. CONCLUSIONS

Spectral parameters such as intercept and midband used in combination with clinical variables such as PSA can dramatically improve our ability to distinguish cancerous from non-cancerous prostate tissue compared to conventional interpretations of ultrasonic B-mode images combined with clinical information. LUTs can effectively translate locally computed spectral-parameter values and global values of PSA levels to TTIs that depict the relative likelihood of cancer throughout the prostate. Real-time implementation of these methods in 2-D TTIs can be used to guide biopsies or plan brachytherapy in the operating room, and 3-D implementations can be used to plan surgical and external-beam radiation treatments. By implication, the methods also may be applicable to monitoring non-surgical treatments or watchful waiting of prostate cancer.

5. ACKNOWLEDGEMENTS

This research is supported in part by NIH/NCI grant CA53561.

We are deeply indebted to the late William R. Fair and Frederic L. Lizzi for their inspirational encouragement and invaluable knowledge.

REFERENCES

1. Feleppa, E.J., Ketterling, J.A., Kalisz, A., Urban, S., Schiff, P.B., Ennis, R.D., Wuu, C.S., Porter, C.R., Fair, W.R., and Gillespie, J.R., "Application of spectrum analysis and neural-network classification to imaging for targeting and monitoring treatment of prostate cancer," in Proceedings of the 2001 Ultrasonics Symposium, pp. 1269–1272, S. Schneider, M. Levy and B. McAvoy (Eds.), IEEE, Piscataway, NJ, 2002.
2. Fair, William R., personal communication, 1992.
3. Feleppa, E.J., Alam, S.K., and Deng, C.X., "Emerging ultrasound technologies for imaging early markers of disease," Disease Markers, 18:249–268, 2004.
4. Feleppa, E.J., Lizzi, F.L., Coleman, D.J., and Yaremko, M.M., "Diagnostic spectrum analysis in ophthalmology: A physical perspective," Ultrasound in Medicine and Biology, 12(8):623–631, 1986.

5. Feleppa, E.J., Ennis, R.D., Schiff, P.B., Wuu, C.S., Kalisz, A., Ketterling, J., Urban, S., Liu, T., Fair, W.R., Porter, C.R., and Gillespie, J.W., "Spectrum-analysis and neural networks for imaging to detect and treat prostate cancer," Ultrason. Imag., 23:135–146, 2001.
6. Metz, CE, "ROC methodology in radiological imaging," Invest. Radiology 21:720–733, 1986.
7. Feleppa, E.J., Porter, C.R., Ketterling, J.A., Lee, P., Dasgupta, S., Urban, S., and Kalisz, A., "Recent developments in tissue-type imaging (TTI) for planning and monitoring treatment of prostate cancer," Ultrason. Imag., 26:163–172, 2004.

DIAGNOSTIC PERFORMANCE OF A COMPUTER-AIDED IMAGE ANALYSIS SYSTEM FOR BREAST ULTRASOUND

M. André, M. Galperin, G. Contro, N. Omid, L. Olson, C. Comstock, K. Richman, M. O'Boyle

Department of Radiology, University of California, San Diego, San Diego VA Healthcare System, San Diego, California USA

Abstract: We developed a sophisticated computer-aided diagnostic system optimized to the specific application of standardizing interpretation of diagnostic breast ultrasound. The implemented Computer-Aided Diagnostic tool was evaluated on a database of 332 cases with findings known ("truth") via biopsy or two-year benign follow up. These same cases were interpreted by a group of four experienced radiologists. Performance of the developed CAD was measured as Sensitivity, Specificity, PPV, NPV and ROC Area (A_Z). For the CAIS A_Z=0.96, which exceeded the performance of four expert radiologists (average A_Z=0.86). A_Z for the radiologists was not significantly different (0.86, 0.85, 0.87, 0.86 ±0.03). Statistical Power for the study was 93%. The excellent performance of CAIS appears to justify further evaluation in a clinical setting to determine its impact on decision making

Key words: Breast cancer; computer-aided diagnosis; image processing; relative similarity; artificial neural network; ROC analysis

1. INTRODUCTION

Currently, breast biopsy serves as the gold standard in the evaluation of breast masses for malignancy. Mammography is the pre-eminent screening procedure with high sensitivity but its lower specificity is well documented.

M.P. André (ed.), Acoustical Imaging, 341–348.

With societal emphasis on early detection of breast cancer, it appears the effort to avoid missing a malignant lesion may have led to a low positive biopsy rate for cancer, between 10–31%. Unfortunately, breast biopsy is neither a benign nor an inexpensive process. Besides affecting patients physically and emotionally, the procedure frequently causes internal scarring, which may obscure the results of future mammograms. With approximately 1,700,000 women undergoing breast biopsy per year, combined with a cost between $750–5000 per procedure, the cost to the U.S.A. healthcare system is significant. Ultrasound is widely regarded as the adjunct procedure of choice to mammography, especially for distinguishing cystic from solid masses for which accuracy is 96–100%. However, earlier studies, in which ultrasound was evaluated largely as a primary screening tool, reported a wide variance in Positive Predictive Value (PPV) and an unsettling range of False Negative (FN) rate from 0.3–30%. These results led to many recommendations still extant that ultrasound be used only to determine cyst from solid and/or for needle guidance.

Work to improve the accuracy of diagnostic breast ultrasound has led to the development of a well-defined rule-based system for describing and interpreting findings in breast ultrasound. The American College of Radiology has developed the structured Breast Imaging Reporting And Data System (BIRADS) and is detailing a program to accredit the clinical practice of breast ultrasound. BIRADS scoring (1–5) for level of suspicion for cancer is based on parameters describing the ultrasound appearance of breast lesions[1,2]. Acceptance and utilization of BIRADS is increasing but it has proven difficult to teach the method, the quality of breast ultrasound may be operator dependent, and there is high variability of lesion description and assessment between radiologists[3,4].

We developed a sophisticated computer-aided diagnostic system for medical imaging applications that was optimized in a companion paper in this volume to the specific application of standardizing interpretation of diagnostic breast ultrasound. This Computer-Aided Imaging System (CAIS) compares a breast mass in question to a database of images with known findings, displays those closest in "Relative Similarity" and computes an estimate of the BIRADS score. The future goal is to utilize the CAIS with the radiologist in the loop. We hypothesize that the specificity of interpretation of breast ultrasound can be significantly improved with no significant change in sensitivity by following a structured objective implementation of the ACR BIRADS method with our CAIS. Lesions of lower level of suspicion such as complex cystic masses may be ruled out as candidates for biopsy with a higher degree of confidence with use of the computer-aided imaging system[5,6].

A recent study demonstrates that precisely applying the BIRADS lexicon is helpful in differentiating benign versus malignant solid masses[4]. Furthermore, this study and others provide evidence that the Negative Predictive Value (NPV) and PPV are high for certain benign and malignant features that are included in our CAIS.

The purpose of this present study was to compare the performance of the CAIS to that of four experienced radiologists on the same set of 332 breast ultrasound images with known findings. The stage of development addressed in this paper corresponds to the solid box in Figure 1 where the performances of two classifiers are compared: Knowledge-Based Relative Similarity and a feed-forward backpropagation Artificial Neural Network. The number of cases required to achieve acceptable statistical power is listed for each stage. The Development and Test functions were completed in the optimization studies described in the companion paper. The final clinical test of impact on decision-making is the last step toward deployment to the clinical setting. The Figure of Merit (FOM), or test metric, for each stage of development is shown in Figure 1.

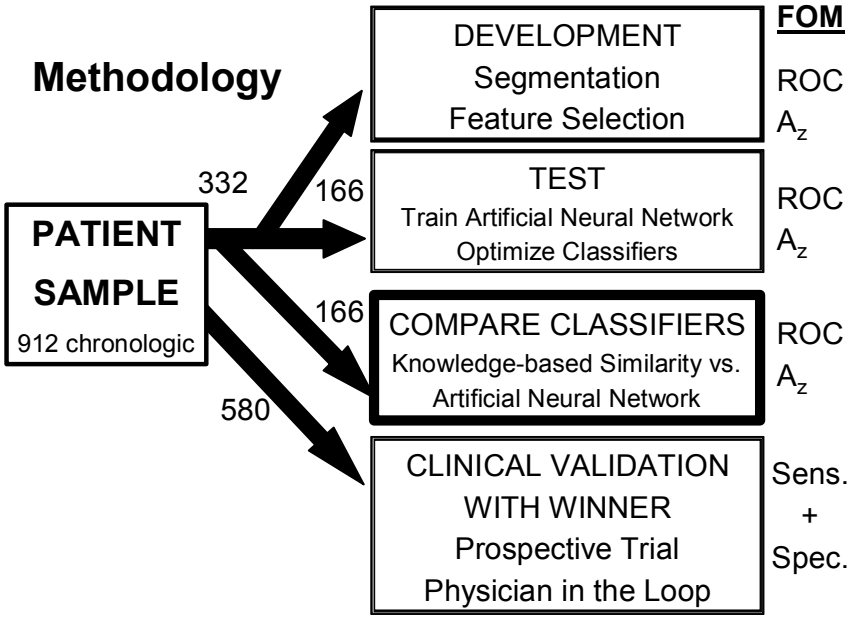

Figure 1. Development of the CAIS.

2. MATERIALS AND METHODS

2.1 Clinical Database of Ultrasound Examinations

Images of 332 breast ultrasound masses were acquired as digital files from the medical center archive and made anonymous. The IRB controlled data were collected in chronological order for patients who had a diagnostic breast sonogram and underwent biopsy or had a two-year negative follow up. We considered carefully the possibility of bias in the distribution of breast lesions in this database and we addressed this possibility in three ways. First, to verify the cancer rate and the distribution of masses among the classes of simple cysts, complex cysts, solid benigns and cancers, we reviewed our entire breast ultrasound radiology reports for the past 36 months. After excluding "no finding" cases in this sample, cancer incidence was consistently 20–25%, which matches that of the template database. Second, we have completed development of a data mining technique to efficiently retrieve in chronological sequence diagnostic ultrasound exams directly from our archive and to verify the radiology report findings with the pathology reports. Third, cases are assembled only in chronological order. After more than four years of developing this technique we recognize the importance of meticulously ensuring that the images we submit for analysis to the computer-aided tool do in fact depict the mass that was actually biopsied or were identified for follow up. The retrieval and verification of patient cases for this study requires significant effort. Cases are excluded if confirmation by either biopsy or 2-year negative follow up cannot be provided or if a concurrent mammogram is not available.

The age range was 40–71 and the database consisted of: 30% simple cysts, 18% intra-cystic masses, 30% solid benign, 22% carcinoma. This distribution of findings follows very closely that of the average mixture in the U.S. reported as 36% cysts, 8% complex cysts, 34% fibroadenomas and 22% malignant[81].

2.2 Computer-Aided Imaging System

The CAIS performs the following steps to produce a BIRADS score (1–5) for the ultrasound image of an unknown mass:

1. Pre-process the unknown ultrasound image to reduce speckle and enhance the borders.
2. Segment the margins of the unknown mass from surrounding structures.

3. Measure the nine features.
4. Compute Relative Similarity to compare the unknown mass to the template database with known findings.
5. Retrieve and display the seven most similar masses.
6. Compute and display the BIRADS score.

Details of each of steps and the procedures to optimize them are described in the companion paper in this volume. The combinations of object features measured in step 3.) above may be represented by an N-dimensional vector **P** used to calculate the "Relative Similarity," **R**, of one lesion to another,

$$\overline{R} = \left(\sum_{k=1}^{L} \left(p_k^t - P_k^t \right)^s \cdot \omega_k \right)^{1/s} \quad (1)$$

A new case with an "unknown" finding is compared directly to the database of stored images and a measure of **R** is computed for different benign and malignant lesions. Similarity is calculated for a particular lesion $\mathbf{P}_{it}$ (the index of this "template" object) compared to the other lesions, $\mathbf{P}_k$ (k=1…L), where L is the number of objects, s is the number of features, although other distance measures may be applied. Figure 2 (below) illustrates this method for a complex cyst compared to a collection of different breast masses. The term Relative Similarity means that the detected lesion is compared not to a hypothetical "golden template" (or "perfect" model) of the disease but rather to the database of previously analyzed patients and the cases most "similar" to the unknown suspicious mass are automatically retrieved and displayed. Only the lesion portion of the stored image that is most similar to the unknown is initially retrieved, so performance is nearly instantaneous. In a previous study Relative Similarity performed significantly better that a feed-forward backpropagation artificial neural network so it was incorporated in the CAIS for this diagnostic study.

3. RESULTS

Four sub-specialty radiologists independently reviewed the US images, provided a BIRADS category score, and were asked to indicate what mass features were depicted in the image following the BIRADS lexicon. Although it was not a part of this study, for future use they were also asked to decide whether to biopsy the mass or not. ROC area results (A_Z in Table 1) between the radiologists were not significantly different and were similar to those reported elsewhere. Although the values of A_Z are comparable, the shapes of the ROC curves are different (Figure 3) and it is interesting to

review the intra-radiologist variability in the traditional measures of performance in Table 1. For the CAIS, A_Z (0.96±0.02) was significantly higher than the radiologists with statistical power of 93%. Radiologists 1 and 3 have comparable results to each other but differ from Radiologists 2 and 4, who appear similar to each other. Further study in the final stage of development is needed to determine the relevance of these inter-reader differences.

Figure 2. Comparison of segmented unknown mass to those most similar.

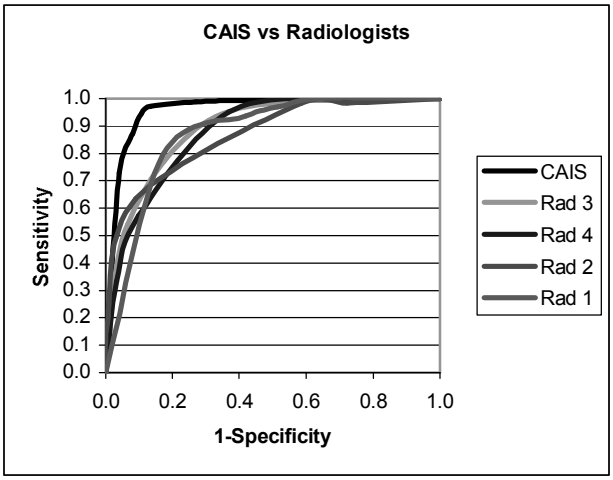

Figure 3. ROC curves for CAIS and Radiologists.

Table 1. CAIS compared to radiologists.

	A_Z	Sensitivity	Specificity	PPV	NPV	Diagnostic efficiency
CAIS	0.96 ±0.02	87.8%	97.3%	90.3%	96.5%	95.2%
Rad1	0.86* ±0.03	93.7%	57.9%	48.0%	95.7%	68.4%
Rad2	0.85* ±0.03	63.5%	90.8%	74.1%	85.7%	82.8%
Rad3	0.87* ±0.03	92.1%	69.1%	55.2%	95.5%	75.8%
Rad4	0.86* ±0.03	57.1%	90.1%	70.6%	83.5%	80.5%

*$p<0.02$ compared to CAIS

4. CONCLUSIONS

The results of this study indicate the performance of the CAIS in a "stand alone" mode is very good in comparison to four experienced radiologists. The success of optimization and the apparent diagnostic performance of this study suggest that the CAIS may be ready to test in a more rigorous clinical environment once the work on the user interface is complete.

We appreciate that in the heat of everyday clinical duties the radiologist is faced with a decision-making task during interpretation of breast ultrasound that is influenced by many factors, not all of which were included in this study. Nonetheless, the diagnostic results of the optimized CAIS classifier using Relative Similarity represent a very high performance exceeding our specified goals.

The next phase of research is to examine how the use of CAIS may impact performance of the radiologists, which will incorporate the subjective clinical factors mentioned above. That is, we proposed to allow the same group of radiologists to utilize the CAIS while interpreting a new set of cases on their own PACS workstation. We will then measure changes in their respective sensitivity and specificity measure inter-reader variability with the statistic kappa. With our clinic's cancer rate we will detect a 5% change in specificity (70–75%) as well as a 10% change in sensitivity (80–90%) with 80% statistical power using a study population of ~580 subjects in a paired two-tailed test[7,8]. Research after this stage will involve assessing

the impact on decision-making by radiologists (for example, biopsy or not) in a true prospective manner, which will constitute a full clinical trial of the final CAIS.

Recent reports continue to demonstrate that radiologists interpret breast ultrasound differently in clinical practice although the potential for accuracy is high. Kolb, et al.,[4] reviewed 11,130 asymptomatic women and found that screening ultrasound in those with dense breasts increased the number of non-palpable invasive cancers by 42%. Overall, ultrasound had 75% sensitivity, 97% specificity, 99.7% NPV, 20.5% PPV and 97% accuracy. We suggest that improvement in performance and standardization may be accomplished by applying the objective analysis of CAIS.

REFERENCES

1. A.T. Stavros, D. Thickman, C.L. Rapp, M.A. Dennis, S.H. Parker, G.A. Sisney, "Solid Breast Nodules: Use of Sonography to Distinguish between Benign and Malignant Lesions," Radiology 196, pp. 123–134, 1995.
2. American College of Radiology: ACR Standards 2000–2001. Reston, VA: American College of Radiology, 2000.
3. T.M. Kolb, J. Lichy, J.H. Newhouse, "Comparison of the performance of screening mammography, physical examination, and breast US and evaluation of factors that influence them: An analysis of 27,825 patient evaluations", Radiology 225:165–175, 2002.
4. A.S. Hong, E.L. Rosen, M.S. Soo, J.A. Baker, "BI-RADS of sonography: Positive and negative predictive values of sonographic features," AJR 184:1260, 2005.
5. M.P. André, M. Galperin, L.K. Olson, et al.: "Improving the accuracy of diagnostic breast ultrasound," Acoustical Imaging 26:453–460, 2002.
6. M.P. André, M. Galperin, C.T. Green, L. Olson, "A Case-Based Reasoning System to Aid Interpretation of Breast Ultrasound Images", SPIE Medical Imaging 5749, 2003.
7. J.A. Hanley, B.J. McNeil, "A method of comparing the areas under receiver operator characteristic curves derived from the same cases," Radiology 148, 839–843 (1983).
8. R.L. Lieber, "Statistical significance and statistical power in hypothesis testing," J Orthopedic Res 8(2), 304–309, 1989.

CLINICAL EXPERIMENTATION OF FEMMINA* AND RULES+ FOR PROSTATE AND BREAST TUMOR DETECTION

(Fast Echographic Multi parameters Multi Image Novel Apparatus)

+(Radiofrequency Ultrasonic Local Estimators)*

L. Masotti, E. Biagi, S. Granchi, D. Bini, F. Ceccarelli, A. Luddi, E. Magrini
Ultrasonic and Non-Destructive Testing Lab, Dept. of Electronics and Telecommunications, Via S. Marta 3, 50 139 Firenze, Italy

Abstract: An echographic method for differentiating pathological regions in biological tissue is presented. The method, named RULES, permits to extract spectral parameters related to the organization and mechanical properties of investigated tissue. The results for breast tumor detection and characterization will be presented in this work together with the results coming from the clinical experimentation on prostate to guide the bioptical sampling

Key words: spectral analysis, breast cancer, prostate cancer, tissue characterization, radio frequency, wavelet

1. INTRODUCTION

An echographic method for investigating biological tissue structure was proposed by the authors two years ago. The method, named RULES, is based on radiofrequency (RF) echographic signal processing. It permits to extract spectral parameters related to the organization and mechanical properties of investigated tissue. Spectral images are produced through a processing procedure, based on a statistical analysis of Local Estimators (LES). They are calculated from the spectral coefficients of Discrete Wavelet Packet Transform. By defining "CONFIGURATION" as a particular set of the LES statistical parameters, a number of possible

M.P. André (ed.), Acoustical Imaging, 349–357.

"CONFIGURATIONS" can be defined for the tissue under test. Image portions, characterized by the same "CONFIGURATION" are considered homogeneous. At this point, the histological analysis of the investigated region allows giving a biological meaning to the concept of "CONFIGURATION", by identifying the nature of these homogeneous portions. A learning procedure permits to establish the number of meaningful "CONFIGURATIONS" related to nature and state/type of a tissue. A hardware-software platform, FEMMINA, dedicated to real-time signal and image processing of continuous sequences of RF frames was employed to support RULES. The results presented in this work, concerning prostate and breast, have demonstrated the RULES capability to differentiate tissue structural organizations by typical "CONFIGURATIONS". Moreover the experimentation demonstrated that for different patients the same pathology was detected by the same "CONFIGURATION". These important results, coming from a continuous RULES refining with the comparison of the histological findings, give to RULES general effectiveness.

2. INVESTIGATION METHOD

The ultrasonic signal collected by the receiving transducer surface appears as a set of wavelet echoes, mutually overlapped of different amplitude. This received signal is named radiofrequency (RF), or "raw" signal. Amplitude and phase information are contained in the RF echo signal[4–7]; amplitude information is related to the mechanical impedance values (density, elastic characteristics) of the backscattering medium, and to ratio of the agglomerations sizes with respect to the wavelength. Phase information, related to the interferences, depends on mutual distances and geometrical organization of the tissue microstructure scatterers. These interferences and reflectivity variations in the time domain are responsible for spectral amplitude modulation in the frequency domain. Furthermore, the non-linear interactions modify the spectral content. As a consequence, the entire band preservation of the RF signal is essential to "read" this amplitude spectrum shape, in order to gain further information for tissue characterization and differentiation purposes. Tissue imaging based on the signal envelope extraction, which partially destroys the information contained in the RF echo signal, can appear lacking in details for tissue characterization.

In this scenario, we proposed the method RULES[1,2,3,8,9] for real time differentiation of the "in vivo" biological tissue type and its status. RULES is a method able to provide a detailed description of the RF signal spectral content for gaining tissue local microstructure information.

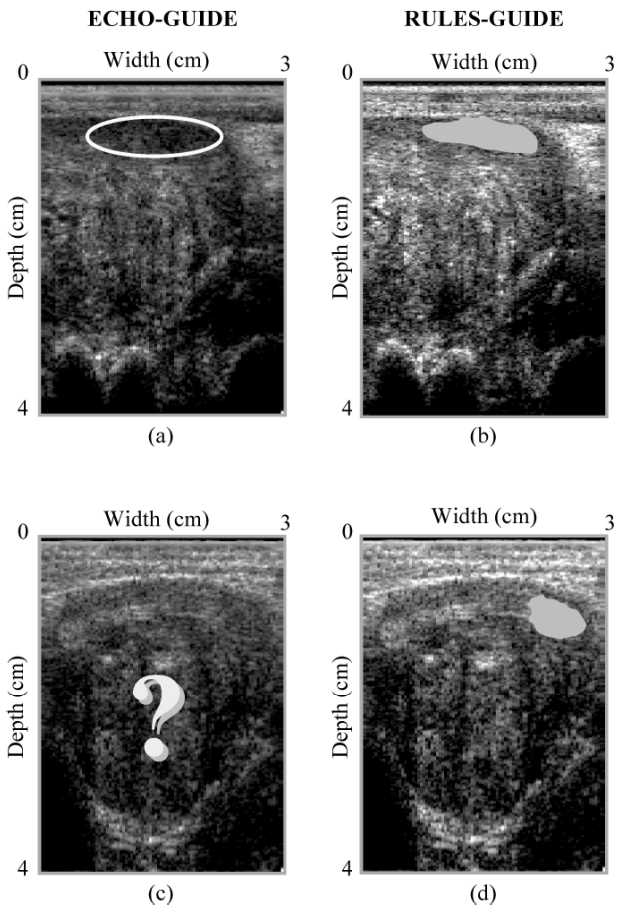

Figure 1. Echographic sections of two different case of prostatic cancer (a), (c). In Fig. (a) tumor appears as an hypoechogenic area and it is detectable by a traditional echography, but in Fig. (c) and (d), cancer exhibits isoechogenic characteristics and it is difficult to be distinguished from the surrounding prostatic tissue. (b) and (d) show shaded regions detected as cancer in (a) and (c) respectively, by the RULES procedure.

In Fig. 1(b) and in Fig. 1(d) tumoral areas, detected by RULES procedure, are presented with grey level code superposition on echographic sections. Biological tissue can be seen as an agglomeration of non-regularly located scatterers, which generate non-stationary, signals[10]. Consequently, the spectral content of the transmitted signal is locally modified and a Time-Frequency Representation (TFR) is required. After evaluating several kind of TFRs, Wavelet Transform is resulted the most suitable for ultrasonic radiofrequency processing, thanks to the good trade off between time and frequency localization and the flexible selection of decomposition basis set[11,12]. The choice of the decomposition basis set, which is constituted by

dilatations and translations of the Mother Wavelet, allowed to employ a wavelet whose shape has a high correlation degree with ultrasonic RF signal back propagated by biological tissue. In order to reduce the computational load without compromising the results quality, the Discrete Wavelet Packets Transform (DWPT)[13] was adopted. This permits an adaptable subdivision of the entire signal spectral band and can be implemented by means of a simple filter cascade. In order to guarantee a high image production rate, DWPT was realized by means of a parallel architecture of the Mallat algorithm,[11] based on the equivalent filters concepts. In this work, the third decomposition level without decimation was chosen, as the best compromise between time and frequency resolution.

The first step of RULES is the acquisition of the RF echographic frames. Each RF track is decomposed in eight bands, derived from the third decomposition level, and eight sets of DWPT coefficients are produced. RULES allows to perform a tissue local characterization because, for each time instant, i.e. depth in the tissue, the eight DWPT coefficients were interpolated by means of a 4th order polynomial. The polynomial coefficients a_0 , a_1 , a_2 , a_3 , a_4 , are used as Local EStimators (LES). For each RF frame, five LES matrixes were calculated. An appropriate rectangular window, which constitutes method spatial resolution cell, is chosen. The window is translated step by step over all the LES matrixes, in order to extract, for each step, the LES histograms. The next processing step leads to the individuation of those RF frame portions, which exhibit similar histogram characteristics for the same Local Estimator. For each LES histogram, similarity criteria are formulated with respect to: most populated classes, occurrence of samples, standard deviation and shape indexes[2]. By defining "CONFIGURATION" a particular set of these statistical parameters, for the five LES, a number of possible "CONFIGURATIONS" can be defined for the under test tissue. Image portions, characterized by the same "CONFIGURATION" are considered homogeneous. The histological analysis of the investigated region allows, first of all, to give a biological meaning to the concept of "CONFIGURATION", by identifying the nature of these homogeneous portions[1,9]. Learning procedure permits to establish the number of meaningful "CONFIGURATIONS" related to nature of a tissue.

The last step of RULES concerns the results visualization. For each recognized "CONFIGURATION" a chromatic or grey code was superposed to the conventional B-Mode image; the different chromatic codes appear in correspondence of different homogeneous areas with histological significance.

3. RESULTS

The experimental laboratory and clinical setup systems are constituted by FEMMINA platform connected to commercial echographs (MEGAS or TECHNOS Ecographs Esaote S.p.A) through a 1 Gbit/s optical fiber link. A 7.5 MHz central frequency ESAOTE linear array probe was employed for both breast and prostate.

In order to reach a high production rate of processed data, we chose to implement the DWPT through a parallel architecture by using a proprietary spectral processing board[14,15] capable of performing FIR digital filtering in real-time with clock frequencies up to 106 MHz and 64x2 16 bit taps.

This electronic board can be programmed to apply up to 32 different filters on the same input signal. Different Wavelet Mother functions were tested. The FEMMINA spectral processing board decomposes every RF signal in eight (third decomposition level) bands. These bands cover the entire spectral width of the echographic signal. The eight sequences of the DWPT coefficients are then transferred to the personal computer completely integrated in the platform, for the successive processing.

The first results concern the prostate. The results obtained from "in vitro" experimental phase guided the method towards the clinical validation phase. The objective was to distinguish Benign Prostatic Hyperplasia (BPH) from cancer with high sensitivity and specificity. The RULES results from the "in vitro" experimentation on 60 cases (375 scan planes) of adenocarcinoma demonstrated, supported by histological analysis, a specificity of 91% and a sensitivity of 93%[16].

Table 1. RULES results (RULES guide) compared with histological findings and TRUSP (TRransrectal UltraSonography of Prostate) detection (echo-guide).

Case number	Histology	Trusp	Rules
17	POSITIVE	POSITIVE	POSITIVE
4	POSITIVE	NEGATIVE	POSITIVE
25	NEGATIVE	NEGATIVE	NEGATIVE
13	NEGATIVE	POSITIVE	NEGATIVE
1	POSITIVE	POSITIVE	NEGATIVE
3	NEGATIVE	POSITIVE	POSITIVE

RULES clinical experimentation on prostate was performed "in vivo" on 63 patients (with mean age of 66 years) undergone to biopsy sampling. Total PSA (Prostatic Specific Antigen) range was included between 1 and 28.7 (mean value of 8). Data acquisition and RULES elaborations were carried out during the examination and the results compared with histological tests.

Traditional method for guiding biopsy sampling on prostatic gland is represented by TRUS (TransRectal Ultra Sonography), which in many cases results to be inefficient such as for isoechogenic and hyperechogenic cancer, as shown in Fig. 1, where two different cases of prostatic cancer are reported. In Fig. 1(a) tumor appears as a hypoechogenic areas and it is easily detectable by TRUS; while in Fig. 1(c), cancer exhibits isoechogenic characteristics and it is difficult to be distinguished from surrounding prostatic tissue. By employing RULES procedure tumoral areas were correctly detected in both cases as shown in Fig. 1(b) and in Fig. 1(d).

In table 1 the results obtained from all the analysed cases, comparing RULES processed data (RULES-guide) and TRUS detection (Echo-guide) with histological findings is reported. Echo-guide and RULES processing correctly identified 17 positive cases and 25 negative cases at histological tests. Four positive cases and 13 negative cases at histological tests were not detected by TRUS while they were successfully detected by RULES. From these results RULES seems to be more sensitive and specific than traditional echographic technique.

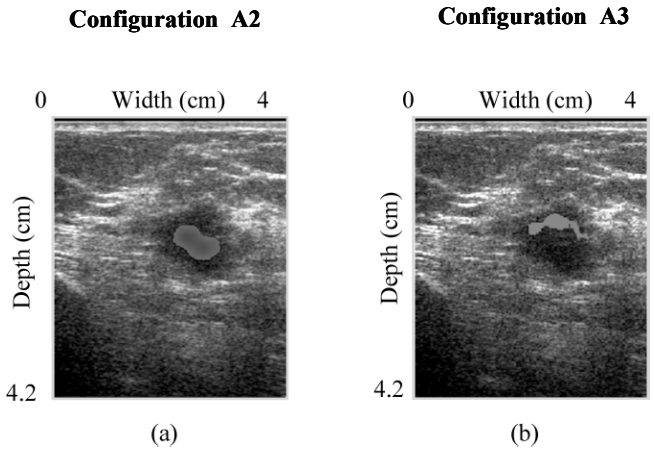

Figure 2. RULES results for breat carcinoma. In figure (a) is reported the carcinoma portion identified by the A2 CONFIGURATION while in (b) the portion individuated by the A3 CONFIGURATION.

By comparing RULES results (RULES-guide) with TRUSP (Echo-guide) RULES seems to be more sensitive and specific. It exhibits 95.5% of sensitivity and 92.7% of specificity while TRUS is characterized by a sensitivity of 72.7% and a specificity of 61%.

The other important “in vivo” experimentation was carried on breast tissue in order to differentiate and localize pathologies with RULES. The clinical validation aim of RULES was to verify its ability to detect

carcinoma. By considering that the breast carcinoma exhibits very heterogeneous tissue organization the RULES learning phase has led us to define five different CONFIGURATIONS for marking different types of carcinoma or inside the same pathological area different regions.

In Fig. 2(a) and in Fig. 2(b) is shown how two different RULES CONFIGURATIONS A2 and A3 mark two different regions of the same tumoral area.

The experimentation was performed in two phases, one learning phase, conducted on 44 patients (13 carcinoma and 31 benign nodules) and a clinical validation phase, carried on 73 patient (23 carcinoma and 50 benign nodules), producing sensitivity and specificity of 93% and 89% respectively. These values are calculated by referring to the all five CONFIGURATIONS.

4. CONCLUSIONS

In this work an investigation method, is described. It allows very interesting results for tissue differentiation and pathology detection.

Typical features of RULES[1], are the direct utilization of RF echo-signal, its capability to manage, the entire spectral content of the RF signal by using different Mother Wavelet in conjunction with different decomposition levels, and to adapt the LES combinations and their statistics to different kind of tissue characterization in dependence on the histological differentiation.

The results presented in this work, for what concerns the prostate and the breast, has demonstrated the RULES capability for individuating typical "CONFIGURATION" able to differentiate tissue structural organizations for each investigated organ. Moreover the experimentation demonstrated that for different patient the same pathology was detected by the same "CONFIGURATION". These important results, which give to RULES general effectiveness, are coming from a continuous refining of RULES with the histological findings comparison.

5. ACKNOWLEDGEMENTS

The authors are grateful to Prof. R. Ponchietti (Dept. of Urology, Univ. of Firenze), Prof. F. Gori (Dept. of Pathology, Univ. of Firenze), Prof. G. Martorana (Dept. of Urology, Univ. of Bologna), Prof. C. Del Favero (Dept. of Radiology, Valduce Hospital of Como) Prof.E. Cassano (European Institute of Oncology of Milano).

This work was partially supported by Bracco Research of Italy.

REFERENCES

1. Masotti, E. Biagi, L. Breschi, S. Granchi, F. Di Lorenzo, E. Magrini, "Tissue dopifferentiation based on radiofrequency echographic signal local spectral content (RULES: Radiofrequency Ultrasonic Local Estimator)," *in Proc. IEEE Ultrason. Symp.*, **1**, 1030–1033, (2003).
2. E. Biagi, L. Breschi, S. Granchi, L. Masotti, "Metodo e dispositivo perfezionati per l'analisi spettrale locale di un segnale ecografico," Italian Patent FI2003A000254, date of filing: Oct. 8, (2003).
3. E. Biagi, L. Breschi, S. Granchi, L. Masotti, "Method and device for spectral analysis of an echographic signal," Italian Patent FI2002A34, date of filing: Feb. 27, (2002), European Patent 03425118.1, date of filing: Feb. 25, (2003), U.S. Patent 10/383674, date of filing: Feb. 25, (2003).
4. M. Scabia, E. Biagi, L. Masotti, "Hardware and software platform for real-time processing and visualization of echographic RF signals," *IEEE Trans. Ultrason., Ferroelect., Freq. Contr.*, **49**(10), 1444–1452, (2002).
5. G. Schmitz, H. Ermert, T. Senge, "Tissue characterization of the prostate using radio frequency ultrasonic signals," *IEEE Trans. Ultrason. Ferroelect. Freq. Contr.*, **46**,126–138, (1999).
6. K.D. Donohue, L. Huang, T. Burks, F. Forsberg, C.W. Piccoli, "Tissue classification with generalized spectrum parameters", *Ultrasound Med Biol*, **27**, 1505–1514, (2001).
7. F.L. Lizzi, D.L. King, M.C. Rorke, J. Hui, M. Ostromolgisky, M.M. Yaremenko, E.J. Feleppa, P. Wai, "Relationship of ultrasonic spectral parameters to features of tissue microstructure", *IEEE Trans. Ultrason. Ferroelect. Freq. Contr.*, **34**, 319–329, 1987.
8. E. Biagi, M. Calzolai, S. Granchi, L. Masotti, M. Scabia, "Real-time processing of the radiofrequency ultrasonic echo signal for on-line spectral maps," *in Proc. 24th Int. Symp. Acoust. Imaging*, **24**, 95–100, (2000).
9. L. Masotti, E. Biagi, A. Acquafresca, L. Breschi, M. Calzolai, R. Facchini, A. Giombetti, S. Granchi, A. Ricci, M. Scabia, "Ultrasonic images of tissue local power spectrum by means of wavelet packets for prostate cancer detection," *in Proc. 26th Int. Symp. Acoust. Imaging*, **26**, 97–104, (2002).
10. G. Georgiou, F.S. Cohen "Tissue characterization using the continuous Wavelet transform part I: decomposition method," *IEEE Trans. Ultrason. Ferroelect. Freq. Contr.*, **48**, 355–363, (2001).
11. I. Daubechies, "Ten lectures on Wavelets," in Cbms-Nsf Regional Conference Series in Applied Mathematics, *Society for Industrial and Applied Mathematics*, Philadelphia, **61**, (1992).
12. S. Mallat, "A theory for multiresolution signal decomposition: The Wavelet representation," *IEEE Trans. Pattern. Anal. Machine Intell.*, **11**(7), 674–693, (1989).
13. M.V. Wickerhauser, "Lectures on wavelet packet algorithms," Technical report, Department of mathematics, Washington University, St. Louis, MO, (1991).
14. E. Biagi, M. Calzolai, S. Granchi, L. Masotti, M. Scabia, "Real-time processing of the radiofrequency ultrasonic echo signal for on-line spectral maps," *in Proc. 24th Int. Symp. Acoust. Imaging* , **24**, 95–100, (2000).
15. L. Masotti, E. Biagi, M. Cerofolini, A. Bertini, M. Calzolai, A. Bigagli, L. Galardi, C. Giovannucci, "Method for enhancing the diagnostic power of ultrasonic scanning system by using real time spectral maps, and device operating by said method," U.S. Patent 6 066 098, May 23, (2000).

16. L.Masotti, E. Biagi, S. Granchi, L. Breschi, E. Magrini, F. Di Lorenzo "Clinical test of Rules", *in 2004 IEEE Trans. Ultrason. Ferroelect. Freq. Contr.*, Joint 50th Anniversary Conference, 2173–2176, (2004).

NON-DESTRUCTIVE EVALUATION

MEASUREMENTS OF PARAMETERS OF LEAKY WAVES USING ULTRASONIC MATERIAL CHARACTERIZATION SYSTEM WITH ELECTRONIC SCANNING

R.Gr. Maev, S.A. Titov
University of Windsor, Windsor, N9B 3P4, Canadna; Institute of Biochemical Physics of RAS, 4 Kosygin St., Moscow, 119991, Russia

Abstract: In this paper, we present an ultrasonic material characterization system with electronic scanning. In this system, leaky acoustic waves are generated by a single transducer whose focus is located at the water-specimen interface, and the spatial field distribution of the reflected wave is recorded by a linear array of receiving transducers. The relative position of the transmitting transducer and the receiving linear array is constant in this experimental setup, and the measurement time is only limited by the time of the wave propagation and speed of the electronic data acquisition system. The parameters of the leaky waves can be obtained by processing the set of the output waveforms

Key words: material characterization; leaky acoustic wave; linear array; mechanical and electronic scanning

1. INTRODUCTION

Recently, many methods have been proposed for quantitative material characterization[1]. In typical measurement scheme, the output voltage of the transducer is recorded as a function of time and relative position of the transducer and the specimen. The velocity and attenuation of the leaky surface acoustic waves can be obtained from the output spatio–temporal data. The experimental arrangements with longitudinal movement of the transducer (the V(z) scheme[2–5]) and lateral translation of the receiving

M.P. André (ed.), Acoustical Imaging, 361–366.

transducer (the V(x) scheme[6–8]) are well known systems. However, the mechanical scanning of the transducer is associated with slow data acquisition, and precision mechanics is required.

In this paper, we consider an ultrasonic material characterization system with electronic scanning. In the system, an unmovable array is used for receiving of leaky waves, which propagate along the specimen–immersion liquid interface under investigation.

2. RAY MODEL OF THE SYSTEM

The ray model of the ultrasonic system is shown in Fig. 1. Suppose the leaky wave propagates along B_1B_2 leaking into upper liquid half–space at the critical angle θ_R. This wave is received by the ultrasonic array having pitch p. The array is tilted at the angle θ_0, and only two of the neighboring elements of the array with centers O_1 and O_2 are shown in Fig. 1.

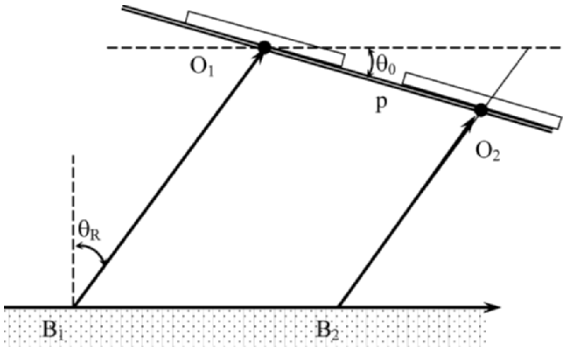

Figure 1. Ray model of the system.

The relative time delay Δt between responses of the leaky wave, received by these two neighbor elements of the array, is related to the critical angle θ_R by the following equation:

$$\Delta t = \frac{p}{C}\sin(\theta_R - \vartheta_0) \tag{1}$$

where C is the sound velocity in the liquid. Using the measured value of Δt, the phase velocity of the non dispersive leaky wave C_R can be calculated according to Snell's law:

$$C_R = \frac{C}{\sin\theta_R} \tag{2}$$

For a particular frequency f_0, the amplitude ratio of the responses of the neighbor elements η can be written as:

$$\eta = \frac{A_2}{A_1} = \frac{\exp(-\alpha \cdot B_1B_2 - \alpha_w \cdot B_2O_2)}{\exp(-\alpha_w \cdot B_1O_1)} \tag{3}$$

where α_w, and α are the attenuation factors of the longitudinal wave in the immersion liquid and the leaky wave, respectively.

$$\eta = \exp\{(-\alpha \cdot \cos(\theta_0 - \theta_R) + \alpha_w \cdot \sin\theta_0) \cdot \frac{p}{\cos\theta_R}\} \tag{4}$$

Using the handbook value of α_w, the critical angle θ_R determined according to Eq. (2), and the measured amplitude ratio η, the attenuation factor of the leaky wave α can be obtained by solving this equation.

3. EXPERIMENT

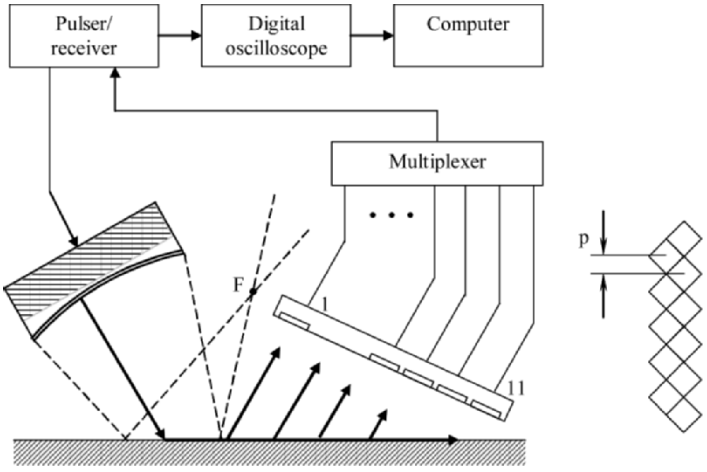

Figure 2. Experimental setup.

The experimental setup is shown in Fig. 2. A leaky wave is generated along the water–specimen interface by a single spherically focused transducer (IS-HR-1/4–20, Xactec Inc., USA). The central frequency of the transducer is 20 MHz, the diameter and focal distances are 6 and 19 mm, respectively. The receiving array consists of 11 identical 1.25 mm square elements located in a zigzag manner as shown in the picture. The pitch of the array is 0.884 mm and the array is tilted at an angle of θ_0=27°.

Relative positions of the array, transmitting transducer and specimen are adjusted in such a way that the wave directly reflected from the interface propagates aside of the array and responses of the array elements are entirely produced by the leaky wave. A standard ultrasonic pulse/receiver with an analog multiplexer are used for acquisition of the output waveforms $V_n(t)$, where n=1…11 is channel number.

Several materials with known properties were tested using this experimental setup. The $V_n(t)$ data recorded for fused quartz, and aluminum alloy are shown in Fig. 3 as grayscale images and waterfall plots. In the graphs, the vertical axes represent the time t, whereas the horizontal axes correspond to the channel number n.

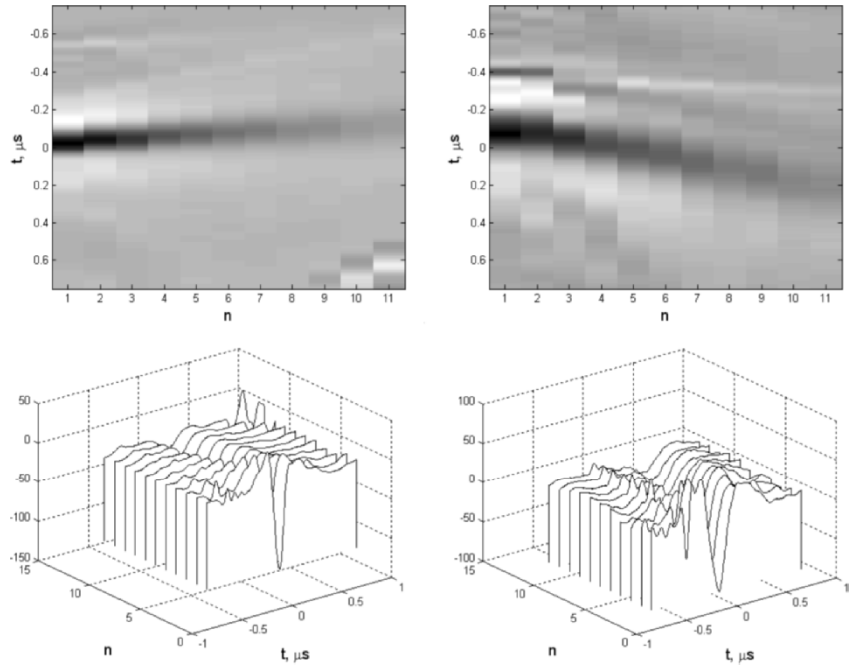

Figure 3. Output waveforms Vn(t) recorded for fused quartz (left) and aluminum alloy (right) presented as grayscale images (upper pictures) and waterfall plots (bottom graphs).

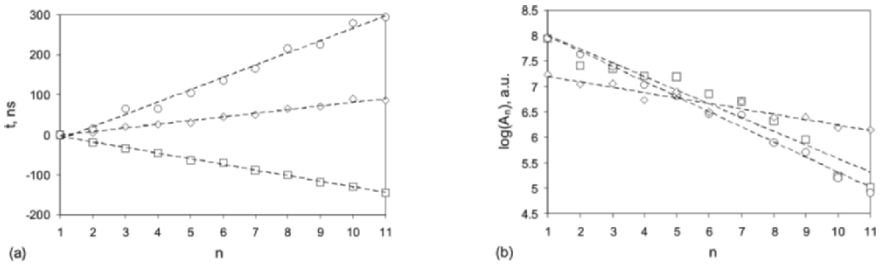

Figure 4. The time of flight (a) and spectral magnitude (b) vs. the channel number n; (o – fused quartz, ◊ – steel, □ – aluminum alloy).

The number of the elements of the array is small (n=11), therefore the discrete structure of the images is quite evident. The slopes and decaying rates of the responses vary between the tested specimens. These responses are produced by the leaky Rayleigh waves and their behavior depends on the elastic properties of the materials.

To measure the velocity of the leaky wave, the time delay t of the negative peak of wave R was determined as a function of n (Fig. 4(a)). The average value of Δt was then calculated, and the velocity C_R was found according to Eqs. (1)–(2) for each material. To estimate the attenuation of the leaky wave, the spectra of the recorded waveforms $S_n(f)$ were calculated first. Then, for a particular frequency f_0=4 MHz, the average value of η was estimated based on the decay of the spectral magnitudes $A_n=|S_n(f_0)|$ with increasing channel number n (Fig. 4(b)). Finally, the attenuation factor of the leaky wave α was found by solving Eq. (4).

4. RESULTS AND DISCUSSION

The values of the velocity C_R and attenuation factor α measured for the test specimens by the proposed ultrasonic material characterization system are summarized in Table 1.

Table 1. Measured and calculated leaky Rayleigh wave parameters.

Material	C_R, m/s	α, 1/mm (f_0=4 MHz)	C_{Rcal}, m/s	α_{cal}, 1/mm (f_0=4 MHz)
Fused quartz	3430	0.30	3426	0.282
Steel	3173	0.10	3163	0.077
Aluminum alloy	2973	0.27	2960	0.235

The leaky Rayleigh wave velocity and attenuation were also calculated from the location of the pole of the reflectance function. To calculate the reflectance function, the velocity of the longitudinal and shear waves were measured for the particular material used in the experiment. The measurement of the bulk wave velocities was conducted according to the ordinary pulse–echo method.

Comparison of measured and calculated values of leaky wave parameters shows a satisfactory agreement, however the attenuation factors obtained by the proposed method are slightly larger than the calculated values because of additional attenuation of ultrasound in a material and diffraction.

REFERENCES

1. A. Briggs, *Acoustic Microscopy* (Clarendon Press, Oxford, 1992).
2. K.K. Liang, G.S. Kino, and B.T. Khuri–Yakub, Material characterization by the inversion of V(z), *IEEE Trans. Sonics and Ultrasonics*, **SU–32**, 213–224 (1985).
3. J. Kushibiki, and N. Chubachi, Material characterization by line–focus–beam acoustic microscope, *IEEE Trans. Sonics and Ultrasonics,* **SU–32**, 189–212 (1985).
4. M.-H. Nadal, P. Lebrun, and C. Gondard, Prediction of the impulse response of materials using a SAM technique in the MHz frequency range with a lensless cylindrical-focused transducer, *Ultrasonics*, **36**, 505–512 (1998).
5. N. Nakaso, K. Ohira, M. Yanaka, and Y. Tsukahara, Measurement of acoustic reflection coefficients by an ultrasonic microspectrometer, *IEEE Trans. Ultrason. Ferroelec. Freq. Contr*., **41**(4), 494–502 (1994).
6. O.I. Lobkis, and D.E. Chimenti, Three–dimensional transducer voltage in anisotropic materials characterization, *J. Acoust. Soc. Amer*., **106**(1), 36–45 (1999).
7. S. Titov, R. Maev, and A. Bogatchenkov. Wide–Aperture, Line–focused Ultrasonic Material Characterization System Based on Lateral Scanning. *IEEE Trans. Ultrason., Ferroelec. Freq. Cont.*, **50**(8), 1046–1056 (2003).
8. M. Pluta, M. Schubert, J. Jahny, and W. Grill, Angular spectrum approach for the computation of group and phase velocity surface of acoustic waves in anisotropic materials, *Ultrasonics*, **38,** 232–236 (2000).

ACOUSTIC IMAGING OF MICROSTRUCTURE AND EVALUATION OF THE ADHESIVE'S PHYSICAL, MECHANICAL AND CHEMICAL PROPERTIES CHANGES AT DIFFERENT CURE STATES

I.A. Severina, A.J. Fabre, E.Yu. Maeva
Centre of Imaging Research and Advanced Material Characterization, University of Windsor, 401 Sunset ave., Windsor, ON, N9B 3P4, Canada

Abstract: Epoxy thermoset adhesives transform during cure from liquid state into the highly cross-linked solid. Cure state of the material depends on condition of the reaction (temperature, pressure, time etc.) and resin/hardener ratio. It is known that the cure degree of the adhesive correlates with adhesion strength, which is critical for structural adhesives used in automotive, aerospace and marine industries. In this work, characterization of cure process of the adhesive with acoustic methods is presented. Evolution of the acoustic and elastic properties (attenuation, sound velocity, density, elastic moduli) during cure reaction was monitored in relation to the substantial physical and chemical changes of the material. These macro parameters of the adhesive were compared with the material's microstructure obtained by high-resolution acoustic microscopy technique in frequencies range of 50–400 MHz. Development of the microstructure of the adhesive as it cures at different conditions has been investigated. Appearance and development of the granular structure on the adhesive interface during cure reaction has been demonstrated. Acoustic images were analyzed by mathematical method to quantitatively characterize distribution of the adhesive's components. Statistical analysis of such images provides an accurate quantitative measure of the degree of cure of such samples. Research results presented in this paper can be useful as a basis for non-destructive evaluation of the adhesive materials

Key words: adhesives; cure monitoring; cure state; acoustic properties; acoustic microscopy

M.P. André (ed.), Acoustical Imaging, 367–374.

1. INTRODUCTION

Adhesive bonding is now accepted in automotive and aerospace industries as a new "classic" joining technique. It has been proven that new structural adhesive bonding can provide high volume assemblies with greater stiffness and better crash performance. Today, non-destructive evaluation of adhesive bond joints is routinely used in the aerospace industry, and its use is growing in automotive and other industries[1]. Ultrasonic methods these days are the most popular NDT technique for use on adhesive joints. Unfortunately, even new generation of high tech NDT instrumentation provides mostly qualitative interpretation when it comes to adhesives bonds. It is still difficult or impossible to determine quantitatively how strong a bond is. The most difficult defects to detect are those related to improper curing.

Evaluation of the cure state of the adhesive and monitoring of cure reaction are key points in studying the adhesive curing process and in improvement of efficiency of polymer processing, in quality assurance. Knowledge of the degree of cure is extremely important with respect to the final cohesive properties that joint is expected to have. A partially cured or incompletely cured adhesive may still contain unreacted compounds that can result in reduced bond strength and poor joint durability. These unreacted compounds can also be a source of contamination in that they can migrate out of the "cured" adhesive over time.

The structural characteristics of polymers like molecular weight, composition of polymer, and crosslink density affect the physical properties of adhesives, which can be represented by glass transition temperature Tg, melting or softening point. The glass transition indicates a transformation of the polymer from a glassy to a rubbery state. As the temperature of the adhesive is raised above its Tg, modification of the material's structure leads to an increase in the effective distance between molecular segments. Glass transition temperature is a very useful physical property measurement that reflects the behavior of polymers in adhesive systems. Also, cure state affects acoustic properties of the material, elastic module and viscosity.

Although the ultrasonic wave propagation is a well-known technique for nondestructive analysis, its application as an analytic technique for measurements of dynamic mechanical properties of polymers is mostly limited to laboratory studies[2–4].

The objective of this work was to evaluate the cure state of the thermoset epoxy-based adhesive with acoustic methods and to visualize development of adhesive microstructure during cure reaction.

2. EVALUATION OF ADHESIVE'S PROPERTIES DURING CURE

Commercial structural epoxy adhesive BETAMATE 1496 that is routinely used in the automotive industry was investigated. Cure monitoring experiments were performed using ultrasonic polymer characterization system in Characterization and Ultrasonic Sensor Group of Industrial Materials Institute (NRC Canada). Monitoring of the adhesive cure was achieved by following sound velocity and attenuation using ultrasonic pulse transmission mode at 2.5 MHz. Monitoring was performed at 120, 140, 160 and 180 ºC.

Isothermal monitoring of adhesive cure at different temperatures is presented in Fig. 1. Sound velocity increases in sigmoidal manner as the reaction proceeds reaching a plateau at the end of reaction. Curing regime (temperature and time of reaction) determine the kinetic and extent of the reaction of adhesive cure. To compare results obtained at different temperatures and evaluate cure state of the adhesive, these sound velocity values were adjusted to scale. Sound velocity of the completely cured adhesive at each specified temperature was accepted as 100% cured adhesive; sound velocity of the uncured adhesive extrapolated to corresponding temperature was taken as 0% of reaction extent. Increase of sound velocity represents dynamics of cure reaction. The slope of the curve increases rapidly with temperature. It takes 10 times longer (20 min. compared to 210) to reach full conversion of adhesive at 120 ºC than at 180 ºC.

Behavior of the acoustic parameters was studied for completely cured adhesive. Attenuation and longitudinal sound velocity as a function of temperature were investigated in 20–200 ºC range with 2 ºC/min. heating rate.

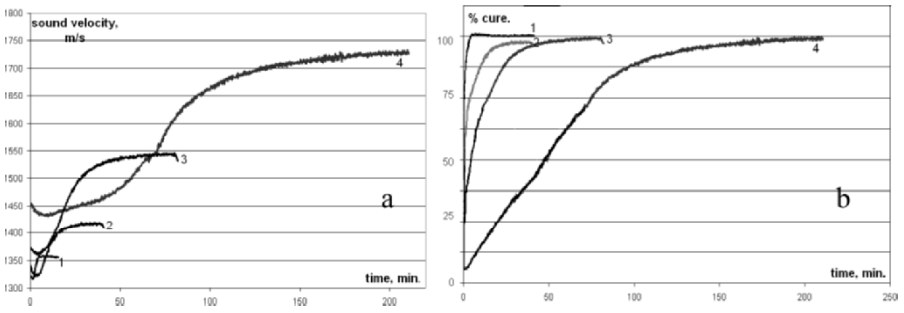

Figure 1. Isothermal cure monitoring of thermoset adhesive at different temperatures. Sound velocity (a) and cure degree (b) time dependence. Cure temperature: 1–180 ºC, 2–160 ºC, 3–140 ºC, 4–120 ºC.

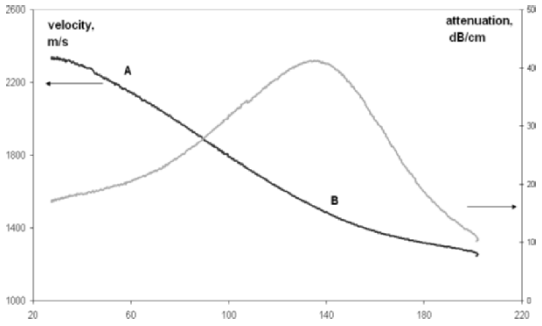

Figure 2. Dependence of acoustic parameters: sound velocity and attenuation of thermoset adhesive on temperature.

Data obtained are presented in Fig. 2. Longitudinal sound velocity decreases as the temperature rises. Attenuation increases to peak at 140 ºC and then decreases. Change of slope in some points indicates regions where transition in the material occurs. This is evident by an increase in the slope of the polymer's specific volume and longitudinal sound velocity as a function of temperature. We have observed two transitions in 25–220 ºC region. At the temperature 70 ºC, slopes of both specific volume and sound velocity (point A) curves are increased. Such behavior is typical to glass transition region. At approx. 160 ºC (point B), sound velocity continues to decrease with decreased slope while the attenuation curve has a well developed maximum indicating relaxation process at this point. It is necessary to note that loss tangent tan δ vs. temperature curve also shows its maximum at this region while specific volume increases monotonically. Maximum in attenuation and loss tangent usually refers to dynamic glass transition [5,6]. Existence of this relaxation at temperatures higher than Tg for epoxy system was also reported by others authors [7,8].

It was found that the dynamic glass transition (point B) is more sensitive to cure state of adhesive than the first one. This transition temperature value was measured as a function of cure degree, which was reached by heating the sample up to, and cooling down from successively increasing temperature and data is represented in Fig. 3. Initial uncured adhesive has a transition at 37 ºC. As the reaction proceeds, this parameter increases gradually until the cure temperature reaches approx. 130 ºC. Then, rapid increase was observed. At the end of cure, transition temperature was approx. 140–150 ºC. Maximal increase of dynamic transition temperature could relate to gelation point of cure. Therefore, transition reflects structural changes during cure of the adhesive and internally linked to the cohesive

properties of the adhesive joint. The value of glass transition temperature in the point A also increases

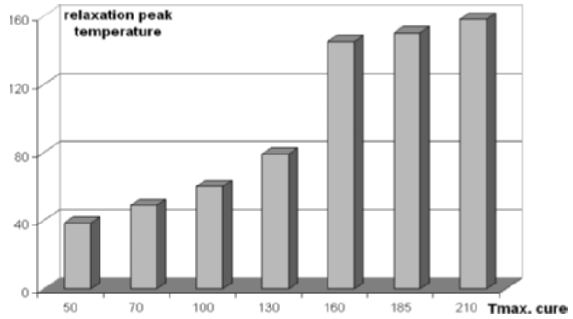

Figure 3. Changes in transition temperature during adhesive cure at elevated temperature.

but in a lesser range from 27 to 70 ºC. Moreover, this region is less expressed and Tg value can be determined with less precision. Acoustic properties (longitudinal sound velocity) of adhesive are linearly dependent on dynamic glass transition temperature value.

For evaluation of cure degree of adhesive in joints that have been cured, a sandwich-like structure, with the adhesive between two metal sheets was prepared. Specimens were cured 3 to 40 min. at the temperature 180 ºC. It is necessary to note that the regime recommended by the manufacturer to reach full cure for this type of adhesive is 30 min. at 180 ºC. Different cure degrees were reached by exposing the samples to selected temperature for different length of time. Longitudinal sound velocity of the adhesive was calculated and data are presented in Fig. 4 along with results of the tensile test. According to both graphs, full cure was reached after 20 min of the reaction. Higher velocity of the cured adhesive is related to stronger contact-three-dimensional network that increases adhesive rigidity and joint strength.

The results obtained show that acoustic measurement can provide information about cure state of the adhesive, its cohesive properties and estimate strength of the joint.

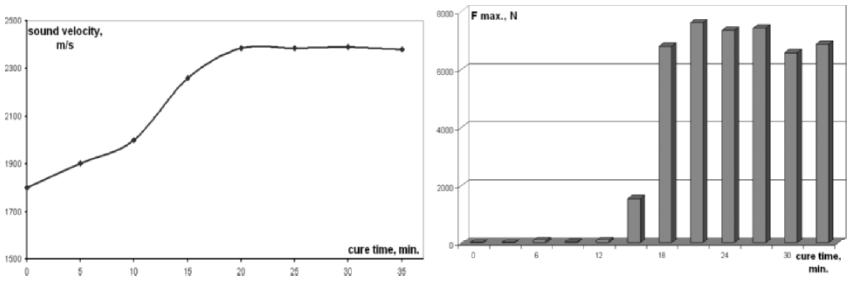

Figure 4. Longitudinal sound velocity changes in adhesive bond joints with cure time (left). Adhesion strength of the joints exposed to 180 ºC different time (right).

3. MICROSTRUCTURE IMAGING OF THE ADHESIVE INTERFACE

Differences in the material's properties can be visualized on the acoustic images of metal/adhesive interface. Twelve identical single lap joints were prepared. Each sample was cured separately for a different length of time, at constant temperature 180 ºC. Acoustic C-scan imaging was performed in reflection mode using Sonix HS-1000 scanning acoustic microscope. A 250 MHz focused transducer was used to produce an 8 bit image of a 1cm^2 region of each sample.

Reflection coefficient R at the interface and, correspondingly, pixel values of a C-scan image depend on the difference of the acoustic impedances Z_2 and Z_1 of two materials

$$I \propto \left(\frac{Z_2 - Z_1}{Z_2 + Z_1} \right) \tag{1}$$

Since the properties of the steel stay constant during the adhesive cure process, the variations in the reflection coefficient value are due to changes in acoustic impedances of the adhesive only. With regard to acoustic impedance definition, these changes are caused by modification in either density or sound velocity. Because shrinkage of the adhesive used is very low, we assume that all changes in acoustic impedance originate from sound velocity modifications. Fig. 5(a)–(c) demonstrates development of the microstructure in the epoxy adhesive/metal interface during cure at 180 ºC. Microstructure of the uncured material does not have a clearly expressed structure. After the material has been exposed to curing conditions, the interface image becomes more contrast; structure of the interface appears

and becomes completely developed by the end of the curing process (30 min.).

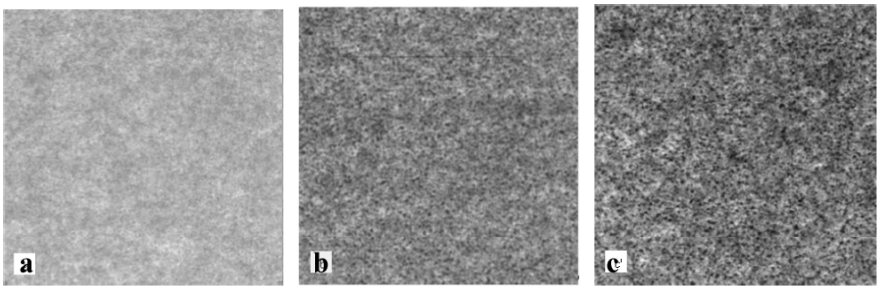

Figure 5. Development of the microstructure of metal-adhesive interface during cure at 180 ºC. Tessonics AM1103 acoustic microscope, 250 MHz. samples were cured for 0 (a), 10 (b) and 35 (c) min.

Each 500x500 pixel image was stored as a matrix in Octave, a software package primarily intended for numerical computations. Each matrix was decomposed into 100 matrices of equal dimensions. Properties such as the minimum value, minimum value, and mean value of the set of matrices were then calculated. Performing measurements on a set of smaller regions allows for the determination of many local maxima and minima which in turn enables one to calculate an error bound. The results were then averaged, producing a result representative of the entire 1cm^2 region. The minimum and maximum intensities of these images were compared. Fig. 6 clearly indicates a decrease in both properties during the curing process, as expected.

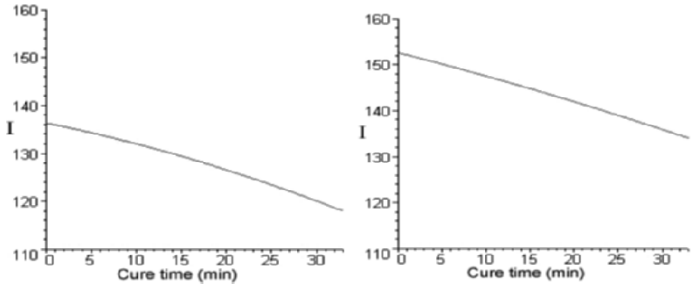

Figure 6. Minimum (left) and maximum (right) intensity as a function of cure time.

4. CONCLUSIONS

An ultrasound method was used for monitoring the cure reaction of thermoset epoxy-based adhesive. Kinetics and extent of the reaction depend on curing conditions (temperature, heating rate, time). Acoustic properties of the adhesive correlates with glass transition temperature that allows estimation of cohesive strength of the adhesive joint. Data obtained by acoustic method are in good correlation with destructive tests. This acoustic technique can be used for evaluating adhesive cure state in an industrial environment. Images of the adhesive/substrate interface reflect changes in properties of the adhesive during cure reaction.

5. ACKNOWLEDGEMENT

The authors are grateful to the Characterization and Ultrasonic Sensor Group, IMI NRC Canada and in particular to Dr. Jen for methodological help and possibility to use research facilities.

This project was supported by NSERC/DaimlerChrysler CRD Grant CRDPJ 263171-02.

REFERENCES

1. D.J. Hagemaier, Adhesive-bonded joints, in: *ASM Handbook Nondestructive Evaluation and Quality Control*, 9th edition, USA, 1996, **17**, pp. 610–640.
2. L. Piche, F. Massines, G. Lessaard, A. Hamel, Ultrasonic characterization of polymers as function of temperature, pressure and frequency, Ultrasonic symposium, 1987 *in Ultrasonic Symposium Proceedings, IEEE 1987,* 1125–1130.
3. L. Piche, Phenomena related to the propagation of ultrasound in polymers (a paradigm for disordered materials) *Ultrasonics Symposium,* 1989. Proceedings, IEEE 1989, 3–6 Oct. **11**, 1989, 599–608.
4. G.S. Constable, A.J. Lesser, E.B. Coughlin, Ultrasonic spectroscopic evaluation of the ring-opening metathesis polymerization of dicyclopentadiene*, J. Pol. Sci. Part B: Polymer Physics* **41**, 1323–1333 (2003).
5. A. Eisenberg, The glassy state and the glass transition in: Physical properties of polymers by J. Mark et al (ACS, Washington, DC, 1993), pp. 61–97.
6. N.T. Nguyen, M. Lethiecq, J.F. Gerald, Glass transition characterization og homogeneous polymers by an ultrasonic method, *Ultrasonics* **22** (4), 323–329 (1995).
7. S.R. White, P.T. Mather, M.J. Smith, Characterization of the cure state of DGEBA-DDS epoxy using ultrasonic, dynamic mechanical and thermal probes, *Pol. Eng. Sci.* **42** (1), 51–67 (2002).
8. M. Maatsukawa, I Nagai, Ultrasonic characterization of polymerizing epoxy resin with imbalanced stoichiometry*, J. Acoust Soc*. Am. **99** (4) 2110–2115 (1996).

APPLICATION OF IMAGES WHEN EVALUATING ULTRASONIC EXAMINATION: RESULTS IN INDUSTRIAL PRACTICE

U. Schlengermann
GE Inspection Technologies GmbH, 50354 Huerth, Germany

Abstract: For testing volumetric objects ultrasonically usually scanning techniques are applied. To achieve a high test speed the pulse repetition frequency is very high and the evaluation of all generated A-scans by an operator is not possible. A solution is to transfer features of the A-scans into a suited image by mathematical operations and to evaluate the results by an acoustical image. The report gives examples for various examination tasks taken from industrial practice for manual and automated ultrasonic testing

Key words: Acoustical imaging, ultrasonic testing, thickness measurement, detection of discontinuities, tests in manufacturing, in-service inspection

1. IMAGING IN NONDESTRUCTIVE TESTING

Historically the first imaging technique in industry was radiography by X-rays, a through-transmission technique using sensitive films as a substrate for the image like photography. Ultrasonic techniques are younger than radiography, but the first ultrasonic imaging techniques used also the radiographic principle: Through-transmission and an acoustically sensitive imaging medium (acoustical camera).

Today ultrasonic testing is done by the pulse-echo technique, which has two advantages:

M.P. André (ed.), Acoustical Imaging, 375–386.

- Access is needed only from one side of the object;
- An echo gives two-fold physical information: the intensity and the time-of-flight of signals.

A disadvantage of the pulse-echo technique is the time needed to build up an image by time-consuming scanning of the object, and to find a substrate to create an image from acoustical parameters. Today the latter can be treated by digital ultrasonic instruments, which deliver digital data to a computer, which can build up an electronic image file immediately. So acoustical online imaging is possible. In contrast to X-ray techniques ultrasound in solids can use different wave modes: longitudinal waves (bulk waves), transverse waves (shear waves), proceeding perpendicular or at an angle to surfaces or even surface waves. The signals for evaluation can result from reflection, diffraction or scattering.

2. TYPES OF ULTRASONIC IMAGES

The typical pulse echo signal is displayed as an A-scan where voltage amplitude A of the piezoelectric transducer is plotted against time-of flight of the echo. When sound velocity is constant, the time-of flight (TOF) is proportional to the distance of the detected object. Figure 1 shows a typical RF-A-scan for immersion technique: Interface echo from the surface (0), an echo from an internal discontinuity (3μs) and the disturbed echo from the back wall (6.5 μs).

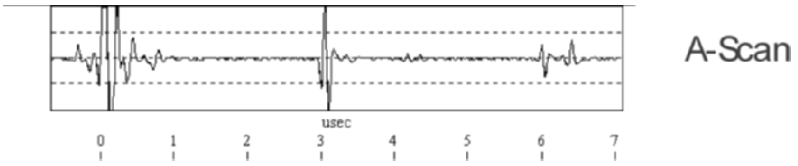

Figure 1. Typical A-scan.

As A-scans sometimes are generated with a repetition frequency of some kHz an operator cannot evaluate them. If the ultrasonic transducer or the object is moving the actual location can be combined with the two acoustical parameters A and/or TOF. That results in three new image types:

- The B-Scan, displaying TOF against location (shift), with colour-coded A.
- The C-scan, displaying two coordinates of location, e.g. rectangular (X,Y) or polar (Φ,R) with colour-coded A.
- The D-scan, displaying two coordinates of location as the C-scan, but with colour-coded TOF.

Table 1 shows the features of these four image types.

Table 1. Definitions of ultrasonic image types.

Type	Coordinates		Amplitude A	TOF t	Function
	Long	Trans			
A-scan			•	•	A = f(t)
B-scan	•		•	•	A = f(L,t)
C-scan	•		•		A = f(L,T)
D-scan	•	•		•	t = f(L,T)

On a steel sample, treated in an environmental test, an ultrasonic scanning was made storing the complete RF-A-scans. The same database was used to generate the images in figure 2, illustrating the different image types as listed in table 1.

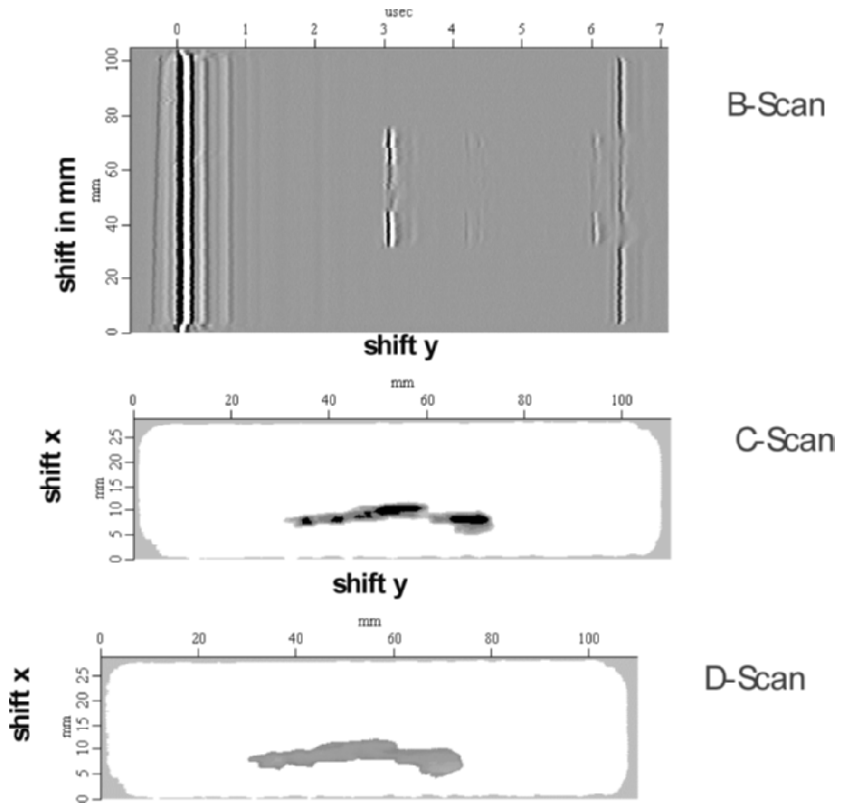

Figure 2. B-Scan, C-Scan, D-scan from the same A-scan-file.

3. EXAMPLES OF ULTRASONIC IMAGES FROM INDUSTRIAL PRACTICE

Examples taken from industrial applications and collected in our laboratory show the versatility of images in ultrasonic nondestructive testing (UT).

3.1 Corrosion Mapping

To detect internal corrosion and erosion on pipelines or vessels by UT the probe is moved manually over the outer surface of the pipe and digital thickness meter shows the actual thickness, but can also show a plot of the measured thickness against the probe shift, which gives an image of the internal contour of the wall in Figure 3. As the wall thickness is calculated from the measured TOF and the known sound velocity this image is a B-scan as defined in table 1.

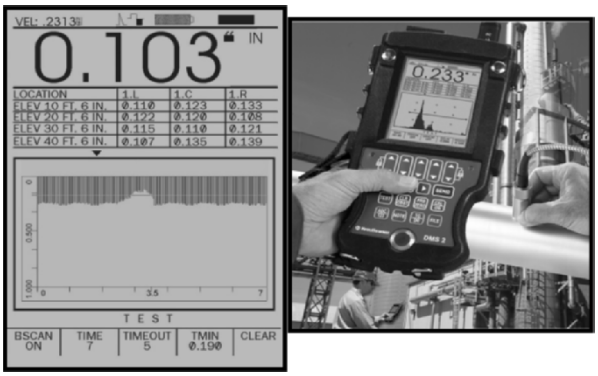

Figure 3. Corrosion mapping in a B-scan.

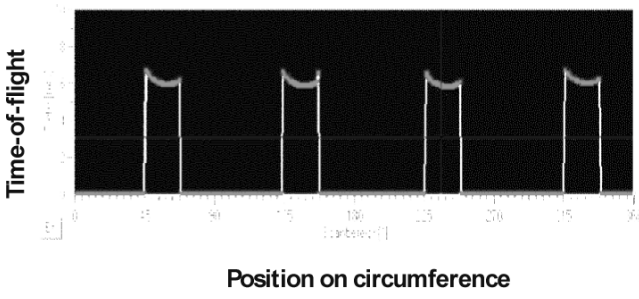

Figure 4. Locating long bore holes in a hydraulic cylinder.

3.2 Locating of Long Bore Holes

When drilling very long bore holes in a hydraulic steel cylinder ultrasound is a perfect tool to locate the end of the drill hole (figure 4). In a simple device the cylinder is rotated and the UT signals are displayed in a D-scan. Plotted against the angle of rotation the TOF shows the perfect location of the holes in depth and position angle.

3.3 Testing of Railway Rails in Track

Re-examining suspicious areas of rails in track by B-scan imaging unveils details which cannot be evaluated when running with the test car at full speed. A B-scan from data collected by a straight-beam probe shows reflections from the top of two boltholes but also the strong echo from a horizontal crack connected to one of the bolt holes (Figure 5).

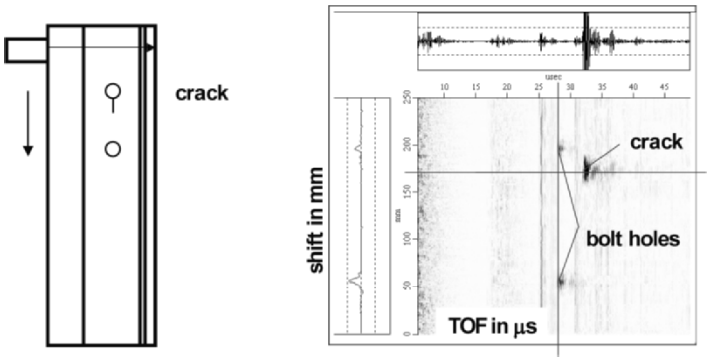

Figure 5. Imaging of a bolt hole crack in a rail by straight-beam.

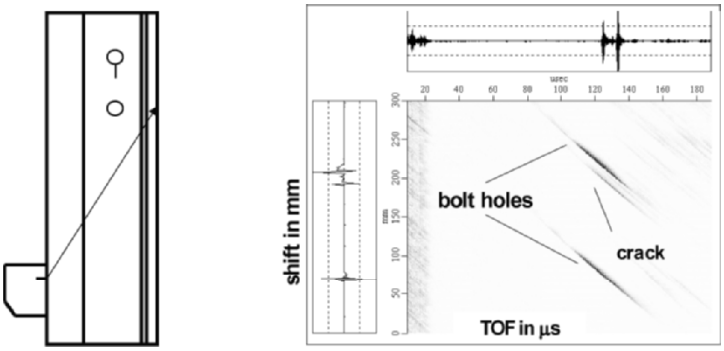

Figure 6. Imaging of a bolt hole crack in a rail by angle beam.

If the same rail is inspected by an inclined ultrasonic beam, the B-scan looks quite different (figure 6). When approaching the holes the TOF decreases and because the beam has a certain width the same reflector is seen from different positions of the probe. The result in the B-scan is a so-called amplitude-locus-curve. As the distance of the crack from rail surface is different from the bore holes its curve is shown separated from the hole. The distance between crack curve and hole curve is a measure of the crack extension.

3.4 Rating of Hydrogen Attack in Steel Samples

Steels used in corrosive environment have to show their performance in hostile environments to get the certification for the special application in pipelines, vessels or bridges. A typical test for steel grades used for oil & gas pipelines is the HIC test (resistivity against hydrogen-induced cracking). Figure 2 shows a typical B-scan of a HIC steel sample: Surface echo at the left, back wall echo at the right side. Approximately in the center is the image of a HI crack. It shades the back wall echo partially. Additionally multiple echoes from the crack can be identified. The final statement is: A semi-transparent HIC with unconnected parts (compare also C-scan and D-scan of the same object in figure 2).

In industrial production the results from a batch of steel samples are combined in C-scans from which the damaged area and some quality ratios according to specifications are calculated automatically as shown in Figure 7.

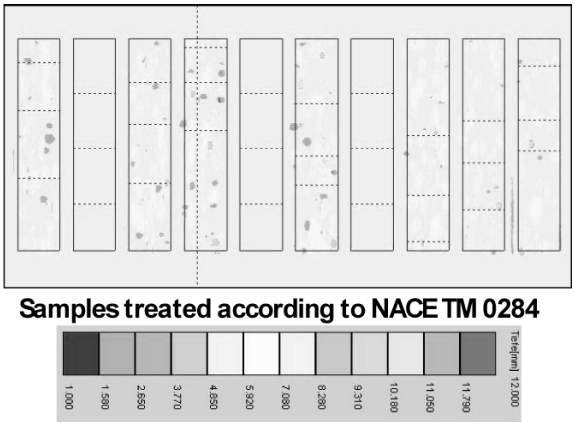

Figure 7. Evaluation of results from HIC samples using C-scans.

3.5 Evaluation of Grain Structure in Brass

Depending on the structure of alloys and on heat treatment brass of the same chemical composition may show quite different grain structures that are unwanted for machining and forming. Figure 8 gives an example how grain structure changes on a perfect brass cylinder from one end to the other. The change of ultrasonic scattering can be easily imaged in a B-scan, plotting the time-of-flight against angle of rotation. Not only the increasing scattering is shown but also the increasing TOF in spite of the perfect cylindrical shape, i.e. the sound velocity decreases from one end to the other.

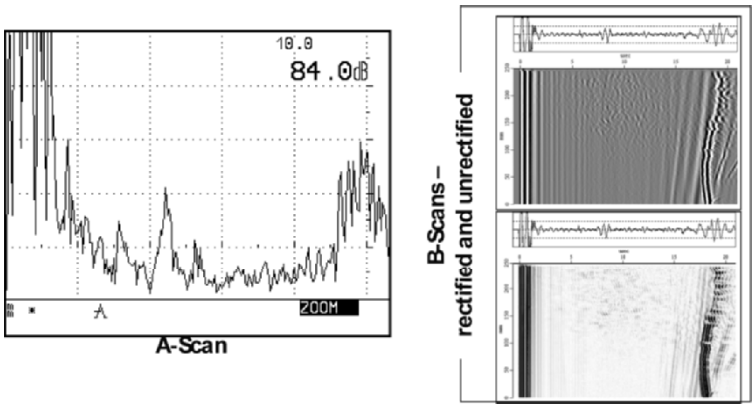

Figure 8. Evaluation of grain structure in brass.

3.6 Testing of Composite - Fiber-Reinforced Materials

Ultrasonic imaging can be used to detect faults and failures on composite materials in manufacturing stage as well as in service.

Both types of UT images, B-cans and C-scans offer projections in three orthogonal planes like computer-aided drawings.

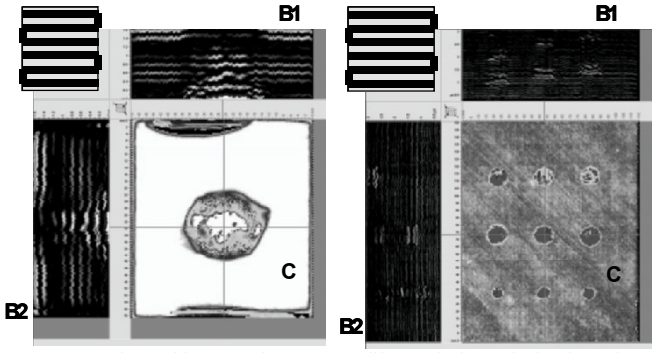

Figure 9. (a) Imaging of impact damage on fiber-reinforced plastics; (b). Imaging of eliminations on fiber-reinforced plastics.

Figure 9a gives an example for evaluation of an impact on a fiber-reinforced plate. The C-scan shows only the position of the surface damage whereas the attached B-scans show the status of the different internal layers and reveal the in-depth penetration of the impact.

Figure 9b in contrary shows the same style of imaging on production defects (here artificial delaminations). The B-scans clearly reveal size and depth position of the delaminations.

3.7 Testing of Railway Axles in the Built-in Condition

Railway axles are suffering from oscillating loads and impacts. These can generate circumferential cracks especially in the areas of the wheel seats, bearing seats or brake disc seats. For older type underground rail vehicles a mechanized installation was developed to test all axles periodically in the built-in condition. On the standing vehicle in the depot the test is executed from the end faces of the axles by moving the ultrasonic probe on a full circle storing 720 A-scans per revolution. From the data in this A-scan file B-scans are generated showing the reflection from the contour of the axle and possible reflections from surface cracks. Figure 10 shows the details of the axles and the typical B-scan. Because the sound beam is parallel to the surface the image looks like a C-scan, but as TOF is plotted against position (grey-coded A), it really is a B-scan.

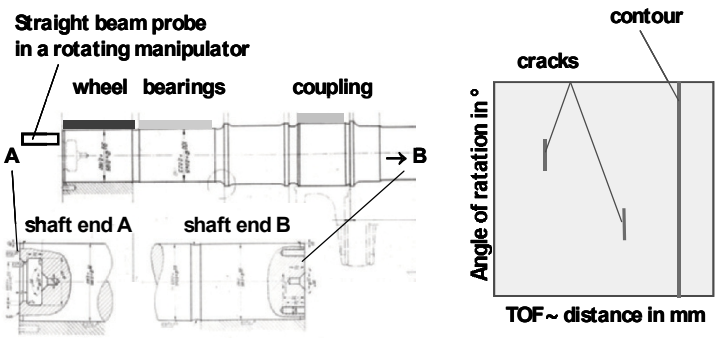

Figure 10. In-service inspection of a built in axle of a rail vehicle.

3.7.1 Testing Welded Joints using Diffracted Waves

With fusion welds in metals possible defects have to be evaluated by determining their length and depth extension. A modern tool to gain these values is the time-of-flight diffraction technique (TOFD) where the TOF of signals diffracted at the boundaries of a discontinuity are plotted against

probe shift (grey-coded A), i.e. a B-scan is generated. Figure 11 shows an example on a steel plate with a defective weld.

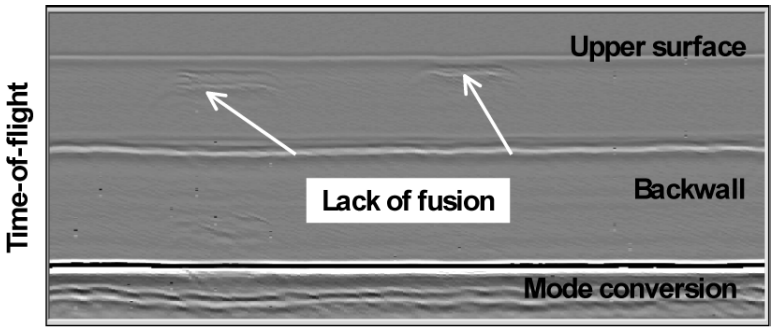

Figure 11. Weld testing using the TOFD technique.

3.7.2 Imaging by Phased Array Probes

With electronically controlled transducers in an array the sound beam can be changed in shape and direction by time delays. This gives an excellent tool to collect data from reflecting or scattering obstacles in an object under different conditions, e.g. focusing, or directions. For fast automated ultrasonic testing procedures two examples are given, how images are used in the evaluation process and on the other hand to renounce imaging in order to gain high test speed by only evaluating some essential parameters from the imaging process.

3.7.3 Automated Testing of Dismounted Railway Axles

Wheel sets of high-speed passenger trains are periodically tested for circumferential cracks at defined areas. The tests are carried out by automated installations when the wheel sets are dismounted to be machined on a lathe and when the bearings are to be replaced. Because there are only a few areas available to place an ultrasonic probe phased array probes are used. Four phased array probes have fixed positions. The direction of the sound beam is changed electronically between 35° and 70° very fast during one revolution of the wheel set. Only signals close to the surface (surface cracks) are evaluated and displayed as C-scans on the circumference of the axle. Only the sections covering the areas of the axle that have to be inspected are displayed as stripes in the plot which is generated on-line to allow the operator to stop and to restart the process if the system runs out of order. The on-scale images immediately are compared to master images

of reference wheel sets of the same type containing reference flaws. Figure 12 shows the installation and an image of the test results from one side of an axle (bearing seat, wheel seat and brake disk seat).

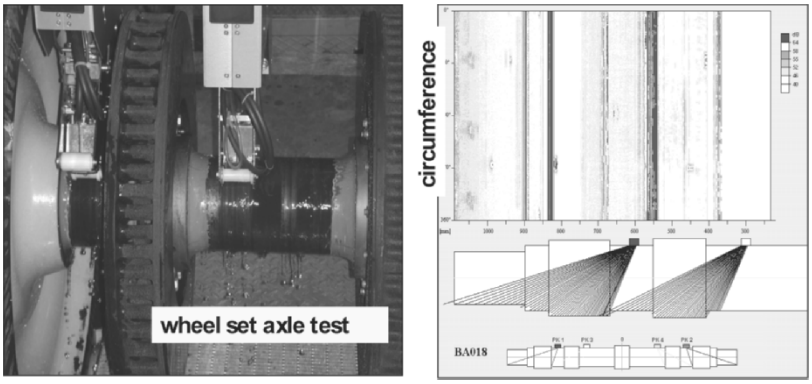

Figure 12. Automated testing of dismounted railway axles.

3.7.4 Automated Testing of Steel Tubes and Rods

Tubes and rods for pressure or construction purposes have to be ultrasonically tested on their entire volume in the production flow. To cover the volume very fast moving mechanical parts are replaced by electronically steered sound beams, i.e. by phased array probes. The interaction of typical (not acceptable) inside and outside surface defects can be studied in B-scans generated from the received A-scans. This is a very helpful tool at the development stage. Figure 13 shows the typical A-scans and a related B-scan on a reference tube.

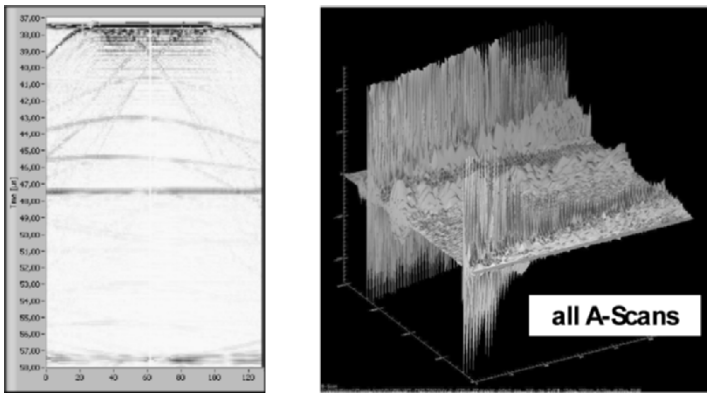

Figure 13. Full B-scan from reference defects in a tube.

But in production test there is no time to generate and to evaluate complete images. For automated classification and sorting of the test objects only some part of the imaging algorithm is used to immediately gain the information needed for the classifying decision by the computer. Figure 14 shows the typical multiple reflections inside a tube wall and part of the B-scan information used to classify inside and outside defects at production speed. Only for maintenance purposes a service technician displays full A-scans and B-scans. On automated operation only bars and signal lights show the proper operation of the test installation.

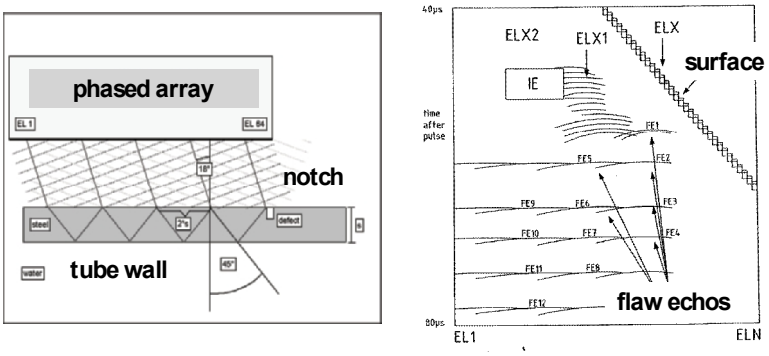

Figure 14. Classifying defects in tubes and rods (patented).

4. SUMMARY

The main requirements for the application of ultrasonic images in industry are:

- Maximizing the speed of evaluation.
- Minimizing the information needed to classify the tested objects.
- Standardizing the processes to proof a defined quality of the tested objects.

So contrary to applications of imaging in medical ultrasonic diagnosis, in nondestructive testing imaging is more a tool at the development stage than in industrial manufacturing. As shown by the examples out of production and maintenance of mass products the automated generation of images followed by immediate automated evaluation of these images is a roundabout way. As the digital information from the collected A-scans can be evaluated directly by sophisticated algorithms imaging of UT results is more a favorite of human operators but not necessarily of automated testing

installations. Screening a large electronic file of information for unexpected features, for unacceptable deviations from a standard may be different from human evaluation of an optical image. Nevertheless, intelligent algorithms of evaluation may serve both.

INNOVATIVE POWER AMPLIFIER AND TRANSDUCER TECHNOLOGIES FOR HIGH FREQUENCY, BROADBAND SONAR ARRAYS

K.R. Erikson, G. Zipfel, S.C. Butler, G.S. Edelson, E.M. Will
BAE Systems, Advanced Science & Technology, Box 868, Nashua, NH 03061-0868, USA; Summit Applied Research, 64 Canoe Brook Parkway, Summit, NJ 07901; Naval Undersea Warfare Center, Fleet Sensors and Cables Engineering Branch, Code 1516, Bldg. 1170, Newport, RI 02840

Abstract: Advances in high frequency power amplifier and transducer technologies developed as part of the ONR High Frequency Broadband Array (HFBBA) Program are discussed. The HFBBA system uses optimized, co-developed power amplifiers and transmitter transducers, and receiver transducers co-located with the transmitter transducers. This innovative approach provides a scalable, exceptionally compact, efficient system. Initial test results of a fully populated 6x6 element array demonstration system are presented

Key words: Sonar, array, Tonpilz, power amplifier

1. INTRODUCTION

The purpose of the High Frequency Broadband Array Program (HFBBA), sponsored by the Office of Naval Research of the US Navy, was to explore the use of the most advanced electronic and transducer technologies together with modern software techniques in a sonar array. Although the specific frequency ranges of the array cannot be disclosed, the frequency is higher than most human hearing and the bandwidth is multi-octave. One design goal was a compact, scalable, complete "system in a box" that could be contained in an enclosure on the outside of a vessel with a minimum number of hull penetrations.

M.P. André (ed.), Acoustical Imaging, 387–397.

Although initially the plan was to develop a sparse, vernier array, the current program demonstrated a more traditional, "fully populated" 6x6 array. The fully populated array, in which the array elements are contiguous, is most suitable for applications with minimal available aperture. In most conventional sonar systems, using the same aperture for transmitting and receiving dictates using the same transducer for transmitting and receiving.

In the HFBBA, however, a novel, "Push-pull" Triple Resonance Tonpilz transducer was used as a transmitter with a separate Co-polymer receiver transducer mounted on the head mass. This "dual-mode" transducer eliminated the requirement for a Transmit/Receive (T/R) switch in the front end electronics. The requirement for high peak power (multi-kilowatt), long pulses (up to 1 sec) with a moderate duty cycle (< 10%) in an extremely compact package was met by a novel "push-pull" power amplifier.

The HFBBA system design is briefly described. The power amplifier and transducer design are discussed in detail and initial test results of the transmitting portion of the system are presented.

2. HFBBA SYSTEM DESIGN

Figure 1 depicts the "wet end" panel with AC power for the electronics and DC power for the power amplifier brought in from the interior or "dry end" of the vessel through separate cables and hull penetrating connectors. Bi-directional communications between the dry-side PC-based signal processing and control and the panel are passed through a single optical fiber. This eliminates channel-to-channel crosstalk in the signals passing through the hull. In the test configuration described below, 100 meter cables connected the two sides to enable testing at depth. Multiplexing and digital signal conditioning of all 36 channels were performed with a single Renesas Digital Signal Processor (DSP) and a single Xilinx Vertex II Field Programmable Gate Array (FPGA).

DIMUS (Digital Multibeam Steering)[1], a time delay and sum beamforming technique with simple memory lookups was selected for receive beamforming to avoid computationally intensive interpolation. This technique, now widely used, was invented in early 60's by Victor Anderson at Marine Physical Laboratory (Scripps) at the University of California, San

Diego[4]. The HFBBA implementation used >25x oversampling, a cost effective approach with modern A/D's and inexpensive memory.

Note that the transmitter transducer and receiver transducer are electrically isolated. Elimination of the T/R switch avoids loss of power in the switch, added noise in the receiver from the switch and enables perfect impedance matching of the receiver transducer to the preamplifier for optimal signal to noise.

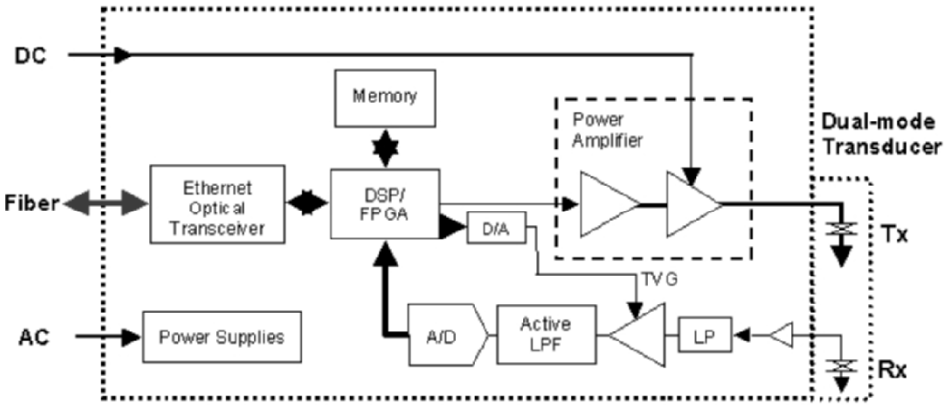

Figure 1. HFBBA - System Block Diagram.

The receiver circuit is conventional, with a preamplifier in close proximity to the receiver transducer, a passive low-pass (LP) filter, an amplifier with digitally controlled time-varying gain (TVG), an active low-pass filter and a 16-bit A/D converter digitizing at 1 MHz. Samples from each channel are stored in buffers in the FPGA and selectively read out and summed by the DSP (the DIMUS method).

3. TRANSMITTER CHANNEL

The transmitter channel (Fig. 1) is completely digital from the PC through the output of the pulse-width modulated power amplifier. Pre-computed waveforms are sent from the PC through the fiber to the DSPalong with a beam steering direction. The DSP calculates the correct element-to-element time delays and buffers the delayed waveforms in the FPGA. Upon receiving a transmit command, the waveforms are sent to the power

amplifier. Figure 2 is a schematic diagram of the unique "push-pull" power amplifier.

3.1 Power Amplifier Technology

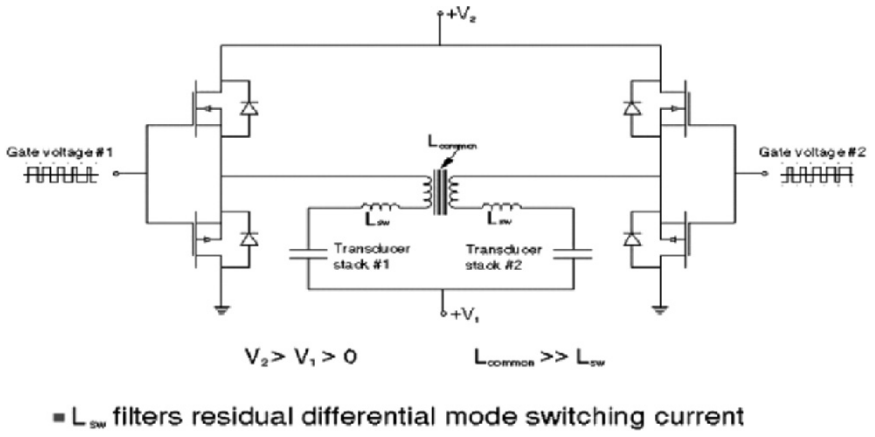

Figure 2. "Push-pull" Switched Power Amplifier (Summit Applied Research Patent Pending).

The switching power amplifier volume is less than 150 cm^3 (9 in^3) in this prototype and can output up to 1 kVA. DC Power is brought in separately for the power stage. Out-of-phase pulse width patterns are sent to each leg of the "H-bridge" power circuit from a pre-driver (shown in Fig. 1). Note that the transducer stack is divided in two parts. Each stack is thus 180º out of phase with respect to the other and is directly driven, eliminating the need for a voltage step-up transformer.

Conventional power amplifiers require an inductor to match the capacitive load of the transducer stack. This inductor must pass the currents associated with the high drive levels and are often nearly as large as the transducer itself. Furthermore, energy is wasted as the energy cycles back and forth between the transducer and the inductor in the resonant circuit.

In the "push-pull" amplifier, energy flowing out of one-half of the transducer stack is stored in the other half for reuse. Elimination of the transformer and inductor thus results in a major savings in size and weight as well as an improvement in efficiency.

Figure 3 is a photograph of the prototype power amplifier. Two channels are mounted back-to-back on a copper heat sink. In a production configuration, the size of the amplifier would be substantially reduced.

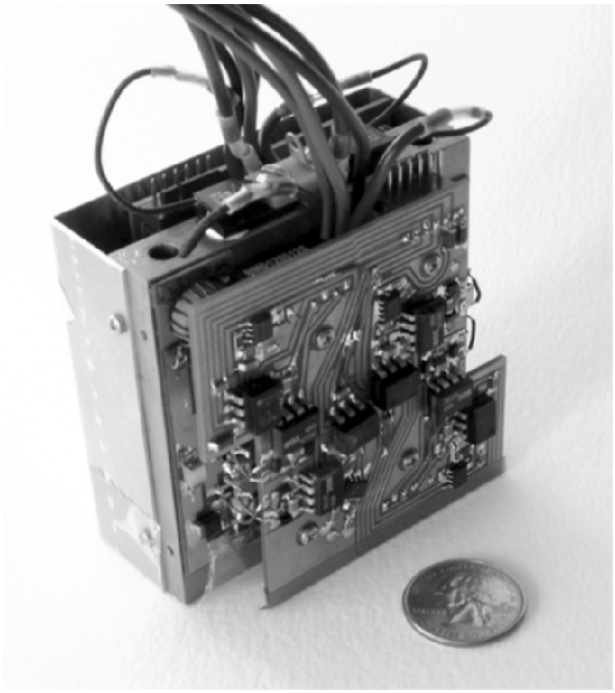

Figure 3. "Push-pull" Switched Power Amplifier
(Summit Applied Research Prototype).

4. TRANSDUCER TECHNOLOGY

As shown in Fig. 2, the power amplifier requires that the transducer stack be divided into two equal portions. Figure 4(a) is a schematic drawing of a conventional Tonpilz transducer, the most common high power transducer used at higher frequencies. The "push-pull" version with divided stack is shown in Fig. 4(b). By reversing the polarity of one stack with respect to the other, the out-of-phase electrical drive becomes an in-phase mechanical force.

With co-fired, multi-layered ceramic drive stacks[2], transducer elements can be driven at 1/10th the conventional voltage, enabling direct drive from the power FET's in the power amplifier and eliminating a transformer.

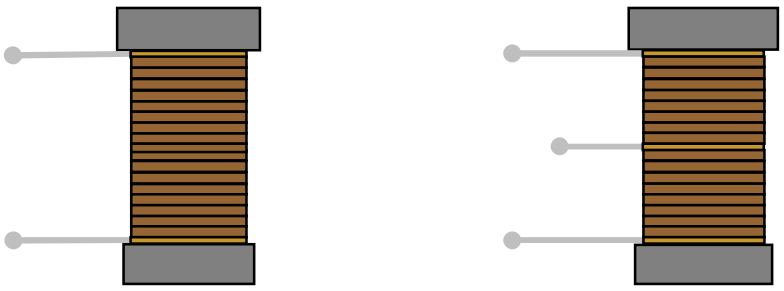

Figure 4. (a) Conventional two-wire Tonpilz transducer;
(b) Three wire "Push-pull" Tonpilz transducer with polarization opposed, half stacks. (BAE Systems Patent Pending).

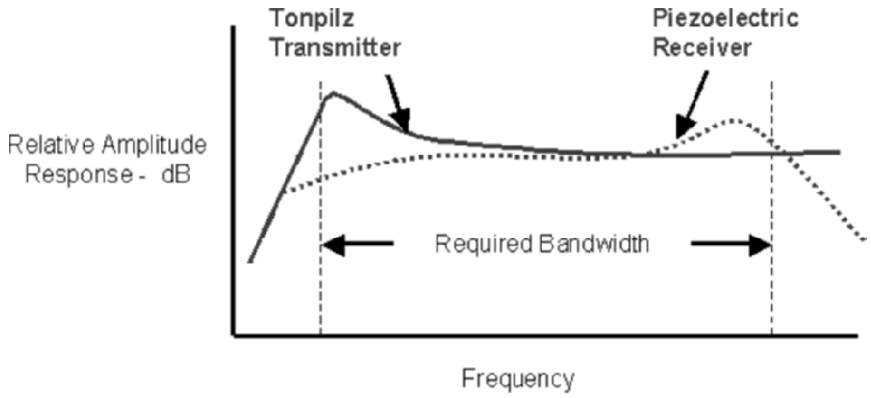

Figure 5. Independent optimization of transmitter and receiver transducer technologies.

Separating the transmitter and receiver electrically also enables use of different transducer technologies and independent optimization of performance. Figure 5 describes one example. A Tonpilz transmitter has

response *above* its first resonance frequency, whereas a piezoelectric receiver has flat response *below* its first resonance frequency. The combined effect of these two responses is normalized amplitude of the received signal over the frequency band of interest.

Figure 6 is a drawing of the final transducer configuration that combines an independent Co-Polymer Tile[3] Hydrophone and a Triple- Resonance Tonpilz[4] transmitter using the push-pull or split stack of Fig. 5. The Co-polymer Hydrophone Tile consists of piezoelectric thin film of PVDF (vinylidene fluoride) combined with TrFE (trifluoroethylene) to form P(VDF-TrFE)[7]. The Tile is composed of a 1.5 mm layer of Copolymer film sandwiched between two 0.25 mm aluminum plates.

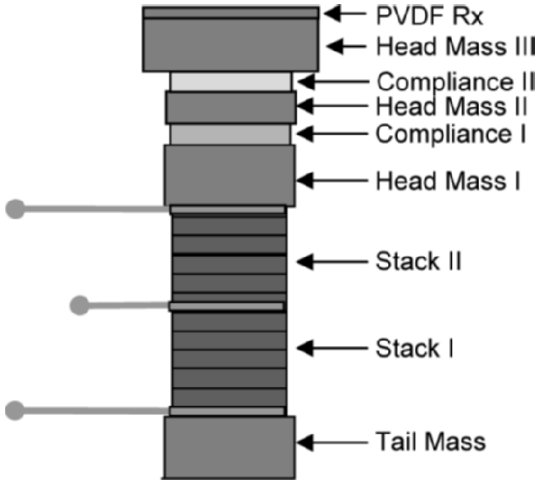

Figure 6. Triple Resonance Tonpilz Transducer
(US patent 6,822,373, Stephen Butler)
with Co-located Co-polymer Receiver
incorporating Push-pull technology.

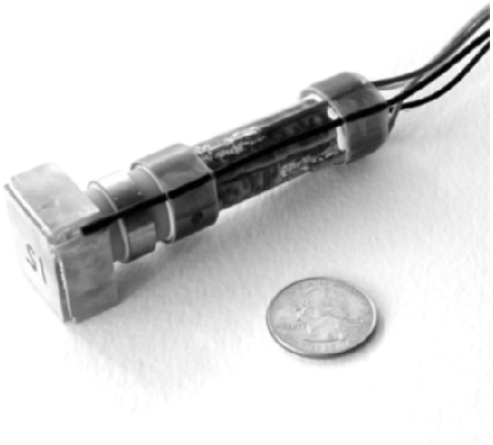

Figure 7. Push-pull, triple resonant Tonpilz transmitter transducer with co-located PVDF receiver.

Figure 7 is a photograph of the final transducer. A small diameter coaxial cable is attached to the receiver transducer. A 6x6 square array of these elements was used in the HFBBA system. This array had enough elements to demonstrate a functional system, although in most applications a larger array would be required.

5. TEST RESULTS

Figure 8 presents measured array source level data obtained with a hydrophone at the Naval Undersea Warfare Center Acoustic Open Tank Measurement Facility at a test depth of 2.3 m and separation distance of 2 m[5,6]. The measurements were made using standard gated pulse techniques[8]. The three resonance frequencies $f_o/2$, f_o and $2f_o$ are clearly evident. The vertical axis is Relative Sound Pressure Level - dB.

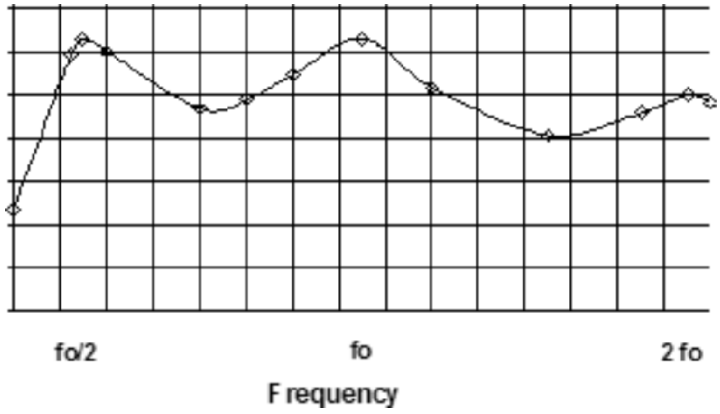

Figure 8. Relative Array Source Level Response.

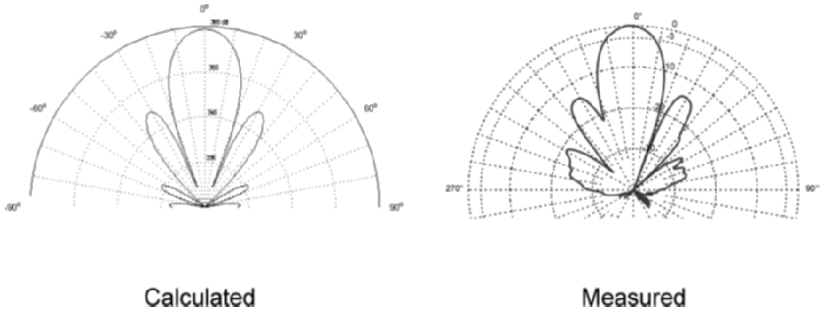

Figure 9. Array Beam Pattern – Unsteered.

Figures 9 and 10 are a plot of relative calculated and measured transmitter array directivity. Departures from the calculated beam pattern are thought to due to non-uniform response of the elements, since no attempt was made to calibrate individual output levels.

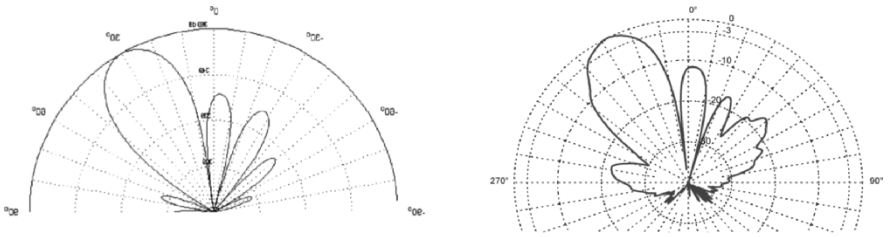

Figure 10. Array Beam Pattern - Steered at -30 degrees.

6. CONCLUSION

The HFBBA Program demonstrated digital I/O, DSP signal conditioning, novel power amplifiers and novel transducers in a single array package. We believe this compact, modular design will play an important role in the sonar systems of the future.

7. ACKNOWLEDGEMENT

The authors would like to thank Jan Lindberg of the Office of Naval Research (US Navy) Code 321, Maritime Sensing for his support of this work.

8. IN MEMORIAM

The first author would like to remember Fred Lizzi, PhD, a colleague, friend and fellow member of the Hertz Group.

REFERENCES

1. Kenneth Erikson, “Push-pull Tonpilz Transducer”, patent pending, assigned to BAE Systems, Inc.
2. Stephen Butler, US Patent 6,822,373, “Broadband Triple Resonant Transducer”, assigned to the United States of America (Navy).

3. Summit Applied Research, Inc. patent pending.
4. V.C. Anderson, "Digital Array Phasing", J. Acoustical Soc. Am., Vol. 32, no. 7, pp. 867–870, 1960.
5. TRS Technologies, Inc., State College, PA. http://trstechnologies.com.
6. Measurement Specialties Inc., Sensors Division, Hampton VA.
7. Stephen C. Butler, "Integrated Co-Fired Triply Resonant Broadband Projector and Co-Polymer Hydrophone Transducer", Proceedings of the Institute of Acoustics, Sonar Transducers and Numerical Modeling in Underwater Acoustics at National Physical Lab. Teddington, UK, 21–22 March 2005, Vol. 27 Pt.1.2005.
8. S.I. Nikolov and J.A. Jensen, "Application of different spatial sampling patterns for sparse-array transducer design", Proc. Ultrasonics Intl., pp. 921–922, 1999.

DIRECT AND POST-COMPRESSED SOUND FIELDS FOR DIFFERENT CODED EXCITATIONS

Experimental Results

A. Nowicki, Z. Klimonda, M. Lewandowski, J. Litniewski, P.A. Lewin, I. Trots

Institute of Fundamental Technological Research, 00-049 Warsaw, Poland; Drexel University, Philadelphia, PA 19104, USA

Abstract: Coded ultrasonography is intensively studied in many laboratories due to its remarkable properties; increased penetration depth, signal to noise (SNR) gain and improved axial resolution. However, no data concerning the spatial behavior of the pressure field generated by coded bursts transmissions were yet reported. This work reports the results of investigations using five different excitations schemes: two and sixteen periods sine bursts, 8 μs chirp (1 MHz bandwidth), and sinusoidal sequences phase modulated with 13 bits Barker code and 16 bits Golay complementary codes. Flat, circular transducer with 15 mm diameter, 2 MHz center frequency and 50% bandwidth was used in all experiments. The data were recorded using PVDF membrane hydrophone and collected using computerized scanning system developed in our laboratory. The results of measured pressure field distributions before and after compression were compared to those recorded using standard ultrasonographic short pulse excitation. The comparison clearly indicated increase in the SNR of the decoded pressure fields. Also, the modification of the spatial pressure field distribution, especially in the intensity and shape of the sidelobes, was apparent. As coded sequences are relatively long, intuitively, the beam shape or directivity pattern would be expected to be very similar to those produced by a long sine burst. Whereas the outcome of the experiments confirmed that this is correct for non-compressed distributions of the examined signals, in the case of the compressed sound fields, especially those generated for binary Golay sequences, the field patterns exhibited characteristics corresponding to those obtained using short, wideband bursts

Key words: coded excitation; ultrasound imaging; spatial field distribution

M.P. André (ed.), Acoustical Imaging, 399–407.

1. INTRODUCTION

Coded transmission techniques were extensively studied in radar systems[1], however, only in the past decade these techniques were also introduced into acoustic imaging[2–7]. The primary interest in applying these technique in medical ultrasound imaging is due to their ability to improve the quality of the image by enhancing signal to noise ratio (SNR) without the need to increase the peak pressure amplitudes of the probing waves. It is well known that both axial and lateral resolution increases with increasing frequency, however, in tissue, attenuation increases linearly with increasing frequency leading to decrease in the penetration depth. Although this loss in penetration could be partially compensated by increasing the excitation voltage driving pulse-echo transducer, in practice, such solution is not possible. This is because in medical ultrasound imaging the peak acoustic pressure amplitudes are limited for a given application by the maximum allowable value of the Mechanical Index[8].

Several coded excitation systems were described in the literature in the last decade[2–7]. However, none of these papers contained information on the spatial distribution of the field produced by an imaging transducer driven by a coded excitation. Such information could be helpful in optimizing the design of imaging transducers employed in imaging systems designed for coded excitation.

This paper describes the results of the measurements showing the spatial behavior of the pressure field generated obtained by transmitting coded bursts and using five different excitations schemes at 2 MHz center frequency. These schemes included two and sixteen periods sine bursts, 8 μs chirp of 1 MHz bandwidth, sinusoidal sequences phase modulated with 13 bits Barker code, and 16 bits Golay complementary codes.

2. CODED TRANSMISSION

The difference between the standard, short burst excitation pulse-echo imaging technique and the coded one can be conveniently discussed referring to Eq. (1), which describes cross-correlation of the received echoes *e(t)* with the replica of the transmitted signal *s(t)*.

$$R(\tau) = \int_{-\infty}^{\infty} s(t)e(t-\tau)dt \tag{1}$$

It should be noted that the emitted signal *s(t)* has a characteristic signature depending on the code used and also that its duration is, in general, significantly longer than that of the conventional pulse-echo signal used in ultrasound imaging systems. Function $R(\tau)$ represents the results of matched filtering, which provides time compression of the received echoes. As demonstrated in the following, this compression restores the axial resolution along with a considerable increase in signal to noise ratio (SNR).

Depending on the coding algorithm two classes of waveforms, namely, amplitude and phase modulated, can be distinguished. In addition, phase modulation can be either continuous or discrete. Linear frequency modulated waveform, belongs to the class of continuous phase modulation whereas Barker and Golay pair sequences are representatives of discrete (either positive or negative "pi") phase modulation.

Three different codes and their corresponding autocorrelation functions examined in this paper are briefly discussed below. Fig. 1a shows an excitation signal corresponding to linear chirp modulation while its autocorrelation function is depicted in Fig. 1b. Barker code of length 13 together with its autocorrelation function is shown in Fig. 2a and 2b, respectively. Finally, two sets of voltage-time plots associated with Golay codes are depicted in Fig. 3.

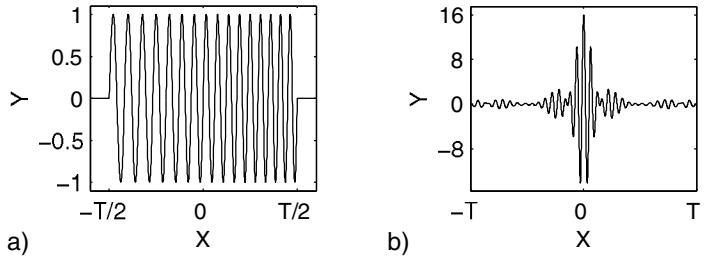

Figure 1. Linear modulation – chirp signal (a) and its autocorrelation function (b).

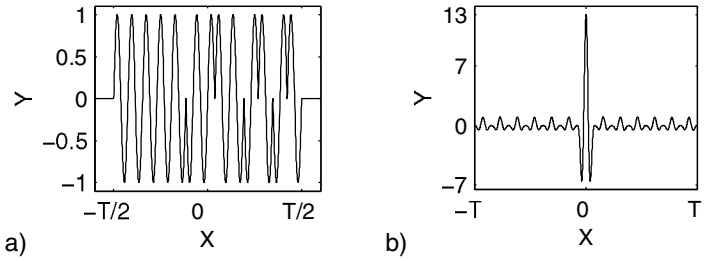

Figure 2. Barker code of length 13 (a) and its autocorrelation function (b).

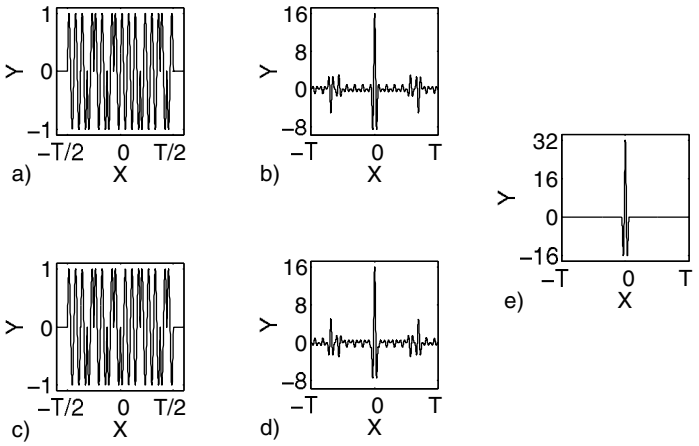

Figure 3. Golay codes (a,c), its autocorrelation functions (b,d) and the sum of autocorrelation functions (e).

A closer examination of Figs. 1 and 2 indicates that the autocorrelation functions of the codes considered exhibit time (range) sidelobes. These sidelobes are undesirable because their presence introduces artifacts in ultrasonic image and affects its quality. The shape and magnitude of the sidelobes level depend on the code applied. For linear non-apodized chirp the level of the sidelobes is 13.2 dB below the main peak. This value is independent on the time-bandwidth product and the only way to lower this value is to perform weighting in time or frequency domain[10].

The most widely used binary codes are Barker sequences, similar to those shown in Fig. 2. For this code the autocorrelation function peak is equal to N (N is the number or length of the code) and the sidelobes level is constant and varies between +1 and –1. Also, the compression ratio in the Barker code is proportional to the length of the code. The Golay complementary codes[9] of Fig. 3 deserve some additional attention here because they exhibit an interesting property that could be employed in ultrasound imaging systems. As shown in Fig. 3e, the sum of autocorrelation functions of Golay sequence pairs has virtually no sidelobes (Figs. 3a and 3c). This property follows from the reversed signs of the compressed sidelobes' amplitudes as shown in Figs. 3b and 3d.

3. MEASUREMENT SYSTEM

The block diagram of the measurement set up is shown in Fig. 4. Five different codes were generated making use of a PC computer that controlled

the arbitrary function generator (LeCroy 9109, USA). The output signal from the generator was fed to power amplifier (ENI 3100LA, USA) that drove unfocused, 2 MHz, 15 mm diameter acoustic source having 50% fractional bandwidth. The spatial field distributions were recorded using wideband PVDF polymer membrane hydrophone probe (Sonora Medical Systems model Sonic 804-201, Longmont, CO, USA). The 2 MHz source was mounted on the custom designed xyz micromanipulator controlled by the PC, and was driven by different excitation signals. The PC software allowed the field to be probed along the acoustic axis of the 2 MHz source and in an arbitrary plane perpendicular to the axis, so effectively it facilitated 3D field distribution to be examined. The minimum distance from the 2 MHz source at which the scan was carried out was 30 mm. The pressure amplitude of the ultrasonic field was measured in 5 mm intervals along the z axis of the source and in 1 mm intervals laterally along x axis. More specifically, the scan was performed up to the distance of +/–30 mm in the positive and negative x direction and from 30 to 130 mm in the positive z direction. At each scanning point, the peak-to-peak pressure amplitude was recorded by the hydrophone probe. Maximum pressure amplitudes produced by the 2 MHz planar transducer have not exceeded 1.5 MPa. The output signal measured by the hydrophone was then amplified with the help of RITEC BR-640 (CT, USA), displayed on the sampling oscilloscope (HP 54503A, Agilent, USA) and transferred to the PC for storing and printing.

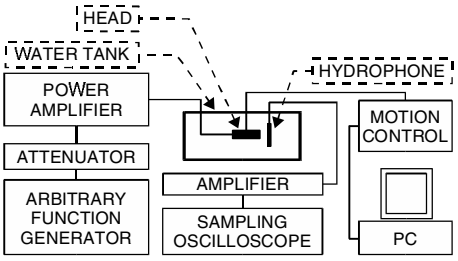

Figure 4. Measurement setup.

To compare the results of the field distributions generated by coded excitation to those encountered at the output of conventional pulse-echo imaging equipment, the set of excitation signals included a 2 and 16 cycles 2 MHz tone burst was included.

4. RESULTS

The results of the spatial field distributions obtained are presented in Figs. 5 through 12, where the isobars are shown in 6 dB intervals. The sidelobes are clearly visible in the field distributions corresponding to uncompressed signals, shown on the left hand side figures. More specifically, Fig. 5 shows the field generated by 16 periods of 2 MHz tone burst excitation and Fig. 7 depicts the field distribution corresponding to uncompressed chirp signal. Similarly, the sidelobes are visible in Figs. 9 and 11 illustrating the fields related to uncompressed Barker and Golay pair, respectively. In contrast, the corresponding field distributions shown in the right-hand side Figs. 8, 10 and 12 demonstrate that compression process has reduced significantly the sidelobes levels. The field distributions of Figs. 8, 10 and 12 could be compared with the reference one presented in Fig. 6. The field distribution of Fig. 6 corresponds to two cycle, 2 MHz tone burst excitation and, as noted above, mimics the field characteristic of that produced by a conventional, pulse-echo ultrasound imaging equipment. It is interesting to note that there are virtually no sidelobes in the field distributions corresponding to Barker (Fig. 10) and complementary Golay (Fig. 12) codes. In addition, for these two codes, it can be seen that compression or matched filtering resulted in narrowing of the main lobes in comparison with the ones measured with the signals that were uncompressed (Figs. 9 and 11). Comparison of the uncompressed and compressed signals unveiled that compression process increased signal-to-noise-ratios: about 7 dB for Barker code, 14 dB in case of chirp excitation, and 15 dB for Golay pair.

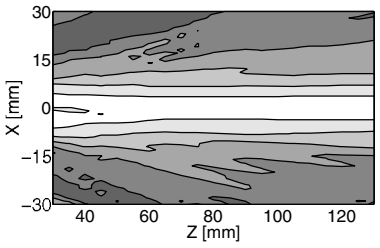

Figure 5. 16 cycles of sine.

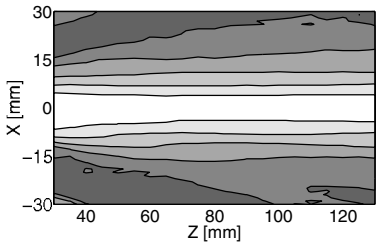

Figure 6. 16 cycles of sine.

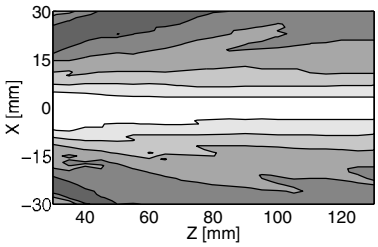

Figure 7. Non-compressed chirp.

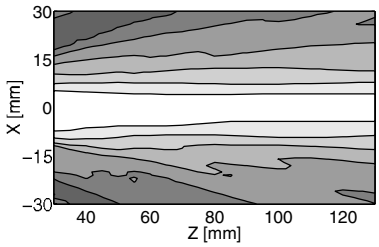

Figure 8. Compressed chirp.

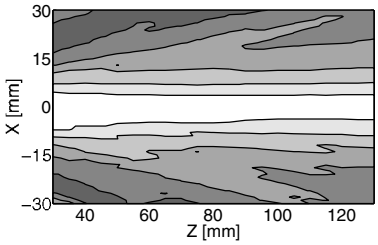

Figure 9. Non-compressed Barker code.

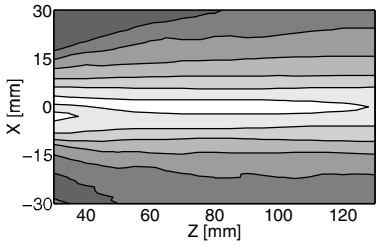

Figure 10. Compressed Barker code.

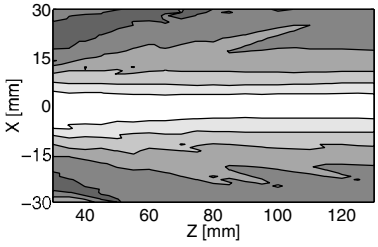

Figure 11. Non-compressed Golay pair element.

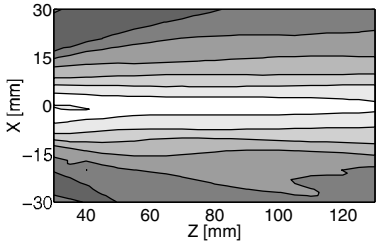

Figure 12. Sum of compressed Golay pair elements.

5. CONCLUSIONS

As coded sequences are relatively long, intuitively, their beam shape or directivity patterns would be expected to resemble those produced by a long sine burst, i.e. narrowband excitation. Indeed, the results presented above indicate that the field distributions corresponding to uncompressed signals are similar to those obtained using relatively long, 16 cycles tone burst excitation. In contrast, for short signals corresponding to relatively wide bandwidth, one would expect the sidelobes to be suppressed. This is corroborated by the results obtained with compressed signals; directivity patterns shown in Figs. 8, 10 and 12 are very similar to those obtained using short, wideband burst excitation, corresponding to conventional pulse-echo ultrasound systems (see Fig. 6). In conclusion, matched filtering of coded signals or pulse compression results in a strong reduction of spatial sidelobes level, despite the relatively long pulse duration of the excitation signal.

The primary motivation of this work was to gain an insight into the spatial distribution of the fields produced by different coded excitations and their possible impact on image resolution. The additional reason for the image quality improvement is associated with the increase in the S/N ratio of the received echoes obtained as a result of matched filtering. However, this aspect of coded excitation was not examined here. The results of this work may be useful in clinical imaging applications where enhancement in dynamic contrast is desirable.

6. ACKNOWLEDGEMENT

This study was supported by the State Committee for Scientific Research, Poland (grant No. 4 T08D 010 24).

REFERENCES

1. M.N. Cohen, in: *Airborne Pulsed Doppler Radar*, edited by G. Morris and L. Harkness (Artech House Publishers, Boston · London, 1996), pp. 173–214.
2. B. Haider, P.A Lewin and K.E. Thomenius, Pulse Elongation and Deconvolution Filtering for Medical Ultrasonic Imaging, *IEEE Transactions on Ultrasonics, Ferroelectrics And Frequency Control*, **45**, 98–113 (1988).
3. M. O'Donnell, Coded excitation system for improving the penetration of real-time phased-array imaging systems, *IEEE Transactions on Ultrasonics, Ferroelectrics and Frequency Control*, **39**(3), 341–351 (1992).

4. T.X. Misaridis, K. Gammelmark, Ch.H Jorgensen, N. Lindberg, A.H. Thomsen, M.H. Pedersen and J.A. Jensen, Potential of Coded Excitation in Medical Ultrasound Imaging, *Ultrasonics,* **38**, 183–189 (2000).
5. A. Nowicki, W. Secomski, J. Litniewski and I. Trots, On the application of signal compression using Golay's codes sequences in ultrasound diagnostic, *Archives of Acoustics,* **28**(4), 313–324 (2003).
6. V. Behar and D. Adam, Parameter optimization of pulse compression in ultrasound imaging systems with coded excitation, *Ultrasonics*, **42**(10), 1101–1109 (2004).
7. M. Pollakowski and H. Ermert, Chirp Signal Matching and Signal Power Optimization in Pulse-Echo Mode Ultrasonic Nondestructive Testing, *IEEE Transactions on Ultrasonics, Ferroelectrics And Frequency Control*, **41**(5), 665–659 (1994).
8. National Electrical Manufactures Association (NEMA), NEMA Acoustic Output Measurement Standard for Diagnostic Ultrasound Equipment, UD-3-1993, NEMA and AIUM (American Institute of Ultrasound in Medicine) Standard for Real Time Display of Thermal and Mechanical Acoustic Output Indices on Diagnostic Ultrasound Equipment.
9. M.J.E. Golay, Complementary Serries, *IRE Trans. Inf. Theory*, **IT-7**, 82–87 (1961).
10. T. Missaridis, Ultrasound Imaging Using Coded Signals, PhD thesis, (Center for Fast Ultrasound Imaging, Technical University of Denmark, 2001).

ELASTIC PROPERTIES OF CLAY MINERALS DETERMINED BY ATOMIC FORCE ACOUSTIC MICROSCOPY TECHNIQUE

M. Kopycinska-Müller, M. Prasad, U. Rabe, W. Arnold
Fraunhofer Institute for Nondestructive Testing, IZFP, Saarbrücken; Center for Rock Abuse, Colorado School of Mines (currently at National Institute for Standards and Technology, Boulder, CO)

Abstract: Seismic wave propagation in geological formations is altered by the presence of clay minerals. Knowledge about the elastic properties of clay is therefore essential for the interpretation and modeling of the seismic response of clay-bearing formations. However, due to the layered structure of clay, it is very difficult to investigate its elastic properties. We measured elastic properties of clay using atomic force acoustic microscopy (AFAM). The forces applied during the experiments were not higher than 50 nN. The adhesion forces were measured from the pull-off forces and included into our calculations by means of the Derjaguin-Mueller-Toporov model for contact mechanics. The obtained values of the elastic modulus for clay varied from 10 to 17 GPa depending on various parameters that describe the dynamics of a vibrating beam

Key words: Atomic Force Acoustic Microscopy, clay minerals, elastic modulus, hydration state

1. INTRODUCTION

Clay is one of the most common sedimentary minerals on Earth. Seismic wave propagation in geological formations is altered by the presence of clay minerals. When the clay is load bearing, it forms a weak link between larger and stronger components of various geological structures. Fig. 1 shows a comparison between scanning electron (SEM), atomic force (AFM), and scanning acoustic microscopy (SAM) images of sandstone. Fig. 1a (from du Bernard et al. 2003) illustrates location of clay particles around quartz

M.P. André (ed.), Acoustical Imaging, 409–416.

grains. Although, topography changes were too large (Fig. 1b) to make quantitative measurements on such samples, SAM images (Fig. 1c) do show lower impedance for clay as compared to quartz. Presence of clay alters the elastic and plastic behavior of the composite material significantly. And so, knowledge about the elastic properties of clay is essential for interpreting and modeling the seismic response of clay-bearing formations. However, the layered structure of clay (see Fig. 2) makes this a challenging measurement. There are many problems associated with elastic properties measurements of clay minerals with standard pulse transmission techniques. Clay "booklets" usually consist of many layers with thicknesses in the range of few nm.

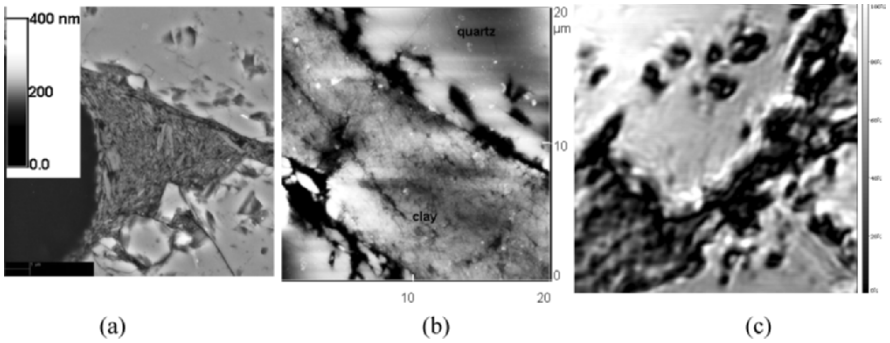

Figure 1. Comparison between (a) SEM, (b) AFM, and (c) SAM images of a contact zone in a thin section of sandstone with clay cements. 2a shows the alignment of the clay around quartz grains in the contact. However, topographic effects dominate (2b). The SAM image shows that clays have lower impedance (darker color) that the quartz (lighter color).

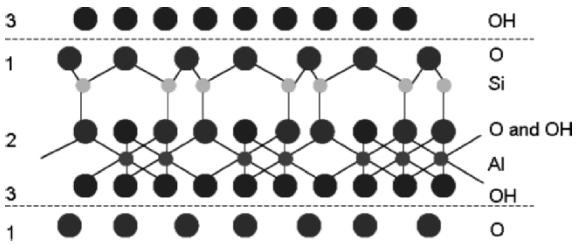

Figure 2. Structure of Kaolinite (adapted from Velde, 1992). The layered silicate structure 1–3 is held together to other sheets by the attraction force between the oxygen and hydroxyl ions.

In the following, we present measurements of elastic properties of clay minerals (dickite) and mica particles using atomic force acoustic microscopy (AFAM). This technique is a dynamic enhancement of the atomic force

microscope (AFM) technique and its principles are described in details elsewhere (Rabe et. al, 1996, 1998, 2000). Sample preparation is explained in Prasad et al. (2002).

2. TOPOGRAPHY MEASUREMENTS

Topography images were first obtained in contact mode using a triangular cantilever with a low spring constant. The imaged structures were not stable and it was observed that scanning the sample surface in the contact mode actually damaged the sample. Therefore, tapping mode AFM was considered more suitable for imaging this material. Tapping mode not only ensures higher lateral resolution but also protects the sample structures better. The AFM topography imaging results are presented in Fig. 3a, which shows a typical clay booklet structure. One can clearly see a stack of seven thin layers, each with a thickness less than 1 nm (as given by Velde, 1992). The image size was 1 μm x 1 μm with a height scale of about 10 nm in Fig. 3b.

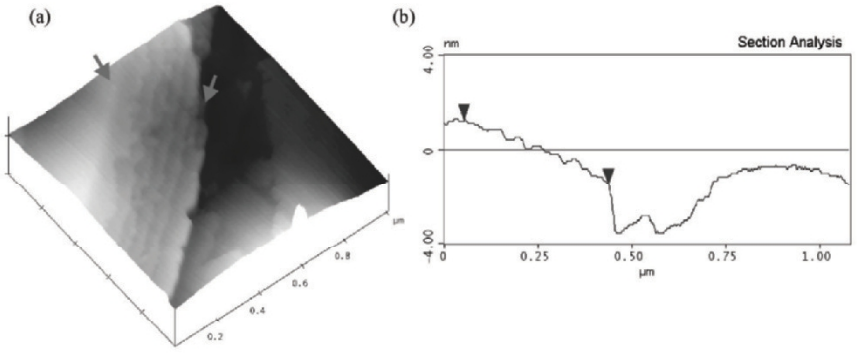

Figure 3. AFM topography image of dickite (a). The arrows mark location of the cross-section shown in (b). The size of the image is 1 μm × 1 μm. Here typical clay booklets can be observed. As can be seen in (b) the height scale is about 10 nm. As the vertical distance between the two marked points is about 3 nm it can be concluded that the thickness of the clay layers is less than 1 nm.

3. AFAM CONTACT RESONANCE SPECTRA

It was difficult to obtain AFAM images of the clay samples, as the layers of clay slid during imaging as discussed in Prasad, et al. (2002). This problem could be reduced when the cantilever contacted the sample surface

only at a single point. Thus, AFAM spectra at single points were measured in order to determine the elastic properties of clay without imaging the sample. The spring constant of the cantilever used in these experiments was 1.5 N/m. The free resonance frequencies of the cantilever were 66.88 kHz and 420.39 kHz for the first and the second mode, respectively. The contact resonance spectra for the first and second mode were measured at 10 different locations on the sample surface at two different static loads of 30 and 45 nN. A fused quartz sample was the first choice as a reference sample.

Preliminary results showed, however, that the clay sample was much more compliant than the fused quartz sample. In order to improve the accuracy of the measured values, additional measurements were made on polystyrene that has an elastic modulus lower than that of clay. Mica particles were mingled with the clay. Since the AFAM measurements were made at random locations, occasionally the tip came into contact with mica instead of clay. The properties of mica are closer to those of fused quartz than to clay, so it was possible to identify and interpret the measurements on mica. Fig. 4a and 4b shows examples of normalized contact-resonance spectra measured on clay, polystyrene, mica and fused quartz. Contact-resonance frequencies measured on clay are slightly higher than the frequencies detected on polystyrene and lower than the contact-resonance frequencies measured on mica and fused quartz. This difference is greater for the second contact-resonance frequencies. The relative difference in the contact resonance frequencies for different materials depends on the mode of the cantilever vibration (Turner et al. 1997).

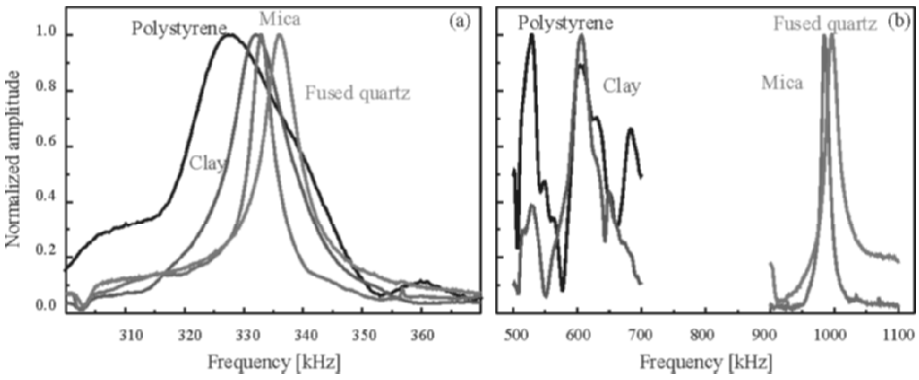

Figure 4. Contact-resonance spectra measured on polystyrene, clay, mica, and fused quartz. The relative frequency of the contact-resonance peaks implies that the indentation modulus of clay lies between than that of polystyrene and that of mica and fused quartz. The differences are minimal for the first contact-resonance frequency (a) but are much larger for the second contact-resonance frequency (b). The spectra shown here were normalized to emphasize the differences in the position of the contact resonance frequency (from Prasad et al. 2002).

The AFAM spectra were measured in sweep mode. Twenty-five spectra were measured at each location for each static load. The curves presented in Fig. 4 were obtained by averaging the 25 measured spectra. All of the average values of the first and the second contact resonance frequencies are shown in Fig. 5a and b. The error bars represent the standard deviation of 25 measurements. In most cases, the standard deviation is so small, that the error bars are actually smaller than the size of the symbol that represents the value of the resonance frequency. Large error bars correspond to measurements during which the contact resonance frequency changed, probably due to the sliding of the booklets. Fig. 5 shows that in almost all cases, the measured spectra behaved like those in Fig. 4. The differences between the values of the first contact resonance frequency measured on the fused quartz and the clay sample are small. In a few cases, the first resonance frequency measured on the clay sample is actually higher than the resonance frequency measured on the fused quartz sample. Such behavior was previously observed for these types of AFM cantilever (Kopycinska-Mueller, 2005). The second contact resonance frequency measured on the clay sample is lower than the corresponding frequency for the fused quartz sample by about 400 kHz.

4. RESULTS AND DISCUSSION

The resonance frequencies (Fig. 5) were used to determine the tip position parameter L_1/L and then to calculate the local tip-sample contact stiffness k^* (for example, Rabe et al. 1996, 2000, 2002). The optimum value of L_1/L was found to be 0.873. One can calculate an error value Δk^* defined as a difference of the stiffness calculated for the two modes separately at the determined value of L_1/L $\Delta k^* = 100\% \times 2(k^*(f_1)-k^*(f_2))/(k^*(f_1)+k^*(f_2))$. The smaller the value of Δk^* better the agreement between the measured contact resonance frequencies and the dynamic beam model. The results obtained for k^* and Δk^* (Fig. 6(a)) show that the values of k^* calculated for fused quartz are twice as large as k^* values obtained for the clay sample. Fig. 6(b) can also be noticed that there is a significant difference in Δk^* calculated for the clay and for the fused quartz sample. For the clay sample, the difference between the values of k^* calculated for the first and second modes is smaller than 20 %. An equivalent calculation performed for the fused quartz sample yielded $\Delta k^* = 110$ %. The value of L_1/L determined was not optimal for all of the measured contact-resonance frequencies. $L_1/L = 0.909$ is the value obtained for the resonance frequencies measured on the fused quartz sample only. Because more resonance frequencies were measured on the clay sample than on the fused quartz sample, the calculated value of L_1/L will be weighted

toward the values of the frequencies measured on the clay sample. These results suggest that the tip-position L_1/L relates not only to the physical tip position but also to the elastic properties of the sample and to the measured contact mode. As the first contact resonance frequency measured on fused quartz was pinned, there is a strong suspicion that the ratio of the vertical and lateral forces acting between the tip and the sample for the first mode is different from the same ratio for the second mode. This may alter the results of the calculation, as the different dynamic of the pinned modes is not included into analytical model of the vibrating beam. Note that all inconsistencies in contact stiffness evaluation are assigned to L_1/L. Future work could involve modifying the physical model to also account for the Eigenmodes of the cantilever.

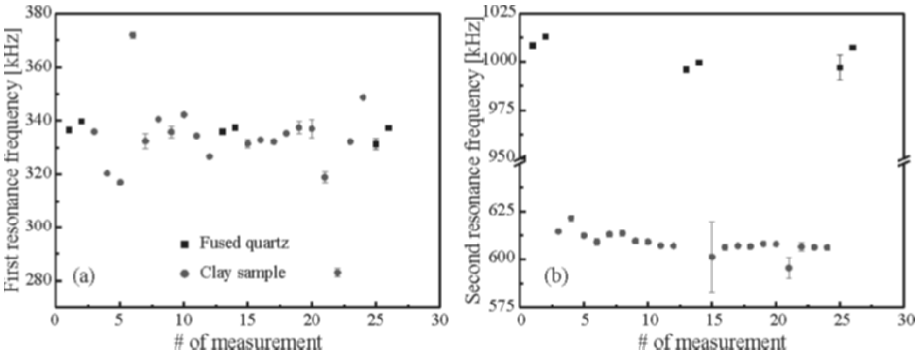

Figure 5. (a) First and (b) second contact-resonance frequency measured on fused quartz (■) and clay (●). Each resonance frequency was measured at static loads of 30 nN and 45 nN. The spectra were measured in sweep mode. Results presented here are the average values of 25 measured resonance frequencies. In some cases, the contact-resonance frequency changed significantly during the measurement giving rise to large standard deviations. Note the break in y-scale between 650 and 950 kHz in (b).

The tip position parameter has a strong impact on the value calculated for the local tip-sample contact stiffness. Table 1 compares the values of k^* calculated for the fused quartz sample using $L_1/L = 0.873$ and 0.909. As can be seen in Table 1, the calculated values of k^* differ significantly when different values of L_1/L are assumed. The values of k^*obtained for $L_1/L = 0.909$ are about 50% higher than those obtained for $L_1/L = 0.873$. The values of k^* used for the reference sample affect the calculated elastic properties of the clay sample. For example, the average value of the indentation modulus M_{clay} calculated for the clay sample is 16.9 GPa ± 6.3 GPa if the values of k^* for quartz with $L_1/L = 0.873$ are used. However, when the values of k^* for quartz calculated for $L_1/L = 0.909$ are used, the average value of $M_{clay} = 9.9$ GPa ± 3.3 GPa. Taking into account the additional reference measurement

on the polystyrene sample for which M is approximately 3.8 GPa, the result M = 9.9 GPa ± 3.3 GPa is likely to be closer to the real properties of clay. Currently, there are no other measurements of the elastic properties of clay for comparison. Theoretical estimates available (Berge and Berryman, 1995) yield a value for the Young's modulus of clay of 10–12 GPa.

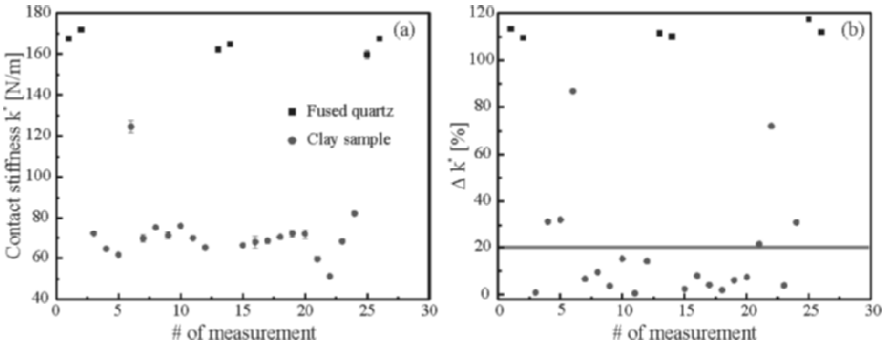

Figure 6. (a) k^* calculated from the resonance frequencies measured on the fused quartz and clay samples at a fixed $L_1/L = 0.873$. (b) Δk^* in the values of $k^*(f_1)$ and $k^*(f_2)$ calculated for this value of L_1/L. Δk^* varies strongly depending on the elastic properties of the sample. For the clay sample, Δk^* is less than 20 % in almost all cases. For the fused quartz sample, however, Δk^* is greater than 100 %, indicating that the chosen value of L_1/L is not optimal.

Table 1. Impact of the tip-position parameter L_1/L on the tip-sample contact stiffness k*, calculated for the measurements on the fused quartz sample. The values of k^* calculated using a tip-position determined from the entire set of measurements ($L_1/L = 0.873$) are significantly lower than the values of k^* calculated at tip position of $L_1/L = 0.9090$, the value determined from the fused quartz measurements only.

Measurement #	Static load [nN]	$L_1/L = 0.873$		$L_1/L = 0.909$	
		k^* [N/m]	Δk^* [%]	k^* [N/m]	Δk^* [%]
1	30	167.57	113.21	234.42	76.18
	45	171.89	109.59	246.24	70.02
2	30	162.37	111.36	222.36	71.51
	45	164.86	110.00	228.73	69.25
3	30	159.79	117.50	214.39	83.59
	45	167.65	111.95	234.97	73.69

5. CONCLUSIONS AND FUTURE WORK

We have shown that the Young's modulus for clay measured with AFAM lies between 10 – 15 GPa. The measurement uncertainty of our measurements is estimated at ± 8 GPa. These results have been very encouraging. For the future we plan to make measurements as functions of

varying water content by drying and baking of the clay minerals and by varying humidity in the sample through a controlled environmental chamber (Hurley and Turner, 2004).

6. ACKNOWLEDGEMENT

We acknowledge the support of the sponsors Colorado School of Mines - University of Houston Fluids / DHI Consortium and the National Science Foundation (Grant No. EAR 0074330).

REFERENCES

1. Berge, P.A., and Berryman, J.G., 1995, Realizability of Negative Pore Compressibility in Poroelastic Composites, Journal of Applied Mechanics 62, 1053–1062.
2. Du Bernard, X., Prasad, M., and Reinstaedtler, M., 2003, The effect of cementation on the seismic properties of sandstones, Proc. Int. Symp. Acoustical Imaging, Eds. W. Arnold and S. Hirsekorn, 27, 399–405.
3. Hurley, D.C., and Turner, J.A., 2004, J. Appl. Phys. 95, p. 2403.
4. Kopycinska-Mueller, M., 2005, On the elastic properties of nanocrystalline materials and the determination of elastic properties on a nanoscale using the atomic force acoustic microscopy technique: PhD thesis, Technical Faculty of Saarland University, Saarbruecken (*in preparation).*
5. Prasad, M., Kopycinska, M., Rabe, U., and Arnold, W., 2002, Measurement of Young's modulus of clay minerals using Atomic Force Acoustic Microscopy, Geophysical Research Letters, Vol. 29, #8, 13-1–13-4.
6. Rabe, U., Janser, K., and Arnold, W., 1996, Vibrations of free and surface-coupled atomic force microscopy cantilevers: theory and experiment, Rev. Sci. Instrum. 67, p. 3281–3293.
7. Rabe, U., Turner, J., and Arnold, W., 1998, Analysis of the High-Frequency Response of Atomic Force Microscope Cantilevers, Appl. Phys. A 66, S277–S282.
8. Rabe, U., Amelio, S., Kester, E., Scherer, V., Hirsekorn, S., and Arnold, W., 2000, Quantitative Determination of Contact Stiffness Using Atomic Force Acoustic Microscopy Ultrasonics, 38, 430–437.
9. Rabe, U., Amelio, S., Kopycinska, M., Hirsekorn, S., Kempf, M., Göken, M., and Arnold, W., 2002, Imaging and Measurement of Local Mechanical Material Properties by Atomic Force Acoustic Microscopy, Surf. Interface Anal. 33, p. 65–70
10. Turner, J., Hirsekorn, S., Rabe, U., and Arnold, W., 1997, High-Frequency Response of Atomic-Force Microscope Cantilevers, J. Appl. Phys. 82, 966–970.
11. Velde, B., 1992, Introduction to clay minerals, chemistry, origins, uses and environmental significance, Chapman and Hall, London, United Kingdom.

PHYSICS AND MATHEMATICS

THREE-DIMENSIONAL ACOUSTIC TISSUE MODEL: A COMPUTATIONAL TISSUE PHANTOM FOR IMAGE ANALYSES

J. Mamou, M.L. Oelze, W.D. O'Brien, Jr., J.F. Zachary
Department of Electrical and Computer Engineering, University of Illinois at Urbana-Champaign; Department of Bioengineering, University of Illinois at Urbana-Champaign; Department of Veterinary Pathobiology, University of Illinois at Urbana-Champaign

Abstract: A novel methodology to obtain three-dimensional (3D) acoustic tissue models (3DATMs) is introduced. 3DATMs can be used as computational tools for ultrasonic imaging algorithm development and analysis. In particular, 3D models of biological structures can provide great benefit to better understand fundamentally how ultrasonic waves interact with biological materials. As an example, such models were used to generate ultrasonic images that characterize tumor tissue microstructures. 3DATMs can be used to evaluate a variety of tissue types. Typically, excised tissue is fixed, embedded, serially sectioned, and stained. The stained sections are digitally imaged (24-bit bitmap) with light microscopy. Contrast of each stained section is equalized and an automated registration algorithm aligns consecutive sections. The normalized mutual information is used as a similarity measure, and simplex optimization is conducted to find the best alignment. Both rigid and non-rigid registrations are performed. During tissue preparation, some sections are generally lost; thus, interpolation prior to 3D reconstruction is performed. Interpolation is conducted after registration using cubic Hermite polynoms. The registered (with interpolated) sections yield a 3D histologic volume (3DHV). Acoustic properties are then assigned to each tissue constituent of the 3DHV to obtain the 3DATMs. As an example, a 3D acoustic impedance tissue model (3DZM) was obtained for a solid breast tumor (EHS mouse sarcoma) and used to estimate ultrasonic scatterer size. The 3DZM results yielded an effective scatterer size of 32.9 (±6.1) μm. Ultrasonic backscatter measurements conducted on the same tumor tissue *in vivo* yielded an effective scatterer size of 33 (±8) μm. This good agreement shows that 3DATMs may be a powerful modeling tool for acoustic imaging applications

Key words: Registration; 3D reconstruction; tissue characterization

M.P. André (ed.), Acoustical Imaging, 419–426.

1. INTRODUCTION

This contribution presents a set of strategies to reconstruct three-dimensional (3D) acoustic tissue models (ATMs) from consecutive two-dimensional (2D) stained histologic sections of a mouse sarcoma tumor. The 3D reconstruction strategies are familiar to the medical imaging and image/signal processing communities. Tissue preparation (sectioning, etc.) is challenging and leads to a 3D dataset with artifacts that need to be accounted for in order to obtain accurate 3D models. Specifically, all the sections do not have the same contrast. Also, during imaging the pathologist manually aligns one section to the next consecutive. This alignment is approximate and fine-tuning registration needs to be conducted. Finally, during sectioning of the tissue some of the sections are lost. Therefore, sections need to be interpolated post registration for accurate reconstruction of 3D volumes. Thus, this study addresses signal and image processing strategies to obtain accurate 3D histologic volumes (3DHV) from the 2D histologic sections.

The reconstructed 3DHVs can be used as 3D computational phantoms for different wave propagation simulations and as imaging algorithm development tools. For example, 3DHVs are converted to 3DATMs by assigning acoustic properties to every voxel (i.e., speed of sound, density, attenuation, etc.), then computational algorithms could be used to solve acoustic wave equations to study wave propagation phenomena in tissue. Furthermore, techniques were recently developed to estimate ultrasonic scatterer properties from 3D impedance maps (i.e., 3DATMs where every voxel was assigned an acoustic impedance value) [1]. These estimates are believed to have diagnostic potential for detecting and diagnosing disease. Scatterer size estimates were obtained from the 3D impedance map (3DZM) obtained from the mouse sarcoma and compared to ultrasonic measurements obtained *in situ* from the same tumor.

This 3D reconstruction study was conducted as a first step of a very ambitious project that is trying to establish connections between ultrasonic scattering signatures and tissue microstructure for noninvasive diagnostics. Hence, 3DATMs can be used for better understanding the complicated interactions of ultrasound waves with biological material.

2. TISSUE PREPARATION AND IMAGING

Three-dimensional reconstruction strategies are developed and demonstrated with a murine sarcoma tumor model. The EHS (Englebreth-Holm-Swarm) cell line (ATCC - CRL-2108, American Type Culture Collection) is a transplantable sarcoma in C57BL/6 mice. This tumor grows subcutaneously

and produces extracellular matrix (ECM) components such as laminin, collagen IV, entactin, and heparan sulfate proteoglycan. The tumor was allowed to grow until it was of sufficient size for harvesting.

Sections of the EHS sarcoma were fixed by immersion in 10% neutral-buffered formalin, embedded in paraffin, sectioned at 3-μm thickness, mounted on glass slides, and stained with hematoxylin and eosin (H&E) for evaluation. The processes of fixation, paraffin infiltration, and sectioning of the EHS sarcoma for histopathologic evaluation causes a minor degree of inherent tissue shrinkage that is small, but indeterminate for each section. In addition, it is not possible to obtain 200 serial sections (one section after another) without the loss of some sections in the series due to technical difficulties in tissue sectioning. EHS sarcoma sections, mounted on glass slides, were examined and captured using a Nikon Optophot-2 light microscope equipped with a Sony color video camera.

A board-certified pathologist via a microscope stage manually registered each image with the proceeding image. This manual registration process is very labor-intensive and imprecise; therefore, an automatic registration algorithm was developed. For the EHS dataset, the optical images measured laterally 400 μm by 300 μm. The EHS dataset contained 200 sections of which 54 sections (26%) were lost during tissue preparation. Each bitmap image measured 640 pixels by 480 pixels with 8-bit accuracy for each red, green and blue (RGB) component.

3. THREE-DIMENSIONAL RECONSTRUCTION

Obtaining a 3DATM (or a 3DZM) from 2D sections involves four signal and image processing steps. 1) The contrast of the sections is equalized because the uptake of stain, in general, is not uniform; nor is the video capture intensity necessarily the same from section to section. 2) A fine-tuning registration is conducted. 3) For the missing sections, interpolation is performed. 4) The resulting 3DHV is converted to a 3DZM by assigning an acoustic impedance value to each voxel.

3.1 Contrast Equalization

Consecutive histologic sections generally have different contrasts. Each section may have been stained for a slightly different duration and/or may be slightly different in thicknesses, thus resulting in variability of stain uptake. Equalization was conducted for each of the three-color components (i.e., red, green and blue) of each image.

Specifically, let H_c denote the cumulative histogram of image I (for one of the color components). Thus, $H_c(\alpha)$ is the number of pixels with intensity level $\leq\alpha$ in the image. Then, the equalizing transform is given by:

$$\alpha' = 255\frac{H_C(\alpha)}{N}, \tag{1}$$

where N is the total number of pixels in the image and the 255 factor has been added so that the new intensity is in the range 0–255 (because $N \geq H_c \geq 0$). α' is the new intensity value for of the pixels that had an intensity value of α.

3.2 Registration

Registration or alignment is an essential step in the 3D reconstruction because if the consecutive sections are not aligned correctly, then the resulting 3DATM will yield misleading or incorrect results. For our 3D modeling, each section needs to be aligned with the next. Specifically, we are trying to determine the best transformation to apply to an image I_2 so that it is the most similar to the original and adjacent image I_1. Hence, the registration algorithm is composed of three main parts: set of transformations, similarity measure and optimization.

The rigid transformation set, S_r, is composed of rotations and translations (it has three degrees of freedom (DOFs), two translational and one rotational). The non-rigid transformation set, S_{nr}, is composed of just about any conceivable adjustable parameter. In the present work S_r was used as it is a reasonable choice considering the error sources in the initial manual alignment of the images. However, a subset of S_{nr} limited to the affine transformations (S_{af}) was also considered because this class of transforms (6 DOFs) can in particular compensate for the unknown inherent tissue shrinkage and shearing that occur during tissue preparation.

Once the image I_2 is transformed it is necessary to quantify how $T(I_2)$ is similar to I_1. Let us define $F(I,J)$ as a function that quantifies the similarity between image I and image J. Many choices are possible for F. However, it has been shown that the functions F based on information theory concepts (entropy) are usually very robust. Thus, the normalized mutual information (NMI) was used as a similarity measure [2].

The next step is to update the transform ($T \rightarrow T'$) so that $F(I_1,T(I_2)) > F(I_1,T'(I_2))$, where T and T' belong to the set of transforms. Many optimization algorithms rely on the possibility of evaluating or easily estimating the gradient and/or the Hessian of the similarity function (with

respect to the transformation's DOFs). These techniques are not readily applicable to the NMI measure. Popular algorithms that bypass the need for derivatives are Powell's algorithm and the simplex method. Powell's algorithm optimizes each of the transformation's DOFs one by one. The simplex method considers all DOFs simultaneously. The latter was used in the present work [3].

3.3 Missing Section Interpolation

When tissue is sectioned, some sections are lost or destroyed. Therefore, it is necessary to interpolate the missing sections to avoid further artifacts in the 3D tissue model. To interpolate the missing voxels, cubic Hermite polyno–mials were used. Specifically, the 3D interpolation was first reduced to several 1D interpolations by considering the 1D signal formed by following the intensity at the same pixel location from one section to the next (and for each of the three color bands). Thus, this 1D signal was regularly sampled but has missing samples. To interpolate missing samples, the Hermite interpolation searches for a third-order polynomial (i.e., four unknowns) to match the value and the slopes of the signal on both sides of the "hole". Thus, the scheme leads to four equations to find four unknowns.

3.4 Acoustic Impedance Assignment

To convert each pixel value to appropriate acoustic impedance value a color-threshold algorithm was used on every H&E stained bitmap image. Tissue proteins stained with eosin have shades of color ranging from very light pink to dark pink, depending on the concentration of protein within the structure. This differential staining allowed for the recognition of unique microstructures in the tissue. A range of colors corresponding to an identified microstructure in the stained bitmap images was then assigned a single color. The new single color was thus representative of the acoustic impedance for that tissue microstructure. For each pixel of the same color in the color-thresholded bitmap image the same acoustic impedance value was assigned.

4. SCATTERER SIZE ESTIMATION

The backscattered intensity, I_{bs}, due to an incident plane wave on a weakly inhomogeneous medium can be written as [4]:

$$I_{bs} = Ak^4 \left| \iiint \frac{\Delta z}{z} e^{-2ikr_0} dv_0 \right|^2 , \quad (2)$$

where A is proportionality constant and z is the acoustic impedance. The power spectrum of the relative impedance variations can be easily extracted from the backscattered intensity. A Gaussian form factor was chosen to model ultrasonic scattering because it is the form factor chosen for ultrasonic evaluation of the sarcoma. The scatterer size is then estimated by fitting the Gaussian FF to the power spectrum of the 3DZM [1].

5. RESULTS

The 3D reconstruction strategies were applied to the EHS dataset. Figure 1a shows 43 consecutive sections of the original EHS dataset. These sections were subimages of size 218 μm by 156 μm (i.e., 350 by 250 pixels) of the original 400 μm by 300 μm EHS images. Among these 43 consecutive sections, 7 were missing (including 4 consecutive sections). The sections were misaligned and the contrast between sections was also slightly different. The misalignment can be observed by following the pink quasicircular structure (muscle) from one section to the next. Also, sections 8 and 17 have slightly better contrast than their neighboring sections.

Figure 1b shows the reconstructed 43-section dataset. To align the images, affine registration was used. Figure 1b shows that all the reconstructed images have a very similar contrast, that is, none of the sections visually stand out as clearly darker or lighter than the others. The sections were also aligned, as can be seen by following the oblique structures in the top left corner. The interpolated missing sections were of lower quality than the others; note that the interpolated missing sections were not as sharp and contained some edge artifacts, particularly for the four reconstructed images of the four consecutive missing sections.

Figure 2a shows a 3D rendering of the 3DZM from the 43-section dataset of Figure 1b. Figure 2b shows the deduced 3DZM for which seven distinct impedance values were used: 2.00 Mrayl for the nuclear heterochromatin (black), 1.85 Mrayl for the nuclear euchromatin (blue), 1.70 and 1.65 Mrayl for the extracellular matrix (dark red/red), 1.60 for the vascular space/whole blood (white), and 1.58 and 1.55 for the cytoplasm (green/yellow).

The scatterer size estimation was then conducted on the 3DZM (Figure 2b). The 3DZM results yielded an effective scatterer size of 32.9 (±6.1) μm.

Ultrasonic backscatter measurements conducted on the same tumor tissue *in vivo* yielded an effective scatterer size of 33 (±8) μm.

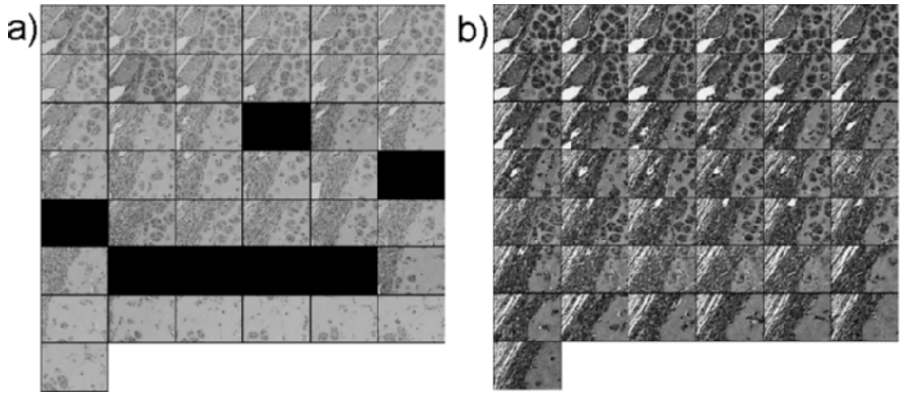

Figure 1. a) Forty-three-section dataset from the EHS dataset. Sections are of size 218 μm by 156 μm (i.e., 350 by 250 pixels). Sections are subimages of size 218 μm by 156 μm (i.e., 350 by 250 pixels) of the original 400 μm by 300 μm EHS sections. The sections were consecutive from left to right and top to bottom. Black fields symbolize missing sections. b) Reconstruction of the 43-section EHS dataset. Contrast of the available sections was equalized. Each section was affine-registered with the next available section. Missing sections were Hermite-interpolated post equalization and post registration.

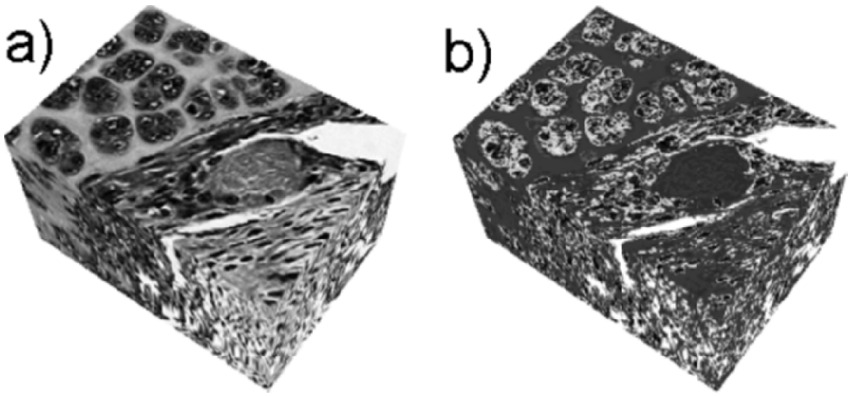

Figure 2. a) 3D rendering from the reconstructed 43-section dataset (Fig. 1b). Volume is of size 218 μm by 156 μm by 129 μm (depth). b) 3D rendering of the deduced 3DZM. The 3DZM was deduced by using a 7-level color-threshold algorithm on each reconstructed section.

6. CONCLUSIONS

A new set of strategies was proposed to obtain 3D acoustic tissue models from adjacent histologic sections. The strategies were illustrated using a 200-section dataset from a mouse sarcoma tumor. Imperfections of the original histologic dataset were carefully accounted for. First, contrast of all the sections was equalized and affine registration was conducted to ensure that all the sections were perfectly aligned. Then, sections lost during tissue preparation were interpolated. Finally, to deduce a 3DZM from this 3DHV acoustic impedance values were assigned using a 7-level threshold algorithm. An ultrasonic tissue characterization scheme was developed to obtain ultrasonic scatterer size estimates from the 3DZM. 3DZM estimates for the sarcoma 3DZM were found to be virtually the same as those obtained on the same sarcoma with ultrasound. This excellent agreement demonstrates that 3DATMs may be a powerful modeling tool for acoustic imaging applications.

7. ACKNOWLEDGEMENT

The authors would like to thank James P. Blue. Work supported by the University of Illinois Research Board.

REFERENCES

1. J. Mamou, M.L. Oelze, W.D. O'Brien, Jr., and J.F. Zachary, "Identifying ultrasonic scattering sites from 3d impedance maps," *J. Acoust. Soc. Am.*, pp. 413–423, 2005.
2. C. Studholme, D.L.G. Hill., and D.J. Hawkes, "An overlap invariant entropy measure of 3d medical image alignement," *Pattern Recogn.*, vol. 32, pp. 71–86, 1999.
3. J.A. Nelder., and R. Mead, "A simplex method for function minimization," *Computer J.*, vol. 7, pp. 308–313, 1965.
4. P.M. Morse., and K.U. Ingard, *Theoretical acoustics*, McGraw-Hill, New York, NY, 1968.

QUANTUM ACOUSTICAL IMAGING

W.S. Gan
Acoustical Technologies Singapore Pte Ltd, 209-212 Innovation Center, NTU, 16 Nanyang Drive, Singapore 637722, Republic of Singapore. Tel: (65)67913242, Fax:(65)67913665. Email address: wsgan@singnet.com.sg

Abstract: So far all forms of acoustical imaging are diffraction limited and so their resolution limit obeys Rayleigh's criterion, that is $\lambda/2$, where λ is the sound wavelength. In this paper, we apply quantum theory to acoustical imaging and obtain the resolution limit given by the effective de Broglie wavelength λ/N where N is the number of entangled phonons. Entanglement is a general quantum phenomenon. It occurs for photons and likewise also for phonons. We demonstrate that phonons entanglement is feasible and we propose a quantum acoustical imaging system

Key words: Rayleigh's criterion, phonons entanglement, de Broglie wavelength, quantum acoustical imaging system

1. INTRODUCTION

So far all forms of acoustical imaging are diffraction limited and so their resolution limit obeys Rayleigh's criterion that is $\lambda/2$, where λ is the sound wavelength. The shortcomings of acoustical imaging compared with other forms of imaging such as X-ray imaging, nuclear magnetic resonance imaging and positron emission tomography is resolution problem. In order to improve the resolution of acoustical imaging and bring acoustical imaging to the nanometer resolution level, we propose quantum acoustical imaging. Sound wave has quantum mechanical characteristics but most of today's

M.P. André (ed.), Acoustical Imaging, 427–434.

acoustical imaging technology does not depend upon this quantum nature and in fact ignores it altogether. Classical or semi-classical approaches to modeling the behavior of sound are sufficient to understand the behavior of most acoustical imaging devices.

2. PHONONS ENTAGLEMENT

It is well known that entanglement is a general quantum phenomenon. It occurs in light giving rise to photons entanglement[1]. It should also occur for sound waves, giving rise to phonons entanglement[2]. Here we formulate a theory for entangled imaging. We developed a numerical model, based on the Wigner representation that simulates the propagation of the three waves inside a realistic crystal including the effects of diffraction spatial and temporal walk-off, and temporal dispersion. Here we will focus on some key results for a conceptual experimental scheme suited to discuss the wave-particle aspects at a macroscopic level. We also used an analytic approach, valid in terms of the unitary transformation:

$$\begin{aligned} &a_i^{out}(\vec{q},\Omega) = U_i(\vec{q},\Omega)a_i^{in}(\vec{q},\Omega) + v_i(\vec{q},\Omega)a_j^{in}(-\vec{q},-\Omega) \\ &i \neq j = S,I \end{aligned} \tag{1}$$

linking signal/idler (S/I) fields at the input with those at the output face of the nonlinear crystal. $a_i(\vec{q},\Omega)$ in/out are annihilation operators of plane-wave modes, $\vec{q}$ being the transverse wave vector and Ω the shift from the carrier frequency. For brevity of notation, we drop in the following the frequency argument from all the formulas (even if we took it into account in our calculations). When the transformation equivalent to (1) in a *Schrödinger*-like picture is applied to the input vacuum state of the S/I fields, we obtain the output entangled states:

$$\left|\varphi\right\rangle = \prod_{\vec{q}}\{\sum_{n=0}^{\infty} C_n(\vec{q})\left|n,\vec{q}\right\rangle_S \left|n,-\vec{q}\right\rangle_I\} \tag{2}$$

where $\left|n,\vec{q}\right\rangle_{S/I}$ denotes a Fock state with n phonons in mode $\vec{q}$ of S/I beam and $c_n(\vec{q})\{U_s(\vec{q})V_I(-\vec{q})\}^n\left|U_s(\vec{q})\right|^{-(2n+1)}$. Moreover,

$$\left|C_n(\vec{q})\right|^2 = \frac{\left\langle n(\vec{q})\right\rangle^n}{[1+\left\langle n(\vec{q})\right\rangle]^{n+1}} \tag{3}$$

where $\langle n(\vec{q})\rangle$ is the average number of phonons in mode $\vec{q}$.

For down-conversion process, $\langle n(\vec{q})\rangle << 1$, then Eq. (2) reduces to

$$|\varphi\rangle = \prod_{\vec{q}}\{C_0(\vec{q})|0,\vec{q}\rangle_S|0,-\vec{q}\rangle_I + \sum_{\vec{q}}\{C_1(\vec{q})|1,\vec{q}\rangle_S|1,-\vec{q}\rangle_I \prod_{\vec{q}_1\neq\vec{q}} C_0(\vec{q}_1)|0,\vec{q}_1\rangle_S|0,-\vec{q}_1\rangle_I\} \tag{4}$$

In this case, which we refer to as the microscopic case, one detects coincidences of single phonon pairs; in application to imaging, the image is reconstructed from a statistics over a large number of coincidences.

Here we focus instead on the case in which the average phonon number per mode is not negligible, so that all the terms of the expansion (2) are relevant (we call it the macroscopic case). In this case, the entanglement is with respect to phonon number, and this model predicts perfect correlations in the S/I phonon numbers detected on two symmetric modes $\vec{q}$ and $-\vec{q}$.

An interesting analytical limit is that of a short crystal, where diffraction and walk-off along the crystal become negligible. The coefficients U_i and V_i in Eq. (1) become practically constant with respect to q and can be replaced by their value $\vec{q} = 0$. Back-transforming Eq. (1) to the real space, one obtains input/output relations local in the position $\vec{x}$ in the crystal output plane ("near field"), and corresponding output state reads

$$|\varphi\rangle = \prod_{\vec{x}}\{\sum_{n=0}^{\infty}\{C_n(\vec{q}=0)|n,\vec{x}\rangle_S|n,\vec{x}\rangle_I\} \tag{5}$$

where $|n,\vec{x}\rangle$ is the Fock state with n phonons at point $\vec{x}$. In this limit, there is ideally a perfect correlation in the number of S/I phonons detected at the same near field position.

Superposition is one of the most distinctive features of quantum theory and has been demonstrated in numerous single-particle interference experiments. Quantum entanglement, the coherent superposition of states in multi-particle systems, yields more complex phenomena. One important type of multi-particle experiment uses path-entangled number states, which exhibit pure higher-order interference and the potential for applications in imaging[3].

The following example shows the origin of multi-particle interference more clearly. Here single-phonon interference occurs owing to the spatial separation of two modes of propagation a1 and b1 for a single particle entering the interference scheme at the first beamsplitter. Varation of the path length induces a phase shift $\Delta\phi$ and thus gives rise to detection probabilities $P_{a2} \propto 1+\cos\Delta\phi$ and $P_{b2} \propto 1-\cos\Delta\phi$ in each of the two output modes a2 and b2 behind the exit beamsplitter. Two-phonon interference occurs when a1 and b1 are the modes of propagation for a state of two indistinguishable phonons, that is, a biphonon state

$$|\varphi\rangle = \frac{1}{\sqrt{2}}(|2\rangle_{a1}|0\rangle_{b1} + e^{j2\Delta\phi}|0\rangle_{a1}|2\rangle_{b1}) \tag{6}$$

It represents a path-entangled two-phonon state, which exhibits pure two-particle interference at the output beamsplitter. The probability to find two phonons in either mode a2 or b2 then oscillates with $P_{a2,a2} \propto 1+\cos(2\Delta\phi)$ and $P_{b2,b2} \propto 1-\cos(2\Delta\phi)$, respectively, while the single-phonon detection probabilities P_{a2} and P_{b2} remain constant.

In the generalized case of an N-particle interference, the N phonons will be in a superposition of being in either mode a1 or b1, resulting in

$$|\varphi\rangle = \frac{1}{\sqrt{2}}(|N\rangle_{a1}|0\rangle_{b1} + e^{jN\Delta\phi}|0\rangle_{a1}|N\rangle_{b1}) \tag{7}$$

In other words, the paths are entangled in phonon number. Here $|N\rangle_{a1}(|N\rangle_{b1})$ indicates the N-particle Fock state in spatial mode a1(b1) respectively and $N=0$ represents an empty mode. The phase modulation $N\Delta\phi$ increases linearly with the particle number N, which is the origin of all entanglement – enhanced interference scheme. In particular, the N-phonon detection probability in each of the interference outputs would vary as $P_N \propto 1\pm\cos(N\Delta\phi)$. It has therefore been suggested that an effective de Broglie wavelength λ/N could be attributed to the quantum state. This resembles the case of a heavy massive molecule consisting of N atoms; though here the particles are in no way bound to each other.

3. ENTANGLEMENT IS A PREREQUISITE FOR DISTRIBUTED QUANTUM IMAGING

A quantum two-particle system in an entangled state exhibits effects that cannot be attained with any classically correlated system, no matter how strong the correlation.

Consider an entangled two-phonon source described by the state probability amplitude $Q(x,x') = Q(x)\delta(x-x')$, in which case the two-phonon state is

$$\left|\varphi\right\rangle = \int dx \quad Q(x)\left|1_x, 1_x\right\rangle \tag{8}$$

where the reduced density operators of the individual phonons are

$$\rho_1 = \rho_2 = \int dx \left|Q(x)\right|^2 \left|1_x\right\rangle\left\langle 1_x\right|,$$

so that

$$P(x_1,x_2) \propto \left|\int dx Q(x) h_1(x_1,x) h_2(x_2,x)\right|^2 \tag{9a}$$

$$P_j(x_j) \propto \int dx \left|Q(x)\right|^2 \left|h_j(x_j,x)\right|^2, \quad j = 1,2, \tag{9b}$$

$$\begin{aligned} &\overline{P}_j(x_j) \propto \iint dx dx' Q(x) Q^*(x') g_k(x,x') h_j(x_j,x) h_j{}^*(x_j,x), \\ &\quad j,k = 1,2, \quad j \neq k \end{aligned} \tag{9c}$$

with $g_k(x,x') = \int dx'' h_k(x'',x) h_k^*(x'',x')$, k = 1, 2. Evidently, $\overline{P}_j(x_j) \neq P_j(x_j)$, j = 1, 2.

To check whether distributed quantum imaging can be achieved without entanglement, we take a mixed state that exhibits the strongest possible classical correlations, i.e. one for which

$$\rho = \int dx|\gamma(x)| \, |1_x,1_x\rangle\langle 1_x,1_x| \tag{10}$$

with $\int dx \ \gamma(x) = 1$. This state represents a superposition of phonon-pair emission probabilities from various locations x. The density operators of each phonon taken individually are $\rho_1 = \rho_2 = \int dx\gamma(x)|1_x\rangle\langle 1_x|$, which are identical to those of the entangled source if $\gamma(x) = |Q(x)|^2$. In this case, then

$$P(x_1,x_2) \propto \int dx\gamma(x)|h_1(x_1,x)|^2|h_2(x_2,x)|^2 \tag{11a}$$

$$P_j(x_j) \propto \int dx\gamma(x)|h_j(x_j,x)|^2, \quad j=1,2, \tag{11b}$$

$$\overline{P}_j(x_j) \propto \int dx\overline{\gamma}_k(x)|h_j(x_j,x)|^2, \quad j,k=1,2, \quad j\neq k \tag{11c}$$

where $\overline{\gamma}_k(x) = \gamma(x)\int dx'|h_k(x',x)|^2$, $k=1,2$. The result in Eq. (11b) is similar to that in Eq. (9b). As a result of Eqs. (11a)-(11c), the distributed quantum imaging scheme truly requires entanglement in the source and cannot be achieved using a classical source correlations but without entanglement.

4. ENTANGLEMENT AND THE RESOLUTION LIMIT

In this paper, we investigate the propagation of entangled phonons through an interferometric acoustical imaging setup. Exploiting the quantum mechanical nature of sound, an interferometric acoustical imaging technique may beat the Rayleigh diffraction limit. Entangled phonons serve as the source beams and the beamsplitter constrains them to reach the target closer than they would in a classical system. In this technique, two initially entangled phonons incident on opposite sides of a beam splitter would be routed to two grazing incidence acoustic mirrors. One of the paths would lead directly to a target, while the other would include a phase shifter before the target. Classically speaking, sound interferes in such a setup, yielding an

intensity pattern that varies as both a slowly and quickly varying function of phase shift. The slow variation limits the spatial resolution to the Rayleigh diffraction limit.

According to quantum mechanics, however, the setup beats that limit. The beamsplitter correlates the phonons even more. Each generates a new state with equal probability amplitudes for presence on both the upper and lower paths.

In a sense, the position-state of each phonon is linked to the other. Once one of each phonon strikes a given location on the target, the partner is constrained to move on the same path. More importantly, the resultant intensity pattern varies with only the high spatial frequency of the semiclassical solution, eliminating the lower frequency term and thus halving the minimum spot size at the target.

An acoustical imaging system based on multiple entangled phonons would be even more impressive. Essentially N phonons entangled state offers a resolution enhancement that varies with N. The challenge is to reliably generate such entangled phonons.

5. PROPOSED IMAGING SYTEM

Quantum-entangled phonons have been produced in $KTaO_3$[2]. Our proposed quantum acoustical imaging system is shown below:

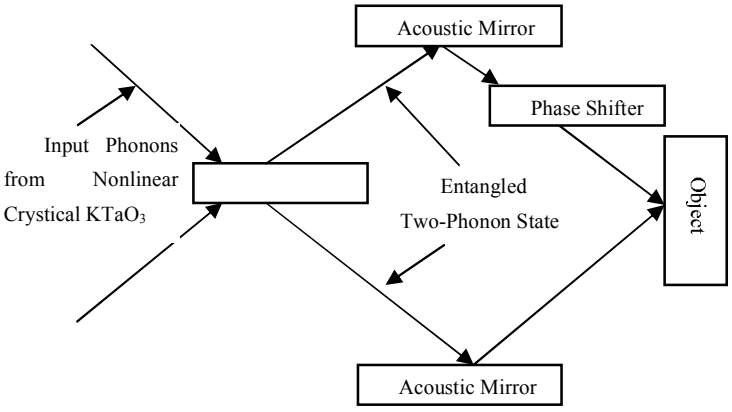

Figure 1. Quantum Acoustic Imaging System.

6. CONCLUSIONS

Quantum acoustical imaging system is feasible. If experimentally demonstrated, it could beat the diffraction limit and achieve a resolution limit of $\lambda/2N$ where N is the number of entangled-phonons achieved.

REFERENCES

1. K. Edamatsu, R. Shimizu, and T. Itoh, Measurement of the photonic de Broglie wavelength of entangled photon pairs generated by spontaneous parametric down-conversion, Phy. Rev. Lett. **89**, 213–601 2002.
2. R.D. Merlin, Control of electron coherences with coherent phonons, University of Michigan Internal Report, 1999.
3. H. Lee, P. Kok, and J.P. Dowling, in Proc. Sixth Int. Conf. on Quantum Communication, Measurement and Computing (eds. J.H. Shapiro, and O. Hirota) 223–229, (Rinton Press, Princeton, 2002).

A STUDY OF PULSE-ECHO IMAGE FORMATION USING NON-QUADRATIC REGULARIZATION WITH SPECKLE-BASED IMAGES

R. Lavarello, F. Kamalabadi, W.D. O'Brien, Jr.
Bioacoustics Research Laboratory, Coordinated Science Laboratory, Department of Electrical and Computer Engineering, University of Illinois at Urbana-Champaign, 405 North Mathews,Urbana, IL 61801 USA

Abstract: **Objective:** B-mode imaging is a standard way of presenting results when pulse-echo data acquisition is used. Inverse approaches have been explored to a limited extent. The goals of this study are to explore the feasibility and effectiveness of regularization by: (a) evaluating the quality of the reconstruction of speckle-based images as a function of imaging parameters (i.e., bandwidth of the transducer, f/number, and distance between region of interest (ROI) and focal region), and (b) comparing the reconstructed images with those obtained by conventional imaging techniques (e.g., B-mode and synthetic aperture focusing techniques (SAFT)). **Methodology:** Two-dimensional pulse-echo data from a single-element focused transducer with center frequency of 6 MHz and focal distance of 19 mm were simulated using fractional bandwidths of 33%, 50% and 100%, f/numbers of 1, 2 and 3, and distances between ROI and focus of 0, 2.5 and 5 mm. A minimum scatterer density of 4 scatterers per resolution cell was used. The images were reconstructed using non-quadratic regularization. Because the desired image was known, the normalized mean squared error (MSE) was used as a quantitative indicator of reconstruction performance. The reconstructed images were also evaluated by visual inspection. **Results:** The best reconstructions were achieved when the ROI was at the focus, the bandwidth was 100% and the f/number was 1, for which the MSE was 25% for a 20-dB signal-to-noise ratio (SNR). The MSE increased as the bandwidth decreased, the f/number increased, and the distance between ROI and focus increased. The bandwidth was the most sensitive parameter, increasing the MSE up to 86% for a SNR of 20 dB. For all cases, parameter selection techniques such as the L-curve and generalized cross-validation (GCV) gave a close

M.P. André (ed.), Acoustical Imaging, 435–443.

approximation to the image with the best visual appearance. **Conclusion:** For speckle-based images the inversion using regularization gave better results than conventional techniques for high SNR. A lower bound of 20 dB was found for this study. Below this threshold contrast information and most of the image features were lost during the reconstruction process in order to control the distortion due to the noise. Further work will be required to improve the stability of the forward model and to use more appropriate *a priori* model information in order to use this technique in a more realistic scenario including the effect of modeling errors

Key words: Inverse problems; non quadratic regularization; speckle-based images

1. INTRODUCTION

B-mode, synthetic aperture focusing techniques (SAFT) and array imaging have been studied for a long time and their limitations are well documented[1]. Such techniques suffer from spatial resolution limitations due to the finite size of the resolution cell of the imaging system, i.e., the area (or volume) that corresponds to the smallest resolvable detail, and contrast resolution limitations due to the presence of sidelobes. Because ultrasonic imaging is coherent, when there are many scatterers randomly distributed in a resolution cell, their reflections may interfere constructively or destructively depending on their relative position to the transducer generating spots of brightness and darkness in the image. For focused systems, these spots tend to have a size on the order of the focal region and the resulting image will have a granular appearance resulting in speckle-based images[2]. Speckle is very common in ultrasound medical imaging because body tissue is a semitransparent media. If the point spread function has a wide mainlobe or high-level sidelobes, the spots generated by the speckle can mask regions of low contrast.

Inverse problem approaches[3] and regularization techniques, such as truncated singular value decomposition (TSVD)[4], total variation[5], total least squares[6] and others[7], have already been used in acoustical imaging and their effectiveness have been explored to a limited extent. It is of special importance to compare the performance of this class of techniques with that which can be obtained using conventional acoustic imaging methods. Speckle based images are proposed as targets of reconstruction because of the limitations of conventional techniques in dealing with these type of images. The goals of this study are to explore the feasibility and effectiveness of regularization by: (a) evaluating the quality of the reconstruction of speckle-based images as a function of imaging parameters

(i.e., bandwidth of the transducer, f/number, and distance between region of interest (ROI) and focal region), and (b) comparing the reconstructed images with those obtained by conventional imaging techniques (e.g., B-mode and SAFT).

2. METHODOLOGY

The ROI is a square region with axial (or beam) axis x and lateral (or scanning) axis y. The pulse-echo data are acquired at locations u_L, $L \in [1, q]$. The received signal is sampled at discrete times t_k, $k \in [1, p]$. The time signal recorded at the position u_L is denoted by $g_{u_L}(t)$. The ROI is also discretized, with the discrete values of x and y denoted by x_i, $i \in [1, n]$ and y_i, $i \in [1, m]$. The reflectance of the ROI will be assumed to be constant in each pixel and will be denoted by r_{x_i, y_j}. The spatially-variant impulse response of the transducer, i.e., the signal that would be received if a point target of unitary amplitude were at the coordinates $(\hat{x}, \hat{y})$ relative to the transducer, will be denoted by $s_{\hat{x},\hat{y}}(t)$.

Neglecting multiple scattering, the received pulse-echo data when the transducer is placed at the location u_L will be the sum of the impulse responses of all the pixels inside the ROI scaled by the corresponding values of the reflectance. The two-dimensional sequences $g(t, u_L)$ and $r(x_i, y_j)$ are stacked as vectors to form a pair of one-dimensional sequences in order to express the problem as a set of linear equations. With this reordering, the forward model can be written in matrix form as:

$$\begin{bmatrix} \begin{bmatrix} s_{x_1,y_1-u_1}(t_1) \\ s_{x_1,y_1-u_1}(t_2) \\ \vdots \\ s_{x_1,y_1-u_1}(t_p) \end{bmatrix} \begin{bmatrix} s_{x_2,y_1-u_1}(t_1) \\ s_{x_2,y_1-u_1}(t_2) \\ \vdots \\ s_{x_2,y_1-u_1}(t_p) \end{bmatrix} \cdots \begin{bmatrix} s_{x_n,y_m-u_1}(t_1) \\ s_{x_n,y_m-u_1}(t_2) \\ \vdots \\ s_{x_n,y_m-u_1}(t_p) \end{bmatrix} \\ \vdots \\ \begin{bmatrix} s_{x_1,y_1-u_q}(t_1) \\ s_{x_1,y_1-u_q}(t_2) \\ \vdots \\ s_{x_1,y_1-u_q}(t_p) \end{bmatrix} \begin{bmatrix} s_{x_2,y_1-u_q}(t_1) \\ s_{x_2,y_1-u_q}(t_2) \\ \vdots \\ s_{x_2,y_1-u_q}(t_p) \end{bmatrix} \cdots \begin{bmatrix} s_{x_n,y_m-u_q}(t_1) \\ s_{x_n,y_m-u_q}(t_2) \\ \vdots \\ s_{x_n,y_m-u_q}(t_p) \end{bmatrix} \end{bmatrix} \begin{bmatrix} r_{x_1,y_1} \\ r_{x_2,y_1} \\ r_{x_3,y_1} \\ \vdots \\ r_{x_n,y_m} \end{bmatrix} = \begin{bmatrix} \begin{bmatrix} g_{u_1}(t_1) \\ g_{u_1}(t_2) \\ \vdots \\ g_{u_1}(t_p) \end{bmatrix} \\ \vdots \\ \begin{bmatrix} g_{u_q}(t_1) \\ g_{u_q}(t_2) \\ \vdots \\ g_{u_q}(t_p) \end{bmatrix} \end{bmatrix} \tag{1}$$

Because the forward model matrix S is ill-conditioned, generalized Tikhonov regularization[8] has been used to solve this equation system. This corresponds to solving the following minimization problem:

$$\hat{\mathrm{r}} = \arg\min_{\mathrm{r}} \{ \|\mathrm{g} - \mathrm{S}\mathrm{r}\|_2^2 + \alpha^2 \sum \left(|\mathrm{L}\mathrm{r}|^2 + \beta \right)^{\frac{\mathrm{k}}{2}} \} \tag{2}$$

where g, r and S are the pulse-echo data, the unknown reflectivities and the forward model matrix, respectively. The first term in Eq.2 corresponds to the LMS solution to the linearized problem. The second term, which is included to stabilize the inverse problem, is the l_k norm ($\|.\|_k^k$) of a linear transformation of the unknown vector r using a matrix operator L. β is a small constant to allow the differentiation of the second term around zero for $k \leq 1$. α is known as the regularization parameter and controls the amount of regularization imposed on the solution. L was chosen to be the identity matrix because it is known to have filtering effects similar to TSVD[9] and is a natural way of regularizing an ill-posed problem. The performance of the reconstruction was quantified using the normalized mean square error (MSE), defined as:

$$\mathrm{MSE} = 100 \left\| \hat{\mathrm{r}} - \bar{\mathrm{r}} \right\|_2^2 / \left\| \bar{\mathrm{r}} \right\|_2^2 \tag{3}$$

where $\bar{\mathrm{r}}$ and $\hat{\mathrm{r}}$ are the true and reconstructed images respectively, both logarithmically compressed using a dynamic range of 40 dB.

Automatic parameter selection is an important aspect in regularization. Both general cross-validation (GCV) and L-curve[10] were tested to select the best choice of the parameter α for fixed k and β.

To test the quality of the reconstructions, two-dimensional pulse-echo data were simulated using Field II[11] corresponding to a single-element focused transducer with center frequency of 6 MHz (wavelength λ=250 μm with a speed of sound of 1500 m/s) and focal distance of 19 mm. Fractional bandwidths of 33%, 50% and 100%, f/numbers of 1, 2 and 3, and distances between ROI and focus of 0, 2.5 and 5 mm were used for the simulations. The ROI used in the simulations is shown in Figure 1. It consists of two concentric regions, the inner one having a diameter of 1 mm. The mean scatterer reflectivity in the outer region is 10 times larger than the one of the inner region. The scatterer density is 4 per λ^2. Because the largest bandwidth and smallest focal number used are 100% and 1 respectively, the minimum number of scatterers per resolution cell is roughly equal to 4.

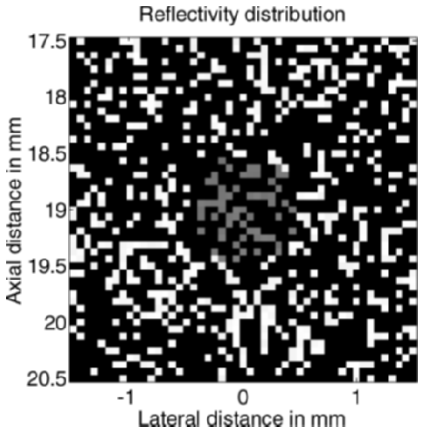

Figure 1. Reflectivity distribution used for the simulations.

3. SIMULATIONS

The simulations were performed by changing one physical parameter at a time among the bandwidth, the f/number and the distance to the focus, in order to analyze the individual effects of these parameters. For low SNR, the choice of k=2 and k=0.5 yields solutions that are oversmoothed or too sparse respectively. The choice of k=1 represents a tradeoff between these two behaviors and hence the results corresponding to that particular choice

will be shown here. With k=1 the performance was somewhat insensitive to the choice of the parameter β, which was finally chosen to be 10^{-7}. Both the L-curve and GCV yielded very similar results for this study, so only the GCV results are presented.

The MSE curves in Figure 2 indicate that among bandwidth, focal number and distance to focus, the bandwidth had the largest effect on the performance of the simulations. For an SNR of 20 dB, the MSE corresponding to a bandwidth of 100% is close to 25%, whereas for a bandwidth of 33% the error was roughly 86%. For the same SNR, the error corresponding to changing the f/number to 3 is only 56% and the error corresponding to changing the distance between the focus and the ROI is only 35%. The differences in changing the f/number from 2 to 3 or the distance between ROI and focus from 2.5 to 5 mm are not discernible from the MSE curves.

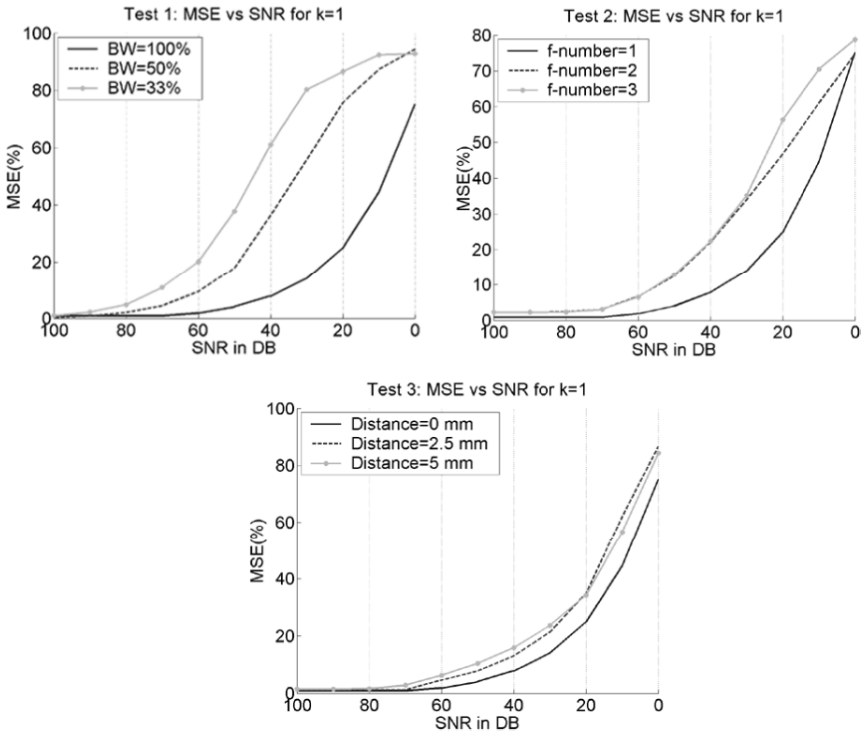

Figure 2. MSE curves for regularization reconstructions. Left top: effect of changing the bandwidth. Right top: effect of changing the f/number. Bottom: effect of changing the distance to the focus.

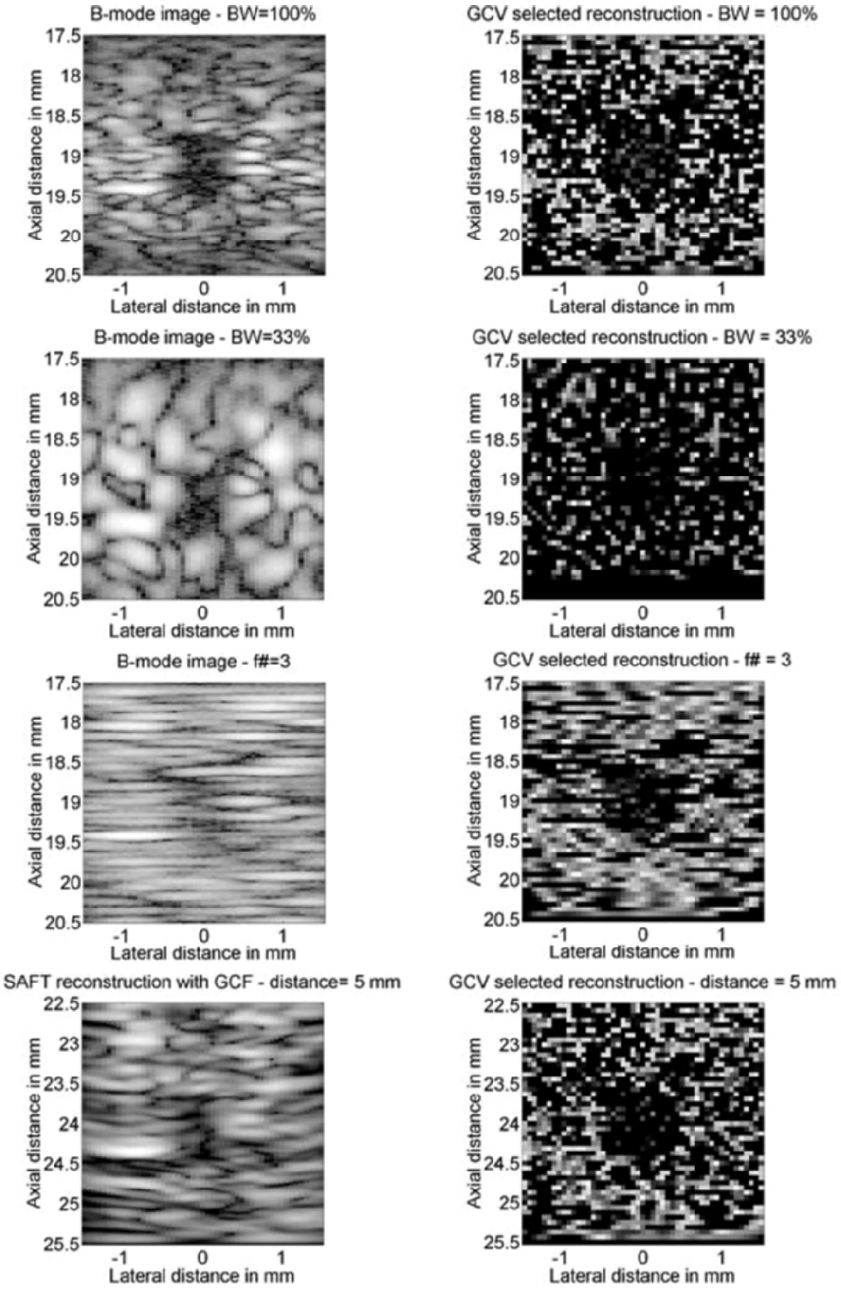

Figure 3. Reconstructed images for SNR=20 dB. First row: BW = 100%, f/# = 1 and distance to focus = 0 mm. Second row: BW = 33%, f/# = 1 and distance to focus = 0 mm. Third row: BW = 100%, f/# = 3 and distance to focus = 0 mm. Fourth row: BW = 100%, f/# = 1 and distance to focus = 5 mm.

Figure 3 shows the images corresponding to conventional techniques and regularization. The left column shows the B-mode (for the case of change in bandwidth and f/number) and SAFT (for the change of distance to the focus) images. The regularization reconstructed images selected using GCV are shown on the right column.

4. CONCLUSIONS

The performance of conventional imaging techniques such as B-mode and SAFT is mainly limited by the size of the resolution cell of the imaging system. This factor also has an impact on the performance of regularization techniques by determining the lower threshold for the SNR for which these approaches yield an image of better quality. A larger bandwidth, smaller f/number and smaller distance between ROI and focus result in better performance as measured by the MSE for fixed SNR. A lower bound of 20 dB for the SNR was found for this study. Below this threshold, contrast information and most of the image features were lost during the reconstruction process in order to control the distortion due to the noise. Further work will be required to improve the stability of the forward model and to use more appropriate *a priori* model information in order to use this technique in a more realistic scenario including the effects of modeling errors.

REFERENCES

1. Gordon S. Kino. Acoustic waves: devices, imaging, and analog signal processing. Prentice Hall, Inc (1997)
2. Christoph B. Burckhard. Speckle in ultrasound B-mode scans. *IEEE Transactions on Sonics and Ultrasonics*, **25**(1), 1–6 (1978)
3. Fredrik Lingvall, Tomas Olofsson and Tadeusz Stepinski. Synthetic aperture imaging using sources with finite aperture: deconvolution of the spatial impulse response. *Journal of the Acoustical Society of America,* **114**(1), 225–234 (2003)
4. Hesham Desoky, Abou Bakr M. Youssef and Yasser M. Kadah. Reconstruction using optimal spatially variant kernel for B-mode ultrasound imaging. *SPIE Medical Imaging 2003: Ultrasonic Imaging and Signal Processing*, 147–153 (2003)
5. Xiadong Zhang and Shira Broschat. A comparison of material classification techniques for ultrasound inverse imaging. *Journal of the Acoustical Society of America,* **111**(1), 457–467 (2002)
6. Chao Liu, Yuanmei Wang and Pheng Ann Heng. A comparison of truncated total least squares with Tikhonov regularization in imaging by ultrasound inverse scattering. *Physics in Medicine and Biology,* **48**(15), 2437–2451 (2003)

7. William C. Karl and Mujdat Cetin. Edge preserving image reconstruction for coherent imaging applications. *IEEE International Conference on Image Processing*, 481–484 (2002)
8. William C. Karl and Mujdat Cetin. Feature-enhanced synthetic aperture radar image formation based on non quadratic regularization. *IEEE Transactions on Image Processing,* **10**(4), 623–631 (2001)
9. Heinz W. Engl, Martin Hanke and Andreas Neubauer. Regularization of inverse problems. Kluwer Academic Publishers (1996)
10. C. R. Vogel. Non-convergence of the L-curve regularization parameter selection method. *Inverse Problems,* **12**(4), 535–547 (1996)
11. J.A. Jensen and N.B. Svendsen. Calculation of pressure fields from arbitrarily shaped, apodized, and excited ultrasound transducers. *IEEE Transactions on Ultrasonics, Ferroelectrics and Frequency Control*, **39**(2), 262–267 (1992)

ANALYTICAL SOLUTIONS OF THE KDV-KZK EQUATION

W.S. GAN
Acoustical Technologies Singapore Pte Ltd, 209-212 Innovation Center, NTU, 16 Nanyang Drive, Singapore 637722, Republic of Singapore. Tel: (65)-67913242, Fax:(65)67913665. Email address: wsgan@singnet.com.sg

Abstract: The KdV-KZK equation for fluids developed by me was presented at the ICSV 11 in St. Petersburg in July 2004. In this paper, I made an attempt on the analytical solutions of this equation using the perturbation method. Some physical interpretation of the solutions is given. A brief introduction to KdV-KZK equation for solids is given

Key words: analytical solutions, perturbation method, dissipation, dispersion, nonlinearity, diffraction, shock wave, solitons, chaos theory

1. INTRODUCTION

We developed the KdV-KZK equation for fluids in a paper presented at the 11th ICSV in St. Petersburg in July 2004. The KdV-KZK equation covers all basic physical mechanisms of sound propagation in fluids: diffraction, nonlinearity, absorption, and dispersion. Mark Hamilton's group[1] in University of Texas has used a numerical method to solve an augmented Burgers equation using splitting procedure and incremental step approach by giving equal weights to all the four physical mechanisms. This does not reflect the actual phenomenon because dispersion may be predominant over

M.P. André (ed.), Acoustical Imaging, 445–452.

diffraction etc. and so only gives approximation results. In this paper, we use a rigorous approach by using analytical method.

2. PERTURBATION METHOD USED

The KdV-KZK equation is given as

$$\frac{\partial}{\partial\tau}\left(\frac{\partial P}{\partial z}-\frac{\partial^2 P}{\partial c_0^3\rho_0}\frac{\partial^2 P}{\partial\tau^2}-\frac{\varepsilon}{c_0^3\rho_0}P\frac{\partial P}{\partial\tau}+\gamma\frac{\partial^3 P}{\partial\tau^3}\right)=\frac{c_0}{2}\Delta_\perp P \tag{1}$$

where P = acoustic pressure, z = direction of sound propagation, $\tau = t - z/c_0$, ε = parameters of nonlinearity, c_0 = sound velocity, $b = \zeta + 4\eta/3$ where ζ and η are the bulk and shear viscosity. ρ_0 = density of fluid and $\gamma = c_p/c_v$ = adiabatic index where c_p and c_v are the specific heats at constant pressure and constant volume.

With perturbation method and writing

$$P = P^{(1)} + P^{(2)} + P^{(3)} \tag{2}$$

First perturbation, we write

$$\frac{\partial}{\partial\tau}\left(\frac{\partial P^{(1)}}{\partial z}-\frac{b}{\partial c_0^3\rho_0}\frac{\partial^2 P^{(1)}}{\partial\tau^2}\right)-\frac{c_0}{2}\Delta_\perp P^{(1)}=0 \tag{3}$$

where $\Delta_\perp = \partial^2/\partial x^2 + \partial^2/\partial y^2$ is the Lagrangian in transverse coordinates.

Here our solutions are given in the light of the simple modes of operation of a parametric radiator. The processes whereby low-frequency waves are formed in the field of nondiffracting plane and spherically diverging high-frequency beams are considered. We will consider waves of high intensity (high acoustic Reynolds number) and that the profile of the wave contains a discontinuity.

The solution of Eq. (3) for a biharmonic high-frequency pump can be written as

$$P^{(1)} = \frac{1}{2} A_1(r,z) e^{iw_1\tau} + \frac{1}{2} A_2(r,z) e^{iw_2\tau} + c.c. \tag{4}$$

The complex amplitudes $A_{1,2}$ satisfy the parabolic equation of diffraction theory:

$$\frac{\partial A}{\partial z} + \alpha A = \frac{1}{2ik}\left(\frac{\partial^2 A}{\partial r^2} + \frac{1}{r}\frac{\partial A}{\partial r}\right) \tag{5}$$

where αA describes the attenuation of the high-frequency waves.

For second perturbation, we have

$$\frac{\partial}{\partial \tau}\left(\frac{\partial P^{(2)}}{\partial z} - \frac{b}{2c_0^3\rho_0}\frac{\partial^2 P^{(2)}}{\partial \tau^2}\right) - \frac{c_0}{2}\Delta_\perp P^{(2)} = \frac{\varepsilon}{2c_0^3\rho_0}\frac{\partial^2 P^{(1)^2}}{\partial \tau^2} \tag{6}$$

Substituting in Eq. (4), we have

$$\frac{\varepsilon}{2c_0^3\rho_0}\frac{\partial^2 P^{(1)^2}}{\partial \tau^2} = -\frac{\varepsilon\Omega^2}{4c_0^3\rho_0} A_1(r,z) A_2^*(r,z) e^{i\Omega\tau} + c.c. \tag{7}$$

where Ω = difference angular frequency.

Substitute the expression Eq. (7) into the right hand side of Eq. (6) and seek its solution by inspection in the form

$$P^{(2)} = \frac{1}{2} P(r,z) e^{i\Omega r} + c.c. \tag{8}$$

We obtain the following equation for the complex amplitude of the difference frequency wave $P_{-}(r,z)$ in place of Eq. (6) :

$$\frac{\partial P_{-}}{\partial z} + \alpha_{-} P_{-} - \frac{1}{2ik} \Delta_{\perp} P_{-} = i \frac{\varepsilon \Omega}{2 c_0^3 \rho_0} A_1 A_2^* \tag{9}$$

Here the term that describes the damping of the difference frequency wave is eliminated with the help of the substitution $P_{-} \rightarrow P_{-} \exp(-\alpha_{-} z)$. Thus Eq. (9) becomes

$$\frac{\partial P_{-}}{\partial z} - \frac{1}{2ik} \Delta_{\perp} P_{-} = i \frac{\varepsilon K}{2 c_0^2 \rho_0} A_1 A_2^* e^{-\alpha z} = Q(r,z) \tag{10}$$

where α_{-} = damping coefficient of difference frequency wave, K = wave number of the difference frequency wave, $\alpha = \alpha_1 + \alpha_2 - \alpha_{-} = 2/l_a$ = effective attenuation coefficient, A_1, A_2^* = functions satisfying the parabolic equation Eq. (5) without account of attenuation.

To solve Eq. (10), we assume the beams to be cylindrically symmetric (circular). Using the Hankel transforms :

$$\begin{aligned} P_{-}(r,z) &= \int_0^{\infty} \tilde{P}(v,z) J_0(vr) v dv, \\ \tilde{P}(v,z) &= \int_0^{\infty} P_{-}(r,z) J_0(vr) r dr \end{aligned} \tag{11}$$

then Eq. (10) reduces to

$$\frac{d\widetilde{P}}{dz} = i\frac{v^2}{2k}\widetilde{P} = \widetilde{Q}(v,z) \tag{12}$$

where $\widetilde{Q} = \frac{i\varepsilon K}{2c_0^2\rho_0} e^{-\alpha z}\int_0^\infty A_1 A_2^{*} J_0(vr) r dr$ (13)

is the Hankel transform of the right hand side of Eq. (10). The solution of Eq. (12) with zero condition at the boundary z=0 has the form

$$\widetilde{P} = \int_0^z \widetilde{Q}(v,z')\exp(i\frac{v^2}{2k}(z-z'))dz' \tag{14}$$

Carrying out the inverse Hankel transformation, we find the desired solution of Eq. (10)

$$P_{-}(r,z) = \int_0^\infty J_0(vr)vdv\int_0^z \widetilde{Q}(v,z')\exp(\frac{iv^2}{2k}(z-z'))dz' \tag{15}$$

This solution is valid for any distributions of complex amplitudes of the high-frequency waves A_1 and A_2 on the surface of the pump transducer. Substituting any of the solutions of the parabolic equation in this form, the corresponding solution for the difference-frequency wave can be obtained.

For third perturbation, we have

$$\frac{\partial}{\partial\tau}\left(\frac{\partial P^{(3)}}{\partial z}-\frac{b}{2c_0^3\rho_0}\frac{\partial^2 P^{(3)}}{\partial\tau^2}\right)-\frac{c_0}{2}\Delta_\perp P^{(3)} = \frac{\varepsilon}{2c_0^3\rho_0}\frac{\partial^2 P^{(2)^2}}{\partial\tau^2}-\gamma\frac{\partial^3 P^{(2)}}{\partial\tau^3} \tag{16}$$

We know that the KdV-KZK equation is an extension of the KdVB equation to include diffraction effect. So the solution of the KdVB equation should throw some lights on the possible solution of the KdV-KZK equation. The solution of the KdVB equation describes a shock wave as a transition between two constant velocity values. This transition can have oscillations due to the dispersion. At low δ where $\delta=\frac{b}{2c_0^3\rho_0}$ the first oscillations are quite close to solitons (solitons correspond to a closed separatrix). In the latter case a nonstationary solution can be developed as well, describing a slowly decaying soliton.

Hence, let us seek a solution in the form of a soliton

$$P=\frac{P_0}{\cosh^2(\tau+bz/\Delta)} \tag{17}$$

where b = constant = $\frac{\varepsilon P_0}{c_0^3\rho_0 3}$ and $\Delta=\sqrt{\frac{12\gamma}{(\varepsilon/c_0^3\rho_0)P_0}}$.

Substituting Eq. (17) into Eq. (16), should give some light on the solution of the KdV-KZK equation.

3. ANALYTICAL SOLUTION OF THE KDV-KZK EQUATION USING CHAOTIC THEORY

The KdV-KZK equation is a nonlinear differential equation. There is a theorem stating that any nonlinear differential equation does possess a regime within which its solutions are chaotic. Using the above theorem, the KdV-KZK equation should have some chaotic solution subject to certain conditions on its parameters. The KdVB equation has some soliton solution. X. N. Chen and R. J. Wei[2] show that some solitons do possess chaotic characteristics. I feel that it is very promising to find analytical solutions of the KdV-KZK equation in the light of chaotic theory.

4. EXTENSION OF THE KDV-KZK EQUATION TO SOLIDS

There has been extension of the KZ equation from fluids to solids such as M. S. Cramer and M. F. Andrew's[3] work. In this paper, they consider a weakly nonlinear, weakly diffracting, two dimensional shear waves propagating in a prestrained hyper elastic solid. A modification of the classical KZ equation is derived using a systematic perturbation scheme. Both dissipative and non-dissipative materials are considered. The principle effect of the prestrain is seen to be the inclusion of a quadratic nonlinearity to the cubic nonlinearity found n the case of zero prestrain. Further results include the shock jump relations and the prediction of shocks having a speed which is identical to the nonlinear wave speed ahead of or behind the shock. The main difference of the KZ equation for fluids and for solids is the inclusion of elasticity and stress-strain relations in the equation. Also the Lagrangian coordinates instead of the Euler coordinates have to be used to account for the strain parameter.

5. CONCLUSION

The analytical solution for the KdV-KZK equation is possible. Analytical solutions for the KdVB equation are well established. Compared with the KdVB equation, the KdV-KZK equation only has one extra term and it will not introduce much complexity. It would be also useful to find numerical solutions of the KdV-KZK equation but would be different from that of the Lee-Hamilton method[1] which gives equal importance to each of the physical mechanism. KdV-KZK equation for fluids will find application in

aerodynamics, underwater acoustics. Its extension to solids will find applications in medical imaging and in nonlinear nondestructive evaluation.

REFERENCES

1. Y.S. Lee, and M.F. Hamilton, Time-domain modeling of pulsed finite-amplitude sound beams. J.A.S.A. 97, 906–917 (1995).
2. X.N. Chen, and R.J. Wei, Chaotic motion of a non-propagating soliton through a period-doubling route, Selected Papers of Wei Rongjue, Nanjing University Press, 1998.
3. M.S. Cramer, and C. Webb, A Zobolotskaya-Khokhlov equation for cubic and near cubic nonlinearity, AIAA paper, 98, 2957 (1988).

SYNTHETIC APERTURE FOCUSING OF ECHOGRAPHIC IMAGES BY MEANS OF PULSE COMPRESSION

L. Masotti, E. Biagi, M. Scabia
Laboratorio Ultrasuoni e Controlli Non Distruttivi, Università di Firenze

Abstract: A novel technique for focusing echographic images inspired by Synthetic Aperture Radar focusing algorithms is presented. Pulse compression both in depth and lateral directions is used. Problems arising from the different geometry of the echographic case with respect to radars are solved through a remapping in the frequency domain. Experimental results demonstrating the improvement in resolution are shown

Key words: chirp coding, coded excitation, SAFT, ultrasonic imaging, resolution, pulse compression

1. INTRODUCTION

It is interesting to study the widely different paths undertaken in the field of echography and in the field of Synthetic Aperture Radars (SAR) in order to achieve focusing.

An echograph typically obtains its focused image by transmitting, for each line of sight, a short pulse through a certain "sub-aperture" of an array probe; each element of this sub-aperture is excited with a delay calculated according to the geometric law for focusing at the desired depth for each transmission focus. The received ultrasonic echoes are beam-formed by adding together the signals received by the elements of the same "sub-aperture" (or a similar one centered at a different position along the array) with delays that vary over time (i.e. depth) in order to achieve a correct focusing in reception at each portion of depth from which ultrasonic echoes originate; this technique is commonly referred to as "dynamic focusing". It must be observed that, considering the much lower propagation speed of

M.P. André (ed.), Acoustical Imaging, 453–459.

ultrasound when compared to electromagnetic waves, the delays required to implement this focusing technique for the echographic case are orders of magnitude higher (thus physically realizable) than those that would be required for the same kind of focusing applied to a SAR; this is the main reason why echographic focusing was never employed in SARs. Furthermore an advantage of echographic focusing is of being a very direct approach and thus its light computational load makes it suitable for real-time implementation. However this technique does not provide uniform resolution across the image and, more importantly, it produces artifacts around point scatterers, as shown in Fig. 1.

The advances in processing power of modern digital electronics open the possibility to apply to echography more complex focusing algorithms in real-time such as those employed in SAR. While there are a few examples in the literature of application of chirped signals to the case of echography [1], the pulse compression technique centered on "chirps" is the basis of SAR operation. SAR systems employ this technique both for "range" compression (i.e. depth of an ultrasonic image) by actually transmitting a linearly frequency modulated signal and for "azimuth" compression (i.e. lateral focusing).

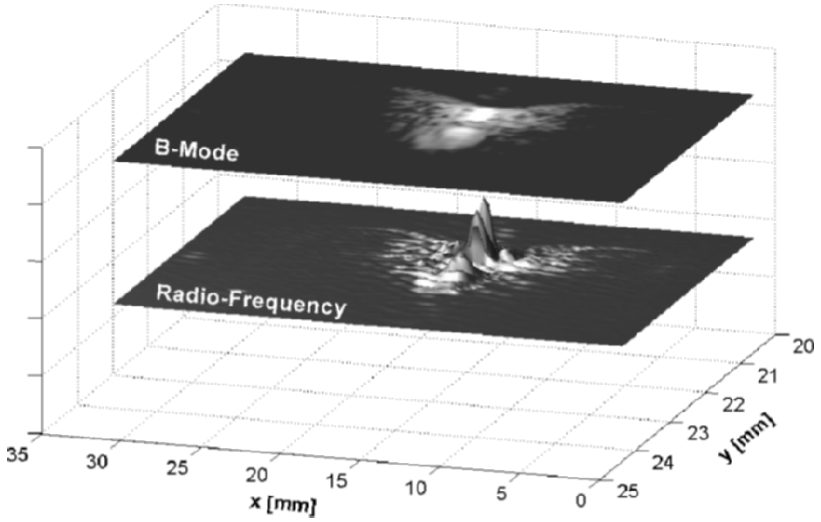

Figure 1. Echographic section of a plastic wire of diameter 0.4 mm in water, obtained transmitting an ultrasound beam with a frequency of 6.67 MHz by a digital commercial echograph (mod MEGAS, ESAOTE) with a linear array probe (ESAOTE LA13) and traditional focusing technique. Upper image: B-Mode. Lower image: relative Radio-Frequency signal.

In this work we tackle the problem of applying the SAR focusing technique to echographic signals. In the case of ultrasound the geometry involved does not allow direct application of the SAR focusing technique. The method that we propose, labeled ICARUS (Imaging pulse Compression Algorithm through Remapping of UltraSound), operates a remapping of the Radio-Frequency (RF) ultrasonic image in the frequency domain in order to correctly perform the SAR focusing also in the echographic case.

Theoretical analysis, simulations and experimental results, some of which are reported in this work, demonstrated how SAR focusing employed through ICARUS can improve the resolution of echographic images.

2. ICARUS

The algorithm we propose is based on the use of linearly frequency modulated signals, transmitted and received through a single element of an ultrasonic linear array probe along a lateral scan of the region under investigation. The echographic image is made up by juxtaposition of the various tracks separately received by each transducer of the probe. The transmit and receive ultrasonic beams are completely unfocused. Like in SAR systems, this situation can be equivalently interpreted as if the transducer was fixed and the scatterer was moving in the direction opposite to the scan. The focusing process is achieved by applying ICARUS directly to RF data (Fig. 2).

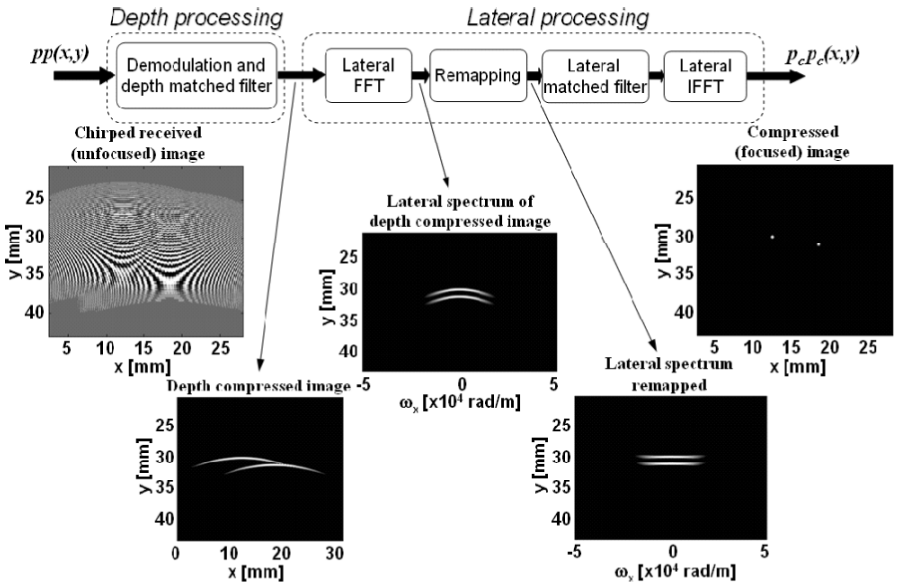

Figure 2. Block-diagram of ICARUS technique with received and focused images and intermediate results.

ICARUS consists of two blocks: first, we have a depth (y coordinate) processing and then a lateral (x coordinate) processing. Depth processing consists of coherent demodulation and matched filtering of each vertical track. Lateral processing consists of matched filtering of each lateral track after remapping in the (ω_x, y) domain, where ω_x is the lateral spatial frequency. This remapping in the (ω_x, y) domain is the core of our algorithm and it is necessary because the unfocused received images are strongly affected by curvature. This curvature is due to the different distances (times of flight) between a scatterer and the transducers of the array probe. As it is shown in the second image in Fig. 2, the echoes of different scatterers can be cross-coupled in the 2D spatial domain (x, y); however in the frequency-spatial domain (ω_x, y) these same echoes are separated (third image in Fig. 2). Therefore in this domain we can compensate the curvature of the echo of each scatterer (fourth image in Fig. 2) and then apply the matched filter in the lateral direction. It is possible to use a lateral matched filtering because the received RF frame presents a frequency modulation in the lateral direction as well, due to the different distances between the scatterer and the various elements of the array probe. The final result is the last image in Fig. 2, where it is possible to observe how two different scatterers were focused through ICARUS.

Theoretical analysis of ICARUS[2] allowed us to identify some advantages of this method when compared to traditional focusing: 1) Resolution throughout the image is uniform, due to the fact that axial resolution is dependent on bandwidth, while lateral resolution is dependent on angular dimension of the radiation pattern of the transducer. Both of these resolutions are independent from the actual position of the scatterer. This theoretical result is valid in the ideal case of a propagation medium without frequency selective attenuation. However, the resolution-loss along depth is much lower in ICARUS focusing than in traditional echographic focusing, where it is also caused by the geometry involved in the delay-and-add method and not only by frequency-selective attenuation. 2) Resolution is improved with respect to traditional focusing techniques due to the use of matched filters in both vertical and lateral directions.

3. EXPERIMENTAL RESULTS

A commercial digital echograph (Megas, Esaote S.p.A., Florence) was modified for generating the required signals (chirps) and unfocused beam patterns. A 7.5 MHz central frequency 128 elements linear array probe was used (LA13, Esaote S.p.A., Florence). The elements of this probe were driven in compound mode in order to obtain a 256 tracks image. Since the employed probe has a 0.36 mm pitch, the tracks of the presented image are spaced at 0.18 mm. The FEMMINA platform (Fast Echographic Multi-parametric Multi-Image Novel Apparatus)[3] was used to acquire and to process Radio-Frequency signals in order to produce the ICARUS focused images in real-time. Results confirm the expected resolution improvement.

Fig. 3 shows a section of a calibrated test object (mod. 414 B, Radiation Measurements Inc.) focused with both the ICARUS method and a standard delay-and-add method [4,5]. In the first image (Fig. 3, left) a linearly frequency modulated excitation signal is used, sweeping from 5 to 10 MHz in 20 μs; in the second image (Fig. 3, right) the excitation signal is a standard single-cycle 6.67 MHz pulse and traditional focusing is applied. ICARUS achieves better resolution over the whole image and less invasive artifacts, which makes the image sharper and reveals details otherwise masked. ICARUS is also capable of resolving the tissue-mimicking speckle much more clearly.

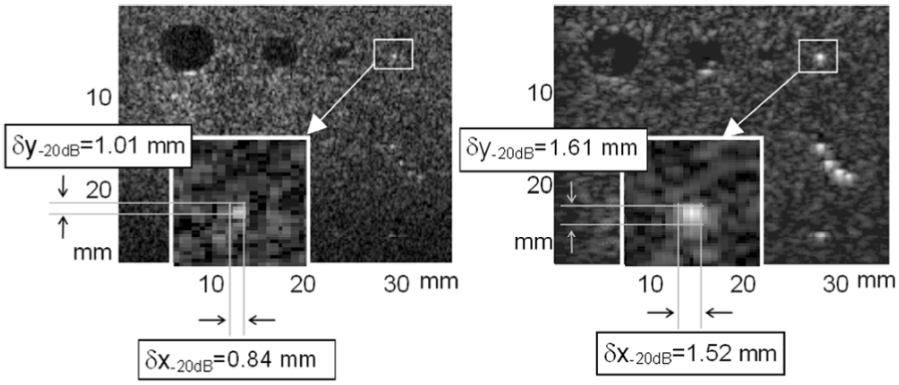

Figure 3. Calibrated Test Object section, focused with ICARUS method (left), standard method (right). Sizes of wires in the test object are calculated at -20 dB.

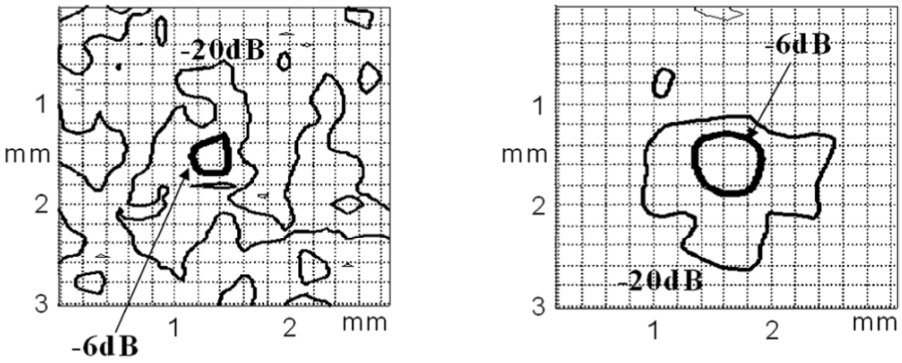

Figure 4. Modulus contour curves around the pointed out spot of Fig. 3. -6 dB, -20 dB curves are shown in decreasing thickness.

The resolutions obtained with the two methods are compared in Fig. 3 and Fig. 4 by observing the modulus of the focused images around the marked spots: a 0.1 mm nylon wire of the test-object is resolved as a 0.84 x1.01 mm spot in the ICARUS image and as a 1.52 x1.61 mm spot in the traditionally focused image (both cases at -20 dB).

Tests with other objects (wires or bubbles in water) and even *in-vivo* tests show similar improvements with respect to traditional focusing.

4. CONCLUSIONS

This paper describes a novel echographic focusing technique inspired by SAR algorithms. Because of the different geometry, SAR algorithms can not be directly applied to the ultrasonic case. We developed a method called ICARUS based on pulse compression of linearly frequency modulated signals that, through a remapping in the frequency domain, permits an improvement in resolution of echographic images in both depth and lateral directions. Experimental results demonstrated the validity of our method in improving resolution of echographic images: by applying pulse compression in both dimensions, it is possible to reach a -20 dB resolution of 1.01 mm (depth) and 0.84 mm (lateral) to be compared with the resolution achieved with traditional focusing on the same echograph and with the same probe: 1.61 mm and 1.52 mm respectively.

REFERENCES

1. Pollakowski, M., Ermert, H., "Chirp Signal Matching and Signal Power Optimization in Pulse-Echo Mode Ultrasonic Nondestructive Testing", IEEE Trans. Ultrason., Ferroelec., Freq. Contr., vol. 41, no 3, September 1992, Pages: 655–659.
2. Biagi, E., Masotti, L., Scabia, M., Rossi, I., Dreoni, N., "ICARUS. Metodo di focalizzazione di un'immagine ecografica e relativo sistema ecografico". Italian Patent n° FI2002A000228.
3. Scabia, M., Biagi, E., Masotti, L., "Hardware and software platform for real-time processing and visualization of echographic radiofrequency signals". IEEE Trans. Ultrason., Ferroelec., Freq. Contr., vol. 49, no. 10, October 2002, Pages 1444–1452.
4. Biagi, E., Masotti, L., Rossi, I., Scabia, M., "Synthetic Aperture Technique For Echographic Focusing Based On Pulse Compression", IEEE Ultrasonic Symposium Proc., September 2004, Pages 1425–1428.
5. Biagi, E., Dreoni, N., Masotti, L., Scabia, M., "ICARUS: Imaging pulse Compression Algorithm through Remapping of UltraSound", IEEE Trans. Ultrason., Ferroelec., Freq. Contr., In Press.

ACOUSTICAL IMAGING WITH NEGATIVE REFRACTION

W.S. Gan
Acoustical Technologies Singapore Pte Ltd, 209-212 Innovation Center, NTU, 16 Nanyang Drive, Singapore 637722, Republic of Singapore. Tel: (65)67913242, Fax:(65)67913665. Email address: wsgan@singnet.com.sg

Abstract: It is well known that the resolution limit of acoustical images is limited by diffraction to $\lambda/2$ where λ is the sound wavelength. Negative refraction proposed by Veselago in 1968 shows possibility of defeating the diffraction limit. His work is for electromagnetic waves. Recently it has been shown experimentally that negative refraction can be achieved for both electromagnetic waves and sound waves by using photonic crystals and phononic crystals respectively. John Pendry proposed the concept of 'perfect lens' using negative refraction for electromagnetic waves. In this paper, we propose a 'perfect lens' for sound waves and an acoustical imaging system incorporating the 'perfect lens' is also outlined

Key words: Negative refraction, photonic crystals, phononic crystals, perfect lens, multiple scattering, KKR approach, evanescent waves, scanning acoustical microscope, resolution limit

1. INTRODUCTION

It is well known that the resolution limit of acoustical images is limited by diffraction to $\lambda/2$, where λ is the sound wavelength. Negative refraction

M.P. André (ed.), Acoustical Imaging, 461–466.

proposed by Veselago in 1968 shows possibility of defeating the diffraction limit. His work is for electromagnetic waves. No attention was paid to his work until recently because it was not possible to produce materials with negative refraction. During the past few years, there are several groups able to fabricate photonic crystals with negative refraction[2] characteristics. In this paper, we propose the extension of Veselago's theory to acoustic waves with the purpose of acoustical imaging in mind. In 2000, Johen Pendry[3] proposed the concept of 'perfect lens' using negative refraction for electromagnetic waves. This lens is able to overcome diffraction limit and is independent of wavelength. The reason is that it is able to focus not only the far field wave field but also the nonpropagating evanescent wave field. Thus it is able to provide sub wavelength details. Also this type of lens can be made of only a thin slab and does not have the fabrication difficulties of spherical lens. During recent months, there are groups in China[4] and in Canada[5] able to fabricate phononic crystals capable of negative refraction. The Chinese group even design a microlens of thin slab shape with focusing effect based on negative refraction. This gives us the confidence of proposing a 'perfect acoustic lens'. The concept of 'perfect acoustic lens' is not mentioned in the paper of the Chinese group[4].

2. DERIVATION OF TRANSMISSION COEFFICIENT FOR A PERFECT ACOUSTIC LENS

Consider the sound velocity field $\underline{v}$ in front of the acoustic lens. The components of the field will be given by some 2D Fourier expansion

$$\underline{v}(\underline{r},\, t) = \sum_{k_x,\, k_y} \underline{v}(k_x,\, k_y) \exp(ik_x x + ik_y y + ik_z z - i\omega t) \tag{1}$$

where we choose the axis of the lens to be the z-axis. The acoustic field equation tells us that

$$k_z = + \sqrt{\omega^2 c^{-2} - {k_x}^2 - {k_y}^2}, \quad \omega^2 c^{-2} > {k_x}^2 + {k_y}^2 \tag{2}$$

The function of the lens is to apply a phase correction to each of the Fourier components so that at some distance beyond the lens the fields reassemble to

a focus and an image of the sound source appears. However, for larger values of the transverse wave vector

$$k_z = +i\sqrt{k_x^{\,2} + k_y^{\,2} - \omega^2 c^{-2}}, \quad \omega^2 c^{-2} < k_x^{\,2} + k_y^{\,2} \tag{3}$$

These evanescent waves decay exponentially with z and no phase correction will restore them to their proper amplitude. They are effectively removed from the image which generally comprises only the propagating waves. Since the propagating waves are limited to

$$k_x^{\,2} + k_y^{\,2} < \omega^2 c^{-2} \tag{4}$$

the maximum resolution in the image can never be greater than

$$\Delta = \frac{2\pi}{k_{\max}} = \frac{2\pi c}{\omega} = \lambda \tag{5}$$

Material with negative refractive index will focus sound wave even when in the form of a parallel-sided slab of material. The sound wave will obey Snell's laws of refraction at the surface as sound wave inside the medium makes a negative angle with the surface normal. The other characteristic of the system is the double focusing effect revealed by a simple ray diagram. Sound wave transmitted through a slab of thickness d_2 located at distance d_1 from the source comes to a second focus when

$$z = d_2 - d_1 \tag{6}$$

Calculations confirm that all of the energy is perfectly transmitted into the medium but in a strange manner. Transmission of energy in the +z direction requires that, in the medium

$$k_z' = -\sqrt{\omega^2 c^{-2} - k_x^{\,2} - k_y^{\,2}} \tag{7}$$

Overall the transmission coefficient of the medium is

$$T = tt' = \exp(ik_z' d) = \exp(-i\sqrt{\omega^2 c^{-2} - k_x^{\,2} - k_y^{\,2} - d}) \tag{8}$$

Where d is the slab thickness and the negative phase results from the choice of wave vector given by causality. It is this phase reversal that enables the medium to refocus sound by canceling the phase acquired by the sound wave as it moves away from its source.

Remarkably, the medium can also cancel the decay of evanescent waves. The challenge here is that such waves decay in amplitude, not in phase as they propagate away from the object plane. Therefore to focus them we need to amplify them rather than to correct their phase. We shall show that evanescent waves emerge from the far side of the medium enhanced in amplitude by the transmission process. This does not violate energy conservation because evanescent waves transport no energy, but nevertheless, it is a surprising result.

To calculate the transmission through both surfaces of the slab, we must sum the multiple scattering events,

$$\begin{aligned} T &= tt'\exp(ik_z'd) + tt'r'^2\exp(3ik_z'd) + tt'r'^4\exp(5ik_z'd) + \cdots \\ &= \frac{tt'\exp(ik_z'd)}{1-r'^2\exp(2ik_z'd)} \end{aligned} \tag{9}$$

where t and r are the transmission coefficient and reflection coefficient at the interface within the medium respectively, t' and r' are the transmission coefficient and reflection coefficient at the interface between the medium and the vacuum respectively.

3. CALCULATION OF WAVE FIELD PATTERN USING A FOURIER IMAGING TECHNIQUE

Here the transmission coefficient is equivalent to the transfer function. Let $F_0(k_x, k_y)$ represent the Fourier spectrum of the sound wave transmitted by the lens and $F_i(k_x, k_y)$ represent the Fourier spectrum of the sound wave from the object incident onto the lens. Then

$$F_0(k_x, k_y) = \frac{tt'\exp(ik_z'd)}{1-r'^2\exp(2ik_z'd)} F_i(k_x, k_y) \tag{10}$$

The spatial image wave field pattern is given by the inverse Fourier transform of $F_0(k_x, k_y)$:

$$f_0(x,y) = \frac{1}{(2\pi)^2} \int_0^{k_x} \int_0^{k_y} \frac{tt' \exp(ik_z' d)}{1 - r'^2 \exp(2ik_z' d)} F_i(k_x, k_y) \exp[i2\pi(xk_x + yk_y)] dk_x dk_y \tag{11}$$

4. RESOLUTION LIMIT

X. Zhang and Z. Liu[4] have shown that by using phononic crystals they are able to achieve negative refraction. Using the effect of negative refraction, they can fabricate a super lens which can break through the traditional limitation of Rayleigh resolution limit and achieve a transverse size (full size at half-maximum) of the image spot as 0.14λ. John Pendry[3] using a 'perfect lens' also based on negative refraction achieved even better resolution. In this paper we follow John Pendry's[3] method of constructing the 'perfect lens' by incorporating the evanescent waves and we hope to defeat the Rayleigh resolution limit.

5. PROPOSED ACOUSTICAL IMAGING SYSTEM

We proposed a scanning acoustical microscopic (SAM) system making use of the acoustic lens capable of negative refraction. The acoustic lens has to be made of phononic crystals as proposed by X. Zhang and Z. Liu.[4] Our SAM system will have to be modified in design. The transducer producing the ultrasonic waves will have to incident on the object first. Then the object wave will go onto the acoustic lens of negative refraction and the image will be formed after transmission through the lens.

To achieve the effect of collection of the evanescent waves, special design of the system is required.

6. CONCLUSIONS

We have shown that the concept of a 'perfect acoustic lens' is possible. The most difficult part would be the design of the acoustical imaging system which can make use of this 'perfect lens'.

REFERENCES

1. Veselago, V.G., The electrodynamics of substances with simultaneous negative values of ε and μ, Sov. Phys. Usp. **10**. 509 (1968).
2. Foteinopoulou, S., and Soukoulis, C.M., Negative refraction and left-handed behavior in two-dimensional photonic crystals, P. Rev. B **67**, 235107-1-235107-5 (2003).
3. Pendry, J.B., Negative refraction makes a perfect lens, P. Rev. Letts. 3966–3969 (2000).
4. Zhang, X., and Liu, Z., Negative refraction of acoustic waves in two-dimensional phononic crystals, App. Phys. Letts. **85**, 341−343 (2004).
5. Yang, S., Page, J.H., Liu, Z., Cowan, M.L., Chan, C.T., and Sheng, P., Focusing of sound in a 3D phononic crystal, P. Rev. Lett, **93**, 024301-1-024301-4 (2004).

EPILOGUE

FREDERIC L. LIZZI, ENG.SC.D.

Frederic L. Lizzi, Eng.Sc.D., died peacefully in his home in Manhattan, NY on Saturday, 8 January 2005. Dr. Lizzi was born 11 December 1942 in Brooklyn, NY.

Dr. Lizzi received his Bachelor of Arts degree in electrical engineering from Manhattan College in 1963, his Master of Science degree in bioengineering from Columbia University in 1965 and his Engineering Science Doctorate degree in bioengineering from Columbia University in 1971. His doctoral dissertation was entitled, "Transient radiation patterns in ophthalmic ultrasound".

In 1967, Dr. Lizzi became an employee of Riverside Research Institute (RRI) in New York City as a Member of the Research Staff. In 1973, he became an Assistant Manager of Optics, and in 1976, he became the Manager of the Biomedical Engineering Laboratories at RRI. He led RRI's biomedical engineering studies since the early 1970s and became the Research Director of the Biomedical Engineering Laboratories in 1984. Dr. Lizzi holds several patents in medical ultrasound technology that he developed at RRI. Since 1994, he was the Chief Technical Advisor for Spectrasonics, Inc., of Wayne, PA. Dr. Lizzi was Adjunct Professor of Ophthalmic Physics at the Weill Medical College of Cornell University since 1979, and Adjunct Professor of Applied Physics at Columbia University since 1997.

Dr. Lizzi is internationally recognized as a pioneering and leading investigator in advanced medical ultrasound, including diagnostic and therapeutic applications of ultrasound, which he investigated on theoretical, experimental, and clinical levels. He was an active leader in several professional societies including the American Institute of Ultrasound in Medicine (AIUM), Acoustical Society of America (ASA), World Federation of Ultrasound in Medicine and Biology (WFUMB), and International Society for Diagnostic Ultrasound and Ophthalmology. Dr. Lizzi was a Fellow of the AIUM and the ASA, and served on the Board of Governors of the AIUM from 1985 to 1988 and the International Society for Therapeutic Ultrasound since 2002. He helped to organize many international scientific meetings and conferences, and served as a guest editor and editorial advisor for scientific journals such as Ultrasound in Medicine and Biology and Transactions of the Institute of Electrical and Electronics Engineers. Dr. Lizzi received many prestigious professional awards including the William J. Fry Memorial Award of the AIUM in 1986; the Presidential Recognition Award of the AIUM in 1988 and again in 1996; the Pioneer Award of the AIUM and WFUMB in 1988, the Mayneord Award of the British Institute of Radiology in 1990, and the Joseph Holmes Pioneer Award of the AIUM in 1994. The journal, Ultrasound in Medicine and Biology, gave him the Best Clinical Paper Award in 1984 and the Best Technical Paper Award in 1986.

Dr. Lizzi was the Principal Investigator on many research projects funded by the National Institutes of Health, beginning in the 1970s with pioneering studies of high-frequency ultrasound in ophthalmology. In these ophthalmic investigations, Dr. Lizzi developed novel means of characterizing tissue for diagnostic purposes, and he studied safety and therapeutic aspects of high-frequency ultrasound. These seminal research efforts continue to the present day applied to organs such as the prostate, breast and heart as well as to the eye in a broad range of contemporary, very-high-frequency-ultrasound and high-intensity-ultrasound studies in Dr. Lizzi's laboratories and in research centers around the world.

Dr. Lizzi is survived by his wife Mary, his son, Joseph, his daughter, Marian, his mother, and three sisters.

Subject Index

Author Index